INNOVATIONS IN COASTAL EROSION RISK ASSESSMENT AND MITIGATION

EDITED BY: Giuseppe Barbaro, Giandomenico Foti and Felice D'Alessandro
PUBLISHED IN: Frontiers in Marine Science

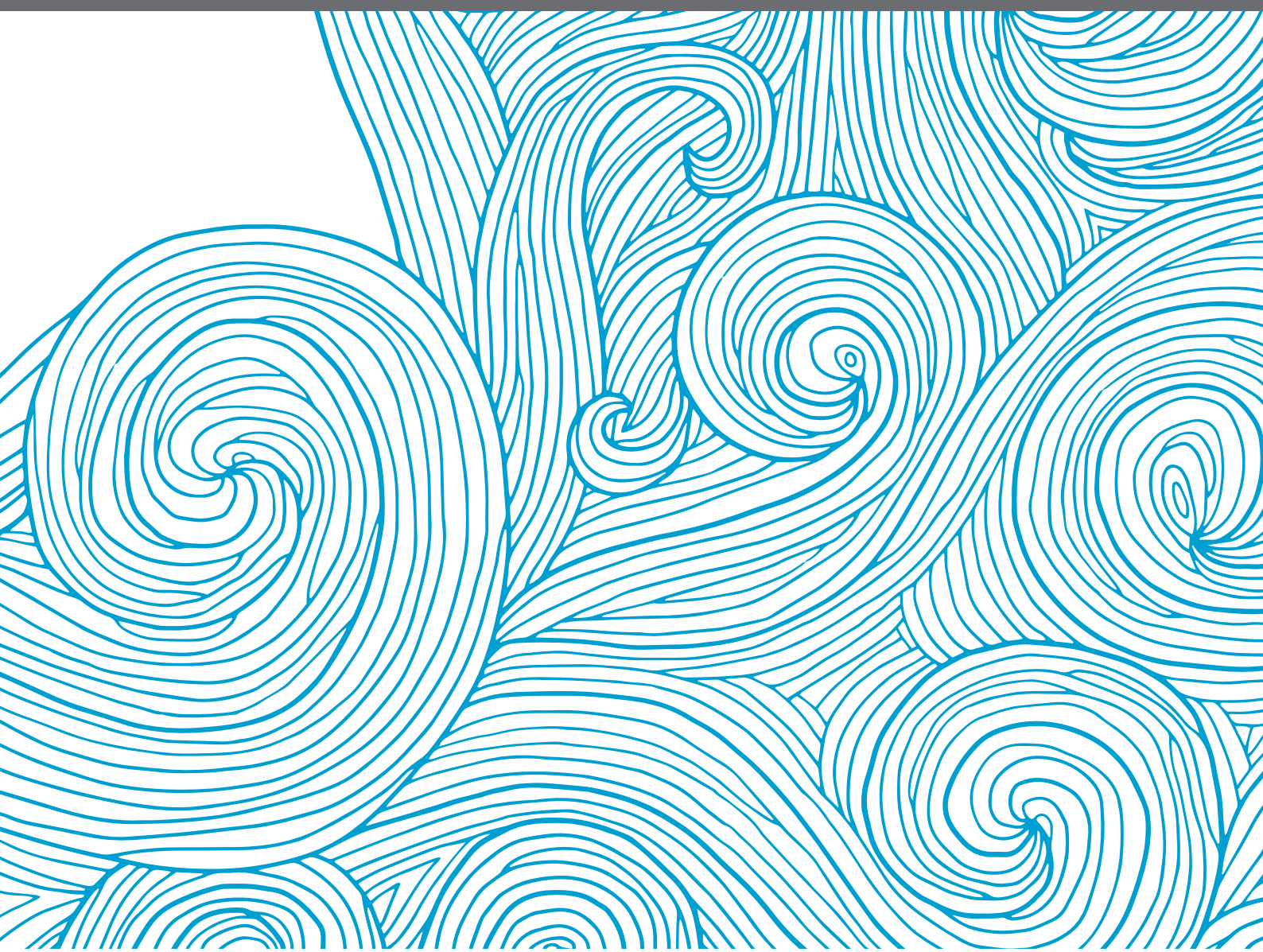

frontiers Research Topics

frontiers

ISSN 1664-8714
ISBN 978-2-83250-693-6
DOI 10.3389/978-2-83250-693-6

About Frontiers

Frontiers is more than just an open-access publisher of scholarly articles: it is a pioneering approach to the world of academia, radically improving the way scholarly research is managed. The grand vision of Frontiers is a world where all people have an equal opportunity to seek, share and generate knowledge. Frontiers provides immediate and permanent online open access to all its publications, but this alone is not enough to realize our grand goals.

Frontiers Journal Series

The Frontiers Journal Series is a multi-tier and interdisciplinary set of open-access, online journals, promising a paradigm shift from the current review, selection and dissemination processes in academic publishing. All Frontiers journals are driven by researchers for researchers; therefore, they constitute a service to the scholarly community. At the same time, the Frontiers Journal Series operates on a revolutionary invention, the tiered publishing system, initially addressing specific communities of scholars, and gradually climbing up to broader public understanding, thus serving the interests of the lay society, too.

Dedication to Quality

Each Frontiers article is a landmark of the highest quality, thanks to genuinely collaborative interactions between authors and review editors, who include some of the world's best academicians. Research must be certified by peers before entering a stream of knowledge that may eventually reach the public - and shape society; therefore, Frontiers only applies the most rigorous and unbiased reviews.
Frontiers revolutionizes research publishing by freely delivering the most outstanding research, evaluated with no bias from both the academic and social point of view. By applying the most advanced information technologies, Frontiers is catapulting scholarly publishing into a new generation.

What are Frontiers Research Topics?

Frontiers Research Topics are very popular trademarks of the Frontiers Journals Series: they are collections of at least ten articles, all centered on a particular subject. With their unique mix of varied contributions from Original Research to Review Articles, Frontiers Research Topics unify the most influential researchers, the latest key findings and historical advances in a hot research area! Find out more on how to host your own Frontiers Research Topic or contribute to one as an author by contacting the Frontiers Editorial Office: frontiersin.org/about/contact

INNOVATIONS IN COASTAL EROSION RISK ASSESSMENT AND MITIGATION

Topic Editors:
Giuseppe Barbaro, Mediterranea University of Reggio Calabria, Italy
Giandomenico Foti, Mediterranea University of Reggio Calabria, Italy
Felice D'Alessandro, University of Milan, Italy

Citation: Barbaro, G., Foti, G., D'Alessandro, F., eds. (2022). Innovations in Coastal Erosion Risk Assessment and Mitigation. Lausanne: Frontiers Media SA.
doi: 10.3389/978-2-83250-693-6

Table of Contents

04 ***Editorial: Innovations in Coastal Erosion Risk Assessment and Mitigation***
Giandomenico Foti, Giuseppe Barbaro and Felice D'Alessandro

08 ***Technical and Social Approaches to Study Shoreline Change of Kuakata, Bangladesh***
Nazla Bushra, Rubayet Bin Mostafiz, Robert V. Rohli, Carol J. Friedland and Md Adilur Rahim

21 ***Critical Shear Stress for Erosion of Sand-Mud Mixtures and Pure Mud***
Dake Chen, Jinhai Zheng, Chi Zhang, Dawei Guan, Yuan Li and Yigang Wang

40 ***Vulnerability Analysis of Episodic Beach Erosion by Applying Storm Wave Scenarios to a Shoreline Response Model***
Tae-Kon Kim, Changbin Lim and Jung-Lyul Lee

55 ***Challenges and Opportunities in Coastal Shoreline Prediction***
Kristen D. Splinter and Giovanni Coco

63 ***Regime Shifts in Future Shoreline Dynamics of Saudi Arabia***
Arjen Pieter Luijendijk, Etiënne Kras, Vasiliki Dagalaki, Robin Morelissen, Ibrahim Hoteit and Roshanka Ranasinghe

75 ***Vulnerability Evolution of Coastal Erosion in the Pearl River Estuary Great Bay Area Due to the Influence of Human Activities in the Past Forty Years***
Chao Cao, Kai Zhu, Feng Cai, Hongshuai Qi, Jianhui Liu, Gang Lei, Zijian Mao, Shaohua Zhao, Gen Liu and Yan Su

90 ***Shoreline Evolutionary Trends Along Calabrian Coasts: Causes and Classification***
Giandomenico Foti, Giuseppe Barbaro, Giuseppina Chiara Barillà, Pierluigi Mancuso and Pierfabrizio Puntorieri

108 ***Multicriteria Decision Analysis to Assist in the Selection of Coastal Defence Measures: Involving Coastal Managers and Professionals in the Identification and Weighting of Criteria***
Philippe Sauvé, Pascal Bernatchez and Mathias Glaus

129 ***Application of Airborne LiDAR Measurements to the Topographic Survey of the Tidal Flats of the Northern Jiangsu Radial Sand Ridges in the Southern Yellow Sea***
Haifeng Zhang, Lian Wang, Yifei Zhao, Jicheng Cao and Min Xu

142 ***Numerical Simulation of the Locality of Erosional Damages by Storm Waves in Searching for Measures to Conserve Bonggil Beach, Korea***
Jong Dae Do, Jae-Youll Jin, Byunggil Lee, Weon Mu Jeong, Jin Yong Choi, Sang Kwon Hyun, Kihyun Kim and Yeon S. Chang

164 ***Seasonal Changes in Beach Resilience Along an Urbanized Barrier Island***
Ernesto Tonatiuh Mendoza, Alec Torres-Freyermuth, Elena Ojeda, Gabriela Medellín, Rodolfo Rioja-Nieto, Paulo Salles and Imen Turki

frontiers | Frontiers in Marine Science

TYPE Editorial
PUBLISHED 20 October 2022
DOI 10.3389/fmars.2022.1066989

OPEN ACCESS

EDITED AND REVIEWED BY
Charitha Bandula Pattiaratchi,
University of Western Australia,
Australia

*CORRESPONDENCE
Giandomenico Foti
giandomenico.foti@unirc.it

SPECIALTY SECTION
This article was submitted to Coastal Ocean Processes, a section of the journal Frontiers in Marine Science

RECEIVED 11 October 2022
ACCEPTED 13 October 2022
PUBLISHED 20 October 2022

CITATION
Foti G, Barbaro G and D'Alessandro F (2022) Editorial: Innovations in coastal erosion risk assessment and mitigation.
Front. Mar. Sci. 9:1066989.
doi: 10.3389/fmars.2022.1066989

Editorial: Innovations in coastal erosion risk assessment and mitigation

Giandomenico Foti[1]*, Giuseppe Barbaro[1] and Felice D'Alessandro[2]

[1]Mediterranea University of Reggio Calabria, Civil, Energy, Environmental and Material Engineering (DICEAM) Department, Reggio Calabria, Italy, [2]University of Milan, Department of Environmental Science and Policy, Milan, Italy

KEYWORDS

coastal erosion, shoreline changes, sea storms, extreme events, anthropogenic pressure, vulnerable coastal regions, multicriteria decision analysis approach, remote sensing

Editorial on the Research Topic:
Innovations in coastal erosion risk assessment and mitigation

Introduction

This Research Topic focused on coastal erosion risk. This is a current and important topic as it involves many of the world's coastal areas (Luijendijk et al., 2018; Mentaschi et al., 2018). Generally, coastal erosion is caused by an alteration of coastal and river dynamics both due to the action of natural factors and to the increase in anthropogenic pressure (Besset et al., 2019; Bombino et al., 2022), mainly observed in the second half of the last century after the end of the Second World War (Ozpolat and Demir, 2019). All of this influences the shoreline position, which is the most important geoindicator of shoreline evolution (Boak and Turner, 2005). From this point of view, remote sensing and GIS (Geographical Information Systems) techniques allow us to accurately identify the shoreline position and to estimate the shoreline changes over the years (Moore, 2000; Apostolopoulos and Nikolakopoulos, 2021; Boumboulis et al., 2021). Furthermore, anthropogenic pressure causes an increase in impermeable surfaces with negative consequences on the vulnerability of the territory under the action of natural events such as floods and sea storms (Fiori et al., 2014). Climate change can also contribute to coastal erosion by the increasing of sea levels and of frequency and intensity of extreme weather events (Yang et al., 2015; Mavromatidi et al., 2018).

Due to the various issue of this topic, to protect and manage coastal areas all the natural and anthropogenic factors that influence coastal and river dynamics should be analyzed. From this point of view, many coastal erosion risk assessment methodologies have been defined. These methodologies differ from each other mainly about the large differences in the factors analyzed by each methodology, depending by the coastal regions analyzed, and about the scale of application (Narra et al., 2017; Pantusa et al., 2018; Viavattene et al., 2018).

Research topic summary

Eleven papers have been published in this Research Topic, ten of which are Original Research and the other are a Perspective paper. Below is a summary of the main objectives of each paper.

Many papers have focused on shoreline changes, especially in vulnerable coastal regions. Among these, Bushra et al. (2021) analyzed the coast of Kuakata, in south-central Bangladesh, Foti et al. (2022) analyzed the coast of Calabria, a region in southern Italy, and Luijendijk et al. (2022) analyzed the coast of Saudi Arabia. In all the papers remote sensing and GIS techniques have been widely used and the causes of the shoreline erosive phenomena were analyzed. In addition, the first paper used participatory rural appraisal (PRA) tools which revealed the societal impacts caused by the shoreline changes. Instead, the second paper proposed a classification of erosive trends at different time scales, based on a shoreline variation rate while the third paper evaluate the future shoreline changes due to sea level rise under a moderate emissions scenario, RCP 4.5, and a high emissions scenario, RCP 8.5. Vulnerability to coastal erosion was analyzed by Cao et al. (2022) in 15 counties and districts along the coast of the Pearl River Estuary Great Bay Area. This study selects 12 evaluation indices from five perspectives for analysis, including coastal characteristics, hydrodynamic forces, economics, population, and coastal reconstruction. Also, this study used analytic hierarchy process (AHP) method, Technique for Order Preference by Similarity to an Ideal Solution (TOPSIS) method, independent weight method, Jenks natural breaks method (Jenks), exposure-sensitivity-adaptation (ESA) model and obstacle degree method to construct a coastal erosion vulnerability evaluation system for the study area.

Other papers have focused on the effects of sea storms and extreme events such as typhoons. Among these, Kim et al. (2021) provided a vulnerability analysis of beach erosion along the east coast of South Korea with few tidal ranges. This analysis was carried out through a beach vulnerability curve (BVC) by applying a storm wave scenario, function of the peak wave height, to a shoreline response model (SLRM) of bulk model type. The performance of the BVC was tested by comparison with long-term shoreline observation data and showed good agreement under high wave conditions, which is more meaningful for vulnerability analysis. Instead, Do et al. (2022) carried out a numerical simulation, using Telemac-2D and XBeach, of the dune erosion due to Typhoon Tapah occurred in Boggil Beach, Korea, in September 2019. Furthermore, these models were also used to evaluate the effects of measure to preserve the beach from future storm attacks, such as submerged breakwater and submerged groin.

Among other papers, Sauvé et al. (2022) used a multicriteria decision analysis (MCDA) approach through PROMETHEE method to evaluate and hierarchize coastal defense measures (CDMs) in four study sites in the province of Quebec, Canada, with distinct geomorphological, hydrodynamic, ecological, and socio-economic characteristics. Mendoza et al. (2022) proposed a Coastal Resilience Index from Remote Sensors (CRIfRS) for an urbanized coast of the Northern Yucatan coast. This index was divided into five categories, was based on aerial photogrammetry, was applicable on regional and local scale and depends on three indicators: beach width, coastal structure influence area, and vegetation coverage. Chen et al. (2021) analyzed the erosion threshold of sand-mud mixtures through a theoretical analysis of the momentum balance of a sand particle or a mud parcel under the initial motion condition and developed a formula for the critical shear stress of sand-mud mixtures, which also applies for pure sand and mud. Compared with the existing formulae for sand-mud mixtures, the developed formula is much easier for application as it has few coefficients. Zhang et al. (2022) analyzed the reliability of Airborne LIDAR system with an integrated 3D laser scanner for coastal tidal flat where it is difficult to carry out topographic and marine surveys such as the Yangkou Port area of Rudong County in Jiangsu Province, China.

Finally, Splinter and Coco's (2021) Perspective paper analyzed the current state of shoreline modeling at the sub-century timescale and provided an outlook on future challenges and opportunities ahead (Figure 1).

Conclusions

The main aims of this Research Topic were to analyze coastal erosion risk. However, the great variety of factors that influence coastal erosion risk make it a multidisciplinary Topic, as highlighted by the published papers. The most debated topics were shoreline changes, the vulnerability of coastal areas and the

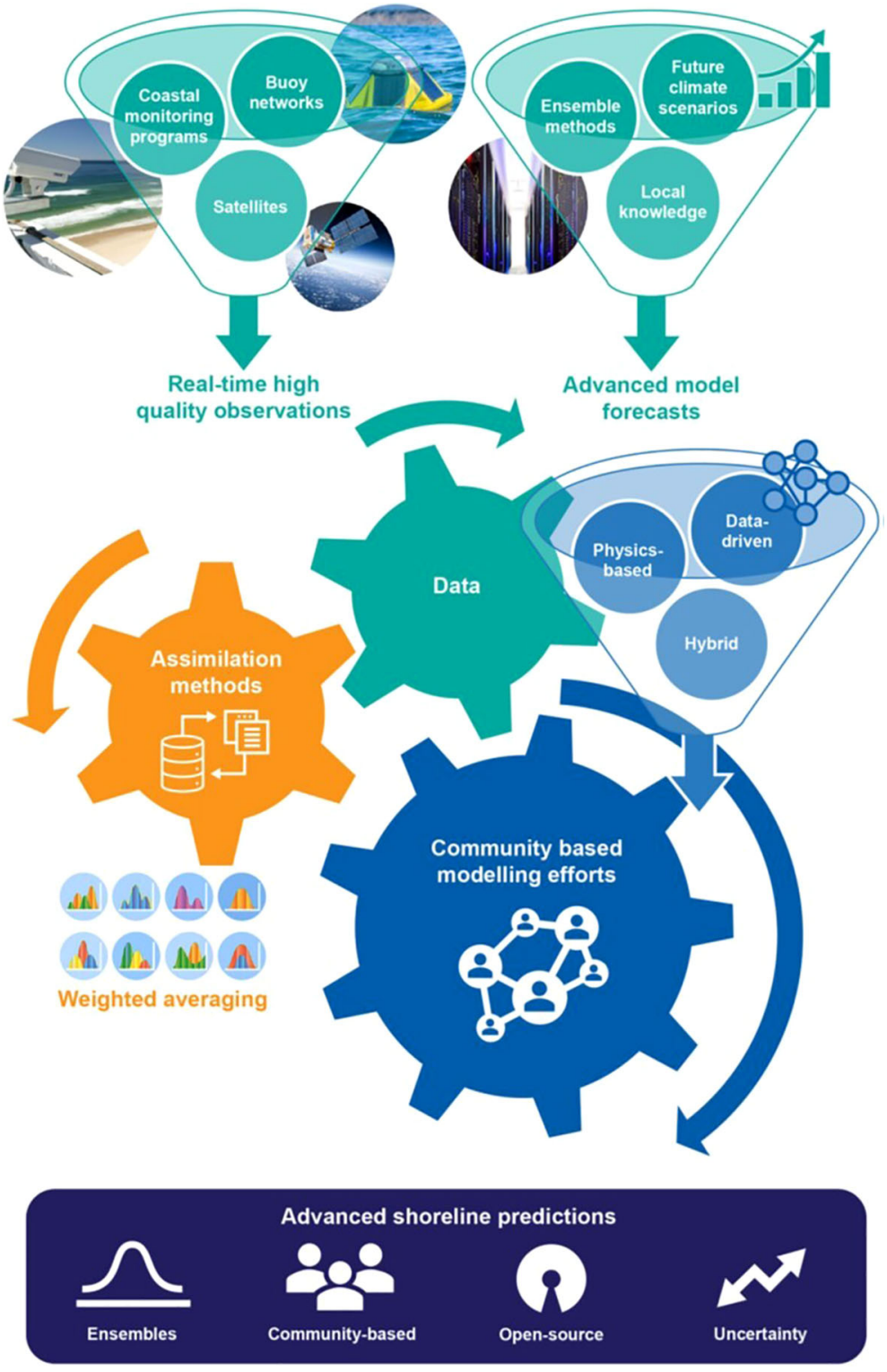

FIGURE 1
A framework for future shoreline change modeling (Splinter and Coco, 2021).

related methods of analysis, and the effects of sea storms and extreme events such as typhoons. Most of the papers used remote sensing, testifying the growing importance in the analysis and understanding phases of various phenomena, including coastal ones. Therefore, this Research Topic has significantly contributed to scientific advances in the complex field of coastal risk.

Author contributions

GB developed the idea for this Research Topic, and he was editor of a paper. GF and FD'A were co-Topic Editors and were editors of five and four papers, respectively. All three authors co-wrote this Editorial and approve the submitted version.

Conflict of interest

The authors declare that the research was conducted in the absence of any commercial or financial relationships that could be construed as a potential conflict of interest.

Publisher's note

References

Apostolopoulos, D., and Nikolakopoulos, K. (2021). A review and meta-analysis of remote sensing data, GIS methods, materials and indices used for monitoring the coastline evolution over the last twenty years. *Eur. J. Remote Sens.* 54 (1), 240–265. doi: 10.1080/22797254.2021.1904293

Besset, M., Anthony, E. J., and Bouchette, F. (2019). Multi-decadal variations in delta shorelines and their relationship to river sediment supply: An assessment and review. *Earth-Sci. Rev.* 193, 199–219. doi: 10.1016/j.earscirev.2019.04.018

Boak, E. H., and Turner, I. L. (2005). Shoreline definition and detection: a review. *J. Coast. Res.* 21 (4), 688–703. doi: 10.2112/03-0071.1

Bombino, G., Barbaro, G., D'Agostino, D., Denisi, P., Foti, G., Labate, A., et al. (2022). Shoreline change and coastal erosion: The role of check dams. first indications from a case study in calabria, southern Italy. *Catena* 217, 1–13. doi: 10.1016/j.catena.2022.106494

Boumboulis, V., Apostolopoulos, D., Depountis, N., and Nikolakopoulos, K. (2021). The importance of geotechnical evaluation and shoreline evolution in coastal vulnerability index calculations. *J. Mar. Sci. Eng.* 9 (4), 423. doi: 10.3390/jmse9040423

Fiori, E., Comellas, A., Molini, L., Rebora, N., Siccardi, F., Gochis, D. J., et al. (2014). Analysis and hindcast simulations of an extreme rainfall event in the Mediterranean area: The Genoa 2011 case. *Atmos. Res.* 138, 13–29. doi: 10.1016/j.atmosres.2013.10.007

Luijendijk, A., Hagenaars, G., Ranasinghe, R., Baart, F., Donchyts, G., and Aarninkhof, S. (2018). The state of the world's beaches. *Sci. Rep.* 8, 1–11. doi: 10.1038/s41598-018-24630-6

Mavromatidi, A., Briche, E., and Claeys, C. (2018). Mapping and analyzing socio-environmental vulnerability to coastal hazards induced by climate change: an application to coastal Mediterranean cities in France. *Cities* 72, pp. doi: 10.1016/j.cities.2017.08.007

Mentaschi, L., Vousdoukas, M. I., Pekel, J. F., Voukouvalas, E., and Feyen, L. (2018). Global long-term observations of coastal erosion and accretion. *Sci. Rep.* 8 (1), 12876. doi: 10.1038/s41598-018-30904-w

Moore, L. J. (2000). Shoreline mapping techniques. *J. Coast. Res.* 16, 111–124.

Narra, P., Coelho, C., Sancho, F., and Palalane, J. (2017). CERA: an open-source tool for coastal erosion risk assessment. *Ocean Coast. Manage.* 142, pp. doi: 10.1016/j.ocecoaman.2017.03.013

Ozpolat, E., and Demir, T. (2019). The spatiotemporal shoreline dynamics of a delta under natural and anthropogenic conditions from 1950 to 2018: A dramatic case from the Eastern Mediterranean. *Ocean Coast. Manage.* 180, 104910. doi: 10.1016/j.ocecoaman.2019.104910

Pantusa, D., D'Alessandro, F., Riefolo, L., Principato, F., and Tomasicchio, G. (2018). Application of a coastal vulnerability index. a case study along the apulian coastline, Italy. *Water* 10 (9), 1–16. doi: 10.3390/w10091218

Viavattene, C., Jiménez, J. A., Ferreira, O., Priest, S., Owen, D., and McCall, R. (2018). Selecting coastal hotspots to storm impacts at the regional scale: a coastal risk assessment framework. *Coast. Eng.* 134, 33–47. doi: 10.1016/j.coastaleng.2017.09.002

Yang, Z., Wang, T., Voisin, N., and Copping, A. (2015). Estuarine response to river flow and sea-level rise under future climate change and human development. *Estuarine Coast. Shelf Sci.* 156, 19–30. doi: 10.1016/j.ecss.2014.08.015

frontiers in Marine Science

ORIGINAL RESEARCH
published: 13 August 2021
doi: 10.3389/fmars.2021.730984

Technical and Social Approaches to Study Shoreline Change of Kuakata, Bangladesh

Nazla Bushra[1], Rubayet Bin Mostafiz[1], Robert V. Rohli[1], Carol J. Friedland[2] and Md Adilur Rahim[3]*

[1] *Department of Oceanography and Coastal Sciences, Louisiana State University, Baton Rouge, LA, United States,*
[2] *Bert S. Turner Department of Construction Management, Louisiana State University, Baton Rouge, LA, United States,*
[3] *Department of Civil and Environmental Engineering, Louisiana State University, Baton Rouge, LA, United States*

In recent years, shoreline determination has become an issue of increasing importance and concern, especially at the local level, as sea level continues to rise. This study identifies the rates of absolute and net erosion, accretion, and shoreline stabilization along the coast of Kuakata, a vulnerable coastal region in south-central Bangladesh. Shoreline change was detected by applying remote sensing and geographic information system (RS-GIS)-based techniques by using Landsat Thematic Mapper (TM), Landsat 8 Operational Land Imager (OLI) and Thermal Infrared Sensor (TIRS) satellite images at 30-m resolution from 1989, 2003, 2010, and 2020. The band combination (BC) method was used to extract the shoreline (i.e., land-water boundary) due to its improved accuracy over other methods for matching with the existing shoreline position. This study also used participatory rural appraisal (PRA) tools which revealed the societal impacts caused by the shoreline changes. Coupling RS-GIS and PRA techniques provides an enhanced understanding of shoreline change and its impacts because PRA enriches the RS-GIS outcomes by contextualizing the findings. Results show that from 1989 to 2020, a total of 13.59 km^2 of coastal land was eroded, and 3.27 km^2 of land was accreted, suggesting that land is retreating at about 0.32 km^2 yr^{-1}. Results from the PRA tools support this finding and demonstrate that fisheries and tourism are affected by the shoreline change. These results are important in Kuakata, a major tourist spot in Bangladesh, because of the impacts on fisheries, recreation, resource extraction, land use planning, and coastal risk management.

Keywords: shoreline change, remote sensing, GIS, coastal erosion and accretion, Landsat TM, participatory rural appraisal, Kuakata, Bangladesh

OPEN ACCESS

Edited by:
Giandomenico Foti, Mediterranea University of Reggio Calabria, Italy

Reviewed by:
Chandrasekar Nainarpandian, Manonmaniam Sundaranar University, India
Polina Lemenkova, Institute of Physics of the Earth, Russian Academy of Sciences (RAS), Russia

****Correspondence:***
Nazla Bushra
nbushr1@lsu.edu

Specialty section:
This article was submitted to Coastal Ocean Processes, a section of the journal Frontiers in Marine Science

Received: *25 June 2021*
Accepted: *26 July 2021*
Published: *13 August 2021*

Citation:
Bushra N, Mostafiz RB, Rohli RV, Friedland CJ and Rahim MA (2021) Technical and Social Approaches to Study Shoreline Change of Kuakata, Bangladesh. Front. Mar. Sci. 8:730984. doi: 10.3389/fmars.2021.730984

INTRODUCTION

The coast is a unique geologic, ecological, and biological domain that supports resource extraction, biodiversity, recreation, aesthetics, and trade—all amid natural hazard risk. Thus, coastal land-use planning and risk management are critical. Micro-scale (i.e., at local levels) hazard risk assessment is important to inform planning efforts aimed at reducing losses from various natural hazards (Mostafiz et al., 2020a,b). Determination of region-specific shoreline morphometric changes is of particular concern to better characterize the changing risk to its inhabitants.

These shoreline changes are important in general, as the Center for Climate Systems Research and The Earth Institute of Columbia Climate School (2006) estimated that the world population living within 60 miles of a coastline in 2025 would increase by 35 percent above 1995 levels. But shoreline changes are particularly important in coastal south Asia, including Bangladesh, where the coastline is considered highly vulnerable to sea level rise (Oppenheimer et al., 2019) not only because of the gentle slope of the deltaic formation (Brammer et al., 1996; Akter et al., 2016) but also because of the dense population (Penning-Rowsell et al., 2013), amid the threats of anticipated accelerating sea level rise related to global climate change (Huq et al., 1996; Alam et al., 2018) and local subsidence (Hanebuth et al., 2013). One area on the Bangladesh coastline that is of particular concern is near the resort town of Kuakata, where both fluvial and marine processes dominate the shoreline while storm surges (Mitra et al., 2013) and human intervention (Brammer, 2014; Bushra et al., 2016) exacerbate vulnerability to hazards.

Identification of the land-water interface is not an easy task, especially where the fluvial and marine processes are present simultaneously. Satellite imagery provides the opportunity to identify precisely the changes of shoreline over time. Several studies have quantified shoreline change using satellite images at relatively active coastal zones. For example, Chen (1998) used sequential SPOT imagery and tidal measurements to detect shoreline changes on the western coast of Taiwan. Since Chen (1998), others have used satellite imagery to detect shoreline changes of Port Said, Egypt (Elkoushy and Tolba, 2003); Tanzania (Makota et al., 2004); eastern (Maiti and Bhattacharya, 2009; Chand and Acharya, 2010; Pritam and Prasenjit, 2010; Mukhopadhyay et al., 2012), southern (Kumaravel et al., 2013; Mujabar and Chandrasekar, 2013), and western India (Deepika et al., 2014); Bangladesh (Sarwar and Woodroffe, 2013); the Persian Gulf (Niya et al., 2013); Vietnam (Tran Thi et al., 2014); Indonesia (Yulianto et al., 2019); the Gulf of Oman (Ghaderi and Rahbani, 2020); Reggio Calabria, Italy (Barbaro et al., 2017; Foti et al., 2019; Barillà et al., 2020); and the Arctic (Zagorski et al., 2020).

In Bangladesh, shoreline studies are typically linked to climate change impacts and sea level change (Ali, 2000; Sarwar, 2013; Zaman et al., 2018). Scientists at the Centre for Environmental and Geographic Information Services (Centre for Environmental and Geographic Information Services (CEGIS), 2009) found that Bangladesh's landmass increased by 20 km^2 annually over the 1973–2005 period. Models suggest that the natural accretion occurring in Bangladesh for hundreds of years along the estuaries will continue for decades or centuries into the future (Centre for Environmental and Geographic Information Services (CEGIS), 2009). Yet many people living along the coast of Bangladesh have observed anecdotally that sea levels are rising on human time scales. Locals suggest that while new land is emerging, more land is disappearing (Brammer, 2014; Ahmed et al., 2018).

Rahman (1999) described the morphometric properties of Kuakata beach along with the sand grain uniformity and properties. Rahman et al. (2013) examined shoreline shifting rates via satellite imagery available from 1973 to 2010, with results describing the locations and rates where erosion and accretion dominate. Islam et al. (2013) analyzed multi-temporal satellite images of the Kuakata shoreline from 1973 to 2012 and concluded that it is an unstable shoreline where both erosion and accretion were taking place over the study period, but erosional activities were dominating the coastline, especially over the eastern region.

While previous remote-sensing-based work is useful and must be updated to include the most recent observations, research is also needed that uses technical and societal approaches simultaneously, where causality can be assessed through direct observation. The observational evidence by the local community is important, as their intergenerational familiarity with their homeland precedes and includes the Satellite Era; their perception can be a great contribution for analyzing impacts and future planning. Although Bushra et al. (2014, 2016) explained the physical processes driving the modification of the Kuakata coast, no previous study has identified and quantified the micro-scale shifting of the shoreline while incorporating both physical and social perspectives. This task is subjective and time-consuming, as seasonal variations and tidal influences complicate the determination of the shoreline boundary (Boak and Turner, 2005).

This study addresses the extent of shore erosion, accretion, and stabilization along the coast of Kuakata using remote sensing (RS) and geographic information systems- (GIS-) based methods, to provide a basis for assessing the current and potential economic and environmental impacts of the present condition. Along with detecting the shoreline applying RS-GIS technique, this study also incorporates the perceptions of community members who face the consequences over time by applying participatory rural appraisal (PRA) tools.

While geophysical research is mostly confined to the application of a technical approach, this research demonstrates that applying PRA can be important for demonstrating causation and consequences of the shoreline change, and can even approximate the outcomes of the quantitative analysis. Coupling RS-GIS and PRA is important because studying shoreline change would contribute little without listening to ideas for improving lives and livelihoods which is often neglected in shoreline studies. In an age of multiplicity of knowledge systems, integration of technical and societal approaches is important to advance socio-economic development, particularly in less developed countries, where community participation contributes substantially toward understanding (Puri, 2007). In such cases, PRA tools can be more effective for sustainable development and policy implementations. Several studies (e.g., Brodnig and Mayer-Schönberger, 2000; Mialhe et al., 2015; Koeva et al., 2020) have recognized the potential influence of the community in decision making. Application of PRA tools facilitates social interactions in formal and informal ways, allowing excavation of information that would be difficult to assemble by technical analysis alone. Occupational practices and traditional knowledge determine societal settings and these are related to local resources which get modified by shoreline change. Proper integration of RS-GIS and PRA tools and sharing the outcomes can be complementary to each other and this can improve the stewardship of available resources to cope with future challenges. Therefore, this study could play a significant role in governmental initiatives to

mitigate consequences. The techniques used in this study are unique in terms of incorporating both technical and social approaches, and the outcome will be valuable for future land use planning, investment strategies, and hazard mitigation planning.

MATERIALS AND METHODS

Study Area

The dynamic coast of Bangladesh is constantly deformed and reshaped by sediments carried by the three mighty river systems: the Ganges, Brahmaputra, and Meghna rivers. While there is a net accumulation of sediment (delta building) at the river mouth (Broadus, 1993; Amin, 2008), a substantial amount of sediment is entrained by waves and currents. Sediment replenishment plays an important role in deltaic stability by hindering natural compaction and subsidence (Dixon et al., 2006) and is thus considered one of the main factors in this coastal zone for shoreline changes caused by sea level rise (Amin, 2008; Emran et al., 2019). Along with a gentle slope into the Bay of Bengal, this wide sandy beach area has patches of mangrove trees behind it which withstand the perpetual forces of the tides. In addition, population dynamics (Ericson et al., 2006) of this coastal area and how the shoreline change may affect livelihoods (Mukherjee et al., 2019) are important considerations.

Kuakata, situated on the central coast of Bangladesh on the western side of the Meghna estuary at the sedimentary outlet of the Padma, Meghna, and Brahmaputra, is selected as the study area because of the dynamic nature of its shoreline and its economic and cultural significance. The convex shape of the Kuakata coast (**Figure 1**) invites the significant, simultaneous impact of erosion and accretion from both fluvial and marine processes. About 41 percent of the cyclones originating in the Bay of Bengal travel through this funnel-shaped central region each year, such as Cyclone Sidr in 2007 (Ikeuchi et al., 2017), which makes the central coast of Bangladesh vulnerable to storm surge (Paul and Rahman, 2006). A complete analysis of processes that shape the landscape in this tidal-to-fluvial transition zone of Bangladesh is beyond the scope of this research but is detailed effectively elsewhere (Goodbred and Kuehl, 1999; Wilson and Goodbred, 2015; Bomer et al., 2019).

From a human-environment-interactions perspective, Kuakata is an economically active zone that offers access to fisheries and commerce, proximity to rich agricultural lowlands, and recreational opportunities, which form the basis for economic opportunities for a large community. The percentages of jobs in agriculture, fishing, commerce, service, agricultural laborer, wage laborer, and "other" in this region are approximately 45.6, 5.7, 10.0, 3.6, 18.9, 4.6, and 11.7, respectively (Bangladesh Bureau of Statistics, 2009). While 19 percent of Kuakata's land is classified as agricultural, this percentage is decreasing gradually, as the land is in high demand for commercial development, particularly by the recently emerging tourism industry. The inland area of Kuakata is protected from tidal waves by an earthen flood embankment, which was constructed few hundred meters away from the shoreline (Rahman et al., 2013). The extension of the embankment/levee and newly created roads has increased this demand further.

Technical Approach

The shoreline change is detected over an approximately four-decade interval by comparing satellite imagery from 12 January 1989, 19 December 2003, and 30 January 2010 using Landsat Thematic Mapper (TM) imagery, and 11 February 2020 using Landsat 8 Operational Land Imager (OLI) and Thermal Infrared Sensor (TIRS) satellite images, all at 30 m resolution. These dates are selected to enhance shoreline delineation by balancing the needs for clear sky cover, low tides, and maintenance of a similar time in the dry season, all amid the limitation of a once-in-sixteen-day flyover by the satellite sensor (United States Geological Survey (USGS), 2021). For unavoidable cases of tidal interference, tidal data are used to verify the tidal condition at the acquisition time, and the exact shore line position is determined by adding or subtracting the tidal data. Although several tidal stations managed by the Bangladesh Water Development Board exist, none with reliable, continuous records are located on Kuakata. Mirzaganj (Station ID—SW19), located ∼61.0 km northwest from the study area, is the nearest tidal station with a continuous record of the daily semi-diurnal tidal conditions, ranging from 0.01 m at neap tide to 2.04 m at spring tide at the Barisal-Buriswar River; its data are applied to approximate the tidal condition at the image acquisition time.

Band Combination (BC; Dwivedi and Rao, 1992; Sutikno et al., 2020), Ratio Transformation (RT; Mavraeidopoulos et al., 2019), Normalized Difference Vegetation Index (NDVI; Carlson and Ripley, 1997; Huang et al., 2021), and Normalized Difference Water Index (NDWI; Gao, 1996; Su et al., 2021) algorithms are often used to extract the shoreline from the land/water boundary. Among the four methods of shoreline detection, BC—a method of combining bands with wavelengths of the electromagnetic spectrum sensitive to shoreline detection, is selected primarily because of its higher accuracy of boundary-matching with the already georeferenced, cross-checked Local Government Engineering Department (LGED) maps. For the BC method, combining the TM's Bands 4 (0.76–0.90 μm), 5 (1.55–1.75 μm), and 7 (2.08–2.35 μm), and Bands 5 (0.85–0.88 μm), 6 (1.57–1.65 μm), and 7 (2.11–2.29 μm) for OLI and TIRS, provides the best result for shoreline detection (United States Geological Survey, 2020). This is because these bands operate in the best spectral region to emphasize land-water contrast, distinguishing water bodies in a darker tone from other land use categories in a lighter tone. This sets a sharp contrast between the land-water boundary, as for both Landsat Image types Band 7 spectral has a strong water absorption region and a strong reflectance region for soil and rock, thereby causing water bodies to appear in dark tones and exposed land surfaces to appear in bright tones. Thus, the combination of these three bands results in the most accurate and distinct shoreline boundary. A minimal percentage of inaccuracy in boundary detection may be caused by diurnal tidal variations, vegetation coverage, and indistinguishable land-water area in Landsat satellite images.

The accuracy of the extracted shorelines is verified with georeferenced standard maps collected from the LGED of

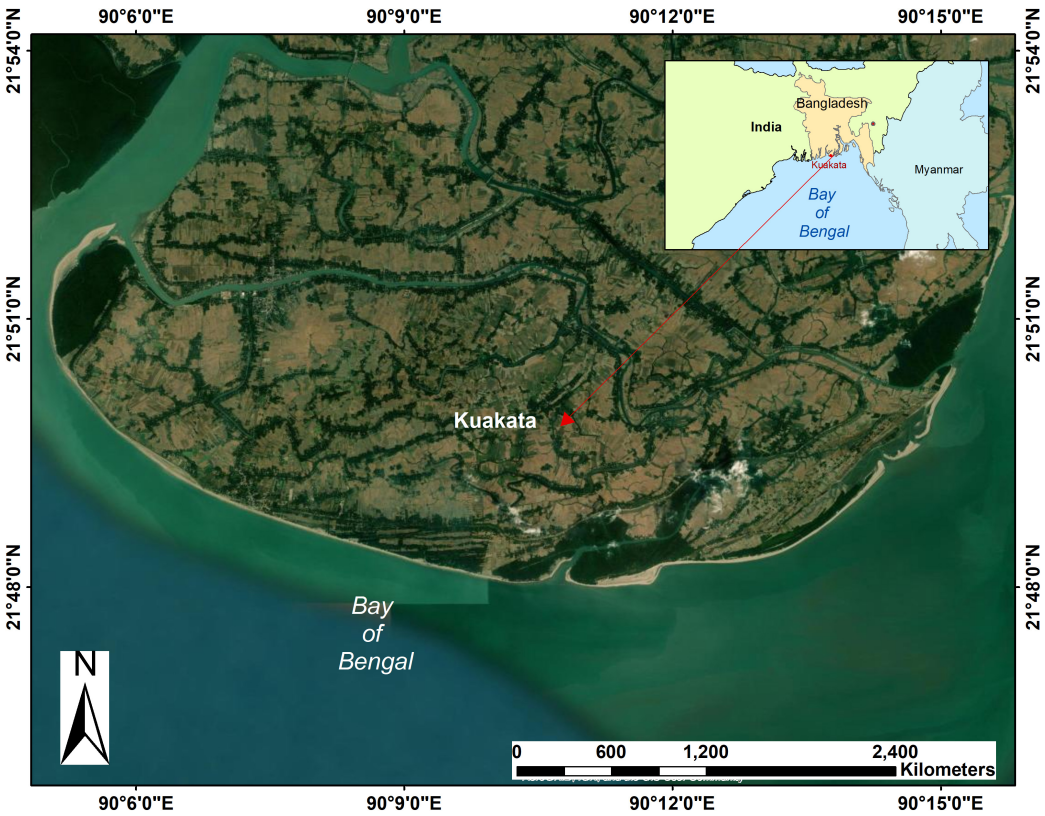

FIGURE 1 | Location of study area.

Bangladesh. The position is also cross-checked with the recorded ground control point (GCP) data, which are used for quality control. Also, 2010 is considered as the reference year to detect shoreline change.

The GIS and RS tools, Integrated Land and Water Information System (ILWIS) and ArcGIS® Desktop, are used for image processing, geometric correction, visual interpretation, and manual digitization to develop a vector data series for each of the images, to compare and measure the changes. The vector line dataset enables the comparison of shoreline shift over the years and vector polygon data series facilitates measurement of the rate of shoreline accretion and erosion using GIS tools. Application of GIS and RS is also required for ground truthing, which is done by conducting field verifications and GCP data collection using Global Positioning System (GPS) for more accurate measurements. The RS-GIS technique tests and quantifies the information collected from PRA tools.

Societal Approach

Most research on shoreline change is directed toward using technical tools and applications rather than incorporating the human perceptive. PRA (Chambers, 1994; Kukielka et al., 2016), a growing family of research methods, involves a series of qualitative multidisciplinary approaches to learning about local-level conditions and individual perspectives based on first-hand knowledge, experiences, and intergenerational accumulated wisdom. The PRA tools described below were implemented in 2010 to elucidate the major causes and impacts of coastline shifting associated with the different natural settings and livelihoods, including forest, agriculture, aquaculture, fishing, fish drying, sea salt production, and trading. The PRA employed here relies on field observations and group meetings with communities and stakeholders, such as fisherman, farmers, small business owners, and tourism-related employees. More specifically, PRA verifies the results through a transect walk (Dooley et al., 2018; Schäffler et al., 2021), timeline (historical mapping) analysis (Mueller et al., 2010; Tomlinson et al., 2018), cause and effect diagram (Holme and Chalauisaeng, 2006; Saja et al., 2021), key informant interview (KII; Chenais et al., 2015; Balgah, 2016; Nicholson and Valentine, 2019; Dureab et al., 2021; Roothaert et al., 2021), and focus group discussion (FGD; Shamsuddin et al., 2007; Ng et al., 2021). These tools emphasize the following questions: What is the perception about shoreline change along the coast of Kuakata? What is the rate of this change? Is the face of change (i.e., erosion or accretion) happening similarly along the entire coast? What natural and/or anthropogenic features are affecting the rate of change? How have the local people adopted their livelihood to this change? What is the impact of this change?

The main aim of the transect walk is to observe land use from the 30 m buffer zone of the Bay of Bengal to 500 m inland. Six transect walks were conducted in the central and western-central

parts of the island while avoiding the mangrove forests and sand dune piles. The land use pattern is generalized to a cross section profile, with the help of pre-downloaded Google imagery, GPS, and local knowledge, to convey the impact of shoreline change on coastal land use and livelihood patterns.

The timeline analysis is designed to appraise the historical change in people's observations. This analysis facilitates acquisition of substantive qualitative information regarding the chronology of shoreline change in a short amount of time across a remote area poorly covered by PRA study. The timeline analysis is based on the assumption that to understand past events it is necessary to identify the shoreline location over time, cause of changes, and impacts due to the change. Twelve people, in groups of six, participated in drawing the relative shoreline positions over time, from that provided to them in a timeline table. They then offered their opinions on the causes and impacts of the changes. The majority (i.e., four to five from each group) of the participants were fishermen who live near the coast. Based on the common responses from the two groups, numbers in the table have been reported.

The cause and effect diagram is also implemented to assess causes of changes and their impacts, based on the participant opinions. It involves a visual tool to help the participants to compare the relative importance of the causes and effects due to shoreline change in a tree-like diagram where the consequences (effects) of shoreline change are represented by the trunk of the tree diagram, while physical mechanisms (causes) which result from those consequences by accelerating shoreline change are shown as roots. Three different groups (one with ten fishermen, another group of ten farmers, and six small businessmen associated with tourism activities) participated separately to complete the tree diagram.

The purpose of the KII is to assign local specification of the consequences and investigate common impacts and adaptation measures. Relying on the list of issues found from the transect walk, timeline analysis, and cause and effect diagram, a descriptive question structure was formed to allow free flow of information for collecting in-depth and spontaneous responses from the two key interviewees about the shoreline change that they have observed over the years and its impact on the community's livelihood. The key informants are from two different backgrounds who were interviewed individually, after obtaining their written consent, to determine their perceptions of the causes of shoreline change and its impacts on local people. At the time, one of the interviewees was a surveyor with 35 years of professional experience regarding land use survey and land use change. Another key informant was a land developer and was still working there for a land reclamation project. Notes taken during the interview process were evaluated and elaborated shortly afterward.

Finally, one group of ten fishermen and a separate group of ten farmers participated in two FGDs, as it became apparent that they are the primary victimized occupational groups from the change of shoreline. They were asked whether they have noticed coastal accretion or erosion and the effects or impacts of this land change.

RESULTS AND DISCUSSION

Findings From Remote Sensing and GIS

The Kuakata shoreline has shifted inward (**Figure 2**). The central and eastern regions have a retrograding shoreline on a net basis, and the western part of the western region of the island has an elongating shoreline, likely owing to fluvial deposition. The BC method reveals that erosional activity is more prominent than accretional activity. The western horn of the island is elongating because of accretion. In the central and eastern coast both erosional and accretional processes have taken place to modify the coastline. The shoreline change implies that Kuakata's seaward coast is dominated by the effects of erosional activities and/or sea level rise. Approximately 13.59 km^2 of land has been lost, and 3.27 km^2 land has been gained since 1989, resulting in a net loss of 10.32 km^2 of land over the last four decades. The fastest accretion rate across the study period is for the eastern zone, at 0.05 $km^2\ yr^{-1}$ (**Table 1**), despite a net shoreline retreat. The central zone has the most rapid erosion rate, at 0.19 $km^2\ yr^{-1}$ and the strongest net rate of shoreline retreat (**Table 1**), likely because of less fluvial impact and marine influence.

Comparison between the range of years 1989–2003, 2003–2010, and 2010–2020 provides a more detailed perspective. The erosion rate from 2003 to 2010 (0.76 $km^2\ yr^{-1}$) exceeded that from 1989 to 2003 (0.46 $km^2\ yr^{-1}$) and 2010 to 2020 (0.18 $km^2\ yr^{-1}$). At the same time, the accretion rate was less from 2003 to 2010 (0.07 $km^2\ yr^{-1}$) than from 1989 to 2003 (0.13 $km^2\ yr^{-1}$) and 2010 to 2020 (0.09 $km^2\ yr^{-1}$). Thus, land loss from 2003 to 2010 exceeded that from 1989 to 2003 and 2010 to 2020. For the entire range of years (i.e., from 1989 to 2020), the erosion rate was 0.44 $km^2\ yr^{-1}$, and the rate of accretion was 0.11 $km^2\ yr^{-1}$. These relationships are depicted graphically by region in **Figure 3**, with specific locations where net accretion and erosion occurred during the sub-intervals shown in **Figure 4**. Only very small coastal areas, mostly in the west, have net accretion, with net erosion elsewhere. The results corroborate those of other studies (Shibly and Takewaka, 2012; Bushra, 2013; Islam et al., 2013; Mitra et al., 2013; Rahman et al., 2013) which concluded that erosion dominates over accretion in this region. For example, Islam et al. (2013) found that from 1973 to 2012 the erosion rate was 0.29 $km^2\ yr^{-1}$, and the rate of accretion was 0.09 $km^2\ yr^{-1}$ in the Kuakata.

Application of PRA Tools

In addition to the satellite image study and geospatial interpretation, The PRA tools described in the previous sections provide new information.

Figure 5 summarizes the results of the transect walk. According to the local people, the establishment of embankments since 1966 and the presence of fluvial tidal creeks, canals, and sand dunes have important roles in maintaining the stable shoreline in the central zone and accretion in the eastern zone. The locals believe that the western part is protected by a newly formed extension of the embankment

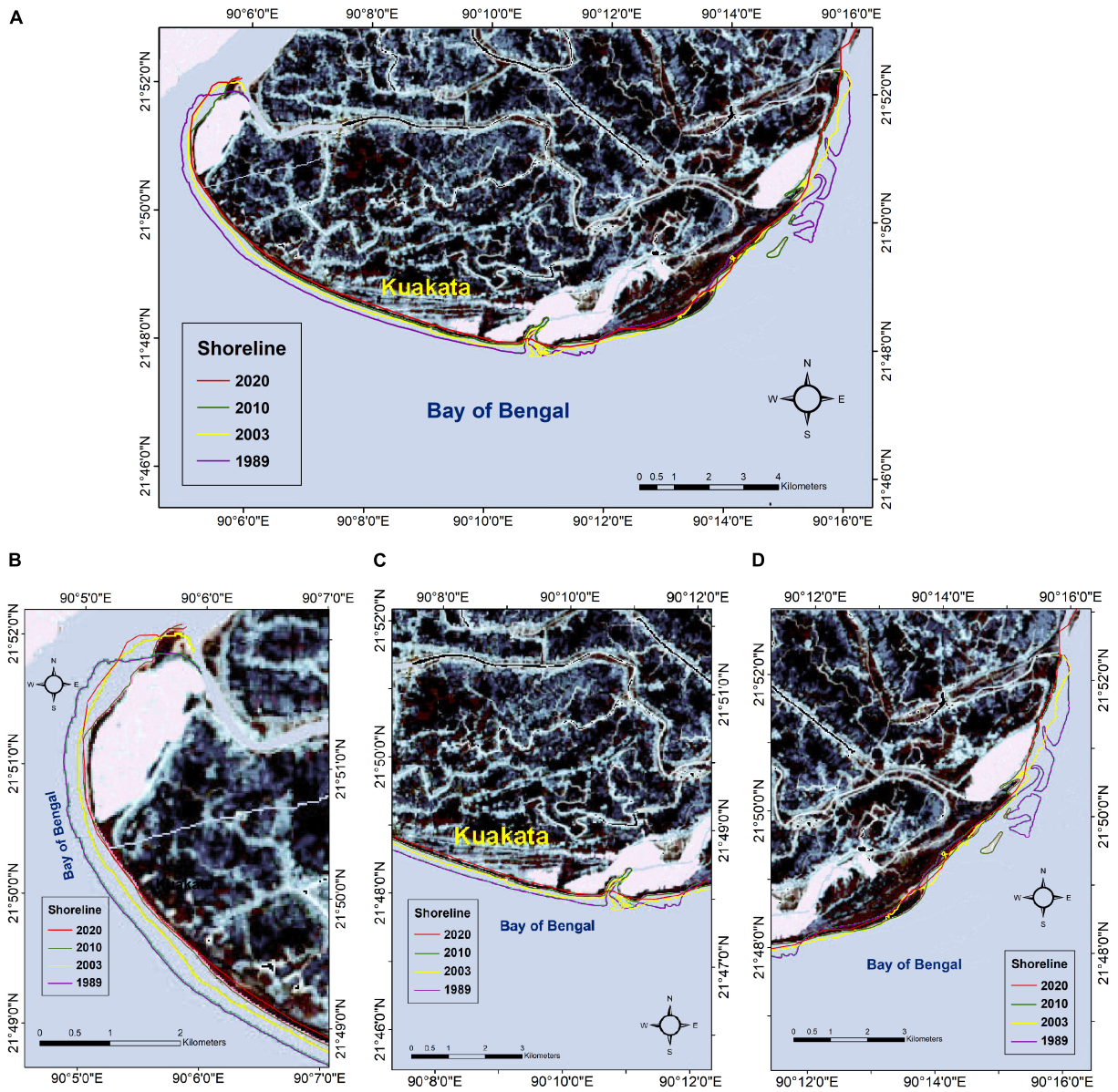

FIGURE 2 | Position of Kuakata's seaward shoreline by year; **(A)** overall, **(B)** western, **(C)** central, and **(D)** eastern part of the study area. Notice the elongating shoreline in the western extreme of the western zone, and the unevenness of the retreat over time, particularly in the eastern zone.

TABLE 1 | Measurements of coastal land area changes by accretion and erosion (in km^2).

Time period	Western zone		Central zone		Eastern zone		Total	
	Accretion	Erosion	Accretion	Erosion	Accretion	Erosion	Accretion	Erosion
1989–2003	0.24	2.33	0.60	2.56	0.99	1.60	1.83	6.49
2003-2010	0	1.63	0.01	2.15	0.50	1.54	0.51	5.32
2010-2020	0.77	0.46	0.10	1.05	0.06	0.27	0.93	1.78
1989-2020	1.01	4.42	0.71	5.76	1.55	3.41	3.27	13.59

which was built after Cyclone Aila destroyed the previous one in 2009, and even though erosion still persists, the rate is less than in years before embankment construction. The satellite imagery confirms this observation, as for the western zone over the 2010–2020 period, erosion was 0.46 km^2, but over the 1989–2003 and 2003–2010 periods it was

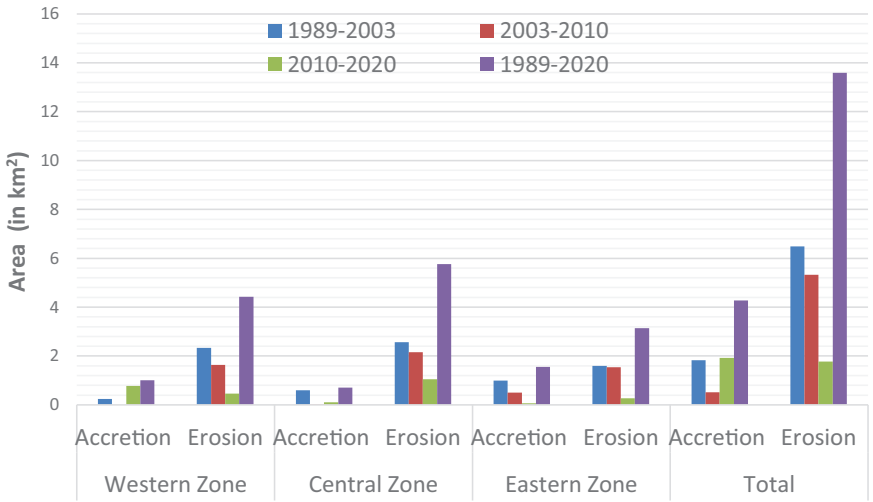

FIGURE 3 | Kuakata coastal land area changes by zone (from 1989 to 2020).

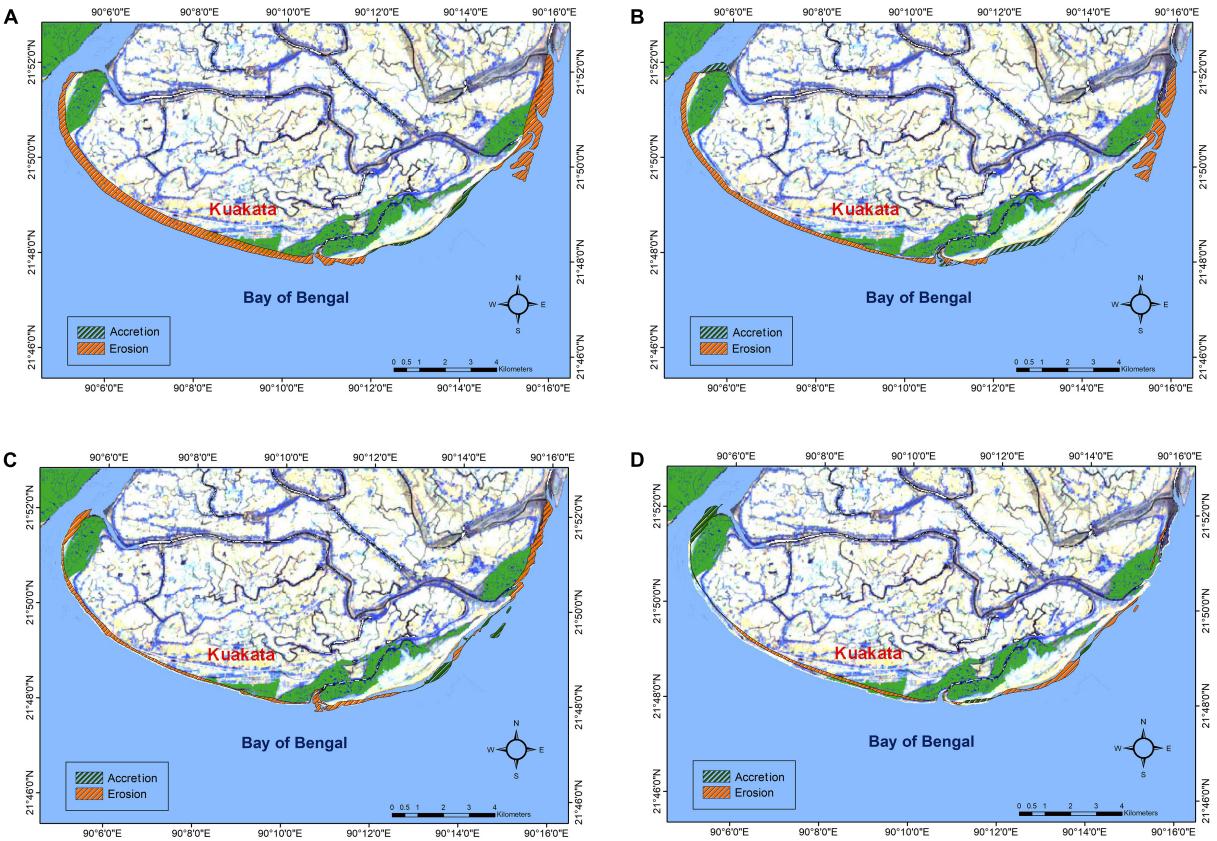

FIGURE 4 | Erosion and accretion at Kuakata coast from **(A)** 1989 to 2020, **(B)** 1989 to 2003, **(C)** 2003 to 2010, and **(D)** 2010 to 2020. Notice the very small coastal areas, mostly in the west, of net accretion, and net erosion elsewhere.

2.33 km^2 and 1.63 km^2, respectively. During the transect walk, the local community confirms that among all major economic activities fishing and tourism were affected most by shoreline erosion.

The timeline analysis reveals that except for the Cauer Char (L8) area (**Figure 6**), which is situated at the eastern side of the landmass, the shoreline has retreated inland substantially (**Table 2**). This finding corroborates the results from the satellite

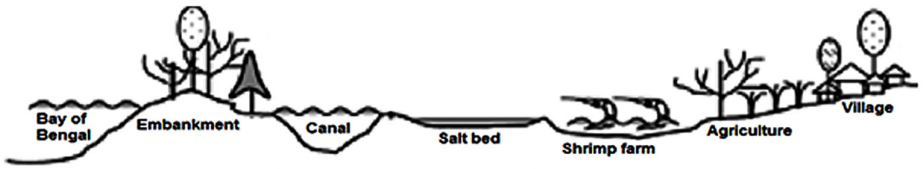

Landuse	Bay of Bengal	Embankment	Canal	Salt bed	Shrimp Farm	Agriculture	Settlement
Resources	Fish, shrimp, oyster, mussel	Land, tree, grass, local shops	Water, fish, shrimp, mussel	Land	Shrimp, fish	Land, crops	Tree, livestock
Activities	Fishing, navigation	Local transport, grazing, temporary living	Water supply, navigation, shrimp fry collection	Concentrate sea water, salt production	Pond preparation, management, harvesting	Cultivation of rice, vegetable, betel leaf	Housing, gardening, poultry, social forestry
Land type		Tidal land		Tidal land, plain land	Tidal land, plain land	Plain land	Plain land
Problem/ Issues	Erosion, accretion, water, pollution, storm surge	Hamper adaptation of aquatic organisms	Water contamination	Land ownership, rainwater, salt price fluctuation	Low production, diseases, water pollution, land use conflicts	Utilization of pesticides and chemical fertilizers	Lack of safe drinking water, toilet, electricity, transportation, education
Opportunities	Domestic consumption and export of fishery resources, employment	Protection shelter	Community livelihood	Salt and high saline water selling	Family consumption of fish, shrimp export, employment	Family consumption, selling of products	Family consumption, selling chickens, ducks, goats, cows, and different fruits

FIGURE 5 | Transect walk analysis showing land use patterns in central Kuakata.

imagery analysis. According to the local people, at Lebur Char (L1) and Khajura (L2), the shoreline had been reduced by about 7–8 km from 1989 to 2003 and about 2.5 km from 2003 to 2010. The Computer (L3) and Mirabari (L4) areas had shown nearly the same amount of erosion for 1989–2003 and about 1.5–2.5 km of erosion for 2003–2010. In comparison to the above area, the Ghatla (L5), Jhauban (L6), and Gangamoti (L7) locations had less shoreline erosion, which was about 5 km for the years 1989–2003 and 1–7.5 km for 2003–2010. Though the Cauer Char (L8) did not exist in 1989, its establishment was prominent in 2003, and it became extended by about 2 km from 2003 to 2010.

Both RS-GIS and PRA outcomes (**Tables 1**, **2**) establish that in the western (Lebur Char, Khajura, and Computer) and central (Mirabari, Ghatla, and Jhauban) zones, erosional activity is dominating over accretion. The concave shape of the coast also explains why the central zone is more responsive to these factors. In the eastern zone (Cauer Char), accretion is dominating. These findings corroborate those of Rahman et al. (2013), who found that from 1973 to 2010 the western part of Kuakata beach suffered an average erosion of 350–450 m. **Table 2** shows that, on average from 1989 to 2010, the erosion rate in Lebur Char, Khajura, and Computer is approximately 500 m yr^{-1}.

The cause and effect diagram (**Figure 7**) depicts the main causes of shoreline change in that locality, as expressed by community members. Most prominent among the community-identified causes are marine and climatic actions for shoreline erosion, including tide, current, wave actions, tidal flood, cyclone, storm surges, and sea level rise. A few people mentioned that in some parts of Kuakata, accretion activities caused by sedimentation by fluvial and marine actions and landform structure are occurring. This accretion occurs along the low gradient and gentle slope of the continental shelf and is enhanced by construction of the embankment and polders at the coastal boundary. Landfilling at the shoreline boundary and destruction of sand dunes, which accelerate the wave/wind action inland, are also the causes for shoreline modification at the coastal boundary. Respondents concur that the shoreline is mainly retreating, but there are some accretional activities in some parts of the lands

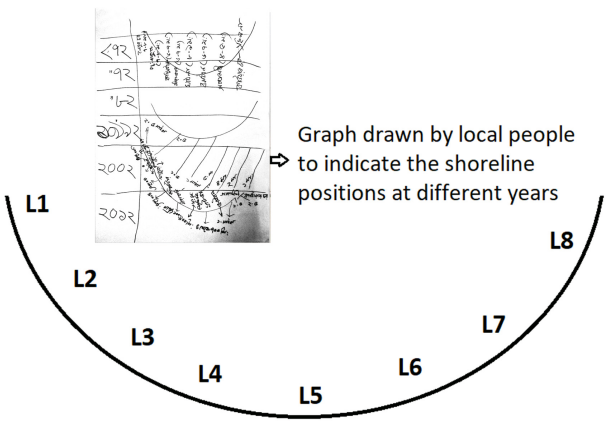

FIGURE 6 | Comparative position of local places along the shoreline according to the local people.

TABLE 2 | Tentative positions of the shoreline at different locations from the embankment, according to the timeline analysis by local people.

Local Place Name	Position of the Shoreline from the Embankment (km) Assessed by Local People			Erosion/Accretion (km)		
	1989	2003	2010	1989-2003	2003-2010	1989-2010
Lebur Char (L1)	11.0-12.0	3.0-4.0	0.55-0.60	8.0	2.45-3.4	10.45-11.4
Khajura (L2)	11.0-12.0	3.0-4.0	0.50-0.55	8.0	2.5-3.45	10.5-11.45
Computer (L3)	10.0-11.0	2.0-3.0	0.44-0.50	8.0	1.56-2.5	9.56-10.5
Mirabari (L4)	10.0-11.0	1.5-2.0	0.11-0.15	8.5-9.0	1.39-1.85	9.89-10.85
Ghatla (L5)	12.0-13.0	7.0-8.0	0.45-0.50	5.0	6.55-7.5	11.55-12.5
Jhauban (L6)	10.0-11.0	5.0-6.0	1.0-1.3	5.0	4-4.7	9.0-9.7
Gangamoti (L7)	7.0-8.0	2.0-3.0	2.0-2.1	5.0	0-0.9	5.0-5.9
Cauer Char (L8)	Did not exist	1.0-2.0	4.0	1.0-2.0	2.0-3.0	3.0-5.0

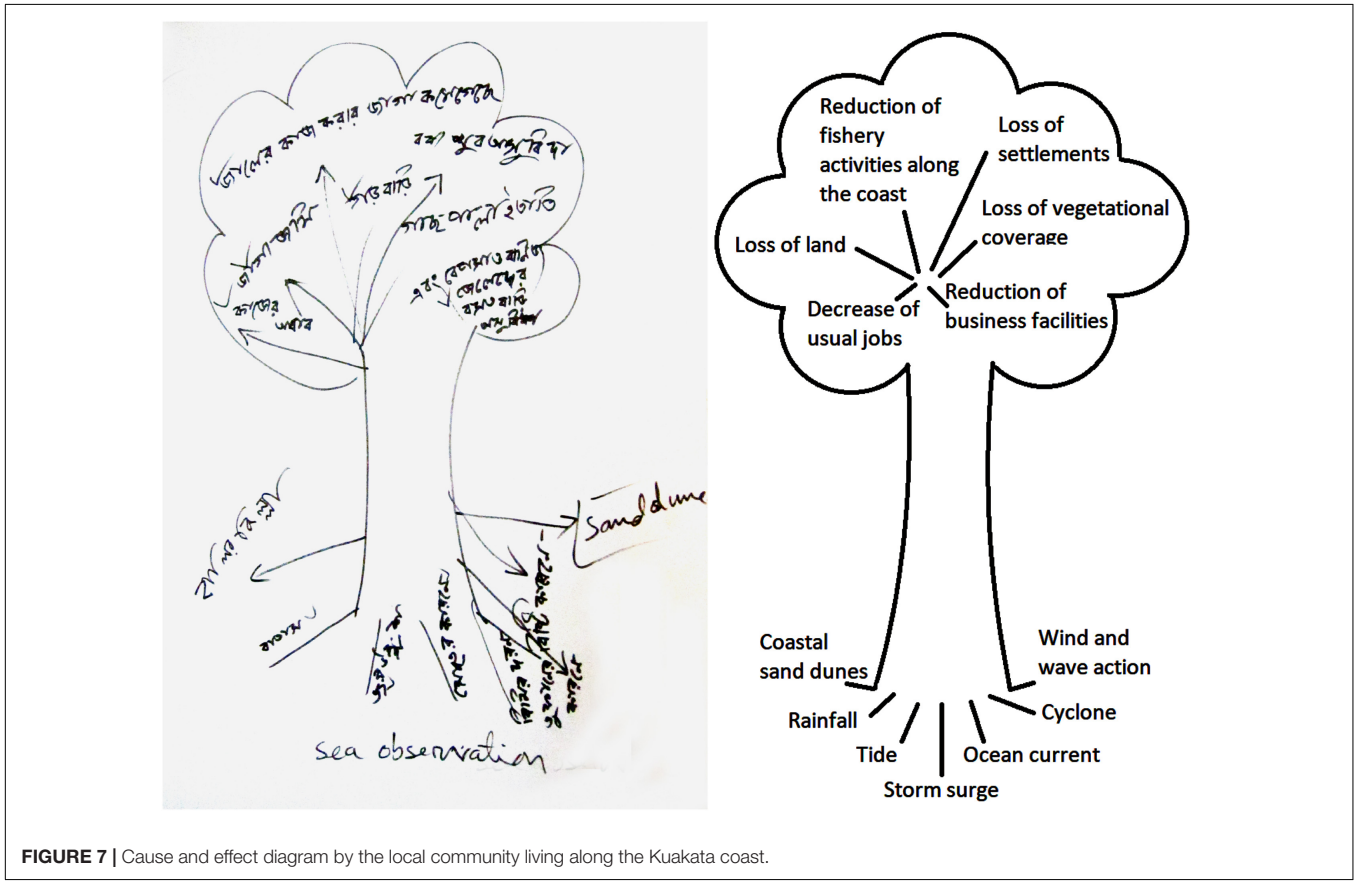

FIGURE 7 | Cause and effect diagram by the local community living along the Kuakata coast.

where the fluvial and marine processes have deposited sediments over the last 20 years. The main causes of shoreline change and their subsequent effects are listed in **Table 3**.

The key informant who was a surveyor expressed that poor coastal management, monitoring, and maintenance are among the causes of coastal land degradation and land loss, rather than natural processes. The informant who at the time was a land developer expressed that by being a famous tourist spot in Bangladesh, land reclamation has accelerated over the last 30 years, and that initially no one monitored the process of land cover change for commercial purposes (i.e., building hotels, resorts, and shopping complexes). That same informant noted that the excavation of sand from the sea was also destroying many dune fields. The informant also noted that these are common occurrences for the development of many hotels along the beachside. Such activities ultimately result in disruption of the natural processes and acceleration of coastal erosion. Both key informants agree that the lack of planning and proper implementation of laws and legislation for coastal management and maintenance are responsible for this coastal land degradation. Although the government has undertaken some initiatives to maintain this famous tourist spot, land reclamation by the developer and the development of high-rise buildings continues.

TABLE 3 | Major causes and their subsequent effects of shoreline change on the Kuakata coast.

	Causes	Effects
Shoreline erosion	Erosional activities caused by tidal flood, cyclone, storm surges; marine action (tide, current, wave); and sea level rise	Land inundation, loss of land and vegetational coverage, loss of settlements, disruption of livelihood/change of livelihood
Shoreline accretion	Accretional activities caused by sedimentation, marine action, landform structure, sand agglomeration by ocean currents caused by sand dune subsidence, beach structure, continental slope/shelf, construction of embankments/polders, landfilling	Land gaining, increase of social conflict, imbalance in eco-system

According to the fishermen in the FGD, marine waves, ocean currents, and tides are the major causes of shoreline change. The participants felt that these regular phenomena are more prevalent during the monsoon season, which causes land loss and shoreline erosion. In addition to these regular phenomena, the recent increase in the frequency of coastal cyclones and in the intensity of storm surge (Bushra, 2016; Bushra et al., 2019) and tidal flooding have accelerated the erosional process along the coast. As these phenomena destroy the vegetation coverage, sand dune fields, and sand piles along the coast, the erosional effects of regular waves, currents, and tides are exacerbated. Because the seasonal winds typically blow from the southwest, the erosional activities are more prominent along the west coast of Kuakata. Thus, the fishing community has less buffer zone around the seashore for their fishing activities.

The farmers noted that as the sea encroaches on their homeland, they themselves become more dependent on shrimp cultivation rather than cropping. According to the respondents, saltwater intrusion complicates the problem even more. As the sea is advancing, windblown sand from the beach has become so abundant on their fertile land that it can become uncultivable. The farmers who have land near the coast sometimes face enormous pressure from land developers and are sometimes swindled into selling their land to occupiers. They have also mentioned that the establishment of the embankment has acted as a barrier to many tidal creeks and canals inland, causing flow diversion or discontinuous and reduced flow sedimentation. These problems invite further unobstructed encroachment by the sea.

While fluvial processes contribute considerably to seaward shoreline advancement through delta building, embankment/levee construction has hindered that process. On the other hand, establishment of the embankment reduces coastal erosion from waves, tides, ocean currents, and storm surges, thus protecting the coast from marine processes. It is difficult to evaluate which processes—fluvial or marine—contribute more toward coastal land formation and therefore the shoreline change. Not surprisingly, farmers emphasized the fluvial processes, which bring sediments to nourish their agricultural lands, while the fishermen are more concerned about marine processes.

CONCLUSION

Shoreline change in Bangladesh has great implications regarding coastal ecosystem health, biodiversity, economic livelihood, and land use practices. The people of the coastal area face the consequences of this change. Precise determination of the shoreline rates of change is needed to prepare for coastal hazards, risks, and land use planning (Nicholls and Klein, 2005).

Comparison between the shorelines of satellite images consistently showed that on a net basis from 1989 to 2020, erosional activity on the Bangladesh coast is more prominent than accretional activity. Regionally erosional, activity is more prominent in the western and central zone, and accretion occurs more in the eastern zone. Even though erosion was greater in the central zone (5.76 km^2) over the same period, it decreased gradually over time. Thus, spatial analysis along with the temporal representation of the dynamic coastline of Kuakata signifies that western and central parts of the shoreline are shifted inward noticeably. From 1989 to 2020, 3.27 km^2 of coastal land has been gained while 13.59 km^2 of land has been eroded across the Kuakata coastline. These results support those from previous research (Shibly and Takewaka, 2012; Bushra, 2013; Islam et al., 2013; Mitra et al., 2013; Rahman et al., 2013) that suggested that the shoreline retreat had been occurring in this area at least up to 2012. On a more encouraging note, in the last decades the accretion rate has increased and the erosion rate has decreased from the previous decades.

Application of PRA supports the quantitative results of shoreline change from satellite imagery by addressing the impacts of erosion, accretion, and stable shoreline along the Kuakata coast qualitatively. PRA provides information regarding the basis of this erosion and accretion and their effects on the coastal livelihood pattern. The implementation of PRA tools establishes the basis for describing the extent of economic and environmental effects of present shoreline erosion and accretion. PRA results imply that the establishment of the embankment protects the zones from erosional activities, while the presence of fluvial tidal creeks and sand dunes plays a greater role for the stable zones. Economic activities, especially fishing and tourism, are affected by the erosional effects of shoreline change. The local people identify marine and climatic factors as the main causes of the shoreline change. The key informants reported that monitoring and proper management are needed for future maintenance of the coast as the coastal area has attracted the attention of land developers, particularly because of the area's desirability as a tourist resort. Over the years, coastline retreat inland reduces the fishing activity while agricultural lands are also diminishing due to saltwater intrusion, loss of fertility due to sand aggregation and canals/creeks diversion, and land reclamation by the developer for commercial purposes. Collectively the information from this PRA implies that, on a net basis, the rate of erosion exceeds that of accretion along the coast of Kuakata. The PRA result that shoreline change,

specifically shoreline erosion, is such a concern, particularly due to its continuation over the years, provides hope that proper land management strategy, policy implementation, and appropriate risk reduction approaches, as well as social, behavioral, and communal responses, may be successful.

Accurate shoreline delineation is needed for application sciences (e.g., ship navigation, environmental change management, coastal development, and flood prediction). A comprehensive shoreline change analysis and its impact can be evaluated by applying technological approaches accompanied by on-the-scene input from local community members who observe the changes and their impacts daily. This research is important not only for measuring shoreline change over time, but for policy makers and land use managers for future land use planning related to costal shoreline change. Next steps in effective analysis may include monitoring the shoreline by means of repeated surveys to correct the seasonal variability induced by intense storms, with public input. More efficient methods for data extrapolation would reach an effective compromise between accuracy, cost, and time. Regardless, however, effective monitoring requires the development of technologies and social science approaches capable of providing useful contributions to enhance sustainability of this important coastal environment.

DATA AVAILABILITY STATEMENT

The raw data supporting the conclusions of this article will be made available by the authors, without undue reservation.

AUTHOR CONTRIBUTIONS

NB developed the methodology, collected and analyzed the data, and developed the initial text. RM provided assistance in data collection, organized the manuscript, edited the text, and revised the text to conform to reviewer recommendations. RR edited initial and late drafts of the text. CF revised the text. MR verified the calculations and edited the text. All authors contributed to the article and approved the submitted version.

FUNDING

This project has been completed as a requirement of a degree program under South Asian Water (SAWA) Fellowship Programme.

ACKNOWLEDGMENTS

We appreciate the assistance and support of A.K.M. Saiful Islam and Mashfiqus Salehin, professors of the Institute of Water and Flood Management (IWFM), Bangladesh University of Engineering and Technology (BUET), and Md. Ali Haider, Assoc. Prof., Department of Geography and Environmental Studies, University of Chittagong, for their guidance and suggestions throughout the course of this project work, and Kuakata's local people for their assistance in collecting field data and participating in PRA methods.

REFERENCES

Ahmed, A., Drake, F., Nawaz, R., and Woulds, C. (2018). Where is the coast? Monitoring coastal land dynamics in Bangladesh: an integrated management approach using GIS and remote sensing techniques. *Ocean Coast. Manag.* 151, 10–24. doi: 10.1016/j.ocecoaman.2017.10.030

Akter, J., Sarker, M. H., Popescu, I., and Roelvink, D. (2016). Evolution of the Bengal Delta and its prevailing processes. *J. Coast. Res.* 32, 1212–1226. doi: 10.2112/JCOASTRES-D-14-00232.1

Alam, G. M., Alam, K., Mushtaq, S., and Filho, W. L. (2018). How do climate change and associated hazards impact on the resilience of riparian rural communities in Bangladesh? Policy implications for livelihood development. *Environ. Sci. Policy* 84, 7–18. doi: 10.1016/j.envsci.2018.02.012

Ali, A. (2000). *Vulnerability of Bangladesh Coastal Region to Climate Change with Adaptation Options*. Dhaka: Bangladesh Space Research and Remote Sensing Organization (SPARRSO), 34–58.

Amin, S. M. N. (2008). *Studies on Coastal Environments in Bangladesh*. House: A.H. Development Publishing.

Balgah, R. A. (2016). Applying participatory rural appraisal to unlock gender group differences in some communities in rural Cameroon. *Asian J. Agric. Ext. Econ. Sociol.* 12, 1–11. doi: 10.9734/AJAEES/2016/28327

Bangladesh Bureau of Statistics (2009). *Statistical Yearbook of Bangladesh. Ministry of Planning, Government of Bangladesh, Dhaka, Bangladesh*. Available online at: http://203.112.218.65:8008/PageSiteMap1.aspx?MenuKey=7 (accessed July 18, 2021).

Barbaro, G., Fiamma, V., Barrile, V., Foti, G., and Ielo, G. (2017). Analysis of the shoreline changes of Reggio Calabria (Italy). *Int. J. Civil Eng. Technol.* 8, 1777–1791.

Barillà, G. C., Foti, G., Barbaro, G., and Puntorieri, P. (2020). "Shoreline changes of a pocket beach: a remote sensing application, Proc. SPIE 11524," in *Proceedings of the 8th International Conference on Remote Sensing and Geoinformation of the Environment (RSCy2020)*, Vol. 11524, (Bellingham, WA: International Society for Optics and Photonics), 1152425. doi: 10.1117/12.2571212

Boak, E. H., and Turner, I. L. (2005). Shoreline definition and detection: a review. *J. Coast. Res.* 21, 688–703. doi: 10.2112/03-0071.1

Bomer, E. J., Wilson, C. A., and Datta, D. K. (2019). An integrated approach for constraining depositional zones in a tide-influenced river: insights from the Gorai River, Southwest Bangladesh. *Water* 11:2047. doi: 10.3390/w11102047

Brammer, H. (2014). Bangladesh's dynamic coastal regions and sea-level rise. *Clim. Risk Manag.* 1, 51–62. doi: 10.1016/j.crm.2013.10.001

Brammer, H., Asaduzzaman, M., and Sultana, P. (1996). "Effects of climate and sea-level changes on the natural resources of Bangladesh," in *The Implications of Climate and Sea–Level Change for Bangladesh*, eds R. A. Warrick and Q. K. Ahmad (Dordrecht: Springer), 143–203. doi: 10.1007/978-94-009-0241-1

Broadus, J. M. (1993). "Possible impacts of, and adjustments to, sea level rise: the case of Bangladesh and Egypt," in *Climate and Sea Level Change: Observations, Projections and Implications*, eds R. A. Warrick, E. M. Barrow, and T. M. L. Wigley (Cambridge: Cambridge University Press), 263–275.

Brodnig, G., and Mayer-Schönberger, V. (2000). Bridging the gap: the role of spatial information technologies in the integration of traditional environmental knowledge and western science. *Electron. J. Inf. Syst. Dev. Ctries.* 1, 1–15. doi: 10.1002/j.1681-4835.2000.tb00001.x

Bushra, N. (2013). *Detecting Changes of Shoreline at Kuakata Coast Using RS-GIS Techniques and Participatory Approach. Post Graduate Diploma Project, Institute of Water and Flood Management, Bangladesh University of Engineering and Technology*. Available online at: http://lib.buet.ac.bd:8080/xmlui/handle/123456789/4186 (accessed June 24, 2021).

Bushra, N. (2016). *Modeling Tropical Cyclone Storm Surge and Wind Induced Risk along the Bay of Bengal Coastline Using a Statistical Copula*. LSU Master's Thesis. 251. Available online at: https://digitalcommons.lsu.edu/gradschool_theses/251 (accessed July 18, 2021).

Bushra, N., Islam, M. S., and Khan, A. U. (2014). Natural processes on coastal sand dune dynamics of Kuakata: a geographical analysis. *Dhaka Univ. J. Earth Environ. Sci.* 3, 9–14.

Bushra, N., Islam, M. S., and Khan, A. U. (2016). Dune morphology of Kuakata coast in Bangladesh. *J. NOAMI* 33, 91–102.

Bushra, N., Trepanier, J. C., and Rohli, R. V. (2019). Joint probability risk modelling of storm surge and cyclone wind along the coast of Bay of Bengal using a statistical copula. *Int. J. Climatol.* 39, 4206–4217. doi: 10.1002/joc.6068

Carlson, T. N., and Ripley, D. A. (1997). On the relation between NDVI, fractional vegetation cover, and leaf area index. *Remote Sens. Environ.* 62, 241–252. doi: 10.1016/S0034-4257(97)00104-1

Center for Climate Systems Research and The Earth Institute of Columbia Climate School (2006). *It's 2025. Where do most people live?* Available online at: https://www.earth.columbia.edu/articles/view/919 (accessed July 18, 2021).

Centre for Environmental and Geographic Information Services (CEGIS) (2009). *Monitoring Platform Developments in the EDP (Estuary Development Program) Area Using Remote Sensing, Dhaka, Bangladesh*. Available online at: https://www.cegisbd.com/ (accessed July 18, 2021).

Chambers, R. (1994). The origins and practice of participatory rural appraisal. *World Dev.* 22, 953–969. doi: 10.1016/0305-750X(94)90141-4

Chand, P., and Acharya, P. (2010). Shoreline change and sea level rise along coast of Bhitarkanika wildlife sanctuary, Orissa: an analytical approach of remote sensing and statistical techniques. *Int. J. Geomatics Geosci.* 1, 436–455.

Chen, L. C. (1998). Detection of shoreline changes for tideland areas using multi-temporal satellite images. *Int. J. Remote Sens.* 19, 3383–3397. doi: 10.1080/014311698214055

Chenais, E., Sternberg-Lewerin, S., Boqvist, S., Emanuelson, U., Aliro, T., Tejler, E., et al. (2015). African swine fever in Uganda: qualitative evaluation of three surveillance methods with implications for other resource-poor settings. *Front. Vet. Sci.* 2:51. doi: 10.3389/fvets.2015.00051

Deepika, B., Avinash, K., and Jayappa, K. S. (2014). Shoreline change rate estimation and its forecast: remote sensing, geographical information system and statistics-based approach. *Int. J. Environ. Sci. Technol.* 11, 395–416. doi: 10.1007/s13762-013-0196-1

Dixon, T. H., Amelung, F., Ferretti, A., Novali, F., Rocca, F., Dokka, R., et al. (2006). Subsidence and flooding in New Orleans. *Nature* 441, 587–588.

Dooley, K. E., Dobbins, C., and Edgar, L. D. (2018). Using participatory rural appraisal for a community needs assessment in Timor-Leste. *J. Int. Agric. Ext. Educ.* 25, 63–73. doi: 10.5191/jiaee.2018.25405

Dureab, F., Hussain, T., Sheikh, R., Al-Dheeb, N., Al-Awlaqi, S., and Jahn, A. (2021). Forms of health system fragmentation during conflict: the case of Yemen. *Front. Public Health* 9:805. doi: 10.3389/fpubh.2021.659980

Dwivedi, R. S., and Rao, B. R. M. (1992). The selection of the best possible Landsat TM band combination for delineating salt-affected soils. *Int. J. Remote Sens.* 13, 2051–2058. doi: 10.1080/01431169208904252

Elkoushy, A. A., and Tolba, E. R. A. (2003). *Prediction of Shoreline Change by Using Satellite Aerial Imagery*. Available online at: https://www.isprs.org/proceedings/XXXV/congress/yf/papers/1.pdf (accessed June 24, 2021).

Emran, A., Rob, M. A., and Kabir, M. H. (2019). "Coastline change and erosion-accretion evolution of the Sandwip Island, Bangladesh," in *Environmental Information Systems: Concepts, Methodologies, Tools, and Applications (pp. 1497-1509)*, (Hershey, PA: IGI Global). Available online at: https://www.igi-global.com/chapter/coastline-change-and-erosion-accretion-evolution-of-the-sandwip-island-bangladesh/213005 (accessed July 18, 2021).

Ericson, J. P., Vörösmarty, C. J., Dingman, S. L., Ward, L. G., and Meybeck, M. (2006). Effective sea-level rise and deltas: causes of change and human dimension implications. *Global Planet. Change* 50, 63–82. doi: 10.1016/j.gloplacha.2005.07.004

Foti, G., Barbaro, G., Bombino, G., Fiamma, V., Puntorieri, P., Minniti, F., et al. (2019). Shoreline changes near river mouth: case study of Sant'Agata River (Reggio Calabria, Italy). *Eur. J. Remote Sens.* 52 (Suppl. 4), 102–112. doi: 10.1080/22797254.2019.1686955

Gao, B. C. (1996). NDWI—A normalized difference water index for remote sensing of vegetation liquid water from space. *Remote Sens. Environ.* 58, 257–266. doi: 10.1016/S0034-4257(96)00067-3

Ghaderi, D., and Rahbani, M. (2020). Detecting shoreline change employing remote sensing images (Case study: Beris Port-east of Chabahar, Iran). *Int. J. Coast. Offshore Eng.* 3, 1–8.

Goodbred, S. L. Jr., and Kuehl, S. A. (1999). Holocene and modern sediment budgets for the Ganges-Brahmaputra river system: evidence for highstand dispersal to flood-plain, shelf, and deep-sea depocenters. *Geology* 27, 559–562.

Hanebuth, T. J. J., Kudrass, H. R., Linstädter, J., Islam, B., and Zander, A. M. (2013). Rapid coastal subsidence in the central Ganges-Brahmaputra Delta (Bangladesh) since the 17th century deduced from submerged salt-producing kilns. *Geology* 41, 987–990. doi: 10.1130/G34646.1

Holme, R., and Chalauisaeng, B. (2006). The learner as needs analyst: the use of participatory appraisal in the EAP reading classroom. *Engl. Specif. Purp.* 25, 403–419. doi: 10.1016/j.esp.2006.01.003

Huang, S., Tang, L., Hupy, J. P., Wang, Y., and Shao, G. (2021). A commentary review on the use of normalized difference vegetation index (NDVI) in the era of popular remote sensing. *J. For. Res.* 32, 1–6. doi: 10.1007/s11676-020-01155-1

Huq, S. U., Ahmed, A. U., and Koudstaal, R. (1996). "Vulnerability of Bangladesh to climate change and sea level rise," in *In Climate Change and World Food Security*, ed. T. E. Downing Vol. 37, (Berlin: Springer), 347–379. doi: 10.1007/978-3-642-61086-8_14

Ikeuchi, H., Hirabayashi, Y., Yamazaki, D., Muis, S., Ward, P. J., Winsemius, H. C., et al. (2017). Compound simulation of fluvial floods and storm surges in a global coupled river-coast flood model: model development and its application to 2007 Cyclone Sidr in Bangladesh. *J. Adv. Model. Earth Syst.* 9, 1847–1862. doi: 10.1002/2017MS000943

Islam, A. Z. M. Z., Kabir, S. M. H., and Sharifee, M. N. H. (2013). High-tide coastline method to study the stability of Kuakata coast of Bangladesh using remote sensing techniques. *Asian J. Geoinform.* 13, 23–29.

Koeva, M., Stöcker, C., Crommelinck, S., Ho, S., Chipofya, M., Sahib, J., et al. (2020). Innovative remote sensing methodologies for Kenyan land tenure mapping. *Remote Sens.* 12:273. doi: 10.3390/rs12020273

Kukielka, E. A., Jori, F., Martínez-López, B., Chenais, E., Masembe, C., Chavernac, D., et al. (2016). Wild and domestic pig interactions at the wildlife–livestock interface of Murchison Falls national Park, Uganda, and the potential association with African swine fever outbreaks. *Front. Vet. Sci.* 3:31. doi: 10.3389/fvets.2016.00031

Kumaravel, S., Ramkumar, T., Gurunanam, B., Suresh, M., and Dharanirajan, K. (2013). An application of remote sensing and GIS based shoreline change studies–a case study in the Cuddalore District, East Coast of Tamilnadu, South India. *Int. J. Innov. Technol. Explor. Eng. (IJITEE)* 2, 211–215.

Maiti, S., and Bhattacharya, A. K. (2009). Shoreline change analysis and its application to prediction: a remote sensing and statistics based approach. *Mar. Geol.* 257, 11–23. doi: 10.1016/j.margeo.2008.10.006

Makota, V., Sallema, R., and Mahika, C. (2004). Monitoring shoreline change using remote sensing and GIS: a case study of Kunduchi area, Tanzania. *Western Indian Ocean J. Mar. Sci.* 3, 1–10.

Mavraeidopoulos, A. K., Oikonomou, E., Palikaris, A., and Poulos, S. (2019). A hybrid bio-optical transformation for satellite bathymetry modeling using sentinel-2 imagery. *Remote Sens.* 11:2746. doi: 10.3390/rs11232746

Mialhe, F., Gunnell, Y., Ignacio, J. A. F., Delbart, N., Ogania, J. L., and Henry, S. (2015). Monitoring land-use change by combining participatory land-use maps with standard remote sensing techniques: showcase from a remote forest catchment on Mindanao, Philippines. *Int. J. Appl. Earth Observ. Geoinform.* 36, 69–82. doi: 10.1016/j.jag.2014.11.007

Mitra, M. C., Rahman, M. A., and Bin-Shafique, S. (2013). "Erosion of Kuakata Beach and its protection by beach nourishment," in *Proceedings of the 23rd International Offshore and Polar Engineering Conference. International Society of Offshore and Polar Engineers*. Available online at: https://onepetro.org/ISOPEIOPEC/proceedings-abstract/ISOPE13/All-ISOPE13/ISOPE-I-13-511/13516 (accessed July 18, 2021).

Mostafiz, R. B., Friedland, C. J., Rohli, R. V., and Bushra, N. (2020a). "Assessing property loss in Louisiana, U.S.A., to natural hazards incorporating future projected conditions," in *American Geophysical Union Conference, NH015-002*. Available online at: https://ui.adsabs.harvard.edu/abs/2020AGUFMNH0150002M/abstract (accessed July 18, 2021).

Mostafiz, R. B., Friedland, C. J., Rohli, R. V., Gall, M., Bushra, N., and Gilliland, J. M. (2020b). Census-block-level property risk estimation due to extreme cold temperature, hail, lightning, and tornadoes in Louisiana, United States. *Front. Earth Sci.* 8:521. doi: 10.3389/feart.2020.601624

Mueller, J. G., Assanou, I. H. B., Guimbo, I. D., and Almedom, A. M. (2010). Evaluating rapid participatory rural appraisal as an assessment of ethnoecological knowledge and local biodiversity patterns. *Conserv. Biol.* 24, 140–150. doi: 10.1111/j.1523-1739.2009.01392.x

Mujabar, P. S., and Chandrasekar, N. (2013). Shoreline change analysis along the coast between Kanyakumari and Tuticorin of India using remote sensing and GIS. *Arab. J. Geosci.* 6, 647–664. doi: 10.1007/s12517-011-0394-4

Mukherjee, N., Siddique, G., Basak, A., Roy, A., and Mandal, M. H. (2019). Climate change and livelihood vulnerability of the local population on Sagar Island, India. *Chin. Geograph. Sci.* 29, 417–436. doi: 10.1007/s11769-019-1042-2

Mukhopadhyay, A., Mukherjee, S., Ghosh, S., Hazra, S., and Mitra, D. (2012). Automatic shoreline detection and future prediction: a case study on Puri Coast, Bay of Bengal, India. *Eur. J. Remote Sens.* 45, 201–213. doi: 10.5721/EuJRS20124519

Ng, Y. P., Pheh, K. S., Panirselvam, R. R., Chan, W. L., Lim, J. B. Y., Lim, J. T. Y., et al. (2021). Malaysian stakeholder perspectives on suicide-related reporting: findings from focus group discussions. *Front. Psychol.* 12:1745. doi: 10.3389/fpsyg.2021.673287

Nicholls, R. J., and Klein, R. J. T. (2005). "Climate change and coastal management on Europe's coast," in *Managing European Coasts, 199-226. Environmental Science*, eds J. Vermaat, W. Salomons, L. Bouwer, and K. Turner (Berlin: Springer). doi: 10.1007/3-540-27150-3_11

Nicholson, J., and Valentine, A. (2019). Key informants specify core elements of peer supports for parents with serious mental illness. *Front. Psychiatry* 10:106. doi: 10.3389/fpsyt.2019.00106

Niya, A. K., Alesheikh, A. A., Soltanpor, M., and Kheirkhahzarkesh, M. M. (2013). Shoreline change mapping using remote sensing and GIS case study: Bushehr Province. *Int. J. Remote Sens. Appl.* 3, 102–107.

Oppenheimer, M., Glavovic, B. C., Hinkel, J., van de Wal, R., Magnan, A. K., Abd-Elgawad, A., et al. (2019). "Sea level rise and implications for low-lying Islands, coasts and communities," in *IPCC Special Report on the Ocean and Cryosphere in a Changing Climate*, eds H. O. Poñrtner, D. C. Roberts, V. Masson-Delmotte, P. Zhai, M. Tignor, and E. Poloczanska. Available online at: https://www.ipcc.ch/srocc/chapter/chapter-4-sea-level-rise-and-implications-for-low-lying-islands-coasts-and-communities/ (accessed June 24, 2021).

Paul, A., and Rahman, M. (2006). Cyclone mitigation perspectives in the Islands of Bangladesh: a case of Sandwip and Hatia Islands. *Coast. Manag.* 34, 199–215. doi: 10.1080/08920750500531371

Penning-Rowsell, E. C., Sultana, P., and Thompson, P. M. (2013). The 'last resort'? Population movement in response to climate-related hazards in Bangladesh. *Environ. Sci. Policy* 27, S44–S59. doi: 10.1016/j.envsci.2012.03.009

Pritam, C., and Prasenjit, A. (2010). Shoreline change and sea level rise along coast of Bhitarkanika wildlife sanctuary, Orissa: an analytical approach of remote sensing and statistical techniques. *Int. J. Geomatics Geosci.* 1, 436–455.

Puri, S. K. (2007). Integrating scientific with indigenous knowledge: constructing knowledge alliances for land management in India. *MIS Q.* 355–379.

Rahman, M. A., Mitra, M. C., and Akter, A. (2013). Investigation on erosion of Kuakata sea beach and its protection design by artificial beach nourishment. *J. Civil Eng. (IEB)* 41, 1–12.

Rahman, M. M. (1999). *Analysis of the Beach Materials at the Kuakata Coast. M. Eng. Thesis, Department of Water Resources Engineering, Bangladesh University of Engineering and Technology*. Available online at: http://lib.buet.ac.bd:8080/xmlui/handle/123456789/276 (accessed June 25, 2021).

Roothaert, R., Mpogole, H., Hunter, D., Ochieng, J., and Kejo, D. (2021). Policies, multi-stakeholder approaches and home-grown school feeding programs for improving quality, equity and sustainability of school meals in northern Tanzania. *Front. Sustain. Food Syst.* 5:43. doi: 10.3389/fsufs.2021.621608

Saja, P., Woźny, A., and Bednarova, L. (2021). Risk management in the context of COVID-19 pandemic in an enterprise–Ishikawa cause-and-effect diagram. *Syst. Saf.* 3, 253–259. doi: 10.2478/czoto-2021-0026

Sarwar, M. G. M. (2013). "Sea-level rise along the coast of Bangladesh," in *Disaster Risk Reduction Approaches in Bangladesh*, eds R. Shaw, F. Mallick, and A. Islam (Tokyo: Springer), 217–231.

Sarwar, M. G. M., and Woodroffe, C. D. (2013). Rates of shoreline change along the coast of Bangladesh. *J. Coast. Conserv.* 17, 515–526. doi: 10.1007/s11852-013-0251-6

Schäffler, L., Kappeler, P. M., and Halley, J. M. (2021). Mouse lemurs in an assemblage of Cheirogaleid primates in Menabe Central, Western Madagascar–three reasons to coexist. *Front. Ecol. Evol.* 9:149. doi: 10.3389/fevo.2021.585781

Shamsuddin, M., Alam, M. M., Hossein, M. S., Goodger, W. J., Bari, F. Y., Ahmed, T. U., et al. (2007). Participatory rural appraisal to identify needs and prospects of market-oriented dairy industries in Bangladesh. *Trop. Anim. Health Prod.* 39, 567–581. doi: 10.1007/s11250-007-9062-9

Shibly, A. M., and Takewaka, S. (2012). Morphological changes along Bangladesh coast derived from satellite images. *Proc. Coast. Eng.* 3, 41–45.

Su, H., Peng, Y., Xu, C., Feng, A., and Liu, T. (2021). Using improved DeepLabv3+ network integrated with normalized difference water index to extract water bodies in Sentinel-2A urban remote sensing images. *J. Appl. Remote Sens.* 15:018504. doi: 10.1117/1.JRS.15.018504

Sutikno, S., Hidayati, N., Rinaldi, Nasrul, B., Putra, A., and Qomar, N. (2020). "Classification of tropical peatland degradation using remote sensing and GIS technique," in *Proceedings of the AIP Conference Proceedings*, Vol. 2255, (Melville, NY: AIP Publishing LLC), 070022. doi: 10.1063/5.0013881

Tomlinson, K. R., Bailey, A. M., Alicai, T., Seal, S., and Foster, G. D. (2018). Cassava brown streak disease: historical timeline, current knowledge and future prospects. *Mol. Plant Pathol.* 19, 1282–1294. doi: 10.1111/mpp.12613

Tran Thi, V., Tien Thi Xuan, A., Phan Nguyen, H., Dahdouh-Guebas, F., and Koedam, N. (2014). Application of remote sensing and GIS for detection of long-term mangrove shoreline changes in Mui Ca Mau, Vietnam. *Biogeosciences* 11, 3781–3795. doi: 10.5194/bg-11-3781-2014

United States Geological Survey (USGS) (2021). *What are the Acquisition Schedules for the Landsat Satellites?* Available online at: https://www.usgs.gov/faqs/what-are-acquisition-schedules-landsat-satellites?qt-news_science_products=0#qt-news_science_products (accessed July 18, 2021).

United States Geological Survey (2020). *Landsat 8 Band Designations*. Available online at: https://www.usgs.gov/media/images/landsat-8-band-designations (accessed June 24, 2021).

Wilson, C. A., and Goodbred, S. L. Jr. (2015). Construction and maintenance of the Ganges-Brahmaputra-Meghna delta: linking process, morphology, and stratigraphy. *Annu. Rev. Mar. Sci.* 7, 67–88. doi: 10.1146/annurev-marine-010213-135032

Yulianto, F., Suwarsono, S., Maulana, T., and Khomarudin, M. R. (2019). The dynamics of shoreline change analysis based on the integration of remote sensing and geographic information system (GIS) techniques in Pekalongan coastal area, Central Java, Indonesia. *J. Degraded Min. Lands Manag.* 6, 1789–1802. doi: 10.15243/jdmlm.2019.063.1789

Zagorski, P., Jarosz, K., and Superson, J. (2020). Integrated assessment of shoreline change along the Calypsostranda (Svalbard) from remote sensing, field survey and GIS. *Mar. Geodesy* 43, 433–471. doi: 10.1080/01490419.2020.1715516

Zaman, S., Sujauddin, M., and Khan, N. A. (2018). "Assessment of the climate change-induced vulnerabilities of coastal regions and adaptation practices of arable agriculture in Bangladesh," in *The Environmental Sustainable Development Goals in Bangladesh*, eds S. A. Selim, S. K. Saha, R. Sultana, and C. Roberts (London: Routledge), 69–82.

Conflict of Interest: The authors declare that the research was conducted in the absence of any commercial or financial relationships that could be construed as a potential conflict of interest.

Publisher's Note: All claims expressed in this article are solely those of the authors and do not necessarily represent those of their affiliated organizations, or those of the publisher, the editors and the reviewers. Any product that may be evaluated in this article, or claim that may be made by its manufacturer, is not guaranteed or endorsed by the publisher.

frontiers in Marine Science

ORIGINAL RESEARCH
published: 14 October 2021
doi: 10.3389/fmars.2021.713039

Critical Shear Stress for Erosion of Sand-Mud Mixtures and Pure Mud

Dake Chen[1,2,3,4†], Jinhai Zheng[1], Chi Zhang[5†], Dawei Guan[2], Yuan Li[2] and Yigang Wang[2]*

[1] Key Laboratory of Coastal Disaster and Protection (Hohai University), Ministry of Education, Nanjing, China, [2] College of Harbour, Coastal and Offshore Engineering, Hohai University, Nanjing, China, [3] State Key Laboratory of Coastal and Offshore Engineering, Dalian University of Technology, Dalian, China, [4] State Key Laboratory of Estuarine and Coastal Research, East China Normal University, Shanghai, China, [5] State Key Laboratory of Hydrology-Water Resources and Hydraulic Engineering, Nanjing, China

The erosion threshold of sand-mud mixtures is investigated by analyzing the momentum balance of a sand particle or a mud parcel in the mixture bed surface, and a formula for the critical shear stress of sand-mud mixtures is developed, which also applies for pure sand and mud. The developed formula suggests that the variation of the critical shear stress of sand-mud mixtures over mud content is mainly caused by the varying dry bulk density of the mud component in the mixture. The developed formula reproduces well the variation of the critical shear stress of sand-mud mixtures over mud content and can predict the critical shear stress of both sand-mud mixtures and pure mud in the process of consolidation. The developed formula promises to be convenient for application by relating the critical shear stress to mud content and the dry bulk density of sediment.

Keywords: critical shear stress, erodibility of sediment, erosion threshold, mixed sediment, mud, sand-mud mixtures, multi-fraction sediment

OPEN ACCESS

Edited by:
Felice D'Alessandro, University of Milan, Italy

Reviewed by:
Liqin Zuo, Nanjing Hydraulic Research Institute, China
Eugeny Buldakov, University College London, United Kingdom

****Correspondence:***
Chi Zhang
zhangchi@hhu.edu.cn

†ORCID:
Dake Chen
orcid.org/0000-0002-5160-589X
Chi Zhang
orcid.org/0000-0003-2708-4286

Specialty section:
This article was submitted to Coastal Ocean Processes, a section of the journal Frontiers in Marine Science

Received: *21 May 2021*
Accepted: *23 September 2021*
Published: *14 October 2021*

Citation:
Chen D, Zheng J, Zhang C, Guan D, Li Y and Wang Y (2021) Critical Shear Stress for Erosion of Sand-Mud Mixtures and Pure Mud. Front. Mar. Sci. 8:713039. doi: 10.3389/fmars.2021.713039

INTRODUCTION

The erosion of sediment is one of the controlling processes of sediment dynamics in aquatic systems. It concerns various domains, including geomorphology, pollutant transport, dredging activities, scour around structures, landward retreat of shorelines, bank failure, etc. (Sanford and Maa, 2001; Mostafa et al., 2008; Chen et al., 2017; Kurdistani et al., 2019; Zheng et al., 2020; Li et al., 2021). Assessment of the erodibility of sediment has therefore been of interest to numerous scientists and engineers. The particle size is one of the most critical factors affecting the erodibility of sediment. According to the particle size, sediments can be classified into gravel, sand, silt, and clay. Coarse-grained sediments, such as coarse silt, sand and gravel, are usually non-cohesive. Sediments comprised primarily of fine silt and clay exhibit cohesion, and therefore are often referred to as cohesive sediments or mud (Mehta and Partheniades, 1982; Van Rijn, 1993). The physicochemical properties of non-cohesive sediment and cohesive sediment are strikingly different. As a result, the erodibilities of non-cohesive and cohesive sediments have been separately studied in the past several decades (Van Ledden et al., 2004; Le Hir et al., 2011).

Non-cohesive sediment is eroded as individual particles. The erosion resistance of non-cohesive sediment is mainly provided by the submerged weight of the sediment, which leads to express the erosion threshold as a function of the size, shape and density of the particles (Miller et al., 1977; Chiew and Parker, 1994). For cohesive sediment, the interparticle attractive force coming from electrochemical effects is much more significant than the gravitational force and plays a dominant role in the erosional behavior and property (Righetti and Lucarelli, 2007). Experimental

studies have shown that cohesive sediment is eroded as aggregates (i.e., surface erosion) at low bed shear stresses and as lumps or chunks of bed material (i.e., mass/bulk erosion) at high bed shear stresses (Partheniades, 1965; Mehta, 1989; Sanford and Maa, 2001; Winterwerp et al., 2012). The erosion threshold of cohesive sediment has been found to increase with increasing degree of compactness of sediment when other physicochemical properties of the sediment are controlled. Some empirical relationships were also developed between the critical shear stress and physical properties of cohesive sediments, including wet or dry bulk density (Tang, 1963; Owen, 1970; Dou, 2000; Amos et al., 2004; Xu et al., 2015; Zuo et al., 2017), water content (Jacobs et al., 2011), solid volume fraction (Kusuda et al., 1984; Mehta and Parchure, 2000), solid/void volume ratio (Wu et al., 2017) and yield stress (Zhang and Yu, 2017; Zhang et al., 2017). As the erodibility of cohesive sediment is also affected by factors like mineralogy, pore water chemistry, temperature, organic content, biological actions, etc., those relationships between the erosion threshold and the physical properties are often modified by these influences. Summaries on the theories and models for predicting the erosion threshold and rate of non-cohesive and cohesive sediments could be found in the studies of Zhu et al. (2008); Le Hir et al. (2011), and Chen et al. (2018, 2021).

In many natural environments, e.g., estuary, delta, mangrove forests, muddy and silty coasts, non-cohesive sediment and cohesive sediment are not completely separated and often occur as sand-mud mixtures (Carniello et al., 2012; Mehta and Letter, 2013). Compared with pure sand and pure mud, the erodibility of sand-mud mixtures has not been well-understood. A few experiments have been conducted to investigate the erodibility of sand-mud mixtures in the past decades (Torfs, 1995; Panagiotopoulos et al., 1997; Sharif, 2003; Le Hir et al., 2008; Jacobs et al., 2011; Ye et al., 2011; Smith et al., 2015; Van Rijn, 2020). These experiments have shown that sand-mud mixtures behave like cohesive sediments if they contain enough cohesive particles, otherwise like non-cohesive sediments (Torfs, 1995; Panagiotopoulos et al., 1997). The critical shear stress of sand-mud mixtures has been found significantly correlated to mud content. For non-cohesive mixtures, the critical shear stress generally increases with increasing mud content (Torfs, 1995; Le Hir et al., 2008; Smith et al., 2015). In some cases, a slight decrease in the sand threshold was sometimes observed for very low mud fractions (Torfs et al., 2000; Barry et al., 2006). Barry et al. (2006) attributed this decrease to viscous lubrication induced by clay-sized particles in the bed pore fluid. For cohesive mixtures, the critical shear stress increases monotonously with increasing mud content or firstly increases with mud content up to an optimum mud content then decreases slowly with further increasing mud content until 100% mud (Nalluri and Alvarez, 1992; Sharif, 2003; Ye et al., 2011; Smith et al., 2015; Van Rijn, 2020).

Those experiments of sand-mud mixtures have shown that the mixtures behave differently from pure sand and pure mud. Applying the formulae developed for pure sand and pure mud to sand-mud mixtures would induce massive errors. Van Ledden (2003) developed an empirical formula for the critical shear stress of sand-mud mixtures, which is expressed as a function of the mud content, the critical mud content, the critical shear stresses of pure sand and pure mud:

$$\tau_{cr} = \begin{cases} \tau_{crs}\left(1+p_m\right)^{\beta_v}, p_m \le p_{mcr} \\ \frac{\tau_{crs}\left(1+p_{mcr}\right)^{\beta_v}-\tau_{crm}}{1-p_{mcr}}\left(1-p_{mcr}\right)+\tau_{crm}, p_m > p_{mcr} \end{cases} \quad (1)$$

where τ_{cr} is the critical shear stress of sand-mud mixtures; p_m is mud content; p_{mcr} is the critical mud content (about 10–15%), below which the mixture is cohesionless and above which the mixture exhibits cohesion; τ_{crs} and τ_{crm} are the critical shear stresses of pure sand and pure mud, respectively; β_v is an empirical coefficient between 0.75 and 1.25. Ahmad et al. (2011) developed a similar formula for the critical shear stress of sand-mud mixtures. Compared with the formula of Van Ledden (2003), their formula is simpler:

$$\tau_{cr} = e^{\zeta\left(1-1/p_s\right)}\tau_{crs} + \left(1-p_s\right)\tau_{crm} \quad (2)$$

where p_s is sand content (i.e., the fraction of sand in the mixture); and ζ is an empirical coefficient between 0.1 and 0.2. The formulae of Van Ledden (2003) and Ahmad et al. (2011) involve the critical shear stress of pure mud. However, both Van Ledden (2003) and Ahmad et al. (2011) did not give a solution to determine the critical shear stress of pure mud for a given sand-mud mixture, which limits the application of their formulae in practice. Recently, Wu et al. (2017) developed a formula for the critical shear stress of sand-mud mixtures by analyzing the force balance on a sediment parcel beginning to erode from the bed surface:

$$\tau_{cr} = \tau_{crL} + \left(\tau_{crmc} - \tau_{crL}\right)\exp\left[-\alpha\left(\frac{p_s}{p_m}\right)^{\beta_w}\right] \quad (3)$$

where τ_{crL} is the critical shear stress for mixtures with low mud contents, $\tau_{crL} = \tau_{crs} + 1.25\left(\tau_{crmc} - \tau_{crs}\right)\min\left(p_m, 0.05\right)$; τ_{crmc} is the critical shear stress for erosion of mud corresponding to the porosity of the mud component in a sediment mixture; α and β_w are two coefficients. The value of α is related to the sand median diameter d_s : $\alpha = 0.42\exp\left(-3380d_s\right)$. The value of β_w is set as constant 1.2. Wu et al. (2017) assumed τ_{crmc} could be calculated by the formula for the critical shear stress of pure mud. Based on their collected data of pure mud, they developed an empirical formula for the critical shear stress of pure mud:

$$\tau_{cr} = 10.29r^{1.7} \quad (4)$$

where r is the solid/void volume ratio, $r = \left(1-\phi_m\right)/\phi_m$, with ϕ_m being the mud porosity. As the coefficient 10.29 in Eq. (4) may vary for different muds, Wu et al. (2017) suggested τ_{crmc} could be calculated by:

$$\tau_{crmc} = \tau_{crc}\left(\frac{r}{r_c}\right)^{1.7} \quad (5)$$

where τ_{crc} is a known critical shear stress for reference, which can be the critical shear stress in the case of 100% mud or another high mud content if the pure mud is not tested; r_c is the solid/void volume ratio of the mixture/mud corresponding to the reference critical shear stress. Chen et al. (2018) also developed a formula

for the critical shear stress of sand-mud mixtures based on the analysis of the balance of forces on a single particle of the mixture:

$$\tau_{cr} = \theta_{cr0}\left(\rho_s - \rho\right) gd + \theta_{cr1}\rho\frac{1}{d_m}\left(\frac{\rho_{sdm}}{\rho_{pm}}\right)\left(\frac{1}{\rho_{sdm}}\frac{p_m\rho_d\rho_{ps}}{\rho_{ps} - p_s\rho_d}\right)^{m+1} \quad (6)$$

where d and ρ_s are the representative size and density of primary particles of the mixture, respectively; θ_{cr0} is the critical Shields parameter of non-cohesive sediment which is of a diameter d and particle density ρ_s ; ρ is density of water; d_m and ρ_{pm} are the diameter and density of primary particles of the mud component of the mixture, respectively; ρ_d is the dry bulk density of the mixture; ρ_{ps} is the density of sand particles; ρ_{sdm} is the stable dry bulk density of the mud component (which is the dry bulk density of the mud component when it gets fully consolidated); θ_{cr1} and m are coefficients, $\theta_{cr1} = 6.20 \times 10^{-8}$ m^3 s^{-2} and $m = 1.55$. The formula of Chen et al. (2018) applies not only to sand-mud mixtures but also to pure sand and mud. However, the stable dry bulk density of the mud component involved in the formulation is difficult to determine for a given sand-mud mixture, limiting the application of their formula.

The present study aims to develop a formula for the critical shear stress of sand-mud mixtures. The developed formula promises to be simple and easily applied in practice. It also should cover the full range of the mud content, i.e., it applies for pure sand, pure mud and sand-mud mixtures. The formula development, testing and discussion are described in the following sections.

THEORETICAL FRAMEWORK FOR INCIPIENT MOTION CONDITION OF SAND-MUD MIXTURES

Particle Cohesion

The cohesion between the fine-grained particles arises from electrochemical effects and is often modulated by biochemical factors (e.g., mucopolysaccharide binding) (Mehta and Lee, 1994). The biochemical effect is not considered in this study, leaving a focus on the particle cohesion from electrochemical actions. The fine-grained particles usually carry net negative charges which attract cations in water to form a double-layer water film coating the particles. The coating water film cannot transfer hydrostatic pressure. Therefore, the water pressure would induce an additional force acting on the overlapping area when the water films coating the neighboring particles overlap. This additional force induced by water pressure has been verified by the experiment with cross-quartz fibers (Deriagin and Malkin, 1950). Some researchers have considered the additional force induced by water pressure as one of the origins of the cohesive force between fine-grained particles (e.g., Dou, 1962, 2000; Han, 1982; Zhang, 2012). Since there is a fundamental difference between the force induced by water pressure and the cohesive force arising from electrochemical actions, we prefer to consider them two different forces. The additional force induced by water pressure is not taken into account in this study because most of the existing erosion tests of sand–mud mixtures and pure mud were conducted in small-depth water flumes.

The van der Waals attraction has been generally believed to be responsible for particle cohesion from electrochemical effects in cohesive sediments (Han, 1982; Lick et al., 2004; Righetti and Lucarelli, 2007; Ternat et al., 2008). For two spherical particles of equal diameter, the van der Waals force f_c between them is given by (Hamaker, 1937):

$$f_c = \frac{A_h}{24}d_m\frac{1}{l_\Delta^2} \quad (7)$$

where d_m is the diameter of the cohesive particles; l_Δ is the separation distance between two particles (i.e., the smallest distance between the surfaces of the particles); A_h is the Hamaker constant which reflects the strength of the van der Waals force, with its value typically between 10^{-19} and 10^{-21} J. The Hamaker constant A_h is a function of the interacting particles and the intervening medium (Mehta, 2014). Therefore, its value is site-specific as the mineral compositions and pore water environments of cohesive sediments from different sites are usually different.

The van der Waals force is a short-range force with its effective acting range typically within ∼0.1 μm (Hoath, 2016). As the fine cohesive particles usually form loosely structures called aggregates or flocs, the separation distance between neighboring particles could be far larger than the effective acting range of the van der Waals force, i.e., the van der Waals force is not always effective between neighboring particles. Studies have shown that the van der Waals force is significant between two contacted cohesive particles and negligible between two particles not contacted directly (Han, 1982). **Figure 1** shows the distinction between a separation distance between two contacted particles (l_Δ) and a separation distance between two neighboring particles that are not contacted with each other (i.e., $s - d_m$ in which s is the distance between two neighboring particles). The separation distance between two contacted particles is generally on the same order of magnitude as the thickness of the water films coating the fine particles. The average separation distance $s - d_m$ between neighboring particles is usually on the same order of magnitude as the particle diameter. During the consolidation of cohesive sediment, the particle packing becomes dense and the cohesive force gets enhanced. Therefore, the average separation distance between two contacted particles is positively correlated to the average separation distance between two neighboring particles. And the two average separation distances decrease with increasing the compactness degree of the sediment. As a first approximation, it is assumed that the dimensionless average separation distance l_Δ/δ (where δ is the thickness of the water film coating the cohesive particles) between two contacted particles is proportional to the dimensionless average separation distance $\left(s - d_m\right)/d_m$ between neighboring particles, i.e.,

$$\frac{l_\Delta}{\delta} = \eta\frac{s - d_m}{d_m} \quad (8)$$

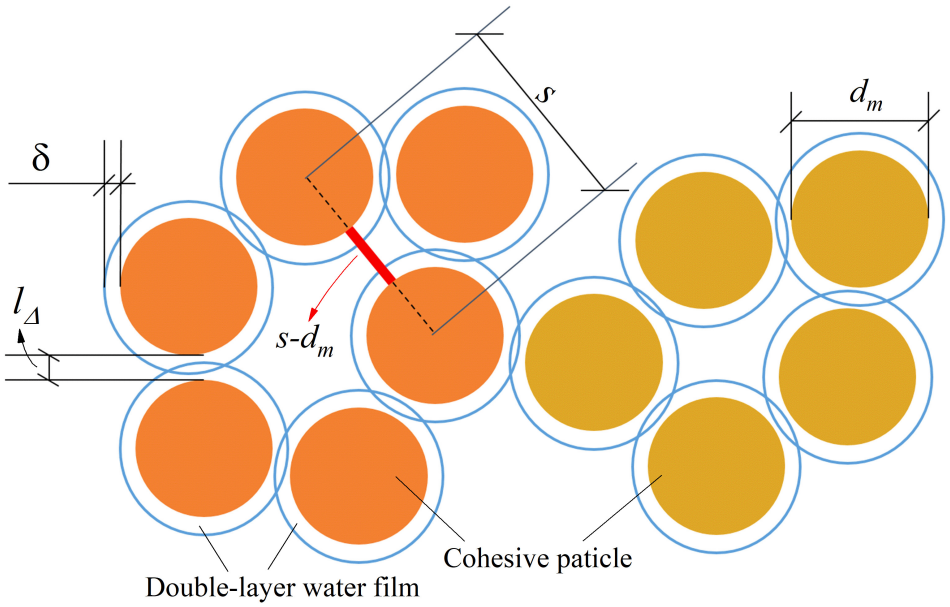

FIGURE 1 | The distinction between a separation distance between two contacted particles (l_Δ) and a separation distance between two neighboring particles not contacted with each other ($s - d_m$).

where η is a coefficient.

The average (center-to-center) distance between neighboring particles s could be estimated from the dry bulk density of the mud component (Ternat et al., 2008):

$$\frac{d_m^3}{s^3} = \frac{\rho_{dm}}{\rho_{pm}} \tag{9}$$

Substituting Eqs. (8, 9) into Eq. (7), the van der Waals force between two contacted cohesive particles could be estimated by:

$$f_c = \frac{A_h}{24\eta^2\delta^2} d_m \left[\left(\frac{\rho_{dm}}{\rho_{pm}} \right)^{-1/3} - 1 \right]^{-2} \tag{10}$$

Incipient Motion Analysis of Sand-Mud Mixtures

The erosion behavior of sand-mud mixtures has been found related to the network structure of mixtures (Van Ledden et al., 2004; Jacobs et al., 2011; Wu et al., 2017). There are two typical network structures of sand-mud mixtures. When the mud content is low, the sand particles contact each other and form a skeleton, with the mud particles filling the voids formed between the sand grains (**Figure 2A**). This kind of mixture (referring to as sand-dominated mixtures hereafter) behaves as non-cohesive or less cohesive (Torfs, 1995; Van Ledden et al., 2004; Wu et al., 2017). The erosion process of these mixtures is governed by the sand component and occurs in the form of the detachment of particles of sand and flocs of mud. When the mud content is high, there are sufficient mud particles to prevent grain-to-grain contact of the sand particles, and consequently, the sand particles lose contact with each other and "float" in the mud matrix (**Figure 2B**). This kind of mixture (called mud-dominated mixtures hereafter) behaves as cohesive and the typical two erosion modes of cohesive sediment can occur (Torfs, 1995; Smith et al., 2015; Wu et al., 2017).

Consider a flat horizontal sand-dominated mixture bed and a flat horizontal mud-dominated mixture bed exposed to unidirectional flow. The erosion processes of the sand-dominated mixtures and the mud-dominated mixtures are, respectively, governed by the sand component and the mud component (Torfs, 1995; Van Ledden et al., 2004; Wu et al., 2017). Here we take the detachment of a sand particle in the bed surface as the incipient motion criterion of the sand-dominated mixtures and the entrainment of a cohesive sediment parcel (which may be a cohesive sediment floc or aggregate) in the bed surface as the incipient motion criterion of the mud-dominated mixtures.

The sand particles in sand-dominated mixtures have been found usually coated by a thin layer of the mud particles (Revil et al., 2002; Duteil et al., 2020; Van Rijn, 2020; Worden et al., 2020). The phenomenon is often documented as grain coating and ascribed to the adhesive force (the attraction/bonding between two particles of different media), diagenesis, biological actions, etc. (Duteil et al., 2020; Worden et al., 2020). Here, we assume that the sand particles in the sand-dominated mixtures are coated by a thin layer of the mud particles, and when a sand particle is disrupted from the bed surface, the coating layer is entrained together with the sand particle (**Figure 3**). This assumption has an advantage that in the analysis of the incipient motion of the sand particle, the adhesive forces between the sand particle and mud particles could be left out of consideration, which makes it easier to study the incipient motions of the sand-dominated mixtures and the mud-dominated mixtures in the same theoretical framework.

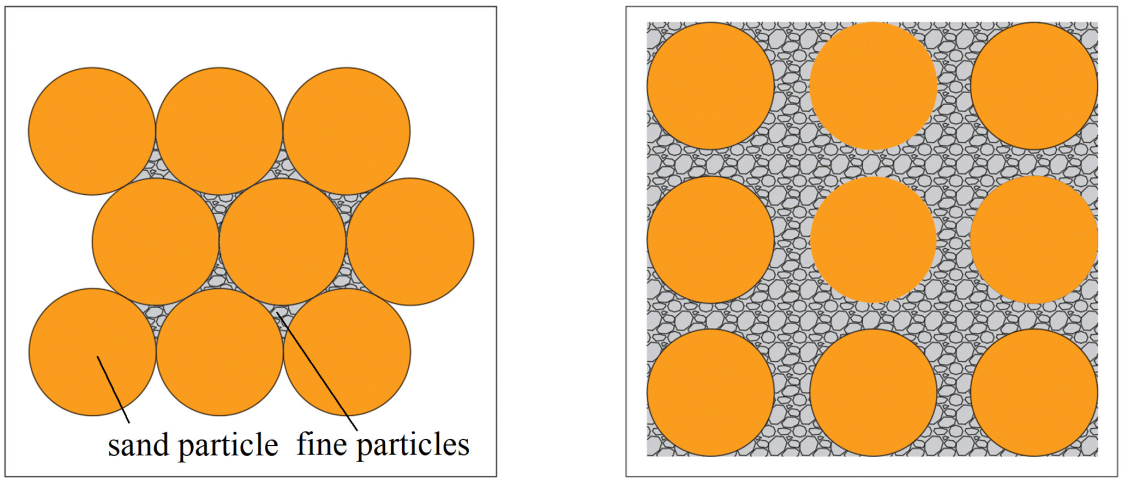

FIGURE 2 | Network structures of **(A)** sand-dominated mixtures and **(B)** mud-dominated mixtures.

Figure 3 shows the incipient motion condition of a sand particle (or a cohesive sediment parcel) belonging to a sand-dominated mixture (or a mud-dominated mixture). The forces acting on the sand particle or the mud parcel include the drag force F_d , the lift force F_l , the effective gravitational force G and the additional force F_c which is the resultant force of the interparticle attractive forces (the van der Waals forces) between the mud particles in the surface of the parcel or the coating layer of the sand particle and those surrounding mud particles. Considering the entrainments of the sand particle and the mud parcel are usually completed within a very short period, both the sand particle and mud parcel are assumed rigid bodies. The momentum balance equation for the critical condition of the incipient motions of the sand particle and the mud parcel is given by:

$$F_d k_1 d_r + F_l k_2 d_r = G k_3 d_r + F_c k_4 d_r \tag{11}$$

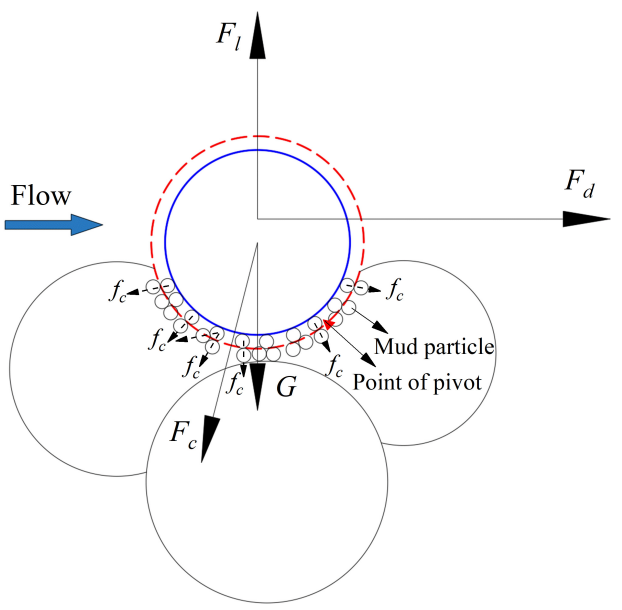

FIGURE 3 | Forces acting on a sand particle (or a mud parcel) in the surface of a sand-dominated mixture (a mud-dominated mixture). For the sand-dominated mixture, regard the blue circle as a sand particle and the red circle as the coating layer; for the mud-dominated mixture, regard the red circle as a mud parcel.

where d_r is a representative diameter, which refers to the diameter of sand particles for sand-dominated mixtures or the average diameter of mud parcels for mud-dominated mixtures, i.e., $d_r = d_s$ for $p_m \leq p_{mcr}$ and $d_r = d_a$ for $p_m > p_{mcr}$, with d_s being the diameter of the sand particle and d_a being the diameter of the mud parcel; $k_1 d_r$, $k_2 d_r$, $k_3 d_r$, and $k_4 d_r$ are the moment arms of the drag force F_d , lift force F_l , submerged weight G and resultant cohesive force F_c , respectively, with k_1 , k_2 , k_3 , and k_4 set as the proportionality coefficients.

The drag and lift forces are given by $F_d = C_d \rho u_b^2 \alpha_1 d_r^2$ and $F_l = C_l \rho u_b^2 \alpha_1 d_r^2$, respectively (Dou, 2000; Righetti and Lucarelli, 2007; Vollmer and Kleinhans, 2007; Wu et al., 2017), where C_d and C_l are drag and lift coefficients, respectively; ρ is the density of water; u_b is the flow velocity near the bed surface and α_1 is the area shape factor of the sand particle or the mud parcel.

The effective gravitational force G is given by $G = \alpha_2 \left(\rho_{pr} - \rho\right) g d_r^3$, where α_2 is a volumetric shape coefficient; g is the gravitational acceleration and ρ_{pr} is the density of the sand particle or the mud parcel, i.e., $\rho_{pr} = \rho_{ps}$ for $p_m \leq p_{mcr}$ and $\rho_{pr} = \rho_{pa}$ for $p_m > p_{mcr}$ with ρ_{pa} being the density of the mud parcel. For the sand-dominated mixtures, the effective weights of the mud particles in the thin coating layer are negligible due to the thin layer and the small size of the mud particles.

The resultant force F_c could be obtained by integrating those cohesive forces coming from the mud particles surrounding the motion-initiating sand particle or mud parcel: $F_c = k_5 n c_n f_c$, where f_c is the cohesive force (the van der Waals force) between two contacted mud particles; n is the number of mud particles coating the motion-initiating sand particle or the number of mud particles in the buried surface of the motion-initiating mud parcel; c_n is the coordination number, i.e., the average number of the contacted particles of a mud particle; k_5 is a coefficient. According to Meissner et al. (1964), c_n is a function of the volume fraction of solids:

$$c_n = 2\exp\left(2.4\frac{\rho_{dm}}{\rho_{pm}}\right) \tag{12}$$

where ρ_{dm}/ρ_{pm} denotes the volume fraction of solids of the mud component. n could be calculated by: $n = (1-\eta_\Delta)\,\pi d_r^2 N$, where $(1-\eta_\Delta)\,\pi d_r^2$ denotes the buried surface area of the sand particle or the mud parcel in which η_Δ is the relative protruding height of the sand particle or mud parcel into the flow from the bed surface; and N is the number of mud particles per unit area of the buried surface of the sand particle or the mud parcel. Assuming the sizes of the sand particle and the mud parcel are far larger than the size of the mud particles, N could be estimated by:

$$N\frac{\pi}{6}d_m^3\rho_{pm} = \rho_{dm}s \tag{13}$$

where d_m and ρ_{pm} are the diameter and density of the mud particles, respectively; s is the average distance between neighboring particles and ρ_{dm} is the dry bulk density of the mud component of the mixture. Considering Eqs. (9, 13), n is given by:

$$n = 6(1-\eta_\Delta)\frac{d_r^2}{d_m^2}\left(\frac{\rho_{dm}}{\rho_{pm}}\right)^{2/3} \tag{14}$$

Considering Eqs. (10, 12, 14), the resultant force F_c is given by:

$$F_c = \frac{A_h k_5(1-\eta_\Delta)}{2\eta^2\delta^2}\frac{d_r^2}{d_m}\left(\frac{\rho_{dm}}{\rho_{pm}}\right)^{2/3}\left[\left(\frac{\rho_{dm}}{\rho_{pm}}\right)^{-1/3}-1\right]^{-2}\exp\left(2.4\frac{\rho_{dm}}{\rho_{pm}}\right) \tag{15}$$

Substituting the expressions for F_d , F_l , G, and F_c into Eq. (11), the near-bed flow velocity for the incipient motion of sediment, $u_{b,cr}$, is given by:

$$u_{b,cr} = \left\{\frac{\alpha_2 k_3}{\rho\alpha_1\left(k_1C_d+k_2C_l\right)}(\rho_{pr}-\rho)gd_r + \frac{A_h k_4 k_5(1-\eta_\Delta)}{2\rho\alpha_1\left(k_1C_d+k_2C_l\right)\eta^2\delta^2}\frac{1}{d_m}\left(\frac{\rho_{dm}}{\rho_{pm}}\right)^{2/3}\left[\left(\frac{\rho_{dm}}{\rho_{pm}}\right)^{-1/3}-1\right]^{-2}\exp\left(2.4\frac{\rho_{dm}}{\rho_{pm}}\right)\right\}^{1/2} \tag{16}$$

Assuming the log law of velocity is valid near the bed, the near-bed flow velocity could be calculated by (Wu et al., 2017; Zhang and Zou, 2019; Li et al., 2020):

$$u_b = 5.75u_*\log\left(30.2\frac{z_b\chi}{k_s}\right) \tag{17}$$

where z_b is the elevation where the drag force acts on the sediment particle or parcel; χ is the correction factor of Einstein (Einstein, 1950) and k_s is the equivalent roughness height. Both z_b and k_s are related to the size of the sediment particle or parcel.

Substituting Eq. (17) into Eq. (16) and considering $u_* = \sqrt{\tau_b/\rho}$ in which τ_b is the bed shear stress, the critical shear stress of sand-mud mixtures τ_{cr} could be obtained:

$$\tau_{cr} = \frac{\alpha_2 k_3}{\alpha_1\left(k_1C_d+k_2C_l\right)\left[5.75\log\left(30.2z_b\chi/k_s\right)\right]^2}(\rho_{pr}-\rho)gd_r + \frac{A_h k_4 k_5(1-\eta_\Delta)\alpha_1^{-1}\eta^{-2}\delta^{-2}}{2\left(k_1C_d+k_2C_l\right)\left[5.75\log\left(30.2z_b\chi/k_s\right)\right]^2}\frac{1}{d_m}\left(\frac{\rho_{dm}}{\rho_{pm}}\right)^{2/3}\left[\left(\frac{\rho_{dm}}{\rho_{pm}}\right)^{-1/3}-1\right]^{-2}\exp\left(2.4\frac{\rho_{dm}}{\rho_{pm}}\right) \tag{18}$$

According to Eq. (18), the critical shear stress of sand-mud mixtures consists of two parts which are, respectively, contributed by the effective weight of the sand particle or the mud parcel (corresponding to the first term on the right side of the equation) and the cohesive strength from the mud component (corresponding to the second term). By ignoring the cohesion between particles [i.e., ignoring the second term in the right side of Eq. (18)], Eq. (18) is reduced to:

$$\frac{\tau_{cr}}{(\rho_{pr}-\rho)gd_r} = \frac{\alpha_2 k_3}{\alpha_1\left(k_1C_d+k_2C_l\right)\left[5.75\log\left(30.2z_b\chi/k_s\right)\right]^2} \tag{19}$$

The left hand side of Eq. (19) is the critical Shields parameter. This yields

$$\theta_{cr0}\left(d_{r*}\right) = \frac{\alpha_2 k_3}{\alpha_1\left(k_1C_d+k_2C_l\right)\left[5.75\log\left(30.2z_b\chi/k_s\right)\right]^2} \tag{20}$$

where $\theta_{cr0}\left(d_{r*}\right)$ is the critical Shields parameter of non-cohesive sediment of a particle diameter d_r and d_{r*} is the dimensionless diameter, defined as $d_{r*} = d_r\left[\left(\rho_{pr}/\rho-1\right)g/\upsilon^2\right]^{1/3}$. $\theta_{cr0}\left(d_{r*}\right)$ could be calculated from the Shields diagram or by the formula of Soulsby and Whitehouse (1997):

$$\theta_{cr0}\left(d_{r*7}\right) = \frac{0.3}{1+1.2d_{r*}} + 0.055\left(1-\exp\left(-0.02d_{r*}\right)\right) \tag{21}$$

Substituting Eq. (20) into Eq. (18), the critical shear stress of sand-mud mixtures is given by:

$$\tau_{cr} = \theta_{cr0}\left(d_{r*}\right)(\rho_{pr}-\rho)gd_r + A\frac{1}{d_m}\left(\frac{\rho_{dm}}{\rho_{pm}}\right)^{2/3}\left[\left(\frac{\rho_{dm}}{\rho_{pm}}\right)^{-1/3}-1\right]^{-2}\exp\left(2.4\frac{\rho_{dm}}{\rho_{pm}}\right) \tag{22}$$

where $A = 0.5A_h k_4 k_5 (1-\eta_\Delta)\alpha_1^{-1}\eta^{-2}\delta^{-2}(k_1 C_d + k_2 C_l)^{-1}[5.75 \log(30.2 z_b \chi / k_s)]^{-2}$.

The erosion threshold of the mud-dominated mixtures mainly depends from the cohesive strength of the mud component. Therefore, the first term on the right side of Eq. (22) could be negligible for mud-dominated mixtures. As a result, Eq. (22) can be further written as

$$\tau_{cr} = \begin{cases} \theta_{cr0}\left(d_{s*}\right)\left(\rho_{ps}-\rho\right) g d_s + A\frac{1}{d_m}\left(\frac{\rho_{dm}}{\rho_{pm}}\right)^{2/3} \\ \left[\left(\frac{\rho_{dm}}{\rho_{pm}}\right)^{-1/3}-1\right]^{-2} \exp\left(2.4\frac{\rho_{dm}}{\rho_{pm}}\right), p_m \le p_{mcr} \\ A\frac{1}{d_m}\left(\frac{\rho_{dm}}{\rho_{pm}}\right)^{2/3}\left[\left(\frac{\rho_{dm}}{\rho_{pm}}\right)^{-1/3}-1\right]^{-2} \\ \exp\left(2.4\frac{\rho_{dm}}{\rho_{pm}}\right), p_m > p_{mcr} \end{cases} \quad (23)$$

where p_m is mud content and p_{mcr} is the critical mud content beyond which the mixture is a mud-dominated mixture or pure mud and below which the mixture is a sand-dominated mixture or pure sand.

Equation (23) is the formula we develop for predicting the critical shear stress of sand-mud mixtures. It covers the full range of mud content from 0 to 100%, i.e., it also applies for pure sand and pure mud. When the mud content is 0%, Eq. (23) is reduced into the widely used formula for non-cohesive sediment: $\tau_{cr} = \theta_{cr0}\left(d_{s*}\right)\left(\rho_{ps}-\rho\right) g d_s$. When the mud content is higher than 0 but lower than the critical mud content, i.e., $0 < p_m \le p_{mcr}$, the mixture occurs in a sand-dominated structure and its critical shear stress is a function of the diameter of the sand particles, the diameter of the mud particles and the dry bulk density of the mud component. When the mud content is beyond the critical mud content, i.e., $p_m > p_{mcr}$, the mixture occurs in a mud-dominated structure or as pure mud. For this case, the critical shear stress is a function of the diameter of the mud particles and the dry bulk density of the mud component (or of the pure mud).

When applying Eq. (23) to a specific mixture, the dry bulk density of the mud component in the mixture needs to be determined first. As the mud particles fill in the space between the sand particles, the dry bulk density of the mud component in a mixture could be estimated by $\rho_{dm} = \rho_d p_m / (1-\varphi_s)$, where φ_s is the volume fraction of sand particles. Considering $\varphi_s = \rho_d p_s / \rho_{ps}$, the dry bulk density of the mud component in a mixture is then calculated by:

$$\rho_{dm} = \frac{\rho_d p_m}{1 - \rho_d p_s / \rho_{ps}} \quad (24)$$

Equation (24) shows the dry bulk density of the mud component is 0 for pure sand and equal to the dry bulk density of the mud when the mud content is 100%.

There are two coefficients in Eq. (23): p_{mcr} and A. According to the existing experiments of sand-mud mixtures, the erosion mode of mixtures changes from non-cohesive to cohesive at a mud content of approximately 5–15%. As some sand-dominated mixtures could also exhibit weak cohesive behavior, the upper value, 15%, is used for the critical mud content in this study, i.e., $p_{mcr} = 15\%$. The value of A not only reflects the cohesion strength of the mud component, but also is related to the roughness of the mixture bed surface. Currently, it is difficult to determine the value of A as some coefficients in the expression for A are usually unknown, e.g., A_h , η_Δ , k_4 , and k_5 . Therefore, A is treated as an empirical coefficient that will be determined by the measured data of erosion thresholds.

VALIDITY OF THE DEVELOPED FORMULA IN SAND-MUD MIXTURES

Data of eight groups of sand-mud mixtures collected from four experiments conducted by Torfs (1995); Sharif (2003), Jacobs et al. (2011), and Smith et al. (2015) are used to test the validity of Eq. (23) in sand-mud mixtures. The synopses of the collected data are listed in **Table 1**. Eq. (23) is applied to each group of data in this section. A best-fit value of A is adopted for each dataset, which was obtained by the regression analysis of the data. We also test the formulae of Van Ledden (2003); Ahmad et al. (2011), Wu et al. (2017), and Chen et al. (2018) using the same datasets. Each dataset and the corresponding testing results are described below.

Experimental Data of Torfs (1995)

Torfs (1995) conducted a series of erosion experiments of artificial mixtures of sand and clay mineral in a straight flume with a rectangular cross-section. The mixtures were prepared by mixing clay mineral with fine sand and were kept at a constant bulk density around 1,850 kg m^{-3}. Two kinds of clay mineral: kaolinite and montmorillonite, were used in the experiments. The

TABLE 1 | Summary of collected experimental data of sand-mud mixtures and data sources.

Mixture name	Sand size (mm)	Mud size (mm)	Mud/clay content (%)	Critical shear stress (Pa)	Data source
Sand-kaolinite mixtures	0.23	0.0008	0–14.9	0.35–3.048	Torfs, 1995
Sand-bentonite mixtures	0.23	0.008	0–28	0.35–1.837	
Sand-kaolinite mixtures	0.20	0.006	0–100	0.21–1.67	Sharif, 2003
Sand-silt-kaolinite mixtures	0.18	0.004	0–17	0.12–1.6	Jacobs et al., 2011
Sand-silt-bentonite mixtures	0.18	0.002	0–16	0.17–0.99	
Sand-kaolinite mixtures	0.353	0.0038	0–100	0.154–0.881	Smith et al., 2015
Sand-kaolinite-bentonite mixtures	0.353	0.005	0–100	0.168–1.802	
Sand-mud mixtures	0.353	0.0127	0–100	0.168–2.018	

sand is a uniform fine white quartz of a mean diameter around 0.23 mm and does not contain particles smaller than 63 μm. The mud (clay mineral) content varied from 0 to 14.9% for sand-kaolinite mixtures and from 0 to 28% for sand-montmorillonite mixtures. The bed shear stress was estimated by the slope of the energy line which was calculated from the water surface profile. The critical shear stress was defined as the average of the bed shear stresses before and after the onset of erosion. The onset of erosion was reached when sediment is falling into the sediment trap and/or the water samples contain suspended sediment.

As the formulae of Van Ledden (2003) and Ahmad et al. (2011) involve the critical shear stress for erosion of pure mud which is unknown in the two datasets, therefore, only the formulae of Wu et al. (2017); Chen et al. (2018) and Eq. (23) are applied to the two datasets. **Figure 4** compares the calculated and measured critical shear stresses for the sand-kaolinite mixtures and sand-montmorillonite mixtures. For Eq. (23), the best-fit value of A equals 5.75×10^{-6} J m^{-2}. As shown in **Figure 4**, Eq. (17) gives the best estimate of the measurements. The formulae of Wu et al. (2017) and Chen et al. (2018) could only capture the varying trend of the critical shear stress with mud content and both of them tend to underestimate the measured critical shear stresses.

Experimental Data of Sharif (2003)

Sharif (2003) conducted a series of erosion tests of sand-kaolinite mixtures using a straight-through recirculating flume with a rectangular cross-section. The sand used in the experiments has a narrow particle size range from 180 to 212 μm. The median diameter of the sand is about 200 μm. The kaolinite used in the experiments is the industrial-grade pure kaolinite mineral. The mixtures were prepared by mixing the well-sorted fine sand, kaolinite and water with an electrical blender. The mud content varied from 0 to 100%. The mixtures were allowed to consolidate for 48 h before the experiments. For each mixture (or pure mud) bed, the critical shear stresses of the sediment at different depths from the bed surface were measured. Particles from all over the bed starting to erode from the bed was defined as the threshold condition for critical shear stress. The bed shear stress was estimated from the log-law for the vertical velocity distribution and a measured velocity at the center of the bed.

Figure 5 shows the measured and predicted critical shear stress of sand-mud mixtures vary with mud content. Each subfigure represents the results of sediments of different mud contents for the same soil depth. For the formula of Van Ledden (2003), i.e., Eq. (1), p_{mcr} is set as 15% and β_v is set as 1.0. For the formula of Ahmad et al. (2011), i.e., Eq. (2), ζ is set as 0.15. These coefficients are given following the recommendations of Van Ledden (2003) and Ahmad et al. (2011) and are also used in other cases in this study. The best-fit value of A for Eq. (23) is 3.62×10^{-6} J m^{-2} in this case. As shown in **Figure 5**, the calculated critical shear stress by the formulae of Van Ledden (2003) and Ahmad et al. (2011) increases monotonically with increasing mud content, which is not consistent with the measurements. Eq. (23) and the formulae of Wu et al. (2017) and Chen et al. (2018) reproduce well the variation trend of critical shear stress with mud content.

Experimental Data of Jacobs et al. (2011)

Jacobs et al. (2011) conducted a number of erosion tests on artificial sand-mud mixtures using a straight transparent enclosed flume, namely the Erodimetre. The flume is mainly constituted of a small-scale (1.20 m long, 8 cm wide, and 2 cm high) duct where a unidirectional flow can be generated by a recirculating pump. There is a circular cut-off at the bottom of the duct so that a sediment container could be installed where a sediment core can be placed and pushed upwards. During the erosion testing, the surface of the sediment sample was horizontally and vertically leveled with the bottom of the duct. The bottom of the duct was covered with sandpaper of a roughness comparable to the applied sand fraction to decrease differences in roughness with the sample.

The sand-mud mixtures were prepared by mixing fine sand, silt and clay in different proportions. The median particle

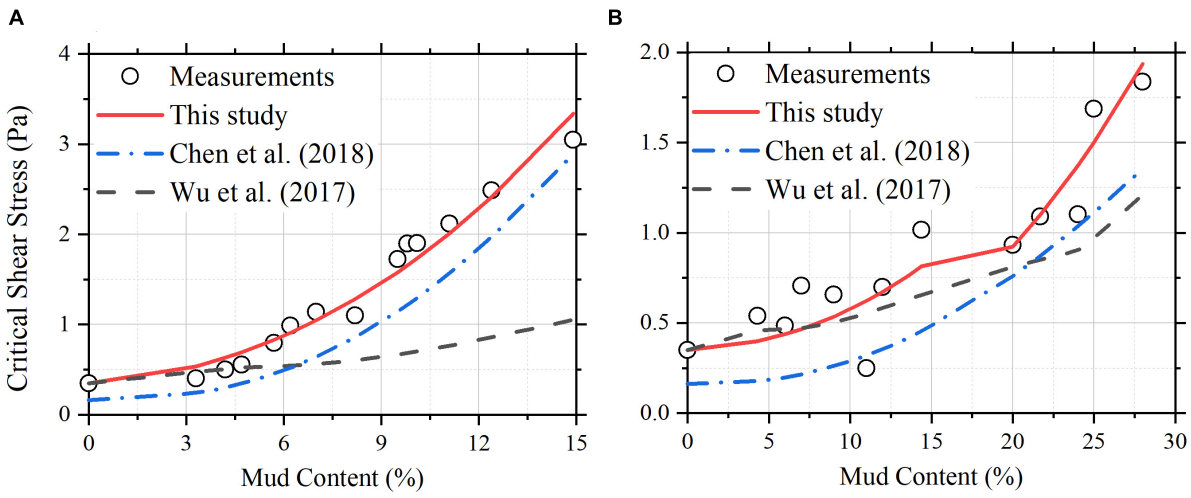

FIGURE 4 | The calculated vs. measured critical shear stresses in the case of Torfs (1995): **(A)** sand-kaolinite mixtures and **(B)** sand-montmorillonite mixtures.

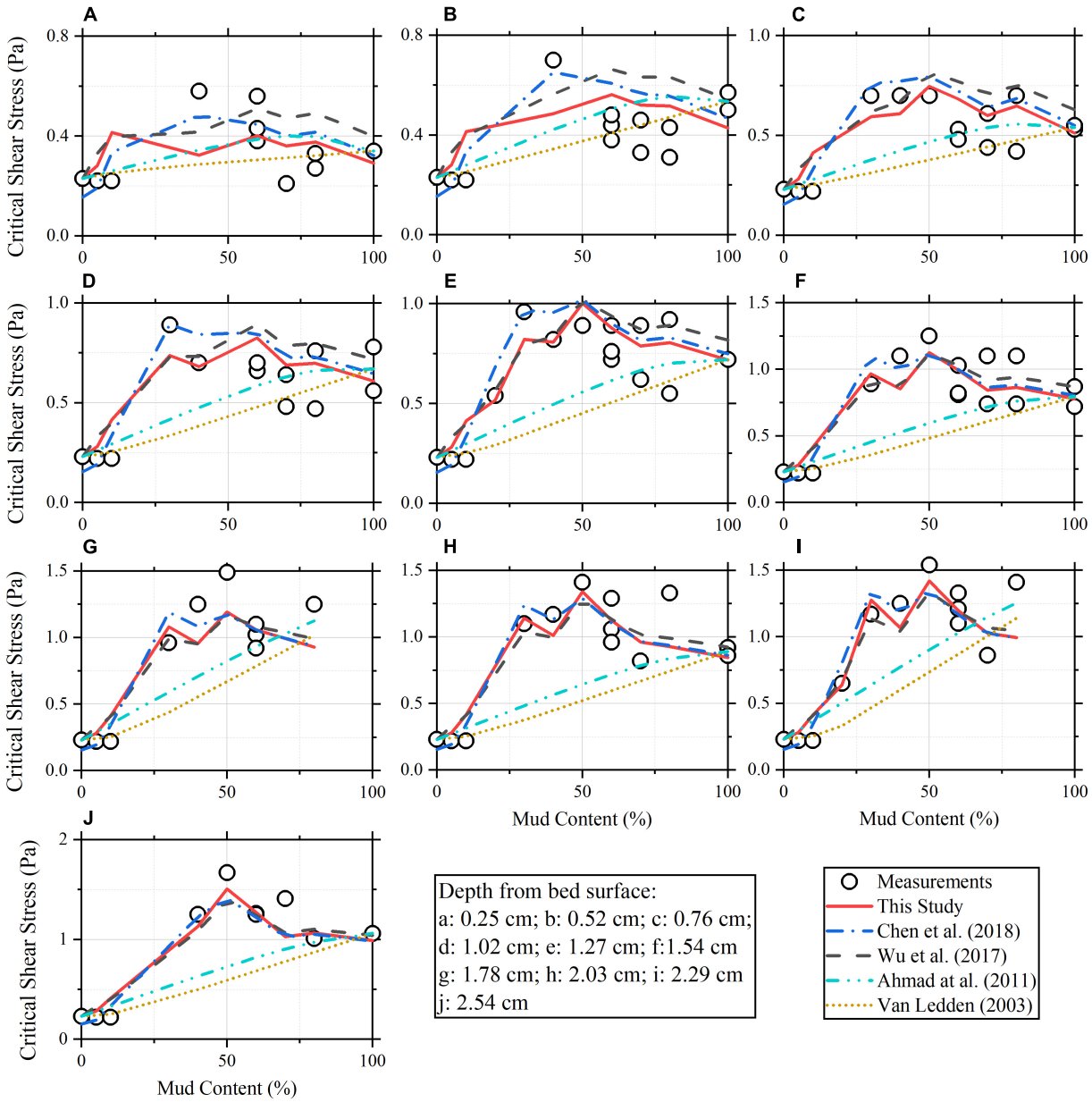

FIGURE 5 | The calculated and measured critical shear stresses vary with mud content for sediment at different soil depths in the case of Sharif (2003): **(A)** 0.25 cm; **(B)** 0.52 cm; **(C)** 0.76 cm; **(D)** 1.02 cm; **(E)** 1.27 cm; **(F)** 1.54 cm; **(G)** 1.78 cm; **(H)** 2.03 cm; **(I)** 2.29 cm; and **(J)** 2.54 cm.

diameters of the sand and silt used in the experiments are 180 and 30 μm, respectively. Two different clay minerals were applied: kaolinite and bentonite. A specific procedure was followed to generate reproducible and homogeneously mixed mixtures. First, sand, silt and clay fractions were oven-dried to disaggregate the material. Next, they were manually mixed for 10 min and placed in a cylindrical container with a removable bottom-lid. Small holes in the bottom and top-lid allow the passage of water and gas. In order to ensure the mixtures being 100% saturated, the containers with dry mixtures were placed in an exsiccator to remove air by lowering the pressure. Then the exsiccator was filled with CO_2, after which the pressure was lowered again to replace enclosed air with CO_2. Subsequently, the mixtures were left for 24 h in the exsiccator, in which a layer of water was present. The combination of the low pressure (reduced surface tension), 100% humidity and the attractive forces of the negatively charged clay particles enables water molecules to activate the clay particles. A layer of 10 cm de-aired and demineralized water was placed on top of the samples. Due to the difference between the atmospheric and the reduced pressure within the exsiccator, water percolated through the mixture thereby completing the saturation procedure.

To prevent consolidation, erosion tests were executed as soon as possible after the generation of the sample. A unidirectional flow generated by a recirculating pump was accelerated step by step (average duration of a step approximately 150–200 s) until the sample was eroded by a few mm. The volume of eroded sand was monitored at a sand trap downstream of the sediment sample, from which the erosion rate of the sand fraction could be derived. The erosion rate of the fine fraction is determined by dividing the time derivative of the continuously recorded turbidity by the surface area of the sample. The erosion threshold of a mixture was selected as the average abscissa of the extrapolated erosion rates assuming a linear relationship between the erosion rate and bed shear stress for both coarse and fine fractions. The bed shear stress was assumed proportional to the square of discharge in the flume, and the drag coefficient has been fitted so that the initiation of movement of the sand used in the experiments is consistent with the critical mobility parameter given by the Shields diagram.

As the mixtures were composed of sand, silt and clay and the clay contents are under 20% for all the mixtures, only Eq. (23) and the formula of Chen et al. (2018) are applied in this case. **Figure 6** shows the measured and calculated critical shear stresses of mixtures varying with clay content. The best-fit value of A for Eq. (23) equals 1.16×10^{-5} J m^{-2} for sand-silt-kaolinite mixtures and 5.93×10^{-6} J m^{-2} for sand-silt-bentonite mixtures. As shown in **Figure 6**, the critical shear stresses calculated by Eq. (23) agree well with the measured values (**Figures 6A,B**), and the formula of Chen et al. (2018) tends to overestimate the critical shear stress at high clay contents (**Figures 6C,D**).

Experimental Data of Smith et al. (2015)

Smith et al. (2015) conducted erosion tests of sand-mud mixtures using the Sedflume, which is a small-scale enclosed duct-type flume (similar to the Erodimetre introduced above). The sand-mud mixtures were prepared by mixing varying fractions of mud with well-sorted quartz sand. The diameter of the sand ranges from 0.25 to 0.50 mm with the median diameter being 0.353 mm. Three different muds were used: kaolinite, mixed 80% kaolinite and 20% bentonite and a natural mud from the lower Mississippi River. The median diameters of the kaolinite, the kaolinite/bentonite mixture clay and the natural mud are 0.0038, 0.005, and 0.0127 mm, respectively. The natural mud has 3.5% organic content according to the test of loss-on-ignition.

Prior to mixing with sand, each mud was slurried with freshwater, and the slurry density was maintained at a density of

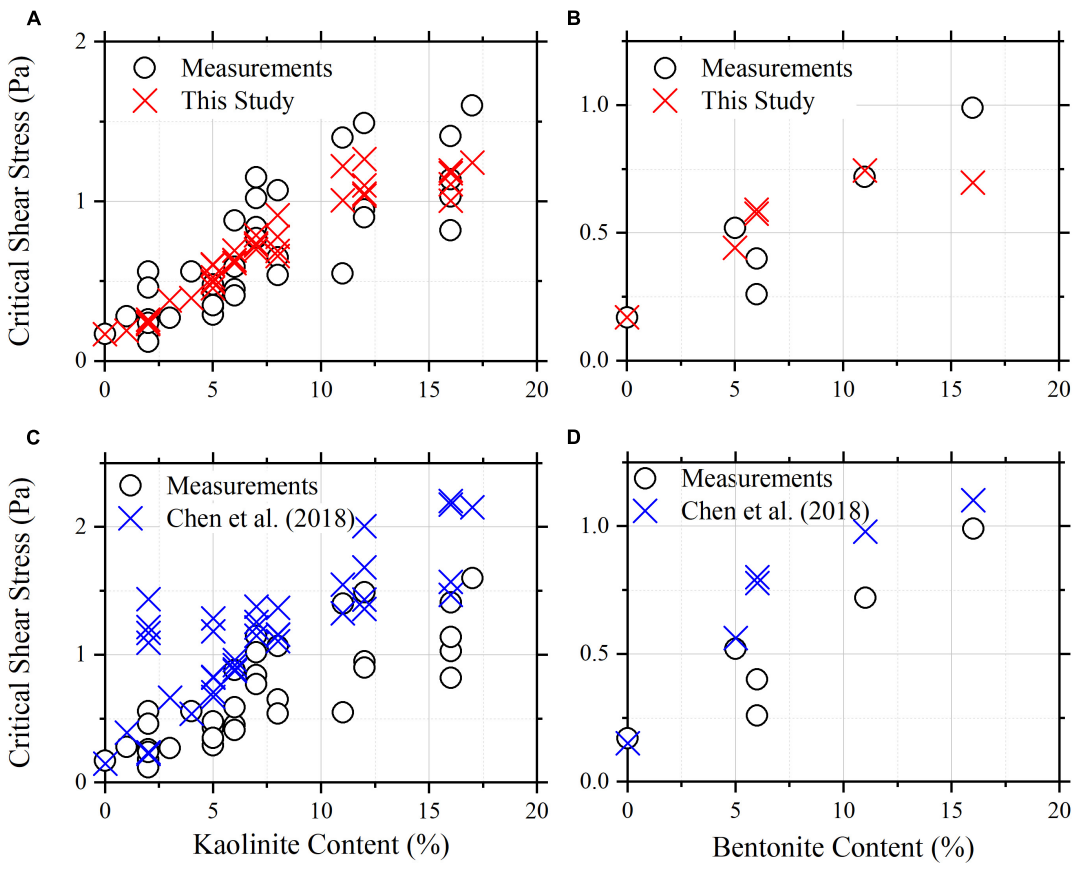

FIGURE 6 | The calculated vs. measured critical shear stresses in the case of Jacobs et al. (2011): **(A,C)** sand-silt-kaolinite mixtures, **(B,D)** sand-silt-bentonite mixtures; **(A,B)** Eq. (23) and **(C,D)** the formula of Chen et al. (2018).

about 1,400 kg m^{-3}. Then an appropriate mass of mud slurry was added to sand to achieve the targeted mud mass fraction. The mixture was then hand-mixed for 3–10 min until mud and sand were evenly distributed throughout the sample. The mixture samples were formed into 10-cm diameters cores by two methods. For fluid mixtures, samples were extruded from a bag into the bottom of a core to minimize gas entrapment. For plastic and granular mixtures, water was added to the mixture to achieve saturation, and the samples were lightly tamped into the core tube in approximately 0.5–1 cm lifts. The prepared sediment cores were allowed to consolidate for 30 days in a 4°C cooler prior to the erosion test.

For each mixture sample, the erosion tests were conducted at five different shear stresses. The critical shear stress was defined as the bed shear stress corresponding to an erosion rate of 10^{-4} cm s^{-1} and obtained by fitting a power law for the erosion rate. The bed shear stress in the Sedflume was determined by the average flow velocity in the flume according to the Darcy equation in which the friction factor was estimated by the Prandtl equation (i.e., both the bed of the flume and the surface of the sediment sample were assumed hydraulically smooth).

Figure 7 shows the measured and calculated critical shear stresses varying with mud content. The formula of Chen et al. (2018) is not applied in this case since the stable dry bulk density of mud cannot be obtained based on the known data. The best-fit value of A for Eq. (23) equals 1.59×10^{-6} J m^{-2} for sand-kaolinite mixtures, 6.42×10^{-6} J m^{-2} for sand-kaolinite-bentonite mixtures and 1.04×10^{-5} J m^{-2} for sand-natural-mud mixtures. As shown in **Figure 7**, the formulae of Van Ledden (2003) and Ahmad et al. (2011) cannot capture well the varying behavior of the critical shear stress with mud content. Eq. (23) and the formula of Wu et al. (2017) reproduce well the critical shear stress of sand-kaolinite-bentonite mixtures (**Figure 7B**) and sand-natural-mud mixtures (**Figure 7C**). However, the latter two formulae can only reproduce the critical shear stress of sand-kaolinite mixtures of mud content lower than 15% and fail to capture well the varying trend of the critical shear stress of sand-kaolinite mixtures of high mud contents (**Figure 7A**). The reason for the latter two formulae failing in capturing the varying trend of the critical shear stress of sand-kaolinite mixtures of high mud contents is probably because the nominal mud contents would be lower than the actual mud contents. For sand-kaolinite mixtures of high mud contents (i.e., fluid mixture samples in the preparing process), the uneven settling of the sand fraction and the mud fraction would occur during the preparing process of the samples. This would lead to that more mud is present in the upper layer of the sample. A modification is made here by assuming the nominal mud contents being 6% lower than the actual mud contents for the sand-kaolinite mixtures of mud content higher than 15%. The calculated critical shear stresses by Eq. (23) and the formula of Wu et al. (2017) after modification are also plotted in **Figure 7A**, which shows better agreements with measurements than before. The uneven settling of the sand fraction and the mud fraction is not significant in sand-kaolinite-bentonite mixtures and sand-natural-mud mixtures. This could be attributed to the mud fractions has much stronger cohesion for sand-kaolinite-bentonite mixtures and sand-natural-mud mixtures, which could also be seen from the higher values of A.

VALIDITY OF THE DEVELOPED FORMULA IN PURE MUD

Nine sets of experimental data of pure mud were collected from literature to test the validity of the developed formula in pure mud. These muds include one group of pure clay mineral, two groups of estuarine mud and six groups of coastal mud. In each experiment, the critical shear stresses of the muds of different bulk densities were measured. The synopsis of the collected data and the data sources are listed in **Table 2**.

Equation (23) is then applied to the nine datasets. For each dataset, the best-fit value of A is used, which was obtained by the regression analysis of the data. The formula of Chen et al. (2018) and Eq. (4) (which was developed by Wu et al. (2017) for calculating the critical shear stress of pure mud) are also applied to each dataset if they are applicable. **Figure 8** shows the application results of those formulae. As shown in **Figure 8**, the formula of Chen et al. (2018) and Eq. (4) only

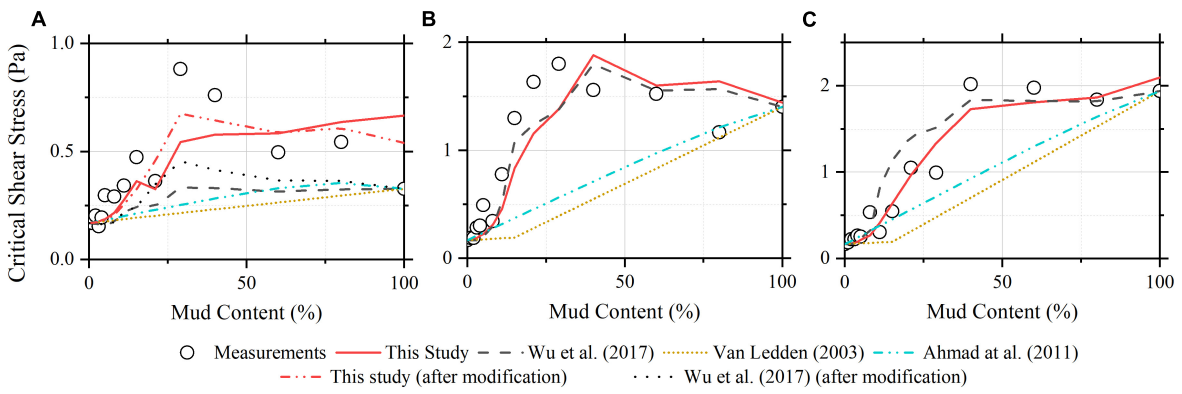

FIGURE 7 | The calculated vs. measured critical shear stresses in the case of Smith et al. (2015): **(A)** the mixtures of sand and kaolinite; **(B)** the mixtures of sand and mixed clay; and **(C)** the mixtures of sand and natural mud.

TABLE 2 | Summary of collected experimental data of pure mud and data sources.

Mud name	Median diameter (mm)	Dry bulk density (kg m^{-3})	Critical shear stress (Pa)	Data source
Pure kaolinite	0.006	385–610	0.34–1.06	Sharif, 2003
Chikugo estuary mud	0.0073	83–277	0.02–0.18	Kusuda et al., 1984
Lianyungang port mud	0.004	173–610	0.12–2.39	Huang, 1989
Lianyungang waterway mud	0.0051	246–634	0.08–1.34	Yang et al., 2018
Hangzhou bay mud	0.0104	415–655	0.19–0.55	Yang and Wang, 1995
Zhejiang coastal mud (location 1/L1)	0.0041	384–520	0.29–0.76	Li et al., 1995
Zhejiang coastal mud (location 2/L2)	0.0054	429–558	0.31–0.73	
Tianjin new port mud	0.0053	121–964	0.02–3.40	Hong and Xu, 1991
Huangmaohai estuary mud	0.007	161–883	0.03–4.19	Xu et al., 2015

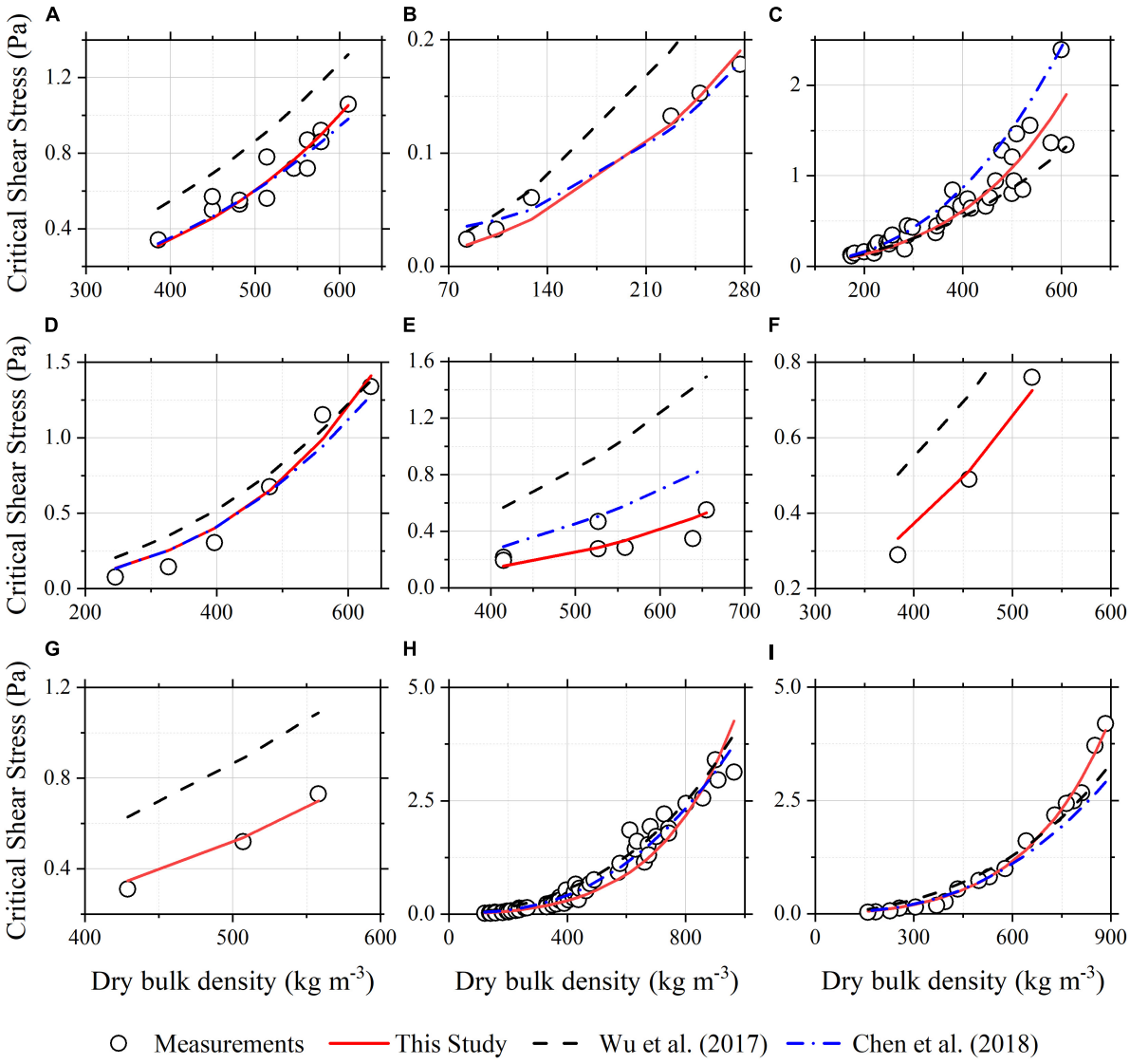

FIGURE 8 | The comparisons of Eq. (23) and the formulae of Wu et al. (2017) and Chen et al. (2018) with the measured critical shear stresses: **(A)** pure kaolinite; **(B)** Chikugo estuary mud; **(C)** Lianyungang port mud; **(D)** Lianyungang waterway mud; **(E)** Hangzhou Bay mud; **(F)** Zhejiang coastal mud (Location 1); **(G)** Zhejiang coastal mud (Location 2); **(H)** Tianjin New Port mud; and **(I)** Huangmaohai Estuary Mud.

reproduce well the critical shear stress of pure mud in a few cases. Eq. (23) gives reasonable estimates of the critical shear stress in all the cases, demonstrating the capacity of the developed formula in pure mud.

DISCUSSION

The Coefficient *A*

The value of A is related to both the cohesion strength of the cohesive component in the sediment and the roughness of the bed surface. The cohesion strength is denoted by the Hamaker constant, which is a function of the particle itself including the mineral composition, the particle shape and the surface roughness, and the pore water environment including the pH value, the sort and concentration of ions. As the mineral composition and the pore water environment of sediment usually vary from site to site, the value of Hamaker constant and the value of A are supposed to be site-specific. The surface roughness of sand-mud mixtures depends on the network structure of mixtures, the aggregation of mud and the occurrence of erosion events (Mitchener and Torfs, 1996; Le Hir et al., 2008; Perkey et al., 2020). Different experimental results of surface roughness of sand-mud mixtures were often reported (Baas et al., 2013; Das et al., 2019). A widely accepted quantitative understanding of the roughness parameter of sand-mud mixtures and its effect on the drag and lift coefficients have not been available. Therefore, A is treated as an empirical coefficient in this study with its value being determined by the measured erosion thresholds.

The threshold of erosion in most existing tests of sand-mud mixtures and pure mud was usually determined by visual observation which is subjective and highly empirical. A universal criterion for the erosion threshold of sediment, especially of cohesive sediments, is not available currently. Therefore, the different criteria for determining the threshold of erosion would also have an effect on the value of A. This makes it more challenging to develop an expression for A.

The best-fit values of A for each dataset of sand-mud mixtures and pure mud are presented in **Table 3**. As shown in **Table 3**, the value of A is generally on the order of magnitude of 10^{-6} or 10^{-5} J m^{-2}. Specifically, the value of A is the range of 1.59×10^{-6}–1.16×10^{-5} J m^{-2} for kaolinite and sand-kaolinite mixtures; 5.93×10^{-6}–9.58×10^{-6} J m^{-2} for sand-bentonite mixtures; 4.89×10^{-6} J m^{-2} for mixtures of sand and kaolinite and bentonite mixed clay; 2.86×10^{-6}–1.04×10^{-5} J m^{-2} for pure mud and sand-mud mixtures.

Although the value of A is site- or sediment- specific, a general or practical value is expected, with which Eq. (23) could give a reasonable estimate of critical shear stress of most of the common sediments. Based on the collected data of sand-mud mixtures and pure mud, a general value of 3.97×10^{-6} J m^{-2} is recommended, which was obtained by the following method. The value of A was allowed to increase from 1.0×10^{-7} J m^{-2} to 1.0×10^{-4} J m^{-2} with a step of 1.0×10^{-8} J m^{-2}. For each value of A, Eq. (23) was applied to all the collected datasets, and the logarithmic root-mean-square error of the calculated critical shear stresses was computed. The logarithmic root-mean-square error is used as a statistical indicator to evaluate the performance of the regression model for the quantity of the measured critical shear stress varies in several orders of magnitude. The general value of A is obtained when the logarithmic root-mean-square error of the calculated critical shear stresses reaches its minimum value. The logarithmic root-mean-square error, denoted as $\log E_{rms}$, is defined by:

$$\log E_{rms} = \sqrt{\frac{1}{M}\sum_{i=1}^{M}\left[\log\left(\frac{\tau_{cr,c,i}+1}{\tau_{cr,m,i}+1}\right)\right]^2} \tag{25}$$

where $\tau_{cr,c,i}$ and $\tau_{cr,m,i}$ are the calculated and measured critical shear stresses, respectively; i is the data index and M is the total number of the collected data.

The comparisons of Eq. (23) and the measured critical shear stresses in all the datasets are shown in **Figures 9A,B**. For **Figure 9A**, the best-fit value of A (see **Table 3**) is used for each dataset; and for **Figure 9B**, the general value of A, 3.97×10^{-6} J m^{-2}, is used for all the datasets. The comparisons of the formulae of Wu et al. (2017) and Chen et al. (2018) with measurements are also shown in **Figures 9C,D**. As shown in **Figure 9**, Eq. (23) with best-fit values of A has the best prediction performance. Eq. (23) with the general value of A also has a good prediction performance, better than the formulae of Wu et al. (2017) and Chen et al. (2018). The average relative error (E), defined as $E = \left[\sum\left(\tau_{cr,c,i}/\tau_{cr,m,i} - 1\right)\right]/M \times 100\%$, is 22.9% for Eq. (23) with best-fit values of A, 34.3% for Eq. (23) with the general value of A, 38.3% for the formula of Chen et al. (2018) and

TABLE 3 | Application results of the developed formula in sand-mud mixtures and pure muds.

Sand-mud mixtures	A (10^{-6} J m^{-2})	Pure mud	A (10^{-6} J m^{-2})
Sand-kaolinite mixtures (Torfs, 1995)	5.75	Pure kaolinite	3.88
Sand-bentonite mixtures (Torfs, 1995)	9.58	Chikugo estuary mud	5.94
Sand-kaolinite mixtures (Sharif, 2003)	3.62	Lianyungang port mud	4.65
Sand-silt-kaolinite mixtures (Jacobs et al., 2011)	11.59	Lianyungang waterway mud	4.18
Sand-silt-bentonite mixtures (Jacobs et al., 2011)	5.93	Hangzhou bay mud	2.86
Sand-kaolinite mixtures (Smith et al., 2015)	1.59	Zhejiang coastal mud	2.86 (L1); 2.98 (L2)
Sand-kaolinite-bentonite mixtures (Smith et al., 2015)	4.89	Tianjin new port mud	2.98
Sand-mud mixtures (Smith et al., 2015)	10.38	Huangmaohai estuary mud	5.18

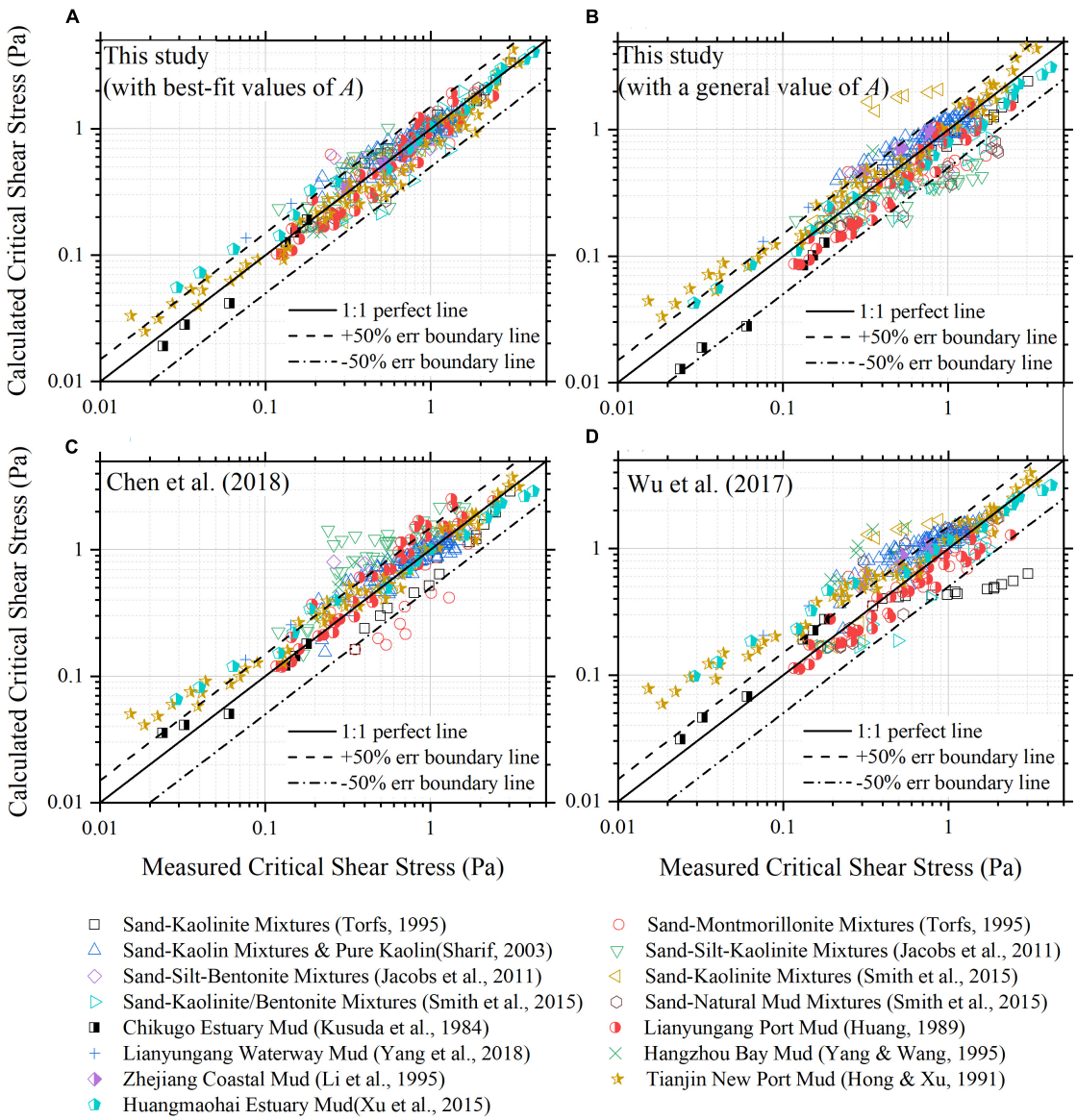

FIGURE 9 | The comparisons of the calculated and measured critical shear stresses in the collected datasets: **(A)** Eq. (23) (in which the best-fit value of A is used for each dataset), **(B)** Eq. (23) (in which a constant value of A is used for all the datasets: 3.97×10^{-6} J m^{-2}), **(C)** the formula of Chen et al. (2018), and **(D)** the formula of Wu et al. (2017).

54.5% for the formula of Wu et al. (2017). For Eq. (23) with best-fit values of A, 90.3 and 99.2% of the collected data points are, respectively, within the range of 50 and 100% error (i.e., $\left|\tau_{cr,c}/\tau_{cr,m} - 1\right| < 0.5$ and $\left|\tau_{cr,c}/\tau_{cr,m} - 1\right| < 1.0$). Accordingly, for Eq. (23) with the general value of A, 79.3 and 97.4% of the data points are, respectively, within the range of 50 and 100% errors; for the formula of Chen et al. (2018), 73.3 and 93.0% of the data points are, respectively, within the range of 50 and 100% errors; and for the formula of Wu et al. (2017), 62.7 and 82.1% of the data points are, respectively, within the range of 50 and 100% errors.

Although Eq. (23) with the general/practical value of A has an acceptable prediction accuracy, it is noted that the value of A could be optimized when Eq. (23) is applied to a specific site. The accurate value of A for a specific site can be determined by applying Eq. (23) to the sediment of known critical shear stress, which could be obtained by a laboratory or field erosion test. Then Eq. (23) can be applied to calculate the critical shear stress of sediments of different mud contents and bulk densities in the site.

Effects of the Network Structure of Sand-Mud Mixtures

Equation (23) indicates that the dry bulk density of the mud component is a more direct factor affecting the erodibility of a mixture than the dry bulk density of the mixture. The variation of

the critical shear stress of sand-mud mixtures with mud content is mainly caused by the varying dry bulk density of the mud component in the mixture. These findings are consistent with previous observations by Migniot (1989); Waeles et al. (2008), Dickhudt et al. (2011); Le Hir et al. (2011), Wu et al. (2017), and Chen et al. (2018). As the network structure of sand-mud mixtures affects the consolidation of sand-mud mixtures, the network structure of sand-mud mixtures would have effects on the dry bulk density of the mud component and also the mixture critical shear stress. Here the effects of the network structure of sand-mud mixtures are investigated using the experimental data of Sharif (2003).

Figure 10 shows the dry bulk density of the mud component (**Figure 10A**) and the critical shear stress calculated by the developed formula (**Figure 10B**) varying with mud content in the case of Sharif (2003). A is taken the value of 3.62×10^{-6} J m^{-2} in the calculations. All the sediments in the experiments were allowed to consolidate for 48 h before the erosion test. The dry bulk density and the critical shear stress of sediment at different depths from the bed surface were measured. Each solid line with markers in **Figure 10** represents the results of sediment samples of different mud contents at the same depths.

Figure 10A shows that the dry bulk density of the mud component increases markedly with increasing mud content from 0 to 10%. With further increase in mud content, the dry bulk density of the mud component first continues to increase and reaches a maximum at an optimum mud content, after that decreases gradually in a slight rate until 100% mud content. The optimum mud content seems to be in the range of 30–50% in this dataset. The dips of the dry bulk density at 40% mud content may be caused by uncertainty in measurements. As generally predicted by the developed formula, the critical shear stress varies with mud content in a similar way as the dry bulk density of the mud component (**Figures 10A,B**).

As shown in **Figure 10A**, the dry bulk density of the mud component does not change with depth for the mud content below 10% and varies with depth when the mud content equals or exceeds 20%. This indicates that the critical mud content for being able to form a sand skeleton is between 10 and 20%. Because when a sand skeleton is formed, the mud particles are in the voids of the sand particles. For such a condition, the mud particles are protected by the sand skeleton, and the sediment depth will have no effect on the consolidation of the mud component. The mud component only consolidates under its self-weight, and therefore, the more mud fraction, the larger the dry bulk density of the mud component. When the mud content is beyond the critical mud content, the complete sand skeleton cannot be formed. For this case, the mud component consolidates under the influence of the effective weight of the overlying layer. Therefore, for the same consolidation time, the deeper sediment depth, the higher the degree of the consolidation of the mud component.

The behavior of the dry bulk density of the mud component increasing first and then decreasing gradually when the mud content is beyond the critical mud content is not well-understood. A reasonable explanation is proposed here. When the mud fraction is not very high, although a complete sand skeleton cannot be formed, some sand particles could still contact each other and form an incomplete skeleton. For this condition, the mud component and the sand component share the load from the effective weight of the overlying layer of sediment. The mud component consolidates under the received load and the self-weight. The more mud fraction means less help from the sand particles and more load received by the mud component. Therefore, a higher mud content will lead to a faster consolidation of the mud component in a mixture. However, if the mud

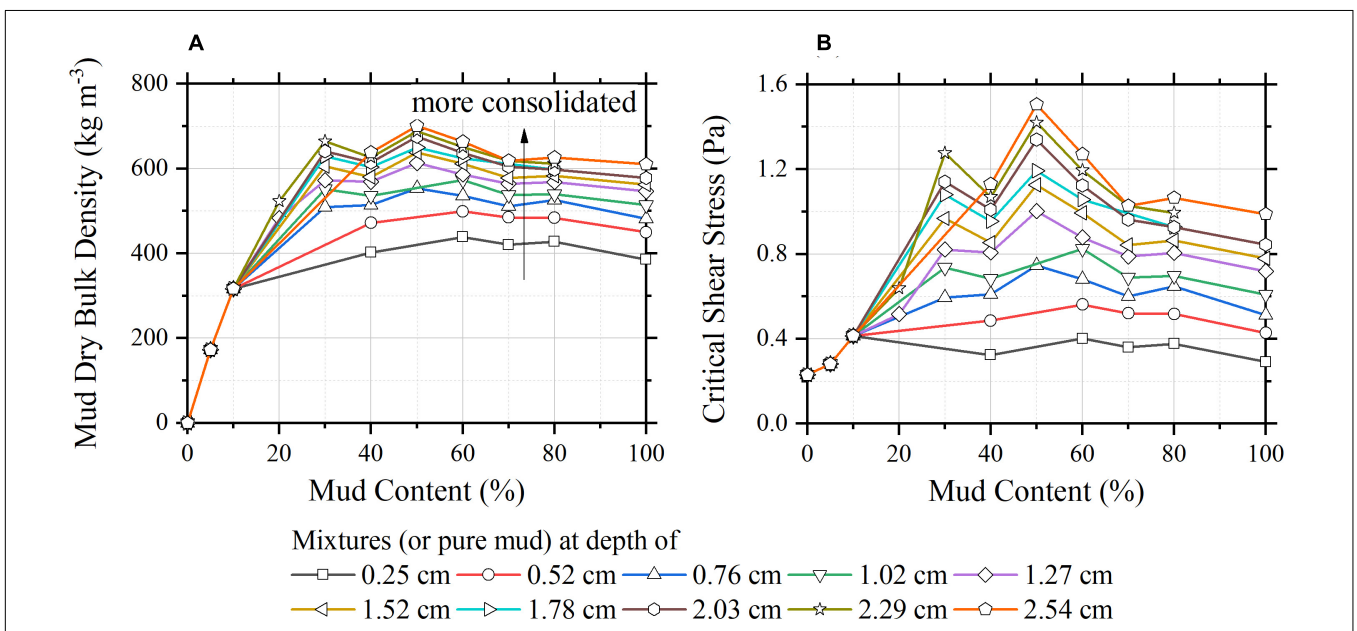

FIGURE 10 | The dry bulk density of the mud component **(A)** and the calculated critical shear stress **(B)** vary with mud content in the case of Sharif (2003).

fraction is high enough that all the sand particles lose contact and are dispersed in the mud matrix. For this condition, the mud component consolidates under the self-weight and the load from the overlying layer. As the sand could assist drainage and the density of the sand particles is higher than that of mud blocks, the increase in the mud content will not benefit the consolidation of the mud component. The more mud fraction and the less sand fraction lead to a lower consolidation rate. Under these two opposing influences, the dry bulk density of the mud component in sand-mud mixtures of the same consolidation time will first increase then decrease.

CONCLUSION

The erosion threshold of sand-mud mixtures has been studied by a theoretical analysis of the momentum balance of a sand particle or a mud parcel under the initial motion condition. A formula for the critical shear stress of sand-mud mixtures was developed, which also applies for pure sand and mud. The developed formula is expressed as a function of the primary particle diameters of the sand and mud components, mud content and the dry bulk density of sediment. Compared with the existing formulae for sand-mud mixtures, the developed formula is much easier for application as it has few coefficients and does not involve the critical shear stress of pure mud and the stable dry bulk density of mud in its expression.

The developed formula can be simplified to the widely used formula for pure sand when the mud content is 0 and has been successfully tested by four sets of experimental data of sand-mud mixtures and nine sets of experimental data of pure mud, which demonstrates the capability of the developed formula in pure sand, pure mud and sand-mud mixtures. The value of A in the developed formula is supposed to be site-specific. According to the collected experimental data, it is generally on the order of magnitude of 10^{-6} or 10^{-5} J m^{-2}. A value of A, 3.97×10^{-6} J m^{-2}, is recommended for general sand-mud mixtures and mud. But it is emphasized that the value of A could be optimized when the developed formula is applied to a specific site.

The developed formula shows that the erosion threshold of sand-mud mixtures is highly affected by the dry bulk density of the mud component. The varying dry bulk density of the mud component in a sand-mud mixture is the main reason for the variation of its critical shear stress with mud content. By analyzing the consolidation behavior of the mud component in mixtures, the effects of the network structure of sand-mud mixtures on the dry bulk density of the mud component and the critical shear stress of sand-mud mixtures were investigated.

DATA AVAILABILITY STATEMENT

The original contributions presented in the study are included in the article/supplementary material, further inquiries can be directed to the corresponding author.

AUTHOR CONTRIBUTIONS

DC and CZ contributed to the conception of the study, the theory development, and manuscript preparation. JZ and YW contributed significantly to the theoretical analysis. DG helped perform the analysis with constructive discussions. YL contributed to the analysis of the data for the work and helped with revising the work. All authors contributed to the article and approved the submitted version.

FUNDING

This work was supported by the National Natural Science Foundation of China (52101310); the Open Research Project of Key Laboratory of Coastal Disaster and Defence (Hohai University), Ministry of Education (201914); the Fundamental Research Funds for the Central Universities, Hohai University (B200202052); the Open Research Fund of State Key Laboratory of Coastal and Offshore Engineering, Dalian University of Technology (LP2020); the Open Research Fund of State Key Laboratory of Estuarine and Coastal Research, East China Normal University (SKLEC-KF202003); the National Natural Science Foundation of China (51879096); the Key Program of National Natural Science Foundation of China (41930538); the Major International (Regional) Joint Research Project of National Natural Science Foundation of China (51920105013); and the National Science Fund for Distinguished Young Scholars (51425901).

ACKNOWLEDGMENTS

The authors would like to thank Liqin Zuo and Eugeny Buldakov for their insightful comments and suggestions, which helped improve the quality of the manuscript.

REFERENCES

Ahmad, M., Dong, P., Mamat, M., Wan Nik, W., and Mohd, M. (2011). The critical shear stresses for sand and mud mixture. *Appl. Math. Sci.* 5, 53–71.

Amos, C., Bergamasco, A., Umgiesser, G., Cappucci, S., Cloutier, D., DeNat, L., et al. (2004). The stability of tidal flats in Venice Lagoon—the results of in-situ measurements using two benthic, annular flumes. *J. Mar. Syst.* 51, 211–241. doi: 10.1016/j.jmarsys.2004.05.013

Baas, J. H., Davies, A. G., and Malarkey, J. (2013). Bedform development in mixed sand–mud: the contrasting role of cohesive forces in flow and bed. *Geomorphology* 182, 19–32. doi: 10.1016/j.geomorph.2012.10.025

Barry, K., Thieke, R., and Mehta, A. (2006). Quasi-hydrodynamic lubrication effect of clay particles on sand grain erosion. *Estuar. Coast. Shelf Sci.* 67, 161–169. doi: 10.1016/j.ecss.2005.11.009

Carniello, L., Defina, A., and D'Alpaos, L. (2012). Modeling sand-mud transport induced by tidal currents and wind waves in shallow microtidal basins: application to the Venice Lagoon (Italy). *Estuar. Coast. Shelf Sci.* 102, 105–115. doi: 10.1016/j.ecss.2012.03.016

Chen, D., Melville, B., Zheng, J., Wang, Y., Zhang, C., Guan, D., et al. (2021). Pickup rate of non-cohesive sediments in low-velocity flows. *J. Hydraulic Res.* 1–11. doi: 10.1080/00221686.2020.1871430

Chen, D., Wang, Y., Huang, H., Chen, C., and Yuan, C. (2017). A behavior-oriented formula to predict coastal bathymetry evolution caused by coastal engineering. *Cont. Shelf Res.* 135, 47–57. doi: 10.1016/j.csr.2017.01.013

Chen, D., Wang, Y., Melville, B., Huang, H., and Zhang, W. (2018). Unified formula for critical shear stress for erosion of sand, mud, and sand-mud mixtures. *J. Hydraul. Eng.* 144:04018046. doi: 10.1061/(Asce)Hy.1943-7900.0001489

Chiew, Y.-M., and Parker, G. (1994). Incipient sediment motion on non-horizontal slopes. *J. Hydraul. Res.* 32, 649–660. doi: 10.1080/00221689409498706

Das, V. K., Roy, S., Barman, K., Chaudhuri, S., and Debnath, K. (2019). Study of clay–sand network structures and its effect on river bank erosion: an experimental approach. *Environ. Earth Sci.* 78:591.

Deriagin, B. I., and Malkin, A. D. (1950). Cohesive forces between quartz fibers in water environments. *Coll. J.* 12, 431–447. (in Russian)

Dickhudt, P. J., Friedrichs, C. T., and Sanford, L. P. (2011). Mud matrix solids fraction and bed erodibility in the York River estuary, USA, and other muddy environments. *Cont. Shelf Res.* 31(Suppl. 10), S3–S13. doi: 10.1016/j.csr.2010.02.008

Dou, G. (1962). Theory for incipient motion of sediment. *Sci. Sin.* 11, 999–1032. (in Russian).,

Dou, G. (2000). Incipient motion of sediment under currents. *China Ocean Eng.* 14, 391–406.

Duteil, T., Bourillot, R., Grégoire, B., Virolle, M., Brigaud, B., Nouet, J., et al. (2020). Experimental formation of clay-coated sand grains using diatom biofilm exopolymers. *Geology* 48, 1012–1017. doi: 10.1130/g47418.1

Einstein, H. A. (1950). *The Bed-Load Function for Sediment Transportation in Open Channel Flows U. G. P. Office*, Vol. 1026. Washington, DC: US Department of Agriculture.

Hamaker, H. C. (1937). The London—van der Waals attraction between spherical particles. *Physica* 4, 1058–1072. doi: 10.1016/s0031-8914(37)80203-7

Han, Q. (1982). Characteristics of incipient sediment motion and incipient velocity. *J. Sediment Res.* 2, 11–26. (in Chinese),

Hoath, S. D. (2016). *Fundamentals of Inkjet Printing: The Science of Inkjet and Droplets*. Weinheim: John Wiley & Sons.

Hong, R., and Xu, S. (1991). Experimental study on incipient of mud in a fluid. *J. Tianjin Univ.* S2, 79–85. (in Chinese),

Huang, J. (1989). An experimental study of the scouring and settling properties of cohesive sediment. *Ocean Eng.* 7, 61–70. (in Chinese),

Jacobs, W., Le Hir, P., Van Kesteren, W., and Cann, P. (2011). Erosion threshold of sand-mud mixtures. *Cont. Shelf Res.* 31, 514–525. doi: 10.1016/j.csr.2010.05.012

Kurdistani, S. M., Tomasicchio, G. R., D'Alessandro, F., and Hassanabadi, L. (2019). River bank protection from ship-induced waves and river flow. *Water Sci. Eng.* 12, 129–135. doi: 10.1016/j.wse.2019.05.002

Kusuda, T., Umita, T., Koga, K., Futawatari, T., and Awaya, Y. (1984). Erosional process of cohesive sediments. *Water Sci. Technol.* 17, 891–901. doi: 10.2166/wst.1985.0188

Le Hir, P., Cann, P., Waeles, B. t., Jestin, H., and Bassoullet, P. (2008). Erodibility of natural sediments: experiments on sand/mud mixtures from laboratory and field erosion tests. *Proc. Mar. Sci.* 9, 137–153. doi: 10.1016/s1568-2692(08)80013-7

Le Hir, P., Cayocca, F., and Waeles, B. (2011). Dynamics of sand and mud mixtures: a multiprocess-based modelling strategy. *Cont. Shelf Res.* 31, S135–S149.

Li, H., Yuan, M., and Zhang, X. (1995). Study on critical motion and erosion of cohesive sediment. *J. Waterway Harb.* 3, 20–26. (in Chinese),

Li, Q., Zeng, Y., and Bai, Y. (2020). Mean flow and turbulence structure of open channel flow with suspended vegetation. *J. Hydrodynam.* 32, 314–325. doi: 10.1007/s42241-020-0020-6

Li, Y., Zhang, C., Chen, D., Zheng, J., Sun, J., and Wang, P. (2021). Barred beach profile equilibrium investigated with a process-based numerical model. *Cont. Shelf Res.* 222:104432. doi: 10.1016/j.csr.2021.104432

Lick, W., Jin, L., and Gailani, J. (2004). Initiation of movement of quartz particles. *J. Hydraul. Eng.* 130, 755–761. doi: 10.1061/(asce)0733-9429(2004)130:8(755)

Mehta, A. J. (1989). On estuarine cohesive sediment suspension behavior. *J. Geophys. Res. Oceans* 94, 14303–14314. doi: 10.1029/jc094ic10p14303

Mehta, A. J. (2014). *An Introduction to Hydraulics of Fine Sediment Transport*, Vol. 38. Hackensack, NJ: World Scientific Publishing Company.

Mehta, A. J., and Lee, S.-C. (1994). Problems in linking the threshold condition for the transport of cohesionless and cohesive sediment grain. *J. Coast. Res.* 10, 170–177.

Mehta, A. J., and Letter, J. V. (2013). Comments on the transition between cohesive and cohesionless sediment bed exchange. *Estuar. Coast. Shelf Sci.* 131, 319–324. doi: 10.1016/j.ecss.2013.07.001

Mehta, A. J., and Partheniades, E. (1982). "Resuspension of deposited cohesive sediment beds," in *Proceedings of the 18th Conference on Coastal Engineering*, Cape Town.

Mehta, A., and Parchure, T. (2000). Surface erosion of fine-grained sediment revisited. *Proc. Mar. Sci.* 2, 55–74. doi: 10.1016/s1568-2692(00)80006-6

Meissner, H., Michaels, A., and Kaiser, R. (1964). Crushing strength of zinc oxide agglomerates. *Ind. Eng. Chem. Process Design Dev.* 3, 202–205. doi: 10.1021/i260011a003

Migniot, C. (1989). Tassement et rhéologie des vases. Première partie. *La Houille Blanche*. 7, 11–29. doi: 10.1051/lhb/1989001

Miller, M., McCave, I., and Komar, P. D. (1977). Threshold of sediment motion under unidirectional currents. *Sedimentology* 24, 507–527. doi: 10.1111/j.1365-3091.1977.tb00136.x

Mitchener, H., and Torfs, H. (1996). Erosion of mud/sand mixtures. *Coast. Eng.* 29, 1–25. doi: 10.1016/s0378-3839(96)00002-6

Mostafa, T. S., Imran, J., Chaudhry, M. H., and Kahn, I. B. (2008). Erosion resistance of cohesive soils. *J. Hydraul. Res.* 46, 777–787. doi: 10.1080/00221686.2008.9521922

Nalluri, C., and Alvarez, E. (1992). The influence of cohesion on sediment behaviour. *Water Sci. Tech.* 25, 151–164. doi: 10.2166/wst.1992.0189

Owen, M. (1970). *A Detailed Study of the Settling Velocities of an Estuary Mud (INT 78)*. Wallingford: H. R. Station.

Panagiotopoulos, I., Voulgaris, G., and Collins, M. (1997). The influence of clay on the threshold of movement of fine sandy beds. *Coast. Eng.* 32, 19–43. doi: 10.1016/s0378-3839(97)00013-6

Partheniades, E. (1965). Erosion and deposition of cohesive soils. *J. Hydraul. Div.* 91, 105–139. doi: 10.1061/jyceaj.0001165

Perkey, D. W., Smith, S. J., and Priestas, A. M. (2020). *Erosion Thresholds and Rates for Sand-Mud Mixtures (ERDC-CHL TR-20-13)*. Vicksburg, MS: U. A. C. o. Engineers.

Revil, A., Grauls, D., and Brévart, O. (2002). Mechanical compaction of sand/clay mixtures. *J. Geophys. Res. Solid Earth* 107:2293.

Righetti, M., and Lucarelli, C. (2007). May the Shields theory be extended to cohesive and adhesive benthic sediments? *J. Geophys. Res. Oceans* 112:C05039.

Sanford, L. P., and Maa, J. P.-Y. (2001). A unified erosion formulation for fine sediments. *Mar. Geol.* 179, 9–23. doi: 10.1016/s0025-3227(01)00201-8

Sharif, A. R. (2003). *Critical Shear Stress and Erosion of Cohesive Soils.* Ph.D thesis. New York, NY: State University of New York at Buffalo.

Smith, J., Perkey, D., and Priestas, A. (2015). "Erosion thresholds and rates for sand-mud mixtures," in *Proceedings of the 13th International Conference on Cohesive Sediment Transport Processes*, Leuven.

Soulsby, R., and Whitehouse, R. (1997). "Threshold of sediment motion in coastal environments Pacific Coasts and Ports' 97," in *Proceedings of the 13th Australasian Coastal and Ocean Engineering Conference and the 6th Australasian Port and Harbour Conference*, Christchurch.

Tang, C. (1963). Law of sediment threshold. *J. Hydraul. Eng.* 2, 1–12. (in Chinese),

Ternat, F., Boyer, P., Anselmet, F., and Amielh, M. (2008). Erosion threshold of saturated natural cohesive sediments: modeling and experiments. *Water Resour. Res.* 44:W11434.

Torfs, H. (1995). *Erosion of mud/sand mixtures.* Ph.D. thesis. Leuven: Katholieke Univeriteit Leuven.

Torfs, H., Jiang, J., and Mehta, A. (2000). Assessment of the erodibility of fine/coarse sediment mixtures. *Proc. Mar. Sci.* 3, 109–123. doi: 10.1016/s1568-2692(00)80116-3

Van Ledden, M. (2003). *Sand-mud Segregation in Estuaries and Tidal Basins*. Delft: Delft University of Technology.

Van Ledden, M., Van Kesteren, W. G. M., and Winterwerp, J. C. (2004). A conceptual framework for the erosion behaviour of sand-mud mixtures. *Cont. Shelf Res.* 24, 1–11. doi: 10.1016/j.csr.2003.09.002

Van Rijn, L. C. (1993). *Principles of Sediment Transport in Rivers, Estuaries and Coastal Seas*, Vol. 1006. Amsterdam: Aqua publications.

Van Rijn, L. C. (2020). Erodibility of mud-sand bed mixtures. *J. Hydraul. Eng.* 146:04019050. doi: 10.1061/(ASCE)HY.1943-7900.0001677

Vollmer, S., and Kleinhans, M. G. (2007). Predicting incipient motion, including the effect of turbulent pressure fluctuations in the bed. *Water Resour. Res.* 43:W05410. doi: 10.1029/2006WR004919

Waeles, B., Le Hir, P., and Lesueur, P. (2008). "A 3D morphodynamic process-based modelling of a mixed sand/mud coastal environment: the seine estuary," in *France Sediment and Ecohydraulics: INTERCOH, 2005. Proceedings in Marine Science*, eds T. Kusuda, H. Yamanishi, J. Spearman, and J. Z. Gailani (Amsterdam: Elsevier) doi: 10.1016/S1568-2692(08)80034-4

Winterwerp, J., Kesteren, W., Prooijen, B., and Jacobs, W. (2012). A conceptual framework for shear flow–induced erosion of soft cohesive sediment beds. *J. Geophys. Res. Oceans* 117:C10020. doi: 10.1029/2012JC008072

Worden, R. H., Griffiths, J., Wooldridge, L. J., Utley, J. E. P., and Armitage, P. J. (2020). Chlorite in sandstones. *Earth Sci. Rev.* 204:103105. doi: 10.1016/j.earscirev.2020.103105

Wu, W., Perera, C., Smith, J., and Sanchez, A. (2017). Critical shear stress for erosion of sand and mud mixtures. *J. Hydraul. Res.* 56, 1–15. doi: 10.1080/00221686.2017.1300195

Xu, D., Bai, Y., Ji, C., and Williams, J. (2015). Experimental study of the density influence on the incipient motion and erosion modes of muds in unidirectional flows: the case of Huangmaohai Estuary. *Ocean Dyn.* 65, 187–201. doi: 10.1007/s10236-014-0803-9

Yang, B., Luo, Y., Jeng, D., Feng, J., and Huhe, A. (2018). Experimental studies on initiation of current-induced movement of mud. *Appl. Ocean Res.* 80, 220–227. doi: 10.1016/j.apor.2018.09.006

Yang, M., and Wang, G. (1995). The incipient motion formulas for cohesive fine sediments. *J. Basic Sci. Eng.* 3, 99–109. (in Chinese),

Ye, Z., Cheng, L., and Zang, Z. (2011). "Experimental study of erosion threshold of reconstituted sediments," in *Proceedings of the 30th International Conference on Ocean, Offshore and Arctic Engineering*, Rotterdam. doi: 10.1115/OMAE2011-50067

Zhang, H. (2012). A unified formula for incipient velocity of sediment. *J. Hydraul. Eng.* 43, 1387–1396. (in Chinese).,

Zhang, M., and Yu, G. (2017). Critical conditions of incipient motion of cohesive sediments. *Water Resour. Res.* 53, 7798–7815. doi: 10.1002/2017WR021066

Zhang, M., Yu, G., La Rovere, A., and Ranzi, R. (2017). Erodibility of fluidized cohesive sediments in unidirectional open flows. *Ocean Eng.* 130, 523–530. doi: 10.1016/j.oceaneng.2016.12.021

Zhang, Z., and Zou, Z. (2019). Application of power law to vertical distribution of longshore currents. *Water Sci. Eng.* 12, 73–83. doi: 10.1016/j.wse.2019.04.004

Zheng, J., Yao, Y., Chen, S., Chen, S., and Zhang, Q. (2020). Laboratory study on wave-induced setup and wave-driven current in a 2DH reef-lagoon-channel system. *Coast. Eng.* 162:103772. doi: 10.1016/j.coastaleng.2020.103772

Zhu, Y., Jinyou, L., Liao, H., Wang, J., Fan, B., and Yao, S. (2008). Research on cohesive sediment erosion by flow: an overview. *Sci. China* 51, 2001–2012. doi: 10.1007/s11431-008-0232-4

Zuo, L., Roelvink, D., Lu, Y., and Li, S. (2017). On incipient motion of silt-sand under combined action of waves and currents. *Appl. Ocean Res.* 69, 116–125. doi: 10.1016/j.apor.2017.10.005

Conflict of Interest: The authors declare that the research was conducted in the absence of any commercial or financial relationships that could be construed as a potential conflict of interest.

Publisher's Note: All claims expressed in this article are solely those of the authors and do not necessarily represent those of their affiliated organizations, or those of the publisher, the editors and the reviewers. Any product that may be evaluated in this article, or claim that may be made by its manufacturer, is not guaranteed or endorsed by the publisher.

GLOSSARY

A, coefficient (J m^{-2}); A_h , Hamaker constant (J); C_d , C_l , drag and lift coefficients (-); c_n , coordination number (-); d_a , diameter of the mud parcel (m); d_m , diameter of cohesive particles (m); d_r , representative diameter (m); d_{r*} , dimensionless diameter of d_r (-); d_s , diameter of sand particles (m); d_{s*} , dimensionless diameter of sand particles (-); E, relative error (-); F_c , resultant cohesive force (kg m s^{-2}); F_d , drag force (kg m s^{-2}); F_l , lift force (kg m s^{-2}); f_c , van der Waals force (kg m s^{-2}); G, effective gravitational force (kg m s^{-2}); g, gravitational acceleration (m s^{-2}); k_1 , k_2 , k_3 , k_4 , k_5 , coefficients (-); k_s , equivalent roughness height (m); l_Δ , separation distance between two (cohesive) particles (m); $\log E_{rms}$, logarithmic root-mean-square error (-); m, exponent (-); N, number of mud particles per unit area of a ruptured surface; n, number of mud particles coating the motion-initiating sand particle or number of mud particles in the buried surface of the motion-initiating mud parcel (-); p_m , mud content (%); p_s , sand content (%); p_{mcr} , critical mud content (%); r, the solid/void volume ratio (-); r_c , the reference solid/void volume ratio (-); s, distance between two neighboring particles (m); u_b , near-bed velocity (m s^{-1}); $u_{b,cr}$, near-bed flow velocity for the incipient motion of sediment (m s^{-1}); u_* , shear velocity (m s^{-1}); z_b , the elevation where the drag force acts on the sediment particle or parcel (m); α , coefficient (-); α_1 , area shape factor of the sand particle or the mud parcel (-); α_2 , volumetric shape coefficient (-); α_2 , volumetric shape coefficient (-); β_v , β_w , coefficients (-); δ , thickness of the water film coating the cohesive particles (m); η , coefficient (-); η_Δ , relative protruding height (-); θ_{cr0} , critical Shields parameter of non-cohesive sediment (-); υ , kinematic viscosity of water (m^2 s); ρ , density of water (kg m^{-3}); ρ_d , dry bulk density of sediment (kg m^{-3}); ρ_{dm} , dry bulk density of the cohesive (mud) component in a mixture (kg m^{-3}); ρ_{pa} , density of the mud parcel (kg m^{-3}); ρ_{pm} , density of cohesive (mud) particles (kg m^{-3}); ρ_{pr} , density of a sand particles or a mud parcel (kg m^{-3}); ρ_{ps} , density of sand particles (kg m^{-3}); ρ_{sdm} , stable dry bulk density of mud (kg m^{-3}); ζ , coefficient (-); τ_b , bed shear stress (Pa); τ_{cr} , critical shear stress (Pa); τ_{crc} , critical shear stress for reference (Pa); $\tau_{cr,c}$, calculated critical shear stress (Pa); τ_{crs} , critical shear stresses of pure sand (Pa); τ_{crm} , critical shear stresses of pure mud (Pa); $\tau_{cr,m}$, measured critical shear stress (Pa); τ_{crL} , critical shear stress for mixtures with low mud contents (Pa); τ_{crmc} , critical shear stress for erosion of mud corresponding to the porosity of the mud component in a sediment mixture (Pa); ϕ_m , mud porosity (-); φ_s , volume fraction of sand particles (-); χ , the correction factor of Einstein (-).

frontiers in Marine Science

ORIGINAL RESEARCH
published: 12 November 2021
doi: 10.3389/fmars.2021.759067

Vulnerability Analysis of Episodic Beach Erosion by Applying Storm Wave Scenarios to a Shoreline Response Model

*Tae-Kon Kim[1], Changbin Lim[1] and Jung-Lyul Lee[2]**

[1] School of Civil, Architectural and Environmental System Engineering, Sungkyunkwan University, Suwon, South Korea,
[2] Graduate School of Water Resources, Sungkyunkwan University, Suwon, South Korea

Recently, because of the influence of climate change on sea level change, there has been growing concern regarding the erosion of beaches, which play a role in reducing the damage caused by coastal disasters. However, despite these concerns, a comprehensive understanding of the morphodynamic relationship between hazard factors and beach erosion is still lacking. Therefore, in this study, a vulnerability analysis of beach erosion was conducted by applying the shoreline response model (SLRM) of bulk model type, which identifies the physical characteristics of relevant coefficients based on the suspended sediment movement processes. To characterize wave energy incidence, storm wave scenario modeling and extreme wave analysis were conducted using wave data of 40 years on the east coast of Korea provided by the National Oceanic and Atmospheric Administration. A dimensionless mathematical function representing the storm wave scenario was proposed as a function of the peak wave height. In addition, to examine whether the beach vulnerability curve (BVC) obtained from the SLRM is valid, it was compared with the long-term shoreline observation data conducted at Maengbang Beach. For the past 9 years, sand sampling and shoreline observations were performed at Maengbang Beach about 5 times a year. However, since observations were performed in time intervals of several months, the direct comparison with model results was impossible, so a comparative analysis through statistical analysis of shoreline variability was performed. The variability of the shoreline for each reference point followed a normal distribution with a standard deviation of approximately 7.1 m. As a result of comparing the BVC results obtained from these statistical characteristics with those obtained from the model, significant similarity was shown in the high wave condition. Finally, the model was performed on two factors (mean wave height and peak wave height) which appear in SWSF and three factors (wave energy at breaking point, beach response factor and beach recovery factor) which appear in SLRM, and by analyzing the results, an approximate formula for the BVC is derived. This novel BVC approximation equation provides an intuitive understanding of the factors that affect beach vulnerability as well as their importance, and estimates the beach buffer section required to prevent coastal facilities from being damaged by erosion during a specific period. The results of this study can help limit reckless coastal development and mitigate erosion damage.

Keywords: storm wave, numerical model, beach response factor, beach recovery factor, extreme wave analysis, shoreline survey, NOAA wave data

OPEN ACCESS

Edited by:
Giandomenico Foti, Mediterranea University of Reggio Calabria, Italy

Reviewed by:
Kyu-Han Kim, Catholic Kwandong University, South Korea
Noujas Varangalil, National Centre for Coastal Research, India

***Correspondence:**
Jung-Lyul Lee
jllee6359@hanmail.net

Specialty section:
This article was submitted to Coastal Ocean Processes, a section of the journal Frontiers in Marine Science

Received: *15 August 2021*
Accepted: *06 October 2021*
Published: *12 November 2021*

Citation:
Kim TK, Lim C and Lee JL (2021) Vulnerability Analysis of Episodic Beach Erosion by Applying Storm Wave Scenarios to a Shoreline Response Model. Front. Mar. Sci. 8:759067. doi: 10.3389/fmars.2021.759067

INTRODUCTION

Numerous research efforts have been made, including establishing concepts and developing models, to evaluate the vulnerability of the coastal environment in relation to coastal disasters and climate change (IPCC, 1996, 2001; UKCIP, 2003; UNDP, 2005; UNFCCC, 2005; Han, 2006; Yook et al., 2011). Although studies often define vulnerability differently, in general, it can be characterized to be receiving a certain amount of impact from external pressure. In particular, the erosion vulnerability of coastal areas, which are prone to coastal disasters because of the effects of climate change, such as sea level changes, is emerging as a research topic of interest. However, despite these efforts, a comprehensive understanding of the hazard factors related to beach erosion and the morphodynamic processes of shoreline retreat is lacking for evaluating beach vulnerability.

Most of the understanding of episodic erosion phenomena is based on statistical analysis of beach erosion survey data or numerical model results that rely on physical parameters related to the sediment process (Mendoza and Jimeńez, 2006; Bosom and Jimeńez, 2011; Oliveira et al., 2014; Ballesteros et al., 2017; Narra et al., 2019; Anfuso et al., 2021). Data analysis has been mainly used for the purpose of finding long-term erosion rates, and short-term erosion has recently become possible with the analysis of CCTV image data. Yates et al. (2009) estimated the convergence position of the shoreline by examining changes in the beach profile as a response to changes in the incoming wave energy via long-term field measurements. In this scenario, if the external hazard is regarded as incoming wave energy and the impact factor is shoreline retreat, the beach vulnerability can be studied. However, their research was limited because the location of the shoreline that ultimately converges when a specific wave energy value was continuously applied. Recently, Park et al. (2019) suggested a methodology for analyzing beach vulnerability by analyzing shoreline data variability observed on the east coast of Korea and the extreme behavior of incident waves. However, the methodology has not been verified because of a lack of long-term wave and shoreline survey data for comparison.

To compensate for these limitations, a method that can quantitatively evaluate beach vulnerability by applying a highly reliable numerical model is required. However, the incidence of wind waves from distant seas to the shore shows an infinitely repeating phenomenon and irregular changes. Therefore, ensuring the reliability of the numerical model is important, and it is also necessary to establish a wave scenario model that considers the characteristics of wave duration. Furthermore, it is necessary to analyze how the duration of the incident wave affects shoreline fluctuations. Specifically, it is necessary to develop a methodology for extracting a vulnerability curve by analyzing long-term wave data and reflecting the influence of the wave duration to determine the maximum receding width of the shoreline. Unlike the wave input conditions used for designing port facilities, the beach response assumes that erosion proceeds according to the incidence of high waves, and when the waves calm, it recovers to its original position. However, there are few cases in which scenario models have been constructed for this purpose. Therefore, in this study, using 40-year National Oceanic and Atmospheric Administration (NOAA) data for the east coast of Korea, a scenario model formula of incident wave height and duration that is dimensionless to the maximum wave height was derived.

Several models have been developed to numerically simulate beach profile responses to identify the causes and develop preventive responses to beach erosion problems caused by storm wave incidence (Larson et al., 1999; Lesser et al., 2004; Roelvink et al., 2009; Deltares, 2018a,b). A shoreline response model of bulk model type was first proposed by Wright et al. (1985a,b). It was used to represent the rate at which the beach state changes and applied the convergence characteristics of beach conditions following storm events in situations where the mechanism of sediment movement in the breaking zone had not yet been elucidated. Later, this equation was also employed for sandbar evolution (Plant et al., 1999) and beach slope change (Madsen and Plant, 2001). Approximately 20 years later, Miller and Dean (2004) proposed a simple governing equation of the ODE type that, based on empirical evidence, relates shoreline change to shoreline position. This equation was calibrated using periodic shoreline data.

The proposed governing equations reveal that the shoreline approaches the equilibrium form for steady-state conditions at approximately exponential rates, which is consistent with laboratory investigations (Swart, 1974) and numerical results (Kriebel and Dean, 1985; Larson et al., 1999). In addition, the recent researches (Yates et al., 2009; Davidson et al., 2013; Toimil et al., 2017) established or examined a shoreline response model using long-term field observations to evaluate its practical applicability. In this study, the ODE type model proposed by Lim et al. (2021) was employed, which derived a correlation of 74% with respect to the wave input and shoreline change observation data used for the blind test of Montaño et al. (2020). Overall, two main constants are employed, the beach response factor and the beach recovery factor, and their physical properties are analyzed by evaluating the horizontal behavior of suspended sediments. However, the peak erosion width indicating the degree of beach erosion vulnerability has not been presented due to the various conditions of wave incidence yet even though the parameters a_r and k_r of the SLRM related to the beach property of erosion vulnerability are determined.

The main objective of this study is to obtain a relational expression for the vulnerability of the shoreline to episodic erosion according to the impact of storm wave energy given as a function of the peak wave height. **Figure 1** shows the detailed research process of applying the SLRM. Section "Extraction of Storm Wave Scenario from NOAA Wave Data" introduces the process of extracting a storm wave scenario function (SWSF) by analyzing NOAA wave data for Maengbang Beach on the east coast of Korea. Section "Derivation of Beach Vulnerability Curve by the Shoreline Response Model" presents a method for deriving the vulnerability curve equation by applying this scenario function to the ODE SLRM, which has been recently proven to exist high reliability. In Section "Beach Vulnerability Curve for Maengbang Beach," in order to analyze the feasibility of this method, the dependence of beach erosional width on wave frequency was obtained using the results of

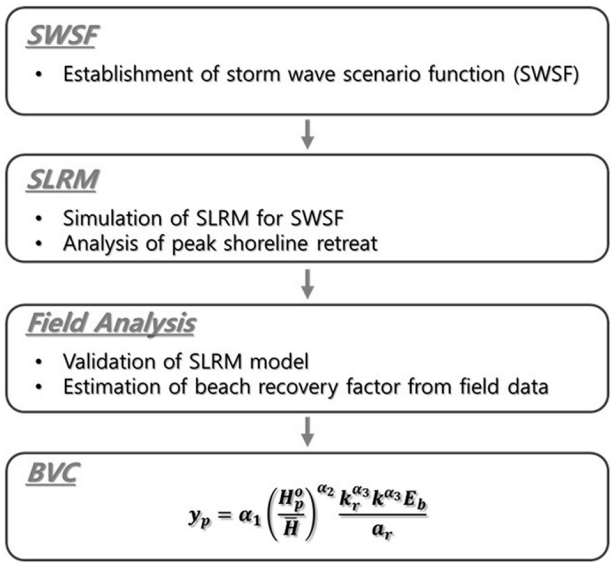

FIGURE 1 | Research processes for deriving a beach vulnerability curve (BVC).

periodic shoreline surveys. In addition, the results of erosion vulnerability are presented in combination with the extreme wave analysis, which corresponds to the most fundamental vulnerability analysis method, and are compared with the results obtained from the SLRM. In Section "Discussion," the effect of duration on erosion vulnerability was discussed by modulating the duration of the SWSF. An approximate formula for erosion vulnerability was also developed by analyzing the influence of factors on erosion vulnerability. Finally, the main conclusions are presented and future research paths are proposed based on the results of this study.

EXTRACTION OF STORM WAVE SCENARIO FROM NOAA WAVE DATA

Study Site

Maengbang Beach, located in Samcheok City, Gangwondo, on the east coast of South Korea, is a linear coast stretching over approximately 4.6 km in the northwest to southeast (NE-SE) direction. The average beach width is approximately 48.0 m, and the shoreline has a mixture of straight and bow shapes. Maengbang Beach is a sandy beach near Osipcheon and Maeupcheon (**Supplementary Figure 1**). **Supplementary Figure 2** shows its tide table and wave rose diagram (Ministry of Ocean and Fisheries, 2017). The study site has a small spring tidal range of 15.6 cm and total tidal range 33.4 cm with little tidal fluctuation, and the annual mean wave incidence at the study site has a significant wave height of 1.14 m and a significant wave period of 7.78 s. The main wave direction in the deep sea shows 39.5°, and compared to the shoreline inclination angle of about 42°, there is a possibility of net littoral drift to the south.

National Oceanic and Atmospheric Administration Wave Data

For the duration of wave actions, wave influence is reflected in the change of beach profiles and most storm waves show a tendency to develop, peak, and then decrease (Corbella and Stretch, 2012). In this study, wave data from NOAA was used for the storm wave scenario model analysis. The annual changes in the significant wave height and significant wave period of Maengbang Beach from 1979 to 2018 are shown in **Supplementary Figures 3,4**, respectively. **Supplementary Figure 5** is a graph showing the annual change of annual mean significant wave height, peak period, and dominant wave direction. **Supplementary Figures 5A,B** show the annual variations of values corresponding to 10% intervals from 10 to 90% from the smallest value out of about 365 × 8 (2920) data every year using wave height and period data at 3 h intervals for 40 years. And **Supplementary Figure 5C** shows the values corresponding to 10% intervals from 10% to 40% in the +/− direction based on 34°N using the wave direction data, showing the change by year for 40 years. It can be seen that the annual mean wave height, period, and wave direction over the past 40 years has been maintained without significant change. Therefore, the amount of long-term change in the wave environment is negligible, and the effect of climate change in this sea area can be found to be very insignificant.

The wave height-period joint probability distribution obtained from the significant wave height-peak period data for these 40 years is shown in **Supplementary Figure 6**, and the corresponding spectrum is shown in **Figure 2**. The frequency spectrum was obtained using the joint distribution by converting the period into frequency (Sorensen, 1993) and wave height into spectrum. The directional spectrum is shown in **Figure 3**. Also, **Figures 2**, **3** show the dotted line results of the spectrum and wave direction distribution obtained at intervals of every 10 years. The peak frequency is 0.12 Hz, and the incoming deep-sea wave direction showing the peak wave energy was calculated to be 25° clockwise from true north.

Analysis of Temporal Evolution of Wave Scenario

In order to reproduce the storm wave scenario for Maengbang Beach, the method proposed by Kim et al. (2021) is adopted in this study. Using 40-year NOAA data (38.5°N, 129.0°E) for Bongpo Beach, located about 111 km north of Maengbang Beach, Kim et al. (2021) normalized the wave height and period data to peak wave height values and the time scale as a function of peak wave height. Therefore, the storm scenario for Maengbang Beach was reproduced similarly using 40-year wave data of NOAA grid point (37.5°N, 129.5°E) closest to Maengbang Beach.

Supplementary Figures 7, **8** show the wave height and wave period scenarios, respectively. The dotted lines indicate the mean and maximum values of all storm wave conditions exceeding a peak wave height in deep water (H_p^o) of 4.5 m. The results show that the curves have a good fit with the extreme wave scenario of the NOAA data. In addition, the scenario function of the storm

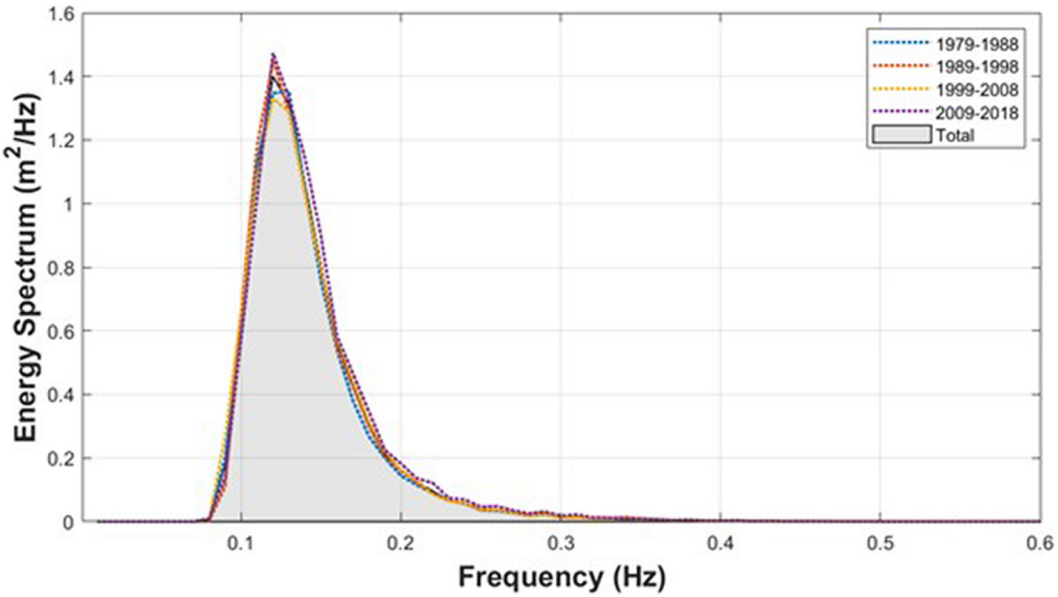

FIGURE 2 | Annual mean wave spectrum at Maengbang coast obtained from the NOAA dataset (1979–2018).

wave height affecting Maengbang Beach is expressed in terms of dimensionless time $t^{'}$, as given in Eq. 1.

$$H'_m = \frac{1}{H_p}\frac{A_H}{(t^{'} - t'_{pH})^5}\exp\left[\left(\frac{B_H - t'_{pH}}{t^{'} - t'_{pH}}\right)^4\right] \quad (1)$$

Where $A_H = 1.28 \times 10^{-9}$, $B_H = 0.00007$, and t'_{pH}=−0.013. The scenario function of the storm wave period can be expressed as:

$$T'_m = \frac{1}{T_p}\frac{A_T}{(t^{'} - t'_{pT})^5}\exp\left[\left(\frac{B_T - t'_{pT}}{t^{'} - t'_{pT}}\right)^4\right] \quad (2)$$

Where $A_T = 4.1 \times 10^{-7}$, $B_T = 0.0042$, and $t'_{pT} = -0.039$. The time is converted to days from the dimensionless time t according to the peak height $H_p^o\ (m)$ as follows:

$$t^{'} = \frac{t_{real}\ (day)}{\left(\frac{H_p^o}{H}\right)^{-0.3}} \times 365 \quad (3)$$

Supplementary Figure 9 compares the time series data wherein the peak wave height and time are dimensionless for wave scenarios with peak wave heights ranging from 4.5 to 7.5 m. These values were obtained using Eq. 1. Similarly, **Supplementary Figure 10** compares the time series data wherein the wave period is dimensionless for wave scenarios with a similar range for peak wave heights. These values were obtained using Eq. 2. The dimensionless time is converted to the real time (*day*) via multiplication with $\left(\frac{H_p}{H}\right)^{-0.3} \times 365$.

Wave Energy at Breaking Point

To apply the SWSF to the SLRM, it is necessary to calculate the wave height at the breaking point using the offshore wave information. If waves are induced in deep water via wave refraction and wave shoaling and they are broken near shore, the height H_b at the breaking point can be obtained according to the law of conservation of energy. In a linear coastal terrain, wherein the isochore line is parallel to the shoreline, assuming that waves break in the shallow water, Eq. 1 can be rearranged in terms of H_b to obtain the following:

$$H_b = \sqrt{\frac{1.56T}{2(gh_b)^{0.5}}}\sqrt{\frac{\cos\theta_0}{\cos\theta_b}}H_0 \quad (4)$$

Then, by substituting $h_b = H_b/\gamma$, where γ is the wave breaking coefficient, the relationship can be reorganized as:

$$H_b = \left[\sqrt{\frac{1.56T}{2(g/\gamma)^{0.5}}}\sqrt{\frac{\cos\theta_0}{\cos\theta_b}}H_0\right]^{4/5} \quad (5)$$

where the wave breaking coefficient γ is assumed to be 0.55, which is the generally applied value for significant wave heights. The wave direction θ_b at the breaking point (assumed to be in shallow water) was obtained by applying Snell's law as follows:

$$\theta_b = \sin^{-1}\left(\sin\theta_0\frac{\sqrt{gh_b}}{1.56T}\right) \quad (6)$$

This effect of refraction is neglected when calculating the breaking wave height, which is the input data of SLRM, from the SWSF of deep sea waves, but Eq. 6 is applied when performing the extreme value analysis on the breaking wave height in Section "Extreme Wave Height Analysis of Incidence Waves". **Figure 4**

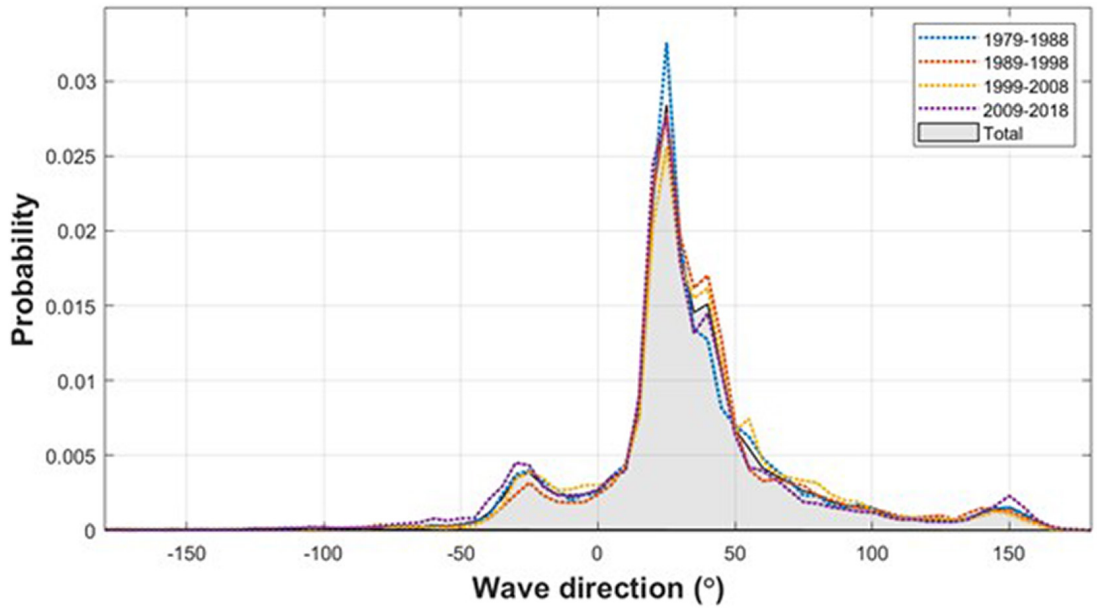

FIGURE 3 | Wave direction distribution at Maengbang coast from the NOAA dataset (1979–2018).

shows the wave scenario functions determined using the peak wave height in deep water H_p^o for the real-time scale t_{real} and the corresponding wave energy at the breaking point.

DERIVATION OF BEACH VULNERABILITY CURVE BY THE SHORELINE RESPONSE MODEL

Governing Equation of the Shoreline Response Model

The governing equation used to determine the maximum retreat width of the shoreline as an indicator of erosion vulnerability is given by Eq. 7. This equation was empirically obtained by Miller and Dean (2004), and recently physical validity has been verified by Lim et al. (2021) by using the horizontal behavior concept of suspended sediment. In addition, applying about 11 years of wave input data (via model prediction) and shoreline data (via CCTV analysis) provided by Montaño et al. (2020), Lim et al. (2021) achieved satisfactory model performance showing a 74% correlation.

$$\frac{dy}{dt} = k_r\left(\frac{E_b}{a_r} - y\right) \tag{7}$$

where y is the shoreline erosion width and k_r is the beach recovery factor, which is related to the recovery speed at which the suspended sediment returns to its original position after erosion. Further, E_b is the energy at the breaking point for the wave scenario model described in Subsection "Analysis of Temporal Evolution of Wave Scenario," and a_r is the beach response factor, which is a positive value in Eq. 7, and its value can be obtained from the sedimentation trend curve equation presented by Yates et al. (2009) or simply from D_{50}, as suggested by Kim and Lee (2018).

Estimating Beach Response and Recovery Factors

Two physical parameters exist in the shoreline response equation (Eq. 7). The first is the beach response factor a_r and the second is the beach recovery factor k_r. The first factor, a_r, can be easily estimated from D_{50}, as described below, while the second factor, k_r, can be obtained from the variation of the shoreline survey data.

Based on Dean's equilibrium beach profile formula, Kim and Lee (2018) proposed a linear relationship between the equilibrium shoreline position S_{eq} (negative value) and wave energy at the breaking point E_b that is similar to the field observations of Yates et al. (2009).

$$S_{eq} = \left[\frac{16}{\gamma}\left(\frac{m_i}{\widetilde{H_b}} - \frac{1}{A^{3/2}\sqrt{\gamma\widetilde{H_b}}}\right)\right]\left(E_b - \overline{E_b}\right) \tag{8}$$

where $\widetilde{H_b}$ is the representative wave height,γ is the breaking coefficient, $\overline{E_b}$ is the annual mean wave energy at the breaking point, and m_i refers to the initial slope, which can be estimated as a function of beach scale factor A as follows:

$$m_i = \frac{f}{A^{3/2}} \tag{9}$$

where A is a function of D_{50} estimated from the table provided by Dean (1977). Yates et al. (2009) found that for Torrey Pines Beach, California, A has a value of $f = 1.51m^{1/2}$ for $D_{50} = 0.23$ mm.

Yates et al. (2009) previously proposed an equation similar to Eq. 8 based on Dean's equation of the equilibrium beach profile,

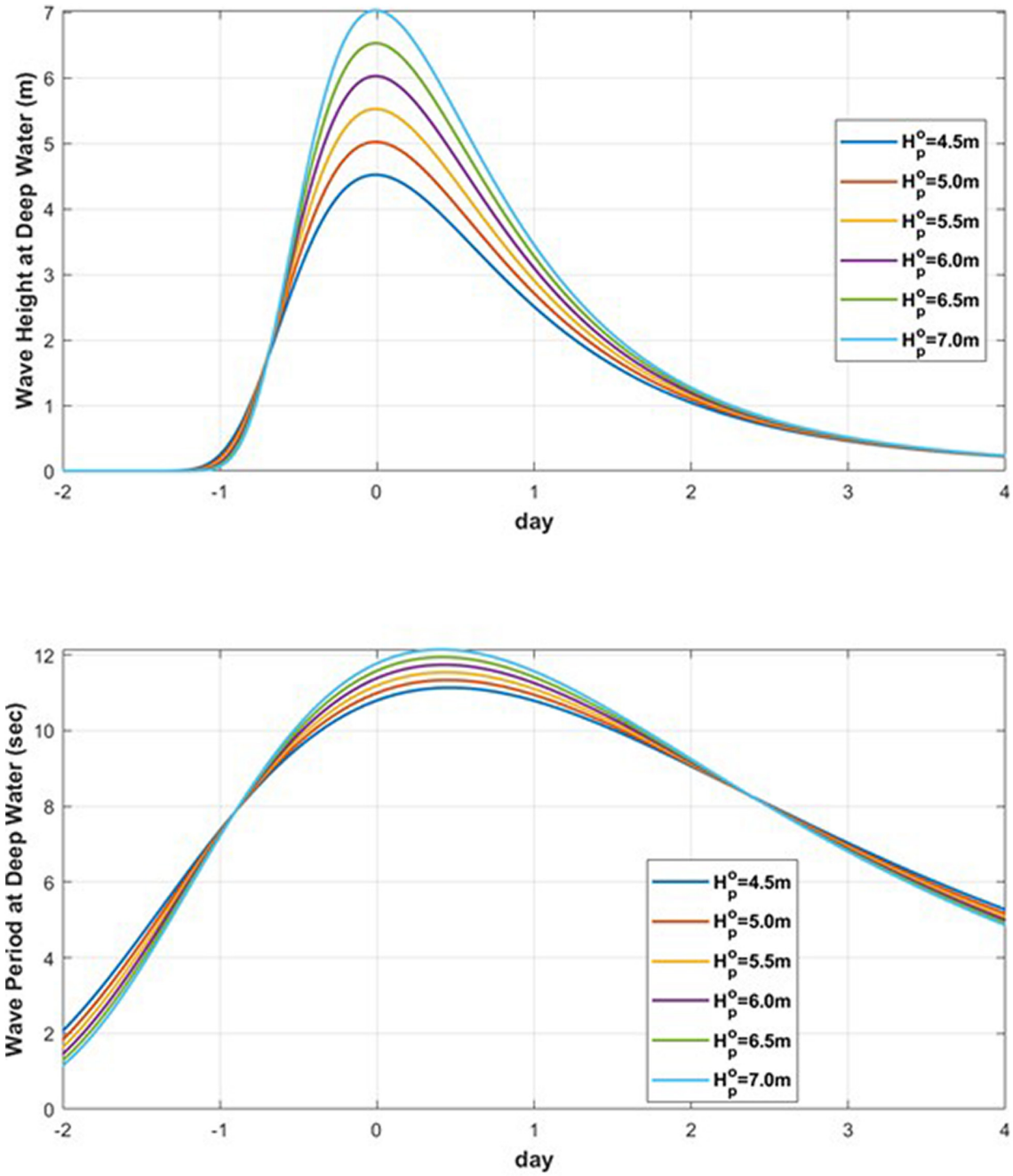

FIGURE 4 | Temporal variation of storm wave height **(Up)** and wave period **(Down)** in deep water with respect to H_p^o.

using which they identified the shoreline erosion/accretion trend according to the wave energy and associated shoreline position of the California coast. Overall, they obtained a linear relationship between wave energy E and shoreline erosion width S_{eq} where erosion and sedimentation are balanced:

$$S_{eq} = -\frac{(E-b)}{a_r} \tag{10}$$

where a_r is a proportional constant between the wave energy and shoreline position, and a larger value indicates lower vulnerability of the beach, and vice versa. Therefore, a_r tends to increase as the grain size increases, and tends to decrease as the grain size decreases. a_r is considered to be a factor indicative of protection against beach erosion because a high value mitigates beach erosion against high waves, and its reciprocal was determined to be the vulnerability proportionality constant in this study. Note that

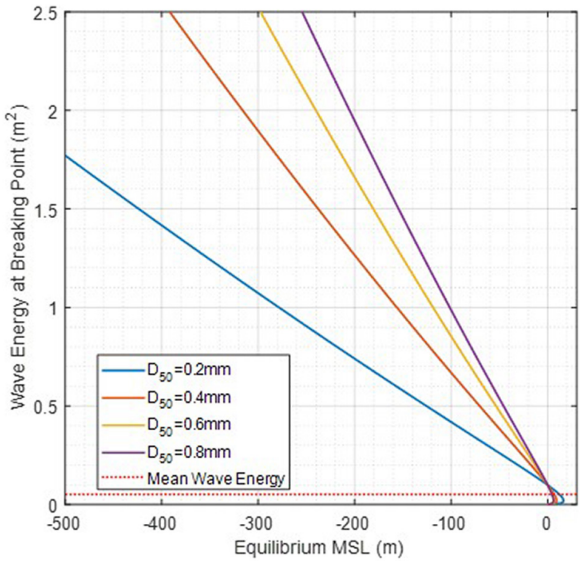

FIGURE 5 | A curve showing the correlation between SL position and energy obtained from Dean's equilibrium beach profile formula.

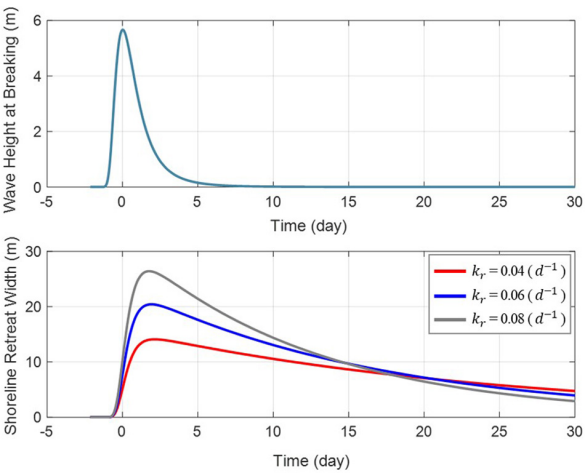

FIGURE 6 | Time evolution of wave scenario and shoreline retreat width for 3 different k_r values.

it is assumed that b in Eq. 10 is relatively negligible for a high wave incidence.

An approximate solution of the proportional constant a_r (negative value) given in Eq. 8 can be obtained using the following equation:

$$a_r \cong \frac{\gamma A^{\frac{3}{2}}}{16}\left(\frac{\widetilde{H_b}}{\sqrt{\frac{\widetilde{H_b}}{\gamma}-f}}\right) \tag{11}$$

According to Eq. 11, $a_r = 0.0018$ m when the sand particle size is 0.1 mm, and $a_r = 0.0111$ m when the sand particle size is 1.0 mm at $\widetilde{H_b} = 6.0\ m$ and $\gamma = 0.55$ (for the significant wave). **Figure 5** shows how the linear relationship between the equilibrium MSL and wave energy at the breaking point changes according to the median particle size. Note that the beach response factor a_r is regarded as a positive value in Eq. 7.

Figure 6 shows the wave scenario at the breaking points, and the numerical solutions of Eq. 7 for $k_r = 0.04$, 0.06, and 0.08 d^{-1}. The results show that the wave input that causes shoreline change lasts for 2–3 days, but the evolution of the shoreline shows that it is affected for more than 30 days before returning to the original initial shoreline position. For $k_r = 0.06\ d^{-1}$, it is estimated that approximately 50 days are required for a 95% recovery after maximum shoreline erosion occurs. In this simulation, $H_p = 6.0$ m and $a_r = 0.007$ m were used for the peak wave height in deep water and beach response factor, respectively.

Predicting Peak Erosion Width Using the SWSF Formula

Figure 7 shows the results obtained using Eq. 7 to determine the peak erosion width for peak wave heights of 4.5, 5.5, 6.5, and 7.5 m. The results of the contour line correspond to the proportionality constants of the vulnerability curves. The ranges of the two factors considered were evaluated based on whether they corresponded to a range of values corresponding to a general sand beach. The temporal change in the wave energy at the breaking point given in Eq. 7 was obtained after converting the significant wave height and peak wave period given by the scenario functions into the wave height at the breaking point.

Based on the ODE in Eq. 7, because dy/dt becomes zero at the time of peak SL retreat, when the elapsed time from the peak wave height passing to the peak erosion retreat is τ, $E_b(\tau)/a_r$ indicates the y_{peak}. Therefore, y_{peak} given as a function of τ is:

$$y_{peak} = \frac{E_b(\tau)}{a_r} \tag{12}$$

Figure 8 shows the results of the τ analysis for $\overline{H} = 1.14$ m. As shown by Eq. 13, τ is a function of only k_r, regardless of a_r.

$$\tau\,(day) \cong \frac{-0.8\ln\left(k_r\right)+0.6}{\left(\frac{H_p^o}{\overline{H}}\right)^{0.22}} \tag{13}$$

where H_p^o is the peak wave height in deep water, H_p^o and $\overline{H}$ have the same unit (m), and k_r has a unit of d^{-1}.

Figure 9 shows a comparison of the BVC obtained from the model results using Eq. 7 and that obtained from the approximate results using Eq. 12 for the three different values of a_r and k_r. Compared with each other, they exhibit satisfactory results.

BEACH VULNERABILITY CURVE FOR MAENGBANG BEACH

In Section "Derivation of Beach Vulnerability Curve by the Shoreline Response Model," it was confirmed that the

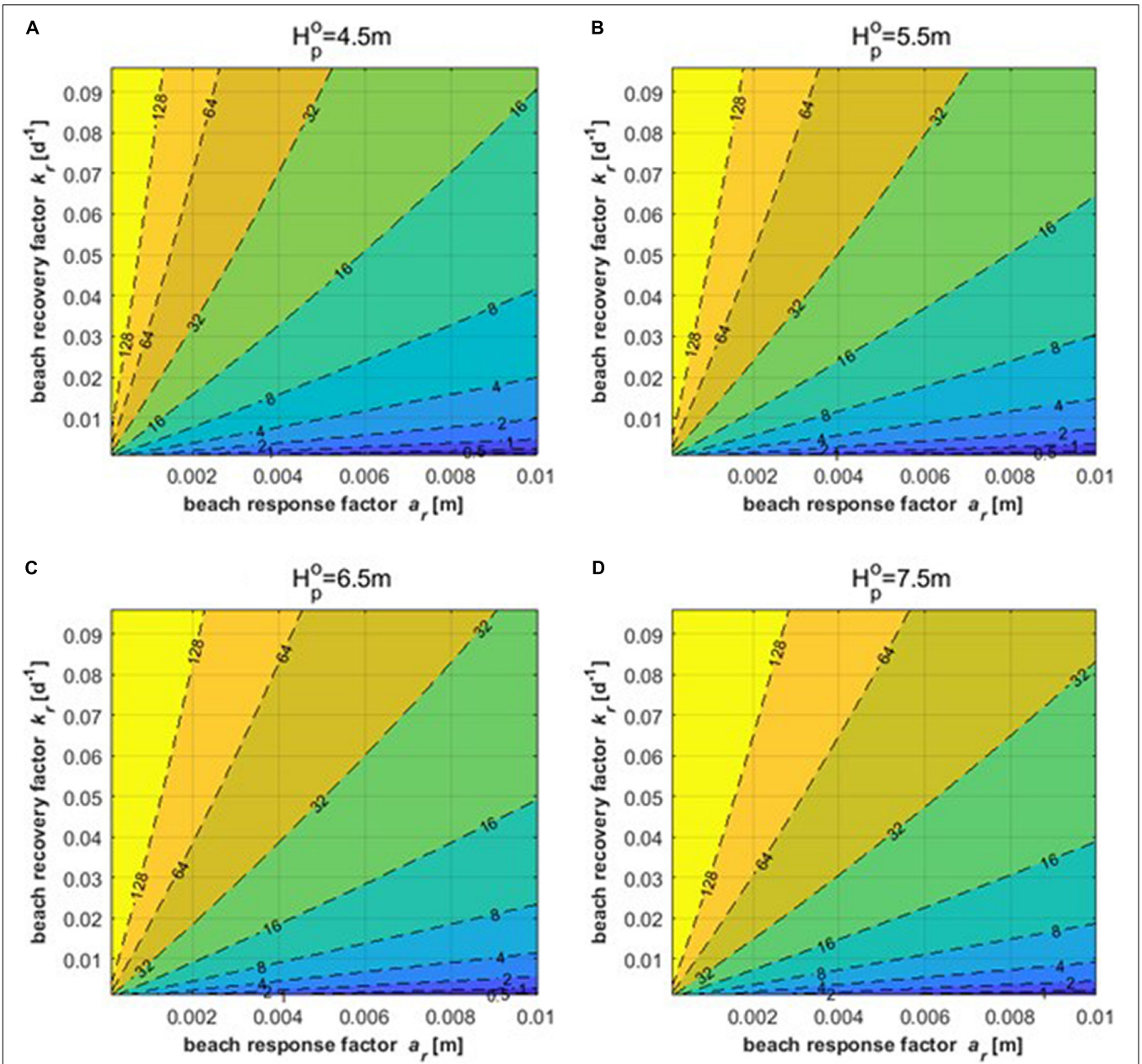

FIGURE 7 | Results of peak SL retreat width according to beach response factor a_r(m) and beach recovery factor $k_r(d^{-1})$ for **(A)** $H_p^o = 4.5\,m$, **(B)** $H_p^o = 5.5\,m$, **(C)** $H_p^o = 6.5\,m$, and **(D)** $H_p^o = 7.5\,m$.

peak erosion width and peak wave energy at the breaking point had a linear correlation without substantial error. The changes in the proportional constant of erosion vulnerability based on a_r and k_r were calculated using the numerical model results. Therefore, if a_r and k_r can be determined, based on the sand properties of the beach, we can obtain the erosion vulnerability of the beach. In this section, we demonstrate the validity of this result by comparing it with the vulnerability curves obtained from analysis of the shoreline survey data observed for approximately 9 years at Maengbang Beach in Korea and the NOAA wave data near Maengbang Beach.

Shoreline Survey at Maengbang Beach

Maengbang Beach is one of the target sites for the erosion status survey of Gangwon-do. This sandy beach, with a total length of 4.6 km, stretches to the southeast, and its main incident waves originate from the northeast. Since 2010, GPS shoreline surveys have been conducted at the site four times a year. Beach profile measurements up to a depth of 15 m, sufficiently deeper than

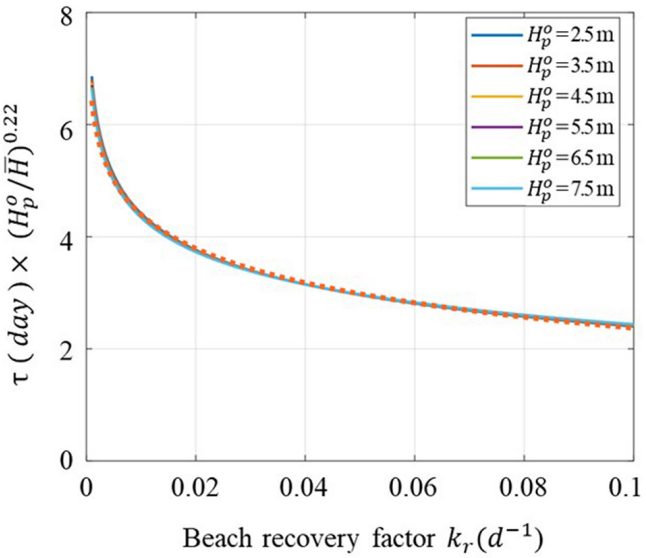

FIGURE 8 | Elapsed time τ from peak wave height to peak erosion width w.r.t the beach recovery factor k_r.

the closure depth, were obtained twice a year at 150 m intervals, and the median particle size survey was conducted in the swash zone. The beach profile was measured by potable GNSS on foot from the survey reference point to a water depth of 1.5 m and from 1.5 m to 15 m water depth was surveyed using a bathymetry survey boat equipped with an echo-sounder (single beam). The GNSS model used for shoreline surveying is GX1230 with an accuracy of H: 3 mm + 0.5 ppm. The echo-sounder used for the bathymetric survey is a single beam, the model name is AquaRoller 200S, and the measurement range is 5 ∼ 200 m. These datasets were utilized as basic data to evaluate the coastal erosion grades (A, B, C, and D). In the event of the erosion of the coast, the datasets serve as basic data for cause analysis.

Figure 10 shows the 13 reference points for the survey conducted at Maengbang Beach, which was divided into four survey zones, wherein the mean shoreline and erosion control line (erosion limit for 30 years) were obtained according to the statistical characteristics of the shoreline data. These two shorelines were used for (1) evaluating the management status of Korean coastal regions in terms of conservation and disaster prevention, and (2) evaluating whether the layout design of soft and hard engineering structures of the coastal improvement projects implemented to reduce coastal erosion are achieving the management target lines (mean target shoreline and erosion prevention line).

The average D_{50} obtained for each zone and the corresponding beach scale factor and beach response factor are listed in **Supplementary Table 1**. Although the average sand particle diameter of Zone 4 was relatively small, the average particle diameter of the entire target beach was 0.656 mm. On the eastern coast of Korea, the net littoral drift flows from the north to the south according to the analysis of long-term wave data and the angle of the coastline (Kim et al., 2001). Owing to this littoral drift environment, the sand on the southern beach may have a finer grain size, but the difference is expected to be small.

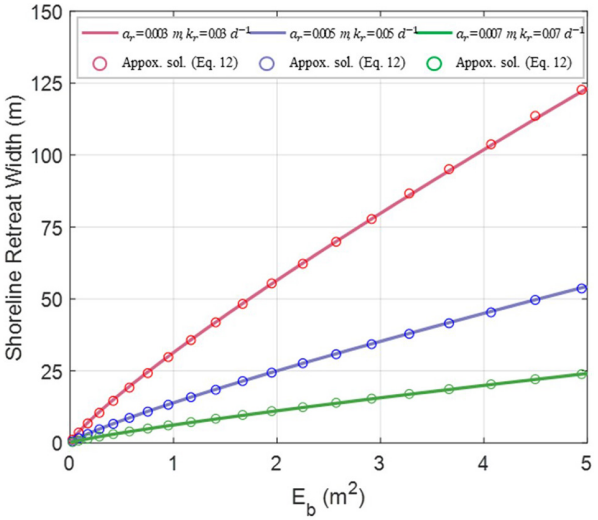

FIGURE 9 | Comparison between model results (Eq. 7) and approximate solutions (Eq. 12) for 3 different points of a_r and k_r.

Variability Analysis Using Shoreline Survey Data

The shoreline survey of Maengbang Beach, the subject of this study's beach response analysis, was conducted about five times a year since 2010 as a major observation item in the coastal erosion survey, and was measured at 13 reference points. In the erosion status survey, the shoreline survey is, in principle, conducted once a season. However, in some cases, shoreline surveys were more carried out once or twice a year. Therefore, it resulted in an average of about five shoreline surveys. **Figure 11** shows the distribution histograms for each survey zone using 192 shoreline survey datasets collected at 13 reference points (see **Figure 10**),

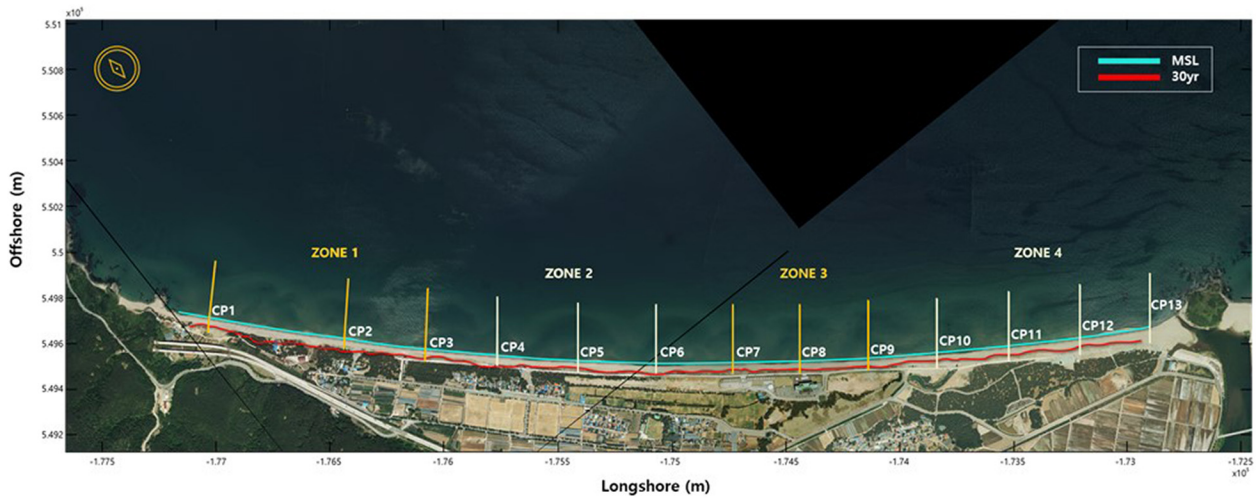

FIGURE 10 | Reference points for median grain size survey, mean shoreline and 30-year erosion control line.

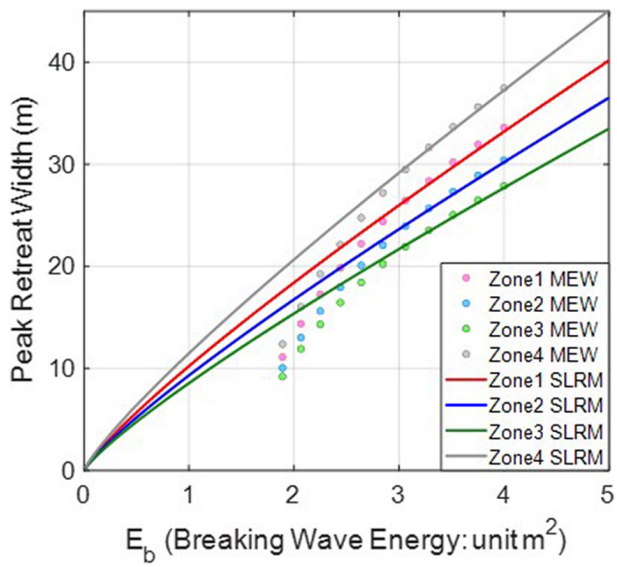

FIGURE 11 | Comparison between MEW and SLRM results.

for which measurements were conducted 47 times from 2010 to 2018. The figure illustrates the probability distribution of the observed shoreline data with reference to the mean values for each zonal reference point. These results were compared to a Gaussian distribution and were found to exhibit high similarity. The statistical frequency analysis of these shoreline observations allows researchers to assess the risk of beach erosion.

Zone 1 is located on the northern side of Maengbang Beach, and Zone 4 is located on the southern side of the beach. The results of each zone reasonably follow a normal Gaussian distribution, and according to their statistical characteristics, the monitored erosion width (MEW) can be obtained for each return period (yr). The standard deviation σ for each zone is listed in **Supplementary Table 2**, as well as the MEW for each zone, which was calculated from the mean value for each return period based on the frequency analysis. These results represent erosion damage by frequency and can therefore be referred to as a risk curve. Conversely, if the extreme wave height analysis result of the NOAA wave data is applied instead of the return frequency, the coastal erosion vulnerability curve (damage curve according to hazards) can be derived.

To verify the normality of the observed shoreline variations, a chi-squared goodness of fit test was performed, confirming that the results follow a normal distribution at the 1% significance level. A qq plot is shown in **Supplementary Figure 12**. **Supplementary Table 2** lists the standard deviation σ of the shoreline survey data for each zone and the MEW for each return period, which was obtained from a variability analysis of the data. The larger the standard deviation, the greater the variability, and thus, the greater the erosion width. Zone 4, which consists of fine sediment, exhibited the highest MEW.

Beach Vulnerability Curve by Shoreline Survey Data

Extreme Wave Height Analysis of Incident Waves

For the extreme wave height analysis, the 40 years long-term wave estimation data provided by NOAA, consisting of 3 h intervals from January 1979 to December 2018, were used. The NOAA deep-sea wave data were converted by applying the shoaling, refraction, and significant wave breaking conditions of Eqs. 4–6 to obtain the wave height at the breaking point. **Supplementary Figure 13** shows the results of the extreme wave height analysis conducted using the Gumbel method, and **Supplementary Table 3** summarizes the extreme wave height at breaking point H_F obtained for each frequency F, which is the reciprocal of the return period. Approximately half of the wave direction components that could not approach the target beach because the wave direction was too wide were excluded from

the extreme distribution analysis. The relationship between the extreme wave height (m) and frequency F (yr^1) is as follows:

$$H_F = -0.5126\, ln\left[-ln\left(1-\frac{F}{365\times 8}\right)\right] + 1.1745 \qquad (14)$$

Analysis of Erosion Vulnerability for Maengbang Beach

As mentioned in Section "Variability Analysis Using Shoreline Survey Data," the MEW for each return period was obtained via an analysis of fluctuations in the monitored shoreline. Therefore, using Eq. 14 to obtain the extreme wave height for each return period, an beach vulnerability curve showing the erosion width for each wave height could be obtained. **Supplementary Table 4** lists the calculated MEW for each zone of Maengbang Beach for each extreme wave height at a breaking point of 4.5 m or higher.

Comparison With Beach Vulnerability Curve From Shoreline Response Model

Figure 11 compares the BVC directly obtained from the extreme breaking wave height and the MEW listed in **Supplementary Table 4** with the BVC numerically obtained by applying the SWSF to the SLRM. In the SLRM, the beach response factor a_r was obtained using Eq. 11 using the sand particle size data, and the beach recovery factor k_r was applied as the value with the best fit, as compared to the MEW data for $E_b > 2.72$ m^2. The k_r values obtained for zones 1–4 were 0.0698, 0.0624, 0.0552, and 0.0796 d^{-1}, respectively. When $H_b > 6.6$ m, at which $E_b > 2.72$ m^2, there is a satisfactory trend, but when $H_b < 6.6$ m, the values interpreted from the observations are lower than the model predictions, and unlike the model predictions, they do not converge to zero. Instead, the values exhibit a convergence to $E_b = 1.73$ m^2, corresponding to the 1-year return period. When the SWSF is shorter than the 1-year return period, the selection of a curve along the maximum coverage line as the scenario model may lead to discrepancies, as shown in **Supplementary Figures 9A, 10A**.

Zones 1 and 4, which are located at the ends of the beach, show slightly larger k_r values than zones 2 and 3. It is presumed that fitting with a larger k_r value is probably because of the greater variability at the beach ends, mainly because of the influence of seasonal littoral sedimentation. While k_r can be determined from the particle size of the sand, estimating its value is difficult and requires additional research with on-site monitoring. Note that this study is limited to analyzing beach vulnerability in the state where a_r and k_r are estimated.

As shown in **Figure 11**, zones 1 and 4, unlike the zones located in the center of the beach, had relatively high k_r values compared to the sand grain size, which may be related to the occurrence of littoral drift due to the incidence of oblique waves at the beach ends. On this basis, considering the loss of suspended sediment due to littoral drift, Eq. 7 is modified as follows:

$$\frac{dy}{dt} = k_r\left(\frac{E_b}{a_r} - \varepsilon y\right) \qquad (15)$$

where ε corresponds to the loss rate of suspended sediment caused by the occurrence of littoral drift. If ε is greater than 1, it is considered that suspended particles are introduced from the outside, and when ε is less than 1, it is considered that particles are discharged to the outside. **Figure 12** shows how the erosion width varies with ε. In particular, when $\varepsilon = 0.2$ is applied to zones 1 and 4, a reasonable k_r is obtained, as compared with that in the surrounding zones. The k_r values obtained for zones 1–4 were 0.0628, 0.0624, 0.0522, and 0.0698 d^{-1}, respectively.

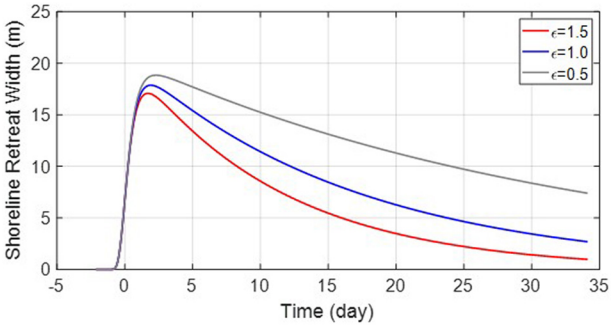

FIGURE 12 | SLRM result according to ε value ($H_p^o = 6.0$ m and $a_r = 0.008$ m).

DISCUSSION

In this study, the SWSF and SLRM were applied to determine the BVC using only cross-shore beach sedimentation based on the values of the beach response factor a_r and beach recovery factor k_r. The BVC may greatly vary depending on the duration of the coast-specific input SWSF, as well as a_r and k_r. Specifically, even with the same peak wave height, the erosion width may vary according to the SWSF when subjected to a limited duration. Therefore, in this section, we attempt to determine the time constraint characteristics of the BVC that is less than equilibrium owing to the effect of a limited duration, as compared with the extreme BVC, which has an equilibrium erosion width and the duration of the incoming wave is infinite. In general, we attempt to determine the time constraint characteristics of a BVC that is not in equilibrium by comparing it with the extreme BVC. The extreme BVC corresponds to the results obtained from the field experiments of Yates et al. (2009). However, note that the resulting erosion width is too high to be realistic, and the actual occurrence of erosion of this magnitude would be catastrophic.

When the equilibrium state is reached, the beach erosion vulnerability is roughly expressed by the wave energy at breaking point E_b and the beach erosion vulnerability factor f_v:

$$ESLP = f_v E_b \qquad (16)$$

where ESLP is the equilibrium shoreline position and f_v is the reciprocal of the beach response factor a_r. This equation is based on Eq. 8, which was modified by ignoring $\overline{E_b}$, as it was considered to be relatively small under high wave conditions. Overall, as the vulnerability factor increases, more beach erosion occurs, indicating that the beach erosion vulnerability increases.

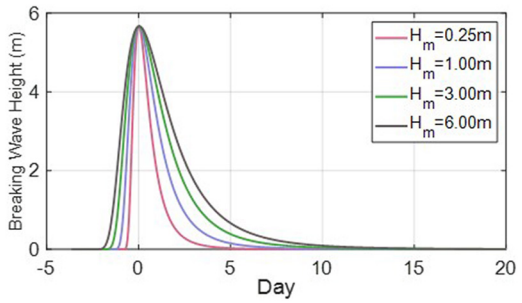

FIGURE 13 | Temporal variation of breaking wave height according to $\overline{H}$ (= H_m) (H_p^o = 6.0 m and a_r = 0.007 m and k_r = 0.08 d^{-1}).

However, the ESLP refers to a virtual erosion state formed by consistant waves incoming with an infinite duration.

Unlike the ESLP, the duration-limited shoreline position (DSLP), which is affected by duration and has a smaller erosion width, can be expressed as follows:

$$DSLP = f_v E_b(\tau) \tag{17}$$

Therefore, the ratio of the erosion width actually generated by the SWSF compared to the equilibrium erosion width can be defined as the shoreline position ratio μ, as follows:

$$\mu = \frac{DSLP}{ESLP} = \frac{E_b(\tau)}{E_b} \tag{18}$$

Supplementary Table 5 lists the calculated τ according to k_r and H_p^o, revealing an elapsed time of approximately 1.5–3 days. **Supplementary Table 6** lists the changes in the μ value defined by Eq. 18. These results are valid for the wave conditions at the Maengbang coast. Unlike the ESLP, which is the result of infinite waves of a certain height, the erosion width of the beach that occurs under the actual duration-limited condition, the DSLP, shows a much smaller erosion width, exhibiting values of only approximately μ = 0.02−0.11. This is because of the characteristics of the real-world incident storm wave scenario, wherein wave energy is not continuously applied at a constant value but increases and then decreases, not allowing an equilibrium state to be reached.

Figure 13 shows $\overline{H}$ has the effect of spreading SWSF laterally. Overall, as $\overline{H}$ increased, the influence of the duration increased. Although $\overline{H}$, which is defined as the mean wave height, is unlikely to be greater than 2 m, we assessed the effect of large $\overline{H}$ values to observe the effect of duration. **Figure 14A** shows that μ becomes larger owing to the effect of longer duration, at constant values of a_r and k_r. Because μ tends to decrease as wave height increases, $H_p^o/\overline{H}$ was applied to eliminate this change and obtain a result that barely changes not only with the wave height but also the $\overline{H}$, as shown in **Figure 14B**. In addition, considering the change in k_r, we obtained the following equation:

$$\mu = \alpha_1 \left(\frac{H_p^o}{\overline{H}}\right)^{\alpha_2} k_r^{\alpha_3} \tag{19}$$

where a_r and k_r have units of m and d^{-1}, respectively, and the three coefficients α_1, α_2, and α_3 have values of 1.5, −0.275, and 0.911, respectively. By inserting Eq. 19 into Eq. 17, we obtain the following equation, which is useful for the practical application of the DSLP:

$$DSLP = \alpha_1 \left(\frac{H_p^o}{\overline{H}}\right)^{\alpha_2} \frac{k_r^{\alpha_3} E_b}{a_r} \tag{20}$$

Thus, the peak erosion width can be conveniently estimated by using Eq. 20 if the incident peak wave information and characteristic coefficients of the beach responses a_r and k_r are determined. This gives an idea of how wide the buffer zone should be to avoid the damage to the hinterland for the return period of interest. However, this result ignores the effect of longshore sediment transport and only considers the cross-shore sediment transport process.

We examined whether Eq. 20 provides a satisfactory solution, as compared with the SLRM result. **Figure 15** shows the results of the comparison under the same conditions as in **Figure 9**, revealing fairly agreeable results.

The reliability of the BVC (Eq. 20) obtained from the shoreline response model was reviewed by comparing the results obtained

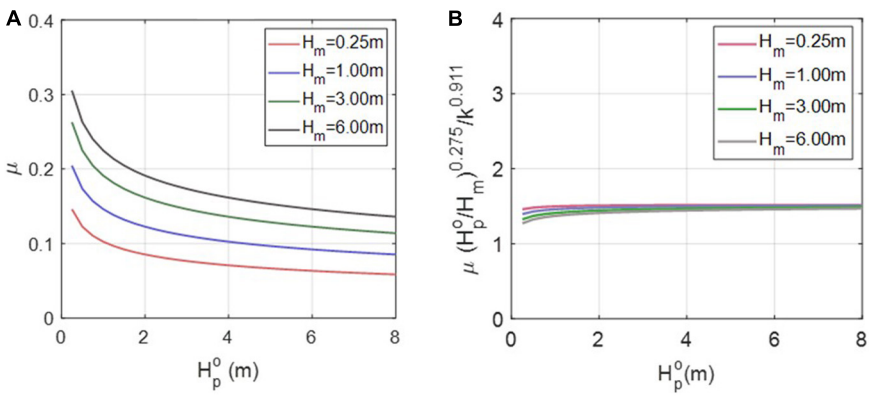

FIGURE 14 | Variation of μ w.r.t H_p^o; **(A)** before scaling with k_r = 0.08 d^{-}1 and **(B)** after scaling.

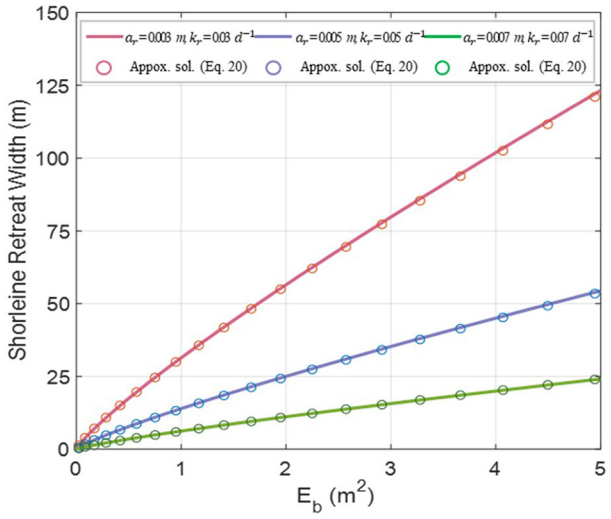

FIGURE 15 | Comparison between model results (Eq. 7) and approximate solutions (Eq. 20) for 3 different points of a_r and k_r.

from the SLRM by applying SWSF with the results obtained from the statistical analysis of periodic shoreline survey data. All of the 47 shoreline survey data taken in the target area are shown in **Supplementary Figure 14**, and the average by statistical analysis and the erosion width by return period are plotted thereon. The applicability of the BVC proposed by Eq. 20 was verified and it was confirmed that it showed satisfactory reliability. **Supplementary Figure 15** shows the results obtained from BVC among the results shown on the three dimensional LiDAR image. The beach recovery factor k_r is the result of considering the effects of littoral drift as described in Section "Comparision with BVC from SLRM".

CONCLUSION

Vulnerability is measured as the degree of damage to hazard intensity. In this study, therefore, the storm wave incident scenario to the target beach expressed in terms of the peak wave height, which is the hazard intensity, was established and the scenarios were applied to the SLRM, and the vulnerability curve was extracted by correlating the result of the erosion width, which is the degree of damage. This methodology can be applied to beaches where there are few tidal ranges. Although it may be slightly affected by other factors, such as berm height and initial slope, these effects are considered to be insignificant.

The storm wave scenario function (SWSF) obtained by analyzing NOAA wave data was used as the input data for the SLRM. The numerical results of the model provided satisfactory results compared with the results of shoreline observations, which were conducted five times a year for 9 years on the eastern coast of Korea. Further, while the model did not provide satisfactory results for wave heights with a return period of approximately 1 year or less, it showed fairly good agreement under high wave conditions, which is more meaningful for vulnerability analyzes.

By analyzing the factors affecting erosion vulnerability via the SLRM, an approximate equation with very good consistency was developed. This equation is given by the peak wave height at deep water H_p^o and the mean wave height $\overline{H}$ in relation to the SWSF, as well as the beach response factor a_r and beach recovery factor k_r in relation to the SLRM. However, although it is not very difficult, the H_p^o needs to be converted to H_b by considering wave shoaling, wave refraction, and wave breaking. This BVC approximation provides an intuitive understanding of the factors that influence beach vulnerability and estimates the length of the beach buffer zone required to prevent erosion damage to hinterland facilities over a specific return period. This is expected to provide essential information for limiting reckless coastal development and mitigating erosion damage.

Herein, the SWSF was determined by analyzing the storm wave scenarios with wave heights of 4.5 m or higher from NOAA wave data, which included long-term wave estimation data over 40 years, at 3 h intervals from January 1979 to December at 38.5°N, 129.0°E near Maengbang Beach. To examine the validity of the BVC obtained from the model results, shoreline surveys were conducted approximately five times a year for 9 years and sand size data were used. In the range of $E_b > 2.72\ m^2$, the results of SLRM and statistical analysis of MEW variability show quite similar patterns, so the prediction of the peak erosion width by SLRM combined with SWSF is considered reasonable. The beach recovery factor k_r in SLRM was applied as the best fit value compared to the MEW data. The k_r value is a physical factor affecting the recovery of the shoreline to its original state, and this value is expected to be related to the grain size of the sand. Future research on this is needed.

Because the tidal wave difference is small along the eastern coast of Korea, the SLRM can be directly applied to the coast. However, in the case of the western coast of Korea and other coastal areas with high tidal variations, the influence of incoming high waves evenly affects the intertidal zone, making it difficult to directly apply the methodology of this study. Therefore, in the future, the SLRM must be improved to assess the erosion vulnerability in coastal areas with high tidal variations, to reflect the effect of tides.

DATA AVAILABILITY STATEMENT

The original contributions presented in the study are included in the article/**Supplementary Material**, further inquiries can be directed to the corresponding author.

AUTHOR CONTRIBUTIONS

T-KK: conceptualization, acquisition of data, visualization, and writing – editing. CL: acquisition of data, visualization, and writing – editing. J-LL: conceptualization, supervision, validation, and writing – original draft and review. All authors contributed to the article and approved the submitted version.

FUNDING

This research was part of the "Practical Technologies for Coastal Erosion Control and Countermeasure" project supported by the Ministry of Oceans and Fisheries, South Korea (Grant No. 20180404).

SUPPLEMENTARY MATERIAL

The Supplementary Material for this article can be found online at: https://www.frontiersin.org/articles/10.3389/fmars.2021.759067/full#supplementary-material

Supplementary Figure 1 | Location of Maengbang Beach and NOAA data coordinate.

Supplementary Figure 2 | Tide table **(A)** and wave rose **(B)** of Maengbang coast.

Supplementary Figure 3 | Time series data of significant wave height (H_S) at Maengbang coast from the NOAA dataset (1979–2018).

Supplementary Figure 4 | Time series data of peak wave period (T_p) at Maengbang coast from the NOAA data (1979–2018).

Supplementary Figure 5 | Temporal change of annual mean wave data from 1979 to 2018: **(A)** annual mean wave height; **(B)** annual mean wave period; **(C)** annual mean wave direction.

Supplementary Figure 6 | Joint probability of wave height (H_S) and wave period (T_S) at Maengbang coast from the NOAA dataset (1979–2018).

Supplementary Figure 7 | Dimensionless wave height scenario model for Maengbang Beach.

Supplementary Figure 8 | Dimensionless wave period scenario model for Maengbang Beach.

Supplementary Figure 9 | Wave scenario models of wave height for Maengbang Beach; **(A)** 4.5 m $\leq H_p^o <$ 5.5 m, **(B)** 5.5 m $\leq H_p^o <$ 6.5 m, **(C)** 6.5 $m \leq H_p^o$, and **(D)** comparison with respect to peak wave heights.

Supplementary Figure 10 | Wave scenario models of wave period for Maengbang Beach; **(A)** 4.5 $m \leq H_p^o < 5.5\ m$, **(B)** 5.5 $m \leq H_p^o < 6.5\ m$, **(C)** 6.5 $m \leq H_p^o$, and **(D)** comparison with respect to peak wave period.

Supplementary Figure 11 | Probability histogram and 30-yr confidence level per zone at Maengbang Beach obtained from shoreline data; **(A)** Zone 1, **(B)** Zone 2, **(C)** Zone 3, and **(D)** Zone 4.

Supplementary Figure 12 | Result of Chi-squared goodness of fit test at Maengbang Beach obtained from shoreline data.

Supplementary Figure 13 | Extreme distribution function between the return period (yr) and extreme breaking wave height H_F (m) obtained from the NOAA data.

Supplementary Figure 14 | Comparison between the erosion width obtained from BVC and monitored erosion width in the study site **(A)** 10-year return period, and **(B)** 30-year return period.

Supplementary Figure 15 | Beach profiles estimated from BVC plotted on the three dimensional LiDAR image.

Supplementary Table 1 | Median grain size D_{50} beach scale factor A and beach response factor a_r for each survey zone at Maengbang Beach.

Supplementary Table 2 | Monitored erosion width (MEW) (negative value; -m unit) with respect to return period.

Supplementary Table 3 | Correlations between the return period and extreme breaking wave height H_F.

Supplementary Table 4 | Monitored erosion width (MEW) for 4 zones according to the breaking wave height H_F.

Supplementary Table 5 | The τ values for deep water wave heights H_p^o for 4 different k_r values.

Supplementary Table 6 | The μ values for each deep water wave heights H_p^o for 4 different k_r values.

REFERENCES

Anfuso, G., Postacchini, M., Dluccio, D., and Benassai, G. (2021). Coastal sensitivity/vulnerability characterization and adaptation strategies: a review. *J. Mar. Sci. Eng.* 9:72. doi: 10.3390/jmse9010072

Ballesteros, C., Jimeńez, J. A., Valdemoro, H. I., and Bosom, E. (2017). Erosion consequences on beach functions along the maresme coast (NW Mediterranean, Spain). *Nat. Hazards* 90, 173–195. doi: 10.1007/s11069-017-3038-5

Bosom, E., and Jimeńez, J. A. (2011). Probabilistic coastal vulnerability assessment to storms at regional scale – application to CataLan beaches (NW Mediterranean). *Nat. Hazards Earth Syst. Sci.* 11, 475–484. doi: 10.5194/nhess-11-475-2011

Corbella, S., and Stretch, D. D. (2012). Multivariate return periods of sea storms for coastal erosion risk assessment. *Nat. Hazards Earth Syst. Sci.* 12, 2699–2708. doi: 10.5194/nhess-12-2699-2012

Davidson, M. A., Splinter, K. D. and Turner, I. L. (2013). A simple equilibrium model for predicting shoreline change. *Coast. Eng.* 73, 191–202. doi: 10.1016/j.coastaleng.2012.11.002

Dean, R. G. (1977). *Equilibrium Beach Profiles: U.S. Atlantic and Gulf Coasts,* Technical Report No. 12. Newark, DE: Department of Civil Engineering. University of Delaware.

Deltares (2018a). *Delft3D-FLOW User Manual: Simulation of Multidimensional Hydrodynamic Flows and Transport Phenomena Including Sediments*. Delft: Deltares.

Deltares (2018b). *Delft3D-WAVE User Manual: Simulation of Shortcrested Waves with SWAN*. Delft: Deltares.

Han, H. J. (2006). *Climate Change Impact Assessment and Development of Adatation Strategies in Korea*. Sejong: Korea Envirionmental Institute.

IPCC (1996). *Climate Change 1995: The Science of Climate Change*, eds J. T. Houghton, L. G. M. Filho, B. A. Callander, N. Harris, A. Kattenberg, and K. Maskell Cambridge: Cambridge University Press.

IPCC (2001). *Climate Change 2001: Impacts, Adaptation* & *Vulnerability, Third Assessment Report*, eds J. J. McCarthy, O. F. Canziani, N. A. Leary, D. J. Dokken, and K. S. White Cambridge: Cambridge University Press, 184.

Kim, A., Lee, J. L., and Choi, B. H. (2001). Analysis of wave data and estimation of littoral drifts for the eastern coast of Korea. *J. Korean Soc. Coast. Ocean Eng.* 13, 18–34.

Kim, T. K., and Lee, J. L. (2018). Analysis of shoreline response due to wave energy incidence using equilibrium beach profile concept. *J. Ocean Eng. Technol.* 32, 116–122. doi: 10.26748/KSOE.2018.4.32.2.116

Kim, T. K., Jeong, J. H., and Lee, J. L. (2021). Shoreline variation analysis by cross-shore sediment transport resulting from effects of storm waves. *J. Coast. Res.* 114, 539–543. doi: 10.2112/JCR-SI114-109.1

Kriebel, D. L., and Dean, R. G. (1985). Numerical simulation of time-dependent beach and dune erosion. *Coast. Eng.* 9, 221–245. doi: 10.1016/0378-3839(85)90009-2

Larson, M., Kraus, N. C., and Byrnes, M. R. (1999). *SBEACH: Numerical Model For Simulating Storm-Induced Beach change*. Report 2Numerical Formulation and Model Tests. Technical Report. CERC-89(9). Vicksburg, MS: U.S. Army Engineer Waterways Experiment Station, 116.

Lesser, G. R., Roelvink, J. A., van Kester, J. A. T. M., and Stelling, G. S. (2004). Development and validation of a three-dimensional morphological model. *Coast. Eng.* 51, 883–915. doi: 10.1016/j.coastaleng.2004.07.014

Lim, C., Kim, T. K., and Lee, J. L. (2021). Shoreline response induced by spatial suspension and recovery processes of wave-induced sediments. *Geomorphology*. (Submitted for review)

Madsen, A. J., and Plant, N. G. (2001). Intertidal beach slope predictions compared to field data. *Mar. Geol.* 173, 121–139. doi: 10.1016/S0025-3227(00)00168-7

Mendoza, E. T., and Jimeńez, J. A. (2006). Storm-induced beach erosion potential on the catalonian coast. *J. Coast. Res.* SI48, 81–88.

Miller, J. K., and Dean, R. G. (2004). A simple new shoreline change model. *Coast. Eng.* 51, 531–556. doi: 10.1016/j.coastaleng.2004.05.006

Ministry of Ocean and Fisheries (2017). *Coastal Erosion Monitoring in Korea Report*. Sejong: Ministry of Ocean and Fisheries.

Montaño, J., Coco, G., Antolnez, J. A. A., Beuzen, T., Bryan, K. R., Cagigal, L., et al. (2020). Blind testing of shoreline evolution models. *Sci. Rep.* 10:2137. doi: 10.1038/s41598-020-59018-y

Narra, P., Coelho, C., and Sancho, F. (2019). Multicriteria GIS-based estimation of coastal erosion risk: implementation to Aveiro Sandy Coast, Portugal. *Ocean Coast. Manag.* 178:104845. doi: 10.1016/j.ocecoaman.2019.104845

Oliveira, A., Jesus, G., Gomes, J. L., Rodrigues, M., Fortunato, A. B., Dias, J. M., et al. (2014). An interactive WebGIS observatory platform for enhanced support of integrated coastal management. *J. Coast. Res.* 70, 507–512. doi: 10.2112/SI70-086.1

Park, S. M., Park, S. H., Lee, J. L., and Kim, T. K. (2019). Erosion control line (ECL) establishment using coastal erosion width prediction model by high wave height. *J. Ocean Eng. Technol.* 33, 526–534. doi: 10.26748/KSOE.2019.110

Plant, N. G., Holman, R. A., and Freilich, M. H. (1999). A simple model for interannul sandbar behavior. *J. Geophys. Res.* 104, 15755–15776. doi: 10.1029/1999JC900112

Roelvink, D., Reniers, A., van Dongeren, A., Van Thiel de Vries, J., McCall, R., and Lescinsky, J. (2009). Modelling strom impacts on beaches, dunes and barrier islands. *Coast. Eng.* 56, 1133–1152. doi: 10.1016/j.coastaleng.2009.08.006

Sorensen, R. M. (1993). *Basic Wave Mechanics : for Coastal and Ocean Engineers*. New York, NY: John Wiley.

Swart, D. H. (1974). *Offshore Sediment Transport and Equilibrium Beach Profiles*. Tech. Rep. Publ. 131. Delft: Delft Hydraulics Lab.

Toimil, A., Losada, I. J., Camus, P., and Díaz-Simal, P. (2017). Managing coastal erosion under climate change at the regional scale. *Coast. Eng.* 128, 106–122. doi: 10.1016/j.coastaleng.2017.08.004

UKCIP (2003). *Climate Adaptation: Risk, Uncertainty, and Decision-Making*. UKCIP Technical Report. Oxford: UKCIP.

UNDP (2005). *Adaptation Policy Framworks for Climate Change: Developing Strategies, Policies, and Measures*. Cambridge, MA: Cambridge University Press.

UNFCCC (2005). *Compendium on Methods and Tools to Evaluate Impacts of, and Vulnerability and Adaptation to, Climate Change; Final Draft Report*. Boulder, CO: Stratus Consulting Inc.

Wright, L. D., Short, A. D., and Green, M. O. (1985a). Short-term changes in the morphologic states of beaches and surf zones: an empirical model. *Mar. Geol.* 62, 339–364. doi: 10.1016/0025-3227(85)90123-9

Wright, L. D., May, S. K., Short, A. D., and Green, M. O. (1985b). "Prediction of beach and surf zone morphodynamics: equilibria, rates of change and frequency response," in *Proceedings of the 19th Coastal Engineering Conference*, 2150–2164.

Yates, M. L., Guza, R. T., and O'Reilly, W. C. (2009). Equilibrium shoreline response: observations and modeling. *J. Geophys. Res.* 114:C09014. doi: 10.1029/2009JC005359

Yook, K. H., Jung, J. H., and Ahn, Y. S. (2011). *A Study on the Coastal Vulnerability Assessment Model to Sea Level Rise*. National Research Council for Economics. Busan: Humanities and Social Sciences & Korea Maritime Institute.

Conflict of Interest: The authors declare that the research was conducted in the absence of any commercial or financial relationships that could be construed as a potential conflict of interest.

Publisher's Note: All claims expressed in this article are solely those of the authors and do not necessarily represent those of their affiliated organizations, or those of the publisher, the editors and the reviewers. Any product that may be evaluated in this article, or claim that may be made by its manufacturer, is not guaranteed or endorsed by the publisher.

frontiers in Marine Science

PERSPECTIVE
published: 20 December 2021
doi: 10.3389/fmars.2021.788657

Challenges and Opportunities in Coastal Shoreline Prediction

Kristen D. Splinter[1]* *and Giovanni Coco*[2]

[1] Water Research Laboratory, School of Civil and Environmental Engineering, UNSW Sydney, Sydney, NSW, Australia,
[2] School of Environment, Faculty of Science, University of Auckland, Auckland, New Zealand

Sandy beaches comprise approximately 31% of the world's ice-free coasts. Sandy coastlines around the world are continuously adjusting in response to changing waves and water levels at both short (storm) and long (climate-driven, from El-Nino Southern Oscillation to sea level rise) timescales. Managing this critical zone requires robust, advanced tools that represent our best understanding of how to abstract and integrate coastal processes. However, this has been hindered by (1) a lack of long-term, large-scale coastal monitoring of sandy beaches and (2) a robust understanding of the key physical processes that drive shoreline change over multiple timescales. This perspectives article aims to summarize the current state of shoreline modeling at the sub-century timescale and provides an outlook on future challenges and opportunities ahead.

Keywords: shoreline, sandy coastline, prediction, waves, uncertainty, equilibrium models, ensemble modeling

OPEN ACCESS

Edited by:
Felice D'Alessandro,
University of Milan, Italy

Reviewed by:
Ali Dastgheib,
IHE Delft Institute for Water Education, Netherlands
Alessandro Romano,
Roma Tre University, Italy

***Correspondence:**
Kristen D. Splinter
k.splinter@unsw.edu.au

Specialty section:
This article was submitted to Coastal Ocean Processes, a section of the journal Frontiers in Marine Science

Received: *03 October 2021*
Accepted: *29 November 2021*
Published: *20 December 2021*

Citation:
Splinter KD and Coco G (2021) Challenges and Opportunities in Coastal Shoreline Prediction. Front. Mar. Sci. 8:788657. doi: 10.3389/fmars.2021.788657

1. INTRODUCTION

Beaches provide essential ecosystem services, including the natural buffering of inland areas from the damaging impacts of waves and elevated water levels during storm events. The coastal zone also provides major economic benefits. The challenge in many coastal areas is that, due to historical planning decisions and perhaps a persistent lack of understanding of the complex dynamic coastline, infrastructure has been inappropriately sited within the active coastal zone. Hence, many new and on-going coastal management projects are needed to deal with the risks associated with coastal erosion.

Coastal erosion can be episodic (storm-driven), show long-term patterns (from seasons to decades) or be chronic (when a trend is established) as a result of both natural (due to changes in water levels and wave characteristics) and anthropogenic causes. Extra-tropical and tropical events can cause widespread and rapid erosion over large areas of the coastline in a matter of hours to days (Castelle et al., 2015; Masselink et al., 2016b; Harley et al., 2017), whereas longer term climate variability (e.g., El-Nino Southern Oscillation, ENSO) can also cause enhanced erosion (or accretion) on time scales of 2–7 years (e.g., Barnard et al., 2015). The issue of changes induced by sea-level rise is also hotly debated (Vitousek et al., 2017a; Cooper et al., 2020; Vousdoukas et al., 2020) because we still lack a clear modeling framework to deal with this even longer temporal scale. For improved shoreline forecasting and coastal management in a dynamic and changing system like the nearshore there is an outstanding need for both long-term, large-scale continuous data sets and improved coastal shoreline prediction models.

2. DATA

Data is fundamental for expanding our understanding of the coastline. Importantly, data also underpins all of our modeling efforts. This is particularly true for hybrid modeling approaches as

described in section 3, that train specific predefined relationships to data. High quality data is even more important for future endeavors to develop predictive models entirely based on data (e.g., machine learning algorithms).

2.1. Shorelines

Historically, a key challenge in our ability to fully understand coastal change has been the lack of long-term, large-scale, high-resolution (in time and space) coastal data sets (Turner et al., 2016; Ludka et al., 2019; Castelle et al., 2020). The result is that many studies on coastal shoreline dynamics have been based on a select few sites and span specific timeframes, thus limiting the universality of the findings. Despite the rather lack of data, we have learned about general principles that control shoreline behavior and the key drivers, including the effects of changing sea-levels (e.g., Brunel and Sabatier, 2009), storminess (e.g., Frazer et al., 2009), climate-driven responses (Barnard et al., 2015), inter-annual variability (e.g., Pianca et al., 2015) and embayment rotation (e.g., Harley et al., 2015).

Recently, the public release of satellite images has provided significant new opportunities for large-scale coastal change studies based on shoreline observations (Luijendijk et al., 2018; Mentaschi et al., 2018; Vos et al., 2019a). Recent open-source toolboxes, for example CoastSat (Vos et al., 2019b) or CASSIE (Almeida et al., 2021), allow for high resolution (order 10 m) bi-weekly shoreline measurements to be obtained at most sandy beaches around the world over the last 30 years. This spatio-temporal resolution of data is a necessary component in shoreline model development and calibration (Splinter et al., 2013). Newer satellites are continuously being added to the data stream providing higher spatial and temporal resolution into the future. As such, satellite data will most likely play an increasing and ongoing role in future, regional scale shoreline modeling efforts via data assimilation (e.g., Vitousek et al., 2017a).

2.2. Waves and Water Levels

When looking at the past, data of the "drivers" of shoreline change, for example waves and water levels, are often readily available as direct observations or numerical hindcasts. A recent paper outlining the priorities for wind-waves research highlighted the need for enhanced buoy networks and high quality bathymetry for nearshore wave predictions (Greenslade et al., 2019). Topographic and bathymetric data collection was also recently listed as a top priority by the Coastal Geosciences community (Power et al., 2021) due to the importance of the links between nearshore bathymetry and beach response, including sediment exchange as well as wave transformation processes. With respect to waves, some coastlines may be considered quite data rich, such as the USA with the NOAA network of buoys, while others rely entirely on global wave models. On complex coastlines, more refined models are needed to capture the complex wave transformation processes from offshore to nearshore in the absence of nearshore buoy networks. These models in turn, require high quality bathymetry data that is expensive to acquire.

The problem becomes insurmountable when looking at the future. Rates of sea-level rise over the next few decades are unknown and available projections depend on global climate models and therefore on the emission scenarios considered, which are also deemed uncertain. Similarly, our ability to predict the details of decadal oscillations in climate variability is extremely limited. However, efforts are being made within the shoreline community to address these (e.g., Antolinez et al., 2016; Montaño et al., 2021). A specific challenge for shoreline prediction is the need for continuous timeseries of forcing conditions. While the wave climate can be derived from global climate models, at present the projections of wave characteristics provide only one temporal sequence of wave conditions. This limits the possibility of assessing, for example, the effect of clustering or chronology of storms on future beach erosion that previous authors have shown to be important (e.g., Coco et al., 2014; Karunarathna et al., 2014; Castelle et al., 2015; Dissanayake et al., 2015; Masselink et al., 2016a,b; Splinter et al., 2016; Angnuureng et al., 2017).

3. MODELS

Models may incorporate a variety of processes, such as those described in **Figure 1**. While models can take on many forms, here we focus on simple models used for daily to multi-year shoreline prediction which form a subset of reduced complexity models. These encompass the "microscale" problem on understanding our coastline at engineering timescales of years to decades and spatial scales of kilometers to tens of kilometers (Wolinsky, 2009). More complex, process-based models, such as XBeach or SBeach are well-suited for short-term (e.g., individual storm response) scenarios but at present they are still not capable of providing robust and reliable predictions of multi-year shoreline change. This model typology, based on the fundamental equations of momentum and mass conservation, could eventually be used to model long-term coastal response, but at present it requires significant computational resources, making it almost impossible to assess how predictions are affected by model uncertainties (in parameters and drivers, for example). The more complex, process-based models also require more calibration data and input data, including the bottom boundary (i.e., bathymetry), tidal currents, and wave-driven currents, making them unsuitable for large regional studies of shoreline change. Here we categorize shoreline models used at engineering timescales into three types: ones that focus on cross-shore process; ones that focus on alongshore processes; and ones that combine these.

3.1. Cross-Shore Models

The most common models used to predict and understand multi-year shoreline change are semi-empirical models (Yates et al., 2009; Davidson et al., 2013; Splinter et al., 2014) based around the equilibrium assumption. The primary forcing component that drives onshore/offshore shoreline movement is waves at the timescales of days to decades. A generalized form of a model considering cross-shore process may take the form:

$$\Delta x(t)_{waves} = f(H(t), T(t), \theta(t), x(t)) \quad (1)$$

FIGURE 1 | Considerations relevant to shoreline modeling at a variety of timescales of interest. (1) Water levels; (2) Waves; (3) Sediment Supply; (4) Human Impact. These may be considered separately, in a combination, or all of them depending on the circumstances. Models can also consider these processes as deterministic or probabilistic.

where $\Delta x(t)$ refers to the cross-shore change in shoreline position (x) as a function of the time-dependant wave height ($H(t)$), wave period ($T(t)$), wave direction ($\theta(t)$), and shoreline position ($x(t)$). Shoreline change at the timescales of hours to days is often quite noisy, such that models are often trained on the resulting time-integral of shoreline change [i.e., shoreline position $x(t)$].

Due to the simplicity of Equation (1), these models require several years of high-resolution data to properly calibrate (Yates et al., 2009; Splinter et al., 2013) and show reasonable skill at predicting shoreline evolution on timescales of individual storms to decades. A key aspect in these models is the inclusion of hysteresis in the system, whereby shoreline change is a function of the present shoreline position (or proxy) in relation to the present wave forcing. The models also assume an unlimited sediment supply is available, with the beach not obstructed by human intervention or other geological features that might limit erosion (e.g., Doria et al., 2016). Approaches to explicitly incorporate the active profile and following the equilibrium principle have also been proposed (e.g., Miller and Dean, 2004; Davidson, 2021). These particular models explicitly include the influence of time-varying water levels, which may be important along coastlines with large tidal variability, large storm surge, or at longer timescales where changes in the mean water level may be important.

At these longer timescales (50–100 year time frames), where changes in mean sea-level may be considered the main driver of shoreline evolution, approaches such as the Bruun Rule (Bruun, 1962) are often employed. These models often consider geomorphic descriptors of the beach profile, such as slope (β), berm/dune height (B) relative to a water level (WL) and may take the form:

$$\Delta x(t)_{WL} = f(WL, \beta, B) \tag{2}$$

This overly simplistic approach, which only considers retreat from rising water levels has been criticized by a number of researchers (e.g., Cooper and Pilkey, 2004; Ranasinghe et al., 2012). Alternative approaches to account for the cross-shore movement of the shoreline due to changes in water levels have also been discussed (e.g., Wolinsky and Murray, 2009; Gutierrez et al., 2011; Rosati et al., 2013; D'Anna et al., 2021b; Davidson-Arnott and Bauer, 2021; McCarroll et al., 2021).

3.2. Alongshore Models

One-line models provide a simplified representation of the beachface and focus on shoreline change as a result of the gradients in alongshore transport resulting from oblique wave action (θ) relative to the orientation of the coastline. These models typically estimate alongshore transport based on breaking waves using the CERC (USACE and Coastal Engineering Research Center, 1984) or Kamphuis (Kamphuis, 1991) formulas and take a simplified form similar to:

$$\Delta x(t, y)_{dy} = f(H(t, y), T(t, y), \theta(t, y), x(t, y)) \tag{3}$$

where both input and output variables are dependant on the alongshore (y) location. However, it is widely accepted that these equations offer an order of magnitude estimate, with local calibration and tuning providing improved results (e.g., Smith

et al., 2009; Ruggiero et al., 2010). These models are most suitable for coastlines with significant gradients in alongshore transport, which may be due to sediment supply, natural features (such as headlands) or human impacts (such as harbors, breakwaters, and groins). Given that gradients in alongshore transport are often relatively small, these models are best suited for long-term (decadal-scale and beyond) studies of shoreline change (e.g., Ruggiero et al., 2010; Anderson et al., 2018).

Other researchers have proposed equilibrium approaches to model the planform of embayed beaches (e.g., Turki et al., 2013; Jaramillo et al., 2021). Much like their sister cross-shore equilibrium models described above, they rely on data to develop simplified relationships between the existing alongshore distribution of the shoreline and the prevailing wave forcing with the underlying physical assumption that beaches will tend to align with the prevailing wave climate direction.

3.3. Combined Approaches to Shoreline Modeling

Building off of established models as described above, a number of simple shoreline models have been proposed that encompass the impacts of cross-shore and alongshore processes (e.g., Vitousek et al., 2017b; Robinet et al., 2018; Antolínez et al., 2019; Roelvink et al., 2020; Alvarez-Cuesta et al., 2021). These models are well-suited for complex coastlines, where the influences of humans, sediment supply, and both alongshore and cross-shore processes contribute to the observed shoreline change. They may take the generalized form of:

$$\Delta x(t,y)_{total} = \Delta x(t)_{waves} + \Delta x(t,y)_{dy} + \Delta x(t)_{WL} \quad (4)$$

As these models also encompass a variety of processes that act at different timescales, these models have also been used for long-term assessment of shoreline variability/change (e.g., Vitousek et al., 2017a; Alvarez-Cuesta et al., 2021).

4. MODEL ADVANCES

4.1. Deterministic vs. Probabilistic Approaches

Many of the above models were developed as deterministic descriptors of shoreline change over time. However, it is critically important to acknowledge that both inputs (i.e., forcing) and model structure (i.e., equations) contain a certain level of error and uncertainty that needs to be included in future shoreline predictions (Ranasinghe, 2020). To that effect, there is a growing body of literature related to predicting future shoreline change that acknowledges the cascades of uncertainty and how these effect long-term shoreline predictions (Le Cozannet et al., 2019; D'Anna et al., 2020, 2021a; Kroon et al., 2020; Toimil et al., 2020, 2021).

To emphasize the importance of acknowledging the uncertainty in wave forcing, Greenslade et al. (2019) listed ensemble and probabilistic wave modeling and forecasting as one of the top 5 priorities for wind-wave research at present. As a start, over the past few decades wave emulators have been developed to address this issue (Davidson et al., 2010, 2017; Antolinez et al., 2016; Anderson et al., 2019; Cagigal et al., 2020). Wave emulators allow for a probabilistic description of wave conditions using techniques such as Monte Carlo sampling. Also with the perspective of providing probabilistic estimates of long-term shoreline change, D'Anna et al. (2021a) developed a framework to address uncertainty related to the unknown future changes in the mean sea level. We believe this is an area where much more work needs to be done to allow for robust future shoreline predictions in an uncertain future.

Uncertainty and error due to model structure has been less well-studied, with the most common approach being an equal-weight ensemble used to estimate the mean and spread of a range of models for a given input scenario (Montaño et al., 2020). While equally weighting all available models provides improved estimates compared to a single model, it has also been acknowledged that certain shoreline models perform better under certain conditions (Montaño et al., 2020; D'Anna et al., 2021a) such that a more dynamic weighting approach to ensemble model output may provide improved model results and more robust estimates of uncertainty and should be considered in future shoreline prediction efforts.

4.2. Timescales of Change

At present the most widely used coastal models assume stationary processes when considering the timescales of days to multi-decade, which by proxy assumes that the systems they model vary within a constrained envelope based on past observations (Yates et al., 2009) or that trends of the past will continue into the future (Luijendijk et al., 2018; Vousdoukas et al., 2020). These assumptions are likely challenged in the face of climate change. Recently, a number of approaches to address non-stationary forcing and model adaptation timescales have been proposed, acknowledging that beaches may adapt over a variety of timescales (e.g., Frazer et al., 2009; Splinter et al., 2016). Many of these have been included acknowledging the simplistic equilibrium-type shoreline models may not be suitable for long-term shoreline prediction (Ranasinghe, 2020). For example, Ibaceta et al. (2020) suggested an ensemble Kalman Filter assimilation technique could track changes in model structure due to changing wave-shoreline feedback. Montaño et al. (2021) and Schepper et al. (2021) separately proposed two different multi-scale model approaches. Montaño et al. (2021) used a Complete Ensemble Empirical Mode Decomposition method that linked different timescales of forcing to the corresponding timescales in the shoreline change. In contrast, Schepper et al. (2021) included upscaling, downscaling and direct forcing methods to link forcing to various timescales of shoreline evolution. These advances hint at ways forward to robustly predict future shoreline changes in a changing and uncertain climate using these simplified reduced complexity models.

5. FUTURE OPPORTUNITIES

Two recent priority setting exercises (Greenslade et al., 2019; Power et al., 2021) found that a number of key priorities in the coastal geosciences and engineering community were related to the need to better understand our coasts now and in the

future. Specifically, high quality temporal and spatial data of both the forcing (waves) and coastlines, enhanced quantification of shoreline change, and improved understanding of extreme events and the quantification of future impacts of climate change on our coasts were listed among the top priorities.

One of the biggest challenges in coastal shoreline forecasting is the ability to predict how coasts may adapt to a range of possible futures. At multiple timescales, planning decisions—be it "do we need to evacuate that house due to risk of an impending storm?" to—"will this

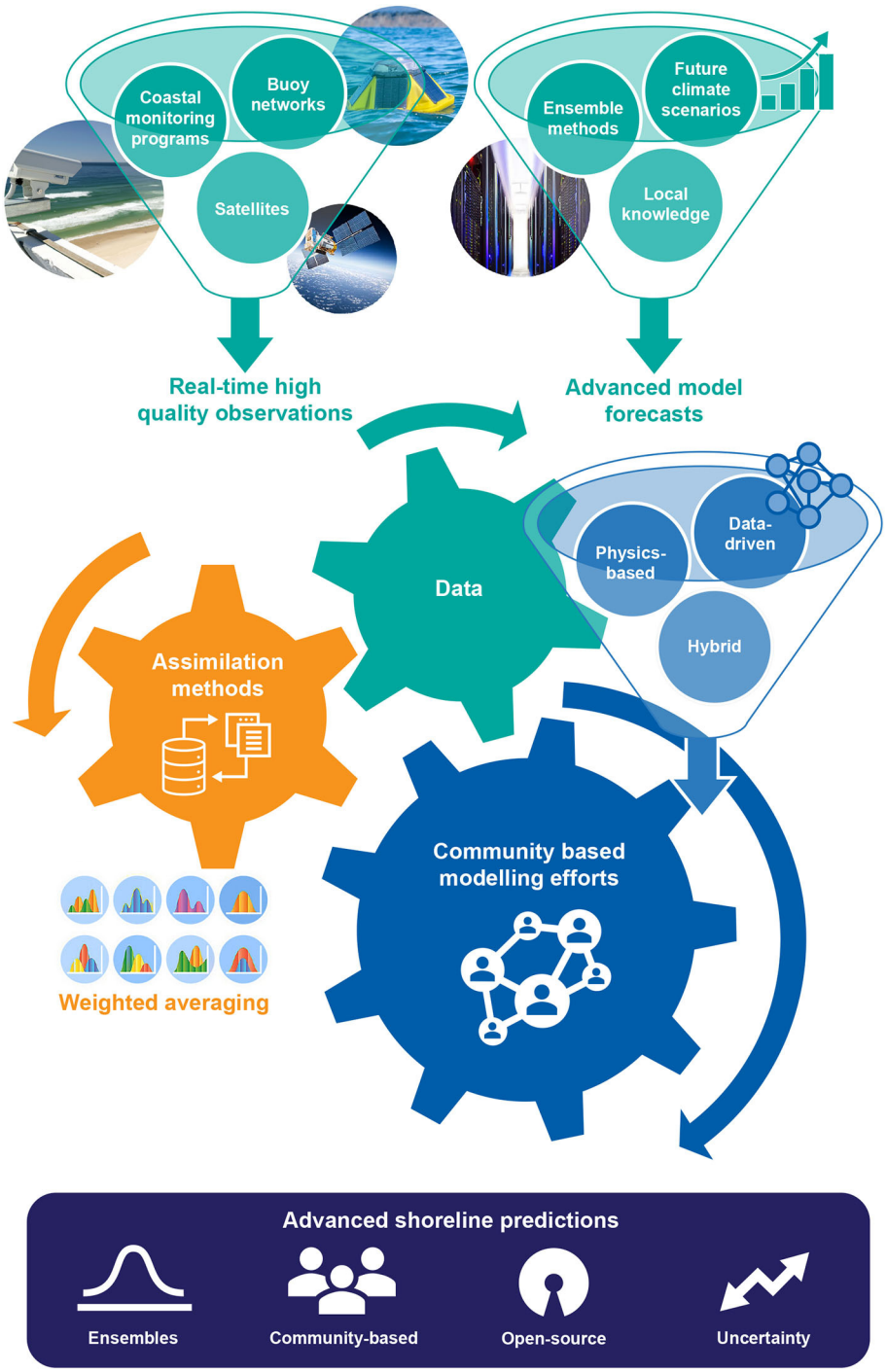

FIGURE 2 | A framework for future shoreline change modeling.

stretch of coast become uninhabitable before the end of the century?" require reliable and robust predictions of shoreline position. To address this, over the last 20 years advancements into modeling of shoreline change at timescales of individual storms to century level predictions have been proposed. To develop more accurate forecast tools for future coastal shoreline change, we recommend the following (also summarized in **Figure 2**):

1. Data is key
   - A continued push for real-time, high frequency and high quality *in-situ* coastal monitoring programs at relevant temporal and spatial scales to better understand the complex ocean/land boundary with a focus to capture the shoreline and nearshore bathymetry.
   - Improved spatial and temporal resolution of the necessary metocean forcing (waves, water levels).
   - Increasing accessibility to the ever growing network of satellite missions and the data they provide.
   - Benchmark data sets openly available for the community to test their models against.
2. Advanced forecasts
   - Reliable and robust forecasts of future wave conditions, in the form of continuous timeseries mode, based on the best climate projections that account for changes in storminess and clustering of storms. This may include the use of alternative approaches, such as surrogate models and emulators.
   - Improved and more frequent use of ensemble methods to bring different forecasts together and address uncertainty associated to model structure.
   - Continue to seek local (traditional) knowledge, particularly at sites that are data poor.
   - Consider new ways of model calibration—based on the ensemble, rather than individual models.
3. Collaboration beats competition
   - A push for more diverse groups to work together to advance the science—this may include engineers, geomorphologists, oceanographers, climatologists, and data scientists for example.
   - An open source approach to improve both process-based models and reduced complexity models on the timescales of interest.
   - Ensemble approaches that use advanced weighting techniques.
4. Learn from new data
   - Acknowledging model structure error and including this in the assimilation process.
   - Incorporating new data streams as they become available.
   - Models that adapt in time to changes in forcing.

Much like the advancements that have been made in climate modeling and wave forecasting on a global scale, workshops and working groups will help to foster the community spirit and rapidly advance the science. We have seen evidence of this already, such as the international ShoreShop (Montaño et al., 2020) and through various national-level programs such as iCOASST (UK), and the National Assessment of Shoreline Change (USA). These models will need to be open source to maximize uptake and development of the community-based efforts. Platforms, such as GitHub and the Community Surface Dynamics Modeling system (https://csdms.colorado.edu/) will become necessary for models to be integrated and developed with proper version control. The community models will ultimately include an "ensemble of ensembles" of shoreline predictions with uncertainty bounds based on the uncertainty of both the inputs (waves/water levels) and of the individual models.

Today's model predictions, no matter which shape or type of model is considered, remain hampered by a variety of uncertainty sources that in some cases can only be partially reduced (e.g., the future wave climate and the large uncertainties associated with the uncertainty in the various emission scenarios used to drive the GCMs). As a result predictions of shoreline change will need to be cast in a probabilistic framework and will require a joint community effort.

DATA AVAILABILITY STATEMENT

The original contributions presented in the study are included in the article/supplementary material, further inquiries can be directed to the corresponding author.

AUTHOR CONTRIBUTIONS

KS and GC came up with the ideas for this perspectives. All authors contributed to the writing and editing of the article.

FUNDING

All authors would like to acknowledge the various funding agencies who in the past have supported their research in shoreline prediction and modeling. These include the Australian Research Council (Discovery and Linkage Program), and the NZ National Hazard Platform.

ACKNOWLEDGMENTS

The authors wish to thank Anna Blacka (UNSW) for her assistance with the graphics and many colleagues that have contributed to shoreline modeling over the past decade and continue to do so in an open and collaborative manner for the further advancement in our field. We also wish to thank the reviewers for their insightful feedback that has improved the manuscript.

REFERENCES

Almeida, L. P., de Oliveira, I. E., Lyra, R., Dazzi, R. L. S., Martins, V. G., and da Fontoura Klein, A. H. (2021). Coastal analyst system from space imagery engine (CASSIE): shoreline management module. *Environ. Modell. Softw.* 140:105033. doi: 10.1016/j.envsoft.2021.105033

Alvarez-Cuesta, M., Toimil, A., and Losada, I. J. (2021). Modelling long-term shoreline evolution in highly anthropized coastal areas. Part 1: model description and validation. *Coast. Eng.* 169:103960. doi: 10.1016/j.coastaleng.2021.103960

Anderson, D., Rueda, A., Cagigal, L., Antolinez, J., Mendez, F., and Ruggiero, P. (2019). Time-varying emulator for short and long-term analysis of coastal flood hazard potential. *J. Geophys. Res. Oceans* 124, 9209–9234. doi: 10.1029/2019JC015312

Anderson, D., Ruggiero, P., Antolinez, J. A. A., Mendez, F. J., and Allen, J. (2018). A climate index optimized for longshore sediment transport reveals interannual and multi-decadal littoral cell rotations. *J. Geophys. Res. Earth Surface* 123, 1958–1981. doi: 10.1029/2018JF004689

Angnuureng, D. B., Almar, R., Senechal, N., Castelle, B., Addo, K. A., Marieu, V., et al. (2017). Shoreline resilience to individual storms and storm clusters on a meso-macrotidal, barred beach. *Geomorphology* 290, 256–276. doi: 10.1016/j.geomorph.2017.04.007

Antolínez, J. A., Méndez, F. J., Anderson, D., Ruggiero, P., and Kaminsky, G. M. (2019). Predicting climate-driven coastlines with a simple and efficient multiscale model. *J. Geophys. Res. Earth Surface* 124, 1596–1624. doi: 10.1029/2018JF004790

Antolinez, J. A. A., Mendez, F. J., Camus, P., Vitousek, S., Gonzales, E. M., Ruggiero, P., et al. (2016). A multiscale climate emulator for long-term morphodynamics (MUSCLE-morpho). *J. Geophys. Res. Oceans* 121, 775–791. doi: 10.1002/2015JC011107

Barnard, P., Short, A. D., Harley, M. D., Splinter, K. D., Vitousek, S., Turner, I. I. L., et al. (2015). Coastal vulnerability across the Pacific dominated by El Ni no/southern oscillation. *Nat. Geosci.* 8, 1–8. doi: 10.1038/ngeo2539

Brunel, C., and Sabatier, F. (2009). Potential influence of sea-level rise in controlling shoreline position on the French Mediterranean Coast. *Geomorphology* 107, 47–57. doi: 10.1016/j.geomorph.2007.05.024

Bruun, P. (1962). Sea-level rise as a cause of shore erosion. *J. Waterways Harbors Coast. Eng. Divis.* 1, 117–130. doi: 10.1061/JWHEAU.0000252

Cagigal, L., Rueda, A., Anderson, D., Ruggiero, P., Merrifield, M. A., Montano, J., et al. (2020). A multivariate, stochastic, climate-based wave emulator for shoreline change modelling. *Ocean Modell.* 154:101695. doi: 10.1016/j.ocemod.2020.101695

Castelle, B., Bujan, S., Marieu, V., and Ferreira, S. (2020). 16 years of topographic surveys of rip-channelled high-energy meso-macrotidal sandy beach. *Sci. Data* 7, 1–9. doi: 10.1038/s41597-020-00750-5

Castelle, B., Marieu, V., Bujan, S., Splinter, K. D., Robinet, A., Sénéchal, N., et al. (2015). Impact of the winter 2013-2014 series of severe Western Europe storms on a double-barred sandy coast: beach and dune erosion and megacusp embayments. *Geomorphology* 238, 135–148. doi: 10.1016/j.geomorph.2015.03.006

Coco, G., Senechal, N., Rejas, A., Bryan, K. R., Capo, S., Parisot, J. P., et al. (2014). Beach response to a sequence of extreme storms. *Geomorphology* 204, 493–501. doi: 10.1016/j.geomorph.2013.08.028

Cooper, J., Masselink, G., Coco, G., Short, A., Castelle, B., Rogers, K., et al. (2020). Sandy beaches can survive sea-level rise. *Nat. Clim. Change* 10, 993–995. doi: 10.1038/s41558-020-00934-2

Cooper, J. A. G., and Pilkey, O. H. (2004). Sea-level rise and shoreline retreat: time to abandon the Bruun Rule. *Glob. Planet. Change* 43, 157–171. doi: 10.1016/j.gloplacha.2004.07.001

D'Anna, M., Castelle, B., Idier, D., Rohmer, J., Le Cozannet, G., Thieblemont, R., et al. (2021a). Uncertainties in shoreline projections to 2100 at Truc Vert Beach (France): role of sea-level rise and equilibrium model assumptions. *J. Geophys. Res. Earth Surface* 126, 1–26. doi: 10.1029/2021JF006160

D'Anna, M., Idier, D., Castelle, B., Le Cozannet, G., Rohmer, J., and Robinet, A. (2020). Impact of model free parameters and sea-level rise uncertainties on 20-years shoreline hindcast: the case of Truc Vert beach (SW France). *Earth Surface Process. Landforms* 45, 1895–1907. doi: 10.1002/esp.4854

D'Anna, M., Idier, D., Castelle, B., Vitousek, S., and Le Cozannet, G. (2021b). Reinterpreting the Bruun Rule in the context of equilibrium shoreline models. *J. Marine Sci. Eng.* 9:974. doi: 10.3390/jmse9090974

Davidson, M. (2021). Forecasting coastal evolution on time-scales of days to decades. *Coast. Eng.* 168:103928. doi: 10.1016/j.coastaleng.2021.103928

Davidson, M., Lewis, R., and Turner, I. (2010). Forecasting seasonal to multi-year shoreline change. *Coast. Eng.* 57, 620–629. doi: 10.1016/j.coastaleng.2010.02.001

Davidson, M., Splinter, K., and Turner, I. (2013). A simple equilibrium model for predicting shoreline change. *Coast. Eng.* 73, 191–202. doi: 10.1016/j.coastaleng.2012.11.002

Davidson, M., Turner, I., Splinter, K. D., and Harley, M. D. (2017). Annual prediction of shoreline erosion and subsequent recovery. *Coast. Eng.* 130, 14–25. doi: 10.1016/j.coastaleng.2017.09.008

Davidson-Arnott, R. G., and Bauer, B. O. (2021). Controls on the geomorphic response of beach-dune systems to water level rise. *J. Great Lakes Res.* (in press). doi: 10.1016/j.jglr.2021.05.006

Dissanayake, P., Brown, J., Wisse, P., and Karunarathna, H. (2015). Effects of storm clustering on beach/dune evolution. *Marine Geol.* 370, 63–75. doi: 10.1016/j.margeo.2015.10.010

Doria, A., Guza, R., O'Reilly, W. C., and Yates, M. (2016). Observations and modeling of San Diego beaches during El Ni no. *Continent. Shelf Res.* 124, 153–164. doi: 10.1016/j.csr.2016.05.008

Frazer, L. N., Anderson, T. R., and Fletcher, C. H. (2009). Modeling storms improves estimates of long-term shoreline change. *Geophys. Res. Lett.* 36:L20404. doi: 10.1029/2009GL040061

Greenslade, D., Hemer, M., Babanin, A., Lowe, R., Turner, I., Power, H., et al. (2019). 15 priorities for wind-waves research: an Australian perspective. *Bull. Am. Meteorol. Soc.* 101, E446–E461. doi: 10.1175/BAMS-D-18-0262.1

Gutierrez, B. T., Plant, N. G., and Thieler, E. R. (2011). A Bayesian network to predict coastal vulnerability to sea level rise. *J. Geophys. Res. Earth Surface* 116, 1–15. doi: 10.1029/2010JF001891

Harley, M., Turner, I., Kinsela, M., Middleton, J., Mumford, P., Splinter, K., et al. (2017). Extreme coastal erosion enhanced by anomalous extratropical storm wave direction. *Sci. Rep.* 7:6033. doi: 10.1038/s41598-017-05792-1

Harley, M. D., Turner, I. L., and Short, A. D. (2015). New insights into embayed beach rotation: the importance of wave exposure and cross-shore processes. *J. Geophys. Res. F Earth Surface* 120, 1470–1484. doi: 10.1002/2014JF003390

Ibaceta, R., Splinter, K. D., Harley, M. D., and Turner, I. L. (2020). Enhanced coastal shoreline modeling using an ensemble Kalman filter to include nonstationarity in future wave climates. *Geophys. Res. Lett.* 47:e2020GL090724. doi: 10.1029/2020GL090724

Jaramillo, C., González, M., Medina, R., and Turki, I. (2021). An equilibrium-based shoreline rotation model. *Coast. Eng.* 163:103789. doi: 10.1016/j.coastaleng.2020.103789

Kamphuis, J. W. (1991). Alongshore sediment transport rate. *J. Waterway Port Coast. Ocean Eng.* 117, 624–640. doi: 10.1061/(ASCE)0733-950X(1991)117:6(624)

Karunarathna, H., Pender, D., Ranasinghe, R., Short, A. D., and Reeve, D. E. (2014). The effects of storm clustering on beach profile variability. *Mar. Geol.* 348, 103–112. doi: 10.1016/j.margeo.2013.12.007

Kroon, A., de Schipper, M. A., van Gelder, P. H., and Aarninkhof, S. G. (2020). Ranking uncertainty: wave climate variability versus model uncertainty in probabilistic assessment of coastline change. *Coast. Eng.* 158:103673. doi: 10.1016/j.coastaleng.2020.103673

Le Cozannet, G., Bulteau, T., Castelle, B., Ranasinghe, R., Wöppelmann, G., Rohmer, J., et al. (2019). Quantifying uncertainties of sandy shoreline change projections as sea level rises. *Sci. Rep.* 9, 1–11. doi: 10.1038/s41598-018-37017-4

Ludka, B. C., Guza, R. T., O'Reilly, W. C., Merrifield, M. A., Flick, R. E., Bak, A. S., et al. (2019). Sixteen years of bathymetry and waves at San Diego beaches. *Sci. Data* 6, 1–13. doi: 10.1038/s41597-019-0167-6

Luijendijk, A., Hagenaars, G., Ranasinghe, R., Baart, F., Donchyts, G., and Aarninkhof, S. (2018). The state of the world's beaches. *Sci. Rep.* 8, 1–11. doi: 10.1038/s41598-018-24630-6

Masselink, G., Castelle, B., Scott, T., Dodet, G., Suanez, S., Jackson, D., et al. (2016a). Extreme wave activity during 2013/2014 winter and morphological impacts along the Atlantic coast of Europe. *Geophys. Res. Lett.* 43, 2135–2143. doi: 10.1002/2015GL067492

Masselink, G., Scott, T., Poate, T., Russell, P., Davidson, M., and Conley, D. (2016b). The extreme 2013/2014 winter storms: hydrodynamic forcing and coastal response along the southwest coast of England. *Earth Surface Process. Landforms* 41, 378–391. doi: 10.1002/esp.3836

McCarroll, R. J., Masselink, G., Valiente, N. G., Scott, T., Wiggins, M., Kirby, J. A., et al. (2021). A rules-based shoreface translation and sediment budgeting tool for estimating coastal change: ShoreTrans. *Mar. Geol.* 435:106466. doi: 10.1016/j.margeo.2021.106466

Mentaschi, L., Vousdoukas, M. I., Pekel, J.-F., Voukouvalas, E., and Feyen, L. (2018). Global long-term observations of coastal erosion and accretion. *Sci. Rep.* 8:12876. doi: 10.1038/s41598-018-30904-w

Miller, J. K., and Dean, R. G. (2004). A simple new shoreline change model. *Coast. Eng.* 51, 531–556. doi: 10.1016/j.coastaleng.2004.05.006

Montaño, J., Coco, G., Antolínez, J. A., Beuzen, T., Bryan, K. R., Cagigal, L., et al. (2020). Blind testing of shoreline evolution models. *Sci. Rep.* 10, 1–10. doi: 10.1038/s41598-020-59018-y

Montaño, J., Coco, G., Cagigal, L., Mendez, F., Rueda, A., Bryan, K. R., et al. (2021). A multiscale approach to shoreline prediction. *Geophys. Res. Lett.* 48:e2020GL090587. doi: 10.1029/2020GL090587

Pianca, C., Holman, R., and Siegle, E. (2015). Shoreline variability from days to decades: results of long-term video imaging. *J. Geophys. Res. C Oceans* 120, 2159–2178. doi: 10.1002/2014JC010329

Power, H. E., Pomeroy, A. W., Kinsela, M. A., and Murray, T. P. (2021). Research priorities for coastal geoscience and engineering: a collaborative exercise in priority setting from Australia. *Front. Mar. Sci.* 8:645797. doi: 10.3389/fmars.2021.645797

Ranasinghe, R. (2020). On the need for a new generation of coastal change models for the 21st century. *Sci. Rep.* 10, 1–6. doi: 10.1038/s41598-020-58376-x

Ranasinghe, R., Callaghan, D., and Stive, M. J. F. (2012). Estimating coastal recession due to sea level rise: beyond the Bruun Rule. *Clim. Change* 110, 561–574. doi: 10.1007/s10584-011-0107-8

Robinet, A., Idier, D., Castelle, B., and Marieu, V. (2018). A reduced-complexity shoreline change model combining longshore and cross-shore processes: the LX-Shore model. *Environ. Modell. Softw.* 109, 1–16. doi: 10.1016/j.envsoft.2018.08.010

Roelvink, D., Huisman, B., Elghandour, A., Ghonim, M., and Reyns, J. (2020). Efficient modeling of complex sandy coastal evolution at monthly to century time scales. *Front. Mar. Sci.* 7:535. doi: 10.3389/fmars.2020.00535

Rosati, J. D., Dean, R. G., and Walton, T. L. (2013). The modified Bruun Rule extended for landward transport. *Mar. Geol.* 340, 71–81. doi: 10.1016/j.margeo.2013.04.018

Ruggiero, P., Buijsman, M., Kaminsky, G. M., and Gelfenbaum, G. (2010). Modeling the effects of wave climate and sediment supply variability on large-scale shoreline change. *Mar. Geol.* 273, 127–140. doi: 10.1016/j.margeo.2010.02.008

Schepper, R., Almar, R., Bergsma, E., de Vries, S., Reniers, A., Davidson, M., et al. (2021). Modelling cross-shore shoreline change on multiple timescales and their interactions. *J. Mar. Sci. Eng.* 9:582. doi: 10.3390/jmse9060582

Smith, E. R., Wang, P., Ebersole, B. A., and Zhang, J. (2009). Dependence of total longshore sediment transport rates on incident wave parameters and breaker type. *J. Coast. Res.* 253, 675–683. doi: 10.2112/07-0919.1

Splinter, K., Turner, I., and Davidson, M. (2013). How much data is enough? The importance of morphological sampling interval and duration for calibration of empirical shoreline models. *Coast. Eng.* 77, 14–27. doi: 10.1016/j.coastaleng.2013.02.009

Splinter, K., Turner, I. L., Davidson, M., Barnard, P., Castelle, B., and Oltman-Shay, J. (2014). A generalized equilibrium model for predicting daily to interannual shoreline response. *J. Geophys. Res. Earth Surface* 119, 1936–1958. doi: 10.1002/2014JF003106

Splinter, K. D., Turner, I. L., Reinhardt, M., and Ruessink, G. (2016). Rapid adjustment of shoreline behavior to changing seasonality of storms: Observations and modelling at an open-coast beach. *Earth Surface Process. Landforms*. 42, 1186–1194. doi: 10.1002/esp.4088

Toimil, A., Camus, P., Losada, I. J., and Alvarez-Cuesta, M. (2021). Visualising the uncertainty cascade in multi-ensemble probabilistic coastal erosion projections. *Front. Mar. Sci.* 8:683535. doi: 10.3389/fmars.2021.683535

Toimil, A., Camus, P., Losada, I. J., Le Cozannet, G., Nicholls, R. J., Idier, D., et al. (2020). Climate change-driven coastal erosion modelling in temperate sandy beaches: methods and uncertainty treatment. *Earth Sci. Rev.* 202:103110. doi: 10.1016/j.earscirev.2020.103110

Turki, I., Medina, R., Coco, G., and Gonzalez, M. (2013). An equilibrium model to predict shoreline rotation of pocket beaches. *Mar. Geol.* 346, 220–232. doi: 10.1016/j.margeo.2013.08.002

Turner, I., Harley, M., Short, A., Simmons, J., Bracs, M., Phillips, M., et al. (2016). A multi-decade dataset of monthly beach profile surveys and inshore wave forcing at Narrabeen, Australia. *Sci. Data* 3:160024. doi: 10.1038/sdata.2016.24

USACE and Coastal Engineering Research Center (1984). *Shore Protection Manual*. US Army Corps of Engineers, Washington, DC.

Vitousek, S., Barnard, P. L., and Limber, P. (2017a). Can beaches survive climate change? *J. Geophys. Res. Earth Surface* 122, 1060–1067. doi: 10.1002/2017JF004308

Vitousek, S., Barnard, P. L., Limber, P., Erikson, L., and Cole, B. (2017b). A model integrating longshore and cross-shore processes for predicting long-term shoreline response to climate change. *J. Geophys. Res. Earth Surface* 122, 782–806. doi: 10.1002/2016JF004065

Vos, K., Harley, M. D., Splinter, K. D., Simmons, J. A., and Turner, I. L. (2019a). Sub-annual to multi-decadal shoreline variability from publicly available satellite imagery. *Coast. Eng.* 150, 160–174. doi: 10.1016/j.coastaleng.2019.04.004

Vos, K., Splinter, K. D., Harley, M. D., Simmons, J. A., and Turner, I. L. (2019b). CoastSat: a Google Earth Engine-enabled Python toolkit to extract shorelines from publicly available satellite imagery. *Environ. Modell. Software* 122:104528. doi: 10.1016/j.envsoft.2019.104528

Vousdoukas, M. I., Ranasinghe, R., Mentaschi, L., Plomaritis, T. A., Athanasiou, P., Luijendijk, A., et al. (2020). Sandy coastlines under threat of erosion. *Nat. Clim. Change* 10, 260–263. doi: 10.1038/s41558-020-0697-0

Wolinsky, M. A. (2009). A unifying framework for shoreline migration: 1. Multiscale shoreline evolution on sedimentary coasts. *J. Geophys. Res.* 114:F01008. doi: 10.1029/2007JF000855

Wolinsky, M. A., and Murray, A. B. (2009). A unifying framework for shoreline migration: 2. Application to wave-dominated coasts. *J. Geophys. Res.* 114:F01009. doi: 10.1029/2007JF000856

Yates, M. L., Guza, R. T., and O'Reilly, W. C. (2009). Equilibrium shoreline response: observations and modeling. *J. Geophys. Res.* 114:C09014. doi: 10.1029/2009JC005359

Conflict of Interest: The authors declare that the research was conducted in the absence of any commercial or financial relationships that could be construed as a potential conflict of interest.

frontiers in Marine Science

ORIGINAL RESEARCH
published: 05 January 2022
doi: 10.3389/fmars.2021.798657

Regime Shifts in Future Shoreline Dynamics of Saudi Arabia

Arjen Pieter Luijendijk[1,2]*, *Etiënne Kras*[1], *Vasiliki Dagalaki*[1], *Robin Morelissen*[1], *Ibrahim Hoteit*[3] and *Roshanka Ranasinghe*[1,4,5]

[1] Deltares, Hydraulic Engineering, Delft, Netherlands, [2] Department of Hydraulic Engineering, Faculty of Civil Engineering and Geosciences, Delft University of Technology, Delft, Netherlands, [3] Physical Science and Engineering Division, King Abdullah University of Science and Technology (Kaust), Thuwal, Saudi Arabia, [4] Department of Coastal and Urban Risk and Resilience, IHE Delft Institute for Water Education, Delft, Netherlands, [5] Water Engineering and Management, Faculty of Engineering Technology, University of Twente, Enschede, Netherlands

The Saudi Arabian tourism sector is growing, and its economy has flourished over the last decades. This has resulted in numerous coastal developments close to large economic centers, while many more are proposed or planned. The coastal developments have influenced the behavior of the shoreline in the past. Here we undertake a national assessment on the state of the coast of Saudi Arabia based on recent data sets on historic and future shoreline positions. While at national scale the shoreline is found to be stable over the last three decades, the Red Sea coast shows a regional-mean retreat rate while the Gulf coast shows a regional-mean prograding behavior. Detailed analysis of the temporal evolution of shoreline position at selected locations show that human interventions may have accelerated shoreline retreat along adjacent shorelines, some of which are Marine Protected Areas. Furthermore, reef-fronted coastal sections have a mean accretive shoreline change rate, while the open coast shows a mean retreat rate. Future shoreline projections under RCP 4.5 and RCP 8.5 show that large parts of the shoreline may experience an accelerated retreat or a change in its regime from either stable or sprograding to retreating. Under the high emission RCP 8.5 scenario, the length of coastline projected to retreat more than doubles along the Red Sea coast, and approximately triples along the Gulf coast in 2100. At national scale, the Saudi Arabian coastline is projected to experience regional-mean retreats of ∼30 m and of ∼130 m by 2050 and 2100 under both RCPs considered in this study. These results indicate that effective adaptation strategies will be required to protect areas of ecological and economic value, and that climate resilience should be a key consideration in planned or proposed coastal interventions.

Keywords: shoreline dynamics, sea level rise (SLR), Saudi Arabia, regime shift, coastal erosion, Persian Gulf, Arabian Gulf

OPEN ACCESS

Edited by:
Giandomenico Foti, Mediterranea University of Reggio Calabria, Italy

Reviewed by:
Giovanni Besio, University of Genoa, Italy
Humood Naser, University of Bahrain, Bahrain

***Correspondence:**
Arjen Pieter Luijendijk
a.p.luijendijk@tudelft.nl

Specialty section:
This article was submitted to Coastal Ocean Processes, a section of the journal Frontiers in Marine Science

Received: *20 October 2021*
Accepted: *13 December 2021*
Published: *05 January 2022*

Citation:
Luijendijk AP, Kras E, Dagalaki V, Morelissen R, Hoteit I and Ranasinghe R (2022) Regime Shifts in Future Shoreline Dynamics of Saudi Arabia. Front. Mar. Sci. 8:798657. doi: 10.3389/fmars.2021.798657

1. INTRODUCTION

The Kingdom of Saudi Arabia is located in the Arabian Peninsula, in southwest Asia. The country's 2.25 million km^2 terrain consists mostly of arid steppe, mountains and sand desert, while the 2,320 km of shoreline span over the Red Sea (ca. 1,760 km) and the Gulf (ca. 560 km). Ninety-nine percent of the Saudi Arabia coast is sandy, interrupted by rocky headlands (Luijendijk et al., 2018). Both on the Red Sea and Gulf, extensive fringing coral reef habitats (1,480 km^2) are found along the coast

and around offshore islands. These reefs together with the mangrove forests (35 km^2) scattered along the Red Sea coast comprise the most significant coastal habitats of the Saudi coast.

Due to the flourishing economy and the growing tourism sector, numerous coastal interventions have been implemented in the last decades in the coastal front of the large economic centers of the country (Jeddah, Khobar, Dammam, Jubail, etc.), driven by the need to create more space for industrial, urban and recreational uses (Halpern et al., 2008; Sheppard et al., 2010). Over the last 30 years, 186 km^2 of Saudi Arabian inland and coastal water surface has been transferred into land while 156 km^2 of its land has been converted into water (Donchyts et al., 2016).

At present, seaside developments (e.g., Red Sea Development Project, NEOM, Economic Cities) are being planned and built, mostly in scarcely populated, pristine areas, with the aim of supporting economic activities and tourism growth. For developers and stakeholders, a smart, future-proof design of the coastal front, in combination with the conservation of the unique physical and ecological characteristics of these coasts, is a primary goal.

Understanding of the natural dynamics of the coast and present state of these rapidly developing coastal zone is therefore of great importance. Acquiring and analyzing information regarding the historical evolution of the coastal system toward its present state can provide useful insight into the influence of the different natural and/or anthropogenic drivers. At a national level, such an analysis has not yet been conducted for Saudi Arabia. Information on historical coastal change can also support the predictions of the future autonomous dynamics of the Saudi coastal systems. Additionally, it can inform the assessment of planned coastal interventions in terms of the type and magnitude of the expected impacts on the natural system, thus contributing to future-proof and sustainable coastal development.

This study investigates long-term historic and projected future shoreline changes for Saudi Arabia, by generating and analyzing detailed state-of-the-art geospatial datasets of historic and future shoreline change. After introducing the study area, data and methods (section 2), the historic long-term shoreline changes, including the temporal variability therein, are discussed (section 3). Thereafter, the projected shoreline changes under two climate change scenarios, and the expected regime shifts in shoreline behavior are discussed. Conclusions of the study are finally presented in section 4.

2. STUDY AREA AND METHODS

2.1. Environmental Conditions

Saudi-Arabia is enclosed by water bodies on both the western and eastern side of the country; the Red Sea (including the Gulf of Aqaba) in the west and the Gulf in the east. The tide in the north Red Sea is semi-diurnal with typical range up to 1 m. Seasonal water level variations are also observed (0.2–0.3 m in the central Red Sea) (Deltares, 2015). Extreme water levels (with return period (RP) of 100 years) in the northern part of the Red Sea are estimated to be between 0.5 and 2 m (Muis et al., 2016; Vousdoukas et al., 2018). Under RCP4.5 (RCP8.5) the projected increase in 100 year RP water levels is 0.2 m (0.4 m) by 2100. The dimensions and layout of the Gulf result in a complex system of tidal standing waves. The tidal characteristics vary over the Gulf, with different areas experiencing diurnal, mixed and semi-diurnal tides (Reynolds, 1993). Tidal range is greater than 1 m everywhere and the highest tidal ranges (up to 4 m) are observed in the northern end of the Gulf and the east side of Qatar (Elshorbagy et al., 2006; Rakha et al., 2007).

The geography of the Red Sea surrounding land masses creates a wind system with dominant directions along the Red Sea axis. The analysis of Langodan et al. (2017) distinguishes different wind systems in the Red Sea. Northwesterly winds associated with storms in the Mediterranean Sea affect the northern part of the basin in the winter (with maximum speed up to 20 m/s) and the entire basin during summer. The southeasterly winds, present mainly in the southern part of the basin, are associated with winter monsoon events in the Arabian Sea. A 30-year regional reanalysis shows decreasing trends in the wind speeds in the area (Langodan et al., 2017). The wind climate in the Gulf is characterized by the presence of seasonal, high-intensity, north, north-easterly winds, the shamals. Summer shamals occur from May to July with velocities 7–13 m/s (Rao et al., 2001; Barlett, 2004) and may last for weeks at a time. Winter shamals affect the region from November to March with wind speeds up to 20 m/s at the center of the Gulf (Al Senafi and Anis, 2015).

The wave climatology in the Red Sea is strongly characterized by the main wind systems. Dominant wave directions in terms of frequency are northwesterly to northerly. In the north part of the Red Sea, H_s mean remains approximately 1 m all year around. Additionally, waves with swell characteristics, associated with the SE winds at the south Red Sea reach the north (Langodan et al., 2017). Energy from southerly waves is especially significant for the high percentiles during Oct-Apr. A 30 year hindcast shows decreasing trends in wave heights in the northern part of the Red Sea (in the order of 5–6 cm in 30 years for the northerly waves and 1 cm for the southerly waves) (Langodan et al., 2020). A decrease in the number of storm events per year related to the northerly and southerly waves is also detected. The prevailing wave direction over the Gulf is northwest to north, following the wind direction. The monthly mean H_s is lower than 1 m over the entirety of the Gulf with the highest values being reached in June and February in the central Gulf area (Kamranzad, 2018).

2.2. Methodology

Nowadays the added value of remote sensing in coastal engineering and coastal zone management is widely acknowledged and several global satellite-derived datasets have been generated (Donchyts et al., 2016; Luijendijk et al., 2018). These datasets can provide valuable information of the historic land-water changes and shoreline evolution since 1984. The historic shoreline change rates have also been used to assess future positions of the shorelines up to 2100 under various climate change scenarios (Vousdoukas et al., 2020). In the present study, these global data sets and methods have been deployed in more detail to conduct a national assessment on historic and future shoreline change of Saudi Arabia.

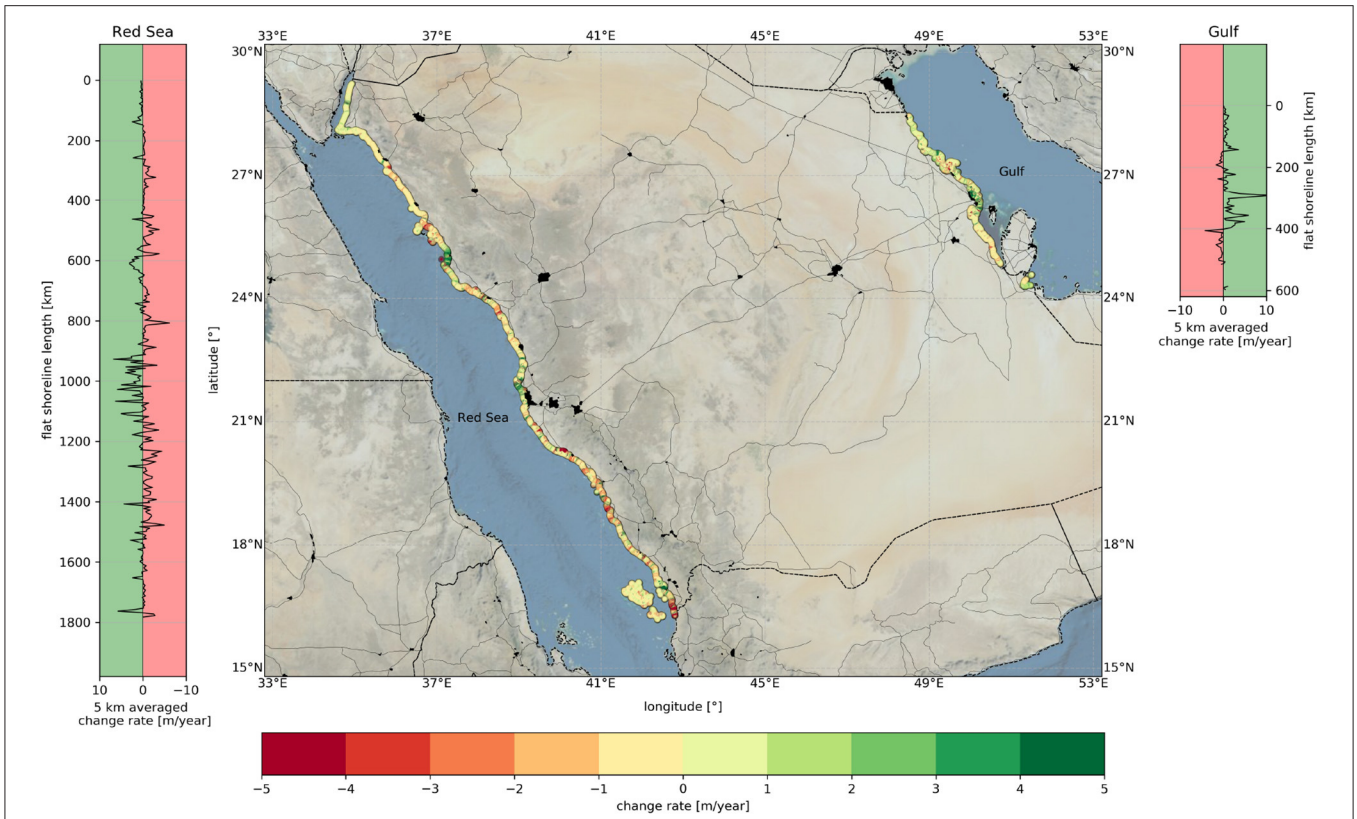

FIGURE 1 | The center panel contains satellite derived annual shoreline change rates for the Saudi Arabian Red Sea and Gulf coast (1984-2016). Urban areas are indicated in black and the road network with thin black lines. Five-kilometer averaged change rates are shown on flat shoreline stretches for the Red Sea (left panel) and the Gulf (right panel). For all panels, negative indicates long-term retreat and positive indicates prograding.

2.2.1. Historic Shoreline Change

Historical shoreline change data for the study area were obtained from the satellite derived shoreline (SDS) data set presented by Luijendijk et al. (2018). This global dataset provides historic annual shoreline positions derived from Landsat satellite imagery from 1984 to 2020 (Luijendijk et al., 2018).

First, yearly top-of-the-atmosphere reflectance composites were generated to remove the effects of clouds, shadows, snow, and ice. Then, the composites were used to estimate an accurate surface water mask using a dynamic thresholding method described in Donchyts et al. (2016). Analysis revealed that the influence of the tidal stage on detected shoreline positions was significantly reduced, which also applied for seasonal variability in wave and beach characteristics (Luijendijk et al., 2018).

Next, the composite images are used to determine the Normalized Difference Water Index (NDWI). The Canny edge detection filter is used to roughly estimate the position of the water-land transition, followed by the use of the Otsu thresholding method (Otsu, 1979) on a buffer polygon around the water-land transition to identify the most probable threshold to classify water and land on the image. The detected water lines at the edge of the water mask are smoothed using a 1D Gaussian smoothing operation to obtain a gradual shoreline avoiding the pixel-induced staircase effect (Luijendijk et al., 2018). A value of three gives the best results based on the four validation cases; meaning that it takes three cells on both sides during the 1D smoothing. The method may result in several shoreline vectors since lakes and small channels are detected. In this case, only the most seaward shoreline position is analyzed.

The validity of the shoreline detection method on sandy beaches has been demonstrated for multiple cases representing different types of beaches, sand, tidal and wave characteristics (Luijendijk et al., 2018). The accuracy of satellite derived shoreline positions is restricted to approximately 15 m over around 30 years (i.e., sub-pixel precision of the maximum spatial resolution (Hagenaars et al., 2017). In terms of shoreline change trends computed from these shoreline position data, trends in the range of –0.5 to +0.5 m/yr are taken to represent stable coastlines.

The automated shoreline detection method produces 37 annual global shorelines (1984–2020) with an alongshore resolution of 30 m. Using the defined transects at a 500 m alongshore spacing, the intersection point of each transect with the aforementioned annual shorelines was determined, which provided a sequence of shoreline positions per transect. The shoreline change rate (m/yr) at each transect is then computed by applying linear regression to all shoreline positions at that location. Ideally, a SDS position is available for each transect

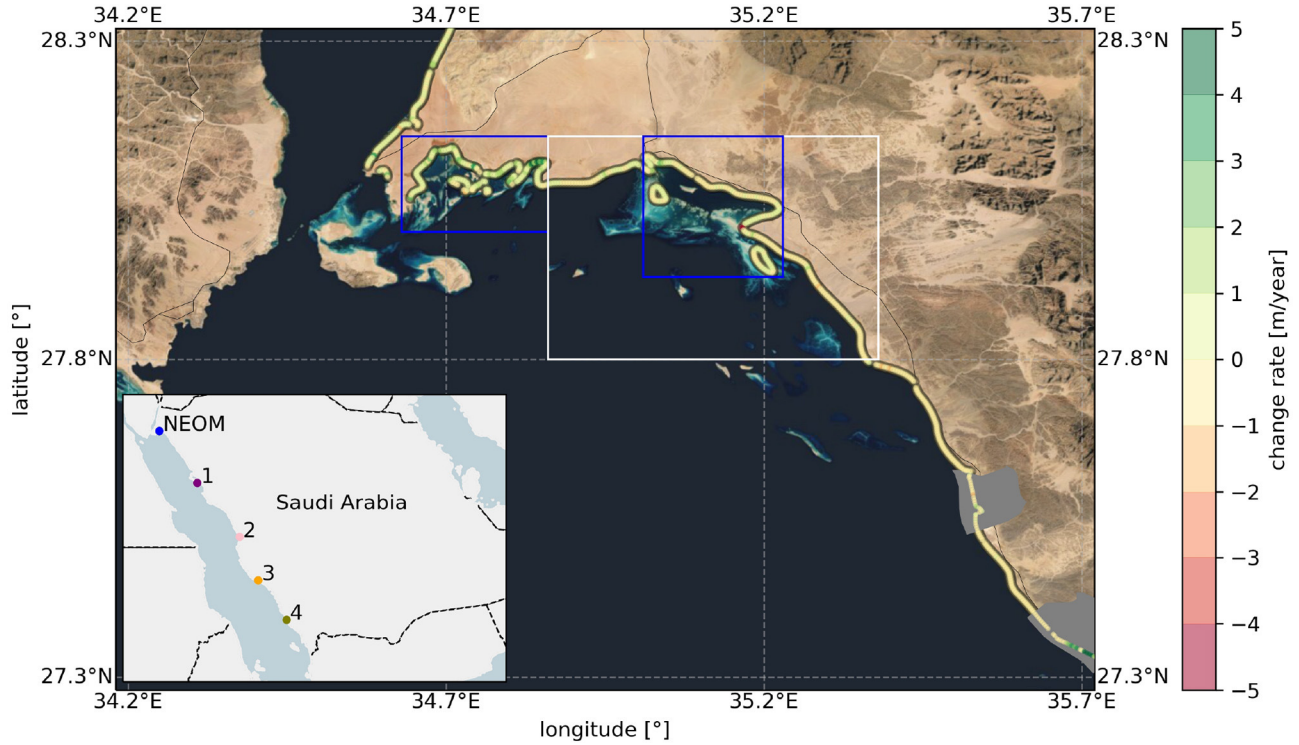

FIGURE 2 | Satellite derived annual shoreline change rates (1984–2016) for the NEOM project site, located on the Red Sea in northwest Saudi Arabia (see blue dot in the small inset). Urban areas (Al Muwaileh and Duba) are marked gray and the road network with thin black lines. The blue polygons indicate reef-fronted coasts, while the white polygon indicates open coasts. All polygons are situated within Ra's Suwayhil/Ra's al-Qasbah Marine Protected Area.

annually. However, the availability of satellite images and cloud cover can limit the number of SDS positions.

For each transect, a linear regression of the form $ax+b+\epsilon$ results in a change rate (a), a cross-shore intercept point with respect to 1984 (b) and a bootstrapped error term (ϵ) representing the reliability of the linear fit for historic shoreline change. To verify whether the change rate based on linear regression can be considered a representative proxy for the underlying data, the uncertainty bandwidth (or standard deviation) should be less than 0.5 m/yr (Luijendijk et al., 2018), which coincides with the limits of the stable regime.

To obtain high resolution time series of shoreline positions at specific sites, the same methods used by Luijendijk et al. (2018) were applied here, albeit using a dynamic (moving) 180-day window as this allows to generate Top of Atmosphere composite images at approximately 16-day intervals. These dynamic composites include seasonal variability in wave and beach characteristics while excluding noise and tidal variations. For this high resolution application, the GEE platform is used to obtain satellite imagery from the NASA Landsat-5 (1984–2013), Landsat-7 (1999-present) and Landsat-8 (2013-present) Operational Land Imager (OLI) sensors and the ESA Sentinel-2 (2015-present) Multi-Spectral Imager (MSI) sensor at a medium and high spatial resolution of 30 and 10 m respectively. Depending on the location on earth, the temporal resolution of the Landsat satellite missions is 16 days, whereas the Sentinel mission has a 5-day revisit time origination from two satellite constellations.

2.2.2. Future Shoreline Change

Estimates of future shoreline projections are obtained by combining data from Vousdoukas et al. (2020) and the historical change rates of Luijendijk et al. (2018). The probabilistic projections of Vousdoukas et al. (2020) explicitly take into account projections of future Relative SLR, spatial variations of coastal morphology, ambient shoreline change trends and future changes in meteorological drivers (for example, storm surge and waves).

In this study, the shoreline change throughout this century has been projected under two RCPs: RCP4.5 and RCP8.5. RCP4.5 may be viewed as a moderate-emission mitigation-policy scenario and RCP8.5 as a high-emissions scenario (Meinshausen, 2011). Here, the study focuses on the evolution of two components of sandy beach shoreline dynamics:

- AC, ambient shoreline dynamics driven by long-term hydrodynamic, geological and anthropic factors;
- R, shoreline retreat due to coastal morphological adjustments to SLR;

In the present study AC was exclusively obtained through the linear interpolation of the shoreline change rates reported

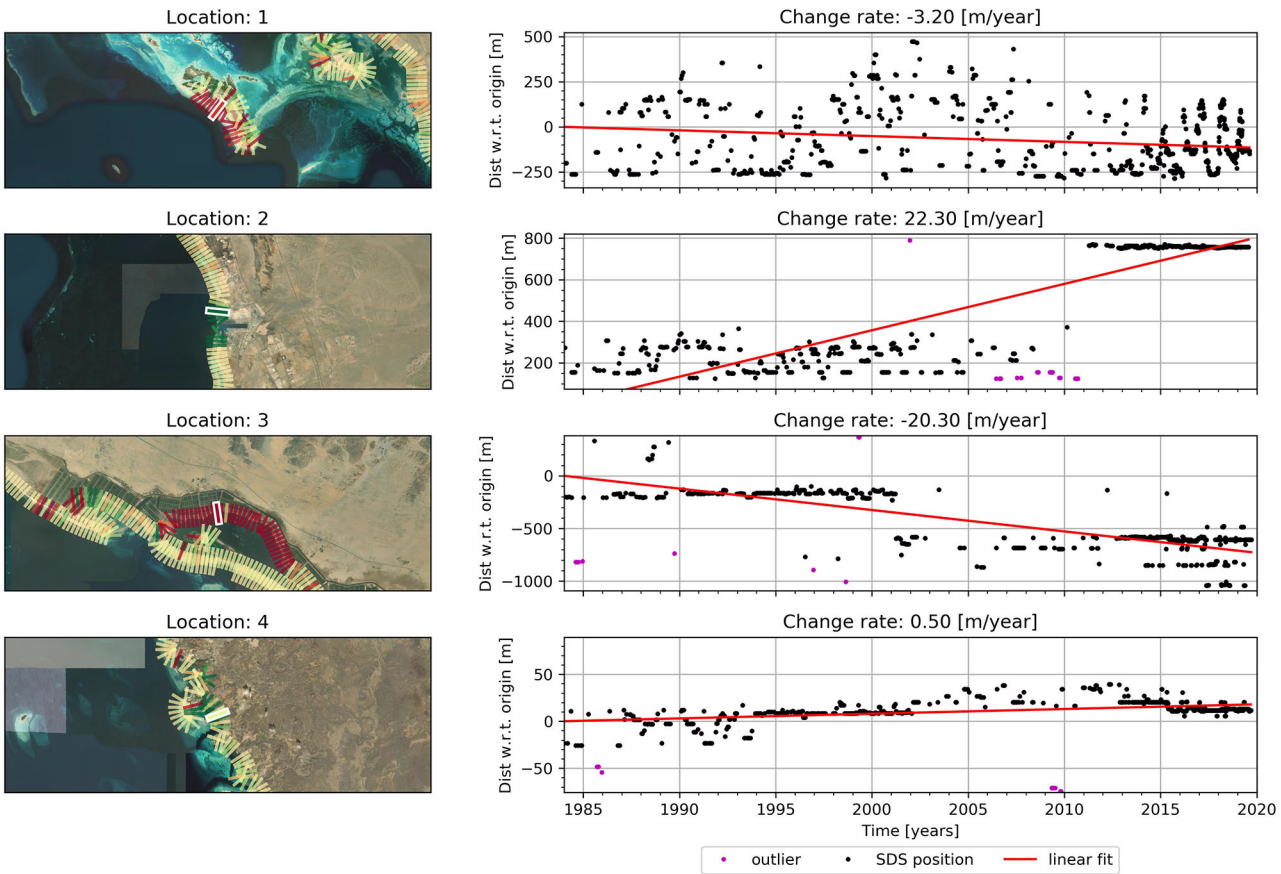

FIGURE 3 | Right panels: high-resolution time series of shoreline positions for the period (1984–2020) for four locations on Saudi Arabia Red Sea coast. The purple dots are identified as outliers following the criteria in Luijendijk et al. (2018). Left panels: geographical location of the selected transect indicated as the white-marked transects.

by Luijendijk et al. (2018); see previous section. Note that Vousdoukas et al. (2020) computed AC combining the shoreline change data sets of Luijendijk et al. (2018) and Mentaschi et al. (2018). The R is directly obtained from Vousdoukas et al. (2020) projections, and represents SLR-driven shoreline retreat, the magnitude of which depends on the amplitude of SLR and the transfer of sediment from the subaerial to the submerged part of the active beach profile, to adjust to rising mean sea levels. The estimation of the equilibrium shoreline retreat R of sandy coasts due to SLR is based on the Bruun rule (Bruun, 1962). This approach builds on the concept that the beach morphology tends to adapt to the prevailing wave climate and is given by:

$$R = SLR/tan\beta$$

where tanβ is the active profile slope. Projections of regional SLR up to the end of this century are available from a probabilistic, process-based approach (Jackson, 2016) that combines the major factors contributing to SLR. Local scale vertical land movements such as land subsidence due to, for example, groundwater extraction are not included in the SLR projections. The tanβ term expresses the slope of the active beach profile, which was based on a global dataset of active beach slopes (Athanasiou et al., 2019). This dataset has been created combining the MERIT digital elevation dataset (Yamazaki et al., 2017) with the GEBCO bathymetry (Weatherall et al., 2015). Beach profiles are generated along each sandy beach transect by combining the above bathymetric and topographic data.

Here, shoreline change projection are derived, by adding the AC and R terms thus obtained, for 2050 and 2100 under RCP 4.5 and RCP 8.5.

3. RESULTS

3.1. National Assessment of Historical Shoreline Change

The center panel in **Figure 1** shows the historic long-term shoreline change rates for the complete shoreline of Saudi Arabia for the period 1984-2016. The mean shoreline change rate for the entire shoreline of Saudi Arabia is 0.06 m/yr. For the Saudi Arabian coast 29% shows shoreline retreat larger than 0.5 m/yr (i.e., the threshold for stable vs. unstable shorelines as per the inherent accuracy level associated with the SDS approach), while

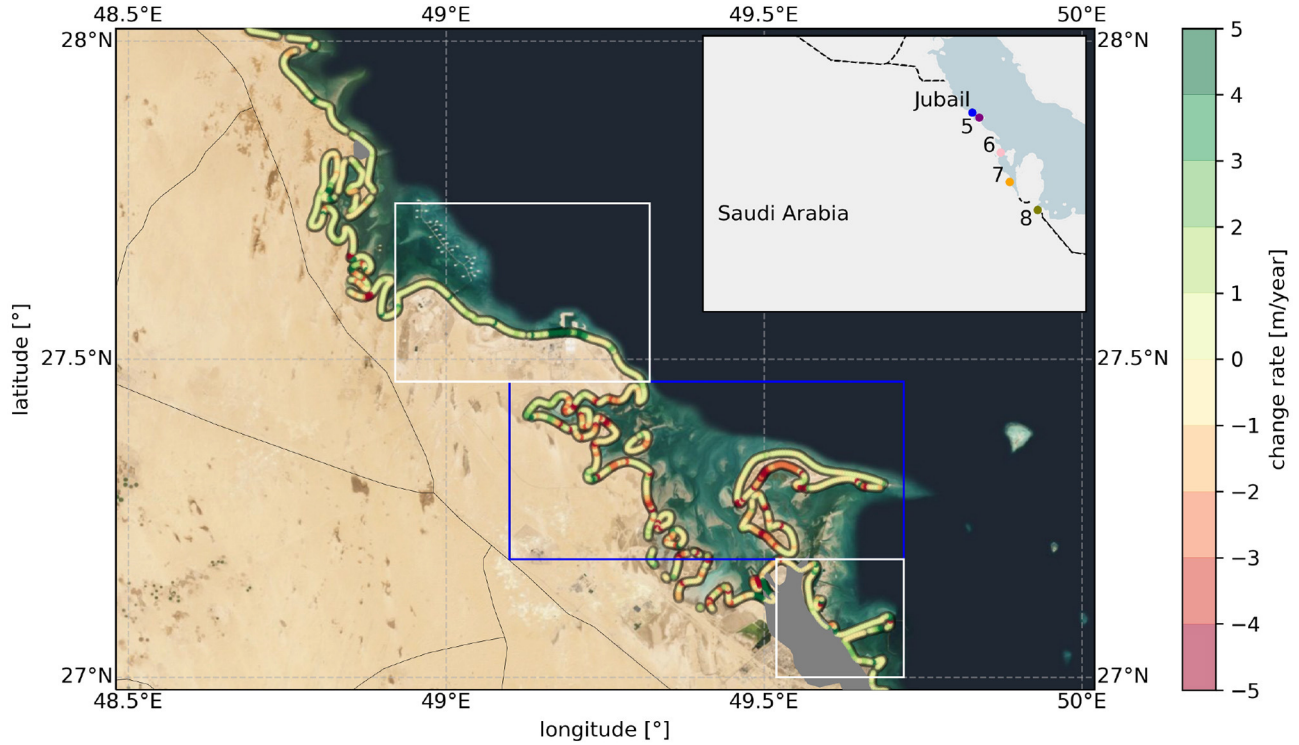

FIGURE 4 | Satellite derived annual shoreline change rates (1984–2016) close to Jubail, located on the Gulf in northeast Saudi Arabia (see blue dot in the small inset). Urban areas (Tanajib and Jubail) are marked grey and the road network with thin black lines. The blue area shows the Jubail Marine Wildlife Sanctuary MPA, while the white polygons indicate areas subject to human interventions.

23% show accretive behavior with change rates larger than 0.5 m/yr. The remaining 48% of the shoreline falls under the category of stable shorelines. As the Saudi Arabian Red Sea and Gulf coasts are different in terms of forcing and physical characteristics, results are discussed separately for the Red Sea and Gulf coast using 5-km averaged change rates as presented in **Figure 1**.

The Saudi Arabian part of the Red Sea coast (including the Gulf of Aqaba) stretches along approximately 1760 km of shoreline. The mean change rate of all transects at the Red Sea coast is retreating with a rate of –0.18 m/year (i.e., retreating). About 19% (334 km) of the Red Sea coast shows a prograding trend, while 32% (563 km) of the coast show a retreating trend. The remaining 49% (863 km) of shoreline is stable.

The Saudia Arabian part of the Gulf coast is approximately 560 km long. The mean change rate of all the Gulf transects is 0.71 m/year (i.e., prograding). About 23% (129 km) exhibits a retreating trend and approximately 32% (179 km) show prograding behavior; the remaining 45% (252 km) of the coast is stable.

The Gulf coast exhibits higher prograding change rates compared to the Red Sea coast (see **Figure 1**). The prograding sections are also here found around economic centers, due to land reclamations and other human developments, while the retreating sections are often located in nature protected areas. Besides, as seen on the sides of **Figure 1**, the Red Sea coast contains higher retreating rates for longer shoreline stretches than the Gulf coast. These retreating sections are mostly located at relatively remote areas, whereas the prograding shorelines are typically found at inhabited areas.

To gain more detailed insights into distinctly different behaviors of the Red Sea and Gulf coasts of Saudi Arabia, below (Section 3.2) we perform a more high resolution analysis of a few selected locations on each coast.

3.2. Regional and Local Analysis

3.2.1. Red Sea Coast

Here we focus on 5 locations along the Red Sea coast (see inset in **Figure 2**). The first location highlights the spatial variations in shoreline behavior, here focusing on differences between an open and a reef-fronted coast. The other four locations are a representative set for the temporal variations of shoreline dynamics found along this coast.

NEOM is a recently announced developments (https://www.neom.com/en-us) which will be located on the Red Sea in northwest Saudi Arabia. The project site, as indicated in **Figure 2** (spanning across the blue and white polygons), is characterized by reef-fronted (blue polygons) and open (white polygon) shorelines known to be part of a 3,700 km^2 planned Marine Protected Area (MPA) called Ra's Suwayhil/Ra's al-Qasbah. At present, there are practically no human interventions on this pristine shoreline managed by the Saudi Wildlife Authority. The shorelines in the blue and white polygons are 135 km and 42 km

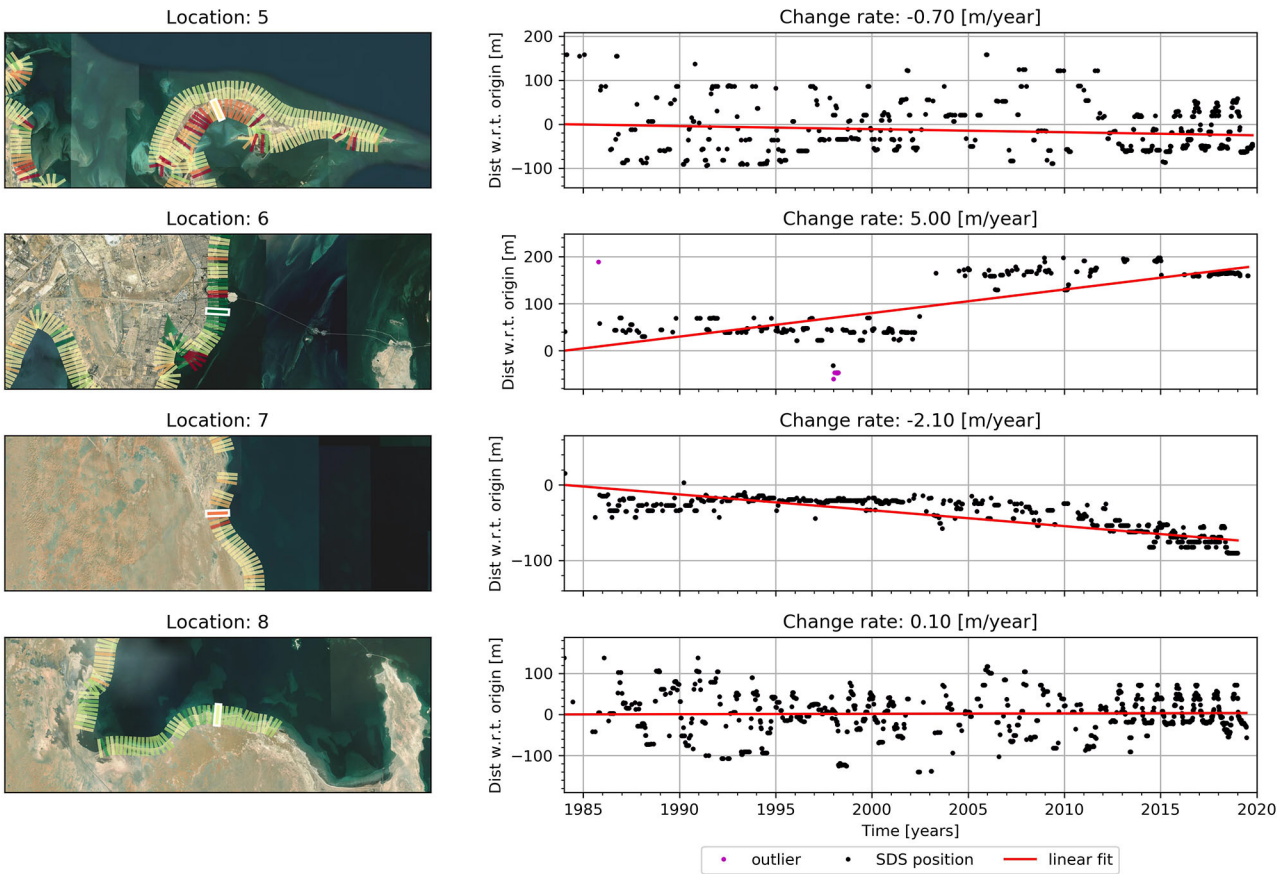

FIGURE 5 | Right panels: high-resolution time series of shoreline positions for the period (1984–2020) for four locations on the Gulf coast of Saudi Arabia. Left panels: geographical location of the selected transect indicated as the white-marked transects.

long, respectively. The reef-fronted shoreline in the west shows a mean prograding change rate of 0.26 m/year, while the transects at the open coast show a mean retreating change rate of –0.09 m/year (see **Figure 2**).

For this specific area, it is found that for 88% of the transects the linear regression is a representative proxy to explain long-term behavior of the shoreline. For more detailed analyses it is useful to study the complete time series signals instead of solely looking into linear change rates. Up to this point, the presented analysis is restricted to annual shoreline positions and its associated linear change rates. Therefore, only natural phenomena or processes acting on at least multi-year timescales are incorporated. However, as explained in the last paragraph of the Methodology section, higher temporal resolution shoreline position data can be derived from the SDS dataset. This opens up the possibility to look into behavior at smaller timescales (like seasonality) within the time series signals as well as to extend the time series to 2020. Such a computationally demanding high temporal resolution analysis is performed for four locations along the Red Sea coast, as indicated with numbered, colored dots in the small inset in **Figure 2**. These locations are selected based on geographical location (nature area vs. developed coast). It gives an overview of the types of time series signals that are present the along the Red Sea shoreline (see **Figure 3**).

Location 1 is located on an island in a remote area that contains a pristine coral reef environment. The time series of shoreline change shows a relatively stable long-term trend, albeit with substantial short-term variability. Seasonal cyclic pattern in shoreline position, up to $\tilde{4}$00 m, can be seen in the data from 2015 onward, due to the availability and inclusion of higher temporal resolution data from the Sentinel-2 satellite mission. Location 2 is located close to a coastal settlement. The time series shows a rather stable shoreline with limited temporal variability up to around 2010. A sudden advancement in shoreline position of $\tilde{6}$00 m can be seen in 2010. This is due to land reclamation (including coastal structures), which has stabilized the shoreline thereon. Location 3 is characterized by an area with a lot of aqua cultural activity. This anthropogenic driver is clearly seen to have an effect on the time series signal. Until 2001, when the aqua cultural activities commenced, this shoreline (which is protected by an offshore island and reefs), has been rather stable. However, around 2001, the shoreline retreated markedly by approximately 400 m, however remaining stable in its retreated position thereafter. Location 4 is located in a sheltered reef

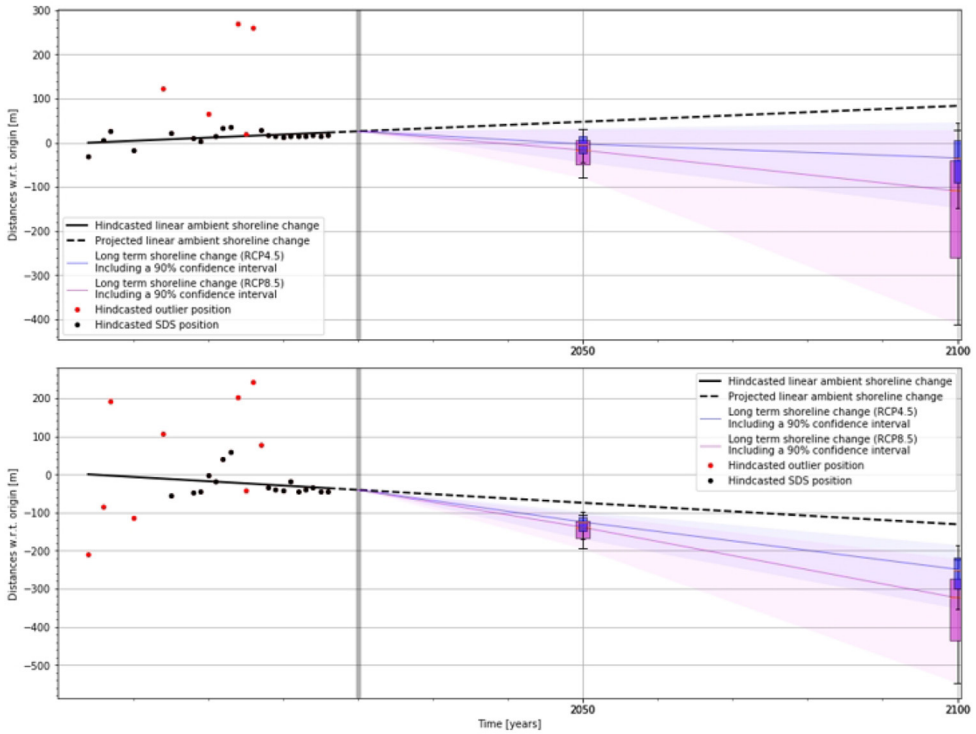

FIGURE 6 | Historic and projected shoreline positions (1984–2100) for two RCP scenarios showing a shift from prograding to retreating for a location at the NEOM site (upper panel) and showing an accelerating retreat at Jubail (lower panel).

environment and has been steadily prograding at a rate of 0.5 m/year with limited short-term variability. In the last decade or so, however, the shoreline at this locations appears to have remained stable.

3.2.2. Gulf Coast

Similar to the Red Sea coast, we focus here on 5 locations along the Gulf coast (see inset in **Figure 4**). The first location highlights the spatial variations in shoreline behavior, here focusing on impacts of human interventions. The other four locations are a representative set for the temporal variations of shoreline dynamics found along this coast.

The Gulf coast of Saudi Arabia has been subjected to large-scale coastal developments, leading to human-engineered systems around its economic centers of Khobar, Dammam and Jubail (see white polygons in **Figure 4**). Between these economic centers, MPA's ensure human interventions are minimal. One of these MPA's is the 2,300 km^2 de facto Jubail Marine Wildlife Sanctuary (see blue polygon in **Figure 4**), of which the state-owned oil enterprise Saudi Aramco is the managing authority (UNEP-WCMC, 2016). The sanctuary is the first MPA in the Arabian Gulf and consists of two coastal embayment systems and five offshore coral islands (Krupp and Khushaim, 1991). The shoreline in the MPA is 290 km long. **Figure 4** shows the satellite derived annual shoreline change rates (1984–2016) in this area. The shoreline in the white polygons shows accretive behavior with a change rate of 1.21 m/year, while the MPA mainly shows shoreline retreat at a rate of -0.77 m/year.

Figure 5 shows the high resolution analysis for four locations along the Gulf coast. Location 5, which is located at a pristine peninsula, shows a cylic, low amplitude (25 m) temporal variability from the year 2013 onward. The years before 2013 indicate a greater, yet non-cylic variability in shoreline positions over time. The time series signal at Location 6 is from a beach that is bounded by two groins and situated in front of a coastal settlement. The data shows a stable trend that incorporates small temporal variability up to around 2003. In 2003, a land reclamation causes a sudden progradation of the shoreline of approximately 150 m. Hereafter, the temporal signal looks similar to its pre-2003 stable state. Location 7 is located at a pristine, undeveloped area. The temporal signal itself shows minor short-term variability while over time the general trend appears to be changing regimes. Up to 1994 it is slightly accretive, then it remains approximately stable for a little less than 10 years. After 2003, the shoreline steadily retreats. Location 8 is also located in an undeveloped area and therefore temporal variability likely caused by environmental forcing conditions. Especially after 2013, the short-term shoreline change becomes noticeably cyclic, as also seen at Location 5.

3.3. Projected Shoreline Changes up to 2100

Timely and sustainable coastal zone management, especially considering the increasing anthropogenic pressure and changing climate, requires knowledge on how shorelines might change

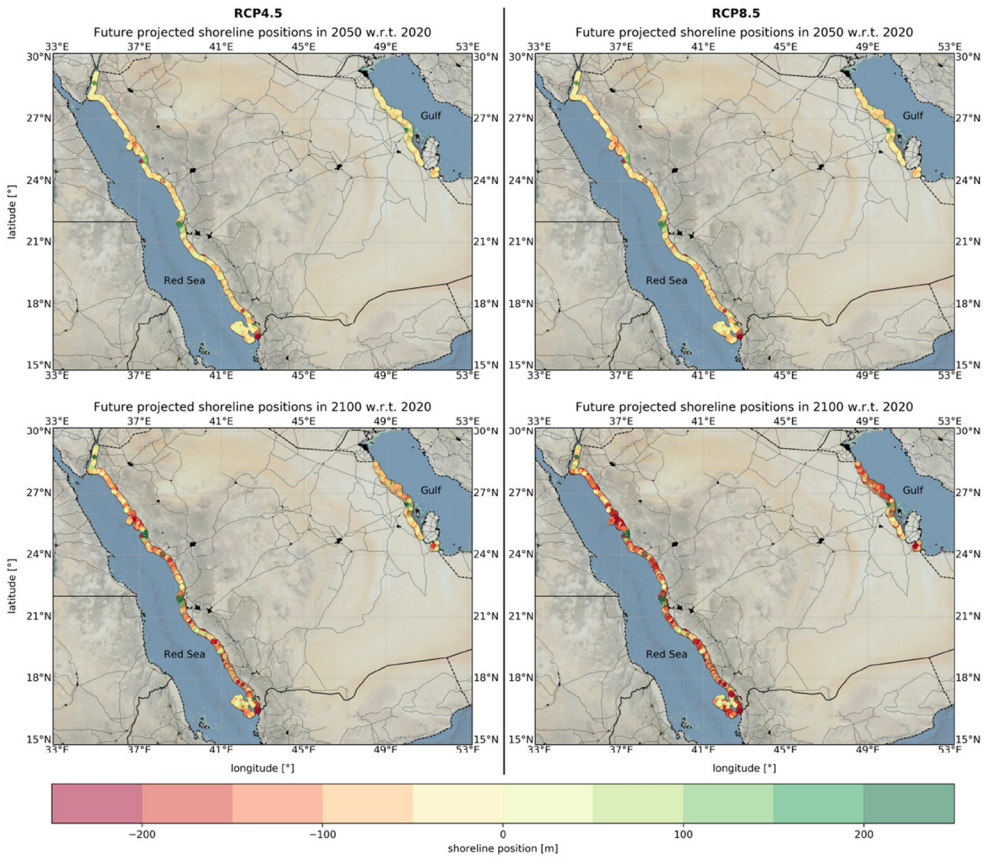

FIGURE 7 | Projected median shoreline positions (relative to 2020) for the Saudi Arabian Red Sea and Gulf coast for the years 2050 and 2100. The panels on the left show outcomes related to greenhouse gas concentration trajectory RCP4.5, while the panel on the right shows results for RCP8.5. Urban areas are marked black and the road network with thin black lines. For all panels, negative indicate retreating shorelines and positive indicate prograding shorelines.

in the future, including uncertainties in future projections. The rate of global sea level rise since 1993 has been greater than that observed over the twentieth century (Church, 2013;). While shoreline change can be the combined result of a range of erosive and accretive phenomena, there is a clear cause and effect relationship between increasing sea levels and shoreline retreat (Bruun, 1962; Ranasinghe and Stive, 2009; Stive, 2010; Ranasinghe, 2016). Climate change will also affect waves and storm surge (Hemer, 2013; Vousdoukas et al., 2018; Morim et al., 2019), which are important drivers of coastal morphology. Therefore, considering the dynamics of extreme weather patterns is also important in assessing potential climate change impacts beyond that of sea-level rise (SLR) alone (Vousdoukas et al., 2020). Future shoreline positions, using combined data from Vousdoukas et al. (2020) and Luijendijk et al. (2018) as discussed in section 2.2.2, are projected for both RCP4.5 and RCP8.5 for the years 2050 and 2100. As example, projections for the presently prograding NEOM site in the north part of the Red Sea show a switch to a retreating regime (see **Figure 6**). Already retreating coastal sections will experience accelerated retreat in the future, which is the case for e.g., Jubail Marine Protected Area (see **Figure 6**).

3.4. Regional Variations of Future Shoreline Positions

Regional projections of shoreline positions (relative to 2020) for the years 2050 and 2100 for both RCP 4.5 and RCP 8.5 are shown in **Figure 7**. At the scale of Saudi Arabia as a whole, regional-mean projections of shoreline retreat by 2050 are 29.0 and 32.1 m for RCP 4.5 and RCP 8.5, respectively. By 2100, these retreats increase to 112.9 and 145.5 m under RCP 4.5 and RCP 8.5, respectively.

At the Red Sea coast, regional mean projections indicate that the shoreline will retreat 31.6 m (RCP4.5) to 35.4 m (RCP8.5) in 2050 with respect to present-day shoreline position. For 2100 an additional retreat of 119.1 m (RCP4.5) to 151.7 m (RCP8.5) is projected due to sea level rise. At the Gulf coast, it is projected that on average the shoreline will retreat an additional mean distance of 20.1 m (RCP4.5) to 21.4 m (RCP8.5) in 2050 and 93.7 m (RCP4.5) to 127.2 m (RCP8.5) in 2100 due to sea level rise.

3.5. Future Regime Shifts in Shoreline Stretches

Analyses of future shoreline positions show that sea level rise may lead to a regime shift in shoreline behavior. The historically

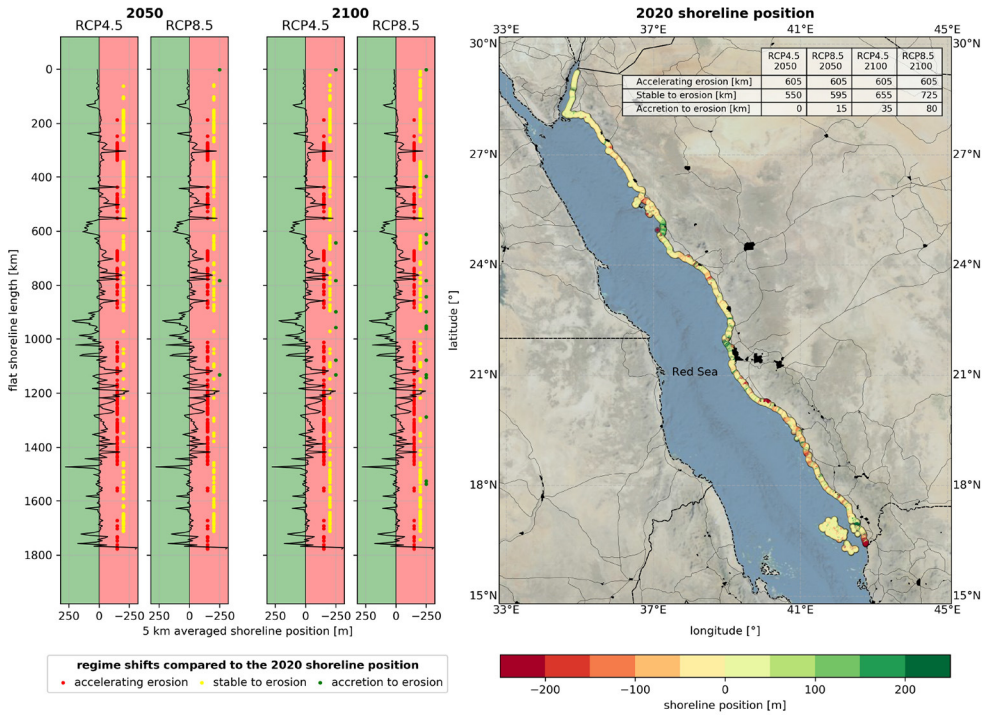

FIGURE 8 | Projected median shoreline positions (relative to 2020) for the Saudi Arabian Red Sea coast for the years 2050 and 2100 for RCP4.5 and RCP8.5. For the map panel, negative indicates retreat and positive indicates prograding trends between 1984 and 2020.

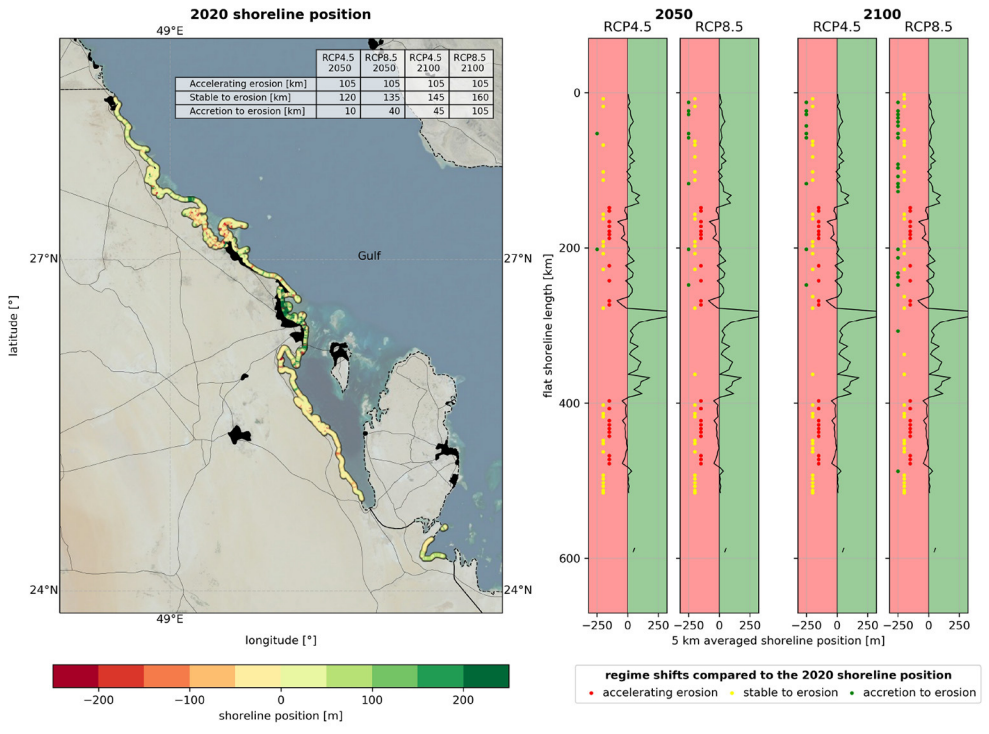

FIGURE 9 | Projected median shoreline positions (relative to 2020) for the Saudi Arabian Gulf coast for the years 2050 and 2100 for RCP4.5 and RCP8.5. For the map panel, negative indicates retreat and positive indicates prograding.

(1984-2020) retreating 5-km averaged coastline stretches (605 km) at the Red Sea coast will all be subject to an acceleration in the rate of retreat by 2050 (see **Figure 8**). In addition, a total length of 550 km that has been stable over the last 35 years will be retreating by 2050 for RCP4.5; 595 km for RCP8.5. This means that, regardless of climate scenario, the length of retreating coastline approximately doubles between 2020 and 2050. In 2100, even more of the Red Sea coastline is projected to change from a stable to retreating regime; i.e., additional 655 km and 725 km under RCP 4.5 and RCP 8.5 respectively. The shift from present-day prograding to retreating behavior is expected to occur at a coastline length of 35 km in 2100 for RCP4.5 and 80 km for RCP8.5. Overall, compared to the 32% of the Red sea coastline that has been retreating over the last 35 years, 63 and 66% of the Red Sea coast is projected to be retreating by 2050, increasing to 71 and 77% by 2100.

For the Gulf coast, the historically retreating 5-km averaged coastline stretches (105 km) will all be subject to an acceleration retreat rate already in 2050 (see **Figure 9**). In addition, a total length of 120 km that has been stable over the last 35 years will in 2050 be retreating for scenario RCP4.5; for RCP8.5 this will be a length of 135 km. In 2100 even longer coastline lengths will change from a stable to retreating regime; i.e., 145 km for RCP4.5 and 160 km for RCP8.5. The shift from prograding to retreating behavior is expected to occur at a coastline length of 45 km in 2100 for RCP4.5 and 105 km for RCP8.5. All in all, where nowadays 23% is retreating, in 2050 46% will be retreating in case of RCP4.5 and 54% for RCP8.5, while in 2100 this will be further increased to 57% for RCP4.5 and 70% for RCP8.5. This means that the length of coastline subject to retreat more than triples for the Gulf coast.

4. CONCLUSIONS

This study presented a national assessment of the state of the coast of Saudi Arabia using two state-of-the-art data sets of historical and future shoreline change. At national scale, the shoreline of Saudi Arabia has been stable over the 1985–2016 period with a long-term change rate of 0.06 m/year. At a more granular scale, the Red Sea and Gulf coast of Saudi Arabia show substantial differences in long-term shoreline dynamics over the same historical period. The former has experienced a regional-mean retreat rate of –0.18 m/year, while the latter has experienced a regional-mean progradation rate of 0.71 m/year. A detailed analysis of bi-weekly shoreline positions shows that human interventions in both Red sea and Gulf coasts have changed the natural shoreline dynamics substantially.

At several of the Red Sea locations where the bi-weekly resolution analysis was done, coastal developments appear to accelerate the retreat along adjacent coastlines. Furthermore, reef-fronted coastal sections show a mean prograding behavior, while the nearby open coastal sections show a retreating trend. Shoreline evolution in the Gulf coast behaves rather differently. Here too, human interventions have lead to step-changes in shoreline position at a few coastal sections. The SDS data for the Gulf shows a change rate of 1.21 m/year, while the marine protected areas show a remarkable mean retreat rate of 0.77 m/year. This may be an indication that the economy-driven coastal developments trigger significant erosion in the adjacent (marine protected) areas.

Future projections of shoreline change indicate that large Saudi Arabian shoreline stretches will be subject regime shifts (e.g., stable to retreating) in coastline behavior under both RCP 4.5 and RCP 8.5, and that these regime changes could be taking place already. Projections show that the length of retreating shorelines along the Red sea coast could more than double by 2100 (RCP 8.5), while this length could triple along the Gulf coast by 2100 (RCP 8.5). Considering the entire Saudi Arabian coastline, projections indicate regional-mean retreats of around 30 m and of around 130 m by 2050 and 2100 under both RCPs considered. These projections highlight the need for timely and sustainable coastal zone management, to protect the areas with large economic and ecological values while also ensuring climate resilience in planned or proposed coastal interventions.

DATA AVAILABILITY STATEMENT

Publicly available datasets were analyzed in this study. This data can be found here: https://shorelinemonitor.deltares.nl; https://data.jrc.ec.europa.eu/collection/liscoast.

AUTHOR CONTRIBUTIONS

AL and RR conceived the idea of the study. AL, EK, and VD co-worked on the analysis and visualization and wrote the manuscript together with RR. RM and IH reviewed the manuscript. All authors contributed to the article and approved the submitted version.

FUNDING

This research was funded by King Abdullah University of Science and Technology and the Deltares Strategic Research Program Seas and Coastal Zones. RR is partly supported by the AXA Research Fund.

REFERENCES

Al Senafi, F., and Anis, A. (2015). Shamals and climate variability in the northern arabian/persian gulf from 1973 to 2012. *Int. J. Climatol.* 35, 4509–4528. doi: 10.1002/joc.4302

Athanasiou, P., van Dongeren, A., Giardino, A., Vousdoukas, M., Gaytan-Aguilar, S., and Ranasinghe, R. (2019). Global distribution of nearshore slopes with implications for coastal retreat. *Earth Syst. Sci. Data* 11, 1515–1529. doi: 10.5194/essd-11-1515-2019

Barlett, K. (2004). *Dust storm forecasting for al udeid ab, qatar: an empirical analysis*. Master Thesis, Air Force Institute of Technology, Wright-Patterson Air Force Base, Ohio.

Bruun, P. (1962). Sea-Level Rise as a Cause of Shore Erosion. *J. Waterw. Harb. Coast. Eng. Div.* 8, 117–130. doi: 10.1061/jwheau.0000252

Church, J. A., Clark, P. U., Cazenave, A., Gregory, J. M., Jevrejeva, S., Levermann, A., et al (2013). *Sea Level Change*. Cambrige: Cambridge University Press. p.385

Deltares (2015). *Red Sea MetOcean Database*. Technical report 1210078-000-HYE-0010.

Donchyts, G., Baart, F., Winsemius, H., Gorelick, N., Kwadijk, J., and van de Giesen, N. (2016). Earth's surface water change over the past 30 years. *Nat. Clim. Chang* 6, 810–813. doi: 10.1038/nclimate3111

Elshorbagy, W., Azam, M., and Taguchi, K. (2006). Hydrodynamic characterization and modeling of the arabian gulf. *J. Waterway Port Coastal Ocean Eng.* 132, 47–56. doi: 10.1061/(ASCE)0733-950X(2006)132:1(47)

Hagenaars, G., de Vries, S., Luijendijk, A. P., de Boer, W. P., and Reniers, A. J. H. M. (2017). On the accuracy of automated shoreline detection derived from satellite imagery: a case study of the sand motor mega-scale nourishment. *Coastal Eng.* 133, 113–125. doi: 10.1016/j.coastaleng.2017.12.011

Halpern, B. S., Walbridge, S., Selkoe, K. A., Kappel, C. V., Micheli, F., D'Agrosa, C., et al. (2008). A global map of human impact on marine ecosystems. *Science* 319, 948–952. doi: 10.1126/science.1149345

Hemer, M., Fan, Y., Mori, N., Semedo, A., and Wang X. L. (2013). Projected changes in wave climate from a multi-model ensemble. *Nat. Clim. Chang.* 3, 471–476. doi: 10.1038/nclimate1791

IPCC (2019). *Climate Change and Land: an IPCC special report on climate change, desertification, land degradation, sustainable land management, food security, and greenhouse gas fluxes in terrestrial ecosystems* eds P.R. Shukla, J. Skea, E. Calvo Buendia, V. Masson-Delmotte, H.-O. Pörtner, D. C. Roberts, P. Zhai, R. Slade, S. Connors, R. van Diemen, M. Ferrat, E. Haughey, S. Luz, S. Neogi, M. Pathak, J. Petzold, J. Portugal Pereira, P. Vyas, E. Huntley, K. Kissick, M. Belkacemi, J. Malley.

Jackson, L. P., and Jevrejeva, S. (2016). A probabilistic approach to 21st century regional sea-level projections using rcp and high-end scenarios. *Glob. Planet. Change* 146, 179–189. doi: 10.1016/j.gloplacha.2016.10.006

Kamranzad, B. (2018). Persian gulf zone classification based on the wind and wave climate variability. *Ocean Eng.* 169, 604–635. doi: 10.1016/j.oceaneng.2018.09.020

Langodan, S., Cavaleri, L., Pomaro, A., Vishwanadhapalli, Y., Bertotti, L., and Hoteit, I. (2017). The climatology of the red sea part 2: the waves. *Int. J. Climatol.* 37, 4518–4528. doi: 10.1002/joc.5101

Langodan, S., Cavaleri, L., Portilla, J., Abualnaja, Y., and Hoteit, I. (2020). Can we extrapolate climate in an inner basin? the case of the red sea. *Glob. Planetary Change* 188:1035151. doi: 10.1016/j.gloplacha.2020.103151

Luijendijk, A., Hagenaars, G., Ranasinghe, R., Baart, F., Donchyts, G., and Aarninkhof, S. (2018). The state of the world's beaches. *Sci. Rep.* 8:6641. doi: 10.1038/s41598-018-24630-6

Meinshausen, M., and S. S. C. K. (2011). The rcp greenhouse gas concentrations and their extensions from 1765 to 2300. *Clim. Change* 109:213. doi: 10.1007/s10584-011-0156-z

Mentaschi, L., Vousdoukas, M., Pekel, J.-F., Voukouvalas, E., and Feyen, L. (2018). Global long-term observations of coastal erosion and accretion. *Sci. Rep.* 8:12876. doi: 10.1038/s41598-018-30904-w

Morim, J., Hemer, M., Wang, X. L., Cartwright, N., Trenham, C., Semedo, A., et al. (2019).Robustness and uncertainties in global multivariate wind-wave climate projections. *Nat. Clim. Chang.* 9, 711–718. doi: 10.1038/s41558-019-0542-5

Muis, S., Verlaan, M., Winsemius, H., Aerts, J., and Ward, P. (2016). A global reanalysis of storm surges and extreme sea levels. *Nat. Commun.* 7:11969. doi: 10.1038/ncomms11969

Otsu, N. (1979). Threshold selection method from gray-level histograms. *IEEE Trans. Syst. Man. Cybern.* 9, 62–66. doi: 10.1109/TSMC.1979.4310076

Rakha, K., Al-Salem, K., and Neelamani, S. (2007). Hydrodynamic atlas for the arabian gulf. *J. Coastal Res.* 550–554.

Ranasinghe, R., and Stive, M. (2009). Rising seas and retreating coastlines. *Clim. Change.* 97, 465–468. doi: 10.1007/s10584-009-9593-3

Ranasinghe, R. W. M. R. J. B. (2016). Assessing climate change impacts on open sandy coasts: A review. *Earth Sci. Rev.* 160, 320–332. doi: 10.1016/j.earscirev.2016.07.011

Rao, P. G., Al Sulaiti, M., and Al ?Mulla, A. H. (2001). Winter shamals in qatar, arabian gulf. *Weather* 56, 444–451. doi: 10.1002/j.1477-8696.2001.tb06528.x

Reynolds, R. (1993). Physical oceanography of the Gulf, Strait of Hormuz, and the Gulf of Oman-Results from the Mt Mitchell expedition. *Mar. Pollut. Bull.* 27, 35–59. doi: 10.1016/0025-326x(93)90007-7

Sheppard, C., Al-Husiani, M., Al-Jamali, F., Al-Yamani, F., Baldwin, R., Bishop, J., et al. (2010). The gulf: a young sea in decline. *Mar. Pollut. Bull.* 60, 13–38. doi: 10.1016/j.marpolbul.2009.10.017

Stive, M. J., Ranasinghe, R., and Cowell, P. J. (2010). "Sea level rise and coastal erosion," in *Handbook of Coastal and Ocean Engineering*, eds Y. C. Kim (Los Angeles, LA: California University Press), 1023–1037.

Vousdoukas, M., Mentaschi, L., Voukouvalas, E., Verlaan, M., Jevrejeva, S., Jackson, L., et al. (2018). Global probabilistic projections of extreme sea levels show intensification of coastal flood hazard. *Nat. Commun.* 9:2360. doi: 10.1038/s41467-018-04692-w

Vousdoukas, M. I., Ranasinghe, R., Mentaschi, L., Plomaritis, T. A., Athanasiou, P., Luijendijk, A., et al. (2020). Sandy coastlines under threat of erosion. *Nat. Clim. Chang* 10, 260–263. doi: 10.1038/s41558-020-0697-0

Weatherall, P., Marks, K., Jakobsson, M., Schmitt, T., Tani, S., Arndt, J. E., et al. (2015). A new digital bathymetric model of the world's oceans. *Earth Space Sci.* 2, 331–345. doi: 10.1002/2015EA000107

Yamazaki, D., Ikeshima, D., Tawatari, R., Yamaguchi, T., O'Loughlin, F., Neal, J., et al. (2017). A high-accuracy map of global terrain elevations: accurate global terrain elevation map. *Geophys. Res. Lett.* 44, 5844–5853. doi: 10.1002/2017GL072874

Conflict of Interest: The authors declare that the research was conducted in the absence of any commercial or financial relationships that could be construed as a potential conflict of interest.

Publisher's Note: All claims expressed in this article are solely those of the authors and do not necessarily represent those of their affiliated organizations, or those of the publisher, the editors and the reviewers. Any product that may be evaluated in this article, or claim that may be made by its manufacturer, is not guaranteed or endorsed by the publisher.

frontiers in Marine Science

ORIGINAL RESEARCH
published: 25 March 2022
doi: 10.3389/fmars.2022.847655

Vulnerability Evolution of Coastal Erosion in the Pearl River Estuary Great Bay Area Due to the Influence of Human Activities in the Past Forty Years

Chao Cao[1,2,3,4,5,6†], Kai Zhu[2†], Feng Cai[1,3,4,5,6*], Hongshuai Qi[1,3,4,5,6], Jianhui Liu[1,3,4,5,6], Gang Lei[1,3,4,6], Zijian Mao[2], Shaohua Zhao[1,3,4], Gen Liu[1,3,4,6] and Yan Su[2]*

[1] Third Institute of Oceanography, Ministry of Natural Resources, Xiamen, China, [2] College of Civil Engineering, Fuzhou University, Fuzhou, China, [3] Fujian Provincial Key Laboratory of Marine Ecological Conservation and Restoration, Xiamen, China, [4] Key Laboratory of Marine Ecological Conservation and Restoration, Ministry of Natural Resources, Xiamen, China, [5] Fujian Provincial Station for Field Observation and Research of Island and Costal Zone in Zhangzhou, Xiamen, China, [6] Southern Marine Science and Engineering Guangdong Laboratory (Zhuhai), Zhuhai, China

OPEN ACCESS

Edited by:
Giandomenico Foti,
Mediterranea University of Reggio Calabria, Italy

Reviewed by:
Meilin Wu,
South China Sea Institute of Oceanology (CAS), China
Kerrylee Rogers,
University of Wollongong, Australia

***Correspondence:**
Chao Cao
caochao@tio.org.cn
Feng Cai
caifeng@tio.org.cn

†These authors have contributed equally to this work

Specialty section:
This article was submitted to Coastal Ocean Processes, a section of the journal Frontiers in Marine Science

Received: 03 January 2022
Accepted: 23 February 2022
Published: 25 March 2022

Citation:
Cao C, Zhu K, Cai F, Qi HS, Liu JH, Lei G, Mao ZJ, Zhao S, Liu G and Su Y (2022) Vulnerability Evolution of Coastal Erosion in the Pearl River Estuary Great Bay Area Due to the Influence of Human Activities in the Past Forty Years. Front. Mar. Sci. 9:847655. doi: 10.3389/fmars.2022.847655

Under the dual effects of global climate change and intensive human development activities, vulnerability to coastal erosion in bay areas is becoming increasingly serious. This study focuses on 15 counties and districts along the coast of the Pearl River Estuary (PRE) Great Bay Area and selects 12 evaluation indices from five perspectives for analysis, including coastal characteristics, hydrodynamic forces, economics, population and coastal reconstruction. The analytic hierarchy process (AHP) method, Technique for Order Preference by Similarity to an Ideal Solution (TOPSIS) method, independent weight method, Jenks natural breaks method (Jenks), exposure-sensitivity-adaptation (ESA) model and obstacle degree method are used in conjunction with the above indices to construct a coastal erosion vulnerability evaluation system for the PRE. The results show that coastal erosion vulnerability in the PRE is low in the eastern hilly area and high in the central and western delta areas. Coastal characteristics, coastal lowlands and protection capability are the main controlling elements of erosion. The PRE experienced an era of rapid economic development from 1980 to 2010, and coastal erosion vulnerability gradually increased, with a cost of ecological environment destruction. Then, an era of coastal zone ecological restoration supported by policy protection occurred from 2010 to 2020. Compared with three major bay areas with similar developed economies worldwide, the PRE is characterized by comparatively late but rapid economic development. Notably, the development and utilization efficiency of coastal zones is very high, the duration of damage to the ecological environment is short, and the effects of ecological repair and restoration are obvious. The results of this study provide a reference for economic development and ecological restoration in the bay areas of China and provide scientific guidance for coastal zone development, management and planning.

Keywords: coastal erosion, vulnerability assessment, evolution process, impact of human activities, the Pearl River Estuary Great Bay Area

INTRODUCTION

Coastal erosion is a common phenomenon associated with geological hazards, coastline migration and subbed erosion in intertidal and subtidal zones (Cai et al., 2009). This phenomenon is accelerated by sea level rise issues caused by global warming, frequent storm surges and human activities (Li et al., 2015; Phong et al., 2017; Flor-Blanco et al., 2021). The number of coastal cities worldwide increased from 472 to 2,129 between 1950 and 2015 (Stronkhorst et al., 2018). At the same time, coastal areas are densely populated areas that are home to high-economic-value activities, such as those in the industrial, transportation, and tourism sectors (Rangel-Buitrago et al., 2018). Many cities, people and businesses are being threatened by coastal erosion, and immeasurable losses could occur. Since China's reform and expansion in 1978, the study area has experienced rapid urbanization, rapid population growth, frequent shoreline reconstruction, and frequent reclamation activities, and the low-lying Pearl River Delta has been severely affected by marine disasters. Frequent natural disasters have influenced many residents, and coastal areas with many high-value buildings are threatened by erosion. The erosion of sandy shorelines is prevalent in the study area. The Guangdong Provincial Government has selected some shore sections of Huidong County, Huiyang District, Longgang District, and Nansha District as coastal erosion priorities, among which the gold coast of Huiyang District is seriously eroded. Additionally, historical data indicate that hard artificial revetments, mainly seawalls, have been eroded by storm surges, and outburst events have regularly occurred (Chen et al., 2010). The threat of coastal erosion in the PRE coastal zone system is high, and the current coastal erosion situation is bleak.

Therefore, the vulnerability of coastal zones to coastal erosion disasters needs to be effectively evaluated to quantify the potential amount of loss and the degree of damage. Like most studies in the twentieth century, early evaluations of coastal erosion vulnerability based on factors such as sea level rise, coastal geomorphology, elevation, coastal slope, coastline change, land use, tidal range and wave height (Pendleton et al., 2010; Yin et al., 2012; Jana and Bhattacharya, 2013), focused too much on the effects of natural or climatic conditions on coastal zone systems, leading to exaggerated effects of natural factors. As social factors, such as gross domestic product (GDP), fiscal expenditure, population density, value of coastal buildings, proportion of artificial shoreline, and reclamation area were considered in studies of coastal erosion vulnerability (Cai et al., 2019; Zhu, 2019; Wang X. T. et al., 2021), vulnerability evaluation systems have been improved, and vulnerability hazards can now be comprehensively assessed. However, the number of evaluation factors is not directly related to the accuracy of the evaluation system because the evaluation factors will be highly correlated (McLaughlin and Cooper, 2010). With the optimization of index systems, mathematical methods for coastal vulnerability assessment have evolved from the simple place vulnerability index (PVI), coastal social vulnerability index (SVI) and coastal vulnerability index (CVI) models (Boruff et al., 2005; Duriyapong and Nakhapakorn, 2011) into the analytic hierarchy process (AHP) (Hoque et al., 2018), fuzzy mathematical (Luo et al., 2013) and cloud model methods (Zhu et al., 2018; Cai et al., 2019) for assessing vulnerability. The AHP is a reliable method to deal with multicriteria analysis (Roy et al., 2021), and most coastal erosion vulnerability assessments are based on this method. With the introduction of geographic information system (GIS) technology, the results of coastal erosion vulnerability assessments can be effectively visualized (Li et al., 2015). Jenks is a map classification method in GISs, that can group similar values most appropriately and maximize the differences among various classes. This method has achieved good results in vulnerability zoning of the Chittagong District and Bangladesh coast (Miah et al., 2020). System vulnerability includes three main factors: exposure, sensitivity and adaptation (ESA). Exposure refers to the degree of interference in the system caused by natural and human-made external factors. Sensitivity refers to the inherent vulnerability within a system, and adaptability is the ability of a system to return to its original state under the effects of external disturbances (Swami and Parthasarathy, 2021). The ESA concept has been coupled with coastal vulnerability in studies of coastal areas in South East Queensland, Australia, and the Korean coast (Sano et al., 2015; Kang et al., 2018). However, few scholars have coupled ESA models with coastal erosion vulnerability. The TOPSIS method can comprehensively and objectively reflect the dynamic change trend of the research object (Li and Damen, 2010), which has been verified and applied by many experts from various fields (Yang et al., 2018). The obstacle degree model can obtain the main influencing factors restricting the development of the research object, and is widely used in the study of ecology, environmental carrying capacity and vulnerability (Wu and Hu, 2020; Wang X. Y. et al., 2021; Yang and Shuai, 2021). TOPSIS method and obstacle degree model can well explain the temporal and spatial variation laws and main influencing factors of China's delta urban agglomeration in the fields of sustainable development and air quality (Gao et al., 2019; Liang et al., 2021; Xu et al., 2021); however, few scholars apply them to the evaluation of coastal erosion vulnerability. The Pearl River Delta, where the Pearl River Estuary (PRE) Bay Area is located, has been studied in detail; specifically, the spatiotemporal evolution of urbanization, coastlines, and wetland types has been considered (Li and Damen, 2010; Yang et al., 2020, 2021; Guo et al., 2021), but few studies have examined the temporal and spatial changes in coastal erosion vulnerability and quantitatively evaluated vulnerability.

In this study, 15 coastal counties and districts in the Great Bay Area of the PRE were used as evaluation units, and each decade between 1980 and 2020 was divided into an evaluation period, with a total of 5 periods. According to previous studies and regional characteristics, the impact of natural and socioeconomic conditions on the coastal zone is considered at the same time, and 12 evaluation indices were selected from 5 perspectives: coastal characteristics, hydrodynamic forces, economics, population and coastline reconstruction. The AHP, independent weight, TOPSIS, Jenks, ESA and obstacle degree methods were applied to comprehensively calculate the erosion vulnerability indices and grades for each coastal evaluation unit. Additionally, an obstacle degree model was used to evaluate the temporal and spatial

distributions of the ESA characteristics in the coastal zone of the PRE, and analyses of the main controlling elements and indices affecting the spatial and temporal distributions of coastal erosion vulnerability in the Great Bay Area were performed.

Through weight, vulnerability calculation and factor analysis method, we hope to find out the temporal and spatial variation law and main influencing factors of coastal erosion vulnerability in the Pearl River Estuary Bay area since the reform and opening up. The assessment results can provide a scientific basis and practical experience for coastal zone protection and vulnerability assessment and contribute to government decision-making.

MATERIALS AND METHODS

Study Area

The PRE is located in the southeast coast of Guangdong Province, China (111. 35°∼115.47° E, 21.45°∼24.40°N). It is a bay area composed of 9 cities in Guangdong Province, China, including Guangzhou, Shenzhen, Foshan, Zhuhai, Dongguan, Zhongshan, Jiangmen and Zhaoqing (except Hong Kong and Macao special administrative regions). The evaluation units of this study are 15 coastal counties and districts in the PRE (Both Dongguan City and Zhongshan City have only district along the coast, **Figure 1**).

The study area covers a land region of approximately 17,915 km^2, of which nearly one-third of the area is low, flat and vulnerable to coastal erosion caused by sea level rise. Approximately 63.1% of hard artificial shorelines in the PRE are resistant to natural erosion over long-term periods. The study area is located in the PRE, which is severely affected by marine hazards. Since 1970, 277 tropical cyclones have affected the PRE (Ye et al., 2020), accompanied by strong winds, large waves, and rainstorms, which have considerably increased the vulnerability of the area to coastal erosion (Han et al., 2010). The permanent population of the study area is approximately 33.6 million (according to statistics from China's seventh census), and the population density is as high as 1,874 people/km^2. Thus, this region is one of the most densely populated and urbanized areas in China, and the coastal zone system is under enormous pressure. As of 2020, 87.6% (944 km) of the coastline in the study area was disturbed by human activities, and approximately 597 km^2 of sea area has been reclaimed. Frequent and intense human activities have changed the morphology and length of the coastline, causing irreversible changes to the coastal zone (Manuel et al., 2015). From the initial low-production-value economic structure based on farming and breeding to the current high-value industries with coastal tourism, business districts, ports and docks, the losses caused by coastal erosion were immeasurable.

Establishment of an Index System

The AHP method decomposes complex problems into various constituent factors and then groups these factors according to

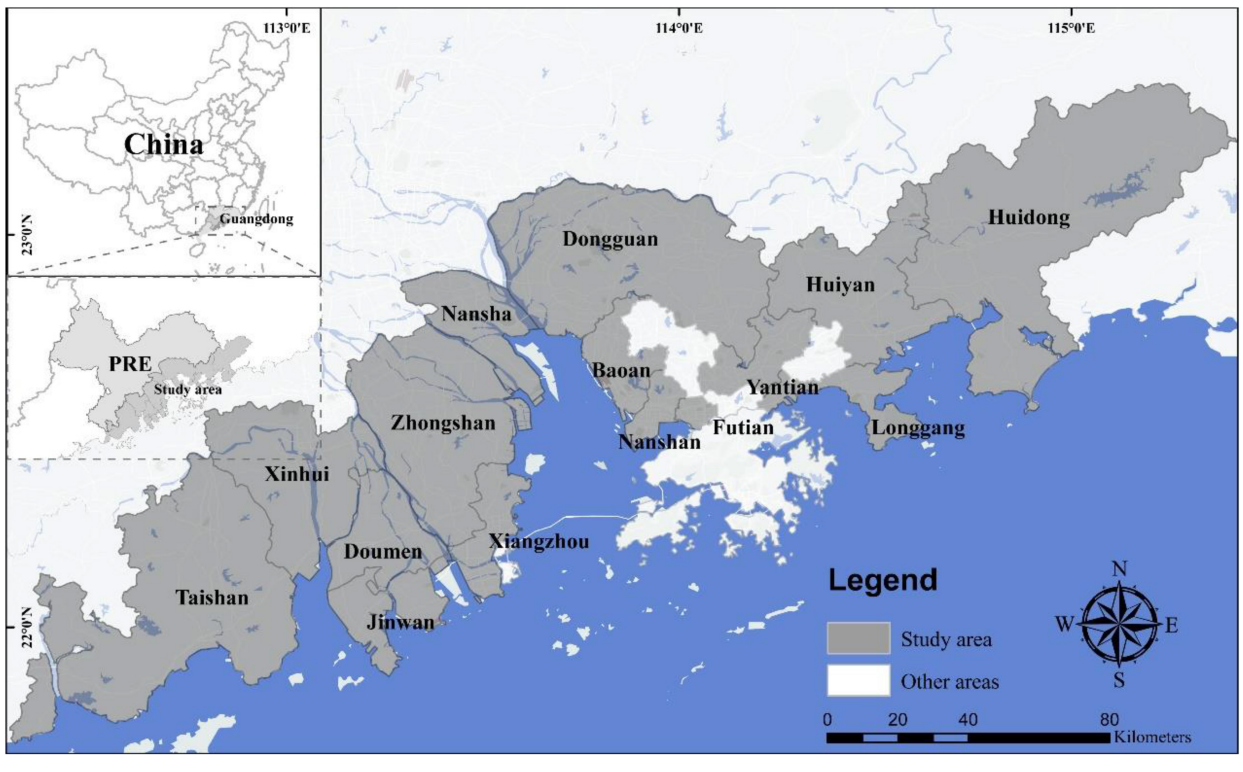

FIGURE 1 | ThePRE is located in the southeast coast of Guangdong Province, China. The study area encompasses 15 counties and districts along the PRE coast (study areas are gray, and other areas are white).

the dominant relationship to form a hierarchical evaluation system. A top-down evaluation hierarchy was constructed using the AHP method, with natural and socioeconomic conditions used to establish the element layer. Five factors, namely, coastal characteristics, hydrodynamic conditions, economic conditions, demographic conditions and shoreline modifications, were used to establish the index layer, and 12 indicators, among which include coastal lowlands, storm surges and GDP, were used to construct the factor layer (**Figure 2**, P1). **Table 1** lists the indices used for coastal erosion vulnerability evaluation in the study area and the corresponding data sources.

Computational Method

The data processing method in this study consists of weight calculation and the TOPSIS method. The weight is composed

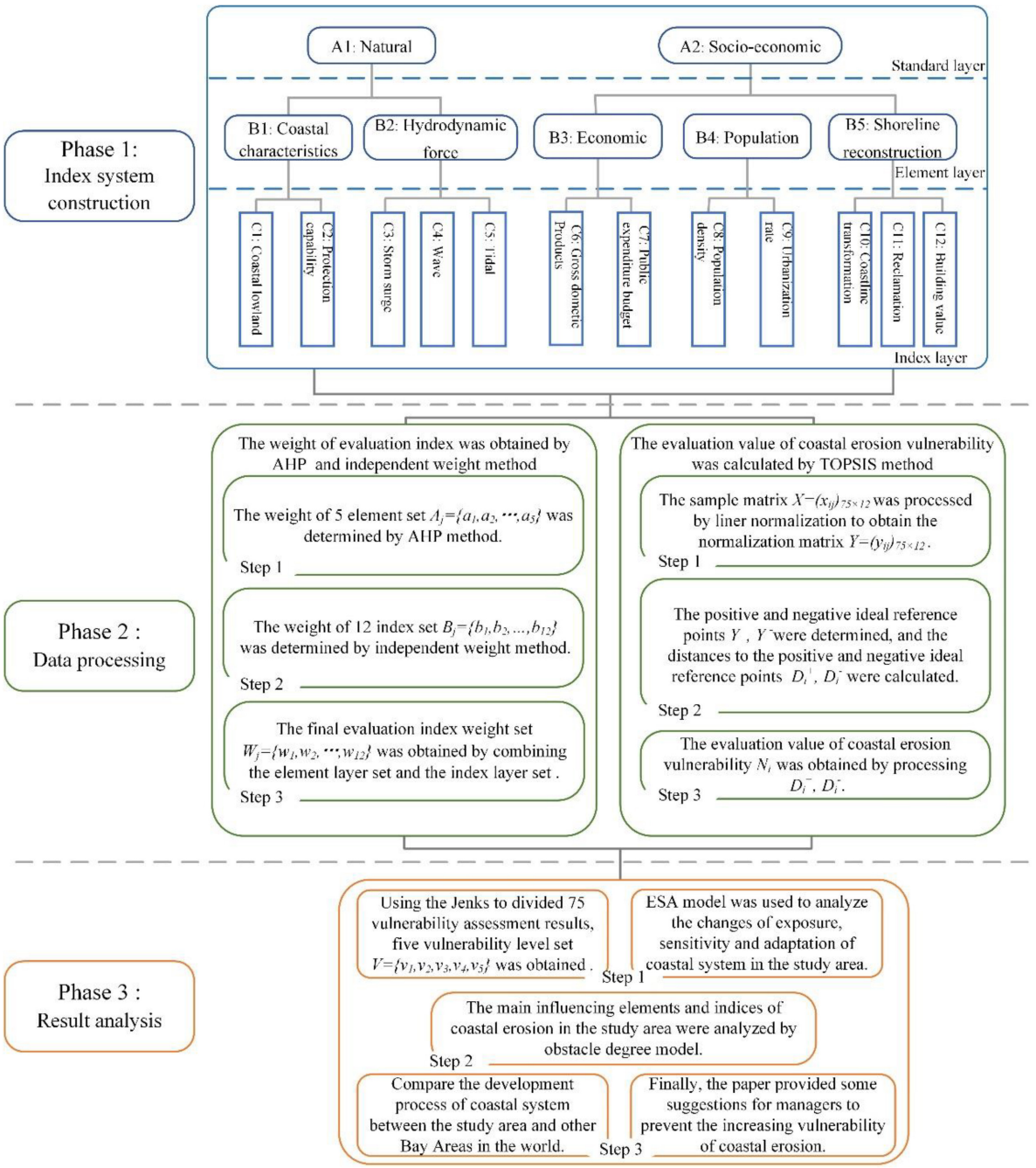

FIGURE 2 | Flow chart of the technical methods used in this study. This study consists of three phases: Index system construction, data processing and analysis of the results. The corresponding tables of numerical symbols and acronyms in this paper are described in **Supplementary Table 1**.

TABLE 1 | Indicators used in the integrated coastal erosion vulnerability assessment.

Indices (attributes)	Implication	Formulation	Reference	Accuracy (indices unit)
C1 Coastal lowlands +	The rise in sea level caused by global warming will seriously affect low-lying islands and low-elevation coastal areas. In this paper (Susmita et al., 2010; Ahmed et al., 2021), the continuous coastal zone with an elevation of less than 10 m is defined as the coastal lowland zone (Mcgranahan et al., 2007).	The proportion of the area with an elevation less than 10 m to the total area	ASTER GDEM; Landsat	30 m (%)
C2 Protection capability +	Sandy, bedrock, and biological coastlines are considered to determine the natural ability of the coastal to mitigate coastal erosion (Williams et al., 2018; Zhu et al., 2018; Armenio et al., 2021).	Percentage of protected coastline	Site investigations; Landsat	30 m (%)
C3 Storm surges +	The storm surge caused by a typhoon will directly affect the coastal zone (Castelle et al., 2015).	$\sum_i^{S_i}$, where S is the typhoon wind speed in the impact evaluation unit and i is number of typhoons	China Typhoon Network (weather.com.cn)	1 m/s (m/s)
C4 Waves +	Wave actions cause erosion at the foot of revetment slopes, and storm surge water levels rise after a typhoon passes (Phan et al., 2013; Armenio et al., 2021).	Annual average effective wave height in an evaluation unit	Copernicus Marine Service (CMEMS) (marine.copernicus.eu)	0.2° (m)
C5 Tides -	Microtidal coastal areas are more likely to experience acute erosion than are macrotidal coastal areas. Additionally, the larger the tidal range is, the larger the amount of deposition is, which is beneficial to tidal flat development in delta areas (Qi et al., 2010; Wang X. T. et al., 2021).	Annual average tidal range in an evaluation unit	Tidal contour maps; tidal level station data (Xiao, 2003; Ma, 2005)	0.01 m (m)
C6 Gross domestic product -	The main disaster reduction factors include government investment in disaster reduction, effective financial resource allocation and personal disaster recovery, which are mainly reflected in the general GDP and public expenditure budget (Zhu, 2019).	Per capita GDP in an evaluation unit	Statistical yearbooks form each era	10,000 yuan (yuan)
C7 Public expenditure budget -		Per capita public budget expenditures in an evaluation unit	Statistical yearbooks from each era	10,000 yuan (yuan)
C8 Population density +	With high population densities and high urbanization rates, coastal zones are highly affected by erosion, which can lead to damage to high-value residential and industrial buildings. Sparsely populated areas suffer from the same coastal erosion processes but require less protection (Jana and Bhattacharya, 2013; Armenio et al., 2021).	$\frac{\text{Total population}}{\text{Unit area}}$	Census data and Statistical yearbooks from each era; Landsat	10,000 persons (per km^2)
C9 Urbanization rate +		Ratio of urban population to total population	Census data and Statistical yearbooks from each era	10,000 persons (%)
C10 Coastline transformation +	Coastline reconstruction and reclamation activities have led to the conversion of many natural coastlines to artificial coastlines. In this process, the sea area is lost, the sediment balance in the original coastal zone system is disrupted, and the threat of coastal erosion may remain (Cai et al., 2019).	Percentage of artificial coastline	Site investigations; Landsat	30 m (%)
C11 Reclamation +		Cumulative reclamation area	Site investigations; Landsat	30 m (km^2)
C12 Building value +	The higher the economic value of buildings along a coastline is, the greater the potential loss due to coastal erosion (Zhu et al., 2018). Type 1, undeveloped area; Type 2, agricultural cultivation; Type 3, urban construction land; Type 4, Industrial transport; Type 5, commercial, real estate and parks	$\frac{\text{Type 1} \times 1 + \text{Type 2} \times 2 + \text{Type 3} \times 3 + \text{Type 4} \times 4 + \text{Type 5} \times 5}{\text{Total coastline length}}$	Site investigations; Landsat	30 m

(+) indicates that the value of the indicator is positively correlated with vulnerability, and (–) is the opposite. Due to the limitations of the data acquisition methods, the C4 and C5 data are consistent in 5 periods, and the remaining data are the most recent data for each period. In the early years, some counties and districts were not established, and missing data were replaced with the lowest or average values. ***Supplementary Table 2*** *shows the specific establishment process of the formulation.*

of the subjective weight AHP method and objective weight independent weight method (**Figure 2**, P2).

Jenks is used to classify the vulnerability evaluation results. The changes in exposure, sensitivity and adaptability in the study area over the past 40 years were analyzed by the ESA model. The obstacle degree model is used to analyze the main vulnerability factors. Then, the results of this study are compared with other regions, and the similarities and differences in coastal zone system development in the study area are obtained. Finally, this study puts forward some

suggestions to provide a reference for management decision-making (**Figure 2**, P3).

Evaluation Index Weight Calculations

The AHP method determines the relative importance of each factor through pairwise comparison between elements, and then obtains the weight value of each element by synthesizing the judgment of decision-makers. The independence weight method is an objective weight method. The idea of this method is to use the collinearity between indicators to determine the weight. The method was used to establish the top-down evaluation hierarchy between the element layer and factor layer in the evaluation system for coastal erosion vulnerability, and the AHP method was used to calculate the weight set $A_j = \{a_1, a_2, \cdots, a_5\}$ for the five factors in the element layer. The 12 evaluation factors were first determined by the independent weight method, and the weight set $B_j = \{b_1, b_2, \cdots, b_{12}\}$ was obtained. Then, the weight set $W_j = \{w_1, w_2, \cdots, w_{12}\}$ was obtained for the 12 evaluation indices by the joint weighting of sets A_j and B_j (**Supplementary Table 3**).

Coastal Erosion Vulnerability Assessment

The TOPSIS method is a comprehensive evaluation method with distance as the evaluation standard. This method combines the size of data to determine the positive and negative ideal solutions and the distance between positive and negative ideal solutions, and finally obtains the proximity value. The set of weights $W_j = \{w_1, w_2, \cdots, w_{12}\}$ was substituted into the weighted TOPSIS method for calculation.

(i) Dimensionless index processing. The sample matrix $X = (x_{ij})_{75\times12}$ (**Supplementary Table 4**), consisting of 75 evaluation units and 12 evaluation indices, was processed by linear normalization to obtain the normalization matrix $Y = (y_{ij})_{75\times12}$ (**Supplementary Table 5**).

Positive indices:

$$y_{ij} = \frac{x_{ij} - \min(x_j)}{\max(x_j) - \min(x_j)} + 0.001 \quad (1)$$

Negative indices:

$$y_{ij} = \frac{\max(x_j) - x_{ij}}{\max(x_j) - \min(x_j)} + 0.001 \quad (2)$$

The purpose of adding 0.001 to formula 1 and 2 is to prevent the divisor from being 0 in subsequent calculations.

(ii) The positive and negative ideal reference points were determined, and the distances to the positive and negative ideal reference points (**Supplementary Tables 6A,B**) were calculated.

$$Y^+ = \left\{Y_1^+, Y_2^+, \ldots, Y_{12}^+\right\} = \left\{max\ y_{ij}\right\} \quad (3)$$

$$Y^- = \left\{Y_1^-, Y_2^-, \ldots, Y_{12}^-\right\} = \left\{min\ y_{ij}\right\} \quad (4)$$

$$D_i^+ = \sqrt{\sum_{j=1}^{12} w_j \left(y_{ij} - Y_j^+\right)^2}\ (i = 1, 2, \ldots, 75) \quad (5)$$

$$D_i^- = \sqrt{\sum_{j=1}^{12} w_j \left(y_{ij} - Y_j^-\right)^2}\ (i = 1, 2, \ldots, 75) \quad (6)$$

(iii) The coastal erosion vulnerability assessment values were obtained.

$$N_i = \frac{D_i^-}{D_i^+ + D_i^-} \qquad N_i \in (0, 1) \quad (7)$$

The greater the assessment value is, the more severe the level of coastal erosion vulnerability is.

Analysis of Computational Results

Vulnerability Levels of Subareas

The Jenks method will set its boundary where the difference in data values is relatively large. The method was used for the 75 evaluation units to classify the calculated coastal erosion vulnerability values $N_i = \{n_1, n_2, \cdots, n_{75}\}^T$ into a set of 5 levels with the smallest standard deviation within groups and the largest standard deviation between groups: low vulnerability, moderately low vulnerability, medium vulnerability, moderately high vulnerability, and high vulnerability $V = \{v_1, v_2, \cdots, v_5\}$, and the results are presented in the map.

ESA Analysis of Coastal Zone

The ESA model consists of three elements: exposure, sensitivity and adaptation. Exposure represents the extent to which a coastal zone system is disturbed by external conditions, sensitivity represents the degree of inherent vulnerability in a coastal zone system, and adaptation represents the ability of a coastal zone to resist coastal erosion. Storm surges, waves, coastline transformation and reclamation were used as exposure evaluation indicators. Additionally, coastal lowlands, population density, urbanization rate and building value were used as sensitivity evaluation indicators. Finally, tides, GDP and the public expenditure budget were used as adaptation evaluation indicators. The 12 evaluation indices were regrouped according to the ESA model, and the above calculation steps (Section "Coastal Erosion Vulnerability Assessment" steps i–iii) were repeated. Then, the weighted TOPSIS method was applied to obtain the exposure, sensitivity and adaptation values for the 75 evaluation units in the studied coastal zone system. Exposure and sensitivity evaluation values are positively correlated with coastal erosion vulnerability, with large values reflecting large contributions to coastal erosion vulnerability. The opposite trend was observed for the adaptation indicators.

Analysis of the Main Factors

The obstacle degree model obtains the obstacle degree of each factor vulnerability of the evaluation unit by analyzing the weight of the evaluation index and its specific value. To explain the spatial variation in the vulnerability to coastal erosion in the study area, the normalization matrix and the weight matrix were processed using the obstacle degree model to obtain the contributions (**Supplementary Tables 7A,B**) of the factors that influence coastal erosion vulnerability in each of the evaluation units in the PRE. The formula is given as follows:

$$O = (o_{ij})_{75\times12} = \frac{y_{ij} \times w_j}{\sum_{j=1}^{12} y_{ij} \times w_j} \quad (8)$$

$$TO = \sum O \quad (9)$$

where *TO* represents the obstacle degree of the element layer, with a value equal to the sum of the evaluation indices for the prior factor layer; the larger the value of the obstacle degree of an evaluation index is, the larger the contribution of this index is to coastal erosion vulnerability.

The Suitability of the Method

This study used the weighted TOPSIS method to calculate values of coastal erosion vulnerability, and presented them on a map, which intuitively reflects the spatial and temporal changes in vulnerability in each county in the PRE region. The results are consistent with the physical process of coastal erosion. Because the span of the data used in this study is as long as 40 years, the quantitative differences among indicators are large in some cases, and the regional and temporal differences are eliminated by using data normalization to obtain comparable evaluation results. The accuracy of the sample data is appropriate, which can effectively distinguish the differences between counties and districts, and the vulnerability calculation results will not lose the sample data information. The independent weight method can eliminate the weight of high correlation factors and prevent the influence of high correlation between factors on the correctness of the evaluation system, which is not the case for other objective weight assignment methods. The Jenks method was used to classify the evaluation results, and the data were divided into five groups of results with the smallest standard deviation within groups and the largest standard deviation between groups. Overall, the vulnerability levels of 75 evaluation units were effectively classified. The ESA model and the obstacle degree model were used to calculate the main factors that influence ESA changes in each county and district for each period in relation to coastal erosion vulnerability, and the results provide effective guidance for shoreline protection in the study area.

RESULTS

Temporal and Spatial Distribution Characteristics

The coastal erosion vulnerability in the 75 evaluation units in the study area was comprehensively evaluated using the improved TOPSIS method and the obstacle degree model, and the evaluation results (N_i values) for the vulnerability of districts and counties in each period were averaged to obtain the overall vulnerability $\bar{N}_i$ of the study area in each period (**Table 2**).

The overall coastal erosion vulnerability value in the study area ranged from 0.478 to 0.526 during the four decades from 1980 to 2020, reaching a maximum value of 0.558 in 2010 and falling back to 0.526 in 2020; overall, coastal erosion vulnerability increased in the first three decades and has gradually decreased in the past decade. The vulnerability of coastal erosion in Futian District started to decline in 2000, and this region displayed the earliest decline in the PRE area (**Table 2**).

The spatial and temporal variations in coastal erosion vulnerability zones, numbers of evaluation units and the vulnerability of each zone in the study area are shown in **Figure 3**. The coastal erosion vulnerability levels in the Futian, Yantian, Longgang, Huiyang, and Huidong Districts, which are located in the eastern part of the study area, are comparatively low, and these districts form an overall low-vulnerability area. Most of the moderately high- and high-vulnerability areas are concentrated in the central and western parts of the PRE, such as the Nansha, Zhongshan, Doumen, Jinwan, Xiangzhou, and Xinhui Districts. During the three decades from 1980 to 2010, the PRE area exhibited a trend of increased vulnerability to coastal erosion, and the overall vulnerability of the PRE area has considerably recovered since 2010, with notably decreasing vulnerability levels in the Nansha District, Dongguan District, Nanshan District, Futian District, and other regions.

TABLE 2 | Evaluation results for coastal erosion vulnerability in each county, district and study area in each period.

Periodcounty and district	1980	1990	2000	2010	2020
Taishan	0.457	0.474	0.494	0.517	0.529
Xinhui	0.494	0.549	0.585	0.594	0.601
Doumen	0.592	0.577	0.596	0.602	0.621
Jinwan	0.531	0.550	0.641	0.646	0.644
Xiangzhou	0.478	0.542	0.603	0.610	0.590
Zhongshan	0.599	0.566	0.601	0.626	0.632
Nansha	0.571	0.553	0.577	0.589	0.520
Dongguan	0.459	0.469	0.526	0.551	0.518
Baoan	0.520	0.504	0.582	0.603	0.552
Nanshan	0.455	0.515	0.562	0.563	0.476
Futian	0.434	0.472	0.516	0.504	0.418
Yantian	0.364	0.407	0.501	0.508	0.429
Longgang	0.418	0.384	0.468	0.491	0.439
Huiyang	0.371	0.362	0.479	0.518	0.492
Huidong	0.429	0.412	0.442	0.455	0.426
$\bar{N}_i$	0.478	0.489	0.545	0.558	0.526

The first 15 rows in the numerical part of the table represent the N_i values of 15 counties, while $\bar{N}_i$, the overall value of the study area, is obtained by averaging the N_i values of 15 counties.

Analysis of Exposure, Sensitivity, and Adaptability

The ESA evaluation results for 75 evaluation units in the study area (**Supplementary Tables 8A–C**) are plotted in **Figures 4**, **5**. Since 1980 and 1990, the sensitivity and exposure of the coastal zone in the study area have increased period by period, and the adaptation level decreased from 1990 to 2010. The level of coastal erosion vulnerability has also increased period by period since 1980. From 2000 to 2020, exposure and sensitivity slowly increased, and adaptation has increased rapidly since 2000, resulting in a reduction in the rate of increase in vulnerability in the study area since 2000. Exposure also decreased in 2020, and adaptation levels significantly improved in the coastal zone, eventually resulting in a decrease in the coastal erosion vulnerability value to 0.526 at the end of 2020, which represented a return to the pre-2000 level (**Table 2** and **Figure 5**).

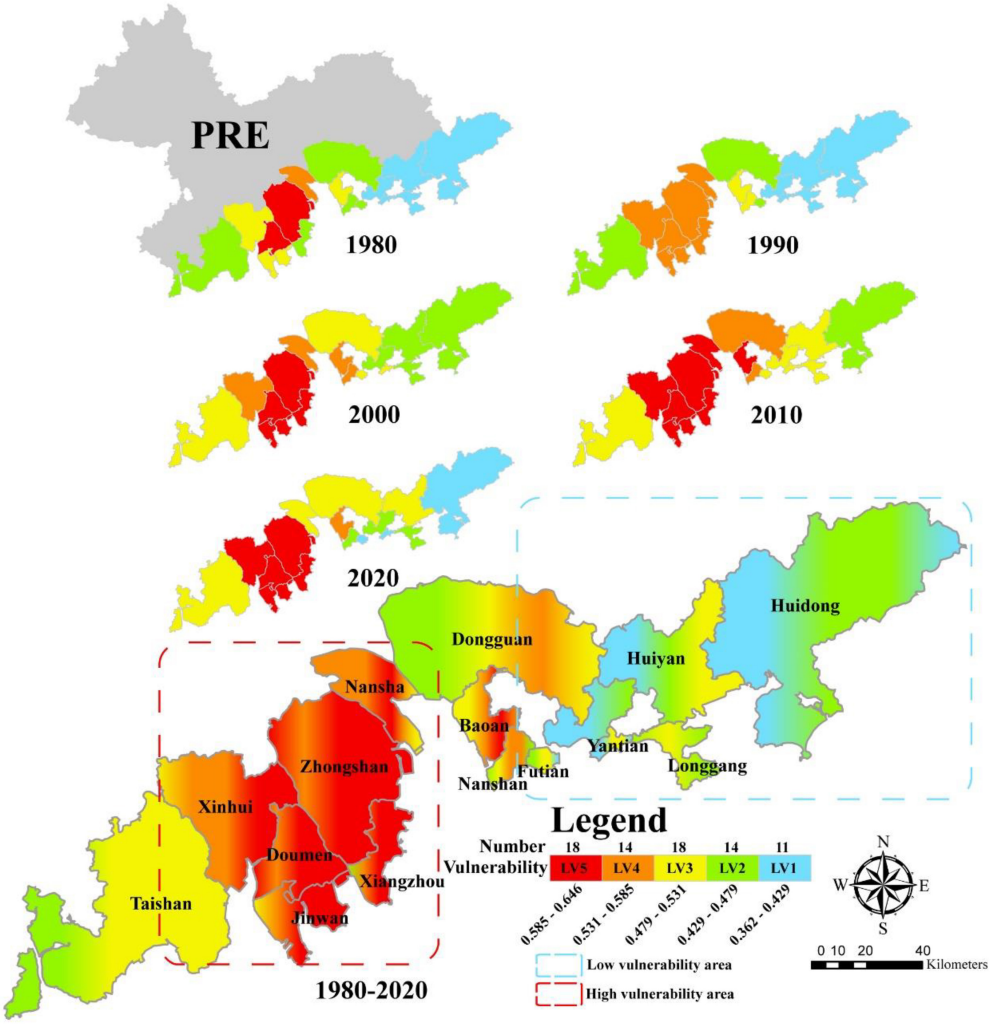

FIGURE 3 | The classification map of coastal erosion vulnerability in each era and the distributions of low-vulnerability and high-vulnerability areas in 15 counties and regions of the study area. Different colors in the color chart represent different vulnerability levels. From left to right, the colors represent high vulnerability (a total of 18 evaluation units in this interval), moderately high vulnerability (14), medium vulnerability (18), moderately low vulnerability (14) and low vulnerability (11). Finally, the evaluation unit is filled with gradient color to reflect the change of their vulnerability level from 1980 to 2020.

The Main Factors

Coastal characteristics, coastal lowlands and protection capability are the main elements and indices influencing coastal erosion vulnerability in the study area. At the same time, the impact of these factors on the high vulnerability area is significantly higher than that on the low vulnerability area. The impact of economic coastal erosion vulnerability in Xiangzhou, Jinwan, Nanshan and other areas near the middle of the study area is lower than that in the areas to the east and west of the study area. Finally, hydrodynamic conditions have a weaker impact on vulnerability to coastal erosion in the central part of the study area than in the areas to the east and west (**Figures 6A,B**).

In 1980, the main factor that increased vulnerability in the study area was the weak economic conditions in China, followed by coastal characteristics and hydrodynamic conditions. From 1980 to 2010, economic conditions contributed increasingly less to the vulnerability of the study area; in contrast, the effects of population conditions and shoreline reconstruction increased. Therefore, the overall vulnerability of the PRE increased, and a 30-year erosion stage began (**Figure 7A**). The Futian District shows a different development process from the entire study area. Since 1980, the impact of element coastal characteristics in Futian on coastal erosion vulnerability has evidently decreased, while the population conditions are the opposite (**Figure 7B**).

DISCUSSION

Coastal zone related vulnerability is affected by both natural and economic conditions, in which natural conditions affect the spatial differences in vulnerability, while social conditions

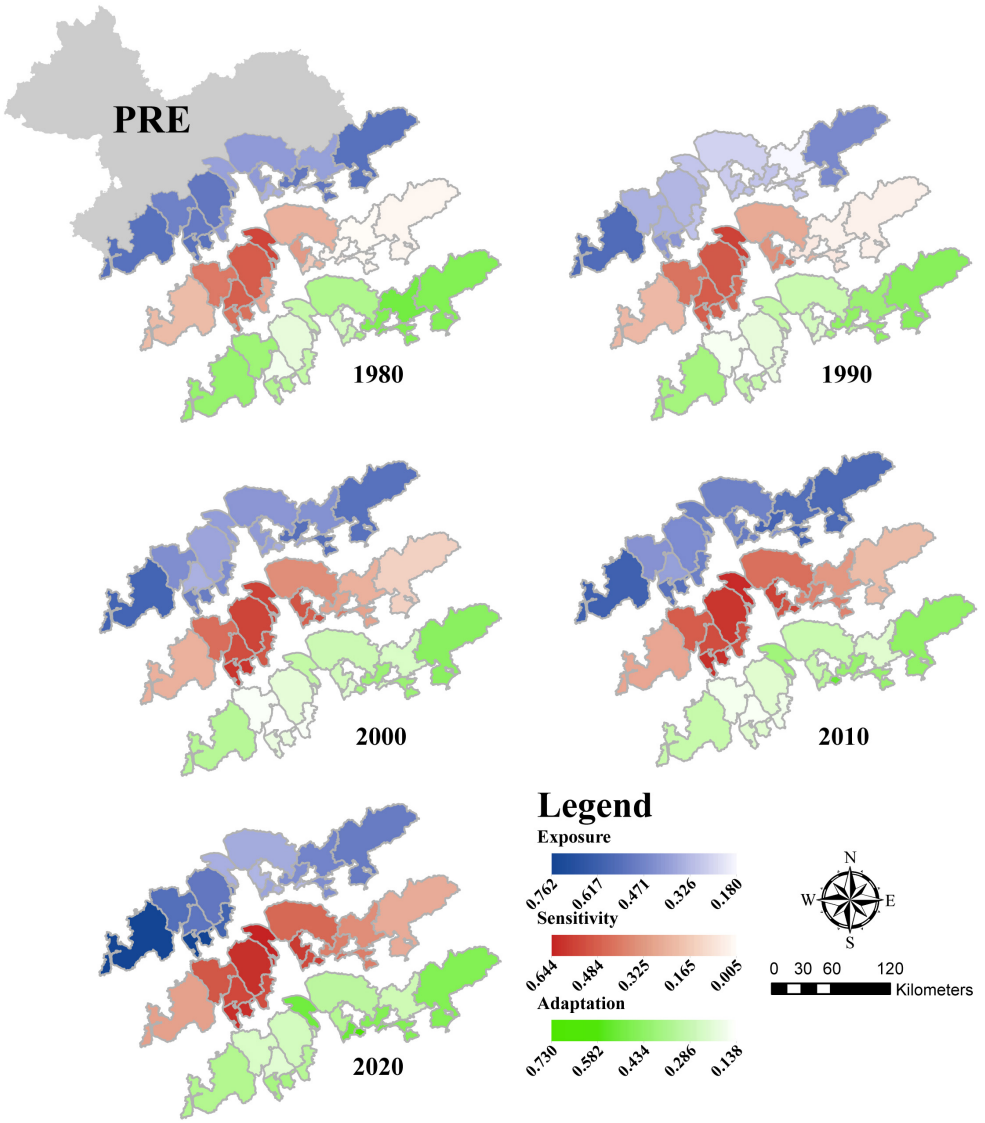

FIGURE 4 | Differences in exposure, sensitivity and adaptation in the coastal zone systems in 15 counties and districts in the study area. The depth and gradient of the three colors in the plots show the differences in ESA values in each county and district.

affect the temporal changes in vulnerability (Boruff et al., 2005; Mani Murali et al., 2013; Bukvic et al., 2020; Wu and Hu, 2020; Yang et al., 2020; Feng et al., 2021). Under natural conditions, slope, regional altitude and shoreline geomorphic type are the main influencing factors. Economic development, urbanization, population growth and policy implementation are the main driving factors affecting vulnerability in social conditions. This finding is consistent with the obstacle analysis results of this study.

Variation in Coastal Erosion Vulnerability

Spatial Variation

The high vulnerability and low vulnerability areas exhibit obvious spatial differences (**Figure 8**). The elevation in the eastern region is generally higher than 10 m, and this region has a large proportion of highly protected coastal sections. Conversely, the central and western regions include more low-elevation and non-protected sections. Since the incoming sand from the Pearl River Basin accumulates in the estuary and bays, leading to the development of complex deltas, the high-vulnerability areas are located within the low-elevation estuarine deltas, which are most affected by sea level rise and storm surges. Most of the coastline has changed from natural shoreline areas with high protective capacities to artificial shorelines dominated by farming (Zhou et al., 2019), with frequent reclamation activities and high-economic-value coastal buildings. As a result, this area is characterized by high exposure, high sensitivity and poor adaptability, and the vulnerability to regional coastal erosion is relatively high (**Figure 5**). However, the main

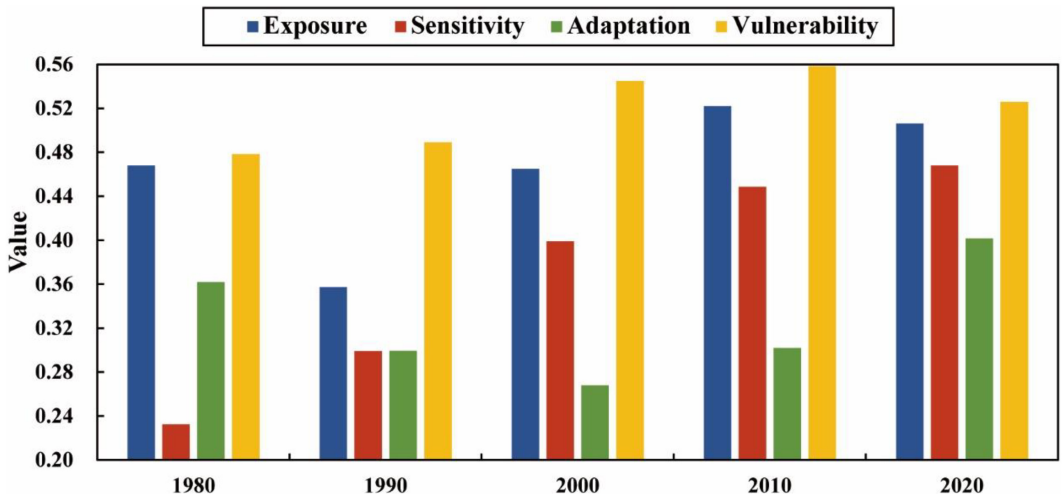

FIGURE 5 | Bar chart showing the changes in exposure, sensitivity, adaptation and erosion vulnerability in the overall coastal zone system in the study area over time.

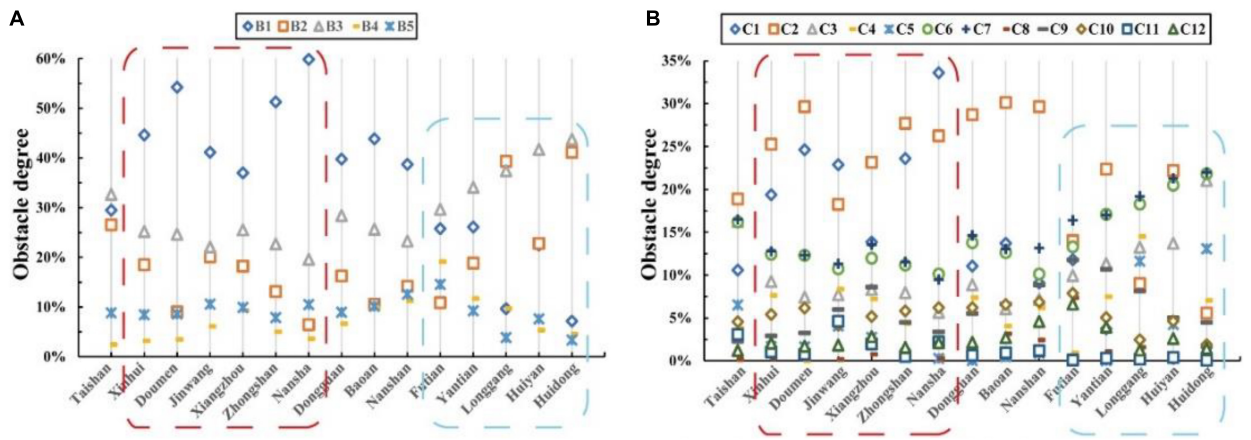

FIGURE 6 | Obstacle degree model analysis of the main elements **(A)** and indices **(B)** that influence coastal erosion in 15 counties and districts and the distribution of coastal characteristic differences in the study area (average of 5 periods). The scope of the high vulnerability area and low vulnerability area is the same as that in **Figure 3**. The specific meaning of the characters in the figure and the corresponding relationship between factors are shown in phase 1 of **Figure 2**.

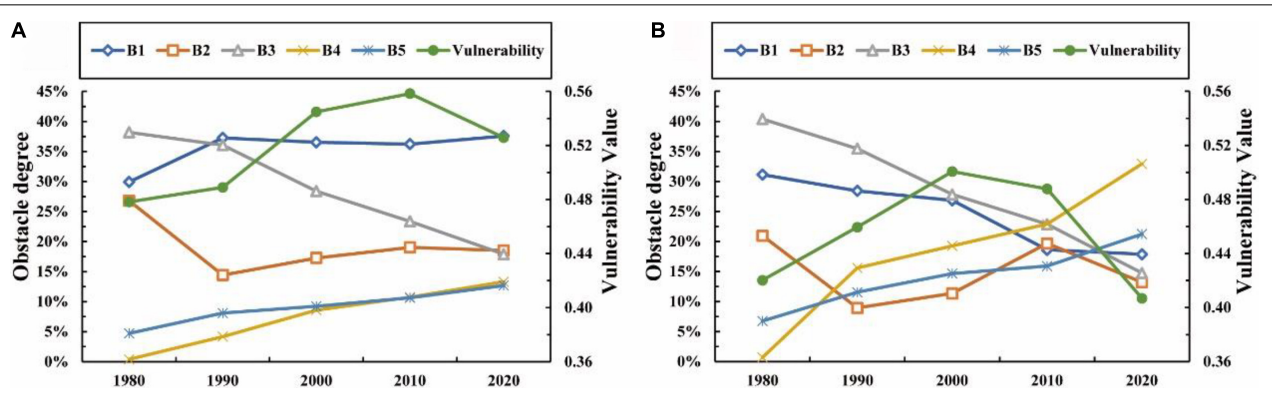

FIGURE 7 | Temporal variations in the main influential elements and vulnerability to coastal erosion in the entire study area **(A)** and Futian District **(B)**. The specific meaning of the characters in the figure and the corresponding relationship between factors are shown in phase 1 of **Figure 2**.

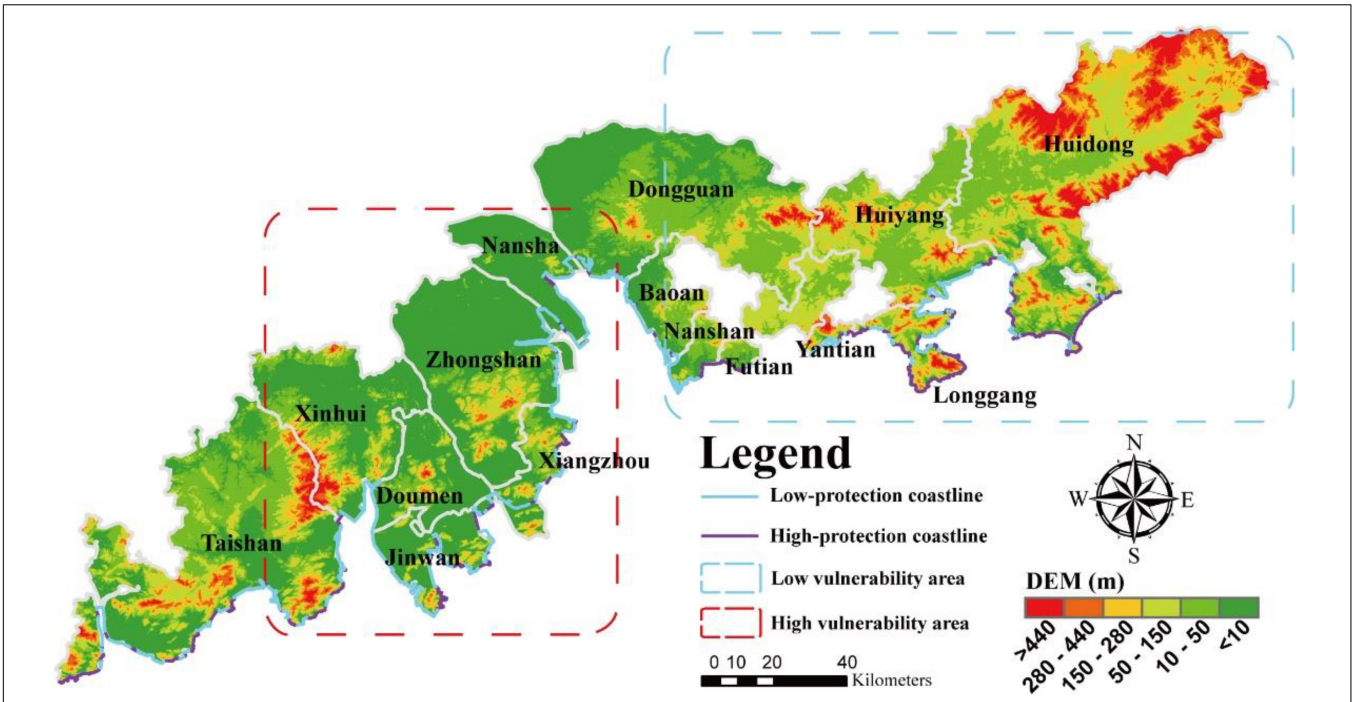

FIGURE 8 | Distribution map of coastal characteristics differences in the study area. Coastal characteristics include coastal lowlands and protection capability, which are reflected in DEM and protection coastline in the figure.

low-vulnerability area is located in a hilly region with high elevations, a predominantly bedrock and sandy shoreline and few artificial revetments. Additionally, the population density in high-elevation areas is low, with sufficient resilience to the threats of climate change and sea level rise. Therefore, the coastal zone system in this region exhibits distinct spatial characteristics in terms of ESA and low vulnerability to coastal erosion.

The cities of Shenzhen and Zhuhai in the central part of the study area play key roles in the Chinese economic system and areas where foreign capital and management strategies have been introduced. Thanks to the favorable policies of reform and expansion and geographical location advantages, Shenzhen and Zhuhai, which are adjacent to Hong Kong and Macau, have healthy industrial structures and rapidly benefit from economic growth. Compared with the economic conditions in the counties on the east and west sides of the study area, the sufficient per capita GDP and public budget expenditures in the central area aid in resisting coastal erosion and restoring the ecological functions of the coastal zone.

The study area is located on the southern coast of China and is frequently affected by tropical cyclones in the Northwest Pacific, which have a long duration and strong impact on the coastal zone. The frequency and intensity of typhoons that make landfall in the PRE area in the central part of the PRE are less than those that make landfall on the east and west sides of this area (Ye et al., 2020); additionally, the wave intensity in the central region is also lower than that in the areas to the east and west regions, which are more open to the sea, and the tidal range in the central area is greater than that in the east and west (Xiao, 2003; Ma, 2005). Therefore, the downstream area of the PRE in the central part of the PRE is less disturbed by both external storm surges and waves, and with a larger tidal range, the adaptability to resist storm surges is strong; consequently, this area is more resilient to storm surges and less vulnerable to hydrodynamic influences on coastal erosion than are other areas.

Variation Over Time

The variation process of coastal erosion vulnerability in the PRE is divided into three stages. Before 1980, the first stage was a period of low coastal erosion vulnerability; then, the second stage was a period of increased vulnerability from 1980 to 2010. The third stage, starting in 2010, was a period of declining vulnerability and restoration of coastal ecosystems (**Figure 9**).

Before the reform and expansion in 1978, the coastline of the study area was mainly used for farming and aquaculture and was relatively underdeveloped compared with coastlines in other regions around the world (Yang et al., 2021). From 1970 to 1980, many typhoons affected the PRE, and the coastal system was greatly disturbed by hydrodynamic variations. At this time, the retention rate of natural shorelines was high due to the absence of large-scale reclamation activities, and the population and urbanization indices were relatively low; thus, the inherent vulnerability of the coastal zone in the PRE was low.

Since 1978, the economy of the study area has rapidly developed, and the total GDP in the nine cities in the PRE is currently approaching ¥ 9 trillion, accounting for approximately 8.8% of China's total GDP in 2020. The adaptability of the coastal system in the PRE has greatly improved, and the impact of economic conditions on erosion vulnerability has begun to

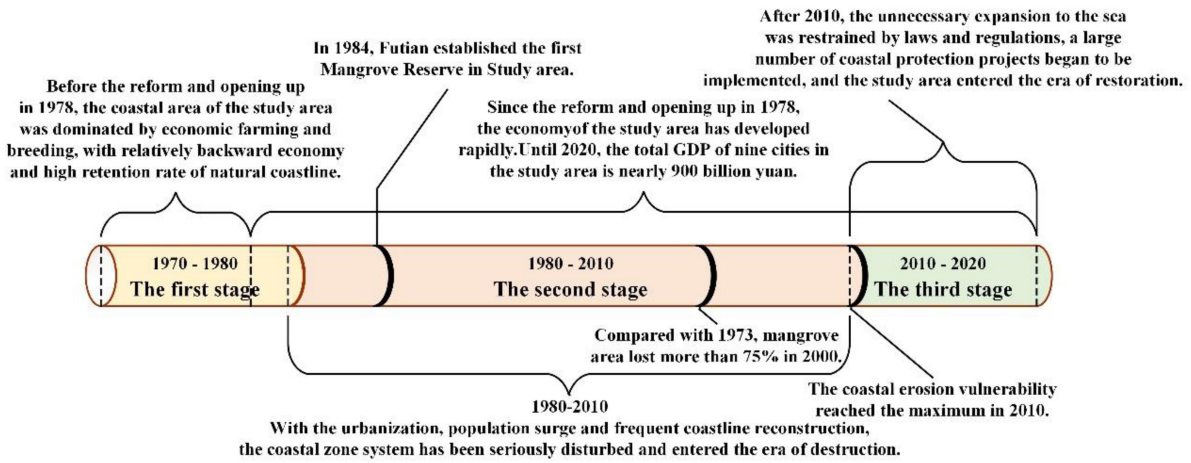

FIGURE 9 | Timeline showing the development process in the study area, which can be divided into three stages. The first stage is the low coastal erosion vulnerability period from 1970 to 1980, the second stage is the period of coastal system damage with vulnerability growth from 1980 to 2010, and the third stage is the period of coastal ecological system recovery with vulnerability decline from 2010 to 2020.

decline. With the expansion of urbanization and reclamation (from 1990 to 2000, the land reclamation area in the PRE reached approximately 233 km^2), the increased population and the increased artificial coastline length in the PRE, infrastructure components, such as airports and docks, have been constructed in traditional farming and breeding areas. Moreover, the value of coastal buildings has increased; therefore, population and coastline reconstruction have increasingly contributed to coastal vulnerability (Zhao et al., 2018; Yang et al., 2020; Guo et al., 2021). The impact of coastal hydrodynamic conditions has increased due to the increasing intensity of typhoons, although the frequency of storm events has generally decreased since 1980 (Ye et al., 2020). The overlapping effects of human activities and environmental conditions have led to a gradual increase in the exposure and sensitivity of coastal systems (**Figure 4**). From 1973 to 2000, the mangrove area in the PRE decreased by more than 75% (Jia et al., 2018), and the resilience of the coastal system significantly decreased (**Figure 4**). With rapid economic development, problems such as decreasing species diversity in coastal systems, increasing coastal erosion, population growth, the disappearance of sea areas and natural coastlines, and declines in coastal protection capabilities have become increasingly serious. Consequently (Wang et al., 2007; Li and Damen, 2010), the vulnerability of coastal erosion continues to increase in the PRE.

Mangrove nature reserves have been established in the Futian District, Dapeng Bay, and Qi'ao Island in Zhuhai since 1984 (Peng et al., 2016). Previous policies established the foundation for large-scale restoration in the PRE, although most measures were implemented after 2010. From 2000 to 2015, 34% of mangrove forests were gradually restored (Jia et al., 2018), and ecological restoration initially achieved positive results. After 2010, local governments realized the risks of massive coastline development and utilization to coastal erosion and successively established restrictive plans such as the "General Plan for the Comprehensive Coastal Protection and Utilization of Guangdong Province," which imposed restrictions on the unnecessary utilization of sea areas and promoted beach restoration and wetland protection activities.

From 2010 to 2018, nearly 70 coastline renovation and restoration projects were established, and investments totaling more than 3 billion yuan occurred. These projects involved wetland ecological restoration, beach erosion protection, sand replenishment, and coral and mangrove restoration. Several major coastal restoration projects have occurred in the PRE, such as the Xianglu Bay Beach Restoration Project in Xiangzhou District, Nansha Shenzhen Bay Mangrove Park and Futian District Mangrove Ecological Park (Zhang et al., 2021).

Coastal Zone Process Over Time

The gulf area is an important base for marine economic activities and tourism. The urbanization and economic development processes in gulf areas can be divided into three periods: Slow economic development, rapid urban economic development, coastal system conflict resolution, policy intervention, and coastal recovery. Other large bay areas worldwide have experienced similar evolutionary processes.

Although these areas have experienced rapid urban and economic development, losses of natural wetlands have occurred, and vulnerability to coastal erosion has increased: more than 90% of the local wetlands have been lost in the approximately 120 years of development in the San Francisco Bay (McPhearson et al., 2013); in approximately 150 years, more than 90% of the natural Bank of Tokyo Bay has been lost, the sea area has been reduced and the shoal has been lost (Furukawa, 2013); finally, over the 160 years of development, 85% of tidal wetlands and 90% of freshwater wetlands in the New York Bay area have been destroyed (McPhearson et al., 2013).

To restore valuable natural resources and slow the irreversible consequences of excessive coastal zone development, local governments have formulated policies to effectively restrain

the further deterioration of the coastal ecosystem. Coupled with effective ecological restoration measures, the harmonious coupling of natural processes and anthropogenic activities could once again occur. Over a 25 years period since 1972, 10 major wetland restoration projects have been implemented and achieved varied results (Williams and Faber, 2001). The "Tokyo Bay Restoration Plan" launched in 2003 has achieved good results (Furukawa and Okada, 2006); After 1974, the abuse and occupation of wetland resources in New York have been fundamentally curbed (Weinberg, 2010).

As a young bay area, the PRE has recently promoted wetland protection and coastal restoration concepts. Due to the high efficiency of policy implementation, the time for the PRE to develop its economy at the expense of the environment is greatly shortened. The PRE entered a period of ecological restoration faster than other bay areas.

Management Recommendations

According to the analytical results, this paper proposes some suggestions to provide information for management decision-making.

First, exposure of the coastal zone system should be reduced, its adaptability should be improved, and the implementation of policies related to coastal zone protection, restoration and reclamation should continue to be promoted. As mentioned above, the study area is located in an economically developed littoral area. The urbanization process and population density are expected to continually increase in the foreseeable future, and the increase in the sensitivity of the coastal system will be irreversible for a long period in the future. The impact of coastal policies on vulnerability has been most obvious in the Futian District (**Figure 7B**). After establishment of the reserve in 1984, the proportion of high-protection coastlines in the Futian District increased, and the impact of coastal characteristics on vulnerability gradually decreased; consequently, the Futian District was the first region to enter the ecological restoration period in the study area, and the advanced coastal zone protection concept achieved good results. The implementation of relevant policies and restoration projects (construction of wetland parks and beach restoration projects) has gradually naturalized the coastline and transformed artificial revetments into near-natural shores, thus avoiding direct damage to the coastal zone caused by human activities but also improving the anti-disturbance and protection capabilities of the coastal ecosystem, reducing the exposure of the coastal system and enhancing adaptability. Relevant policies and restoration projects have prevented further deterioration of coastal vulnerability in the PRE, and this stage represents the beginning of the ecological restoration period in the PRE.

The increased coastal erosion vulnerability caused by natural conditions is difficult for us to control; thus, we need to formulate disaster prevention and mitigation measures to deal with extreme weather and sea-level rise. According to the IPCC report, due to global warming, sea level will continue to rise, and the frequency and intensity of extreme weather will intensify, which will seriously threaten low-lying islands and coastal areas, increasing the threat of coastal erosion due to deterioration of the natural environment over a long time (Han et al., 2010). The study area is a low-lying delta area. Storm surge disasters are very serious. The combination of strong typhoons and spring tides causes a surge in tide level, accompanied by the overflow of sea water caused by strong winds, large waves and rainstorms, which destroys dikes and seriously aggravates the vulnerability of coastal erosion in the PRE Bay area. At the same time, the poor development of the coastline over a long-term period has led to the loss of the coastline's ability to resist natural disasters, which urgently needs to be addressed.

CONCLUSION

The PRE is characterized by low coastal erosion vulnerability in the eastern hilly area and high vulnerability in the central and western deltas. Coastal characteristics, coastal lowlands and protection capability are the main elements and indices related to erosion vulnerability.

The development process of the PRE can be divided into three stages. Before 1980, economic development was slow, and vulnerability to coastal erosion was low. From 1980 to 2010, with the rapid development of the regional economy, the intensity of coastal zone development and coastline utilization increased; consequently, coastal erosion vulnerability increased. With the establishment of ecological restoration policies after 2010, the development and utilization processes in the coastal zone gradually shifted toward ecological repair and restoration, and the vulnerability to coastal erosion gradually decreased. Economic development and GDP inputs are important controlling factors related to coastal erosion vulnerability in each period.

Many bay areas worldwide have experienced rapid economic development at the expense of the ecological environment. With simultaneous development of the economy and utilization of natural resources, restoration to near-natural conditions has been needed in many bay areas; this case was also true in the PRE area. Due to the effectiveness of China's economic policies, although the economy in the study area is still rapidly developing, the local environment is rapidly recovering. The ecological restoration methods used to achieve close-to-natural conditions are effective, and ecological repair and restoration measures have been successful. These cases provide scientific experience for the synergistic development of the economy and the environment in other regions of China.

The PRE is densely populated, and the sensitivity of the coastal zone system will be irreversible for a long time in the future. Therefore, managers should consider how to reduce the coastal erosion vulnerability in the study area from the aspects of exposure and adaptability of coastal zone systems to provide a scientific basis and decision-making for coastal zone protection. At the same time, due to the increased vulnerability of coastal erosion caused by natural conditions, it is difficult for us to control. It is necessary to formulate disaster prevention and mitigation measures to deal with extreme weather and sea-level rise to contribute to the sustainable development of coastal systems.

DATA AVAILABILITY STATEMENT

The datasets presented in this study can be found in online repositories. The names of the repository/repositories and accession number(s) can be found in the article/ **Supplementary Material**.

AUTHOR CONTRIBUTIONS

CC and KZ designed the study, wrote the main manuscript, and prepared all figures. FC and HQ contributed to the improvement of the manuscript. JL, SZ, and GLe contributed to the investigate. KZ, ZM, GLi, and YS contributed to the figure and software. All authors reviewed the manuscript.

FUNDING

This research was funded by the National Natural Science Foundation of China (Grant Nos. 42076058, 41930538, and 42076211), the Scientific Research Foundation of Third Institute of Oceanography, MNR (Grant No. 2019006), the Special Funds for Scientific Research on Marine Public Causes (Grant Nos. 201505012, 201405037, and 200905008), and Comprehensive survey and evaluation of China's offshore Marine resources (Grant No. 908-02-03-04).

ACKNOWLEDGMENTS

We would like to express their sincere thanks to Xiangjin Pan, Xiaojing Zhu and Yazhuang Zhao who have offered support.

SUPPLEMENTARY MATERIAL

The Supplementary Material for this article can be found online at: https://www.frontiersin.org/articles/10.3389/fmars.2022.847655/full#supplementary-material

REFERENCES

Ahmed, N., Howlader, N., Hoque, M. A. A., and Pradhan, B. (2021). Coastal erosion vulnerability assessment along the eastern coast of Bangladesh using geospatial techniques. *Ocean Coast. Manag.* 199:105408. doi: 10.1016/j.ocecoaman.2020.105408

Armenio, E., Mossa, M., and Petrillo, A. F. (2021). Coastal vulnerability analysis to support strategies for tackling COVID-19 infection. *Ocean Coast. Manag.* 211:105731. doi: 10.1016/j.ocecoaman.2021.105731

Boruff, B. J., Emrich, C., and Cutter, S. L. (2005). Erosion hazard vulnerability of US coastal counties. *J. Coast. Res.* 21, 932–942. doi: 10.2112/04-0172.1

Bukvic, A., Rohat, G., Apotsos, A., and Sherbinin, A. D. (2020). A Systematic Review of Coastal Vulnerability Mapping. *Sustde* 12:2822. doi: 10.3390/su12072822

Cai, F., Su, X. Z., Cao, C., Lei, G., Liu, J. H., Yu, F., et al. (2019). *Coastal Erosion Vulnerability Assessment and Demonstration in China*. Beijing: China Ocean Press.

Cai, F., Su, X. Z., Liu, J. H., Li, B., and Lei, G. (2009). Coastal erosion in China under the condition of global climate change and measures for its prevention. *Prog. Nat. Sci.* 19, 415–426. doi: 10.1016/j.pnsc.2008.05.034

Castelle, B., Marieu, V., Bujan, S., Splinter, K. D., Robinet, A., Senechal, N., et al. (2015). Impact of the winter 2013–2014 series of severe Western Europe storms on a double-barred sandy coast: beach and dune erosion and megacusp embayments. *Geomorphology* 238, 135–148. doi: 10.1016/j.geomorph.2015.03.006

Chen, J. Y., Xia, D. X., Yu, Z. Y., and Cai, F. (2010). *Overview Of Coastal Erosion In China*. Beijing: China Ocean Press.

Duriyapong, F., and Nakhapakorn, K. (2011). Coastal vulnerability assessment: a case study of Samut Sakhon coastal zone. *Songklanakarin J. Sci. Technol.* 33, 469–476.

Feng, R. D., Wang, F. Y., and Wang, K. Y. (2021). Spatial-temporal patterns and influencing factors of ecological land degradation-restoration in Guangdong-Hong Kong-Macao Greater Bay Area. *Sci. Total Environ.* 794:148671. doi: 10.1016/j.scitotenv.2021.148671

Flor-Blanco, G., Alcántara-Carrió, J., Jackson, D., Flor, G., and Flores-Soriano, C. (2021). Coastal erosion in NW Spain: recent patterns under extreme storm wave events. *Geomorphology* 387:107767. doi: 10.1016/j.geomorph.2021.107767

Furukawa, K. (2013). Case studies for urban wetlands restoration and management in Japan. *Ocean Coast. Manag.* 81, 97–102. doi: 10.1016/j.ocecoaman.2012.07.012

Furukawa, K., and Okada, T. (2006). "Tokyo Bay: its environmental status—past, present, and future," in *The Environment in Asia Pacific Harbours*, ed. E. Wolanski (Dordrecht, IL: Springer), 15–34.

Gao, H., Yang, W. X., Yang, Y. P., and Yuan, G. H. (2019). Analysis of the air quality and the effect of governance policies in China's Pearl River Delta, 2015–2018. *Atmocz* 10:412. doi: 10.3390/atmos10070412

Guo, H. J., Cai, Y. P., Yang, Z. F., Zhu, Z. C., and Ouyang, Y. R. (2021). Dynamic simulation of coastal wetlands for Guangdong-Hong Kong-Macao Great Bay area based on multi-temporal Landsat images and FLUS model. *Ecol. Indic.* 125:107559. doi: 10.1016/j.ecolind.2021.107559

Han, X. B., Long, J. P., Li, J. B., Chu, F. Y., Zhang, P. P., Xu, D., et al. (2010). Research Progress on the Vulnerability of the Pearl River Delta. *Trop. Geogr.* 30, 1–7. doi: 10.3969/j.issn.1001-5221.2010.01.001

Hoque, M. A. A., Phinn, S., Roelfsema, C., and Childs, I. (2018). Assessing tropical cyclone risks using geospatial techniques. *Appl. Geogr.* 98, 22–33. doi: 10.1016/j.apgeog.2018.07.004

Jana, A., and Bhattacharya, A. K. (2013). Assessment of Coastal Erosion Vulnerability around Midnapur-Balasore Coast, Eastern India using Integrated Remote Sensing and GIS Techniques. *J. Indian Soc. Remote Sens.* 41, 675–686. doi: 10.1007/s12524-012-0251-2

Jia, M. M., Wang, Z. M., Zhang, Y. Z., Mao, D. H., and Chao, W. (2018). Monitoring loss and recovery of mangrove forests during 42 years: the achievements of mangrove conservation in China. *Int. J. Appl. Earth Obs.* 73, 535–545. doi: 10.1016/j.jag.2018.07.025

Kang, T. S., Oh, H. M., Lee, E. I., and Jeong, K. Y. (2018). Disaster Vulnerability Assessment in Coastal Areas of Korea. *J. Coast. Res.* 85, 886–890. doi: 10.2112/SI85-178.1

Li, X., and Damen, M. C. (2010). Coastline change detection with satellite remote sensing for environmental management of the Pearl River Estuary. *China J. Mar. Syst.* 82, S54–S61. doi: 10.1016/j.jmarsys.2010.02.005

Li, X., Zhou, Y. X., Tian, B., Kuang, R. Y., and Wang, L. H. (2015). GIS-based methodology for erosion risk assessment of the muddy coast in the Yangtze Delta. *Ocean Coast. Manag.* 108, 97–108. doi: 10.1016/j.ocecoaman.2014.09.028

Liang, J. Y., Tang, B., Huang, T. T., Jiang, P. P., and You, X. L. (2021). Characteristics and Influencing Factors of Urban Agglomeration Competitiveness in Pearl River Delta. *Adv. Econ. Bus. Manage. Res.* 203, 479–482.

Luo, S. L., Wang, H. J., and Cai, F. (2013). An integrated risk assessment of coastal erosion based on fuzzy set theory along Fujian coast, southeast China. *Ocean Coast. Manag.* 84, 68–76. doi: 10.1016/j.ocecoaman.2013.07.007

Ma, Y. (2005). *Study of determination for the warning tidal level of Guangdong Province*. (Qingdao, SD: Ocean University of China). [Ph D thesis].

Mani Murali, R., Ankita, M., Amrita, S., and Vethamony, P. (2013). Coastal vulnerability assessment of Puducherry coast, India, using the analytical hierarchical process. *Nat. Hazards Earth Sys.* 13, 3291–3311. doi: 10.5194/nhess-13-3291-2013

Manuel, P., Rapaport, E., Keefe, J., and Krawchenko, T. (2015). Coastal climate change and aging communities in Atlantic Canada: a methodological overview of community asset and social vulnerability mapping. *Can. Geogr.Le Géogr. can.* 59, 433–446. doi: 10.1111/cag.12203

Mcgranahan, G., Balk, D., and Anderson, B. (2007). The rising tide: assessing the risks of climate change and human settlements in low elevation coastal zones. *Environ. Urban* 19, 17–37. doi: 10.1177/0956247807076960

McLaughlin, S., and Cooper, J. A. G. (2010). A multi-scale coastal vulnerability index: a tool for coastal managers? *Environ. Hazard.* 9, 233–248. doi: 10.3763/ehaz.2010.0052

McPhearson, T., Maddox, D., Gunther, B., and Bragdon, D. (2013). "Local assessment of New York City: Biodiversity, green space, and ecosystem services," in *Urbanization, Biodiversity and Ecosystem Services: Challenges and Opportunities*, ed. T. Elmqvist (Dordrecht, IL: Springer), 355–383.

Miah, J., Hossain, K. T., Hossain, M. A., and Najia, S. I. (2020). Assessing coastal vulnerability of Chittagong District, Bangladesh using geospatial techniques. *J. Coast. Conserv.* 24:66. doi: 10.1007/s11852-020-00784-2

Pendleton, E. A., Barras, J. A., Williams, S. J., and Twichell, D. C. (2010). *Coastal Vulnerability Assessment of the Northern Gulf of Mexico to Sea-Level Rise and Coastal Change. U.S. Geological Survey Open-File Report 2010–1146*, Reston, VA: U.S. Geological Survey, 1–2. doi: 10.3133/ofr20101146

Peng, Y. S., Zheng, M. X., Zheng, Z. X., Wu, G. C., Chen, Y. C., Xu, H. L., et al. (2016). Virtual increase or latent loss? *Mar. Pollut. Bull.* 109, 691–699. doi: 10.1016/j.marpolbul.2016.06.083

Phan, L. T., Slinn, D. N., and Kline, S. W. (2013). "Wave effects on hurricane storm surge simulation," in *Advances in Hurricane Engineering: Learning From Our Past*, ed. C. P. Jones (New York, NY: ASCE), 753–764.

Phong, N. T., Parnell, K. E., and Cottrell, A. (2017). Human activities and coastal erosion on the Kien Giang coast. *Vietnam. J. Coast. Conserv.* 21, 967–979. doi: 10.1007/s11852-017-0566-9

Qi, H. S., Cai, F., Lei, G., Cao, H. M., and Shi, F. Y. (2010). The response of three main beach types to tropical storms in South China. *Mar. Geol.* 275, 244–254. doi: 10.1016/j.margeo.2010.06.005

Rangel-Buitrago, N., Williams, A. T., and Anfuso, G. (2018). Hard protection structures as a principal coastal erosion management strategy along the Caribbean coast of Colombia. A chronicle of pitfalls. *Ocean Coast. Manag.* 156, 58–75. doi: 10.1016/j.ocecoaman.2017.04.006

Roy, S., Pandit, S., Papia, M., Rahman, M. M., and Hossain, M. S. (2021). Coastal erosion risk assessment in the dynamic estuary: the Meghna estuary case of Bangladesh coast. *Int. J. Disast. Risk Re.* 61:102364. doi: 10.1016/j.ijdrr.2021.102364

Sano, M., Gainza, J., Baum, S., Choy, D. L., Neumann, S., and Tomlinson, R. (2015). Coastal vulnerability and progress in climate change adaptation: an Australian case study. *Reg. Stud. Mar. Sci.* 2, 113–123. doi: 10.1016/j.rsma.2015.08.015

Stronkhorst, J., Levering, A., Hendriksen, G., Rangel-Buitrago, N., and Appelquist, L. R. (2018). Regional coastal erosion assessment based on global open access data: a case study for Colombia. *J. Coast. Conserv.* 22, 787–798. doi: 10.1007/s11852-018-0609-x

Susmita, D., Benoit, L., Siobhan, M., and David, W. (2010). Exposure of developing countries to sea-level rise and storm surges. *Clim. Change* 106, 581–581. doi: 10.1007/s10584-010-9959-6

Swami, D., and Parthasarathy, D. (2021). Dynamics of exposure, sensitivity, adaptive capacity and agricultural vulnerability at district scale for Maharashtra. *India Ecol. Indic.* 121:107206. doi: 10.1016/j.ecolind.2020.107206

Wang, H., Li, Z., Han, G., Han, J., Gao, J., and Xu, T. (2007). Analysis on the ecological footprint in Yellow River Delta and Zhujiang Delta regions. *Ecol. Environ.* 16, 602–608. doi: 10.3969/j.issn.1674-5906.2007.02.066

Wang, X. T., Zhang, W. G., Yin, J., Wang, J., Ge, J. Z., Wu, J. P., et al. (2021). Assessment of coastal erosion vulnerability and socio-economic impact along the Yangtze River Delta. *Ocean Coast. Manag.* 215:105953. doi: 10.1016/j.ocecoaman.2021.105953

Wang, X. Y., Liu, L., and Zhang, S. L. (2021). Integrated model framework for the evaluation and prediction of the water environmental carrying capacity in the Guangdong-Hong Kong-Macao Greater Bay Area. *Ecol. Indic.* 130:108083. doi: 10.1016/j.ecolind.2021.108083

Weinberg, P. (2010). Long Island's Wetland Laws: safeguarding an Irreplaceable Resource. *Mem. Am. Math. Soc.* 26, 2–5. doi: jstor.org/stable/43391917

Williams, A., Rangel-Buitrago, N. G., Pranzini, E., and Anfuso, G. (2018). The management of coastal erosion. *Ocean Coast. Manag.* 156, 4–20. doi: 10.1016/j.ocecoaman.2017.03.022

Williams, P., and Faber, P. (2001). Salt marsh restoration experience in San Francisco Bay. *J. Coastal Res.* 27, 203–211. doi: 10.2307/25736174

Wu, X. L., and Hu, F. (2020). Analysis of ecological carrying capacity using a fuzzy comprehensive evaluation method. *Ecol. Indic.* 113:106243. doi: 10.1016/j.ecolind.2020.106243

Xiao, Y. E. (2003). *Assessment of Coastal Vulnerabliity to Sea-Level Ries: Preliminary Results for the Eoastlines Along the Pearl River Mouth*. (Guangzhou, GD: South China Normal University). [Ph D thesis].

Xu, X. Y., Zhang, Z. H., Long, T., Sun, S. M., and Gao, J. (2021). Mega-city region sustainability assessment and obstacles identification with GIS–entropy–TOPSIS model: a case in Yangtze River Delta urban agglomeration. *China J. Clean. Prod.* 294:126147. doi: 10.1016/j.jclepro.2021.126147

Yang, C., Zhang, C. C., Li, Q. Q., Liu, H. Z., Gao, W. X., Shi, T. Z., et al. (2020). Rapid urbanization and policy variation greatly drive ecological quality evolution in Guangdong-Hong Kong-Macau Great Bay Area of China: a remote sensing perspective. *Ecol. Indic.* 115:106373. doi: 10.1016/j.ecolind.2020.106373

Yang, C. C., Gan, H. Y., Wan, R. S., and Zhang, Y. M. (2021). Spatiotemporal evolution and influencing factors of coastline in the Guangdong-Hong Kong-Macao Great Bay Area from 1975 to 2018. *Geol. China* 48, 697–707. doi: 10.12029/gc20210302

Yang, Q., and Shuai, H. (2021). Spatial and Temporal Variation of Social-Ecosystem Vulnerability and Barrier Factors in Zhangjiajie City. *J. Central South University For. Technol.* 15:12. doi: 10.14067/j.cnki.1673-9272.2021.05.008

Yang, W. C., Xu, K., Lian, J. J., Ma, C., and Bin, L. L. (2018). Integrated flood vulnerability assessment approach based on TOPSIS and Shannon entropy methods. *Ecol. Indic.* 89, 269–280. doi: 10.1016/j.ecolind.2018.02.015

Ye, R. H., Ge, J., Zhang, W. M., and Zhao, H. J. (2020). Statistical analysis on impact from tropical cyclone on Guangdong-Hong Kong-Macao Great Bay Area. *Water Resour. Hydropower Eng.* 51, 37–43. doi: 10.13928/j.cnki.wrahe.2020.S1.007

Yin, J., Yin, Z. E., Wang, J., and Xu, S. Y. (2012). National assessment of coastal vulnerability to sea-level rise for the Chinese coast. *J. Coast. Conserv.* 16, 123–133. doi: 10.1007/s11852-012-0180-9

Zhang, X. H., Wu, L. L., and Huang, H. M. (2021). Achievements,problems and countermeasures of coastline renovation and restoration in guangdong province. *Trans. Oceanol. Limnol.* 43, 140–146. doi: 10.13984/j.cnki.cn37-1141.2021.04.020

Zhao, J. C., Ji, G. X., Tian, Y., Chen, Y. L., and Wang, Z. (2018). Environmental vulnerability assessment for mainland China based on entropy method. *Ecol. Indic.* 91, 410–422. doi: 10.1016/j.ecolind.2018.04.016

Zhou, H. H., Du, J., Nan, Y., Song, K. S., Zhao, B. Y., and Xiang, X. Y. (2019). Landscape Patterns of Coastal Wetlands in Pearl River Delta and Their Changes for 5 Periods since 1980. *Wetl. Sci.* 17, 559–566. doi: 10.13248/j.cnki.wetlandsci.2019.05.009

Zhu, Z. T. (2019). *Study on Assessment Modeling of Coastal Vulnerability to Erosion and its Application*. (Shanghai, SH: East China Normal University). [Ph.D thesis].

Zhu, Z. T., Cai, F., Chen, S. L., Gu, D. Q., Feng, A. P., Cao, C., et al. (2018). Coastal Vulnerability to Erosion Using a Multi-Criteria Index: a Case Study of the Xiamen Coast. *Sustainability* 11:93. doi: 10.3390/su11010093

Conflict of Interest: The authors declare that the research was conducted in the absence of any commercial or financial relationships that could be construed as a potential conflict of interest.

frontiers in Marine Science

ORIGINAL RESEARCH
published: 28 March 2022
doi: 10.3389/fmars.2022.846914

Shoreline Evolutionary Trends Along Calabrian Coasts: Causes and Classification

Giandomenico Foti[1], Giuseppe Barbaro[1], Giuseppina Chiara Barillà[1], Pierluigi Mancuso[2] and Pierfabrizio Puntorieri[1]*

[1] Civil, Energy, Environmental and Material Engineering Department (DICEAM), Mediterranea University of Reggio Calabria, Reggio Calabria, Italy, [2] Public Works Department, Catanzaro, Italy

The issue of coastal erosion currently affects most of the world's coastal territories. This erosion is generally caused by an alteration of coastal and river dynamics both due to the action of natural factors and to the increase in anthropogenic pressure, mainly observed in the second half of the last century after the end of the Second World War. In the future, this issue may be more affected by climate change. This paper describes the shoreline evolutionary trends at different time scale along the Calabrian coasts, a region in southern Italy, in over 50 sample areas. Calabria represents an interesting case study due to its geomorphological peculiarities and due to its considerable anthropogenic pressures, which have caused extensive erosive processes. In addition, this paper analyzes the main causes of these evolutionary trends and classifies them using a quick methodology based on a shoreline variation rate of a fixed area. This is an index-based methodology and is a part of a new generally index-based coastal risk assessment methodology, developed by the Mediterranea University of Reggio Calabria and the Calabria Region and which is currently in progress. The main result is that the sample areas in the erosion classes prevail over those in the advancement class for very long-term, long-term and middle-term time interval while for short-term and most recent time interval the sample areas in the advancement class prevail over those in the erosion classes.

Keywords: coastal erosion, shoreline changes, coastal risk assessment, index-based methodology, remote sensing, GIS

OPEN ACCESS

Edited by:
Roshanka Ranasinghe, IHE Delft Institute for Water Education, Netherlands

Reviewed by:
Goneri Le Cozannet, Bureau de Recherches Géologiques et Minières, France
Ali Dastgheib, IHE Delft Institute for Water Education, Netherlands

****Correspondence:***
Giandomenico Foti
giandomenico.foti@unirc.it

Specialty section:
This article was submitted to Coastal Ocean Processes, a section of the journal Frontiers in Marine Science

Received: *31 December 2021*
Accepted: *25 February 2022*
Published: *28 March 2022*

Citation:
Foti G, Barbaro G, Barillà GC, Mancuso P and Puntorieri P (2022) Shoreline Evolutionary Trends Along Calabrian Coasts: Causes and Classification. Front. Mar. Sci. 9:846914. doi: 10.3389/fmars.2022.846914

INTRODUCTION

Coastal erosion processes currently affect most of the world's coastal areas (Luijendijk et al., 2018; Mentaschi et al., 2018). These processes are caused by many natural and anthropogenic factors that alter both coastal and river dynamics (Komar, 2000; Amrouni et al., 2019; Ozpolat and Demir, 2019; Wang et al., 2019; Zhang et al., 2019; Zhai et al., 2020). In fact, the equilibrium of coastal areas is also influenced by the rivers of the same physiographic unit (Acciarri et al., 2016; Barbaro et al., 2019a; Foti et al., 2019).

The main natural factors are the wave climate (Almar et al., 2015; Kroon et al., 2020), the rainfall events (Dada et al., 2015; Zellou and Rahali, 2019), and the coastal sedimentary balance, which is mainly related to longshore and river transport (Barbaro et al., 2014b; Li et al., 2014; Tomasicchio et al., 2015; Dada et al., 2018; Anthony et al., 2019; Besset et al., 2019).

The main anthropogenic factors are the construction of hydraulic structures such as dams and weirs (Zema et al., 2014), the withdrawal of river sediment (Foti et al., 2020a), the destruction of dune systems (Foti et al., 2022) and the construction of ports and coastal defenses (Barbaro, 2013; Prumm and Iglesias, 2016; Valsamidis and Reeve, 2017). Furthermore, anthropogenic pressure causes an increase in impermeable surfaces with negative consequences on the vulnerability of the territory under the action of natural events such as floods and sea storms (Fiori et al., 2014; Barbaro et al., 2020), especially when concurrent events occur (Barbaro et al., 2019b; Canale et al., 2020). Climate change can also contribute to erosive phenomena by the increasing of sea levels and the frequency and intensity of extreme weather events (Santini, 2011; Yang et al., 2015).

Furthermore, erosive processes can occur at different time scales: instantaneous, seasonal, and long-term. The instantaneous variations are related to the wave action and are more relevant during intense sea storms (Harley et al., 2017). Seasonal and annual variations are linked to the wave action, tides, and currents, generally with erosion during the winter and natural nourishment during the summer months (Short and Trembanis, 2004; Thomas et al., 2011; Barnard et al., 2015). Long-term variations are caused by subsidence, tectonic movements, sea level rise due to climate change (Ranasinghe et al., 2004), and changes in coastal and river sedimentary balance due to anthropogenic actions (Turner, 2006; Bird, 2018).

Therefore, coastal areas represent complex dynamical systems and to protect and manage coastal areas various coastal erosion risk assessment methodologies have been defined here (Anfuso and Del Pozo, 2009; McLaughlin and Cooper, 2010; Ramieri et al., 2012; Torresan et al., 2012; Barbaro, 2016; Satta et al., 2016; Jaranovic et al., 2017; Narra et al., 2017; Satta et al., 2017; Kantamaneni et al., 2018; Mavromatidi et al., 2018; Pantusa et al., 2018; Viavattene et al., 2018; Mucerino et al., 2019; Bruno et al., 2020). From this point of view, it is important to analyze coastal and river dynamics, and to estimate and classify shoreline changes (Boak and Turner, 2005; Mills et al., 2005; Maiti and Bhattacharya, 2009; Maanan and Robin, 2010; Williams et al., 2018; Goncalves et al., 2019; Görmüş et al., 2021; Ngowo et al., 2021). A key element in estimating shoreline changes is the cartography data available. These data include historical cartographies, orthophotos, satellite images, and UAV and Lidar (Light Detection and Ranging or Laser Imaging Detection and Ranging) surveys (Le Mauff et al., 2018; Nicolae-Lerma et al., 2019; Mao et al., 2021). Among these, satellite images have been widely used in recent times for three main reasons: they are free available, they interface well with GIS (Geographical Information Systems) and are provided in infrared spectral bands, therefore the water-land interface is well defined (Duarte et al., 2018; Hagenaars et al., 2018; Qiao et al., 2018; Toure et al., 2019; Vos et al., 2019; Konlechner et al., 2020).

This paper describes the shoreline evolutionary trends at different time scale along the Calabrian coasts, a region in southern Italy, in over 50 sample areas. Calabria is a region in Southern Italy that represents an interesting case study due to its geomorphological peculiarities and due to its considerable anthropogenic pressures, which have caused extensive erosive processes (Barbaro et al., 2014a). In addition, this paper analyzes the main causes of these evolutionary trends and classifies them using a quick methodology based on a shoreline variation rate of a fixed area. This is a quick index-based methodology and is a part of a new generally index-based coastal risk assessment methodology which is currently in progress. The new quick methodology completes and improves the work started by Foti et al. (2020b) and improves the methodology developed by Barbaro (2016), proposing an index based on a shoreline variation rate and classifying the shoreline evolutionary trend into 5 classes. This classification was inspired by that proposed by Ferreira Silva et al. (2017), but it differs from it in the definition of the shoreline variation rate which is the novelty of this methodology and is more representative of the shoreline evolutionary trend than the previous methodologies.

MATERIALS AND METHODS

This section is divided into two parts. The first part describes the geomorphological peculiarities of the study area. The second part describes the quick methodology proposed in this paper to classify the shoreline evolutionary trend.

Site Description

Calabria is a region in southern Italy, located at the tip of the typical Italian "boot" in the center of the Mediterranean Sea enclosed by two seas, the Tyrrhenian and the Ionian, by the Strait of Messina and by the Gulf of Taranto, each of them with different climatic characteristics and with different fetch extensions (**Figure 1**). From the morphological point of view, Calabria is characterized by hills and mountains, with a percentage of less than 10% of flat lands. The main massifs are Pollino, Sila, and Aspromonte, all with a maximum altitude of the order of 2000 m. The main coastal plains are that of Sibari, on the Ionian coast in the Gulf of Taranto, and those of Lamezia Terme and Gioia Tauro, both on the Tyrrhenian coast. Its narrow and elongated shape means that it has over 750 km of coastline, with an alternating mainly sandy and pebbly beaches, and high coasts, with the main headlands are those of Capo Rizzuto, on the Ionian coast, and of Capo Vaticano, on the Tyrrhenian coast.

From a climatic point of view, the Ionian coasts are mainly exposed to the winds of Scirocco, South-East, and Grecale, North-East, while the Tyrrhenian coasts are mainly exposed to the winds of the Mistral, North-West. Regarding the fetch extensions, it varies from a few tens of kilometers within the Strait of Messina and the Gulf of Taranto to several hundred kilometers along various directions in the Ionian and Tyrrhenian seas. These differences lead to a remarkable variability of weather and sea conditions between the different coastal areas which influences the coastal dynamics and that cause meteorological events that damage the territory (Canale et al., 2021). Also, tidal excursion is negligible (Sannino et al., 2015).

Most Calabrian rivers (locally called "fiumare") (Sorriso-Valvo and Terranova, 2006; Sabato and Tropeano, 2014), are characterized by a torrential and irregular hydrological regime,

FIGURE 1 | The Calabrian region (shown with red polygon), in the center of the Mediterranean Sea.

with extensive dry periods and frequent sudden flooding, caused by short and intense rainfalls. Also, many of these rivers have very wide beds with coarse grain size. This combination of hydrological and granulometric characteristics causes high solid transport, and the relative variations can alter the coastal dynamics and the shoreline evolution near the river mouths, as shown by Barbaro et al. (2019a) and by Foti et al. (2019) in the case studies of mouths of the Petrace River and Sant'Agata River, respectively.

To analyze the evolutionary trend and the main erosive causes of the Calabrian coasts, over 50 sample areas with different morphological and anthropogenic characteristics were chosen (**Figure 2** and **Table 1**). In most cases, over 40, anthropized areas have been chosen close to inhabited centers while in the remaining areas there are only scattered houses. In over 20 areas there are coastal defense works and over 10 areas are close to ports. Finally, 3 areas are related to pocket beach, in 4 areas there are dune systems, and over 10 are close to river mouths.

Methodology

The methodology proposed in this paper to classify the shoreline evolutionary trend can be divided into eight phases (**Figure 3**):

1. Acquisition of available cartographic data, such as historical shoreline, orthophotos, and satellite images.
2. Manual digitization of each missing shorelines, using QGIS for orthophotos and using Google Earth Pro for satellite images.
3. Choice and tracking of the transepts representative of each sample area, using QGIS.
4. Estimation of the beach width for each transept, using QGIS.
5. Estimation of the shoreline changes for each transept, using end point rate ("EPR") and net shoreline movement ("NSM") statistics.
6. Estimation of the influence area of each transept, using QGIS.
7. Estimation of the shoreline variation rate of each sample area.
8. Classification of the shoreline evolutionary trend of each sample area based on the shoreline variation rate.

Regarding the last two phases, a quick methodology was developed to classify the shoreline evolutionary trend into five classes, based on the value of the shoreline variation rate index v which is the novelty of this methodology. This index was inspired

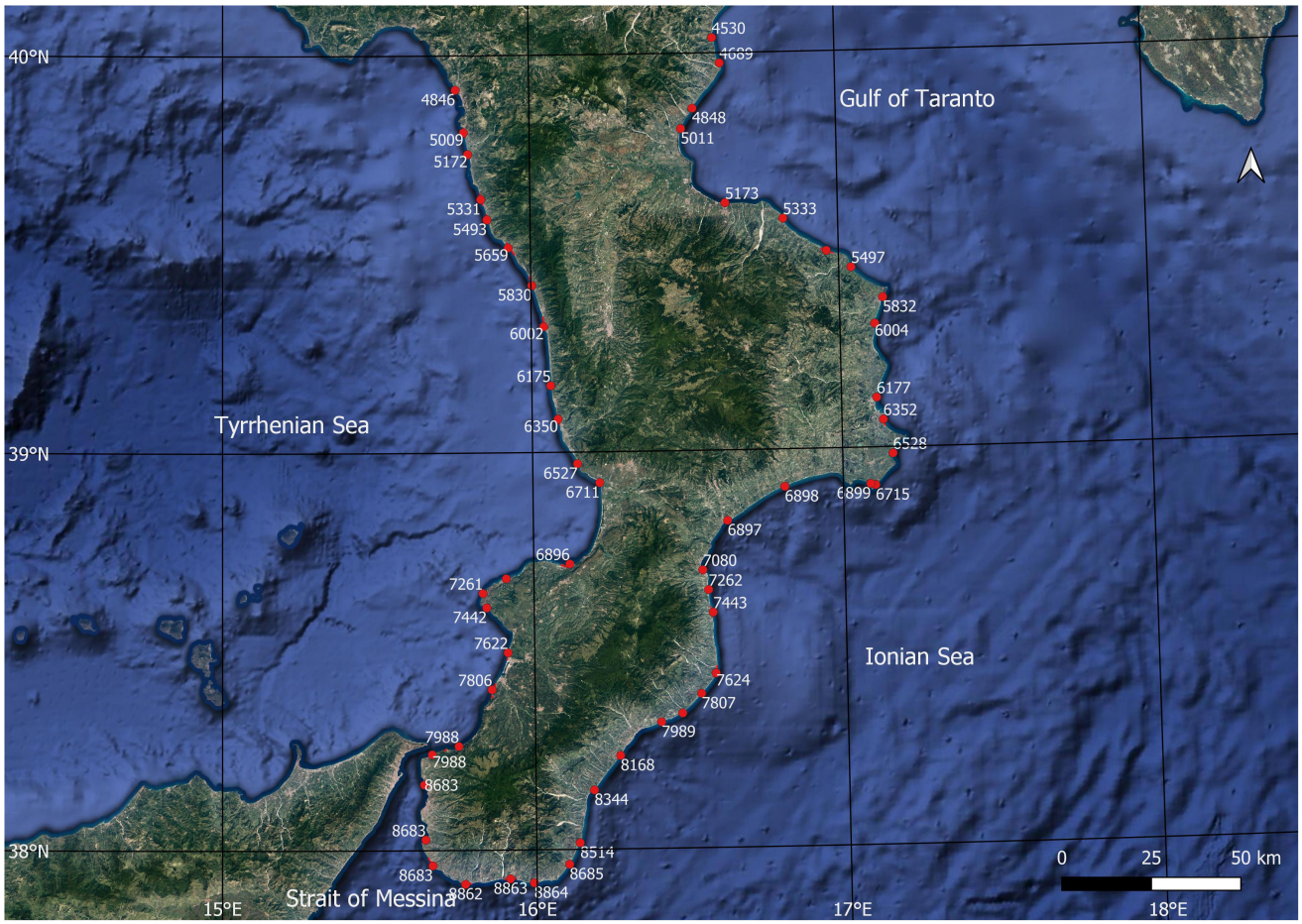

FIGURE 2 | The Calabrian towns examined are identified with a code. Their names are shown in **Table 1**.

by Barbaro's (2016) and this classification was inspired by that proposed by Ferreira Silva et al. (2017).

The shoreline variation rate is calculated with the following formula:

$$\bar{v} = \sum_i v_i \cdot \frac{\triangle A_i}{\triangle A_{tot}}$$

where v_i is the variation rate of the i-th transept evaluated in terms of EPR; ΔA_i is the influence area of the i-th transept, defined as the area between the midpoints of the lines joining the i-th transept with the adjacent ones, and ΔA_{tot} is the sum of the influence areas of all the transepts of the study area. In fact, the shoreline variation rate v is the weighted average shoreline variation rate for each study area, where the weight is given by the influence areas of each transept.

The classes defined by this methodology are advancement ($v > 0.5$), stability ($-0.5 \leq v \leq 0.5$), erosion ($-1 \leq v < -0.5$), intense erosion ($-2 \leq v < -1$), and severe erosion ($v < -2$).

Furthermore, the evaluation of the evolutionary trend of the shoreline was carried out for different timescales as follows: the two most recently available shorelines; a short-term evolutionary trend, with reference to the shorelines available in the last 5 years; a middle-term evolutionary trend, with reference to the shorelines available in the last 20 years; a long-term evolutionary trend, with reference to the shorelines available in the last 30 years; and a very long-term evolutionary trend, with reference to the shorelines available in the past 70 years. For example, with reference to 2020 the time interval would be as follows. Most recent = shorelines of 2020 and 2019; short-term = shorelines from 2016 to 2020; middle-term = shorelines from 2001 to 2020; long-term = shorelines from 1991 to 2020; very long-term = shorelines from 1951 to 2020.

The proposed methodology is more complete than Barbaro's (2016) because it considered the influence area of each transept and because it analyzed the shoreline changes over a time interval of 70 years instead of 15 years, between the 1998–2003, 2003–2008, and 2008–2013 with fixed sub-intervals of 5 years each. However, only a medium-term and a short-term evolutionary trend were analyzed, neglecting a long-term and a very long-term trend. The new methodology has filled this gap. Also, Barbaro's methodology did not analyze evolutionary trends on an annual scale due to the lack of satellite images at that time interval. In fact, only since 2015 are satellite images available on an annual scale for most of the Calabrian coastal areas and this lack was also

TABLE 1 | Sample areas and related code (**Figure 2**).

Sample area	Code	Anthropization	Coastal defense works	Other
Montegiordano	4530	I	G	
Roseto Capo Spulico	4689	I	G	
Trebisacce	4848	I		
Villapiana	5011	S		D
Rossano	5173	I		
Calopezzati	5333	I		
Cariati	5496	I	G	P
Crucoli (Torretta)	5497	I	G	
Cirò Marina	5832	I	B	P
Torre Melissa	6004	I	B	
Crotone (Zigari)	6177	S		
Crotone	6352	I	B	P
Isola Capo Rizzuto (Marinella)	6528	S		PB
Isola Capo Rizzuto	6715	I		
Isola Capo Rizzuto (Le Castella)	6899	S		PB
Cropani	6898	S		D
Catanzaro Lido	6897	I		P
Soverato	7080	I		
San Sostene	7262	S		R
Badolato	7443	S		D, P
Monasterace	7624	I		R
Riace	7807	S		
Caulonia	7990	I		R
Roccella Ionica	7989	I	G	P
Locri	8168	I		
Bovalino	8344	I		
Ferruzzano	8514	S		
Brancaleone	8685	I		
Palizzi	8864	I	B	
Bova Marina	8863	I	B	R
Melito Porto Salvo	8862	I		R
Lazzaro	8683	I	G	
Pellaro	8683	I	G	
Gallico	8683	I	B	R
Porticello	7988	I	M	
Favazzina	7988	I	G	R
Palmi	7806	I		R, P
San Ferdinando	7622	I		R, P
Ricadi (Santa Maria)	7442	I		PB
Capo Vaticano	7261	I	G	R
Tropea	7078	S	G	P
Vibo Marina	6896	I	M	P
Gizzeria	6711	S		D
Falerna	6527	I		
Amantea	6350	I	B	
Belmonte	6175	I		
San Lucido	6002	I	M	
Fuscaldo	5830	I	G	
Cetraro	5659	I	M	P
Sangineto	5493	I	M	
Belvedere	5331	I	M	
Santa Maria del Cedro	5172	S		R
Scalea	5009	I		R
Tortora	4846	I		

B, breakwaters; D, dune systems; G, groynes; I, inhabited center; M, mixed interventions; P, ports; PB, pocket beaches; R, river mouth; S, scattered houses.

filled by the new methodology. In addition, the new methodology differs from that proposed by Ferreira Silva et al. (2017) in the definition of the shoreline variation rate *v*. Finally, the results obtained with the new methodology were compared with those obtained considering the eroded and advanced beach surfaces. This comparison showed that the new methodology was useful, as the results were comparable.

About the other phases, in the first phase various cartography data were compared. In detail, the following have been analyzed: the shapefiles of the historical shorelines of 1954, 1998, 2000, and 2008, taken from the Open Data section of the Calabrian Geoportal[1]; orthophotos of 1989, 1996, 2006, and 2012, taken from the Web Map Service (WMS) of the Open Data section of the Italian Geoportal[2]; and satellite imagery from 2015 to 2020, provided by Google Earth Pro. The shapefile of the shoreline of 1954 has been digitized based on CASMEZ, "*Cassa del Mezzogiorno*," cartography of 1954, in scale 1:10000. The shapefiles of the shorelines of 1998 and 2000 have been digitized based on CTR, "Carta Tecnica Regionale," cartography of 1998 and 2000, both in scale 1:5,000. The shapefile of the shoreline of 2008 has been digitized based on the infrared orthophotos of 2008 in scale 1:5,000. The 1989 and 1996 orthophotos are in black and white, were acquired with a Leica RC30 digital camera and have a scale of 1:10000. The orthophotos of 2006 and 2012 are in color, were acquired with a Leica AD40 digital camera and have a scale of 1:10000. Furthermore, the 2012 orthophotos have pixels of 50 cm. Google satellite images from 2015 to 2020 have variable temporal coverage, from a minimum of three to a maximum of six images depending on the location examined.

Regarding the second phase, the digitalization of each missing shorelines, related to orthophotos and Google satellite imagery, was carried out on a scale of 1:1000 on QGIS and at an eye altitude of 200 m, corresponding to a higher scale, on Google Earth Pro using his spatial analysis tools. The upper limits of the beaches were chosen as the baselines and generally correspond to fixed points such as promenades, roads, and structures or the baseline corresponds with the dune systems in cases where the fixed points are very distant from the beach. About digitization on Google Earth, shorelines and baselines were saved as kml files then saved on QGIS as shapefiles. Baselines were used on QGIS as control points to confirm the accuracy of the procedure.

The digitization phase is characterized by various uncertainties, the main ones concern georeferencing and orthorectification processes, the image resolution, the identification of the wet/dry line or other similar lines, the seasonal cycle of erosion and deposition, and the impact of storms (Boak and Turner, 2005; Hapke et al., 2010). In this phase, uncertainties can be quantified, according to Del Rio and Garcia (2013), through the estimation of the physical component of the error, the scanning error and the georeferencing error. In this case, the reference line chosen was the wet/dry line, the cartography data is all related to the summer period and no storm conditions were observed in any of the data, so the

[1]http://geoportale.regione.calabria.it/opendata, accessed on 15 November 2021.

[2]http://www.pcn.minambiente.it/mattm/servizio-wms/, accessed on 15 November 2021.

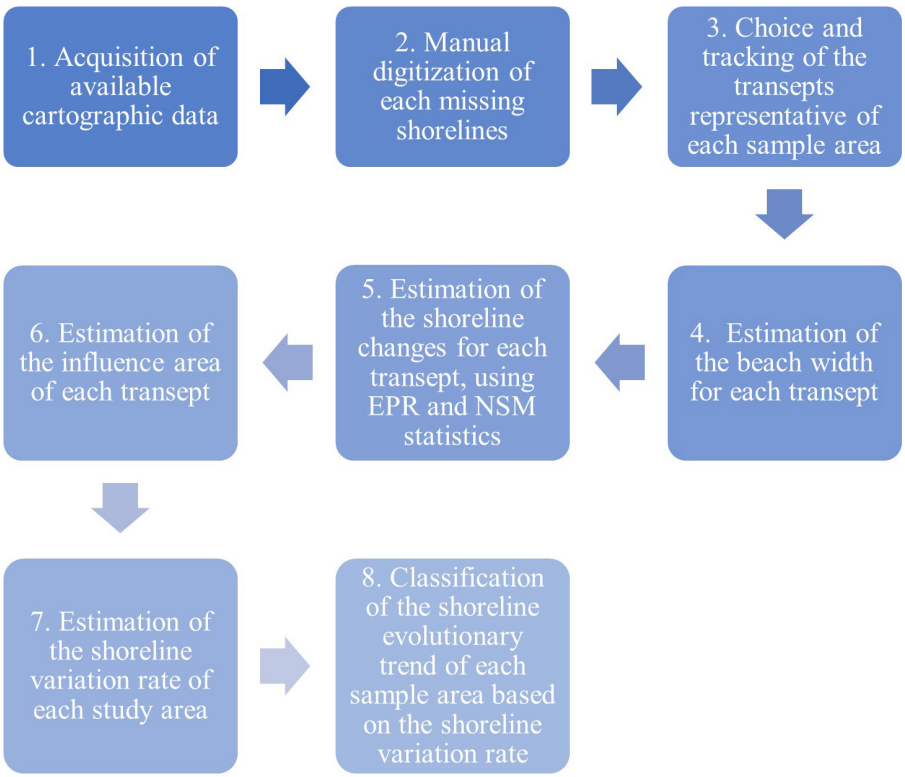

FIGURE 3 | Flow chart of the proposed methodology.

effects of seasonal variation and individual storms on shoreline change are of limited importance. Furthermore, to estimate the tide excursions, the recordings of the tide gages of Crotone and Reggio Calabria were analyzed, the Tide Tables of the Istituto Idrografico della Marina (2020) and the scientific papers were consulted, especially that of Sannino et al. (2015). These sources highlighted that Calabria is a microtidal environment where the tidal excursion is of the order of tens of centimeters. Indeed, the maximum-recorded tide height values are about 25 cm in Reggio Calabria and over 80 cm in Crotone while the minimum recorded tide height values are over −50 cm in Reggio Calabria and over −70 cm in Crotone and the average recorded tide height values are less than 30 cm in Reggio Calabria and about 50 cm in Crotone. Finally, the maximum tide height value reported in the Tide Tables is 25 cm. So, the physical component of the error was estimated using the formula of Allan et al. (2003). The error was estimated, starting from the average and maximum values of the tide height and from the beach slope. This last parameter was estimated using the QGIS Profile tool plugin based on the 1 m side square mesh LIDAR DTMs available on the Italian Geoportal.[3] The beach slope values of the examined locations varied between 1 and 15% so that the estimated error, assuming maximum tide height conditions, was between 1 and 15 m, and the estimated error (assuming minimum tide height conditions) was between 1 and 14 m. However, these are very precautionary values, as the times of the satellite image was not known and, consequently, it is not possible to know the tide conditions at these times. Additionally, the cartography and orthophotos scales are all 1:10000 or less so the scanning errors are of the order of one meter for orthophotos on a scale of 1:10000 and is less than one meter for other sources with a lower scale. On the other hand, regarding the georeferencing error of the Google Earth shorelines, the use of baselines as control points contained the error within a few tens of cm. Finally, since the aim of the paper is the evaluation of the erosion and advancement trends, and not their precise quantification, an accuracy of the order of one meter was considered for estimating the shoreline position and the shoreline changes.

In the third and fourth phases, both developed on QGIS, over 700 transepts representative of each study area were traced. For the choice of the tracing points of the transepts, the following criterion was followed: in the straight and regular beaches an average spacing of the order of a hundred meters was considered, but this was reduced in the presence of coastal structures and in the case of irregular morphologies. Also, for each transept, the distance between the baseline and the shorelines was determined. To automate this process, a point was first inserted at the intersection between each transept and the various shorelines using the line intersection tool. Then, the shortest line function which allows the calculation of the minimum distance between a point and a straight line is used to determine the width of each transept, considering each baseline as straight line.

[3]http://www.pcn.minambiente.it/mattm/, accessed on 15 November 2021.

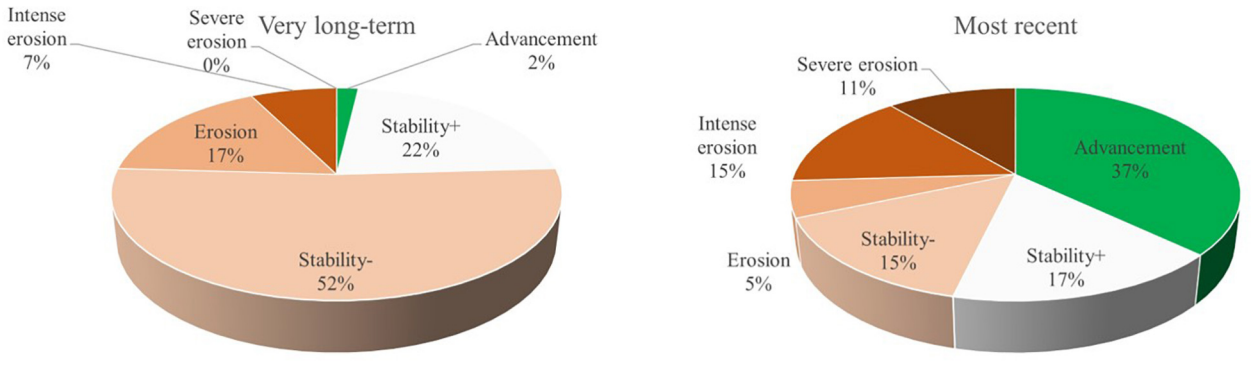

FIGURE 4 | On the **(left)** very long-term shoreline evolutionary trend. To the **(right)** most recent shoreline evolutionary trend.

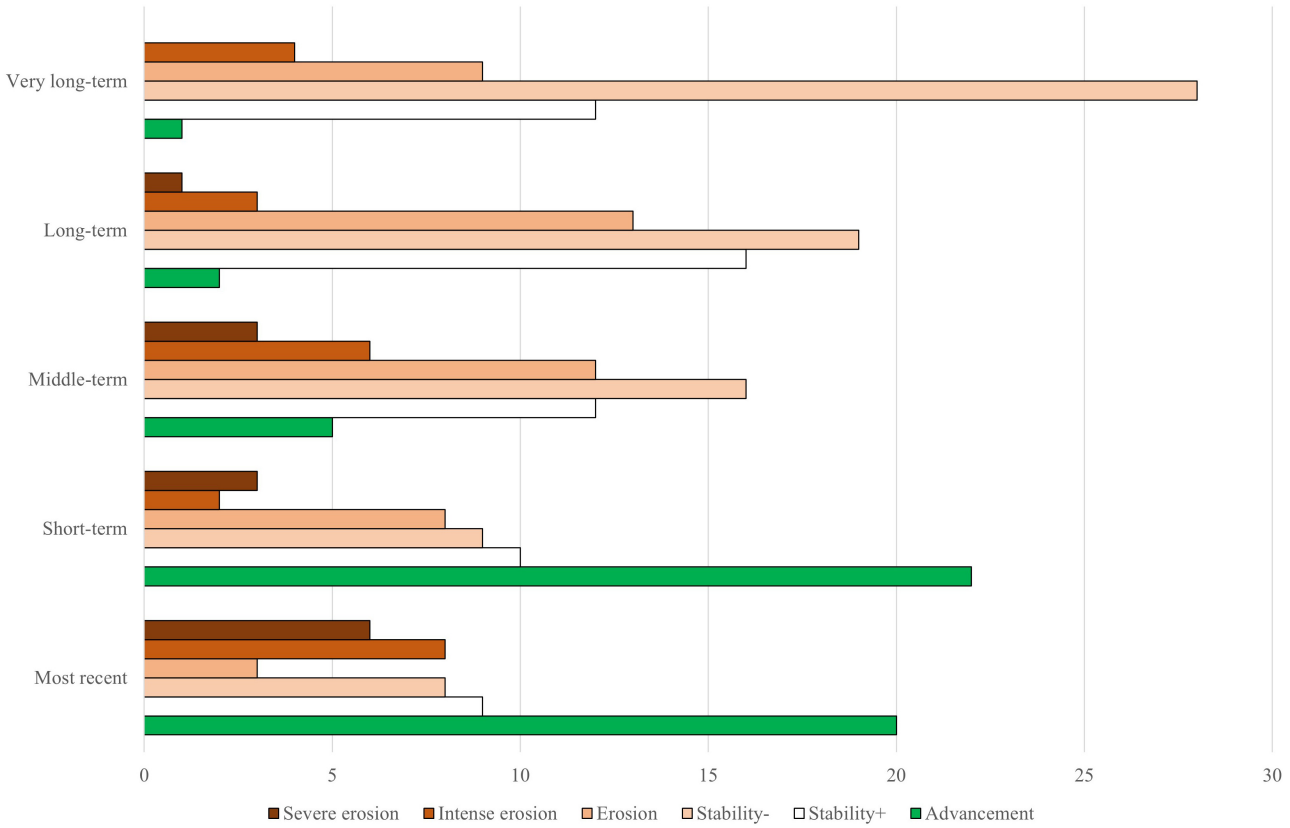

FIGURE 5 | Summary of shoreline evolutionary trends.

For the fifth phase, the NSM and EPR between any two shorelines were calculated. To assess the evolutionary trend of each study area these parameters were also calculated at different time scales being the last 70 years, 30 years, 20 years, 5 years, and finally between the two most recent shorelines available.

Finally, for the sixth phase, QGIS Processing tools were used firstly to draw orthogonal lines to each transept that connect them. The influence area of each transept is the area between the midpoints of the lines joining the examined transept with the adjacent ones and has been calculated using the field calculator.

RESULTS

Tables 2, **3** show a summary of the evolutionary trend for over 50 Calabrian sample areas, according to the classification shown in the previous paragraph. In detail, **Table 2** shows the shoreline evolutionary trend of each sample area while **Table 3** shows the summary of the shoreline evolutionary trends for all areas. In the latter table, the stability class, characterized by both positive and negative shoreline variation rates with values between −0.5 and 0.5 m/year, has been divided into

TABLE 2 | Shoreline evolutionary trend of each sample area.

Sample area	Code	Average shoreline variation rate, *v* [m/year]				
		Most recent	Short-term	Middle-term	Long-term	Very long-term
Montegiordano	4530	−0.22	0.21	0.60	0.16	−0.16
Roseto Capo Spulico	4689	0.19	1.93	0.24	0.10	0.12
Trebisacce	4848	0.07	0.07	−0.35	−0.03	0.14
Villapiana	5011	2.21	2.21	0.53	0.37	0.46
Rossano	5173	−0.26	0.16	0.12	−0.10	−0.12
Calopezzati	5333	−3.19	−0.69	−0.67	−0.55	−0.42
Cariati	5496	0.84	−1.10	−0.39	−0.61	−0.29
Crucoli (Torretta)	5497	−2.11	1.04	−0.96	−0.88	0.12
Cirò Marina	5832	−0.36	−0.08	−1.16	−0.77	−0.38
Torre Melissa	6004	0.16	0.80	0.26	0.01	0.11
Crotone (Zigari)	6177	2.18	−3.58	−1.19	−1.44	−1.29
Crotone	6352	0.54	−0.06	−0.66	0.03	−0.23
Isola Capo Rizzuto (Marinella)	6528	0.25	−0.26	−0.46	−0.17	0.05
Isola Capo Rizzuto	6715	−0.90	2.07	−0.61	−0.14	−0.05
Isola Capo Rizzuto (Le Castella)	6899	−0.04	0.46	−0.49	−0.51	−0.25
Cropani	6898	−1.18	2.50	−0.25	0.21	−0.10
Catanzaro Lido	6897	2.34	0.79	0.07	−0.08	−0.38
Soverato	7080	0.97	2.02	0.13	−0.06	−0.24
San Sostene	7262	0.35	−0.65	−0.68	−0.88	−0.57
Badolato	7443	0.16	1.72	1.04	−0.02	0.63
Monasterace	7624	−1.61	1.19	−0.10	−0.34	−0.77
Riace	7807	0.34	1.40	0.06	0.05	0.2
Caulonia	7990	−5.70	−0.57	−1.04	−1.84	−1.65
Roccella Ionica	7989	1.96	1.48	−0.56	−0.15	−0.06
Locri	8168	−1.04	−0.95	−0.56	−0.26	−0.21
Bovalino	8344	−0.72	−0.16	−0.60	−0.20	−0.33
Ferruzzano	8514	−1.15	−0.37	0.17	0.09	0.01
Brancaleone	8685	−2.09	−0.81	−0.19	−0.17	−0.18
Palizzi	8864	−1.37	0.81	0.26	0.26	−0.31
Bova Marina	8863	−1.84	−0.38	−1.23	−0.87	−0.27
Melito Porto Salvo	8862	−1.03	−0.61	−2.14	−0.96	−0.82
Lazzaro	8683	−0.03	−0.15	−1.15	−0.66	−0.26
Pellaro	8683	0.67	0.30	0.01	−0.15	0.02
Gallico	8683	−0.22	−0.30	−0.25	0.10	−0.36
Porticello	7988	−0.13	0.16	−0.92	−0.12	−0.08
Favazzina	7988	0.21	0.51	−0.25	−0.59	−0.14
Palmi	7806	−0.38	1.33	−0.01	−0.27	−0.96
San Ferdinando	7622	−3.06	−0.66	−0.05	0.01	−0.66
Ricadi (Santa Maria)	7442	1.41	0.08	−0.58	−0.21	−0.14
Capo Vaticano	7261	0.90	−1.84	0.12	0.01	−0.48
Tropea	7078	2.79	0.72	0.92	0.82	0.07
Vibo Marina	6896	2.05	0.48	0.69	0.32	−1.82
Gizzeria	6711	−1.63	−5.49	−1.05	0.60	0.38
Falerna	6527	12.10	8.88	−2.98	−2.37	−0.61
Amantea	6350	−0.84	−0.84	−0.74	−0.68	−0.79
Belmonte	6175	−2.81	−2.81	−0.28	0.48	−0.30
San Lucido	6002	0.20	0.20	−0.15	−0.16	−0.19
Fuscaldo	5830	1.21	0.51	−2.06	−1.56	−0.60
Cetraro	5659	3.59	0.87	−0.42	0.04	−0.79
Sangineto	5493	1.30	0.33	−0.77	−0.32	−1.24
Belvedere	5331	1.73	0.67	−0.23	−0.84	−0.32
Santa Maria del Cedro	5172	2.68	1.32	0.06	−0.23	−0.42
Scalea	5009	2.02	1.74	0.26	0.11	0.29
Tortora	4846	4.17	−0.01	−0.09	−0.69	−0.74

Green, advancement; White, stability; Light brown, erosion; Brown, intense erosion; Dark brown, severe erosion.

TABLE 3 | Summary of shoreline evolutionary trend.

Classification/time interval	Most recent	Short-term	Middle-term	Long-term	Very long-term
Advancement	20	22	5	2	1
Stability	17	19	28	35	40
Erosion	3	8	12	13	9
Intense erosion	8	2	6	3	4
Severe erosion	6	3	3	1	0
Advancement, Stability+	29	32	17	18	13
Erosion, Intense Erosion, Severe Erosion	17	13	21	17	13
Erosion, Intense Erosion, Severe Erosion, Stability-	25	22	37	36	41

*The color scheme is the same as in **Table 2**.*

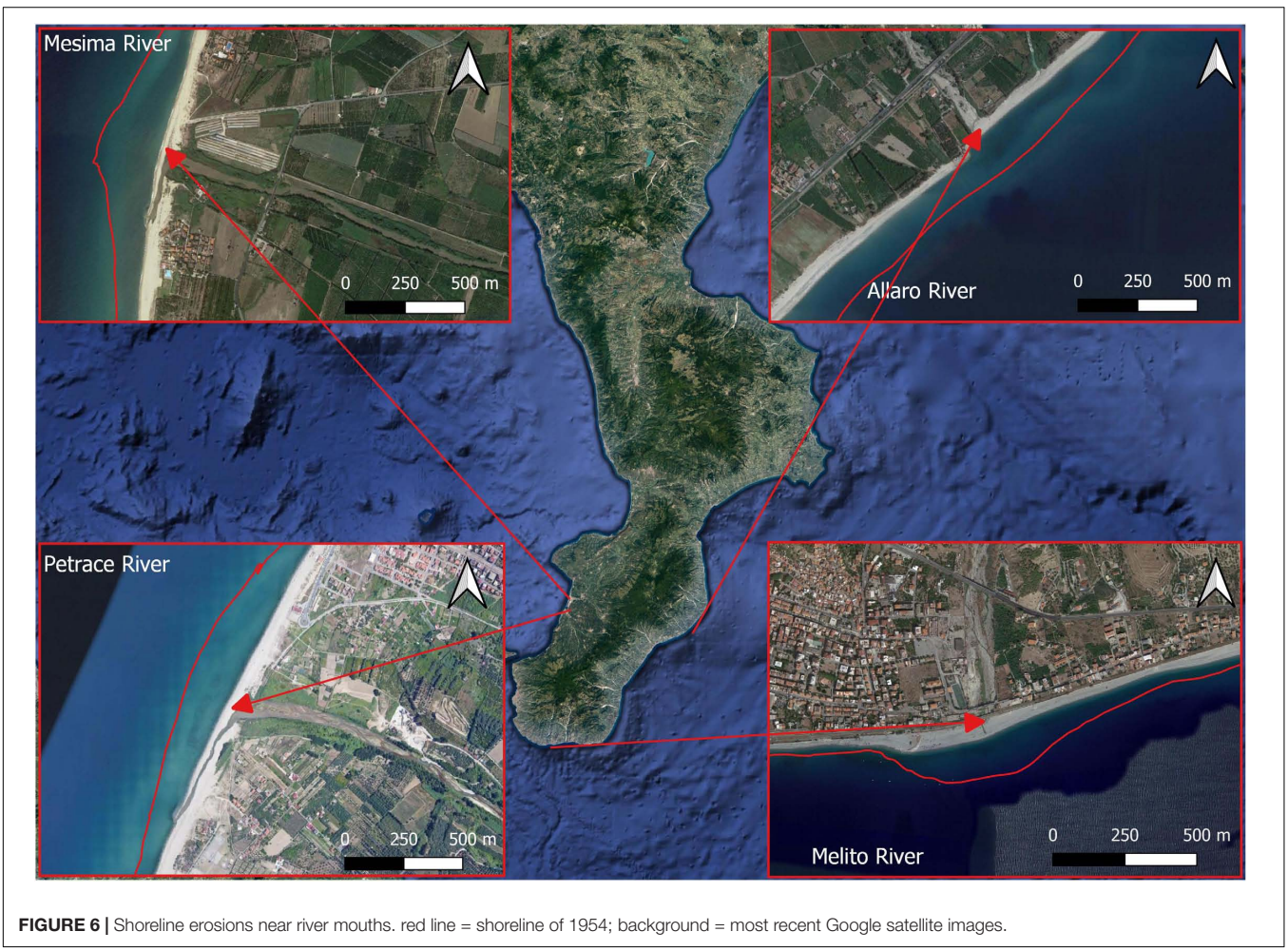

FIGURE 6 | Shoreline erosions near river mouths. red line = shoreline of 1954; background = most recent Google satellite images.

two sub-classes: stability+, where only the positive values have been considered, and stability−, where only the negative values were considered.

These tables show that most of the sample areas are characterized by evolutionary trends that vary depending to the time scale analyzed and only a few sample areas are characterized by evolutionary trends always of the same class. In the latter case, only 5 sample areas are included, where the shoreline evolutionary class is always stability with alternation of stability+ and stability− sub-classes between the various time intervals. Instead, in 6 sample areas, only positive values of the shoreline variation rates are observed, with alternation of advancement and stability+ classes between the various time intervals, and in other 6 sample areas, only advancement and stability classes are observed in all time intervals. On the other hand, in 6 sample areas, there are only erosion and stability classes in all time intervals and in 7 sample areas, only negative values of the shoreline variation rates are observed, with alternation of stability−, erosion, intense erosion and severe erosion classes between the various time intervals, while in 3 sample areas, Caulonia, Melito Porto Salvo, and Amantea, there are only the three erosion classes without the stability− class in all time

FIGURE 7 | Roseto Capo Spulico. **(Large panel)** Baseline (black line) and shorelines of 1954 (red line), 1989 (yellow line), 2000 (green line), and 2006 (brown line) with background Google satellite image of August 2019. **(Small panel)** Overlap between 1954 CASMEZ cartography and Google satellite image of August 2019.

intervals. Finally, in 21 sample areas, both the advancement and the erosion classes are present. Among these sample areas should be mentioned Cariati and Crotone (Zigari), both in the advancement class in most recent but with only negative values of the shoreline variation rates in all other time intervals, with greater values in Crotone (Zigari). Falerna, on the other hand, is largely in the advancement class in the most recent and in the short-term intervals but with strongly negative values of the shoreline variation rates in all the other time intervals. Finally, in various sample area in the Tyrrhenian coast (Fuscaldo, Cetraro, Sangineto, Belvedere, and Tortora), trends like that of Falerna, but with lower values of shoreline variation rates, are observed. This condition of advancement in the most recent and in the short-term intervals and of erosion in the long-term and in the very long-term time intervals does not imply that the current shoreline is in an advanced position compared to that of the 1950s but simply indicates that, after decades of retreat, the shoreline has recently advanced.

Regarding the shoreline variation rates values, there are significant variations depending on the time interval analyzed. In fact, for very long-term the maximum and minimum values are 0.63 m/year in Badolato and −1.82 m/year in Vibo Marina, respectively. For long-term, the maximum and minimum values are 0.82 m/year in Tropea and −2.37 m/year in Falerna. For middle-term, the maximum and minimum values are 1.04 m/year in Badolato and −2.98 m/year in Falerna. For short-term, the maximum and minimum values are 8.8 m/year in Falerna and −5.49 m/year in Gizzeria. Finally, for most recent the maximum and minimum values are 12.1 m/year in Falerna and −5.7 m/year in Caulonia. Among these results, it should be highlighted the case of Badolato, which reaches the maximum values among all the sample areas both for very long-term and for middle-term, and, above all, the case of Falerna, which reaches both the maximum values, for short-term and most recent, that the minimum values, for long-term and middle-term, among all sample areas.

From a temporal point of view, the sample areas in the erosion classes prevail over those in the advancement class for very long-term, long-term and middle-term while for short-term and most recent the sample areas in the advancement class prevail over those in the erosion classes (**Figures 4**, **5**). Instead, the sample areas in the stability class decrease as the time interval decreases. In fact, for very long-term just 1 sample area is in the advancement class while 13 sample areas are in the erosion classes and 40 sample areas are in the stability class, 12 of which are in the stability+ class and the other 28 are in the stability− class.

FIGURE 8 | Villapiana. **(Large panel)** Baseline (black line) and shorelines of 1954 (red line), 1989 (yellow line), 2000 (green line), and 2012 (orange line) with background Google satellite image of October 2019. **(Small panel)** Overlap between 1954 CASMEZ cartography and Google satellite image of October 2019.

For long-term, the sample areas in the advancement class are 2, the sample areas in the erosion classes are 17 and the sample areas in the stability class are 35, 16 of which are in the stability+ class and the other 19 are in the stability− class. For middle-term, the sample areas in the advancement class are 5, the sample areas in the erosion classes are 21 and the sample areas in the stability class are 28, 12 of which are in the stability+ class and the other 16 are in the stability− class. For short-term, the sample areas in the advancement class are 22, the sample areas in the erosion classes are 13 and the sample areas in the stability class are 19, 10 of which are in the stability+ class and the other 9 are in the stability− class. Finally, for most recent time interval the sample areas in the advancement class are 20, the sample areas in the erosion classes are 17 and the sample areas in the stability class are 17, 9 of which are in the stability+ class and the other 8 are in the stability− class.

DISCUSSION

The results described in the previous section show that the sample areas in the erosion classes prevail over those in the advancement class for very long-term, long-term and middle-term while for short-term and most recent the sample areas in the advancement class prevail over those in the erosion classes. These results were analyzed considering both natural and anthropogenic driving factors which influencing shoreline changes, such as the wave climate, the expansion of the inhabited centers with distruction of dune systems and alteration of landward of the beach, and the construction of ports and hydraulic works. Firstly, a general analysis of these factors was carried out. Subsequently, some sample areas where the effects of these driving factors are more representative have been analyzed in detail.

Regarding the wave climate, the peculiar morphology of Calabria exposes it to very different climatic conditions between the Ionian and the Tyrrhenian coasts. Indeed, the Ionian coasts are mainly exposed to the winds of Scirocco, from South-East, and Grecale, from North-East, while the Tyrrhenian coasts are mainly exposed to the winds of the Mistral, from North-West. Also, the fetch extensions vary from a few tens of kilometers within the Strait of Messina and the Gulf of Taranto to several hundred kilometers along various directions in the Ionian and Tyrrhenian seas. These differences lead to a significant variability of sea storms conditions between the various coastal areas which

FIGURE 9 | Badolato. **(Large panel)** Baseline (black line) and shorelines of 1954 (red line) with background Google satellite image of June 2019. **(Small panel)** Overlap between 1954 CASMEZ cartography and Google satellite image of June 2019.

influences the coastal dynamics. In general, the significant wave heights in the Tyrrhenian Sea reach higher maximum values than in the Ionian Sea but in the Tyrrhenian Sea the sea storms are almost entirely concentrated around the sectors coming from the North-West directions while in the Ionian Sea the sea storms can come from a wide range of sectors, from the South-West to North-East directions.

About anthropogenic driving factors, in the second half of the last century, after the end of the Second World War, many of the Calabrian inhabited centers have considerably expanded, especially near the sea. One effect of this expansion is the reduction of the dune systems extension, that is currently equal to one fifth of that of the 1950s. Consequently, in all coastal municipalities where the dune systems were totally destroyed between the 1950s and today and have been replaced by buildings, infrastructures, promenades, etc., coastal erosion processes are observed (Foti et al., 2022). Another important effect of the expansion of the inhabited centers near the sea concerns the alteration of landward of the beach. In fact, like to dune systems, in many locations the new settlements have been built directly on the beach, significantly reducing their width, as in the case of Tortora which will be shown in detail below. Another anthropogenic driving factor concerns the construction of ports. In fact, in Calabria there are currently about twenty ports, just six of which were also present in the 1950s. In addition, in the post-war period the anthropogenic pressure also affected various Calabrian rivers where many hydraulic works were built such as weir, dams, etc. This works has immobilized significant quantities of sediments especially in the valley parts of the river basins, causing significant shoreline retreats near the river mouths. In fact, a peculiarity of Calabrian rivers is high solid transport, whose variations can alter the coastal dynamics and the shoreline evolution near the river mouths, as shown by Barbaro et al. (2019a) and by Foti et al. (2019) in the case studies of mouths of the Petrace River and of the Sant'Agata River, respectively. The rivers with the greatest retreats near the mouth, comparing the shoreline of the 1950s with the more recent one, are Mesima (over 300 m) near San Ferdinando, and Melito, near Melito Porto Salvo, Petrace, near Palmi, and Allaro, near Caulonia (all three over 200 m) (**Figure 6**). Furthermore, in about 20 Calabrian rivers the maximum retreat exceeds 100 m.

It should be noted that most of the anthropogenic driving factors, such as inhabited center and hydraulic works, date back to the first decades after the end of the Second World War.

FIGURE 10 | Caulonia. **(Large panel)** Baseline (black line) and shorelines of 1954 (red line), 1989 (yellow line), and 2000 (green line) with background Google satellite image of June 2019. **(Small panel)** Overlap between 1954 CASMEZ cartography and Google satellite image of June 2019.

In addition, the very long-term and the long-term trends show a prevalence of erosions or stability and only Badolato shows advancement. As will be better described below, the advancement observed in Badolato is related to the construction of a port, therefore the key factors for understanding the very long-term and the long-term evolutionary trends are anthropogenic.

On the other hand, in the new century the construction of new settlements near the sea with alteration of landward of the beaches, the expansion of existing inhabited centers and the construction of new hydraulic works has significantly reduced compared to the previous period. An important consequence of these reductions is that the amount of sediments immobilized in the river basins is also reduced and the amount of sediments that can reach the river mouths can increase. In addition, the short-term and the most recent trends show a prevalence of advancement. This consideration allows us to hypothesize that the short-term and the most recent trend are mainly related to natural factors that alter the sedimentary balance, such as the action of single sea storms or particularly rainy or dry periods.

Finally, it is useful to consider the possible effects of climate change through an analysis of sea level rise according to IPCC (2013), Nerem et al. (2018), Barbaro et al. (2020), and IPCC (2021). These studies show that the average sea level rise is expected to be about 10 cm in the next 20 years, and about 80 cm in the next 100 years. It should be noted that these are estimated values, affected by various uncertainties and which can be exceeded in the presence of worst-case or even catastrophic scenarios, such as the Antarctic collapse. Considering the beach slope values described above, in most of the sample areas this estimated sea level rise would cause linear retreats of the shorelines of the order of a few tens of meters in the next 100 years. Therefore, even in the absence of worst-case or catastrophic scenarios, these retreats can have a significant impact on the Calabrian coasts.

Some sample areas were analyzed in detail below.

Roseto Capo Spulico is a town in the Gulf of Taranto where the shoreline variation rate is always positive and is an example of an advanced shoreline due to the construction of coastal defense works. In fact, until 2006 the beach width was less than 20 m, with modest variations in the shoreline over the years. Between 2006 and 2012 some groynes were built which caused a beach advance by several tens of meters, up to a maximum of 70 m (**Figure 7**).

Villapiana is another town in the Gulf of Taranto where the shoreline variation rate is always positive and the most recent,

FIGURE 11 | Falerna. **(Large panel)** Baseline (black line) and shorelines of 1954 (red line), 2000 (green line), and 2017 (yellow line) with background Google satellite image of June 2019. **(Small panel)** Overlap between 1954 CASMEZ cartography and Google satellite image of June 2019.

short-term and middle-term trend is advancement. Villapiana is one of the few places where the expansion of the inhabited center took place almost entirely behind the existing dune system and the shoreline is currently advanced up to 30 m compared to that of the 1950s (**Figure 8**).

Badolato is a town of the Ionian Sea whose coastal dynamics have been significantly modified, at the beginning of this century, by the construction of a port in a straight coastal area with high longshore transport, as also shown in previous research (Miduri et al., 2017). Indeed, the analysis of the historical shorelines shows a relevant advance south of the port, with maximum value of about 170 m compared to the shoreline of 1950s, with considerable erosion to the north of the port and with periodic obstructions of the port mouth. The advance and the erosion areas are of the same order of magnitude, so they are balanced, as shown in **Table 2**, and the shoreline variation rate always in advance (**Figure 9**).

Caulonia is a town in the Ionian Sea near the mouth of the Allaro river, which is one of the Calabrian rivers at whose mouth the greatest shoreline retreat has been observed, with a maximum value over 200 m compared to the shoreline of 1950s. These retreats affected about 5 km of coastline, both to the left and to the right of the river mouth, causing the destruction of extensive dune systems (**Figure 10**).

Figure 11 shows the very irregular evolutionary trend of Falerna analyzed in the previous section. This trend is caused by anthropogenic pressure through an alteration of landward of the beach. In detail, between 1954 and 1989 shoreline advancement of up to 70 m are observed. In this period, the inhabited center expanded exclusively behind the promenade, which already existed in 1954. Instead, between 1989 and 2006 a shoreline retreat was observed, with a maximum value of about 60 m in the northern part of the inhabited center. In this period some buildings have been built as well as some parking lots instead of portions of the beach. The process of shoreline retreating continued until 2014, especially in the southern part of the inhabited center, with a maximum value exceeding 100 m respect to 1989. Between 2014 and 2017 there was a stability phase, followed by a new shoreline advancement, especially in the southern part of the inhabited center, with a maximum value exceeding 60 m.

Finally, Tortora represents another example of erosive processes caused by anthropogenic pressure like Falerna. In the 1950s, in fact, the town of Tortora was located only in the

FIGURE 12 | Tortora. **(Large panel)** Baseline (black line) and shorelines of 1954 (red line) with background Google satellite image of October 2019. **(Small panel)** Overlap between 1954 CASMEZ cartography and Google satellite image of October 2019.

hills, while on the coast, there was an extensive dune system, with only a few sporadic buildings. Currently, instead of the dune system, the Tortora Marina town has been built, with a promenade and several buildings built not far from the shoreline. Moreover, the beach width is between 30 and a few meters, decreasing toward the north, and a maximum erosion of about 100 m is observed compared to 1954 (**Figure 12**). In recent years, shoreline advancement has been observed especially in the southern part, which explain the irregular evolutionary trend shown in **Table 2**.

CONCLUSION

The paper describes the shoreline evolutionary trends at different time scale along the Calabrian coasts, a region in southern Italy, in over 50 sample areas with different morphological and anthropogenic characteristics such as presence of inhabited centers, scattered houses, ports, coastal defense works, pocket beach, dune systems, and river mouths. The choice of Calabria as a case study is related to its geomorphological peculiarities and due to its considerable anthropogenic pressures, which have caused extensive erosive processes. In addition, this paper analyzes the main causes of these evolutionary trends and classifies them using a quick index-based methodology for classifying the shoreline evolutionary trend into five classes: advancement, stability, erosion, intense erosion, severe erosion. The new methodology differs from the previous methodologies in the definition of the shoreline variation rate of a fixed area that depends on the variation rate of each transept, evaluated in terms of EPR, on the influence area of each transept and of the sum of the influence areas of all the transepts of the fixed area.

The main result is that the sample areas in the erosion classes prevail over those in the advancement class for very long-term, long-term and middle-term time interval while for short-term and most recent time interval the sample areas in the advancement class prevail over those in the erosion classes. The temporal variability of the evolutionary trend may be related to the considerable anthropogenic pressures that occurred in the second half of the last century for very long-term and long-term time interval, and to natural factors for short-term and most recent time interval.

Future developments of this methodology are foreseen. Indeed, annual updates are needed to consider the new Google

satellite images available. Also, this methodology is part of a new generally index-based coastal risk assessment methodology, developed by the Mediterranea University of Reggio Calabria and the Calabria Region and which is currently in progress. Finally, this methodology is of interest in the field of coastal area planning and management and is easily applicable in any other context as it leads to the rapid analysis of cartographic data from different sources using remote sensing and GIS free software.

DATA AVAILABILITY STATEMENT

The original contributions presented in the study are included in the article/supplementary material, further inquiries can be directed to the corresponding author.

AUTHOR CONTRIBUTIONS

GF, GB, and GCB: conceptualization and data curation. GF, GB, GCB, PM, and PP: methodology, validation, writing—review and editing, and visualization. GF and GCB: software and writing—original draft preparation. GF, GCB, and PM: formal analysis and investigation. GB and PM: resources, supervision, and project administration.GB: funding acquisition. All authors have read and agreed to the published version of the manuscript.

FUNDING

This work was funded by the Public Works Department of Calabria Region.

REFERENCES

Acciarri, A., Bisci, C., Cantalamessa, G., and Di Pancrazio, G. (2016). Anthropogenic influence on recent evolution of shoreline between the Conero Mt. and the Tronto R. mouth (southern Marche. Central Italy). *Catena* 147, 545–555. doi: 10.1016/j.catena.2016.08.018

Allan, J. C., Komar, P. D., and Priest, G. R. (2003). Shoreline variability on the high-energy Oregon coast and its usefulness in erosion-hazard assessments. *J. Coast. Res.* 38, 83–105.

Almar, R., Kestenare, E., Reyns, J., Jouanno, J., Anthony, E., Laibi, R., et al. (2015). Response of the Bight of Benin (Gulf of Guinea, West Africa) coastline to anthropogenic and natural forcing, Part 1: wave climate variability and impacts on the longshore sediment transport. *Cont. Shelf Res.* 110, 48–59. doi: 10.1016/j.csr.2015.09.020

Amrouni, O., Hzami, A., and Heggy, E. (2019). Photogrammetric assessment of shoreline retreat in North Africa: anthropogenic and natural drivers. *ISPRS J. Photogramm. Remote Sens.* 157, 73–92. doi: 10.1016/j.isprsjprs.2019.09.001

Anfuso, G., and Del Pozo, J. ÁM. (2009). Assessment of coastal vulnerability through the use of GIS tools in South Sicily (Italy). *Environ. Manag.* 43, 533–545. doi: 10.1007/s00267-008-9238-8

Anthony, E. J., Almar, R., Besset, M., Reyns, J., Laibi, R., Ranasinghe, R., et al. (2019). Response of the Bight of Benin (Gulf of Guinea, West Africa) coastline to anthropogenic and natural forcing, Part 2: sources and patterns of sediment supply, sediment cells, and recent shoreline change. *Cont. Shelf Res.* 173, 93–103. doi: 10.1016/j.csr.2018.12.006

Barbaro, G. (2013). Saline Joniche: a predicted disaster. *Disaster Adv.* 6, 1–3. doi: 10.1017/dmp.2020.417

Barbaro, G. (2016). Master Plan of solutions to mitigate the risk of coastal erosion in Calabria (Italy), a case study. *Ocean Coast. Manag.* 132, 24–35. doi: 10.1016/j.ocecoaman.2016.08.001

Barbaro, G., Bombino, G., Foti, G., Borrello, M. M., and Puntorieri, P. (2019a). Shoreline evolution near river mouth: case study of Petrace River (Calabria. Italy). *Reg. Stud. Mar. Sci.* 29:100619. doi: 10.1016/j.rsma.2019.100619

Barbaro, G., Foti, G., Nucera, A., Barillà, G. C., Canale, C., Puntorieri, P., et al. (2020). Risk mapping of coastal flooding areas. Case studies: scilla and Monasterace (Italy). *Int. J. Saf. Secur. Eng.* 10, 59–67. doi: 10.18280/ijsse.100108

Barbaro, G., Foti, G., Sicilia, C. L., and Malara, G. (2014b). A formula for the calculation of the longshore sediment transport including spectral effects. *J. Coast. Res.* 30, 961–966. doi: 10.2112/jcoastres-d-13-00131.1

Barbaro, G., Foti, G., and Sicilia, C. L. (2014a). Coastal erosion in the South of Italy. *Disaster Adv.* 7, 37–42.

Barbaro, G., Petrucci, O., Canale, C., Foti, G., Mancuso, P., and Puntorieri, P. (2019b). "Contemporaneity of floods and storms. A case study of Metropolitan Area of Reggio Calabria in Southern Italy," in *New Metropolitan Perspectives (NMP) (Reggio Calabria, Italy), Smart Innovation, Systems and Technologies*, Vol. 101, eds F. Calabrò, L. Della Spina, and C. Bevilacqua (Cham: Springer), 614–620. doi: 10.1007/978-3-319-92102-0_66

Barnard, P. L., Short, A. D., Harley, M. D., Splinter, K. D., Vitousek, S., Turner, I. L., et al. (2015). Coastal vulnerability across the Pacific dominated by El Nino/Southern oscillation. *Nat. Geosci.* 8, 801–807. doi: 10.1038/ngeo2539

Besset, M., Anthony, E. J., and Bouchette, F. (2019). Multi-decadal variations in delta shorelines and their relationship to river sediment supply: an assessment and review. *Earth Sci. Rev.* 193, 199–219. doi: 10.1016/j.earscirev.2019.04.018

Bird, E. (2018). "). Coastline changes," in *Encyclopedia of Coastal Science. Encyclopedia of Earth Sciences Series*, eds C. Finkl and C. Makowski (Cham: Springer), doi: 10.1007/978-3-319-48657-4_93-2

Boak, E. H., and Turner, I. L. (2005). Shoreline definition and detection: a review. *J. Coast. Res.* 21, 688–703. doi: 10.2112/03-0071.1

Bruno, M. F., Saponieri, A., Molfetta, M. G., and Damiani, L. (2020). The DPSIR approach for coastal risk assessment under climate change at regional scale: the case of apulian coast (Italy). *J. Mar. Sci. Eng.* 8:531. doi: 10.3390/jmse8070531

Canale, C., Barbaro, G., Foti, G., Petrucci, O., Besio, G., and Barillà, G. C. (2021). Bruzzano river mouth damage to meteorological events. *Int. J. River Basin Manag.* 1–17. doi: 10.1080/15715124.2021.1901725

Canale, C., Barbaro, G., Petrucci, O., Fiamma, V., Foti, G., Barillà, G. C., et al. (2020). Analysis of floods and storms: concurrent conditions. *Ital. J. Eng. Geol. Environ.* 1, 23–29. doi: 10.1016/j.envpol.2018.01.104

Dada, O. A., Li, G., Qiao, L., Asiwaju-Bello, Y. A., and Anifowose, A. Y. B. (2018). Recent Niger Delta shoreline response to Niger River Hydrology: conflicts between forces of Nature and Humans. *J. Afr. Earth Sci.* 139, 222–231. doi: 10.1016/j.jafrearsci.2017.12.023

Dada, O. A., Qiao, L., Ding, D., Li, G., Ma, Y., and Wang, L. (2015). Evolutionary trends of the Niger Delta shoreline during the last 100 years: responses to rainfall and river discharge. *Mar. Geol.* 367, 202–211. doi: 10.1016/j.margeo.2015.06.007

Del Rio, L., and Garcia, F. J. (2013). Error determination in the photogrammetric assessment of shoreline changes. *Natural Hazard.* 65, 238–2397. doi: 10.1007/s11069-012-0407-y

Duarte, C. R., De Miranda, F. P., Landau, L., Souto, M. V. S., Sabadia, J. A. B., Da Silva, C. A., et al. (2018). Short-time analysis of shoreline based on RapidEye satellite images in the terminal area of Pecem Port, Ceara, Brazil. *Int. J. Remote Sens.* 39, 4376–4389. doi: 10.1080/01431161.2018.1457229

Ferreira Silva, S., Martinho, M., Capitao, R., Reis, T., Fortes, C. J., and Ferreira, J. C. (2017). An index-based method for coastal-flood risk assessment in low-lying areas (Costa de Caparica. Portugal). *Ocean Coast. Manag.* 144, 90–104. doi: 10.1016/j.ocecoaman.2017.04.010

Fiori, E., Comellas, A., Molini, L., Rebora, N., Siccardi, F., Gochis, D. J., et al. (2014). Analysis and hindcast simulations of an extreme rainfall event in the Mediterranean area: the Genoa 2011 case. *Atmosp. Res.* 138, 13–29. doi: 10.1016/j.atmosres.2013.10.007

Foti, G., Barbaro, G., Barillà, G. C., and Frega, F. (2022). Effects of anthropogenic pressures on dune systems—case study: calabria (Italy). *J. Mar. Sci. Eng.* 10:10. doi: 10.3390/jmse10010010

Foti, G., Barbaro, G., Bombino, G., Fiamma, V., Puntorieri, P., Minniti, F., et al. (2019). Shoreline changes near river mouth: case study of Sant'Agata River

(Reggio Calabria, Italy). *Eur. J. Remote Sens.* 52(Suppl.4), 102–112. doi: 10.1080/22797254.2019.1686955

Foti, G., Barbaro, G., Manti, A., Foti, P., La Torre, A., Geria, P. F., et al. (2020a). A methodology to evaluate the effects of river sediment withdrawal: the case study of the Amendolea River in Southern Italy. *Aquat. Ecosyst. Health Manag.* 23:465. doi: 10.1080/14634988.2020.1807248

Foti, G., Barillà, G. C., Barbaro, G., and Puntorieri, P. (2020b). Remote sensing and GIS to support coastal erosion risk analysis in Calabria (Italy). *WIT Trans. Eng. Sci.* 129, 67–76. doi: 10.2495/risk200061

Goncalves, R. M., Saleem, A., Queiroz, H. A., and Awange, J. L. (2019). A fuzzy model integrating shoreline changes, NDVI and settlement influences for coastal zone human impact classification. *Appl. Geogr.* 113:102093. doi: 10.1016/j.apgeog.2019.102093

Görmüş, T., Ayat, B., Aydoğan, B., and Tătui, F. (2021). Basin scale spatiotemporal analysis of shoreline change in the Black Sea. *Estuar. Coast. Shelf Sci.* 252:107247. doi: 10.1016/j.ecss.2021.107247

Hagenaars, G., de Vries, S., Luijendijk, A. P., de Boer, W. P., and Reniers, A. J. H. M. (2018). On the accuracy of automated shoreline detection derived from satellite imagery: a case study of the Sand Motor mega-scale nourishment. *Coast. Eng.* 133, 113–125. doi: 10.1016/j.coastaleng.2017.12.011

Hapke, C. J., Himmelstoss, E. A., Kratzmann, M. G., List, J. H., and Thieler, E. R. (2010). *National Assessment of Shoreline Change: Historical Shoreline Change along the New England and Mid-Atlantic Coasts. Open-File Report 1118*. Reston, VA: US Geological Survey, doi: 10.3133/ofr20101118

Harley, M. D., Turner, I. L., Kinsela, M. A., Middleton, J. H., Mumford, P. J., Splinter, K. D., et al. (2017). Extreme coastal erosion enhanced by anomalous extratropical storm wave direction. *Sci. Rep.* 7:6033. doi: 10.1038/s41598-017-05792-1

IPCC (2013). "Climate change 2013: the physical science basis," in *Contribution of Working Group I to the Fifth Assessment Report of the Intergovernmental Panel on Climate Change*, eds T. F. Stocker, D. Qin, G.-K. Plattner, M. Tignor, S. K. Allen, J. Boschung, et al. (Cambridge: Cambridge University Press).

IPCC (2021). "Summary for Policymakers," in *Climate Change 2021: The Physical Science Basis. Working Group I contribution to the Sixth Assessment Report of the Intergovernmental Panel on Climate Change*, eds V. Masson-Delmotte, P. Zhai, A. Pirani, S. L. Connors, C. Péan, S. Berger, et al. (Cambridge: Cambridge University Press).

Istituto Idrografico della Marina (2020). *Tavole di Marea e Delle Correnti di Marea*. Genova: Istituto Idrografico della Marina Italiana.

Jaranovic, B., Trindade, J., Ribeiro, J., and Silva, A. (2017). Using a coastal storm hazard index to assess storm impacts in Lisbon. *Int. J. Saf. Secur. Eng.* 7, 221–233. doi: 10.2495/safe-v7-n2-221-233

Kantamaneni, K., Phillips, M., Thomas, T., and Jenkins, R. (2018). Assessing coastal vulnerability: development of a combined physical and economic index. *Ocean Coast. Manag.* 158, 164–175. doi: 10.1016/j.ocecoaman.2018.03.039

Komar, P. D. (2000). Coastal erosion–underlying factors and human impacts. *Shore Beach* 68, 3–16.

Konlechner, T. M., Kennedy, D. M., O'Grady, J. J., Leach, C., Ranasinghe, R., Carvalho, R. C., et al. (2020). Mapping spatial variability in shoreline change hotspots from satellite data; a case study in southeast Australia. *Estuar. Coast. Shelf Sci.* 246:107018. doi: 10.1016/j.ecss.2020.107018

Kroon, A., de Schipper, M. A., van Gelder, P. H. A. J. M., and Aarninkhof, S. G. J. (2020). Ranking uncertainty: wave climate variability versus model uncertainty in probabilistic assessment of coastline change. *Coast. Eng.* 158:103673. doi: 10.1016/j.coastaleng.2020.103673

Le Mauff, B., Juigner, M., Ba, A., Robin, M., Launeau, P., and Fattal, P. (2018). Coastal monitoring solutions of the geomorphological response of beach-dune systems using multi-temporal LiDAR datasets (Vendée coast. France). *Geomorphology* 304, 121–140. doi: 10.1016/j.geomorph.2017.12.037

Li, X., Zhou, Y., Zhang, L., and Kuang, R. (2014). Shoreline change of Chongming Dongtan and response to river sediment load: a remote sensing assessment. *J. Hydrol.* 511, 432–442. doi: 10.1016/j.jhydrol.2014.02.013

Luijendijk, A., Hagenaars, G., Ranasinghe, R., Baart, F., Donchyts, G., and Aarninkhof, S. (2018). The state of the world's beaches. *Sci. Rep.* 8:6641. doi: 10.1038/s41598-018-24630-6

Maanan, M., and Robin, M. (2010). *Geomatic Solutions for Coastal Environments*. Hauppauge, NY: Nova Science Pub Inc.

Maiti, S., and Bhattacharya, A. K. (2009). Shoreline change analysis and its application to prediction: a remote sensing and statistics based approach. *Mar. Geol.* 257, 11–23. doi: 10.1016/j.margeo.2008.10.006

Mao, Y., Harris, D. L., Xie, Z., and Phinn, S. (2021). Efficient measurement of large-scale decadal shoreline change with increased accuracy in tide-dominated coastal environments with Google Earth Engine. *ISPRS J. Photogramm. Remote Sens.* 181, 385–399. doi: 10.1016/j.isprsjprs.2021.09.021

Mavromatidi, A., Briche, E., and Claeys, C. (2018). Mapping and analyzing socio-environmental vulnerability to coastal hazards induced by climate change: an application to coastal Mediterranean cities in France. *Cities* 72, 189–200. doi: 10.1016/j.cities.2017.08.007

McLaughlin, S., and Cooper, J. A. G. (2010). A multi-scale coastal vulnerability index: a tool for coastal managers? *Environ. Hazards* 9, 233–248. doi: 10.3763/ehaz.2010.0052

Mentaschi, L., Vousdoukas, M. I., Pekel, J. F., Voukouvalas, E., and Feyen, L. (2018). Global long-term observations of coastal erosion and accretion. *Sci. Rep.* 8:12876. doi: 10.1038/s41598-018-30904-w

Miduri, M., Foti, G., and Puntorieri, P. (2017). "Impact generated by Marina of Badolato (Italy) on adjacent coast," in *In Proceedings of the 13th International Congress on Coastal and Marine Sciences, Engineering, Management and Conservation MEDCOAST*, Vol. 2 (Mellieha), 935–945.

Mills, J. P., Buckley, S. J., Mitchell, H. L., Clarke, P. J., and Edwards, J. (2005). A geomatics data integration technique for coastal change monitoring. *Earth Surf. Process. Landf.* 30, 651–664. doi: 10.1002/esp.1165

Mucerino, L., Albarella, M., Carpi, L., Besio, G., Benedetti, A., Corradi, N., et al. (2019). Coastal exposure assessment on Bonassola bay. *Ocean Coast. Manag.* 167, 20–31. doi: 10.1016/j.ocecoaman.2018.09.015

Narra, P., Coelho, C., Sancho, F., and Palalane, J. (2017). CERA: an open-source tool for coastal erosion risk assessment. *Ocean Coast. Manag.* 142, 1–14. doi: 10.1016/j.ocecoaman.2017.03.013

Nerem, R. S., Beckley, B. D., Fasullo, J. T., Hamlington, B. D., Masters, D., and Mitchum, G. T. (2018). Climate-change–driven accelerated sea-level rise detected in the altimeter era. *Proc. Natl. Acad. Sci. U.S.A.* 115, 2022–2025. doi: 10.1073/pnas.1717312115

Ngowo, R. G., Ribeiro, M. C., and Pereira, M. J. (2021). Quantifying 28-year (1991–2019) shoreline change trends along the Mnazi Bay–Ruvuma Estuary Marine Park, Tanzania. *Remote Sens. Appl. Soc. Environ.* 23:100607. doi: 10.1016/j.rsase.2021.100607

Nicolae-Lerma, A., Ayache, B., Ulvoas, B., Paris, F., Bernon, N., Bultreau, T., et al. (2019). Pluriannual beach-dune evolutions at regional scale: erosion and recovery sequences analysis along the Aquitaine coast based on airborne LiDAR data. *Cont. Shelf Res.* 189:103974. doi: 10.1016/j.csr.2019.103974

Ozpolat, E., and Demir, T. (2019). The spatiotemporal shoreline dynamics of a delta under natural and anthropogenic conditions from 1950 to 2018: a dramatic case from the Eastern Mediterranean. *Ocean Coast. Manag.* 180:104910. doi: 10.1016/j.ocecoaman.2019.104910

Pantusa, D., D'Alessandro, F., Riefolo, L., Principato, F., and Tomasicchio, G. R. (2018). Application of a coastal vulnerability index. A case study along the Apulian Coastline, Italy. *Water* 10:1218. doi: 10.3390/w10091218

Prumm, M., and Iglesias, G. (2016). Impacts of port development on estuarine morphodynamics: Ribadeo (Spain). *Ocean Coast. Manag.* 130, 58–72. doi: 10.1016/j.ocecoaman.2016.05.003

Qiao, G., Mi, H., Wang, W., Tong, X., Li, Z., Li, T., et al. (2018). 55-year (1960–2015) spatiotemporal shoreline change analysis using historical DISP and Landsat time series data in Shanghai. *Int. J. Appl. Earth Obs. Geoinform.* 68, 238–251. doi: 10.1016/j.jag.2018.02.009

Ramieri, E., Hartley, A., Barbanti, A., Santos, F. D., Gomes, A., Hilden, M., et al. (2012). Estimating coastal recession due to sea level rise: beyond the Bruun rule. *Clim. Chang.* 110, 561–574. doi: 10.1007/s10584-011-0107-8

Ranasinghe, R., McLoughlin, R., Short, A., and Symonds, G. (2004). The Southern Oscillation Index, wave climate, and beach rotation. *Mar. Geol.* 204, 273–287. doi: 10.1016/s0025-3227(04)00002-7

Sabato, L., and Tropeano, M. (2014). Fiumara: a kind of high hazard river. *Phys. Chem. Earth* 29, 707–715. doi: 10.1016/j.pce.2004.03.008

Sannino, G., Carillo, A., Pisacane, G., and Naranjo, C. (2015). On the relevance of tidal forcing in modeling the Mediterranean thermohailine circulation. *Prog. Oceanogr.* 134, 304–329. doi: 10.1016/j.pocean.2015.03.002

Santini, M. (2011). Methods for assessing coastal vulnerability to climate change. *ETC CCA Techn. Pap.* 1, 1–93.

Satta, A., Puddu, M., Venturini, S., and Giupponi, C. (2017). Assessment of coastal risks to climate change related impacts at regional scale: the case of Mediterranean region. *Int. J. Disaster Risk Reduct.* 24, 284–296. doi: 10.1016/j.ijdrr.2017.06.018

Satta, A., Snoussi, M., Puddu, M., Flayou, L., and Hoult, R. (2016). An index-based method to assess risks of climate-related hazards in coastal zones: the case of Tetouan. *Estuar. Coast. Shelf Sci.* 175, 93–105. doi: 10.1016/j.ecss.2016.03.021

Short, A. D., and Trembanis, A. C. (2004). Decadal scale patterns in beach oscillation and rotation Narrabeen Beach, Australia—time series, PCA and wavelet analysis. *J. Coast. Res.* 202, 523–532. doi: 10.2112/1551-5036(2004)020[0523:dspibo]2.0.co;2

Sorriso-Valvo, M., and Terranova, O. (2006). The Calabrian fiumara streams. *Z. Geomorphol.* 143, 109–125.

Thomas, T., Phillips, M. R., Williams, A. T., and Jenkins, R. E. (2011). Short-term beach rotation, wave climate and the North Atlantic Oscillation (NAO). *Prog. Phys. Geogr. Earth Environ.* 35, 333–352. doi: 10.1177/0309133310397415

Tomasicchio, G. R., D'Alessandro, F., Barbaro, G., Musci, E., and De Giosa, T. M. (2015). Longshore transport at shingle beaches: an independent verification of the general model. *Coast. Eng.* 104, 69–75. doi: 10.1016/j.coastaleng.2015.07.003

Torresan, S., Critto, A., Rizzi, J., and Marcomini, A. (2012). Assessment of coastal vulnerability to climate change hazards at the regional scale: the case study of the North Adriatic Sea. *Natural Hazards Earth Syst. Sci.* 12, 2347–2368. doi: 10.5194/nhess-12-2347-2012

Toure, S., Diop, O., Kpalma, K., and Maiga, A. S. (2019). Shoreline detection using optical remote sensing: a review. *ISPRS Int. J. GeoInform.* 8:75. doi: 10.3390/ijgi8020075

Turner, I. L. (2006). Discriminating Modes of Shoreline Response to Offshore-Detached Structures. *J. Waterway Port Coast. Ocean Eng.* 132, 180–191. doi: 10.1061/(asce)0733-950x2006132:3(180)

Valsamidis, A., and Reeve, D. E. (2017). Modelling shoreline evolution in the vicinity of a groyne and a river. *Cont. Shelf Res.* 132, 49–57. doi: 10.1016/j.csr.2016.11.010

Viavattene, C., Jiménez, J. A., Ferreira, O., Priest, S., Owen, D., and McCall, R. (2018). Finding coastal hotspots of risk at the regional scale: the coastal risk assessment framework. *Coast. Eng.* 134, 33–47. doi: 10.1016/j.coastaleng.2017.09.002

Vos, K., Harley, M. D., Splinter, K. D., Simmons, J. A., and Turner, I. L. (2019). Sub-annual to multi-decadal shoreline variability from publicly available satellite imagery. *Coast. Eng.* 150, 160–174. doi: 10.1016/j.coastaleng.2019.04.004

Wang, J., Zhou, W., Pickett, S. T., Yu, W., and Li, W. (2019). A multiscale analysis of urbanization effects on ecosystem services supply in an urban megaregion. *Sci. Total Environ.* 662, 824–833. doi: 10.1016/j.scitotenv.2019.01.260

Williams, A. T., Rangel-Buitrago, N., Pranzini, E., and Anfuso, G. (2018). The management of coastal erosion. *Ocean Coast. Manag.* 156, 4–20. doi: 10.1016/j.ocecoaman.2017.03.022

Yang, Z., Wang, T., Voisin, N., and Copping, A. (2015). Estuarine response to river flow and sea-level rise under future climate change and human development. *Estuar. Coast. Shelf Sci.* 156, 19–30. doi: 10.1016/j.ecss.2014.08.015

Zellou, B., and Rahali, H. (2019). Assessment of the joint impact of extreme rainfall and storm surge on the risk of flooding in a coastal area. *J. Hydrol.* 569, 647–665. doi: 10.1016/j.jhydrol.2018.12.028

Zema, D. A., Bombino, G., Boix-Fayos, C., Tamburino, V., Zimbone, S. M., and Fortugno, D. (2014). Evaluation and modeling of scouring and sedimentation around check dams in a Mediterranean torrent in Calabria, Italy. *J. Soil Water Conserv.* 69, 316–329. doi: 10.2489/jswc.69.4.316

Zhai, T., Wang, J., Fang, Y., Qin, Y., Huang, L., and Chen, Y. (2020). Assessing ecological risks caused by human activities in rapid urbanization coastal areas: towards an integrated approach to determining key areas of terrestrial-oceanic ecosystems preservation and restoration. *Sci. Total Environ.* 708:135153. doi: 10.1016/j.scitotenv.2019.135153

Zhang, R., Chen, L., Liu, S., Zhang, H., Gong, W., and Lin, G. (2019). Shoreline evolution in an embayed beach adjacent to tidal inlet: the impact of anthropogenic activities. *Geomorphology* 346:106856. doi: 10.1016/j.geomorph.2019.106856

Conflict of Interest: The authors declare that the research was conducted in the absence of any commercial or financial relationships that could be construed as a potential conflict of interest.

Publisher's Note: All claims expressed in this article are solely those of the authors and do not necessarily represent those of their affiliated organizations, or those of the publisher, the editors and the reviewers. Any product that may be evaluated in this article, or claim that may be made by its manufacturer, is not guaranteed or endorsed by the publisher.

frontiers | Frontiers in Marine Science

ORIGINAL RESEARCH
published: 14 April 2022
doi: 10.3389/fmars.2022.845348

Multicriteria Decision Analysis to Assist in the Selection of Coastal Defence Measures: Involving Coastal Managers and Professionals in the Identification and Weighting of Criteria

Philippe Sauvé[1,2*], *Pascal Bernatchez*[1,2,3] *and Mathias Glaus*[4]

[1] Chaire de recherche en géosciences côtières, Université du Québec à Rimouski, Rimouski, QC, Canada, [2] Québec-Océan, Université Laval, Québec, QC, Canada, [3] Centre d'études Nordiques (CEN), Université du Québec à Rimouski, Rimouski, QC, Canada, [4] Laboratoire de la STEPPE-ETS, École de technologie supérieure, Montréal, QC, Canada

OPEN ACCESS

Edited by:
Giuseppe Barbaro,
Mediterranea University of Reggio Calabria, Italy

Reviewed by:
Nikša Jajac,
University of Split, Croatia
Jonathan Pearson,
University of Warwick, United Kingdom

***Correspondence:**
Philippe Sauvé
philippe.sauve@uqar.ca

Specialty section:
This article was submitted to Coastal Ocean Processes, a section of the journal Frontiers in Marine Science

Received: 29 December 2021
Accepted: 21 March 2022
Published: 14 April 2022

Citation:
Sauvé P, Bernatchez P and Glaus M (2022) Multicriteria Decision Analysis to Assist in the Selection of Coastal Defence Measures: Involving Coastal Managers and Professionals in the Identification and Weighting of Criteria. Front. Mar. Sci. 9:845348. doi: 10.3389/fmars.2022.845348

Coastal socio-ecological systems are complex adaptive systems with nonlinear changing properties and multi-scale dynamics. They are influenced by unpredictable coastal hazards accentuated by the effects of climate change, and they can quickly be altered if critical thresholds are crossed. Additional pressures come from coastal activities and development, both of which attracting stakeholders with different perspectives and interests. While coastal defence measures (CDMs) have been implemented to mitigate coastal hazards for centuries, a lack of knowledge and tools available to make informed decision has led to coastal managers favouring the choice of seawalls or rock armours with little consideration for socio-ecological systems features, and stakeholders' priorities. Though it is not currently widely applied in coastal zone management, multicriteria decision analysis (MCDA) is a tool that can be useful to facilitate decision making. PROMETHEE, an outranking method, was chosen to support the multicriteria decision analysis for the evaluation of CDMs in the context of four study sites characterized by distinct environmental features. The aim was to determine the relevance and benefits of a MCDA by integrating coastal zone stakeholders in a participatory decision-making process in order to select CDMs that are better adapted to the whole socio-ecological system. First, in a series of five workshops, stakeholders were asked to identify and weigh criteria that were relevant to their local conditions. Second and third, CDMs were evaluated in relation to each criterion within the local context, then, hierarchized. Initial results show that vegetation came first in three of the four sites, while rock armour ranked first in the fourth site. A post-evaluation of the participatory process indicated that the

weighting phase is an effective way to integrate local knowledge into the decision-making process, but the identification of criteria could be streamlined by the presentation of a predefined list from which participants could make a selection. This would ensure criteria that are standardized, and in a format that is compatible with the MCDA. Coupled with a participatory process MCDA proved to be a flexible methodology that can synthetize multiple aspects of the problem, and contribute in a meaningful way to the coastal engineering and management decision-making process.

Keywords: coastal engineering, coastal defence measure, decision-making, integrated coastal zone management (ICZM), participatory process, coastal protection, multicriteria decision analysis (MCDA), PROMETHEE

1 INTRODUCTION

In most regions of the world, the economic and social benefits in coastal zones tend to increase when population grows together with industrial and recreational activities (Airoldi et al., 2005; Dugan et al., 2011; Gittman et al., 2015). This attracts stakeholders with different perspectives and interests. As any socio-ecological system, coastal environments are complex adaptive systems with nonlinear changing properties and multi-scale dynamics that can be quickly and even irreversibly altered if critical thresholds are crossed. They are affected by multiple drivers of change, and subject to reciprocal feedbacks between social and natural components (Holling and Gunderson, 2002; Gallopín, 2006; Folke, 2016). Coastal systems are also influenced by uncertain coastal hazards, such as erosion and flooding, which are accentuated by the effects of climate change (Nicholls and Cazenave, 2010; Church and White, 2011; Wong et al., 2014; Ranasinghe, 2016).

Coastal defence measures (CDMs) have been implemented to mitigate coastal hazards ever since the establishment of human settlements in coastal zones (Charlier et al., 2005). In the last decades, coastal zone development and the effects of climate change have led to an increase in shoreline armouring, mainly through the implementation of hard coastal defence structures (seawalls and rock armours) (Bernatchez and Fraser, 2012; Sauvé et al., 2020), which can have a significant impact on coastal socio-ecological systems (Moschella et al., 2005; Dugan et al., 2011). In the Canadian province of Quebec, on the coasts of the St. Lawrence Estuary and Gulf, coastal defence structures were implemented as emergency measures, between the 1980s and the early 2000s, and it is still the case today, though to a lesser extent (Boyer-Villemaire et al., 2015). A lack of knowledge and tools available to make informed decisions has led to coastal managers favouring the choice of seawalls or rock armours over other types of CDMs (Friesinger and Bernatchez, 2010; Drejza et al., 2011; Marie et al., 2017). In addition, incomplete scientific knowledge with regard to CDMs effects on different types of coasts, an imbalance in scientific studies worldwide (Sauvé et al., 2022), and uncertainties brought about by varying climate projections (Polasky et al., 2011), all add complexity to the decision-making process, and most certainly play a part in the reluctance by coastal managers to explore lesser known alternatives.

Knowledge and learning process are key to improving the resilience of coastal socio-ecological systems, and overcoming difficulties and uncertainties associated with the complex, and sometimes conflictual environmental management issues (Folke et al., 2005; Garmendia et al., 2010; Koontz et al., 2015). Decision-making, traditionally the sole responsibility of scientists and experts, today tends to involve different stakeholders in an attempt to improve the transparency and flexibility of the process, and to implement measures that are better adapted to the whole socio-ecological system (Reed, 2008; Garmendia et al., 2010; Jones et al., 2014; Marttunen et al., 2017). A participatory process, implemented at an early stage by combining local interests and needs with scientific knowledge, leads to interventions that are better adapted to local socio-cultural and environmental conditions, and allows easier and more accurate monitoring and managing of environmental changes by local communities (Reed, 2008; Jacob et al., 2021).

The decision-making process can also be enhanced by the use of decision support systems which are developed to improve the understanding of complex problems (Westmacott, 2001; National Research Council, 2009). Multicriteria decision analysis (MCDA) is one of the support systems used to facilitate decision making in cases where a variety of alternatives are possible, and depend on multiple and sometimes conflicting criteria. It is based on a pairwise comparison between different alternatives rated against every criterion from a set of pre-defined decision criteria (Scott et al., 2012; Marttunen et al., 2017). Criteria are parameters used to assess how each scenario would contribute to the achievement of a project objective (André et al., 2010). The criteria cover multiple aspects of the issue, while taking into consideration the needs and expectations of local stakeholders (Garmendia et al., 2010). Within the decision-making process, once the problem, the context, and the objective have been established, MCDA is applied, and generally consists of three steps: criteria identification and weighting; scenario evaluation according to each criterion; and scenarios hierarchization (Dodgson et al., 2009). The aim of criteria identification is to select a complete set of criteria that are mutually independent, without duplication, applicable to the local context, and consistent with effects occurring over time (De Bruin et al., 2009). In the scientific literature, criteria identification is typically undertaken by scientists or experts (e.g. Monterroso et al., 2011; Trutnevyte et al., 2011; Chang et al., 2012) or, in more advanced participatory processes, by stakeholders through

questionnaires, workshops, etc. (e.g. Stagl, 2006; Garmendia et al., 2010; Antunes et al., 2011; Garmendia and Gamboa, 2012; Trutnevyte et al., 2012). Criteria weighting can be defined as the measure of the importance of criteria according to stakeholders, experts, and scientists (Stagl, 2006; Garmendia and Gamboa, 2012). A group of stakeholders can agree on a set of criteria without attaching the same importance to each criterion (Garmendia and Gamboa, 2012). For the evaluation of scenarios according to each criterion, and for the scenarios hierarchization, MCDA can be divided into three types of methodology: complete aggregation methods, outranking methods, and iterative, trial-error methods (Maystre et al., 1994; Gamper and Turcanu, 2007; André et al., 2010). Complete aggregation methods allow the comparison of scenarios by aggregating all criteria into a single, synthetized, and exhaustive performance vector (André et al., 2010). Outranking methods, through a preferential reference system, compare scenarios against a set of predefined criteria (Gamper and Turcanu, 2007; André et al., 2010). Iterative, trial-error methods are based on a process that explores the feasibility of scenarios as discussed in successive dialogues with decision-makers (Gamper and Turcanu, 2007). Outranking methods are best suited to holistic land management because they take into account all stakeholders concerns, and integrate them into the analysis (Garmendia and Gamboa, 2012). MCDA outranking methods, such as PROMETHEE and ELECTRE, are generally applied to solve discrete choice problems by focusing on pairwise comparisons between different options (Belton and Stewart, 2002).

While MCDA has been used in many environmental management contexts (Gamper and Turcanu, 2007; Ananda and Herath, 2009) and in engineering problem solving in a marine context (Tavra et al., 2017; Zafirakou et al., 2018; Jajac et al., 2019; Abdel-Basset et al., 2021), to the authors' knowledge, it has not been applied to the evaluation and hierarchization of CDMs. From the review of scientific literature, it appears that cost-benefit analysis (CBA) has been the only decision support system used in such context (Polomé et al., 2005). CBA is based on the evaluation of alternatives in terms of monetary units. It is fairly intuitive and straightforward for some aspects of the coastal system, but it is not appropriate or sophisticated enough when intangible and non-monetary characteristics, like aesthetic values or ecological impacts, are criteria identified as important factors in the decision-making process. The process of monetization leads to giving a monetary value to social or environmental non-market components (McCauley, 2006; Chan et al., 2012; Bryce et al., 2016). In contrast, MCDA is based on evaluation units that are specific to each of the selected criterion, which is one of the reasons why several European Union countries and United Nations' documents recommend the use of MCDA rather than CBA (Gamper and Turcanu, 2007).

Based on the results of an extensive participatory process held in Eastern Quebec, the aim of the present study is to determine the relevance of a multi-criteria decision analysis (MCDA) as a tool to structure and analyze a complex problem related to the selection of CDMs, while taking into account their effect on the socio-ecological system. The study also aims at assessing the benefits of a participatory decision-making process, which involves coastal zone managers and professionals in the identification and weighting of criteria used for the selection of coastal defence measures.

2 METHODS

2.1 Study Sites

The studies were carried out in the Canadian province of Quebec, on the coasts of the Estuary and Gulf of St. Lawrence (EGSL). Four municipalities, characterised by distinct geomorphological, hydrodynamic, ecological or socio-economic features (**Figure 1**), were selected as study sites: Pessamit, Gallix (Sept-Îles), Cap-des-Rosiers (Gaspé), and Baie-des-Capucins (Cap-Chat) (**Figure 2**).

2.2.1 Pessamit

Pessamit is an indigenous community located on the North Shore of the St. Lawrence maritime estuary. Pessamit's coast, which extends over a 12 km span, is mainly composed of unconsolidated cliffs (53.7%), littoral spit (21.0%), salt marsh (20.7%), and beach terrace (4.6%). The tidal range is mesotidal and the offshore significant wave height (95^{th} percentile) is 0.85 m (depth of 132 m). The study site is located on a sandy littoral spit. A wide unvegetated sandy foreshore is present in front of the coast. The study site is a part residential, and part public sector, highly frequented by the local community for a variety of uses and activities: off-road vehicles, boat launching, gatherings, walking, beach activities, archeological site, waterfowl concentration area, etc.

2.1.2 Gallix (Sept-Îles)

Sept-Îles is located on the North Shore of the Gulf of St. Lawrence. The study site, Gallix, is located in the Sainte-Marguerite Bay, which extends along 26.90 km, and is mainly composed of littoral spit (10.4 %), unconsolidated cliff (47.0 %), beach terrace (41.8 %), and rocky shore (0.8 %). The tidal range is mesotidal and the offshore significant wave height (95^{th} percentile) is 0.75 m (depth of 90 m) (Corriveau et al., 2021). The study site is located on a sandy beach terrace, and is characterised by the formation and disappearance of a sandy triangular salient (**Figure 3**). This dynamic is generated by estuarian currents and littoral drift. Storm events, between 2009 and 2017, have caused high shoreline retreat (7.96 m/yr), leading to a shoreline enlargement on the west side of the coastal sector (**Figure 3**). A new salient slightly to the east was formed between 2013 and 2016, and was still present in 2017. That new salient modifies the longitudinal sediment transport processes, leading to an offshore sediment deviation. Sediments are redirected towards the coast, further to the West, resulting in a sediment progradation in the coastal sectors (Corriveau et al., 2019). A rock armour structure is present between the salient formed in 2013-2016, and the high shoreline retreat sector (**Figure 3**). The sandy lower foreshore is partially covered (0-25 %) by a narrow band of macroalgua (mainly *laminaria*

FIGURE 1 | Study sites. **(A)** Pessamit: indigenous community located on a sandy littoral spit with wide unvegetated sandy foreshore. **(B)** Sept-Îles (Gallix): sandy beach terrace with a narrow band of sea cabbage characterised by the formation and disappearance of a sandy triangular salient. **(C1, C2)** Cap-Chat (Baie-des-Capucins): beach terrace of coarse sand, cobbles and pebbles, fronted by a wide vegetated salt marsh. **(D1, D2)** Gaspé (Cap-des-Rosiers): rocky cliff with an unconsolidated top and a lower foreshore of cobbles partially covered by rockweeds.

longicruris). A bar system is also present in front of the study site. The study site is a residential sector, with high scenic and socio-cultural values, and is mainly used by the local community for fishing, nautical and beach activities, gatherings, walking, etc. It is also a waterfowl concentration area, and spawning ground for capelin.

2.1.3 Baie-des-Capucins (Cap-Chat)

Cap-Chat is located on the Gaspé Peninsula on the south shore of the St. Lawrence river. Baie-des-Capucins, a bay located east of Cap-Chat, extends over approximately 3.2 km, and is mainly composed of beach terrace (54.4 %), unconsolidated cliff (15.0 %), rocky cliff (10.3 %), and salt marsh (8.1 %). The study site is located on a beach terrace composed of a mixture of coarse sand, cobbles and pebbles, and by a wide salt marsh vegetated with *spartina alterniflora*. The bay's entrance is partially (1-25%) vegetated with *Zostera marina* and *Fucus* sp. The tidal range is mesotidal and the wave energy is low. The littoral drift is directed towards the inside of the bay. The site is a biodiversity hotspot, and the main activities are nautical activities, walking and fishing. The national road 132 is, in some areas, less than 5 metres from the shoreline.

2.1.4 Cap-des-Rosiers (Gaspé)

Gaspé is located on the Gaspé Peninsula on the south shore of the Gulf of St. Lawrence. Cap-des-Rosiers, a former village annexed to the town of Gaspé, is located at the far north-east end of the Gaspé peninsula. The study site is located on a rocky cliff stretch of coast with an unconsolidated lower (cobbles) foreshore and a rocky infralittoral zone. The lower foreshore is partially (0-25%) covered by macroalgua (mainly *fucaceae*). The tidal range is mesotidal and the offshore significant wave height from ESE-SE reached more than 3 m between November 2017 and 2019 (Savoie-Ferron et al., 2020). The study site is a

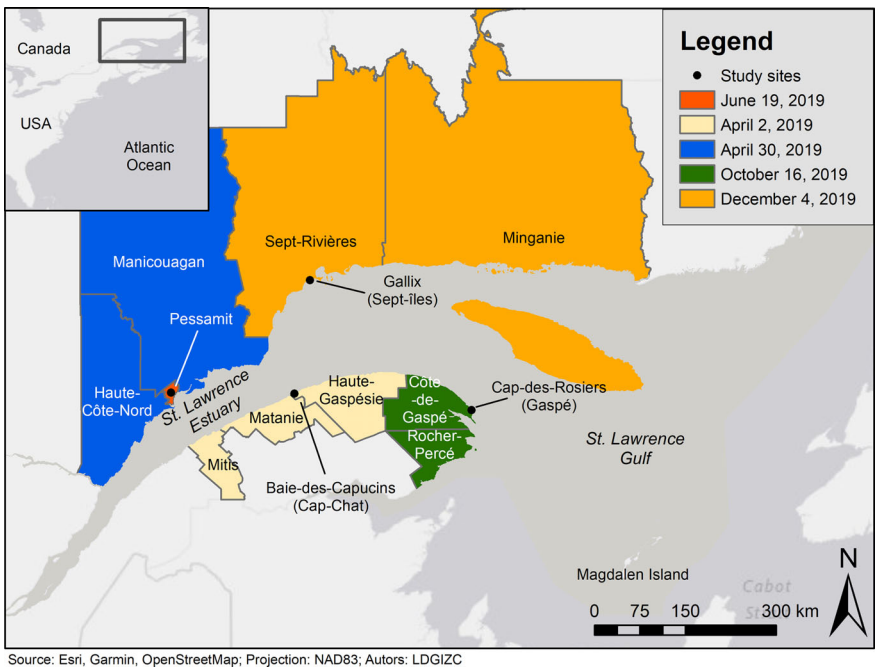

FIGURE 2 | Sites and MRCs from Eastern Quebec included in the study, with the workshops' dates in the legend.

residential sector with low density activities. Still, tourism infrastructures, such as motels, are present in Cap-des-Rosiers due to the proximity of the Forillon National Park, which brings a high volume of tourism during the summer season. The main activities are gatherings and relaxation. Cap-des-Rosiers is a biodiversity hotspot, and has a high socio-cultural value with, among others, the Cap-des-Rosiers lighthouse, the tallest in Canada. The national road 132 is, in some areas, less than 5 metres from the cliff.

2.2 Selection of Coastal Defence Measures to be Evaluated

CDMs that were suitable for each of the four study sites were pre-selected, either by a comity of experts, or by using a coastal defence measure identification algorithm (CDMIA) developed by Sauvé et al. (2022). The number of CDMs can vary from site to site (**Table 1**). The CDMIA processed information that was drawn from 411 published scientific case studies, which included 1709 statements on the effects of CDMs on the environment as observed by the authors of the studies. It then established a correspondence between user-selected environmental features, and those stocked in the database, and it evaluated user-selected CDMs in relation to the specified coastal characteristics by identifying, collating, and rating their effects as observed in similar contexts. Since few CDMs studies have been conducted on rocky cliffs, the CDMs deemed suitable for the terrain at Cap-des-Rosiers, were selected by a comity of experts, instead of through the CDMIA. In the case of Baie-des-Capucins which is characterized by two types of coasts, a beach terrace and a salt marsh, the results of the CDMIA from both types of coasts were combined to select CDMs adapted to such conditions. Also, in Baie-des-Capucins, the low-crested breakwater scenario was based on a living shoreline rock sill concept (Bilkovic et al., 2017). The selected CDMs were then evaluated with the use of a MCDA methodology.

2.3 Multi-Criteria Decision Analysis

For the multi-criteria decision analysis, an outranking method was preferred, as it allows an evaluation between scenarios that initially do not appear to be comparable with each other, and it maintains ranking units that are specific to each criterion (Gamper and Turcanu, 2007; Garmendia and Gamboa, 2012). The PROMETHEE method was chosen as multi-criteria decision-making tool, using the VISUAL PROMETHEE software (VPSolutions, 2013). It was preferred for its stability (Brans et al., 1986), and because it is widely used in environmental management contexts (Behzadian et al., 2010).

2.3.1 PROMETHEE Method

The PROMETHEE method is based on a pairwise comparison between different alternatives, following their assessment $A = \{a_1, a_2, \ldots, a_n\}$ against each criterion c_k ($\Delta_k(a_i, a_j)$) from a defined set of criteria $C = \{c_1, c_2, \ldots, c_m\}$ (equation 1). The variations in the results of the assessments $\Delta_k(a_i, a_j)$ associated with criterion c_k, are translated into a preference index $P[\Delta_k(a_i, a_j)]$ through a preference function, which lies between 0 and 1, 1 being a strong preference, and 0 meaning no preference. In this study, the usual preference function was used; it corresponds to the optimization of values without threshold, that is, larger values are better than lower ones. The multicriteria index $\pi(a_i, a_j)$ is the weighted sum of the preference

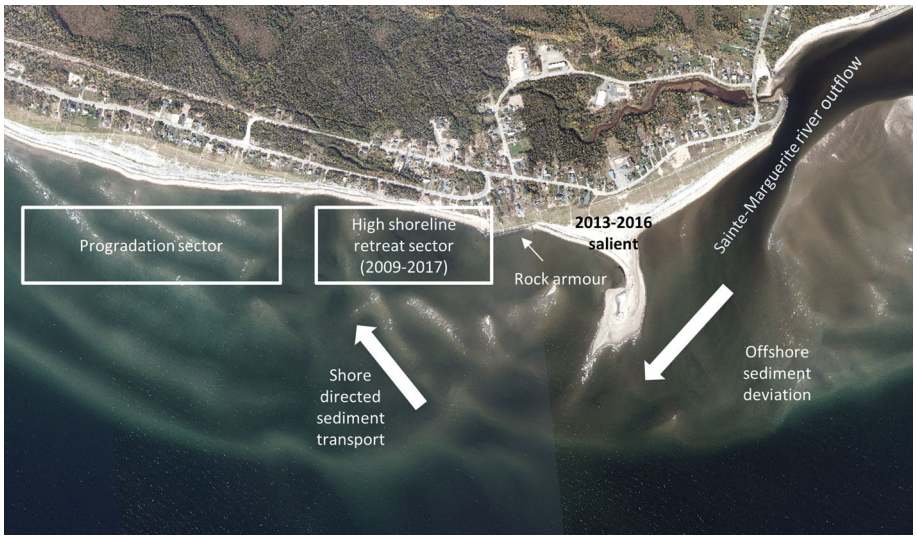

FIGURE 3 | Coastal dynamic illustration from the Gallix study site [modified from Corriveau et al. (2019)].

index P, and is calculated by dividing the preference index by the weight w_k, which is a measure of the importance of the criterion c_k determined by workshop participants (equation 2). The leaving $\Phi^+(a_i)$ and entering $\Phi^-(a_i)$ flows are then calculated in relation to the multicriteria index. The leaving flow expresses the extent to which a_i outranks all other alternatives (equation 3), and the entering flow expresses how much a_i is outranked by all other alternatives (equation 4). Thus, the best alternative has the highest leaving flow and the lowest entering flow. The net flow is the sum of the leaving and entering flows and represents an overall ranking. All criteria were set as maximum with the exception of the criteria whose evaluation was based on the 5 points impact qualitative scale (geomorphological effects, ecological effects and aesthetics). The specificities of the PROMETHEE method are described in the works of Brans et al. (1986) and in the Visual PROMETHEE software's manual (VPSolutions, 2013).

$$\Delta_k(a_i, a_j) = c_k(a_i) - c_k(a_j) \qquad \text{(Equation 1)}$$

$$\pi(a_i, a_j) = \sum_{x \in k} P_k(a_i, a_j) / \sum_k w_k \qquad \text{(Equation 2)}$$

$$\Phi^+(a_i) = \sum_k \pi(a_i, x) \qquad \text{(Equation 3)}$$

$$\Phi^-(a_i) = \sum_{x \in k} \pi(x, a_i) \qquad \text{(Equation 4)}$$

2.3.2 Criteria Identification and Weighting

Coastal zone stakeholders were consulted in the course of two action research projects, with the aim of developing tools to improve coastal planning and protection, and to facilitate the choice of solutions adapted to climate change, in the short, medium and long terms. First, four workshops were organized between April and December 2019, in Eastern Quebec, in the context of the Coastal Resilience project. Stakeholders who were invited to the workshops included administrative personnel and

TABLE 1 | CDMs pre-selected for 3 of the study sites using Sauvé et al., (2022) CDMIA, and in the case of Cap-des-Rosiers, selected by a comity of experts, with the number of CDMs per site.

Study sites			
Pessamit	**Gallix, Sept-îles**	**Baie-des-Capucins, Cap-Chat**	**Cap-des-Rosiers, Gaspé**
CDMs			
Land vegetation	Land vegetation	Vegetation	Rock armour
Foreshore nourishment	Foreshore nourishment	Beach nourishment	Seawall
Permeable groin	Permeable groin	Low crested breakwater	Emerged breakwater
Beach nourishment	Beach nourishment	Permeable groin	Low-crested breakwater
Emerged breakwater	Emerged breakwater		Beach nourishment
Impermeable groin	Impermeable groin		
	Submerged breakwater		
Number of pre-selected CDMs			
6	7	4	5

professionals from local municipalities and coastal MRCs (regional county municipalities), relevant ministries, local and regional organizations, and members of the First Nations (**Table 2**). Second, in June 2019, in the context of a project entitled *Identification de solutions d'adaptation aux aléas côtiers pour augmenter la résilience des communautés des Premières Nations dans un contexte de changements climatiques*, a workshop was organized in Pessamit. Participants to this workshop comprised administrative personnel and professionals from the community. Through various activities, one of the aims was to integrate stakeholders into the decision-making process leading to the implementation of coastal defence measures, by asking them to identify and weigh the CDMs selection criteria (**Figure 4**). The locations of the four study sites and five workshops are shown in **Figure 2**.

For Pessamit, all participants were employees of the municipality, many of them, members of the First Nations; they were all recorded under Municipality rather than First Nations to avoid duplication.

Using an adaptation of the World Cafe methodology (Brown et al., 2005), the participants were separated into rotating discussions groups of between five and fifteen people. The aim was to allow participants to express their views on different subjects related to coastal management, each within a 25-minute time frame. With two facilitators in charge of the discussion, one table was dedicated to discussing relevant criteria to be integrated in the decision-making process for the selection of coastal defence measures.

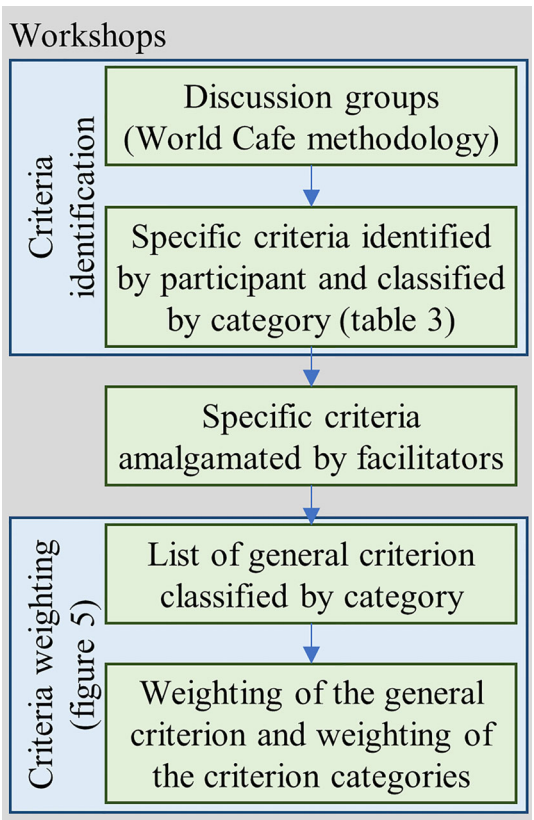

FIGURE 4 | Graphical representation of the method used for the implication of workshop participants in the identification and weighting of the CDMs selection criteria.

At the beginning of the discussion, participants were presented with a brief description of factors affecting the CDMs decision-making process, in order for them to understand the context before identifying the CDMs selection criteria. The question "*In your opinion, which are the criteria to be considered when a coastal defence measure must be selected?*" was asked of participants to start the discussion. Five criteria categories written on cards were presented to participants as a guide (**Table 3**). Specific criteria identified by participants were written on post-it notes and affixed to their corresponding category. The selection criteria identified by participants of one table served as a basis for discussion in the following rotating groups.

A weighting method was established to allow participants to assess the importance of the criteria they previously identified. A three steps classification system was created: first, a list of criteria, as identified by the participants, was compiled; second, from that list, criteria that were similar in nature were amalgamated by the facilitators under a maximum of five general criteria per criteria category; third, the general criteria were grouped under five criteria categories.

Each criteria category was limited to a maximum of five general criteria to limit the total number of criteria, and because it was deemed sufficient to capture and adequately represent all of the criteria identified by the participants. Each general criterion was written on a card with the list of similar criteria originally identified by the participants. The weighting of the general criteria was carried out in two steps. The voting table was divided into six sections: one for each criteria category with its list of general criterion, and one which listed the five criteria categories (**Figure 5**). As a first step, each general criterion card was placed on the voting table under its respective category, with a corresponding voting box. Each participant was given ten tokens per criteria category to weight each general criterion according to the question "*For each criteria category, how important is each criterion when selecting a coastal defence measure?*". As a second step, the five criteria categories' cards were placed in the sixth section, each with a corresponding voting box. As for the previous exercise, participants were given ten tokens to weight the criteria categories according to the question "*How important is each criteria category for the selection of a coastal defence measure?*".

2.3.3 CDMs Evaluation According to Each Criterion

The evaluation of CDMs in relation to each criterion was based on experts' judgement, and on different sources of data such as literature reviews, reports on CDMs, etc. In the PROMETHEE method, different rating scales can be defined, depending on the nature of the criterion. Here, two scales were used: a 9 points qualitative scale for the criteria that lead to the comparison of CDMs' performance relative to each other [very good (9), very good – good, good, good – average, average, average - bad, bad, bad – very bad, and very bad (1)]; and a 5 points impact qualitative scale for the criteria that lead to the evaluation of

TABLE 2 | Number of participants per organisation (MAMH, Ministry of Municipal Affairs and Housing; MELCC, Ministry of Environment and Climate Change; MERN, Ministry of Energy and Natural Resources; MFFP, Ministry of Forests, Wildlife and Parks; MSP, Ministry of Public Security; MSSS, Ministry of Health and Social Services; MTQ, Ministry of Transports; MRC, regional county municipality).

	Coastal resilience project				Innus III project
Organisation	**Haute-Côte-Nord, Manicouagan**	**Sept-Rivières, Minganie**	**Mitis, Matane, Haute-Gaspésie**	**Côte-de-Gaspé, Rocher-Percé**	**Pessamit**
Ministry	**8**	**7**	**5**	**10**	**-**
MAMH	1	1		–	–
MELCC	2	1	1	2	–
MERN	1	1	–	1	–
MFFP	–	1	–	–	–
MSP	3	2	3	2	–
MSSS	–	–	1	–	–
MTQ	1	1	–	5	–
Municipality	**6**	**4**	**1**	**2**	**-**
MRC	–	2	1	1	–
Municipality	6	2	–	1	12
ONG	**2**	**6**	**1**	**5**	**-**
First Nations	**5**	**2**	**1**	**-**	**-**
Total	**21**	**25**	**8**	**17**	**12**

Bold values indicate the sommation of the organisation regroupment.

the direct effects of CDMs on the coastal system [very low (5), low, moderate, high, very high (1)]. Two qualitative scales were used for the evaluation of criteria due to a lack of quantitative local data. For example, the evaluation for the cost related criteria was based on the cost of previous projects at a national scale.

3 RESULTS

3.1 Identified and Weighted CDM Criteria

Following the five workshops, the criteria identified by the participants were standardized with uniform wording, and classified under five categories (**Table 4**). A comprehensive list of sixteen criteria that were mutually independent, without duplication, relevant to the context, and consistent with effects occurring over time, was thus established (**Figure 6**). The list of criteria built during the five workshops was used in the analysis of the four study sites described above, even though only one of the workshops was specific to a study site (Pessamit). Of the remaining workshops, three drew participants from regions around and including a study site, and one was held in a region that did not include a study site (the MRC of Haute-Côte-Nord and Manicouagan).

As shown in **Figure 6**, the identification and weighting of criteria vary between workshops. First, not all criteria were selected in every workshop, as some may not have been relevant or important to the particular context. The adaptability criterion for instance was only identified in the case of Cap-des-Rosiers, while the maintenance and indirect environmental effects were not selected at the Pessamit workshop. Second, the weight assigned to different criteria varied between workshops, and the data range is wide. In general, the average weight is highest for ecological effects and social repercussions. In the case of Baie-des-Capucins, the weight given to the construction cost criterion is the highest among all criteria for all workshops.

For the purpose of weighting analysis, an average baseline can be calculated by dividing 100 percent by the number of identified criteria. For example, in Cap-des-Rosiers, 16 criteria were identified by workshop participants for an average baseline of 6.25%. While the majority of the criteria weight values are close to 6.25%, the ecological effects and social repercussions criteria are nearly twice the average value, which is an indication of the high importance accorded to these criteria by local stakeholders.

3.2 CDMs Evaluation

CDMs evaluation was carried out in two phases: (1) weighting of each CDM in relation to each criterion; (2) final hierarchization.

TABLE 3 | Criteria categories presented to participants.

Criteria categories	Description
Economic context	Criteria related to costs, benefits, economic issues.
Environmental context	Criteria related to environmental impacts.
Social context	Criteria related to acceptability, accessibility, activities, culture.
Project management	Criteria related to planning and execution of construction site.
Technical characteristics	Criteria related to coastal defence measure behaviour, reliability.

TABLE 4 | Standardized criteria identified by participants during the workshops.

Criteria	Definition
Economic context	
Economic repercussions	Indirect economic development benefits.
Construction costs	Initial CDM building costs including cost of materials, labour force, and equipment.
Maintenance costs	Funds required to maintain optimum CDM performance including cost of materials, labour force, and equipment.
Environmental context	
Geomorphological effects	Importance of the modifications generated by the CDM on the morphology of a sediment cell.
Ecological effects	Importance of the modifications generated by the CDM on the ecosystem of a sediment cell.
Indirect environmental benefits	Environmental benefits through the creation or the maintenance of ecological services
Social context	
Social repercussions	Impacts on the community's quality of life and activities, as well as on cultural and patrimonial aspects.
Social perception	Public perception of the CDM.
Aestheticism	Visual impact and potential for the integration of the CDM into the broader landscape.
Project management	
Ability to achieve	Ability to implement a CDM in terms of completion time, and availability of labour force and expertise at the municipal level.
Regulatory liability	Likelihood of the CDM being subject to local regulations and environmental impact assessment.
Technical feasibility	Complexity of the CDM construction depending on the type of structure, availability of materials and accessibility to the site.
Technical characteristics	
Adaptability	Capacity for the CDM to be adapted to changes in the environmental parameters.
Durability	Length of time a CDM can retain its integrity with minimal maintenance.
Efficiency	Ability of the CDM to slow down the retreat of the shoreline and to protect the coastal infrastructures during an event, as long as it is in perfect condition, of standard dimensions and appropriate to local hydro-sediment cell dynamic.
Maintenance	Frequency of maintenance required to preserve the effectiveness of the CDM.

3.2.1 CDMs Evaluation in Relation to Each Criterion

The CDMs evaluation is dependent on each criterion (**Table 5**), and on the socio-ecological features associated with each site. The evaluation scale was adapted to the nature of each criterion.

The evaluation of the CDMs in relation to each criterion and to each study site's socio-ecological features is presented in **Table 6**, with rationale where relevant.

3.2.2 CDMs Hierarchization

The CDMs hierarchization is thereafter presented in diamond shape figures for each study site (**Figure 7**). This shape shows the overall ranking (Φ net) along the vertical axis, as well as the leaving Φ^+ and entering Φ^- flows along the left edges of the diamond. Each CDM is represented by a grey dot. For one CDM to be ranked higher than another, it must outperform it on both the leaving and entering flow axes.

For the Pessamit site, the analysis of the results shows that, according to the workshop participants' preferences, vegetation is ranked first followed by beach nourishment. Despite the large outperformance of vegetation over beach nourishment on the net and leaving flows, their respective entering flows are quite close together, thus weakening the general outperformance of the vegetation option. In third and fourth ranks, while permeable groin outperforms foreshore nourishment on the leaving flow axis, foreshore nourishment outperforms permeable groin on the entering flow. This results in a quasi-tie on the net flow axis. Meanwhile, impermeable groin and emerged breakwater come last, in fifth and sixth ranks, respectively.

For the Gallix site, the vegetation option is ranked first as shown by its significant outperformance over all other CDMs. In second and third ranks, a quasi-tie between beach nourishment and permeable groin on the net flow axis is explained by an outperformance of foreshore nourishment on the leaving flow, and an outperformance of permeable groin on the entering flow. Impermeable groin and foreshore nourishment are also on a quasi-tie in fourth and fifth ranks, respectively, while submerged breakwater and emerged breakwater are ranked sixth and seventh.

The top five CDMs for the Pessamit and Gallix sites are in the same order. Two reasons can explain the similarity. First, their socio-ecological systems are comparable. The environmental characteristics of both sites are low-lying sandy coast with a sandy lower foreshore, mesotidal shoreline, and a low energy environment (<1 m). Also, both sites are part residential part public localities, mostly frequented by the local community for a variety of uses and activities. Due to these similarities, the evaluation of the CDMs in relation to each criterion is equivalent for all criteria with the exception of social perception (**Table 6**). Second, the difference in average weight is below 3 % for seven of the 13 and 15 criteria identified, respectively, in Pessamit and Gallix (**Figure 7**). The local stakeholders' preferences were quite similar in nearly half of the identified criteria, though variances explain differences in the net, leaving, and entering flows between the two sites (**Figure 7**). While the final ranking for the top 5 options is equivalent in both sites, inner differences shown by the above-mentioned three indicators, provide information that is relevant to the decision-makers.

For the Baie-des-Capucins site, the vegetation alternative also outperformed all other CDMs. In second and third ranks, while low-crested breakwater outperformed beach nourishment on the net, and entering flow axes, both are on a quasi-tie on the leaving flows axis. It is to be noted here that, because of the presence of salt marsh, the low-crested breakwater scenario was actually based on a living shoreline rock sill concept (Bilkovic et al., 2017). Finally, permeable groin was ranked fourth.

TABLE 5 | Assessment basis and evaluation scale for the evaluation of CDMs in relation to each criterion.

Criterion	Evaluation scale	Assessment basis
Economic repercussions	qualitative scale	- Pre-existing economic activities on sites
Construction costs	qualitative scale	- Estimations based on Bernatchez et al. (2015) due to a lack of information on CDMs construction and maintenance costs associated with study sites.
Maintenance costs	qualitative scale	- Accessibility to the construction site, availability of materials, and frequency of maintenance.
Geomorphological effects	impact scale	- Information extracted from literature review and expert knowledge
Ecological effects	impact scale	
Indirect environmental benefits	qualitative scale	
Social repercussions	qualitative scale	- Activities practiced on sites
Social perception	qualitative scale	- Results from coastal residents' interviews
Aestheticism	impact scale	- Similarity of materials with the landscape and the creation of visual obstacles
Ability to achieve	qualitative scale	- Availability of expertise and equipment at the Quebec provincial level
Regulatory liability	qualitative scale	- Local regulations
Technical feasibility	qualitative scale	- Accessibility to the site and complexity of the structure
Durability	qualitative scale	- Type of CDMs and their exposure to wave action
Adaptability	qualitative scale	- Information extracted from literature review and expert knowledge
Efficiency	qualitative scale	
Maintenance	qualitative scale	

As for Cap-des-Rosiers, rock armour outperformed all other CDMs, but seawall is a close second. Beach nourishment, low-crested breakwater and emerged breakwater were ranked third, fourth and fifth, respectively. The evaluated CDMs and the final ranking is quite different from the other three sites, which is explained by their significantly dissimilar local conditions.

3.2.3 Robustness Analysis

An analysis was performed to evaluate the robustness of the CDMs hierarchization method in relation to each criterion (**Figure 8**). The circles and triangles show the highest and lowest thresholds at which there is a change in ranking of the top 3 CDMs for a given criterion. For example, in Pessamit under the criterion *Economic repercussions*, the CDM ranked first is outperformed by the CDM ranked second above 21.06%, but it is never outperformed by the CDM ranked third. Also, in Pessamit with regard to the three criteria *Ecological effects*, *Regulatory liability*, and *Technical feasibility*, the circles representing CDMs 1, 2, and 3 are all at 100%. This means that no change occurs in the top 3 CDMs' ranking, no matter the weight attributed to those criteria. An empty criterion cell indicates that the criterion was not identified at the site's workshop.

The grey plus and minus signs show the weighted average plus or minus the standard deviation. For example, if there is no circle or triangle within the range of the standard deviation (between the plus and minus signs), any change to the weight of the criteria would not affect the ranking, which is an indication that the results are robust. In Pessamit and Gallix, the CDMs ranked 1 and 2 are outside the standard deviation range for all criteria, which indicates that the results are robust for the first two CDMs. On the other hand, because CDM ranked 3 sometimes falls within the standard deviation range, it may be outperformed by the CDM ranked 4 if a change occurs in some of the criteria weight values. This shows that the results for CDM ranked 3 are not as robust as the ones for the first two CDMs. In Cap-des-Rosiers, all of the CDMs fall outside of the standard deviation range. This indicates that, in the case of the first three CDMs, the results would not be affected by any change in the criteria weights. In Baie-des-Capucins, the CDM ranked 3 falls within the standard deviation range for the criteria *Construction costs*, and *Social repercussions*. In this case, two out of sixteen criteria would not be enough to change the ranking.

Considering **Figures 6** and **7**, even though the results are not equally robust in all cases, vegetation, beach nourishment, and permeable groin were ranked first, second, and third, respectively, for the three study sites with a sandy low coast (Pessamit, and Gallix). As for Cap-des-Rosiers, with a cliff coast that is naturally reflective, rock armour and seawall were solidly ranked first and second. These results are in line with those obtained through the CDMIA developed by Sauvé et al., (2022), but the MCDA adds a layer of refinement to the assessment.

In Pessamit, the quasi-tie between permeable groin and foreshore nourishment in third and fourth ranks (a) is validated by the robustness analysis, which shows that the lowest and highest thresholds of the CDM ranked 3 (represented by a green triangle and a green dot, respectively), each fall within the standard deviation range in 5 of the criteria (a). In Gallix, the quasi-tie between beach nourishment and permeable groin (b, ranks 2 and 3, respectively) is confirmed by the robustness analysis, which shows the permeable groin's lowest threshold falling within the standard deviation in 3 of the criteria, and the highest threshold, in 6 of the criteria (b). In Baie-des-Capucins, there is no quasi-tie in the CDMs hierachization (c). Indeed, the robustness analysis shows that the thresholds for CDMs ranked 1 and 2 all fall outside of the standard deviation, and even though, in one criterion, the highest threshold

TABLE 6 | Weighting of CDMs in relation to each criterion and sites' characteristics, with relevant rationale.

Criteria	Sites	Rock armour	Seawall	Emerged breakwater	Low-crested breakwater	Submerged breakwater	Impermeable groin	Permeable groin	Beach nourishment	Foreshore nourishment	Vegetation
Economic repercussions	*Pessamit*	–	–	9	–	–	5	5	7	6	5
	Gallix	–	–	9	–	9	5	5	7	6	5
	Baie-des-Capucins	–	–	–	5	–	–	5	5	–	5
	Cap-des-Rosiers	5	5	9	9	9	–	–	5	–	–
	Breakwaters: possible colonization by species of high economic interest. (Baie-des-Capucins: low-crested breakwater option in the salt marsh: expected results would not be the same as for conventional breakwaters). **Nourishments:** none of the municipalities are currently tourist sites; potential for development of tourism in Gallix and Pessamit.										
Construction costs	*Pessamit*	–	–	2	–	–	5	5	3	2	9
	Gallix	–	–	2	–	2	5	5	3	2	9
	Baie-des-Capucins	–	–	–	2	–	–	5	3	–	9
	Cap-des-Rosiers	7	5	2	2	2	–	–	3	–	–
	Breakwaters: offshore construction. **Groins**: land construction. **Beach nourishment:** land construction. **Foreshore nourishment:** offshore construction; same material as beach nourishment. **Vegetation:** very low-cost material.										
Maintenance costs	*Pessamit*	–	–	3	–	–	6	6	2	1	9
	Gallix	–	–	3	–	5	6	6	2	1	9
	Baie-des-Capucins	–	–	–	4	–	–	6	2	–	9
	Cap-des-Rosiers			3	4	–	–	–	2	–	9
	Breakwaters: offshore construction; low to moderate maintenance frequency. **Groins**: land construction; moderate maintenance frequency. **Beach nourishment:** land construction; high maintenance frequency. **Foreshore nourishment:** offshore construction; high maintenance frequency. **Vegetation:** high maintenance frequency; very low-cost material.										
Geomorphologic effects	*Pessamit*	–	–	2	–	–	2	4	4	4	3
	Gallix	–	–	2	–	3	2	4	4	4	3
	Baie-des-Capucins	–	–	–	3	–	–	3	4	–	3
	Cap-des-Rosiers	4	4	2	3	–	–	–	4	–	–
	Breakwaters: beach widening; offshore transport reduction. **Permeable groin**: sediment accumulation; beach widening. (Emerged breakwater and impermeable groin may cause sediment retention. Baie-des-Capucins: accumulation effect reduced due to a low longshore sediment transport). **Nourishments:** increase sediment budget for the sediment cell (at a higher level for beach nourishment. Cap-des-Rosiers: reduce the interaction between cliff and waves). **Vegetation:** sediment stabilisation and sediment accumulation acceleration at a small local scale. **Rock armour and seawall:** effects similar to the natural effects generated by the cliff.										
Ecological effects	*Pessamit*	–	–	2	–	–	3	3	3	3	5
	Gallix	–	–	2	–	2	3	3	3	3	5
	Baie-des-Capucins	–	–	–	3	–	–	3	3	–	5
	Cap-des-Rosiers	4	4	3	3	–	–	–	3	–	–
	Breakwaters: loss of sedimentary habitat; species dispersal, loss of micro-habitats, siltation, water quality degradation. (Baie-des-Capucins: reduce ecological effects due to low hydrodynamism). **Groin**: loss of sedimentary habitat; physical barrier. **Nourishments:** organism burial; increasing temporary turbidity; modification of substrate permeability; ecosystem assemblage modifications. **Vegetation:** coastal ecosystem maintenance. **Enrockement and seawall:** effects similar to the natural effects generated by the cliff.										
Indirect environmental benefits	*Pessamit*	–	–	–	–	–	–	–	–	–	–
	Gallix	–	–	4	–	4	4	5	6	5	8
	Baie-des-Capucins	–	–	–	4	–	–	5	5	–	6
	Cap-des-Rosiers	4	5	6	6	–	–	–	6	–	–
	Rock armour: reduces beach ecosystem width due to encroachment. **Seawall:** limited effects in a context of reflective rocky cliff. **Breakwater:** increase potential ecosystem habitats in Cap-des-Rosiers' rocky environment; reduction of ecological services in sandy Gallix and in Baie-des-Capucins' salt marsh. **Beach nourishment**: increase beach ecosystem width. **Vegetation:** increase of the actual vegetated area in Gallix more than the actual vegetated area in Baie-des-Capucins.										
Social repercussions	*Pessamit*	–	–	3	–	–	3	4	6	6	5
	Gallix	–	–	3	–	3	3	4	6	6	5
	Baie-des-Capucins	–	–	–	4	–	–	4	6	–	5
	Cap-des-Rosiers	5	5	5	5	–	–	–	6	–	–
	Breakwaters and groins: create an obstacle to navigation; potential formation of rip currents; increases the area for recreational use in the medium term. (Permeable groins: similar effects but on a smaller scale. Cap-des-Rosiers: less activities on the beach). **Nourishments:** increased area for recreational use **Vegetation:** no repercussion.										

(Continued)

TABLE 6 | Continued

Criteria	Sites	Rock armour	Seawall	Emerged breakwater	Low-crested breakwater	Submerged breakwater	Impermeable groin	Permeable groin	Beach nourishment	Foreshore nourishment	Vegetation
Social perception	*Pessamit*	–	–	3	–	–	2	2	4	4	7
	Gallix	–	–	8	–	8	6	2	7	7	9
	Baie-des-Capucins	–	–	–	2	–	–	1	2	–	3
	Cap-des-Rosiers	4	9	1	1	–	–	–	1	–	–
Aestheticism	*Pessamit*	–	–	1	–	–	3	3	4	5	5
	Gallix	–	–	1	–	5	3	3	4	5	5
	Baie-des-Capucins	–	–	–	2	–	–	3	4	–	5
	Cap-des-Rosiers	4	3	2	3	–	–	–	4	–	–
	Emerged breakwaters: offshore visual obstacle; no similarity with natural landscape. **Groins:** limited similarity with landscape (for wooden groin). **Beach nourishments:** similarity with the natural landscape. **Vegetation:** strong similarity with the natural landscape.										
Ability to achieve	*Pessamit*	–	–	7	–	–	8	8	7	5	9
	Gallix	–	–	7	–	7	8	8	7	5	9
	Baie-des-Capucins	–	–	–	7	–	–	8	7	–	9
	Cap-des-Rosiers	9	9	7	7	–	–	–	7	–	–
	Breakwaters: expertise to be refined, but present in Quebec; mechanical equipment available. **Groins**: expertise present in Quebec; equipment widely available. **Nourishments:** expertise under development in Quebec; mechanical equipment widely available (land-based sediments); dredging available, but rare and complex from a regulatory point of view. **Vegetation:** expertise available.										
Regulatory liability	*Pessamit*	–	–	1	–	–	3	1	3	1	5
	Gallix	–	–	1	–	1	3	1	3	1	5
	Baie-des-Capucins	–	–	–	1	1	3	1	3	1	5
	Cap-des-Rosiers	5	5	1	1	–	–	–	3	–	–
Technical feasibility	*Pessamit*	–	–	1	–	–	7	7	7	3	9
	Gallix	–	–	1	–	1	7	7	7	3	9
	Baie-des-Capucins	–	–	–	1	–	–	7	7	–	9
	Cap-des-Rosiers	4	3	1	1	–	–	–	7	–	–
	Breakwaters: complex structures with several layers built underwater and offshore. **Groins**: simple structures; land construction. **Nourishments:** relatively simple technique; land and offshore construction sites. **Vegetation:** expertise available.										
Adaptability	*Pessamit*	–	–	–	–	–	–	–	–	–	–
	Gallix	–	–	–	–	–	–	–	–	–	–
	Baie-des-Capucins	–	–	–	–	–	–	–	–	–	–
	Cap-des-Rosiers	4	2	4	4	–	–	–	9	–	9
	Rock armour, Breakwaters: structures can be adapted. **Seawall**: complex to adapt. **Nourishments, vegetation:** adapt naturally.										
Durability	*Pessamit*	–	–	5	–	–	6	6	2	2	1
	Gallix	–	–	5	–	7	6	6	2	2	1
	Baie-des-Capucins	–	–	–	–	–	–	6	2	–	1
	Cap-des-Rosiers	8	9	5	6	–	–	–	1	–	–
	Breakwaters, groins: structures made of materials potentially subject to movement (emerged: continuously exposed to wave action). **Nourishments:** continuously exposed to wave action; unconsolidated materials. **Vegetation:** rare exposure to wave action; low resistance materials.										
Efficiency	*Pessamit*	–	–	7	–	–	5	5	7	6	2
	Gallix	–	–	7	–	6	5	5	7	6	2
	Baie-des-Capucins	–	–	–	7	–	–	5	7	–	2
	Cap-des-Rosiers	7	8	7	7	–	–	–	5	–	–
	Breakwaters: reduce wave energy offshore; lead to sediment deposit. **Groins**: lead to sediment deposit on medium term. **Nourishments:** stabilize or advance the coastline; are dependent on maintenance. **Vegetation:** stabilizes sediment at a minor scale.										
Maintenance	*Pessamit*	–	–	–	–	–	–	–	–	–	–
	Gallix	–	–	6	–	6	6	6	2	2	1
	Baie-des-Capucins	–	–	–	6	–	–	6	2	–	1
	Cap-des-Rosiers	8	7	6	6	–	–	–	2	–	–

falls within the standard deviation for the CDMs ranked three (permeable groin) (c), any change in the criteria weighting would not be enough to affect the final hierarchization. In Cap-des-Rosiers, the CDMs hierarchization is unambiguous (d), and is validated by the robustness analysis which shows that, for all criteria, the top 3 CDMs fall outside the standard deviation (d).

4 DISCUSSION

In order to solve a predefined coastal erosion or flooding problem with a solution that is adapted to the specific socio-ecological context, a variety of scenarios must be considered in a multiphase process before the design and construction phases are undertaken (USACE, 2006). In most cases, decision-making has traditionally been limited to engineers, experts and scientists (Garmendia et al., 2010; Sauvé et al., 2020), and have led to a high rate of shoreline artificiality worldwide, the majority consisting of hard coastal defense structures (Koike, 1996; Valloni et al., 2003; EEA, 2006; Gittman et al., 2015; Cooper et al., 2020; Sauvé et al., 2020). In the past decade, a trend reversal has been observed with the implementation of soft techniques like beach nourishment or vegetation Sauvé et al., (2022), ecological approaches (Morris et al., 2018; Morris et al., 2019) such as Engineering With Nature in the U.S.A. (Bridges et al., 2018) or Building With Nature in The Netherlands (de Vriend and Van Koningsveld, 2012; van Slobbe et al., 2013), and the use of ecological or socio-economic enhancements in the design of hard structures (Evans et al., 2017; Schoonees et al., 2019; Vuik et al., 2019). Still, the decisions regarding the selection of CDMs are not systematically being made through a participatory process (O'Riordan, 2005; Sauvé et al., 2020).

In recent years, decision support tools have been increasingly used in the field of environmental management (Walling and Vaneeckhaute, 2020; Wong-Parodi et al., 2020; Barzehkar et al., 2021). One of the main reasons being the need for a framework to support the meaningful integration of multiple stakeholders in the decision-making process (Wong-Parodi et al., 2020). Such tools help decision-makers address complex and inherently uncertain problems related to socio-ecological systems (Baquerizo and Losada, 2008; Polasky et al., 2011) by objectively structuring and analyzing the information, and by offering multiple solutions for consideration (Walling and Vaneeckhaute, 2020; Wong-Parodi et al., 2020).

4.1 Relevance of MCDA as a Tool to Evaluate CDMs

Cost benefit analysis (CBA) and multicriteria decision analysis (MCDA) are both used for different purposes in environmental and coastal zone management, and in the evaluation of ecosystem services (Horstman et al., 2009; Saarikoski et al., 2016). CBA is often used to analyze CDMs, but rarely through a process of prioritization (Polomé et al., 2005; Boyer-Villemaire et al., 2016; Chow et al., 2017; Thi Oanh et al., 2020). CBA has been used more frequently to assess the cost of CDMs' maintenance, to compare the pros and cons, and the costs of scenarios with or without a CDM (Maia et al., 2015; Ha et al., 2021) or to evaluate a single given solution in monetary terms (Lima et al., 2020). There are two schools of thought regarding CBA and MCDA. The selection of one over the other depends on the project objectives. While CBA can be useful in some contexts (Gamper and Turcanu, 2007; Horstman et al., 2009), MCDA are better suited to the processing of tangible and intangible information obtained when, among others, multiple stakeholders are involved, when all aspects of communities' well-being are taken into consideration, and when scientific uncertainty and spatiotemporal ecological impacts are significant factors in the decision-making process (Wegner and Pascual, 2011; Saarikoski et al., 2016; Alves et al., 2018). CDMs can have different effects on the components of the socio-ecological system, and these effects are usually measured in incommensurable scales and units (Choo et al., 1999). MCDA are best adapted to the evaluation and comparison of CDMs because they allow the simultaneous analysis of dissimilar measurement units that are specific to each criterion (Horstman et al., 2009).

The output reports from the three phases of the MCDA PROMETHEE method combined with the robustness analysis (**Figure 9**) provide the decision-makers with a structured, transparent and integrated analysis, and, as an end result, present alternatives that take stakeholders' preferences into account, and are more likely to be acceptable to all parties (Saaty, 2008; McIntosh et al., 2011; Saarikoski et al., 2016). First, the criteria, identified and weighted by workshop participants, give an indication of the local stakeholders' overall priorities and, more specifically, identifies conflicts and agreements within the consulted group, with regard to each criterion. Decision-makers can use that information, and manage conflictual issues by eliciting further discussion and exploring trade-offs in order to build a consensus around the most suitable solution. Second, the effects of each CDM are evaluated in relation to each criterion. This can be used in the design process to identify conflicts and synergies between CDMs, and to make end users (decision-makers, coastal managers or coastal engineers) aware of the effect of a CDM on individual criteria. Moreover, as mentioned in section 2.3.3, the PROMETHEE method allows the use of different rating scales depending on the nature of each criterion. Thus, when relevant data is available, the accuracy of the results could be improved by using quantitative scale for some of the criteria (e.g. cost related criteria). Third, the CDMs hierarchization, in the diamond figure, shows the interpretation of the results on three axes, and establishes equivalencies between scenarios. For example, in Pessamit and Gallix, there was a quasi-tie between two CDMs. In such cases, the decision-makers should consider both options on the same level. Finally, the robustness analysis gives an indication of how trustworthy the CDMs hierarchization results are. Reflected in the results is the objective of a MCDA, which is not necessarily to point to a unique solution. Rather, it provides a layered structure to facilitate the evaluation of different alternatives, suitable to answer a complex problem. In doing so, MCDA helps the decision-makers examine all aspects of the problem, understand the consequences surrounding the choice

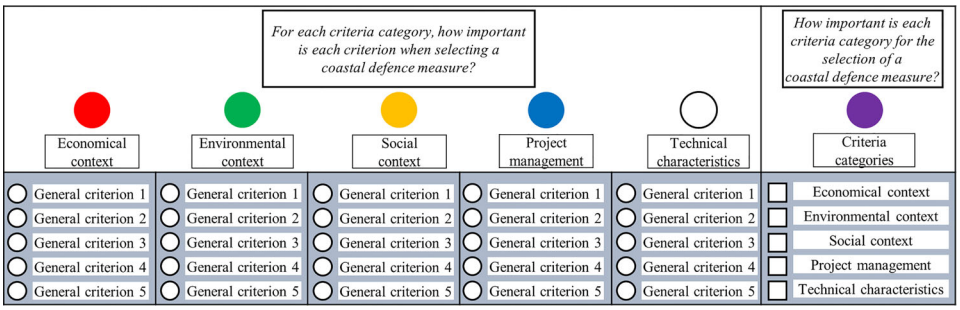

FIGURE 5 | Voting table illustration.

of one or a combination of CDMs, and choose the best alternative in accordance with their priorities and preferences.

In comparison, while CBA, like MCDA, is conducted in a process involving a few sequential steps (Saarikoski et al., 2016; Boardman et al., 2017), these are only related to solving the economic efficiency of scenarios (Wegner and Pascual, 2011). The monetary units used in CBA for the valuation of environmental features can limit the stakeholders in the expression of their preferences (Wegner and Pascual, 2011; Saarikoski et al., 2016). Decision-making based on CBA is focused on an economic perspective, and the analyzed components of the socio-ecological system do not provide as much information to decision-makers, coastal managers and coastal engineers, as MCDA does.

4.2 Analysis of the Participatory Process Involving Criteria Identification and Weighting

Following the uniformization process, a standardized list of 16 criteria was established (**Table 4**), based on the criteria identified by participants during the course of five workshops (**Figure 5**). The identification exercise and subsequent discussions were useful for participants to enhance their understanding of the potential effects of CDMs on socio-ecological systems, and to learn how the relative values attached to each criterion, by different stakeholders, can influence the final decision [e.g. Garmendia and Stagl (2010); Grêt-Regamet et al,. (2017), and Reed (2008)].

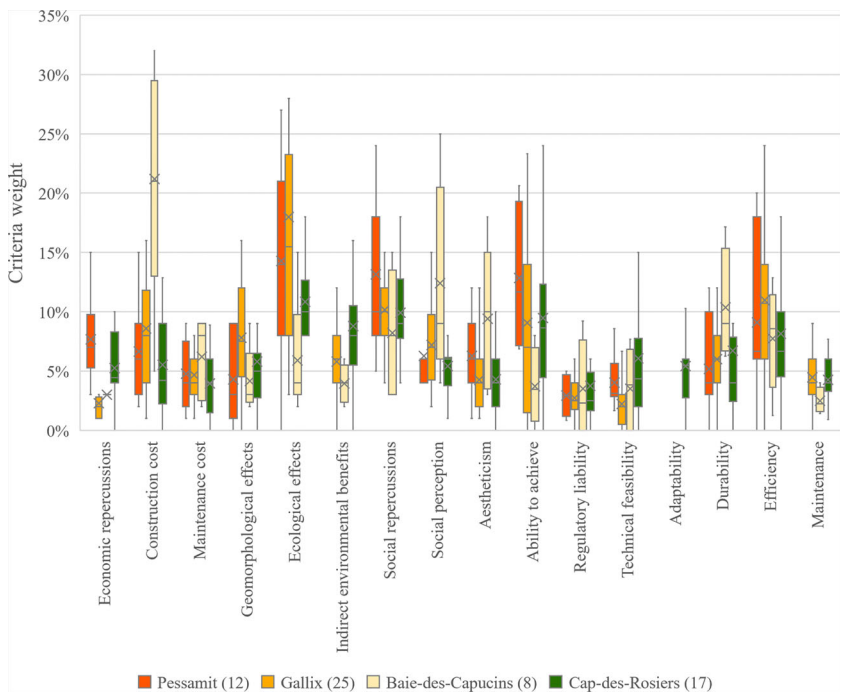

FIGURE 6 | Standardized criteria identified by participants and their weighting range for each workshop. Number of participants per site is indicated in parenthesis.

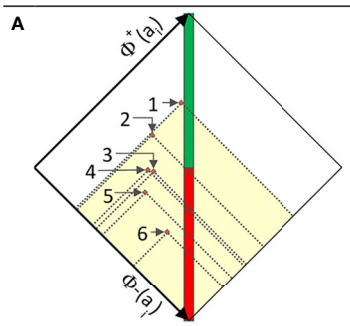

RNK	CDM	net flows (Φ)	leaving flows (Φ^+)	entering flows (Φ^-)
1	Vegetation	0.418	0.686	0.268
2	Beach nourishment	0.209	0.489	0.280
3	Permeable groin	-0.018	0.361	0.379
4	Foreshore nourishment	-0.0282	0.374	0.403
5	Impermeable groin	-0.162	0.280	0.4415
6	Emerged breakwater	-0.418	0.222	0.641

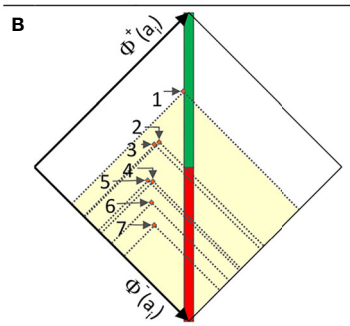

RNK	CDM	net flows (Φ)	leaving flows (Φ^+)	entering flows (Φ^-)
1	Vegetation	0.484	0.723	0.239
2	Beach nourishment	0.158	0.483	0.325
3	Permeable groin	0.146	0.462	0.316
4	Foreshore nourishment	-0.085	0.327	0.412
5	Impermeable groin	-0.094	0.338	0.432
6	Submerged breakwater	-0.231	0.265	0.496
7	Emerged breakwater	-0.378	0.199	0.577

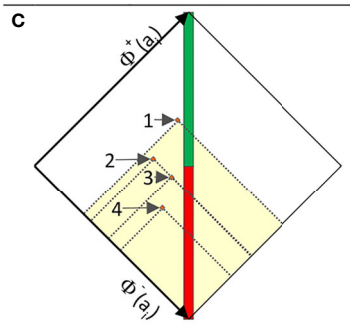

RNK	CDM	net flows (Φ)	leaving flows (Φ^+)	entering flows (Φ^-)
1	Vegetation	0.296	0.614	0.318
2	Low-crested breakwater	0.056	0.411	0.355
3	Beach nourishment	-0.097	0.398	0.495
4	Permeable groin	-0.255	0.293	0.548

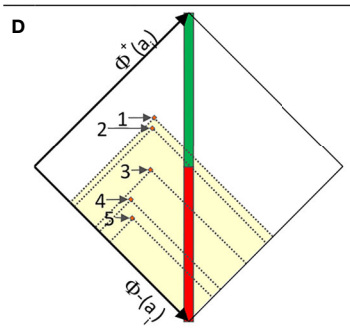

RNK	CDM	net flows (Φ)	leaving flows (Φ^+)	entering flows (Φ^-)
1	Rock armour	0.318	0.547	0.230
2	Seawall	0.249	0.506	0.257
3	Beach nourishment	-0.022	0.367	0.389
4	Low-crested breakwater	-0.215	0.205	0.420
5	Emerged breakwater	-0.330	0.154	0.484

FIGURE 7 | CDMs hierarchization presented in a diamond figure with the net, leaving and entering flows for each study site; **(A)** Pessamit; **(B)** Gallix; **(C)** Baie-des-Capucins; **(D)** Cap-des-Rosiers.

However, the exercise led to an over specificity of the criteria, which happens when different criteria statements have a similar meaning, and when the theoretical basis used for the evaluation cannot reflect the accuracy of each statement. Another issue was the process of synthetizing the criteria identified by participants into a concise standardized list, which had to be achieved in a short time to avoid slowing the pace of the workshop, and to allow enough time for the participants to weigh the criteria. The lack of time may have resulted in the presence of inconsistencies in the categories and groupings created during the workshop. These observations were made during the first workshop of the series. However, the same approach was maintained for reasons of methodology and consistency between workshops. The uniformization of the criteria, identified by the participants,

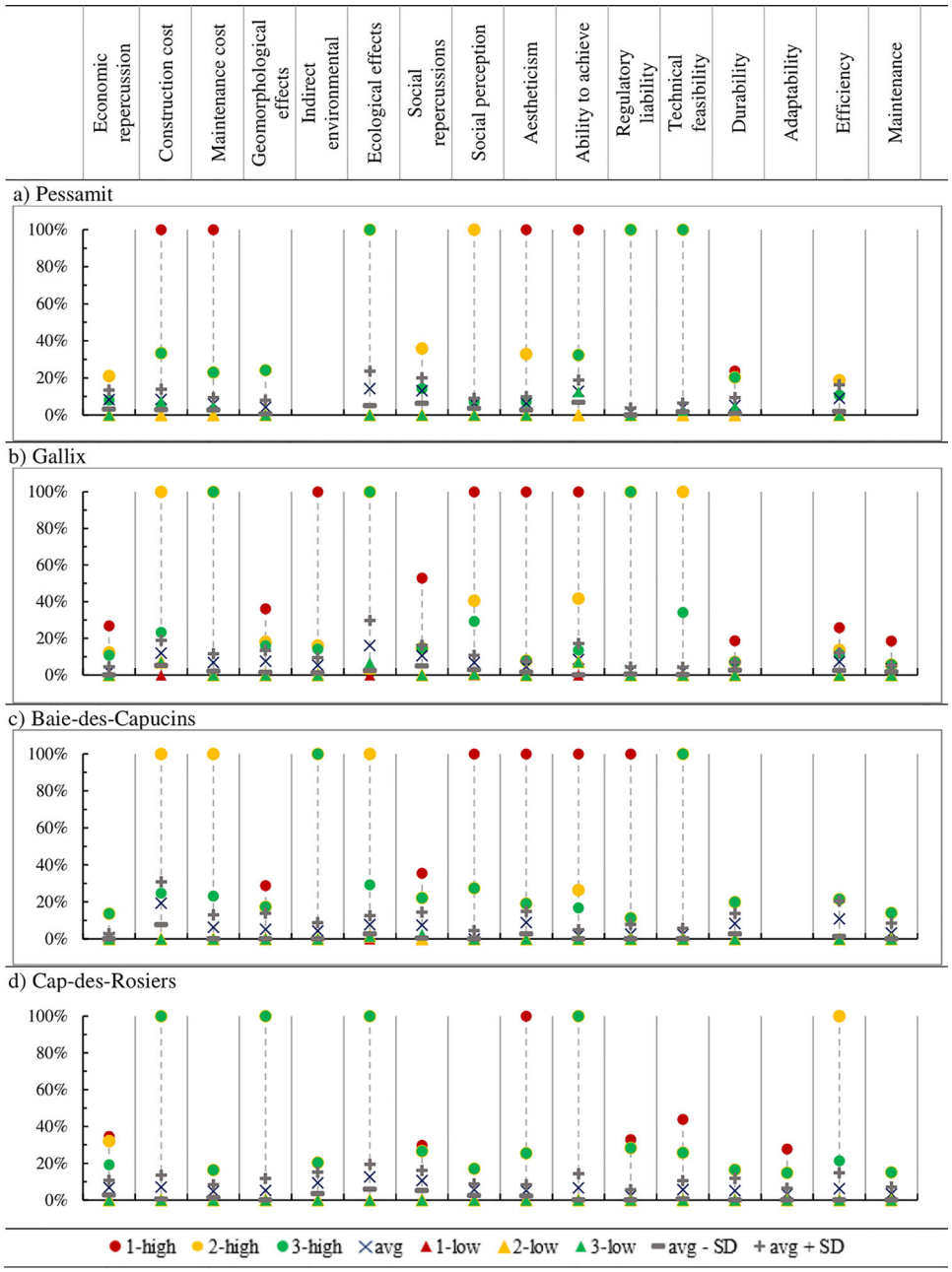

FIGURE 8 | Robustness analysis of CDMs ranked 1 (red), 2 (yellow), and 3 (green), in relation to each criterion for each site **(A)** Pessamit; **(B)** Gallix; **(C)** Baie-des-Capucins; **(D)** Cap-des-Rosiers). The vertical axis shows the average criteria weight in percentage. The circles and triangles show the highest and lowest thresholds at which there is a change in the top 3 ranked CDMs for a given criterion. The blue X shows the criterion weighted average. The grey plus and minus signs show the weighted average plus and minus the standard deviation.

certainly influences the interpretation of the results. Subsequent work regarding the use of multicriteria analysis for the evaluation of CDMs should consider taking advantage of the established list of 16 criteria, in order to avoid a repetition of this phase of the process, and allow more time for the weighting phase. Prior to the workshops, the list can be modified or expanded, depending on the context and environmental conditions.

Despite these drawbacks, the use of multicriteria analysis is advantageous, especially when dealing with complex problems. Its capacity to integrate and process subjective information obtained from local stakeholders in participatory processes, is invaluable to an inclusive decision-making process. In the future, the participatory process could be improved by allowing more time for discussion on the values and weighting of the criteria.

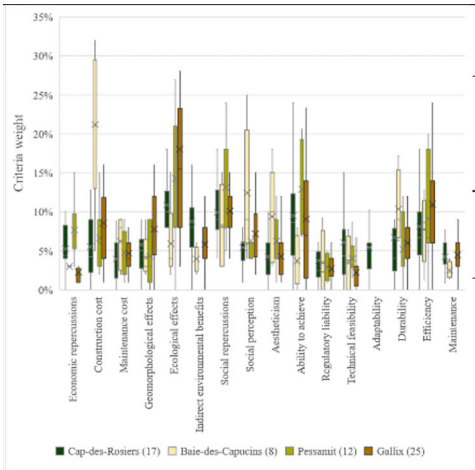

Figure 5

- Preliminary observation on the robustness of the hierarchization: for each criterion, a narrow range in the weighting results indicates high robustness

Criteria	Sites	Enrockment	Seawall	Emerged breakwater	Low-crested breakwater
Social perception	*Pessamit*	-	-	3	-
	Gallix	-	-	8	-
	Baie-des-Capucins	-	-	-	2
	Cap-des-Rosiers	4	9	1	1
Aestheticism	*Pessamit*	-	-	1	-
	Gallix	-	-	1	-
	Baie-des-Capucins	-	-	-	2
	Cap-des-Rosiers	4	3	2	3

Table 6

- Evaluation of the CDMs according to each criterion

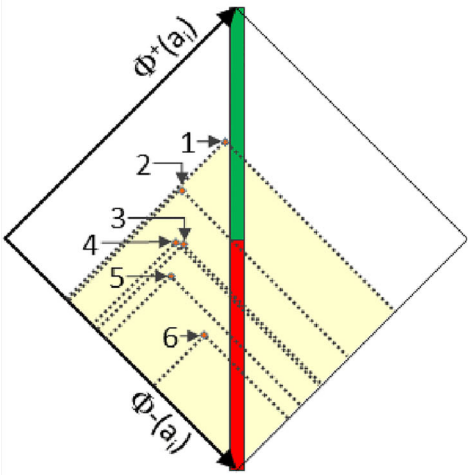

Figure 6

- CDMs hierarchization

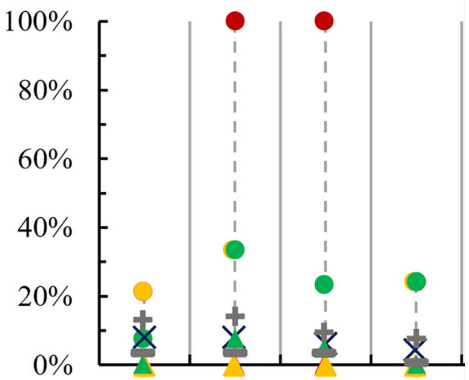

Figure 7

- Analysis and confirmation of observations made at the CDMs hierarchization phase

FIGURE 9 | Illustration of the three phases of the MCDA process and robustness analysis in different report formats.

For instance, participants could be asked to select from a pre-established list of criteria, following a thorough presentation describing the meaning, the scope, and the limits of each criterion. A better understanding of each criterion by participants, would result in a set of criteria that is more accurate, and more representative of their local socio-ecological contexts. Allowing more time to the weighting phase would also possibly result in more accuracy, and narrower ranges in the weighted values.

4.3 Contribution to Coastal Engineering and Management

The proposed MCDA approach is a flexible tool that could contribute to coastal engineering and management by its capacity to structure and analyze the multiple dimensions of a complex problem, that are not necessarily easy to quantify. The method helps compare alternatives in relation to all relevant criteria (Choo et al., 1999; Horstman et al., 2009), while taking into consideration their relative importance, as rated by different local stakeholders. The end result is a better knowledge of the specific context, and is more likely to lead to a solution that is well adapted to the environment in question. This would answer a need raised, in the past, by coastal decision-makers for the necessity to make better decisions related to CDMs (Friesinger and Bernatchez, 2010; Drejza et al., 2011; Marie et al., 2017). The inclusion of coastal managers and professionals in the criteria identification and weighting phases, is in line with a trend to involve more social stakeholders in environmental management

(Reed, 2008; Garmendia et al., 2010; Jones et al., 2014; Marttunen et al., 2017). It gives decision-makers a better understanding of local conditions, priorities and interests, and it enhances the stakeholders' comprehension of all issues related to the interaction between CDMs and socio-ecological systems. The approach is conducive to supporting discussions in a group of stakeholders from different disciplines and functions. Therefore, the solutions emerge from an interdisciplinary exchange process (Gamper and Turcanu, 2007), which contributes to increasing the resilience of the socio-ecological system (Folke, 2016). In three of the four study sectors presented in this article, the MCDA approach made it possible to consider solutions other than rock armour and seawalls which have, up until now, often been implemented in Quebec, regardless of the type of coastal environment (Bernatchez and Fraser, 2012; Sauvé et al., 2020).

5 CONCLUSION

Coastal zone managers and professionals were involved in a participatory process, which led to the identification and weighting of criteria for the purpose of selecting CDMs that are suitable to specific conditions. A multicriteria decision analysis approach was used to evaluate and hierarchize CDMs. The methodology was applied to four study sites in the province of Quebec, Canada: Pessamit, Gallix, Baie-des-Capucins, and Cap-des-Rosiers. The study sites have distinct geomorphological, hydrodynamic, ecological or socio-economic characteristics. PROMETHEE, an outranking method, was chosen to carry out the multicriteria analysis. First, a set of 16 criteria were identified and weighted by participants of five workshops. Second, CDMs were evaluated in relation to each criterion, and according to local socio-ecological features. Third, CDMs were hierarchized using the information obtained in the first two steps. Results show that vegetation holds the first rank in the Pessamit, Gallix, and Baie-des-Capucins sites, while rock armour is first in Cap-des-Rosiers. Still, deeper analysis indicates that, because of their high ranking, beach nourishment and permeable groin are options that are worthwhile considering. Finally, the results are supported by a robustness analysis. The Pessamit, and Gallix sites have similar results, which are explained by the comparability of their environmental characteristics and coastal activities. Findings regarding criteria identification and weighting as a participatory process can be divided in two parts. First, the criteria as identified by workshop participants were too specific, making it difficult to synthetize into a concise and comprehensive list useful for the evaluation of CDMs. To alleviate this problem, this phase of the process could be substituted by a detailed presentation of a pre-established list of criteria, followed by a discussion leading to the selection and weighting, by participants, of relevant criteria from the predefined list. Second, the weighting process was found to be a highly effective way to integrate local knowledge into the decision-making process. The three stages of the multicriteria decision analysis facilitate the decision-making process by presenting the results in a structured, transparent and integrated way, while taking stakeholders' preferences into account. Ultimately, the multicriteria decision analysis coupled with a participatory process is a flexible methodology that structures multiple aspects related to the selection of a CDM. It is a tool that can appreciably improve the coastal engineering and management decision-making process, and contribute to a better understanding of the socio-ecological systems.

DATA AVAILABILITY STATEMENT

The raw data supporting the conclusions of this article will be made available by the authors, without undue reservation.

ETHICS STATEMENT

The studies involving human participants were reviewed and approved by Comité d'éthique de la recherche avec des êtres humains de l'UQAR (CÉR-101-748). The patients/participants provided their written informed consent to participate in this study

AUTHOR CONTRIBUTIONS

PS defined the state of knowledge, developed and executed the methodology, analyzed the data, and wrote the manuscript. PB contributed to the execution of the methodology and the editing of the manuscript. MG contributed to the development and execution of the methodology, the analysis of the results, and the editing of the manuscript. All authors contributed to the article and approved the submitted version.

FUNDING

We are grateful to the Ministère de la Sécurité publique du Québec from his program for natural risks prevention 2013-2020 (CPS 16-17-07 project), to the Ministère de l'Environnement et de la Lutte contre les changements climatiques from the Fonds vert and the Climate Change Action Plan (PACC 2013-2020) of the Government of Québec, and to Natural Resources Canada for its programme on Climate change adaptation (AP660 V205 2017-12-28) for financing the project.

ACKNOWLEDGMENTS

The authors would like to thank all the members of the Research Chair in Coastal Geoscience who participated in consultations organisation and execution, particularly Maud Touchette, Catherine Paul-Hus, Stéphanie Friesinger, and Christian Fraser. We would also like to thank all the workshops participants. Finally, a special thank you to Danielle Allard for the English revision.

REFERENCES

Abdel-Basset, M., Gamal, A., Chakrabortty, R. K., and Ryan, M. (2021). A New Hybrid Multi-Criteria Decision-Making Approach for Location Selection of Sustainable Offshore Wind Energy Stations: A Case Study. *J. Clean. Prod.* 280, 124462. doi: 10.1016/j.jclepro.2020.124462

Airoldi, L., Abbiati, M., Beck, M. W., Hawkins, S. J., Jonsson, P. R., Martin, D., et al. (2005). An Ecological Perspective on the Deployment and Design of Low-Crested and Other Hard Coastal Defence Structures. *Coast. Eng.* 52, 1073–1087. doi: 10.1016/j.coastaleng.2005.09.007

Alves, A., Gersonius, B., Sanchez, A., Vojinovic, Z., and Kapelan, Z. (2018). Multi-Criteria Approach for Selection of Green and Grey Infrastructure to Reduce Flood Risk and Increase CO-Benefits. *Water Resour. Manage.* 32, 2505–2522. doi: 10.1007/s11269-018-1943-3

Ananda, J., and Herath, G. (2009). A Critical Review of Multi-Criteria Decision Making Methods With Special Reference to Forest Management and Planning. *Ecol. Econ.* 68, 2535–2548. doi: 10.1016/j.ecolecon.2009.05.010

André, P., Delisle, C. E., and Revéret, J.-P. (2010). *L'évaluation Des Impacts Sur L'environnement: Processus, Acteurs Et Pratique Pour Un Développement Durable. 3e ed* (Montréal, QC, Canada: Presses internationales Polytechnique).

Antunes, P., Karadzic, V., Santos, R., Beça, P., and Osann, A. (2011). Participatory Multi-Criteria Analysis of Irrigation Management Alternatives: The Case of the Caia Irrigation District, Portugal. *Int. J. Agric. Sustain.* 9, 334–349. doi: 10.1080/14735903.2011.582358

Baquerizo, A., and Losada, M. A. (2008). Human Interaction With Large Scale Coastal Morphological Evolution. An Assessment of the Uncertainty. *Coast. Eng.* 55, 569–580. doi: 10.1016/j.coastaleng.2007.10.004

Barzehkar, M., Parnell, K. E., Mobarghaee Dinan, N., and Brodie, G. (2021). Decision Support Tools for Wind and Solar Farm Site Selection in Isfahan Province, Iran. *Clean. Technol. Environ. Policy* 23, 1179–1195. doi: 10.1007/s10098-020-01978-w

Behzadian, M., Kazemzadeh, R. B., Albadvi, A., and Aghdasi, M. (2010). PROMETHEE: A Comprehensive Literature Review on Methodologies and Applications. *Eur. J. Oper. Res.* 200, 198–215. doi: 10.1016/j.ejor.2009.01.021

Belton, V., and Stewart, T. (2002). *Multiple Criteria Decision Analysis: An Integrated Approach* (Boston, USA: Kluwer Academic Publishers, Springer Science & Business Media).

Bernatchez, P., Dugas, S., Fraser, C., and Da Silva, L. (2015) *Évaluation Economique Des Impacts Potentiels De L'érosion Des Côtes Du Québec Maritime Dans Un Contexte De Changements Climatiques*. Available at: https://www.ouranos.ca/publication-scientifique/RapportBernatchez2015_FR.pdf%5Cnhttps://www.ouranos.ca/programmes/evaluation-economique/.

Bernatchez, P., and Fraser, C. (2012). Evolution of Coastal Defence Structures and Consequences for Beach Width Trends, Québec, Canada. *J. Coast. Res.* 28, 1550–1566. doi: 10.2112/JCOASTRES-D-10-00189.1

Bilkovic, D. M., Mitchell, M. M., La Peyre, M. K., and Toft, J. D. (2017). *Living Shorelines: The Science and Management of Nature-Based Coastal Protection* (Boca Raton: CRC Press).

Boardman, A. E., Greenberg, D. H., Vining, A. R., and Weimer, D. L. (2017). *Cost-Benefit Analysis: Concepts and Practice* (Cambridge, United Kingdom: Cambridge University Press).

Boyer-Villemaire, U., Circé, M., Da Silva, L., Desjarlais, C., and Morneau, F. (2016). *Analyses Coûts-Avantages Des Options D'adaptation En Zone Côtière Au Québec Et Dans Les Provinces Atlantiques* (Montréal: Ouranos), pp. 36.

Boyer-Villemaire, U., Lamari, M., Bernatchez, P., Jacob, J. L., and Nouwodjro, K. (2015). ""Analyse Institutionnelle De La Trajectoire D'adaptation Aux Changements Climatiques Dans Le Québec Maritime," in *Adaptation Aux Changements Climatiques En Zones Côtières: Politiques Publiques Et Indicateurs De Suivi Des Progrès Dans Sept Pays Occidentaux*. Eds. M. Lamari and J. L. Jacob (Québec, Canada: Presses de l'Université du Québec), 77–126.

Brans, J. P., Vincke, P., and Mareschal, B. (1986). How to Select and How to Rank Projects: The PROMETHEE Method. *Eur. J. Oper. Res.* 24, 228–238. doi: 10.1016/0377-2217(86)90044-5

Bridges, T. S., Bourne, E. M., King, J. K., Kuzmitski, H. K., Moynihan, E. B., and Suedel, B. C. (2018). *Engineering With Nature: An Atlas* (Vicksburg, MS: U.S. Army).

Brown, J., Isaacs, D.World Café community. (2005). *The World Café: Shaping Our Futures Through Conversations That Matter* (Oakland, CA: Berrett-Koehler Publishers, Inc).

Bryce, R., Irvine, K. N., Church, A., Fish, R., Ranger, S., and Kenter, J. O. (2016). Subjective Well-Being Indicators for Large-Scale Assessment of Cultural Ecosystem Services. *Ecosyst. Serv.* 21, 258–269. doi: 10.1016/j.ecoser.2016.07.015

Chang, H.-K., Liou, J.-C., and Chen, W.-W. (2012). Protection Priority in the Coastal Environment Using a Hybrid AHP-TOPSIS Method on the Miaoli Coast, Taiwan. *J. Coast. Res* 28, 369–374. doi: 10.2112/JCOASTRES-D-10-00092.1

Chan, K. M. A., Satterfield, T., and Goldstein, J. (2012). Rethinking Ecosystem Services to Better Address and Navigate Cultural Values. *Ecol. Econ.* 74, 8–18. doi: 10.1016/j.ecolecon.2011.11.011

Charlier, R. H., Chaineux, M. C. P., and Morcos, S. (2005). Panorama of the History of Coastal Protection. *J. Coast. Res.* 21, 79–111. doi: 10.2112/03561.1

Choo, E. U., Schoner, B., and Wedley, W. C. (1999). Interpretation of Criteria Weights in Multicriteria Decision Making. *Comput. Ind. Eng.* 37, 527–541. doi: 10.1016/S0360-8352(00)00019-X

Chow, A., Leung, T., and Lee, F. (2017). Benefit-Cost Analysis on Coastal Structures Design for Climate Change Adaptation in Hong Kong. *Coast. Eng. J.* 59, 1–25. doi: 10.1142/S0578563417400058

Church, J. A., and White, N. J. (2011). Sea-Level Rise From the Late 19th to the Early 21st Century. *Surv. Geophys.* 32, 585–602. doi: 10.1007/s10712-011-9119-1

Cooper, J. A. G., O'Connor, M. C., and McIvor, S. (2020). Coastal Defences Versus Coastal Ecosystems: A Regional Appraisal. *Mar. Policy* 111, 102332. doi: 10.1016/j.marpol.2016.02.021

Corriveau, M., Bernatchez, P., and Dugas, S. (2019). "Mise a Jour De La Cartographie Des Marges De Sécurité En Erosion Côtière Pour Le Secteur De Gallix, Municipalité De Sept-Îles: Analyse De L'évolution Côtière Et De La Dynamique," in *Chaire de recherche en géoscience côtière, Laboratoire de dynamique et de gestion intégrée des zones côtières* (Rimouski, Qc, Canada: Université du Québec à Rimouski), pp. 108.

Corriveau, M., Caulet, C., and Bernatchez, P. (2021). "Modélisation Et Cartographie Du Risque De Submersion Côtière De La Région De Sept-Îles, Rapport Intermédiaire," in *Chaire de recherche en géoscience côtière, Laboratoire de dynamique et de gestion intégrée des zones côtières* (Rimouski, Qc, Canada: Université du Québec à Rimouski), pp. 91

De Bruin, K., Dellink, R. B., Ruijs, A., Bolwidt, L., van Buuren, A., Graveland, J., et al. (2009). Adapting to Climate Change in the Netherlands: An Inventory of Climate Adaptation Options and Ranking of Alternatives. *Clim. Change* 95, 23–45. doi: 10.1007/s10584-009-9576-4

de Vriend, H. J., and Van Koningsveld, M. (2012). *Building With Nature: Thinking, Acting and Interacting Differently*. (Dordrecht, the Netherlands: EcoShape, Building with Nature). doi: 10.1080/02513625.2014.925714

Dodgson, J. S., Spackman, M., Pearman, A. D., and Phillips, L. D. (2009). *Multi-Criteria Analysis: A Manual* (London: Department for Communities and Local Government).

Drejza, S., Bernatchez, P., and Dugas, C. (2011). Effectiveness of Land Management Measures to Reduce Coastal Georisks, Eastern Québec, Canada. *Ocean. Coast. Manage.* 54, 290–301. doi: 10.1016/j.ocecoaman.2011.01.001

Dugan, J. E., Airoldi, L., Chapman, M. G., Walker, S. J., and Schlacher, T. A. (2011). ""Estuarine and Coastal Structures: Environmental Effects, A Focus on Shore and Nearshore Structures," in *Treatise on Estuarine and Coastal Science*. Eds. E. Wolanski and D. S. McLusky (Elsevier Inc), 17–41. doi: 10.1016/B978-0-12-374711-2.00802-0

EEA (2006). *The Changing Faces of Europe's Coastal Areas* (Copenhague: European Environment Agency).

Evans, A. J., Garrod, B., Firth, L. B., Hawkins, S. J., Morris-Webb, E. S., Goudge, H., et al. (2017). Stakeholder Priorities for Multi-Functional Coastal Defence Developments and Steps to Effective Implementation. *Mar. Policy* 75, 143–155. doi: 10.1016/j.marpol.2016.10.006

Folke, C. (2016). Resilience (Republished). *Ecol. Soc* 21, 30. doi: 10.5751/ES-09088-210444

Folke, C., Hahn, T., Olsson, P., and Norberg, J. (2005). Adaptive Governance of Social-Ecological Systems. *Annu. Rev. Environ. Resour.*, 441–473. doi: 10.1146/annurev.energy.30.050504.144511

Friesinger, S., and Bernatchez, P. (2010). Perceptions of Gulf of St. Lawrence Coastal Communities Confronting Environmental Change: Hazards and

Adaptation, Québec, Canada. *Ocean. Coast. Manage.* 53, 669–678. doi: 10.1016/j.ocecoaman.2010.09.001

Gallopín, G. C. (2006). Linkages Between Vulnerability, Resilience, and Adaptive Capacity. *Glob. Environ. Change* 16, 293–303. doi: 10.1016/j.gloenvcha.2006.02.004

Gamper, C. D., and Turcanu, C. (2007). On the Governmental Use of Multi-Criteria Analysis. *Ecol. Econ.* 62, 298–307. doi: 10.1016/j.ecolecon.2007.01.010

Garmendia, E., and Gamboa, G. (2012). Weighting Social Preferences in Participatory Multi-Criteria Evaluations: A Case Study on Sustainable Natural Resource Management. *Ecol. Econ.* 84, 110–120. doi: 10.1016/j.ecolecon.2012.09.004

Garmendia, E., Gamboa, G., Franco, J., Garmendia, J. M., Liria, P., and Olazabal, M. (2010). Social Multi-Criteria Evaluation as a Decision Support Tool for Integrated Coastal Zone Management. *Ocean. Coast. Manage.* 53, 385–403. doi: 10.1016/j.ocecoaman.2010.05.001

Garmendia, E., and Stagl, S. (2010). Public Participation for Sustainability and Social Learning: Concepts and Lessons From Three Case Studies in Europe. *Ecol. Econ.* 69, 1712–1722. doi: 10.1016/j.ecolecon.2010.03.027

Gittman, R. K., Fodrie, F. J., Popowich, A. M., Keller, D. A., Bruno, J. F., Currin, C. A., et al. (2015). Engineering Away Our Natural Defenses: An Analysis of Shoreline Hardening in the US. *Front. Ecol. Environ.* 13, 301–307. doi: 10.1890/150065

Grêt-Regamey, A., Sirén, E., Brunner, S. H., and Weibel, B. (2017). Review of Decision Support Tools to Operationalize the Ecosystem Services Concept. *Ecosyst. Serv.* 26, 306–315. doi: 10.1016/j.ecoser.2016.10.012

Ha, S., Tatano, H., Mori, N., Fujimi, T., and Jiang, X. (2021). Cost–benefit Analysis of Adaptation to Storm Surge Due to Climate Change in Osaka Bay, Japan. *Clim. Change* 169, 1–20. doi: 10.1007/s10584-021-03282-y

Holling, C. S., and Gunderson, L. H. (2002). "Resilience and Adaptive Cycle," in *Panarchy - Understanding Transformation in Human and Natural Systems*. Eds. L. H. Gunderson and C. S. Holling (Washington, DC: Island Press), 25–62.

Horstman, A. E. M., Wijnberg, K. M., Smale, A. J., Hulscher, S. J. M. H., Wijnbergt, K. M., and Hiih, H. (2009). Long-Term Coastal Management Strategies: Useful or Useless? *J. Coast. Res.* I, 233–237. https://www.jstor.org/stable/25737572.

Jacob, C., Bernatchez, P., Dupras, J., and Cusson, M. (2021). Not Just an Engineering Problem: The Role of Knowledge and Understanding of Ecosystem Services for Adaptive Management of Coastal Erosion. *Ecosyst. Serv.* 51, 16. doi: 10.1016/j.ecoser.2021.101349

Jajac, N., Kilič, J., and Rogulj, K. (2019). An Integral Approach to Sustainable Decision-Making Within Maritime Spatial Planning-A DSC for the Planning of Anchorages on the Island of Šolta, Croatia. *Sustain ability* 11, 27. doi: 10.3390/su11010104

Jones, R. N., Patwardhan, A., Cohen, S. J., Kumar, P., Barros, R., Dokken, D. J., et al. (2014). ""Foundations for Decision Making," in *Climate Change 2014: Impacts, Adaptation, and Vulnerability. Part A: Global and Sectoral Aspects. Contribution of Working Group II to the Fifth Assessment Report of the Intergovernmental Panel on Climate Change*, vol. 195–228. Eds. C. B. Field, V. R. Barros, D. J. Dokken, K. J. Mach, M. D. Mastrandrea, T. E. Bilir, et al (Cambridge, United Kingdom and New York, NY, USA: Cambridge University Press).

Koike, K. (1996). The Countermeasures Against Coastal Hazards in Japan. *GeoJournal* 38, 301–312. doi: 10.1007/BF00204722

Koontz, T. M., Gupta, D., Mudliar, P., and Ranjan, P. (2015). Adaptive Institutions in Social-Ecological Systems Governance: A Synthesis Framework. *Environ. Sci. Policy* 53, 139–151. doi: 10.1016/j.envsci.2015.01.003

Lima, M., Coelho, C., Veloso-Gomes, F., and Roebeling, P. (2020). An Integrated Physical and Cost-Benefit Approach to Assess Groins as a Coastal Erosion Mitigation Strategy. *Coast. Eng.* 156, 103614. doi: 10.1016/j.coastaleng.2019.103614

Maia, A., Bernardes, C., and Alves, M. (2015). Cost-Benefit Analysis of Coastal Defenses on the Vagueira and Labrego Beaches in North West Portugal. *J. Integr. Coast. Zo. Manage.* 15, 81–90. doi: 10.5894/rgci521

Marie, G., Bernatchez, P., Fraser, C., Touchette, M., Papageorges, S., Coulombe, D., et al. (2017). L'adaptation Aux Aléas Côtiers Dans Un Contexte De Changements Climatiques: Portrait Des Besoins Exprimés Et Des Outils Proposés a L'échelle Des MRC De L'est Du Québec," in *Chaire de Recherche en Géoscience Côtier, Laboratoire de Dynamique Et De Gestion Intégrée Des Zones Côtières* (Rimouski, QC, Canada: Université du Québec à Rimouski).

Marttunen, M., Lienert, J., and Belton, V. (2017). Structuring Problems for Multi-Criteria Decision Analysis in Practice: A Literature Review of Method Combinations. *Eur. J. Oper. Res.* 263, 1–17. doi: 10.1016/j.ejor.2017.04.041

Maystre, L. Y., Pictet, J., and Simos, J. (1994). *Méthodes Multicritères ELECTRE: Description, Conseils Pratiques Et Cas D'application a La Gestion Environnementale* (PPUR presses polytechniques).

McCauley, D. J. (2006). Selling Out on Nature. *Nature* 443, 27–28. doi: 10.1038/443027a

McIntosh, B. S., Ascough, J. C., Twery, M., Chew, J., Elmahdi, A., Haase, D., et al. (2011). Environmental Decision Support Systems (EDSS) Development - Challenges and Best Practices. *Environ. Model. Software* 26, 1389–1402. doi: 10.1016/j.envsoft.2011.09.009

Monterroso, I., Binimelis, R., and Rodríguez-Labajos, B. (2011). New Methods for the Analysis of Invasion Processes: Multi-Criteria Evaluation of the Invasion of Hydrilla Verticillata in Guatemala. *J. Environ. Manage.* 92, 494–507. doi: 10.1016/j.jenvman.2010.09.017

Morris, R. L., Konlechner, T. M., Ghisalberti, M., and Swearer, S. E. (2018). From Grey to Green: Efficacy of Eco-Engineering Solutions for Nature-Based Coastal Defence. *Glob. Change Biol.* 24, 1827–1842. doi: 10.1111/gcb.14063

Morris, R. L., Strain, E. M. A., Konlechner, T. M., Fest, B. J., Kennedy, D. M., Arndt, S. K., et al. (2019). Developing a Nature-Based Coastal Defence Strategy for Australia. *Aust. J. Civ. Eng.* 17, 167–176. doi: 10.1080/14488353.2019.1661062

Moschella, P. S., Abbiati, M., Åberg, P., Airoldi, L., Anderson, J. M., Bacchiocchi, F., et al. (2005). Low-Crested Coastal Defence Structures as Artificial Habitats for Marine Life: Using Ecological Criteria in Design. *Coast. Eng.* 52, 1073–1087. doi: 10.1016/j.coastaleng.2005.09.014

National Research Council (2009). *Informing Decisions in a Changing Climate* (Washington, DC: The National Academies Press). doi: 10.17226/12626

Nicholls, R. J., and Cazenave, A. (2010). Sea-Level Rise and Its Impact on Coastal Zones. *Science (80-.)* 328, 1517–1520. doi: 10.1126/science.1185782

O'Riordan, T. (2005). "Inclusive and Community Participation in the Coastal Zone: Opportunities and Dangers," in *Managing European Coasts*. Eds. J. Vermaat, W. Salomons, L. Bouwer and K. Turner (Berlin, Heidelberg: Springer Berlin Heidelberg), 173–184.

Polasky, S., Carpenter, S. R., Folke, C., and Keeler, B. (2011). Decision-Making Under Great Uncertainty: Environmental Management in an Era of Global Change. *Trends Ecol. Evol.* 26, 398–404. doi: 10.1016/j.tree.2011.04.007

Polomé, P., Marzetti, S., and van der Veen, A. (2005). Economic and Social Demands for Coastal Protection. *Coast. Eng.* 52, 819–840. doi: 10.1016/j.coastaleng.2005.09.009

Ranasinghe, R. (2016). Assessing Climate Change Impacts on Open Sandy Coasts: A Review. *Earth-Sci.s Rev.* 160, 320–332. doi: 10.1016/j.earscirev.2016.07.011

Reed, M. S. (2008). Stakeholder Participation for Environmental Management: A Literature Review. *Biol. Conserv.* 141, 2417–2431. doi: 10.1016/j.biocon.2008.07.014

Saarikoski, H., Mustajoki, J., Barton, D. N., Geneletti, D., Langemeyer, J., Gomez-Baggethun, E., et al. (2016). Multi-Criteria Decision Analysis and Cost-Benefit Analysis: Comparing Alternative Frameworks for Integrated Valuation of Ecosystem Services. *Ecosyst. Serv.* 22, 238–249. doi: 10.1016/j.ecoser.2016.10.014

Saaty, T. L. (2008). Decision Making With the Analytic Hierarchy Process. *Int. J. Serv. Sci.* 1, 83–98. doi: 10.1504/IJSSCI.2008.017590

Sauvé, P., Bernatchez, P., and Glaus, M. (2022). Identification of Coastal Defence Measure Best Adapted to Mitigate Hazards in Specific Coastal Systems: Development of a Dynamic Literature Meta-Analysis Methodology. *J. Mar. Sci. Eng*, 13. doi: 10.3390/jmse10030394

Sauvé, P., Bernatchez, P., Moisset, S., Glaus, M., and Goudreault, M.-O (2022). Case Studies on Coastal Defence Measures: A Meta-Analysis of Literature to Ultimately Improve Decision-Making. *Manag.*; submitted

Savoie-Ferron, F., Goudreault, M.-O., Autret, R., and Bandet, M. (2020). "Suivi Environnemental De Travaux De Rechargement De Plage Et De La Renaturalisation D'une Plage Comme Solution D'adaptation Aux Aléas Côtiers Dans L'estuaire Et Le Golfe Du Saint-Laurent," in *Chaire de recherche en géoscience côtière, Laboratoire de dynamique et de gestion intégrée des zones côtières* (Rimouski, Qc, Canada: Université du Québec à Rimouski), pp. 162. Available at: https://ldgizc.uqar.ca/Web/docs/default-source/default-document-library/savoie-ferron_etal_2020_rapport_final_recharge_corrige_cps-17-18-02.pdf?sfvrsn=60fef139_0.

Schoonees, T., Gijón Mancheño, A., Scheres, B., Bouma, T. J., Silva, R., Schlurmann, T., et al. (2019). Hard Structures for Coastal Protection, Towards Greener Designs. *Estuaries. Coast.* 42, 1709–1729. doi: 10.1007/s12237-019-00551-z

Scott, J. A., Ho, W., and Dey, P. K. (2012). A Review of Multi-Criteria Decision-Making Methods for Bioenergy Systems. *Energy* 42, 146–156. doi: 10.1016/j.energy.2012.03.074

Stagl, S. (2006). Multicriteria Evaluation and Public Participation: The Case of UK Energy Policy. *Land. Use Policy* 23, 53–62. doi: 10.1016/j.landusepol.2004.08.007

Tavra, M., Jajac, N., and Cetl, V. (2017). Marine Spatial Data Infrastructure Development Framework: Croatia Case Study. *ISPRS. Int. J. Geo-Info.* 6, 15. doi: 10.3390/ijgi6040117

Thi Oanh, P., Tamura, M., Kumano, N., and Nguyen, Q. V. (2020). Cost-Benefit Analysis of Mixing Gray and Green Infrastructures to Adapt to Sea Level Rise in the Vietnamese Mekong River Delta. *Sustainability* 12, 1–19. doi: 10.3390/su122410356

Trutnevyte, E., Stauffacher, M., and Scholz, R. W. (2011). Supporting Energy Initiatives in Small Communities by Linking Visions With Energy Scenarios and Multi-Criteria Assessment. *Energy Policy* 39, 7884–7895. doi: 10.1016/j.enpol.2011.09.038

Trutnevyte, E., Stauffacher, M., and Scholz, R. W. (2012). Linking Stakeholder Visions With Resource Allocation Scenarios and Multi-Criteria Assessment. *Eur. J. Oper. Res.* 219, 762–772. doi: 10.1016/j.ejor.2012.01.009

USACE. (2006). "ldquo;Planning and Design Process," in *Coastal Engineering Manual* (Washington, DC, US: U.S. Army corps of Engineers), 17.

Valloni, R., Ferretti, O., Barsanti, M., and Ugolotti, M. (2003). "The Morpho-Sedimentological Types of Italian Coasts and Their Susceptibility to Sea-Level Rise: A First Approximation," in *Quaternary Coastal Morphology and Sea Level Changes* (Puglia, Italy: Final Conference Project IGCP 437), 5–6. Available at: http://www.igcp437finalconference.unisalento.it/AbstractBook/ValloniV_VI.pdf.

van Slobbe, E., de Vriend, H. J., Aarninkhof, S. G. J., Lulofs, K., de Vries, M. B., and Dircke, P. (2013). Building With Nature: In Search of Resilient Storm Surge Protection Strategies. *Nat. Haz.* 66, 1461–1480. doi: 10.1007/s11069-013-0612-3

VPSolutions. (2013). *Visual PROMETHEE 1.4 Manual*. (Bruxelles, Belgium: VPSolutions).

Vuik, V., Borsje, B. W., Willemsen, P. W. J. M., and Jonkman, S. N. (2019). Salt Marshes for Flood Risk Reduction: Quantifying Long-Term Effectiveness and Life-Cycle Costs. *Ocean. Coast. Manage.* 171, 96–110. doi: 10.1016/j.ocecoaman.2019.01.010

Walling, E., and Vaneeckhaute, C. (2020). Developing Successful Environmental Decision Support Systems: Challenges and Best Practices. *J. Environ. Manage.* 264, 16. doi: 10.1016/j.jenvman.2020.110513

Wegner, G., and Pascual, U. (2011). Cost-Benefit Analysis in the Context of Ecosystem Services for Human Well-Being: A Multidisciplinary Critique. *Glob. Environ. Change* 21, 492–504. doi: 10.1016/j.gloenvcha.2010.12.008

Westmacott, S. (2001). Developing Decision Support Systems for Integrated Coastal Management in the Tropics: Is the ICM Decision-Making Environment Too Complex for the Development of a Useable and Useful DSS? *J. Environ. Manage.* 62, 55–74. doi: 10.1006/jema.2001.0420

Wong, P. P., Losada, I. J., Gattuso, J.-P., Hinkel, J., Khattabi, A., McInnes, K. L., et al. (2014). "Coastal Systems and Low-Lying Areas," in *Climate Change 2014: Impacts, Adaptation, and Vulnerability. Part A: Global and Sectoral Aspects. Contribution of Working Group II to the Fifth Assessment Report of the Intergovernmental Panel on Climate Change* (Cambridge, United Kingdom: Cambridge University Press), 361–409.

Wong-Parodi, G., Mach, K. J., Jagannathan, K., and Sjostrom, K. D. (2020). Insights for Developing Effective Decision Support Tools for Environmental Sustainability. *Curr. Opin. Environ. Sustain.* 42, 52–59. doi: 10.1016/j.cosust.2020.01.005

Zafirakou, A., Themeli, S., Tsami, E., and Aretoulis, G. (2018). Multi-Criteria Analysis of Different Approaches to Protect the Marine and Coastal Environment From Oil Spills. *J. Mar. Sci. Eng.* 6, 17. doi: 10.3390/jmse6040125

Conflict of Interest: The authors declare that the research was conducted in the absence of any commercial or financial relationships that could be construed as a potential conflict of interest.

Publisher's Note: All claims expressed in this article are solely those of the authors and do not necessarily represent those of their affiliated organizations, or those of the publisher, the editors and the reviewers. Any product that may be evaluated in this article, or claim that may be made by its manufacturer, is not guaranteed or endorsed by the publisher.

frontiers | Frontiers in Marine Science

ORIGINAL RESEARCH
published: 06 May 2022
doi: 10.3389/fmars.2022.871156

Application of Airborne LiDAR Measurements to the Topographic Survey of the Tidal Flats of the Northern Jiangsu Radial Sand Ridges in the Southern Yellow Sea

Haifeng Zhang[1,2], *Lian Wang*[1], *Yifei Zhao*[1*], *Jicheng Cao*[1] *and Min Xu*[1*]

[1] School of Marine Science and Engineering, Nanjing Normal University, Nanjing, China, [2] Island Research Center, Ministry of Natural Resources (MNR), Fujian, China

OPEN ACCESS

Edited by:
Felice D'Alessandro,
University of Milan, Italy

Reviewed by:
Qinghua Ye,
Deltares, Netherlands
Mei Xuefei,
East China Normal University, China

***Correspondence:**
Yifei Zhao
yfzhao@njnu.edu.cn
Min Xu
xumin0895@njnu.edu.cn

Specialty section:
This article was submitted to Coastal Ocean Processes, a section of the journal Frontiers in Marine Science

Received: 07 February 2022
Accepted: 25 March 2022
Published: 06 May 2022

Citation:
Zhang H, Wang L, Zhao Y, Cao J and Xu M (2022) Application of Airborne LiDAR Measurements to the Topographic Survey of the Tidal Flats of the Northern Jiangsu Radial Sand Ridges in the Southern Yellow Sea. Front. Mar. Sci. 9:871156. doi: 10.3389/fmars.2022.871156

The northern Jiangsu radial sand ridges are typical geomorphic deposit units distributed off the Jiangsu coast. A coastal tidal flat typically develops and provides a good habitat for many migratory birds and benthic organisms. However, topographic surveys of tidal flats have always been difficult in marine surveys because of the dense tidal creek, poor accessibility, and difficulty in setting up control points. In this study, we quickly obtained the point cloud data of the tidal flat near Yangkou Port in the southern part of the radial sand ridges based on an airborne LiDAR system, an integrated 3D laser scanner and a positioning and attitude determination system. We analyzed the adaptabilities of multiple filtering algorithms to tidal flats. In addition, a digital elevation model (DEM) of the tidal flat was constructed and the accuracy was verified with synchronized beach GPS-RTK topographic elevation measurements. The results show that the following: (1) Airborne LiDAR can quickly obtain high precision, high resolution, and a large area of ground point cloud information for tidal flats, overcoming the shortcomings of traditional measurement methods. (2) The triangulated irregular network (TIN) filtering effect is better than that of mathematical morphology and the filtering effect of point cloud normal vector clustering is mediocre. (3) The DEM of the LiDAR point cloud is in good agreement with RTK and the average error of the measurement results is 0.108 m. The error accuracy of the DEM satisfies the surveying specification of a 1:500 topographic map in a flat area, which proves that the airborne LiDAR system can be suitable for tidal flat elevation measurement. Nevertheless, it is possible to provide high precision terrain detection and DEM construction of a tidal flat with the development of airborne infrared and blue-green laser detection radar.

Keywords: airborne LiDAR, DEM, topographic survey, tidal flat, northern Jiangsu radial sand ridges

INTRODUCTION

Tidal flat refers to a muddy coastal intertidal shallow flat, which is the transition zone from land to sea and is located between the mean high tide and mean low tide (Wang and Zhu, 1990; Dyer et al., 2000). As the most important geomorphic component of coastal zones, tidal flats are widely distributed in many coastal zones around the world, including the coast of England, the coast of Wadden in Northern Europe, the banks of the Amazon in French Guiana, Gomso Bay in South Korea, and the coast of China (Mason et al., 1995; Wang, 2002; Ryu et al., 2008; Anthony et al., 2010; Loon-Steensma and Jantsje, 2015). At the same time, tidal flats are also the most sensitive land-sea dynamic interaction areas and have important ecological functions and social and economic values in protecting coastal areas from storm surges, increasing potential land resources, supporting biodiversity, and promoting carbon capture and storage (Murray et al., 2014; Zhang et al., 2017). However, tidal flats are facing serious threats and unprecedented challenges due to human activities, such as the construction of coastal ports and channels, reclamation, and natural factors such as sea level rise, storm surge, and biological invasion. Therefore, the observation of regular topographic changes in tidal flats is critical for coastal protection and sustainable development.

The scale of tidal flats is large in China, ranging from Liaoning in the north to Guangxi in the south, with a total tidal flat coastline length of 4000 km. In particular, the largest and widest tidal flat is distributed in the Jiangsu Province (Wang and Zhu, 1990; Xu et al., 2012). The northern Jiangsu radial sand ridges are typical geomorphic sedimentary units distributed off the coast of Jiangsu Province in China (Wang, 2002). Historically, the Yellow River delivered large amounts of sediment into the South Yellow Sea, especially in 1128-1855 AD, and the tidal flats of the radial sand ridges advanced seaward and formed the largest and most typical muddy coastal tidal flat in China, providing a favorable habitat for many migratory birds and benthic organisms (Zhang, 1984; Liu et al., 2013; Xu et al., 2018; Zhao et al., 2020). In recent decades, the topography of the coastal tidal flat in the radial sand ridges has changed significantly under the influence of sea level rise, global climate change, and human activities. However, the topographic surveys of the tidal flat in the radial sand ridges have always been difficult because of the tidal creek density, poor accessibility in data, and difficulty in setting up control points. At present, the main methods of topographic surveys for the silty tidal flat of the northern Jiangsu radial sand ridges are manual field surveys and remote sensing (Liu et al., 2004; Chen et al., 2010; Gong et al., 2014; Ding et al., 2014; Wang et al., 2018). However, field surveys are restricted because of low efficiency, high cost, limited measurement area of the tidal flat, and inadequate spatiotemporal coverage, although high precision can be obtained. Remote sensing methods for terrain monitoring mainly include the water boundary method and remote sensing water content method (Liu et al., 2012; Li and Gong, 2016; Kang et al., 2017; Li et al., 2018). Although large-scale monitoring can be obtained, there is a horizontal offset error in the calculation of shoreline spatial positioning, resulting in inaccuracy, which, in turn, cannot be used for large-scale mapping of a tidal flat. Oblique photography has a long data processing cycle and difficult image matching technology because of the limited number of image control points that can be arranged, the large amount of field work, and the monotonous texture information of a tidal flat. Airborne LiDAR measurement technology is an effective and innovative technology that integrates laser ranging technology, GPS differential technology, and inertial measurement unit (IMU) technology. As an active remote sensing technology, LiDAR is not limited by time and climate conditions, can provide all-weather observations of the Earth, and can quickly obtain high accuracy, high resolution digital terrain models, and three-dimensional coordinates of ground objects. In addition, LiDAR can also obtain the physical characteristics of the Earth's surface, which cannot be accomplished using passive optical remote sensing. It provides a brand-new technical means for obtaining 3D geographic space information of a coastal zone with high accuracy, which has been widely applied for geological disasters, forests, agriculture, and glaciers (Krabill et al., 2000; Brock and Purkis, 2009; Zhao et al., 2018). Airborne LiDAR is currently the most accurate sensor technology and has a rapidly increasing application in intertidal zones. In recent years, airborne and unmanned aerial vehicle (UAV) platforms have been used in sandy coastal topography, coastal erosion, and marine mapping (Walker et al., 2013; David et al., 2015; Houser et al., 2015). At the same time, it is an efficient method to generate DEM (such unique, wide, gently sloping of tidal flat) in a short time. However, LiDAR technology is rarely used for topographic survey studies of muddy coastal tidal flats due to their gentle slope and shallow water.

In this study, we analyze the adaptability of multiple filtering algorithms in the tidal flat by implementing different filtering algorithms and interpolation algorithms. At the same time, constructing a digital elevation model (DEM) of a tidal flat and the verifying accuracy with synchronized beach GPS-RTK topographic elevation measurements. Our specific objectives were (1) to obtain original airborne LiDAR point cloud data and establish key technologies for generating a DEM of a tidal flat; (2) to discuss the adaptive range of the respective filtering algorithms of those technologies and analyze their advantages and disadvantages by implementing several mainstream filtering algorithms; and (3) to evaluate the influences of different data interpolation methods on DEM accuracy and compare their interpolation efficiency based on the results of the tidal flat control points.

MATERIALS AND METHODS

Study Area

The northern Jiangsu radial sand ridges (NJRSRs) are located between the Sheyang River estuary and the Yangtze River estuary and cover an area of more than 200 km in length and 140 km in width, with a total area of 22,470 km^2 (Wang, 2012). The NJRSRs consist of more than 70 sand ridges and tidal channels ranging up to approximately 25 m in depth, with various dimensions radially centered on the coastal city of Jianggang. The current convergence and divergence between the radial sand ridges are affected by waves and regular semidiurnal tides (Xing et al., 2012). The sediment of the ridge system is composed of silt with median grain sizes ranging from 8~63 μm (Wang and Ke, 1997).

Rudong County is located in the central part of the coast of the NJRSRs, with a total coastline length of 102.59 km (muddy coast), and a sea area of approximately 4758 km^2 of which the tidal flat area is more than 60 km^2, accounting for 1/9 of the total tidal flat area of Jiangsu Province (Jin, 2018). In the offshore sea, sandbanks are scattered and alternate with waterways; there are the Jiangjiasha, Zhugensha, Taiyangsha, Huoxingsha channels and other sand ridges outside the northern coastline, and the Yaosha, Lengjiasha, Lanshayang, and Huangshayang channels are connected to the eastern coastline with good water depth and navigable conditions. The water depth in the offshore intertidal zone is shallow and the sediment grain size components are primarily composed of sand, silt, and clay, with an average grain size of 50.77~171.72 μm, and surface sediments are frequently affected by tidal currents (Huang et al., 2020). According to a 2005 and a 2015 comparative analysis of the measured topographic data of the intertidal tidal flats, the elevation distribution range of this area is between -6.5~1.9 m (1985 National elevation standard), and the net sedimentation volume is 3×10^6 m^3. The most obvious changes in erosion and deposition are concentrated between the ±1 m isobaths, accounting for 72.8% of the area of the survey area (Gu, 2018).

The monitoring area in this study is located on the muddy coast near Yangkou Port in Rudong County, Jiangsu Province (**Figure 1**). The impact of the tidal wave system formed after the confluence of the reflected tidal waves propagated from the Shandong Peninsula has formed a reciprocating current that converges and diverges with Jiang Port as the center (Zhu and Yan, 1998). Under the dynamics of convergent and divergent tidal currents, silty coastal tidal flats are typically developed. The tidal flat has a gentle slope and a large area, with an average width of 6.5 km of the tidal flat, especially in the Tiaozi mud tidal flat, which can reach 14 km. The tides are regular semidiurnal tides with an average tidal range of 2.5 m-4 m, and the measured maximum tidal range was 9.28 m (the largest tidal range recorded in coastal areas in China) in the Huangshayang channel (Ye et al., 1986). In addition, the Yangkou Port is the only port area in Nantong that has the prospect of a 200,000-ton berth construction with wide tidal flat resources and abundant land resources. In recent years, there has been frequent commercialization the Yangkou Port area, including fisheries and aquaculture, port industry, and maritime transportation. The monitoring area in this study is 10.5 km^2, near the Yangkou Port Lingang Industrial Park and the Yellow Sea Bridge (**Figure 1**).

LiDAR Monitoring System

The airborne LiDAR measurement site is located in the Lingang Industrial Park and its outer intertidal zone in Rudong County. The coastline of the measurement area is an artificial coastline, approximately 4 km long. The measurement range is approximately 2 km from the seawall to the sea, with an area of approximately 10.5 km^2 (**Figure 1**). Since the monitoring area is in the intertidal zone, it is submerged at high tide and exposed at low tide. Therefore, we chose to perform airborne LiDAR topographic surveys at low tides.

In this study, a light aircraft equipped with a laser scanning system was selected to obtain the original point cloud data. A total of 16 survey lines were laid out and the numbers of the survey lines were from L1 to L16 (**Figure 2**). The azimuth of the survey lines was determined to be near northwest to southeast and the flight direction angle was 33°~213°. At the same time, a GPS base station was set up in the survey area and its adjacent land area for synchronous observation to realize dynamic DGPS phase difference measurement and positioning. In addition, the 29 tidal flat survey points of tidal flat were measured based on GPS-RTK technology (**Figure 2**). The airborne laser scanning system selected for system is a Leica ALS70-HP Airborne LiDAR equipment, which mainly includes a LS70 laser scanner, SC70 control system box, RCD30 aerial camera, SPAN inertial navigation system, OC62 operation terminal, and other main components. The maximum scanning frequency is 200 Hz, the maximum pulse frequency is 500 kHz, the scanning angle is 45° or 60°, the maximum flight altitude is 3500 m and the minimum flight altitude is 200 m. After iterative processing of the calibration field point cloud result data, the mean square error of the checkpoint was less than 5 cm. The result system adopted

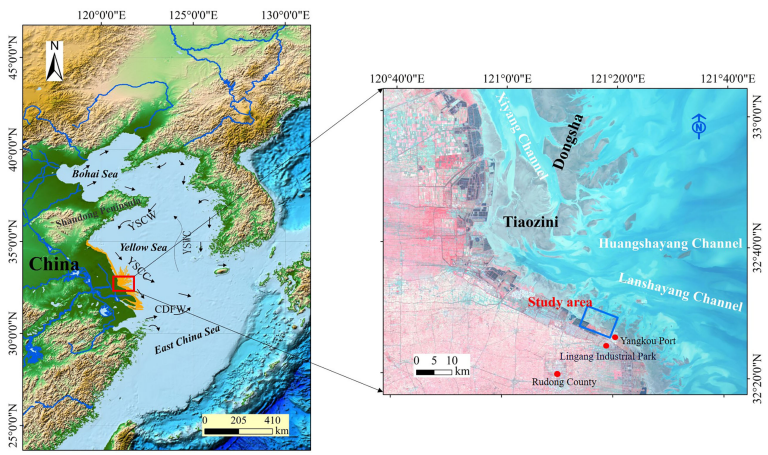

FIGURE 1 | The map of study area.

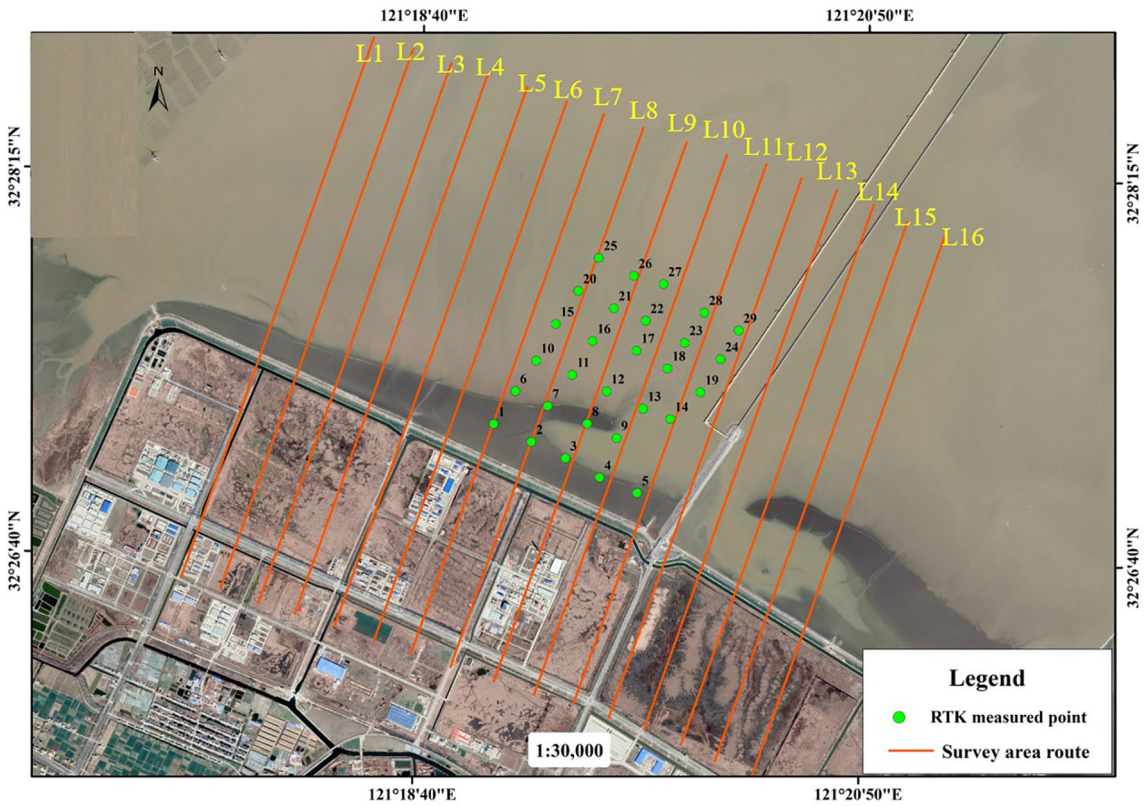

FIGURE 2 | The Monitoring area and GPS-RTK station.

WGS-84 and the elevation system adopted geodetic height system. The specific main technical parameters are shown in **Table 1**.

Ground Elevation Data Collection

To match the requirements of on-site measurement of tidal flats compared to assist aerial platform triangulation, a ground survey was carried out at the same time as the flight survey. TOPCON RTK (Hiper SR) was used in this study for the ground elevation survey. RTK is a measurement technology widely used in recent years because of its use of satellite positioning and the measurement accuracy of observation points is relatively higher, which is more convenient and rapid in tidal flats. The ground survey points were evenly arranged at an interval of approximately 300 m (**Figure 2**). The output result of the RTK elevation survey is in the data under the WGS 84 coordinate system and the elevation datum is the 1985 national elevation datum.

Measurement Methods of the Airborne LiDAR System

An airborne LiDAR laser scanning system integrates an optical mechanical scanner, laser rangefinder, differential GPS (DGPS) receiver, imaging equipment, inertial navigation system (INS), and a central control unit. An aircraft is used as the carrier to obtain three-dimensional coordinates on the ground to generate ground DEM products. An Airborne LiDAR system uses a laser scanning rangefinder emitted from the transmitter to the target, which is

TABLE 1 | Main technical parameters of Airborne LiDAR scanning system.

Laser scanner LS70		**INS SPAN**	
Maximum flying altitude	3500m	System Product Name	SPANOEM638
Minimum flying altitude	200m	IMU sampling frequency	200Hz
Maximum pulsing frequency	500kHz	IMU drift error	0.1°/h
Field angle	75	GPS	GPS Receiver
Scanning mode	Sine waves, triangles, parallel lines	Erro	5~30cm
Maximum sweep frequency	200Hz	Velocity	0.005m/s
Number of echo	unlimited times	Roll, Pitch	0.0025°
Storage	800GB SSD	Heading	0.005°

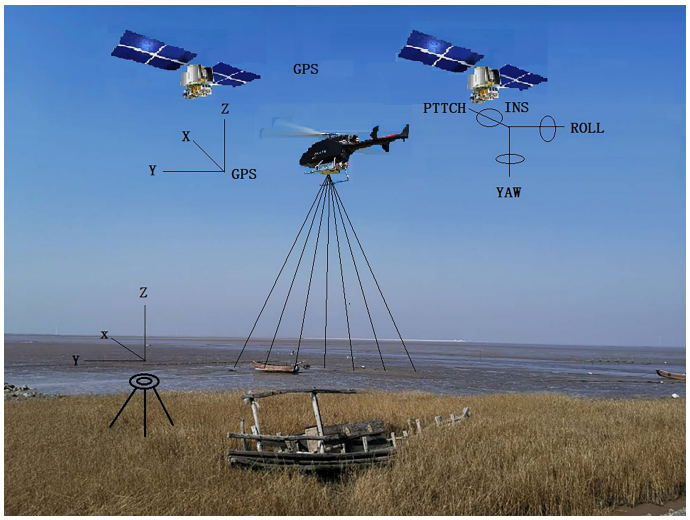

FIGURE 3 | Schematic diagram of airborne LiDAR system.

reflected back to the receiver by the target. There is a certain time difference during this period. By measuring the time difference, the rangefinder can accurately calculate the distance between the target and the launch center. The INS will measure the aircraft heading angle, roll angle, tilt angle, and other parameters during flight. In addition, the GPS system locates the position of the aircraft in real time and accurately calculates the specific coordinate information of the three-dimensional position of the laser point. The system principle is shown in **Figure 3**.

Assuming a vector in three-dimensional space, the starting point coordinates O (X_0, Y_0, Z_0) can be measured, the radial path S from this point to a certain point Pi (X_i, Y_i, Z_i) on the ground is calculated, and the coordinates of point P can be determined through the joint vector calculation of the O coordinates. By accurately obtaining the position of the aircraft platform using GPS or DGPS, the coordinates of the projection center (X_0, Y_0, Z_0) can be determined. Then, a high precision attitude measurement INS is used to obtain the main optical axis attitude data (α, ω, k) at the projection center, and the angle θ between the observation direction and the normal is calculated. The three-dimensional coordinates of any specific point P on the ground can be determined (Sun et al., 2017).

$$\begin{cases} X_i = f_1(X_0, Y_0, Z_0, \alpha, \omega, k, S, \theta) \\ Y_i = f_2(X_0, Y_0, Z_0, \alpha, \omega, k, S, \theta) \\ Z_i = f_3(X_0, Y_0, Z_0, \alpha, \omega, k, S, \theta) \end{cases} \quad (1)$$

Key Technologies of Point Cloud Data Processing

Airborne LiDAR data processing includes data preprocessing and postprocessing. Data preprocessing refers to solving the precise trajectory based on DGPS base station data and GPS and inertial navigation data, and finally generating the original laser point cloud data with the original laser scanning record. Data postprocessing is based on the original point cloud data, performing gross error elimination (including histogram analysis, outlier analysis, shaded relief map and profile map), data filtering (mathematical morphology, irregular triangulation, and point cloud normal vector) and human editors (including shaded relief map, profile map and aerial image). In addition, inverse distance weighted, kriging, and nature neighbor interpolation algorithm were selected to interpolate the filtered ground points and finally generating a DEM and other surveying and mapping products. The technical process of Airborne LiDAR data processing is shown in **Figure 4**.

To obtain the ground information of the laser point cloud more accurately, it is necessary to separate the ground points and nonground points from the point cloud data to retain the real ground point cloud and filter the ground object information and noise extracted from the point cloud (Brzank and Heipke, 2006). At present, the filtering methods of Airborne LiDAR point cloud data include filtering methods based on mathematical morphology (Sui et al., 2010), triangulation progressive encryption methods (Li et al., 2009), filtering algorithms based on slope, and filtering methods based on moving windows (Zhang, 2007). In this paper, a mathematical morphology filtering algorithm, triangulation iterative filtering algorithm, and point cloud vector clustering filtering algorithm are implemented to process relevant data in order to discuss the adaptability of several methods to intertidal tidal flats.

The mathematical morphology filtering algorithm includes basic algorithms such as the expansion operation, corrosion operation, opening operation, and closing operation and analyzes raster data by calculating the maximum, minimum, and average values of the data in the window (Chen, 2014). There are differences between point cloud data processing and image

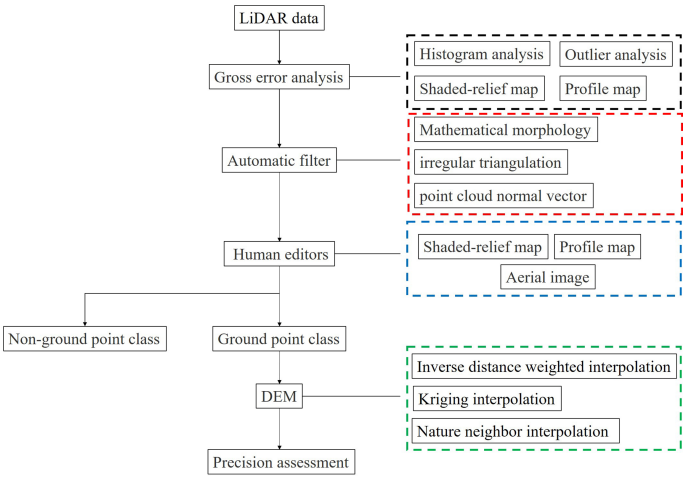

FIGURE 4 | The flow chart of airborne LiDAR data processing.

processing and the emphasis of morphological calculation is elevation rather than pixels. The irregular triangular net filtering algorithm assumes that the selected local area has a relatively flat terrain and the lowest point can be selected to replace the initial seed point in the grid. Then, a sparse triangulation network is constructed to comprehensively judge each point through the triangulation network. A schematic diagram of the triangulation filter is shown in **Figure 5A**.

The irregular triangulation filtering method was formally proposed by Axelsson in the late 20th century (Axelsson, 2000). A point to be determined is represented by P and d represents the distance between the P and the projection surface. The angles between P and the vertices of the projection triangle (V1, V2, V3) are a, b, and c, and then determine the relationship between d, a, b, and c and a set threshold can be determined. If the result is within the threshold, P will be recognized as a ground point and TIN iteration will continue unless no new ground points are added (**Figure 5B**).

Where V1, V2, and V3 represent the vertices of the triangle, respectively. In the same plane, the expressions are as follows:

$$A_x + B_y + C_z + D = 0 \tag{2}$$

where d represents the distance from P to the plane:

$$d = \left| \frac{Ax_p + By_p + Cz_p + D}{\sqrt{A^2 + B^2 + C^2}} \right| \tag{3}$$

S represents the distance from P to the three vertices V1, V2, and V3 of the triangle:

$$S_{V_iP} = \sqrt{(X_{V_i} - X_p)^2 + (Y_{V_i} - Y_p)^2 + (Z_{V_i} - Z_p)^2}, i = 1, 2, 3 \tag{4}$$

and a represents the repetition angle:

$$a = \arcsin \frac{d}{S_{V_iP}} \tag{5}$$

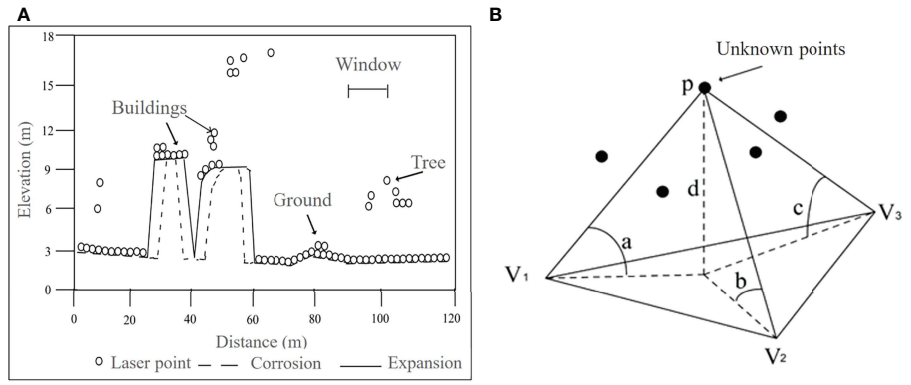

FIGURE 5 | **(A)** Schematic diagram of mathematical morphological filtering; **(B)** principle diagram of triangulation filter.

In addition, a filtering algorithm of point cloud normal vector clustering was also used in this study. The upper and top surfaces of artificial ground objects such as bridges and roofs are relatively horizontal with gentle slopes and most of them are composed of several planes. The normal vectors of point clouds have similar characteristics and the normal vectors of any point are mostly distributed in one or more directions with strong regularity. The feature of a normal vector is affected by the spatial distribution of its neighborhood points. A normal vector is an important geometric characteristic in the point cloud data which can represent the trend of surface changes to a certain extent. With the fluctuation of the surface, the normal vector also changes accordingly. The basic method of point cloud normal vector clustering filtering is to select a seed point from the point cloud data and judge whether it meets the preset judgment standard by calculating the normal vector angle between the seed point and an adjacent point. If the neighboring points meet the criteria, they will belong to an area homogenous with the seed point until no new similar feature points are added in the neighborhood, so as to complete the segmentation of the ground feature point cloud and ground point cloud (Sun et al., 2019).

After the LiDAR data are filtered, there will be data holes in the ground point data. Thus, a data interpolation method can be used to eliminate data holes caused by filtering. The interpolation method is based on the continuous smoothness of the original terrain undulations and it is possible to interpolate the elevation of the neighboring data points to obtain the elevation of a pending point. We further discuss the practical application of three data interpolation methods: inverse distance weighting, kriging, and natural adjacent points in tidal flats.

RESULTS AND DISCUSSION

In May 2019, airborne LiDAR measurements were carried out in the study area and measurements of 10.5 km^2 were obtained. The survey area covered approximately 1,650 m of coastline, extending approximately 1,500 m to land and 2,400 m to sea. A total of 2220.146 thousand point cloud data were obtained from aircraft scanning, with a density of 1.679 points/m^2, a maximum elevation value of 805.450 m, a minimum elevation value of -10.478 m, an average elevation value of 10.603 m, and an elevation standard deviation of 1.655 m (**Figure 6**).

Gross Error Processing

When airborne LiDAR obtains point cloud data, it is highly random and vulnerable to interference from external factors and the scattering and diffraction of laser pulses. A considerable number of noise points (including high points, low points, and outliers) will inevitably appear (Wang, 2011; Zhang et al., 2012), which will affect the accuracy of the data and the construction of the DEM. The point cloud data need to be preprocessed before filtering and classification to eliminate noise points.

In this experiment, data interpolation was performed on the original point cloud data of the study region and to generate the point cloud shading map of the study area. However, it is difficult to eliminate noise points in the tidal flat area with this method. Gross error processing of outlier analysis uses Terrasolid software to eliminate the noise of the original point cloud data. The principle of this algorithm compares the elevation value of a point (the center point) with the elevation value of each point within a given distance. If the center point is significantly lower than the other points, the point will be separated. The set parameter excludes points within 5 m from the points that are lower than the general ground height of 0.5 m. The set parameters exclude points at a radius of 5 m and a high-level error greater than 5 times the standard deviation. The set parameter excludes points within 5m from the point 0.5m below the general ground height, and the radius of parameter elimination is the point with high error greater than 5 times standard deviation within 5m.

According to the profile of the original point cloud data of the study area (**Figure 7A**), it can be found that there is no special regularity in the distribution of gross error points and the number of points around gross error points is relatively small. After analysis, the elevation range of extremely high points is between 168.060 and 805.450 m, and the range of the extremely low points is between -10.478 and 9 m (**Figure 7B**), which provides a certain reference for establishing the histogram gross error analysis threshold.

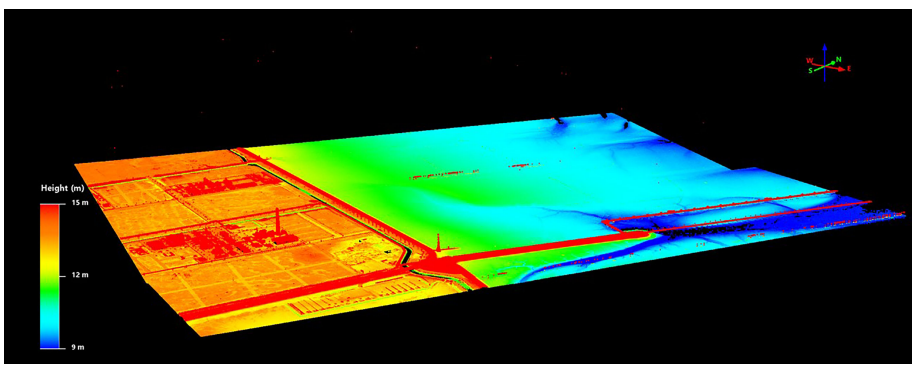

FIGURE 6 | The results of point cloud data.

The abscissa of the point cloud elevation histogram represents the elevation value of the point cloud and the ordinate represents the frequency of occurrence of the elevation value. The number of points with a statistical elevation value less than 8.6 m or greater than 35 m is extremely small and the frequency of normalized elevation values within this range is less than 15 m. Therefore, 35 m is taken as the high point threshold and elevation values greater than this value are eliminated; 8.6 m is taken as the low point threshold and elevation values lower than this value are eliminated. The eliminated gross error points are superimposed with the remote sensing image to further clearly and intuitively analyze the source and distribution of gross error points.

In this experiment, a total of 538 gross error points were eliminated through the outlier analysis, point cloud profile, and elevation statistical histogram, including 354 extremely low points and 184 extremely high points (**Figure 8**). The elevation values of the extremely low points are -10.48~1.47 m and the average elevation value is -2.53 m. The elevation values of the extremely high points are between 36.32 m and 805.45 m and the average elevation value is 92.32m. The extremely low points in the survey area are concentrated and distributed in strips on the east and west sides of the Yellow Sea Bridge and these points do not belong to the surface points, as most of them come from systematic errors. These extremely low points are significantly lower than the tidal flat points because the emitted laser pulses are reflected back to the receiving device multiple times by the tidal flat surface. However, the number of extremely high points in the survey area is small and the distribution is disorderly and without obvious regularity.

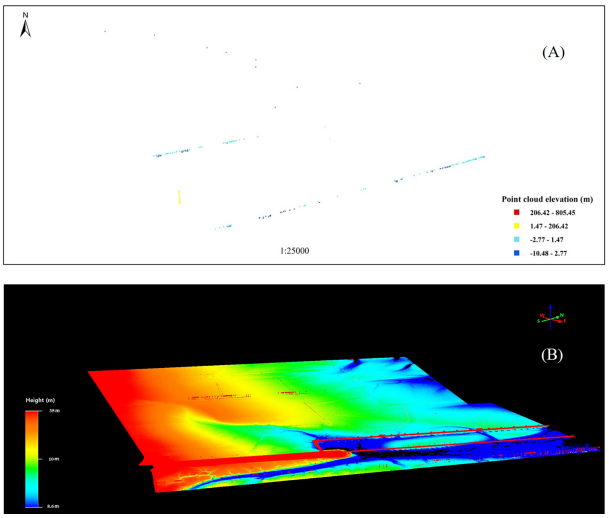

FIGURE 8 | **(A)** The removed gross error points; **(B)** The denoised point cloud data.

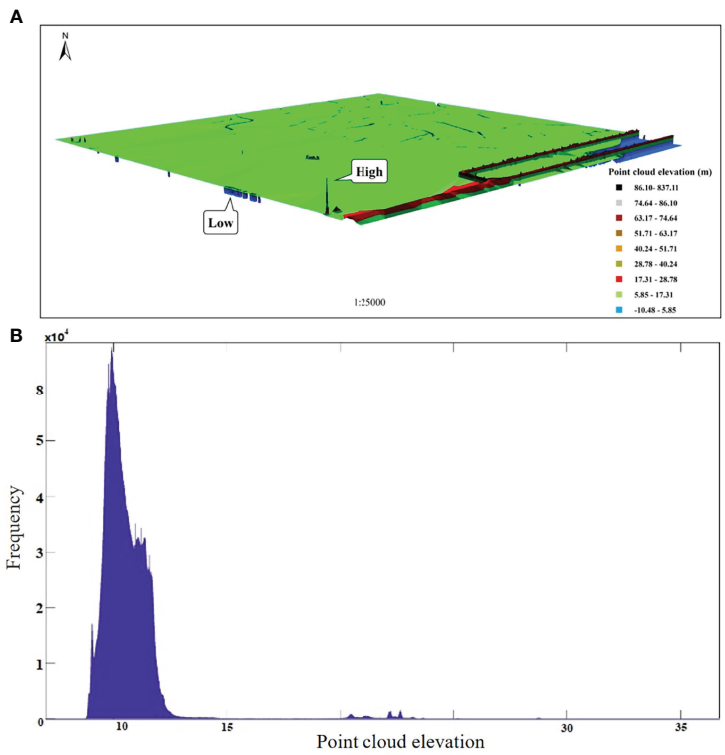

FIGURE 7 | **(A)** the original point cloud data profile; **(B)** the original point cloud data elevation statistical histogram.

In addition, the extremely high points are not ground points and usually come from aerial objects such as birds and low-altitude aircraft. Consequently, there is an obvious height difference between the gross error points, the tidal flat terrain, bridges, and other ground objects. The gross error points can be effectively eliminated through the statistical histogram of the point cloud elevation. The point cloud data, after the gross error is eliminated, is further processed through a specific filtering algorithm.

Filtering Processing

The three filtering methods proposed above are used to perform filtering experiments on the point cloud data after eliminating the gross errors points. The ground points obtained through mathematical morphology filtering, irregular grid TIN filtering, and point cloud normal vector filtering are shown in **Figure 9**.

On this basis, the laser footprint error rate specified by ISPRS is used as an evaluation criterion and it is combined with the actual situation divided into three types of errors to qualitatively evaluate the filtering effect of the three filtering algorithms, e.g., type I error (a ground point error is classified as a nonground point error), type II error (a nonground point is regarded as a ground point error), and total error (Hu et al., 2015). The specific calculation formula is shown in **Table 2**, where 'a' represents the number of ground points correctly classified, 'b' represents the number of ground points that are incorrectly divided into nonground points, 'c' represents the number of nonground points incorrectly divided into ground points, 'd' represents the number of nonground points correctly classified, and 'n' represents the total number of laser points.

Artificial classification was carried out according to the point cloud profile of the study area and aerial photography assisted interpretation, and after filtering by the three algorithms, the type I error, type II error, and total error were calculated respectively (**Table 3**) since there are no standard reference point cloud data in the study area. The purpose of filtering is to restore the real terrain and the number of nonground points and after filtering, the number should be reduced, e.g., the type II error should be minimized.

The type I error of the mathematical morphology filtering method is 0.19%, which is higher than that of the other two algorithms. This kind of error is mostly concentrated on the edges of buildings such as pipe racks and bridges and has

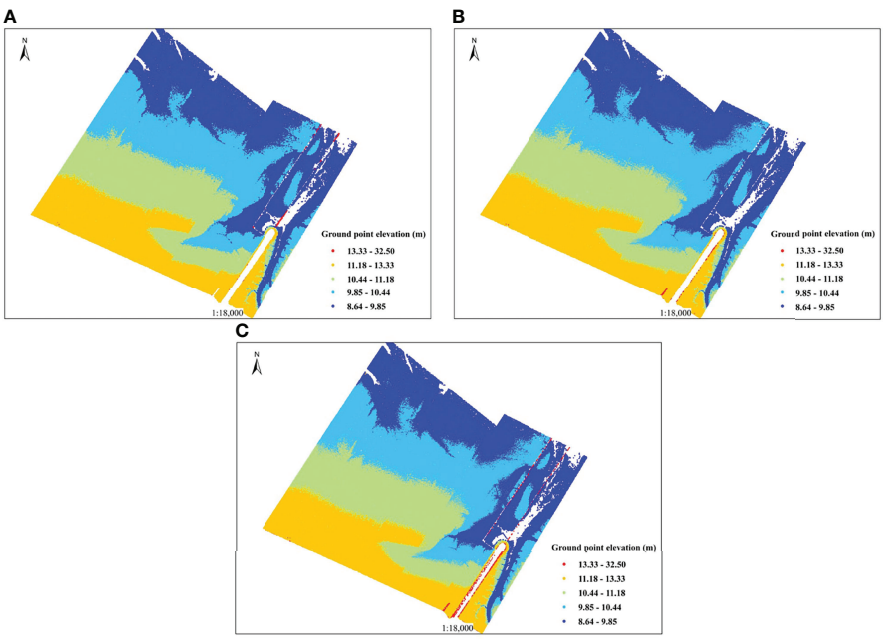

FIGURE 9 | The results of Mathematical morphology filtering (ground points) **(A)**; Irregular Triangulation filtering **(B)**; Point cloud normal vector filtering **(C)**.

TABLE 2 | Error calculation formula.

Reference data	Filtered point cloud data			
	Number of ground points	Number of non-ground points		error
Number of ground points	a	b	e=a+b	b/e × 100% (Type I)
Number of non-ground points	c	d	f=c+d	c/f × 100% (Type II)
Total			m=e+f	(b+c)/n × 100% (Total)

TABLE 3 | Accuracy analysis of filtering results.

Study area	Type I (%)	Type II (%)	Total error (%)
Mathematical morphological filtering	0.19	3.28	0.23
Point cloud normal vector filtering	0.12	3.98	0.32
TIN filtering	0.16	2.84	0.18

relatively obvious terrain fluctuation and results in misclassification. The design principle of the algorithm in this paper is to classify ground points as ground object points as much as possible, so some ground points will be misclassified into ground object points, but such misclassified points have little influence on the subsequent interpolated DEM data in the later period. The key to this algorithm is the setting of the window size. However, there are relatively few ground objects in the tidal flat, so a large number of ground points can be saved and most ground points can be eliminated under the premise of setting an appropriate window size. The data organization form of this algorithm is a regular grid, which reduces the accuracy of the original data and increases the difficulty of filtering.

The type II error and total error distributions of the point cloud normal vector clustering filtering method are 3.98% and 0.32%, respectively, and the filtering effect is relatively poor, which indicates that the algorithm's ability to filter ground objects needs further improvement. The principle of the algorithm is that the normal vector of the point cloud is similar to that of a ground point cloud with a flat roof surface or small curved surface, but the normal vector characteristic of a point depends on the spatial distribution of the surrounding points. For the point cloud data at the boundary of buildings with complex top structures and tall buildings, the algorithm cannot completely filter out the ground objects, and the filtering effect will be especially poor at relatively low point cloud densities. A small part of the tidal flats was flooded around the bridge and the laser points were lost. Thus, the point cloud density is low and the filtering effect is general. In addition, the filtering accuracy of the algorithm is also affected by the determination of neighborhood point sets. The point cloud data of the study area include ground objects with relatively complex top structures, such as pipe racks and electric towers. The point cloud density in some tidal flats is low and lacks prior knowledge of filtering, so the algorithm has certain limitations in tidal flats, resulting in high numbers of type II error and total errors.

The type II error and total error of the irregular triangulation filter method are relatively low, 2.84% and 0.18%, respectively. Under the premise of an appropriate threshold setting, the filtering ability for complex buildings and their surrounding microfeatures is slightly better than that of other two algorithms. The advantage of this algorithm is that the original point cloud data will not be lost and the terrain information can be better preserved. The disadvantage of this algorithm is that it must have prior knowledge of the largest building size and slope in the survey area. If the initial ground point selection effect is not satisfactory, the filtering accuracy will be greatly reduced. In addition, the algorithm needs to be continuously encrypted, which requires a long processing time. The filtering results of the irregular triangulation network filtering algorithm show that the removal effect of this method on different ground objects is considerable (**Figure 6**). Buildings (houses and oil tanks) with large areas and simple structures are well removed. In addition, the higher vegetation (mainly located on both sides of a road) is better filtered because it changes significantly compared to the surrounding terrain. Consequently, the algorithm can better separate obvious ground features.

Construction and Accuracy Verification of the Tidal Flat 3D DEM

After denoising and filtering out the generated laser point cloud data, inverse distance weighted interpolation, kriging interpolation, and the natural neighbor interpolation method based on ArcGIS 10.3 software was used to interpolate the real ground point cloud data of the tidal flat to generate a tidal flat DEM (**Figure 10**). At the same time, five vertical coastal sections were established and the topographic profile was measured using GPS-RTK while the airborne LiDAR system collected the muddy coastal topographic data. The accuracy of the DEM results generated by the airborne LiDAR point cloud is verified based on the synchronized GPS-RTK elevation data (**Table 4**). The section extracted from the point cloud generation DEM obtained using LiDAR is in good agreement with the section point data measured using RTK and shows a consistent trend of change. However, there are large errors in individual points mainly due to the high humidity on the tidal flat or the presence of water. The laser cannot penetrate the water, which has an impact on the accuracy.

Through the analysis of the experimental results of the above three data interpolation methods, the filtered tidal flat point cloud data has no gross error points and no abnormal elevation values. The DEM shading effect map generated by the three interpolation methods of inverse distance weighting, kriging, and natural adjacent points has similar results: good smoothness, strong continuity, and has good interpolation results for the area with missing data. Consequently, the mean square error of DEM elevation processed by inverse distance weighting, natural adjacent points, and Kriging interpolation are 0.112 m, 0.106 m and 0.105 m, respectively, by using two measurement methods to subtract the obtained elevation values (**Table 4**). The average value of the error in the elevation is 0.108 m and the accuracy of the error in the elevation meets the 1:500 topographic map measurement specification for flat areas, indicating that the airborne LiDAR system can be suitable for tidal flat elevation measurement at low tide levels. In addition, the interpolation accuracy of natural adjacent points is equivalent to that of Kriging interpolation in terms of the accuracy of tidal flat DEM, which is higher than that of inverse distance weighted

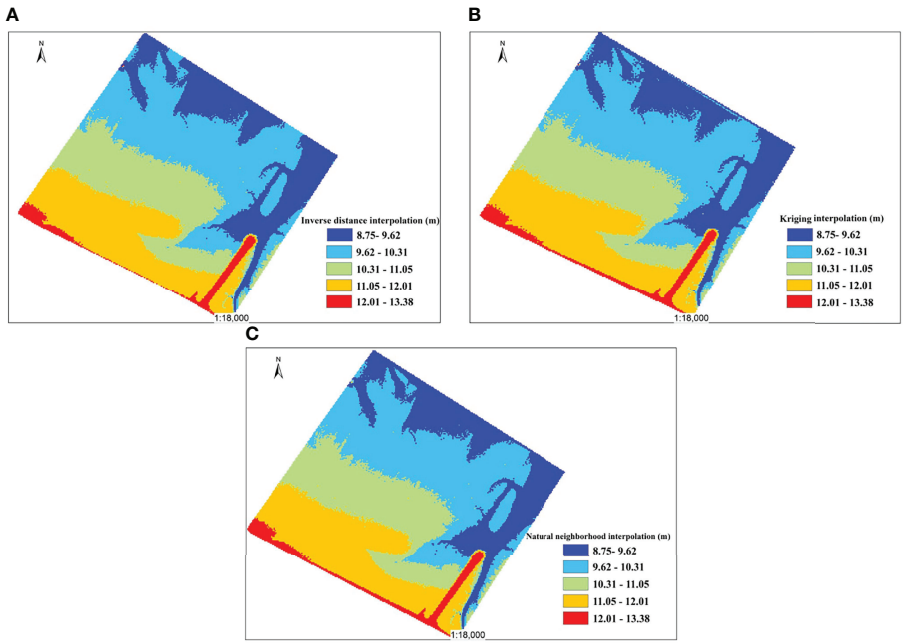

FIGURE 10 | DEM shading map of tidal flat. **(A)** Inverse distance interpolation; **(B)** Kriging interpolation; and **(C)** Natural neighborhood interpolation.

interpolation, but the kriging method has the lowest processing efficiency and takes too long. Therefore, considering the factors of processing efficiency and accuracy, it is recommended to use natural adjacent points for interpolation in the production of tidal flat DEM.

CONCLUSION

In this paper, the LiDAR point cloud data were collected in the Yangkou Port area of Rudong County in Jiangsu Province and the key technology of airborne LiDAR point cloud data postprocessing of typical intertidal tidal flats in Jiangsu were discussed. The airborne LiDAR point cloud data process was designed to quickly generate a high precision tidal flat DEM. The accuracy of tidal flat check points measured in the field was verified using GPS-RTK technology. The results show the following:

1. Airborne LiDAR, as an active remote sensing technology, can quickly obtain high precision, high resolution, and a large area of the ground object parameter information, providing new technical means for the high precision and fast acquisition of three-dimensional tidal flat geographic space information, overcoming the shortcomings of traditional measurement methods.
2. In the process of filtering, mathematical morphology, irregular grid TIN, and point cloud normal vector clustering have better filtering effects for most flat and sparse tidal flats. In general, the TIN filtering effect is

TABLE 4 | The accuracy evaluation of DEM.

Number	GPS-RTK measurement			IDW	Error	NAPI	Error	Kriging	Error
	x	y	z	DEM	Δz	DEM	Δz	DEM	Δz
1	121.317	32.454	11.567	11.642	-0.075	11.642	-0.075	11.638	-0.071
2	121.320	32.452	11.426	11.445	-0.019	11.451	-0.025	11.434	-0.008
3	121.323	32.451	11.360	11.282	0.078	11.283	0.076	11.263	0.097
…									
10	121.321	32.458	10.855	10.914	-0.059	10.907	-0.052	10.923	-0.068
11	121.324	32.457	10.967	10.966	0.001	10.966	0.001	10.970	-0.003
…									
28	121.334	32.462	10.140	10.003	0.137	10.009	0.132	9.971	0.169
29	121.337	32.460	9.993	9.831	0.162	9.841	0.152	9.806	0.187
Error					0.112		0.106		0.105

better, followed by mathematical morphology, and the point cloud vector clustering filtering effect is general. If we have *a priori* knowledge of the topography and features in the survey area, the filtering accuracy will be greatly improved;

3. Based on an airborne LiDAR system with an integrated 3D laser scanner, positioning and attitude system, tidal flat point cloud data can be quickly acquired, a DEM generated, and its accuracy verified with synchronized tidal flat GPS-RTK terrain elevation measurements. The section extracted from the point cloud-generated DEM obtained using LiDAR is in good agreement with the section point data measured by RTK, which shows a consistent change trend. The average error of the measurement results is 0.108 m, and the accuracy of the errors in the elevation meets the 1:500 topographic map measurement specifications for tidal flat. The expected results have been achieved, which further shows that an airborne LiDAR system can be well adapted to the needs of tidal flat elevation measurement at low tide levels.
4. The LiDAR measurements have null values in tidal flat ponding, which will affect the accuracy of the tidal flat topography. The development of airborne infrared and blue-green laser detection radars provide the possibility for high precision terrain detection and DEM construction in the water areas of a tidal flat.

DATA AVAILABILITY STATEMENT

The raw data supporting the conclusions of this article will be made available by the authors, without undue reservation.

AUTHOR CONTRIBUTIONS

HZ: writing—original draft preparation. LW, JC, and HZ: collection and analysis of the data and software. YZ: investigation and validation. YZ and MX: conceptualization, funding acquisition, and project administration. YZ and MX: supervision. All authors contributed to the article and approved the submitted version.

FUNDING

This research was funded by the Marine Science and Technology Innovation Project of Jiangsu Province (No. JSZRHYKJ202002, HY2018-03, JSZRHYKJ202103), and the Nanjing Science and Technology Innovation Project for Overseas Students (1614100001).

ACKNOWLEDGMENTS

The authors would like to thank the reviewers for their valuable comments for the improvement of the manuscript.

REFERENCES

Anthony, E. J., Gardel, A., Gratiot, N., Proisy, C., Allison, M. A., Dolique, F., et al. (2010). The Amazon-Influenced Muddy Coast of South America: A Review of Mud-Bank–Shoreline Interactions. *Earth-Sci. Rev.* 103, 99–121. doi: 10.1016/j.earscirev.2010.09.008

Axelsson, P. (2000). DEM Generation From Laser Scanner Data Using Adaptive TIN Models. *Int. Arch. Photogramm. Remote Sens.* 33, 110–117.

Brock, J. C., and Purkis, S. J. (2009). The Emerging Role of Lidar Remote Sensing in Coastal Research and Resource Management. *J. Coast. Res.* SI (53), 1–5. doi: 10.2112/SI53-001.1

Brzank, A., and Heipke, C. (2006). Classification of Lidar Data Into Water and Land Points in Coastal Areas. *Int. Arch. Photogramm. Remote Sens. Spat. Inform. Sci.* 36, 197–202.

Chen, T. H. (2014). *Digital Image Processing (2nd Edition)* (Beijing, China: Tsinghua University Press)

Chen, J., Wang, Y. G., and Cai, H. (2010). Profile Characteristics Study of the Jiangsu Coast. *Ocean Eng.* 28, 90–96. doi: 10.3969/j.issn.1005-9865.2010.04.013

David, A. S., Zarnetske, P. L., Hacker, S. D., Ruggiero, P., Biel, R. G., and Seabloom, E. W. (2015). Invasive Congeners Differ in Successional Impacts Across Space and Time. *PloS One* 10 (2), e0117283. doi: 10.1371/journal.pone.0117283

Ding, X. R., Zhou, H. H., and Kang, Y. Y. (2014). Geomorphologic Structure Analysis of Radial Sand Ridges. *Geogr. Geo-Inform. Sci.* 30, 32–35. doi: 10.3969/j.issn.1672-0504.2014.04.007

Dyer, K. R., Christie, M. C., Feates, N., Fennessy, M. J., Pejrup, M., and van der Lee, W. (2000). An Investigation Into Processes Influencing the Morphodynamics of an Intertidal Mudflat, the Dollard Estuary, Netherlands: I. Hydrodynamics and Suspended Sediment. Estuar. *Coast. Shelf Sci.* 50, 607–625. doi: 10.1006/ecss.1999.0596

Gong, Z., Jin, C., Zhang, C. K., Li, H., and Xin, P. (2014). Surface Elevation Variation of the Jiangsu Mudflats: Field Observation. *Adv. Water Sci.* 25, 880–887. doi: 10.14042/j.cnki.32.1309.2014.06.017

Gu, J. K. (2018). *Study on Coastal Dynamic Characteristics and Mechanism in Rudong of Jiangsu Province* [Nanjing, China: Nanjing Normal University (master's thesis)].

Houser, C., Wernette, P., Rentschlar, E., Jones, H., Hammond, B., and Trimble, S. (2015). Post-Storm Beach and Dune Recovery: Implications for Barrier Island Resilience. *Geomorphology* 234, 54–63. doi: 10.1016/j.geomorph.2014.12.044

Huang, R. Q., Zhao, Y. F., Liu, Q., and Xu, M. (2020). Grain-Size Characteristics of Surface Sediments and Their Environmental Implication in the Rudong Coastal of Jiangsu Province. *J. Nanjing Norm. Univ.* 43, 91–99. doi: 10.3969/j.issn.1001-4616.2020.01.014

Hu, Y. J., Chen, P. G., Chen, X. Y., Nie, Y. J., and Li, R. (2015). Analysis and Comparison of Airborne Lidar Point Cloud Filtering Algorithms. *J. Surv. Sci. Technol.* 32, 72–77. doi: 10.3969/j.issn.1673-6338.2015.01.015

Jin, L. (2018). *Rudong Yearbook* (Beijing, China: Fangzhi Press).

Kang, Y., Ding, X., Xu, F., Zhang, C., and Ge, X. (2017). Topographic Mapping on Large-Scale Tidal Flats With an Iterative Approach on the Waterline Method. *Estuar. Coast. Shelf Sci.* 190. doi: 10.1016/j.ecss.2017.03.024

Krabill, W., Wright, C., Swift, R., Frederick, E., Manizade, S., Yungel, J., et al. (2000). Airborne Laser Mapping of Assateague National Seashore Beach. *Photogramm. Eng. Rem. Sens.* 66, 65–71. doi: 0099-1-112/00/6601-00OS3.00/0

Li, W., and Gong, P. (2016). Continuous Monitoring of Coastline Dynamics in Western Florida With a 30-Year Time Series of Landsat Imagery. *Remote Sens. Environ.* 179, 196–209. doi: 10.1016/j.rse.2016.03.031

Li, H., Gong, Z., Dai, W. Q., Lu, C., Zhang, X., Cybele, S., et al. (2018). Feasibility of Elevation Mapping Inmuddy Tidal Flats by Remotely Sensed Moisture (RSM) Method. *J. Coast. Res.* 85, 291–295. doi: 10.2112/SI85-059.1

Li, H., Li, D. R., Huang, X. F., and Zhong, C. (2009). Advanced Adaptive TIN Filter for LiDAR Point Clouds Data. *Sci. Surv. Mapp.* 34, 39–40.

Liu, J., Kong, X., Saito, Y., Liu, J., Yang, Z., and Wen, C. (2013). Subaqueous Deltaic Formation of the Old Yellow River (AD 1128–1855) on the Western South Yellow Sea. *Mar. Geol.* 344, 19–33. doi: 10.1016/j.margeo.2013.07.003

Liu, Y., Li, M. C., Cheng, L., Li, F., and Chen, K. (2012). Topographic Mapping of Offshore Sandbank Tidal Flats Using the Waterline Detection Method: A Case Study on the Dongsha Sandbank of Jiangsu Radial Tidal Sand Ridges, China. *Mar. Geod.* 35, 362–378. doi: 10.1080/01490419.2012.699501

Liu, Y. X., Zhang, R. S., and Li, M. C. (2004). Automatic Extracting Method of Land Cover in Jiangsu Tidal Flat. *Remote Sens. Inform.* 123–26. doi: 10.3969/j.issn.1000-3177.2004.01.007

Loon-Steensma, V., and Jantsje, M. (2015). Salt Marshes to Adapt the Flood Defences Along the Dutch Wadden Sea Coast. *Mitig. Adapt. Strat. Gl.* 20, 929–948. doi: 10.1007/s11027-015-9640-5

Mason, D. C., Davenport, I. J., Robinson, G. J., Flather, R. A., and McCartney, B. S. (1995). Construction of an Inter-Tidal Digital Elevation Model by the 'Water-Line'method. *Geophys. Res. Lett.* 22, 3187–3190. doi: 10.1029/95GL03168

Murray, N. J., Clemens, R. S., Phinn, S. R., Possingham, H. P., and Fuller, R. A. (2014). Tracking the Rapid Loss of Tidal Wetlands in the Yellow Sea. *Front. Ecol. Environ.* 12, 267–272. doi: 10.1890/130260

Ryu, J. H., Kim, C. H., Lee, Y. K., Won, J. S., Chun, S. S., and Lee, S. (2008). Detecting the Intertidal Morphologic Change Using Satellite Data. *Estuar. Coast. Shelf Sci.* 78, 623–632. doi: 10.1016/j.ecss.2008.01.020

Sui, L. C., Zhang, Y. B., and Liu, Y. (2010). Filtering of Airborn LiDAR Point Cloud Data Based on the Adaptive Mathematical Morphology. *Acta Geod. Sinica.* 39, 390–396. doi: 10.13203/j.whugis2011.10.017

Sun, X. J., Teng, H. Z., Zhao, J., Wang, Y. F., Zhang, L., and Ye, Q. G. (2017). Airborne LiDAR Coast Topographic Measurement Technology and its Application. *Mar. Survey. Mapp.* 37 (3), 70–78. doi: 10.3969/j.issn.1671-3044.2017.03.017

Sun, W. X., Wang, J., Jin, F. X., and Liang, Z. Y. (2019). A Method of Reference Feature Extraction and Tilt Analysis Based on Point Cloud Normal Vector. *Bull. Surv. Mapp.* 3, 155–158. doi: 10.13474/j.cnki.11-2246.2019.0100

Walker, I. J., Eamer, J. B., and Darke, I. B. (2013). Assessing Significant Geomorphic Changes and Effectiveness of Dynamic Restoration in a Coastal Dune Ecosystem. *Geomorphology* 199, 192–204. doi: 10.1016/j.geomorph.2013.04.023

Wang, Y. (2002). *Radiative Sandy Ridge Field on Continental Shelf of the Yellow Sea* (Beijing, China: China Environ. Sci. Press).

Wang, Y. B. (2011). *Spatial Object Representation Reconstruction and Multi-Resolution Representation Based on Ground LiDAR Point Cloud* (Nanjing, China: Southeast University Press).

Wang, J. (2012). *Coastal Mudflat of Jiangsu Province and its Utilization Potential* (Beijing, China: Ocean Press).

Wang, X., and Ke, X. (1997). Grain-Size Characteristics of the Extant Tidal Flat Sediments Along the Jiangsu Coast, China. *Sediment. Geol* 112, 105–122. doi: 10.1016/S0037-0738(97)00026-2

Wang, X., Xiao, X., Zou, Z., Chen, B., Ma, J., Dong, J., et al. (2018). Tracking Annual Changes of Coastal Tidal Flats in China During 1986–2016 Through Analyses of Landsat Images With Google Earth Engine. *Remote Sens. Environ.* 238, 110987. doi: 10.1016/j.rse.2018.11.030

Wang, Y., and Zhu, D. K. (1990). Tidal Flats in China. *Quaternary Sci.* 10, 291–300. doi: 10.3321/j.issn:1001-7410.1990.04.001

Xing, F., Wang, Y. P., and Wang, H. V. (2012). Tidal Hydrodynamics and Fine-Grained Sediment Transport on the Radial Sand Ridge System in the Southern Yellow Sea. *Mar. Geol.* 291, 192–210. doi: 10.1016/j.margeo.2011.06.006

Xu, M., Li, P. Y., and Lu, P. D. (2012). *Research on Appropriate Reclamation Scale of Prograding Tidal Flat – A Case Study of Jiangsu Province* (Beijing, China: Sci. Press).

Xu, M., Meng, K., Zhao, Y. F., and Zhao, L. (2018). Sedimentary Environment Evolution in East China's Coastal Tidal Flats: The North Jiangsu Radial Sand Ridges. *J. Coastal Res.* 35, 524–533. doi: 10.2112/JCOASTRES-D-18-00006.1

Ye, H. S., Jiang, T. L., Fang, X. Y., and Sun, H. L. (1986). Analysis of Tidal Current and Residual Current in Shoal Area of Hebei Coastal Zone. *Yellow Bohai Sea.* 3, 77–93.

Zhang, R. S. (1984). The Landforming Process of the Yellow River Delta and Coastal Plain in Northern Jiangsu Province. *Acta Geogr. Sinica.* 39, 173–184. doi: 10.11821/xb198402005

Zhang, X. H. (2007). *Theory and Method of Airborne Lidar Measurement Technology* (Wuhan, China: Wuhan University Press).

Zhang, C. K., Gong, Z., Chen, Y. P., Tao, J. F., Kang, Y. Y., Zhou, J. J., et al. (2017). Research Progress and Frontier Issues on Tidal Flat Evolution. *Proc. 18th China Offshore Eng. Sym. (II)*. 7–14.

Zhang, L., Ma, H. C., and Wu, J. W. (2012). Utilization of LiDAR and Tidal Gauge Data for Automatic Extracting High and Low Tide Lines. *J. Remote Sens.* 16, 405–410. doi: 10.11834/jrs.20120448

Zhao, Y. F., Liu, Q., Huang, R. Q., Pan, H. C., and Xu, M. (2020). Recent Evolution of Coastal Tidal Flats and the Impacts of Intensified Human Activities in the Modern Radial Sand Ridges, East China. *Int. J. Env. Res. Pub. He.* 17, 3191. doi: 10.3390/ijerph17093191

Zhao, K., Suarez, J. C., Garcia, M., Hu, T., Wang, C., and Londo, A. (2018). Utility of Multitemporal Lidar for Forest and Carbon Monitoring: Tree Growth, Biomass Dynamics, and Carbon Flux. *Remote Sens. Environ.* 204, 883–897. doi: 10.1016/j.rse.2017.09.007

Zhu, Y. L., and Yan, Y. X. (1998). Study on Hydrodynamic Mechanism of the Formation and Development of Radiating Sandbars in the South Yellow Sea: I. Plane Characteristics of Tidal Current Movement. *Sci. Sin. (Series D)* 28, 403–410.

Conflict of Interest: The authors declare that the research was conducted in the absence of any commercial or financial relationships that could be construed as a potential conflict of interest.

frontiers | Frontiers in Marine Science

ORIGINAL RESEARCH
published: 18 July 2022
doi: 10.3389/fmars.2022.825359

Numerical Simulation of the Locality of Erosional Damages by Storm Waves in Searching for Measures to Conserve Bonggil Beach, Korea

*Jong Dae Do[1], Jae-Youll Jin[1], Byunggil Lee[1], Weon Mu Jeong[2], Jin Yong Choi[3], Sang Kwon Hyun[4], Kihyun Kim[5] and Yeon S. Chang[2]**

[1]East Sea Environment Research Center, Korea Institute of Ocean Science and Technology, Uljin, South Korea, [2]Maritime Information and Communication Technology (ICT) R&D Center, Korea Institute of Ocean Science and Technology, Busan, South Korea, [3]Marine Disaster Research Center, Korea Institute of Ocean Science and Technology, Busan, South Korea, [4]Sekwang Engineering Consultants Company Limited, Seoul, South Korea, [5]Department of Coastal Management, GeoSystem Research Corporation, Gunpo, South Korea

Coastal erosion caused by extreme storms can reduce the value of beaches. Under the scenario of climate change, the storm intensity may increase and the resulting severe erosion can lead to disastrous damages on the beaches. Therefore, it is crucial to find appropriate measures and adaptation plans to conserve the beach from storm attacks. In this study, numerical models were applied to analyze the dune erosion in Boggil Beach, Korea, occurred by Typhoon Tapah in September 2019. Two models were used as Telemac-2D was run in larger domains for producing forcing conditions. XBeach was then applied to simulate the 2019 dune erosion after validation using observational data from a post-event field experiment performed in 2020. The model results showed reasonable agreement with the observational data except for the overestimation of erosion that was likely caused by characteristic pattern of sediment that was a mixture of sand and gravel and the accuracy of model results decreased due to the existence of gravel. The results also confirmed the locality of erosional damage by which the dune erosion was severest in the southern part of the beach. This locality was caused because the water depth was steeper in this area, which kept the wave energy in this area higher than that in the northern part. The uneven distribution of depth was induced by natural and anthropogenic causes. Three cases of model tests were performed to determine an appropriate measure to preserve the beach from future storm attacks – two were to place a submerged breakwater (SB), and one to place a submerged groin(SG). Although the SBs could directly protect the shore from erosion in the lee of the SBs, they could cause additional erosions at unexpected seabed areas. Although the SG was not the best in protecting the beach from the dune erosion, it could minimize the side effect. This measure was also environmentally friendly by keeping the sediments within the coastal cell around the SG so that the beach maintenance could be feasible through replenishment. In addition, the SG could also save the initial cost by reducing its size, and would be more effective, if the recovery process considered, because the SBs would disturb the onshore sediment motions under milder wave conditions. The results of this

OPEN ACCESS

Edited by:
Giandomenico Foti, Mediterranea University of Reggio Calabria, Italy

Reviewed by:
Jianjun Jia, East China Normal University, China
Effi Helmy Ariffin, University of Malaysia Terengganu, Malaysia

***Correspondence:**
Yeon S. Chang
yeonschang@kiost.ac.kr

Specialty section:
This article was submitted to Coastal Ocean Processes, a section of the journal Frontiers in Marine Science

Received: *30 November 2021*
Accepted: *08 June 2022*
Published: *18 July 2022*

Citation:
Do JD, Jin J-Y, Lee B, Jeong WM, Choi JY, Hyun SK, Kim K and Chang YS (2022) Numerical Simulation of the Locality of Erosional Damages by Storm Waves in Searching for Measures to Conserve Bonggil Beach, Korea. Front. Mar. Sci. 9:825359. doi: 10.3389/fmars.2022.825359

study can be applied for decision-making to establish future adaptation plans from storm impacts in Bonggil Beach.

Keywords: coastal erosion, shoreline change, storm waves, xbeach surfbeat, telemac-2D

1 INTRODUCTION

Coastal erosion has become a serious problem in many coastal areas in the world. The reason for the increasing threat on the coasts by erosion may be found from the natural factors such as climate change (Zhang et al., 2004; Masselink and Russell, 2013; Mentaschi et al., 2018) and from the anthropogenic factors such as coastal structures (Syvitski et al., 2005; van Rijn, 2011; Anthony et al., 2015). For example, episodic events of severe coastal erosion would increase when the intensity of storms increases due to the warming of sea surface (Bender et al., 2010; Knutson et al., 2010), and when the equilibrium within a coastal cell could be broken by construction of coastal structures (Do et al., 2021a). Because climate change is an ongoing process and will continue unless robust actions are taken globally, and also because various engineering structures will continue to be built as the coastal communities grow worldwide, the problem of erosion may remain as a significant issue not only at present but also in the future for probably a considerable time. Therefore, it is necessary to develop measures and plans to mitigate the damage by coastal erosion based on proper risk assessment. These assessments and measures should be carefully set up because the impact by coastal erosion is site-specific due to characteristic conditions in a coastal area and sometimes shows locality even within the same area due to the loss of equilibrium by various factors (Oh et al., 2021). Accurate analysis of sediment transport patterns is, therefore, a prerequisite to developing such measures for the site.

The characteristic pattern of sediment transport can be understood by analyzing the short-term and/or long-term sediment budget, the balance between the added and removed sediments within the coastal cell. However, accurate prediction of coastal sediment transport is difficult because the waves carry the sediment both onshore and offshore directions under different conditions. In addition, wave-induced currents and resulting nearshore circulations can lead to complex pattern of sediment transport within the coastal cell, which adds difficulties in understanding their motions. Therefore, the study of coastal sediment transport requires correct information on the hydrodynamic and geographic conditions in the nearshore areas. In addition, factors such as sediment inputs by streams, littoral drift, and outputs in the offshore and longshore directions would be important to understand the balance of the sediment budget within the coastal cell.

In general, the sediments in the beachface move offshore under energetic wave conditions (Russell, 1993), resulting in the shoreline retreat in a short time scale in days or even in hours (Harter and Figlus, 2017; Davidson-Arnott et al., 2019). The eroded shorelines are recovered in months, as a natural process, under mild wave conditions following the storms due to slow but steady onshore sediment motions caused by wave nonlinearity (Hsu and Hanes, 2004), which results in the balance of the shoreline positions without retreat or advancement in the long run. However, under specific conditions such as extraordinary storm waves, the damage on the shore could be too severe so that the recovery process may take a long time of years or even decades (Forbes et al., 2004) because the high wave power under these storms could carry the sediments to the areas where the waves and currents could not affect the sediment motion under normal wave conditions (Do et al., 2019). Sometimes, the damage could hardly be recovered when the coastal structures built to protect the shore were broken (Do et al., 2021a). In order to prevent unexpected damage and to find proper protection plans for beaches of economic and cultural values, therefore, it is important to accurately predict the processes under extreme conditions, considering that the intensity and frequency of major storms may increase in the coming years due to climae change (Bender et al., 2010; Knutson et al., 2010).

In the present study, we observed a severe coastal erosion in Bonggil Beach of the Republic of Korea when Typhoon Tapah attacked the site in late September 2019, which was classified as Categoty 1 tropical cyclone (1-minute maximum sustained wind speed for Category 1 ranges 33-42 m/s). Although the typhoon was not a major storm, it led to huge damages in the beaches located on the east coast of Korea due to the geographical proximity of its path. Specifically, the pattern of damage was distinguished in Bonggil Beach because the erosion showed strong locality as the damage was focused in the southern part of the beach that is separated from the northern part by a nearshore rocky island. In contrast, the typhoon left less severe damage in the northern part that is connected to a stream. In addition to Typhoon Tapah, additional tropical cyclone, Typhoon Mitag, attacked the site consecutively in early October. Typhoon Mitag was classified as Category 2, whose wind speed ranges 43-49 m/s. Considering the unprecedented damage made on the beachface, this study was initiated to analyze and understand the nearshore and beach processes that occurred in the site during the storms, specifically to support the decision-making by the local government to establish appropriate plans to protect and preserve the beach from future threats by similar or even worse storm waves.

For this, we performed field experiments to measure topography and hydrodynamic data and searched for historical records on the site. We also used XBeach model (Roelvink et al., 2009) to simulate the processes during the storm events. Commonly employed area models such as Telemac-2D (Galland et al., 1991) and Delft3D (Roelvink and Van Banning, 1995) have been used to calculate sediment transport, based on the hydrodynamic conditions calculated by the wave and flow modules. However, they are designed to calculate the changes

in seabed elevation, which can be applied to indirectly estimate the shoreline changes. In contrast, the surfbeat mode of XBeach can simulate the morphological changes in the beachface outside the water under extreme wave conditions by resolving the long wave motions with an additional module for avalanching – the slumping of sand from dune face to foreshore under high wave conditions.

In addition, the impacts of sediments that have different sizes at one location can be considered by XBeach in simulating the sediment transport and the resulting morphological changes, using multiple sediment classes with different fractions of each size. One of the characteristic pattern of the sediment in Bonggil Beach was that it was a mixture of sand and gravel. In particular, the spatial distribution of the sand and gavel fractions showed strong loaclity withing the beach area, which required special setting in the input of sediment conditions to reduce modeling error. There were previous studies using XBeach that used multiple sediment classes, especially for the simulation in the gavel (Jamal et al., 2014; McCall et al., 2015) or sand and gravel mixture coasts (Bergillos et al., 2016). However, most of them were 1-dimensional approaches to focus the cross-shore directional sediment transport based on XBeach-G (McCall et al., 2015; Phillips et al., 2020). Recently, 2-dimensinal version of XBeach was used with three sediment classes and their different spatial distributions based on sediment samplings at multiple locations (Gurov and Fomin, 2021). However, their sediments ranged within sand and the impacts by larger sediment grains such as gavel was not examined.

In this study, we investigated the course of the erosional process in the beachface of Bonggil Beach using 2-dimensional Xbeach surfbeat. The model was elaborately setup with the additional application of an area model, Telemac-2D, to provide the forcing conditions by the storm waves to the XBeach. In particular, the sediments were sampled at 72 locations in the beachface and in the water, and the sediment data were classified into two groups of sand and gravel so that the impact of sediment condition could be carefully considered with different sand-gravel fractions at each grid point. The modeling was then focused to generate the exceptional erosion in Bonggil Beach, and thus to analyze the conditions that caused the unusual erosion event. The model was validated based on observational data obtained from field experiments. Once the analysis of the episodic erosion events was completed, additional simulations were performed to search for appropriate measures to mitigate future damages from the attacks of similar or even greater storm events in the study site.

The final goal of this study was then to develop an effective and economic engineering measure to reduce the potential damages by future storm waves, for supporting decision-making to establish conservation plans for Bonggil Beach. Usually, conservation plans for beaches that are vulnarable to storm attacks are established based on the severity of the storms. For exmple, Klima et al. (2012) calculated surge height and wind speed as functions of return period in the areas of Miami-Dade County, United States, and estimated costs and econimic losses using damage models to set up damage reduction protfolios. The present study was not aimed to provide an adaptation plan from storm attacks considering the intensity of future typhoons. Instead, the study was designed to understand the characteristic patern of storm damage spedified in the study site, then to provide possible measures to prevent the similar damage from future storm attacks. Therefore, its study goal was to develop a site-specific engineering measure in Bongil Beach, and the outcome could be confined in this study area, instead of being widely applied for storm adaptation.

The paper is organized as follows. The information of the study site and the damages made by Typhoon Tapah are described in Sections 2.1 and 2.2, respectively. The field experiments performed after the storm event are introduced in Section 3.1. The setup of XBeach and Telemac-2D models in the site is described in Sections 3.2 and 3.3. Validation of the models is described in Section 4.1, and the model results are analyzed in Sections 4.2 and 4.3. The discussions on model outcomes and the suggestions of measures to protect the beach for future storm attacks are provided in Section 5, and the conclusion of the study is in Section 6.

2 BACKGROUND

2.1 Study Site

Bonggil Beach is located on the southeast coast of the Korean Peninsula (**Figure 1A**). It is a 1.8 km long beach whose shoreline is straight in the NNW-SSE direction, facing NEE. **Figure 1B** shows a map of Bonggil Beach, captured from Google Earth on July 4, 2019. The beach consists of a small coastal cell because its northern end is blocked by a set of breakwaters (P1) around a fishing port, and small-sized rocky islands and underwater rocks (P4) are located at the southern end, making the water depth shallower, which disturbs alongshore sediment movement toward further south. In addition, the sediments that are lost from the southern end can hardly be recovered because the shoreline is bent to SSW due to an artificial bank (P5) that was constructed along the shore using tetrapod in order to protect Wolseong Nuclear Power Plant (WNPP). In between the two ends, there is a source of sediment input to the beach through Daejong Stream (P2). One of the most significant features of Bonggil Beach is the rocky island located in the middle of the beach (P3). The island has a diameter of ~50 m and is located ~150 m away from the shore, where the water depth is ~5 m, which disturbs wave propagation, causing a salient in the coast behind the island. This island is culturally important because, according to a legend, this island has been known to be the tomb of a heroic king in Korean history. The island has a name, 'MunMu-daewang-neung' (meaning 'Tomb of Great King MunMu'). For this reason, Bonggil Beach has been one of the most famous beaches in this region where many tourists visit.

The wind and wave condition is moderate in this region as shown with the wind and wave roses in **Figures 2C**, **D**. The wind usually blows from land (WNW) and the wind speed are mostly no greater than 8 m/s. The annual mean significant wave height (H_s) is 0.8 m with the peak wave period of 6.5 s. The most common wave propagation direction is NE and ENE (from the left in **Figure 1B**) as observed from the wave measurement by an AWAC (Acoustic Wave and Current Profiler) located 6.5 km south

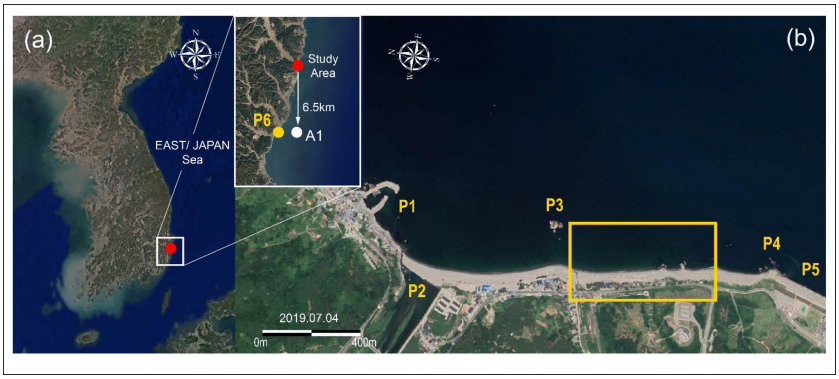

FIGURE 1 | (A) Location of Bonggil Beach in the Korean Peninsula (red dot). In the magnified view of the study area, the location of A1 is marked (white dot) where the wave data were measured during Exp. 1 and 2. **(B)** Google map of Bonggil Beach on July 14, 2019. P1 – P5 mark the locations of the breakwater in the northern end of the beach (P1), the mouth of Daejong Stream (P2), island 'Tomb of Great King MunMu' (P3), rocky islands and underwater rocks in the southern end of the beach (P4) and artificial bank to protect WNPP (P5). The yellow rectangle marks the southern part of the beach, where the damage by erosion was severe. In the panel located in the upper-left corner of **Figure 1B**, the locations of A1 where the wave data in **Figure 4** were measured, and P6 where the severe road destruction in **Figure 3A** occurred are marked.

of Bonggil Beach at a water depth of ~32 m (A1 in **Figure 1A**). In addition to NE, waves are also commonly approaching from SE (from the right in **Figure 1B**). The sediment in Bonggil Beach is characterized as a mixture of sand and pebbles, with their size widely varying from 0.44 mm to 3.22 mm. **Figure 2A** shows a photograph of the beachface in Bonggil Beach on October 24, 2019. The surface of the foreshore (from swash zone to beach berm) is mainly covered by pebbles, whereas the mixture of sand and pebbles are common in the swash zone. Because the sediment in the study site shows characteristic pattern as two types of sediments with clearly different sizes, the measurement was carefully conducted as sediment samples were captured at 72 locations in the beach and in the water (**Figure 2B**). Among them, 30 locations were selected in the beachface (outside water) and 42 locations were inside the water where the sediments were sampled by grab sampler. The details of sediment sampling and the input of sediment data into the numerical model will be described in Section 3.1 and 3.3.

Traditionally, Bonggil Beach has been understood as a depositional beach whose shoreline is gradually advancing due to the excessive input of sediments through Daejong Stream (P2). As shown in **Figure 1B**, the majority part of the stream mouth is blocked by the sediments in the beachface, which has been commonly observed under normal weather conditions. In the rainy season, however, the river mouth is open due to the increased amount of downstream flows that provide sediment to the beach, as shown in **Figure 2C**. It was also reported by the local government that the shoreline positions in the mouth of Daejong Stream are closely related to the precipitation, which indicates that the sediments are carried downstream to the river mouth in heavy rainfalls and transported to the beach, providing a depositional condition in Bonggil Beach.

2.2 Storm Events

On September 22, 2019, Typhoon Tapah passed through the Korean Strait. Tapah was a Category 1 typhoon but caused severe damages, specifically in the southeast coasts of Korea, where the study site is located, due to the proximity of its path. For example, a coastal road in the nearby area (Kyeongju-si Yangnam-myeon) located ~7.0 km south of Bonggil Beach, was destroyed by the storm waves of Typhoon Tapah, as shown in **Figure 3A**. Damage by Tapah was severe in Bonggil Beach, especially in the southern part (yellow rectangle in **Figure 1B**). The two pictures in **Figures 3B, C** compare the beach status before (May 30, 2019) and after (October 9, 2019) the attack of Typhoon Tapah. Before Tapah, a dune was located in the backshore of the beach, and it was covered by grasses. Behind the dune, pine trees were planted protecting the temporary building. After Tapah, however, the dune was severely destroyed, and a steep berm was formed instead. It is also observed that a pine tree was rooted out and laid down in front of the berm. The damage found in **Figure 3C** was too severe, and the natural recovery of the beach seems difficult or may take a long time. After Typhoon Tapah, another tropical cyclone, Typhoon Mitag, attacked the Korean Peninsula on October 3, 2029. Although Mitag was a Category 2 typhoon (max. wind speed 40 m/s), damages made in the study site and in the vicinity were much smaller because its strength became weaker once it landed on the southwestern coast and passed through the peninsula. The wave data measured during Tapah and Mitag are provided in Section 3.1, and the paths of the two typhoons are marked in **Figure 8A**.

3 MATERIAL AND METHODS

3. 1 Field Observations

There are sets of observational data available near the study site for comparisons before and after the event of Typhoon Tapah and Mitag. As shown in **Figure 4**, the AWAC in A1 (**Figure 1B**) measured the wave data during Tapah and Mitag at a water depth of ~32 m (**Figure 4**). The maximum significant wave height (H_s) reached ~7 m on September 22, 2019 when Tapah attacked the site. However, it was much reduced (< 4 m) on October 3, 2019

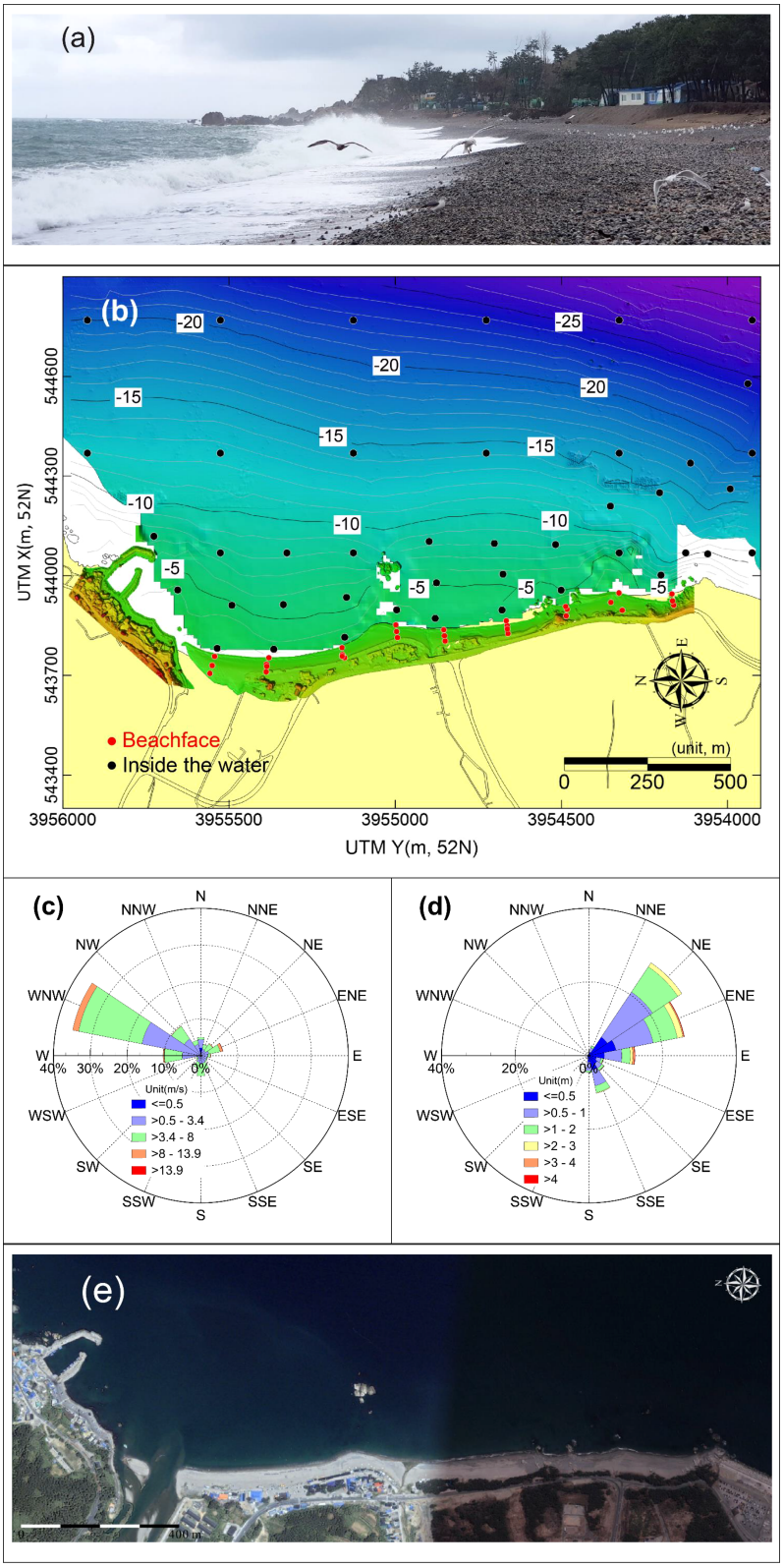

FIGURE 2 | (A) Photograph of the beachface in Bonggil Beach on October 24, 2019, showing the sediment mixture of sand and pebbles. **(B)** Map of the sediment sampling locations, **(C)** wind rose measured at Gampo Port located ~8 km north of the study area, **(D)** wave rose measured at A1 (**Figure 7**) in the study area, **(E)** Google Earth image on July 17, 2011, which shows that the stream mouth was open.

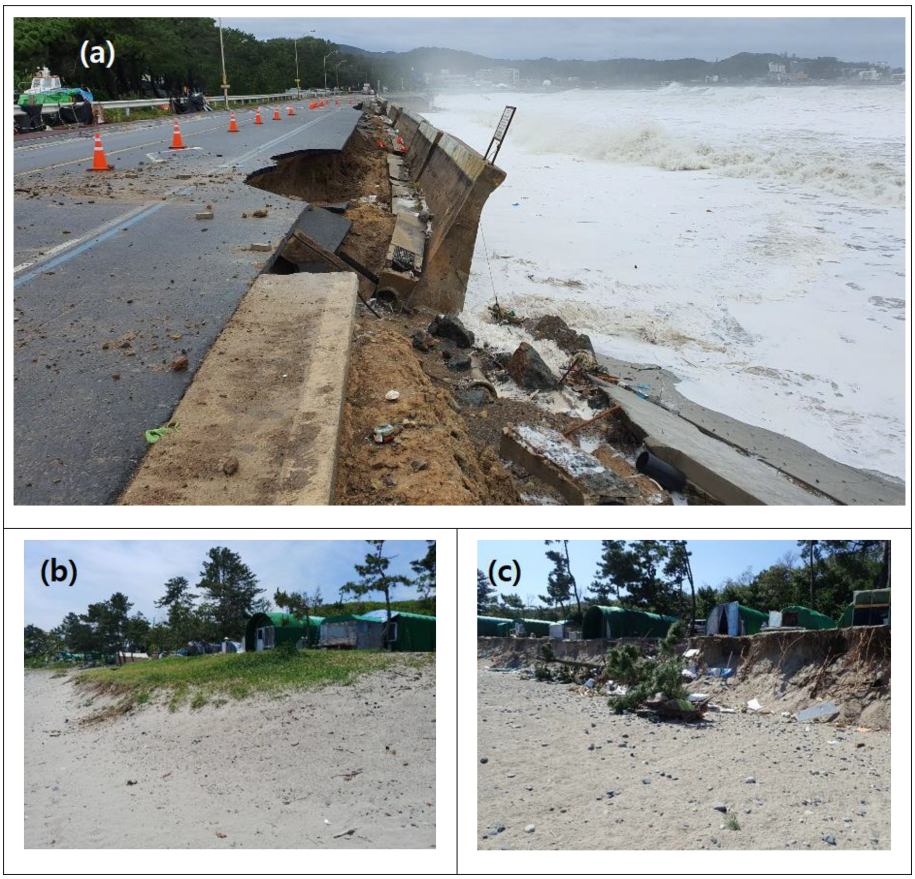

FIGURE 3 | (A) Picture of coastal road destroyed by the attack of Typhoon Tapah, captured from Newsis newspaper (https://newsis.com/view/?id=NISX20190923_0000777231&cID=10899&pID=10800). The road was located ~7.0 km south of Bonggil Beach (P6 in **Figure 1B**) with address of Haebyeongongwon-gil, Yangnam-myeon, Gyeongju-si, Gyeongsangbuk-do, Republic of Korea 38220. **(B)** Picture of the southern part of Bonggil Beach (yellow rectangle in **Figure 1B**) before the attack of Typhoon Tapah (May 30, 2019), and **(C)** picture of the same part of the beach, but after Typhoon Tapah (October 9, 2019).

when Mitag attacked. Because the pictures in **Figures 3A** and **C** were taken after Mitag, it was unclear that the damages in this area were only done by Tapah or by the two consecutive tropical cyclones. However, considering the significant difference in the measured wave height and the witnesses from the dwellers in this area, the damages were presumed to be mostly caused by Tapah. The period of the two storm attacks in **Figure 4** is set as Exp. 1 (September 15 – October 21, 2019), in which the severe coastal erosion in the study site occurred. In addition to the wave measurements, geography data were also available on the site as the profiles, the elevation of beachface, were measured along the perpendicular lines to the coast from October 2019 to October

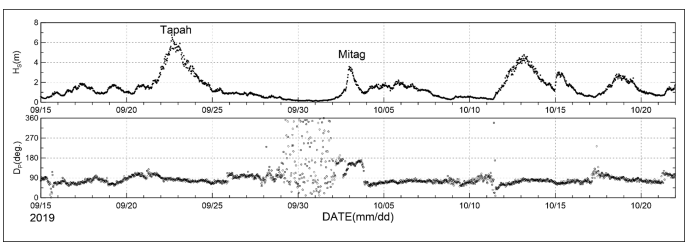

FIGURE 4 | Time series of significant wave height (H_s) and peak wave direction (D_p) from September 15 to October 21, 2019, covering the times of Typhoons Tapah and Mitag, measured by the AWAC at A1 (**Figure 1B**), located 6.5 km south of Bonggil Beach at a water depth of ~32 m. The period of 37 days in **Figure 4** is set as Exp. 1 as it included the period of the erosional event in Bonggil Beach, shown in **Figure 3**. D_p is in degree measured in the clockwise direction from the north (i.e. 45 ° =NE; 90 ° =E; and 135 ° =SE).

2020. **Figure 5A** marks the locations of six profiles (Line 1 – Line 6) on a map measured by a drone on October 20, 2020. The drone was DJI Phantom 4 RTK with takeoff weight of 1.4 kg and diagonal distance of 35 cm, and the three-dimensional meshes were calculated through GCP calibration. The hover accuracy range was ±0.1 m in the vertical and ±0.1 m in the horizontal. The camera resolution was 20 MP, and the GCP RMSE was 4.9 cm and 2.1 cm in the horizontal and 2.5 cm in the vertical. In **Figure 5B**, the beachface elevation data that was measured four times (2019/05/30, 2019/10/09, 2020/09/10, 2020/10/20) before and after the period of Typhoon Tapah and Mitag are compared along with the nine profile lines. The data show high variability with a maximum range of ~3 m, indicating the elevation fluctuated actively in time. However, it does not confirm the specific pattern of erosion or accretion in the site except for Line 7 that is located in the southern part of the beach. Along Line 5, the shoreline was retreated for ~7 m since November 2018 and could not be recovered until October 2020. The location of Line 5 corresponds to the location of severe erosion shown in **Figures 3B**, **C**. Thus the shoreline retreat along Line 5 was likely caused by the storm waves during the attacks of Typhoon Tapah and Mitag.

Because the profile data and the wave measurements from the site were not sufficient to validate the model results, an additional (post-event) field experiment (Exp. 2) was performed from September 15 – October 21, 2020. Exp. 2 was designed to measure geographic and hydrodynamic data such as waves, currents, and suspended sediment concentration using instrument frames that mounted acoustic sensors (Do et al., 2019). During the period of Exp. 2, storm waves also affiliated the southeast coast of, which provided comparable conditions with the times in 2019 when the typhoon Tapah attacked the site. It is noted that the intensity of the storms during Exp. 2 was weaker than that of Tapah in Exp. 1, and the damage by coastal erosion in 2020 was observed to be weaker than that in 2019. The wave condition during Exp. 2 is shown in **Figure 6** when comparing with the model results for validation, and it is not plotted in this section to avoid repetition.

The bathymetry was measured using single-beam (< 3 m) and multi-beam (> 3 m) echosounders, and **Figure 7A** shows the bathymetry data measured on October 21, 2020. The hydrodynamic data were measured during the period of Exp. 2 as well. In **Figure 7A**, the location of the instrument frame (B1) is marked, and **Figure 7B** shows the picture of the frame at B1. The instruments mounted on each frame and their measured data are listed in **Table 1**. The data measured in Exp. 2 are analyzed in Section 4.1. It is noted that, from the bathymetry data in **Figure 7A**, the water depth was deeper in the southern part of the beach (the area where B1 is located). The difference in the water depth can be observed by comparing the distance between the contour lines of -5 m and -10 m. The distance was shorter in the southern part, which indicates that the slope of seabed was steeper in this area. Therefore, the water depth was deeper in the nearshore of the southern part when it was compared at the same distance from the shore.

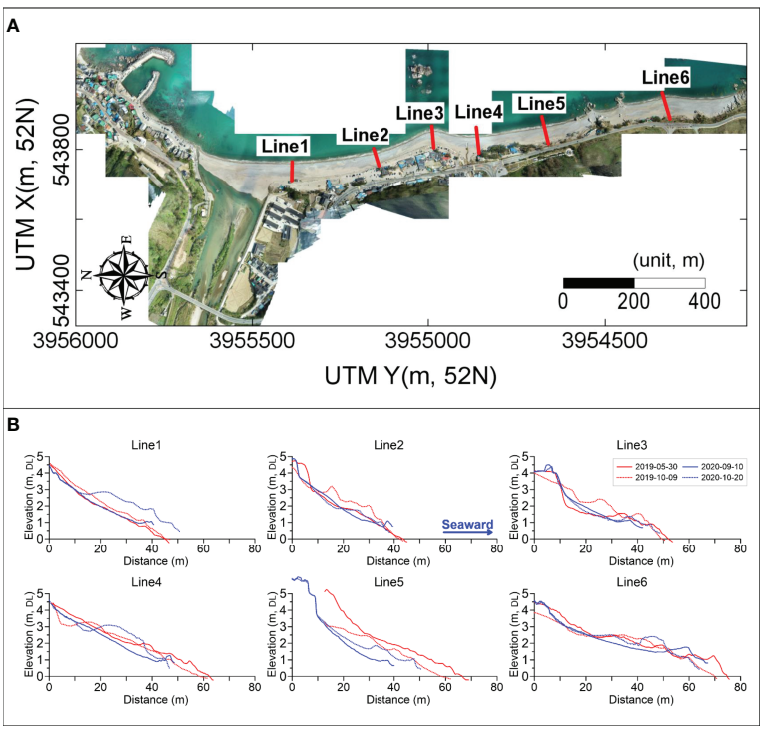

FIGURE 5 | (A) Locations of the six profiles marked on a map measured by a drone survey on October 20, 2015. The profiles were measured four times before and after Typhoon Tapah and Mitag from May 2019 to October 2020. **(B)** Comparisons of profile measurement along the nine lines for the four times on 2019/05/30 (red solid), 2019/10/09 (red dashed), 2020/09/10 (blue solid), 2020/10/20 (blue dashed).

TABLE 1 | List of the instruments mounted on the frame at B1.

Location	Depth	Instruments	Manufacturer	Sampling Interval	Burst Interval	Sampling Frequency	Transducer Frequency	Measurement
129° 29' 10.80" E	~5 m	VECTOR	Nortek AS	600 sec	3600 sec	8 Hz	6 MHZ	Wave parameters and near-bed flow velocities (0.4 m above seabed)
35° 44' 08.41" N		WBL	RBR Ltd.	128 sec	1800 sec	4 Hz	0.2 MHz	Seabed elevation change(0.9 m above seabed)

As described in Section 2.1, the sediment in the study site was a mixture of sand and gravel. In order to carefully analyze the sediment characteristics in this site, therefore, the sediment samples were captured at 72 locations in the beach as well as in the water (the sediments in the water were sampled by grab sampler). D50, D10 and D90 were obtained at each sampling locations. In addition, the proportions of sand, gravel, silt and clay have been obtained at each location (for example, the proportion of sand, gravel, silt and clay at location B20 [one location in the beachface] was 86.75%, 13.25%, 0.00% and 0.00%, respectively, so that the sum of each proportion gave 100% at each location). Based on these sediment proportion data, the sediment facies at each location has been classified into two groups. The two groups are *S* (Sand dominant) and *G* (Gravel dominant). For example, the sediment facies at B20 was classified as *S*. Once the sediment samples at each location are classified, two sediment sizes, D50, were obtained representing the two groups (i.e. D50 = 0.44 mm for group S, whereas D50 = 2.34 mm for Group G). The reason to classify the sediment size into the two groups and obtain the two D50s was to input the two D50s in the model, considering their proportions, which will be described in Section 3.3.

3.2 Numerical Models

In this study, two different models were used to simulate the storm impacts. These models are briefly described in this section as they were introduced in detail by the developers. First, the Telemac -2D (Galland et al., 1991) was employed to generate the wave fields using the wind fields obtained from the Japanese Meteorological Agency (JMA) during the experimental periods. Its results were then applied to produce the time-varying boundary conditions for the XBeach surfbeat (Roelvink et al., 2009) model that was to simulate the seabed topography and shoreline changes by the storm attacks. Telemac-2D is 2DH model package with modules for flows, waves, and sediment transport. This model is characterized by the unstructured mesh system in the horizontal, which has been effectively applied in the coastal regions with complicated topography (Do et al., 2020). Because Telemac-2D only simulated the morphology changes on the seabed but was not to directly calculate the morphological changes along the shore and outside the water, its application for the erosion process in the beachface was limited.

The flow module of Telemac-2D is based on the shallow water equation that solves the depth-averaged momentum equations

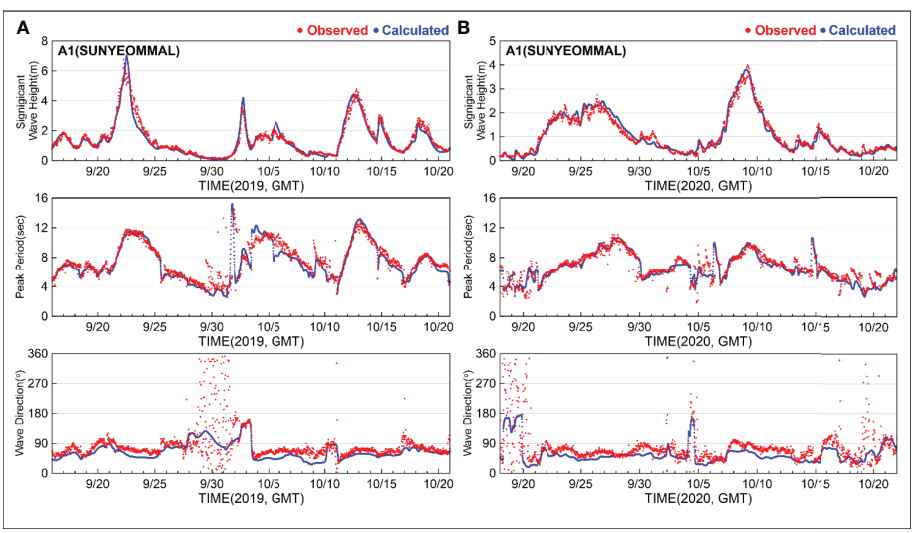

FIGURE 6 | (A) Comparison of significant wave heights (H_s, top panels), peak wave period (T_p, middle), and wave propagation direction (D_p, bottom), between the measured (red dots) and Telemac-2D & Tomawac model (solid blue lines) data at A1 for Exp. 1 (September 15 – October 21, 2019; left panels), and **(B)** for Exp. 2 (September 15 – October 21, 2020; right panels).

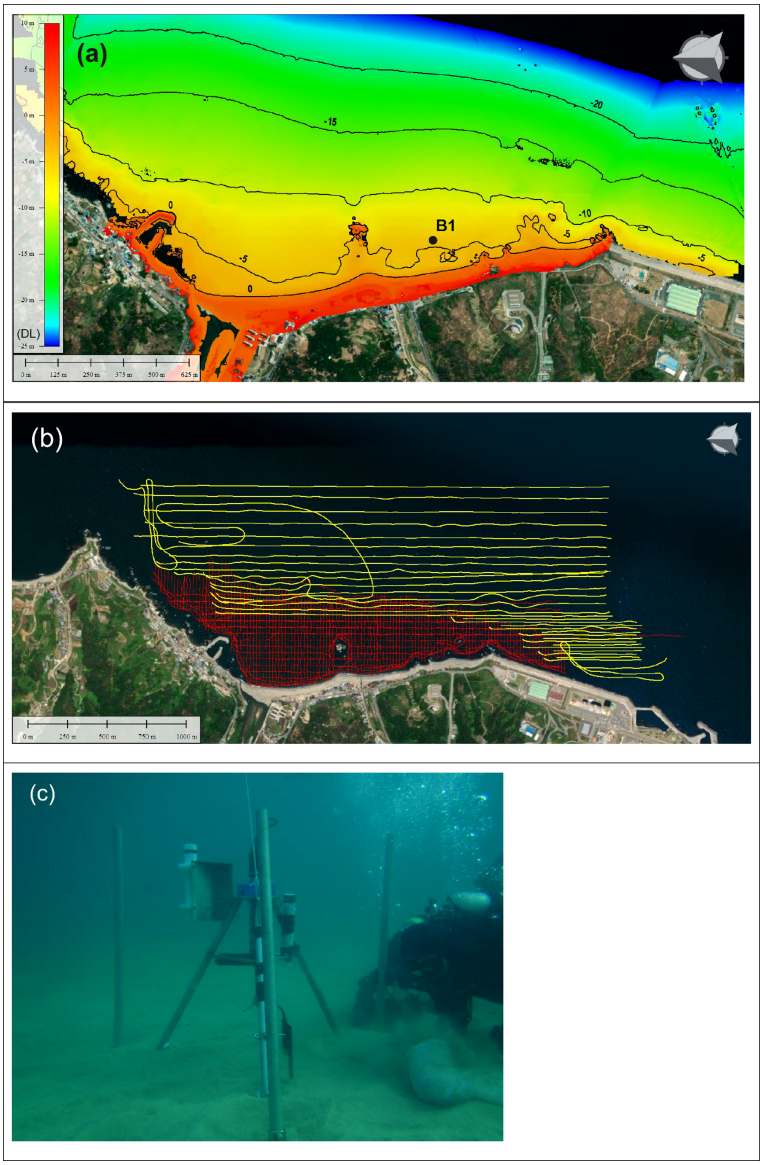

FIGURE 7 | (A) Map of water depths in Bonggil Beach measured by single-beam and multibeam echosounders on October 21, 2020. The single-beam measured data at shallow areas (< 3 m) where the ship with multibeam could not cover. B1 was the location where the instrument frame (**Figure 7B** and **Table 1**) was moored, **(B)** the map of track lines of the bathymetry measurements by single-beam (red) and multi-beam (yellow) echosounders, and **(C)** picture of the underwater-mounted instrument frame.

and continuity equation (Asaro and Paris, 2000; Hervouet, 2000; Robins and Davies, 2011) as:

$$\frac{\partial h}{\partial t} + u\bullet\vec{\nabla}(h) + h\bullet div(\vec{u}) = S_h$$

$$\frac{\partial u}{\partial t} + \vec{u}\bullet\vec{\nabla}(u) = -g\frac{\partial \eta}{\partial x} + S_x + \frac{1}{h}div\left(h\nu_t\vec{\nabla}u\right)$$

$$\frac{\partial v}{\partial t} + \vec{v}\bullet\vec{\nabla}(v) = -g\frac{\partial \eta}{\partial y} + S_y + \frac{1}{h}div\left(h\nu_t\vec{\nabla}v\right)$$

where h is water depth, ν_t is the diffusion coefficient, η is the free surface elevation, S_h S_x and S_y are the source/sink. In the Telemac-2D of this study, the forcing was initially given by the wind fields that were used to generate the wave fields. For the wind fields of the selected storm conditions, JMA was used. The wave fields were generated using the wave module, named 'Tomawac,' which is internally coupled into the Telemac-2D system to generate the wave-induced currents. Tomawac

solves the spectral action balance equation to compute the wave properties such as wave height, period, and wave propagation direction from the wave spectra. Tomawac can also consider the effect of wave diffraction (Holthuijsen et al., 2003) based on the mild slope equation (Berkhoff, 1973). The formulation of the wave action equation is described with the XBeach surfbeat model as it also solves the spectral action balance equation for wave propagation. Once the wave and flow fields are obtained, the sediment transport field can be calculated by solving bedload and suspended load formulas, which then be used to simulate the seabed elevation changes using the morphology module. As already mentioned, the calculation of morphology change is only allowed for the grids inside the water, and the morphological changes outside water are not considered by Telemac-2D. For this reason, Telemac-2D may not be a proper tool for direct evaluation of beachface erosion in the present study, thus used to provide the forcing conditions for the XBeach model in the present study.

The XBeach surfbeat model was able to estimate the rapid changes in the shoreline due to the attacks of storm waves. It is because the model has an additional module, the avalanching module that calculates sand slumping from dune face to foreshore. Thus can be applied to estimate the shoreline evolution. XBeach surfbeat is characterized to resolve the long wave (infragravity) motions, considering that the impacts of long waves are dominant for the shoreline evolution, whereas the shortwaves are often dissipated by breaking and friction when arriving at the shore. Therefore, the surfbeat mode of XBeach does not solve the individual short waves. Instead, it describes the short wave propagation by solving the wave action equation, similar to Telemac-2D, as:

$$\frac{\partial A}{\partial t}+\frac{\partial C_x A}{\partial x}+\frac{\partial C_y A}{\partial y}+\frac{\partial C_\theta A}{\partial \theta}=-\frac{D_w}{\sigma}$$

where $A(x,y,t,\theta)=\frac{S_w(x,y,t,\theta)}{\sigma(x,y,t)}$ is the wave action, θ is the angle of wave incidence, $S_w(x,y,t,\theta)$ is wave energy density, D_w is wave energy dissipation, σ is wave frequency, C_x C_y nd C_θ are wave action propagation speed in the x y and θ direction respectively. The root-mean-square wave height is then calculated from the wave energy spectra as $H_{rms}=\sqrt{8E_w/\rho g}$ where. E_w. is the short wave energy. Once Eqn. (4) is solved, the forcing that generates the long waves is obtained from the radiation stress, which is based on the wave energy variation as:

$$F_x=-\left[\frac{\partial S_{xx}}{\partial x}+\frac{\partial S_{xy}}{\partial y}\right],F_y=-\left[\frac{\partial S_{yy}}{\partial y}+\frac{\partial S_{yx}}{\partial x}\right]$$

where S_{xx} S_{yy} S_{xy} and S_{yx} are the radiation stresses and F_x and F_y are the forcing in the x and y directions, respectively. In XBeach surfbeat, the x axis is located parallel to the coastline, and y -axis is set perpendicular to the shore. The forces in Eqn. (5) are used to generate the long waves *via* the shallow water equation as:

$$\frac{\partial u^L}{\partial t}+u^L\frac{\partial u^L}{\partial x}+v^L\frac{\partial u^L}{\partial y}-fv^L-\nu_h\left(\frac{\partial^2 u^L}{\partial^2 x}+\frac{\partial^2 u^L}{\partial^2 y}\right)=-\frac{\tau_{sx}}{\rho h}-\frac{\tilde{}_{bx}}{\rho h}-g\frac{\partial \eta}{\partial x}+\frac{F_x}{\rho h}$$

$$\frac{\partial v^L}{\partial t}+u^L\frac{\partial v^L}{\partial x}+v^L\frac{\partial v^L}{\partial y}+fu^L-\nu_h\left(\frac{\partial^2 v^L}{\partial^2 x}+\frac{\partial^2 v^L}{\partial^2 y}\right)=-\frac{\tau_{sy}}{\rho h}-\frac{\tilde{}_{by}}{\rho h}-g\frac{\partial \eta}{\partial x}+\frac{F_y}{\rho h}$$

$$\frac{\partial \eta}{\partial t}+\frac{\partial hu^L}{\partial x}+\frac{\partial hv^L}{\partial y}=0$$

where u^L is the Lagrangian velocity which is defined as a particle's distance that travels in one single period of the long wave divided by the corresponding wave period (Wong, 2016). τ_{sx} is wind stress, τ_{bx} is bottom stress, F_x is the forcing in Eqn. (5), h is water depth, ρ is water density, g is gravitation, ν_h is viscosity, f is Coriolis coefficient and η is the water surface elevation of the long waves. The sediment module of XBeach surfbeat solves an advection-diffusion equation as:

$$\frac{\partial hC}{\partial t}+\frac{\partial hCu^E}{\partial x}+\frac{\partial hCv^E}{\partial y}+\frac{\partial}{\partial x}\left[D_x h\frac{\partial C}{\partial x}\right]+\frac{\partial}{\partial y}\left[D_y h\frac{\partial C}{\partial y}\right]=\frac{hC_{eq}-hC}{T_s}$$

where C is volume concentration of sediment, C_{eq} is equilibrium concentration, D_x is sediment diffusivity, T_s is the time of adaptation of entrained sediments. Morphological change in the seabed can be calculated as:

$$\left|\frac{\partial z_b}{\partial t}\right|=\frac{f_{mor}}{(1-P)}\left[\frac{\partial q_x}{\partial x}+\frac{\partial q_y}{\partial y}\right]=0$$

where z_b is seabed level, P is porosity, q_x are sediment flux, f_{mor} is morphology change factor. In the avalanching module, the dune face is set to be slumped when the bed slope exceeds a critical value within one-time step as:

$$\left|\frac{\partial z_b}{\partial x}\right|>m_{cr}$$

where m_{cr} is the critical value. If the condition is satisfied, the dune bed level can be calculated as:

$$\triangle z_b=\left(\left|\frac{\partial z_b}{\partial x}\right|-m_{cr}\right)\triangle x$$

which is used to evaluate the shoreline evolution.

3.3 Model Setup

The Telemac-2D and XBeach surfbeat models were employed for different purposes, as explained in the previous section. The goal of Telemac-2D was to provide the realistic forcing conditions for the XBeach surfbeat runs, and it was run for two large domains, D1 and D2. **Figure 8A** shows the computational domain and unstructured grid system of D1, the largest domain that covered the seas around the Korean Peninsula and parts of the East China Sea and the Northwestern Pacific Ocean. The purpose of D1 runs of Telemac-2D was to provide the forcing conditions for the smaller domain, D2 shown in **Figure 8B**. Telemac-2D in D1 was run to simulate the tide and wave fields so as to compute the tidal elevation, current, wave height, period, and direction along the boundaries of D2.

The unstructured grid system in D1 used 336,264 nodes and 626,069 elements. The tides were composed of the 16 constituents, including M2 and S2. To generate the waves, JMA wind fields were used over the domain with △x and △y of 0.0625 ° and 0.05 °, respectively. In addition to the wind, the air pressure field was applied to increase the model accuracy, specifically during the time of storms. For the air pressure, the data from National Center for Environmental Prediction (NCEP) were applied over the domain with △x and △y f 0.25 °. The JMA and NCEP data were input in the simulation every 3 hours. The model time step, △t was set to 30 s for the tide simulation and 60 s for the wave simulation. In D1, the Telemac-2D model was run for two experimental periods, Exp. 1 and Exp. 2. First, the model was validated based on the observational data available from Exp. 2 as it was run for 37 days September 15 to October 21, 2020. Once the model was validated using the measured data, the model was run from September 15 to October 21, 2019, which was the main run corresponding to Exp. 1 to investigate the impacts of Typhoon Tapah and Mitag on the beach.

Once the model was run over D1, Telemac-2D with Tomawac was run over domain, D2, using the results from the D1 run as

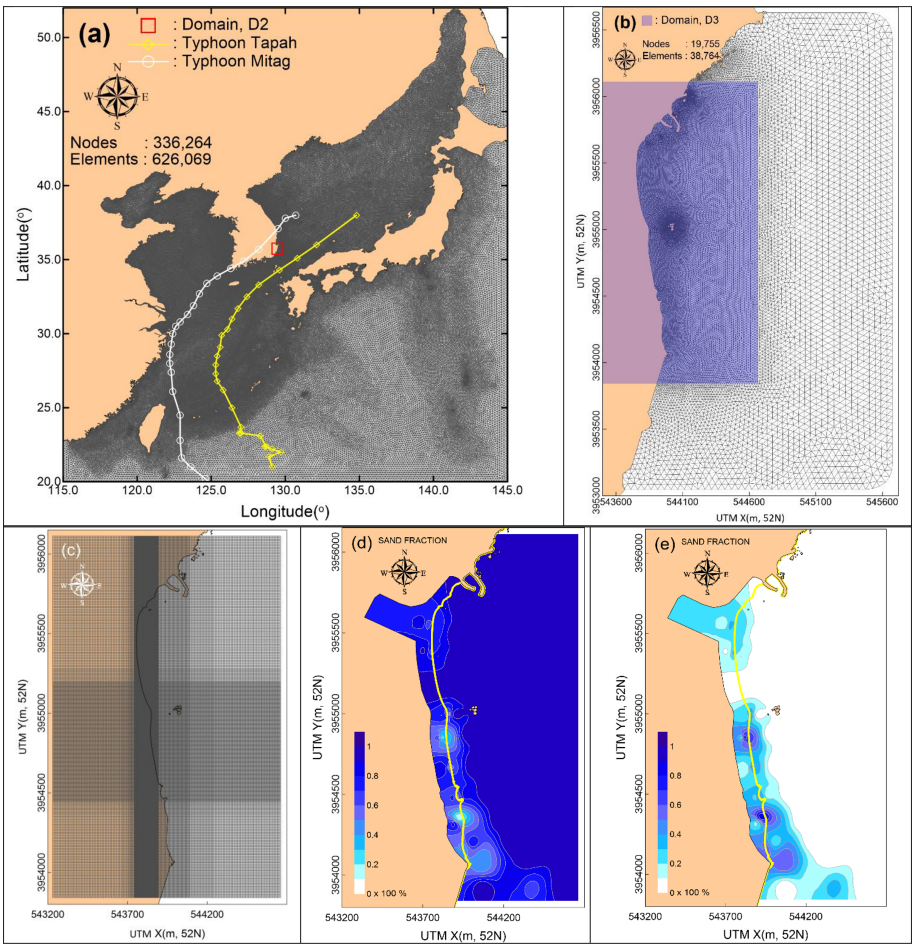

FIGURE 8 | (A) Computational domain and the unstructured meshes in the computational domain, D1, for Telemac-2D. The paths of Typhoon Tapah (yellow) and Mitag (white) are added in **Figure 10A**. **(B)** Computational domain and the unstructured meshes in the computational domain, D2, for Telemac-2D, **(C)** computational domain and the multi-size grids in the computational domain, D3, for XBeach surfbeat **(D)** distribution of sediment for XBeach run over D3 for the erodible area with sand fraction, and **(E)** erodible area with gravel fraction. The yellow and red solid lines in **Figures 8D**, **E** mark the shoreline positions.

the forcing at the boundaries. The computational domain of D2 included the Bonggil Beach and extended to cover a cape in the northern end and the bank of WNPP in the southern end, with the domain size of 2.02 km by 3.58 km in the cross-shore and the longshore direction respectively (**Figure 8B**). The grid system in D2 used 19,755 nodes and 38,784 elements. The purpose of the run over D2 was to provide the forcing conditions for the final XBeach run over the smallest domain, D3. Therefore, the setup of the model was basically same as that over the domain D1 as it was to produce the tide and wave parameters with finer grids within the domain. One difference was that the time-varying conditions along the D2 boundaries were obtained from the outputs of the run over the domain D1, instead of using the wind and air pressure fields. The model was run for Exp. 1 and Exp. 2 as well, corresponding to the D1 runs. The time step was 2 sec for the tide simulation and 10 sec for the wave simulation using Tomawac.

Once the model data using Telemac-2D were obtained, the XBeach surfbeat was run over the smallest domain, D3, using the results from the D2 run as the forcing conditions along the boundaries. The computational domain just covered the Bonggil Beach with the size of 1.43 km by 2.27 km in the cross-shore and longshore direction, respectively (**Figure 8C**). The XBeach model used a multi-grid system to employ finer grids in the middle of the beach and along the shore. The sizes of coarse grids were 307 m and 217 m in the cross-shore and longshore direction, respectively. The sizes of the fine grids ranged from 2.5 m and 10 m (**Figure 8C**). Along the lateral boundaries, the outputs of Telemac-2D run over D2 were applied to provide the forcing conditions. The model was also run for two experimental cases. First, Exp. 2 was run for 37 days from September 15, to October 21, 2020, for model validation. Once it was validated, the model was run to simulate the shoreline changes during Typhoon Tapah and Mitag in Exp. 1. For XBeach surfbeat, semi-empirical parameters were determined for the default settings (Roelvink et al., 2009). The parameters were re-determined based on the laboratory and field measurements from the WTI 2017 (Wettelijk Toets Instrumentarium) project (Van Geer et al., 2015), which were also employed for the two experiments in this study.

In the model, the sediment size could be input differently at each grid point. In addition, two different values of D50s (one for sand and the other for gravel) could be input considering the proportion of each at each grid point. As described earlier, the proportions of the sand (including silt and clay) and gravel were measured at all of the 72 sediment sampling locations, as shown in the new figure (**Figure 2B**). This proportion data have been interpolated/extrapolated in all model grid points, as shown in **Figures 8D**, **E**. Therefore, at each grid point, the fraction of sand and gravel was determined, giving 100% when the two proportions were added. At each grid of the model, the sand (D50 = 0.44 mm) and gravel (D50 = 2.34mm) sizes were input considering the sand and gravel fraction. For example, at the grid point that contained the sampling location B20, there were 4 input parameters for the sediment size as 1) D50_s = 0.44mm; 2) D50_g = 2.34mm; 3) Proportion_Sand = 86.75%; 4) Proportion_Gravel = 13.25%.

4 RESULTS

4.1 Model Validation

The performance of Telemac-2D with Tomawac is examined using the wave measurements at A1. **Figure 6** compares the significant wave heights (H_s), peak wave period (T_p) and wave propagation direction (D_p) between the observation and model data for both Exp. 1 in 2019 and Exp. 2 in 2020. The results show that all three wave parameters were well reproduced by the model during most of the time in both Exp. 1 and 2. Specifically, the modeled H_s nicely agreed even during the storm periods when the maximum H_s reached ~7 m at the time of Typhoon Tapah. During Exp.2, the storm waves (maximum $H_s > 2$ m) were observed two times around September 27 and October 9, 2020. Although the maximum wave heights during the storms in Exp. 2 were lower than those during the storms in Exp. 1 as H_s reached ~2.7 m on September 27 and ~4.0 m on October 9, their periods were longer compared to those in Exp. 1. Considering that the storm impact on sediment transport could increase with storm duration (Almar et al., 2010), it was expected that morphological changes would also be significant during Exp. 2. However, the erosional damage was much weaker for Exp. 2, even though there were two additional typhoons that had greater intensity, Mysak (September 3, 2020; Category 4) and Heishen (September 8, 2020; Category 4), consecutively affiliated the site just before Exp. 2 started, which is discussed in the next section. The modeled wave period, T_p, also nicely matched the observation data except for when T_p abruptly changed. In the case of the wave direction, there were times when the measured data were widely scattered, which was likely due to instrumental error. Except for those times, D_p was also nicely agreed between the two data sets.

Both of the Telemac-2D and XBeach surfbeat model results were also validated through comparison with the hydrodynamic measurements from Exp. 2 (it is noted that the hydrodynamic data were not available for Exp. 1). In **Figure 9**, the longshore (U) and cross-shore (V) velocity measured at B1 during Exp. 2 are compared between the observation and model data. Usually, the velocity magnitude was small as the fluctuation by tidal currents was dominant with a range of ±0.1 m/s in the cross-shore direction, except for the time when the maximum longshore current speed increased up to ~0.5 m/s on October 9, 2020, during the attack of storm waves with maximum H_s of ~ 4 m. In this time, the model result by Telemac-2D was underestimated with a maximum longshore current speed of ~0.2 m/s, whereas XBeach surfbeat was overestimated as its speed reached ~0.7 m/s. Except for this peak, however, the longshore currents were generally in good agreement with the observation with XBeach surfbeat. In the cross-shore direction, the error by Telemac-2D was greater as the current direction was opposite on October 8 – 9, 2020, compared to that by XBeach surfbeat which showed better agreement with the measured data in this period. The better performance in XBeach surfbeat is confirmed in the bottom panels of **Figures 9A**, **B** in which the velocity magnitude was compared between the two models and the observed data, focusing the storm period from October 6, 2020 to October 12, 2020. It shows that the maximum value of current speed of ~0.5 m/s could be modeled by XBeach surfbeat whereas it was

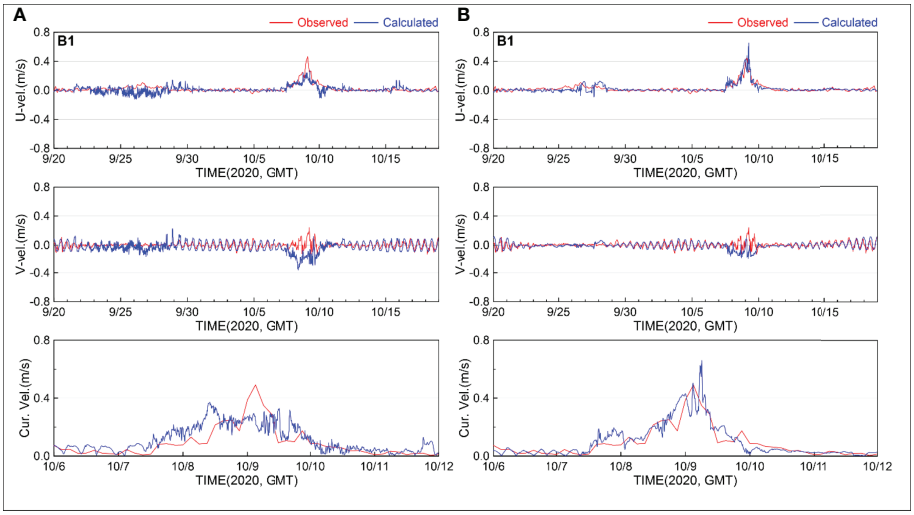

FIGURE 9 | Comparison of measured (red) and model (blue) data between **(A)** Telemac-2D, and **(B)** XBeach surfbeat using the velocity measurements in Exp. 2. Top: longshore (*U*) velocity components (+: north); middle: cross-shore (*V*) velocity components (+: offshore); bottom: velocity magnitude during the storm period from October 6, 2020 to October 12, 2020.

underestimated by Telemac-2D. It is also noted that the tidal currents were more accurately simulated by XBeach surfbeat because the Telemac-2D was slightly overestimated in most times when the tide was dominant. Considering the comparison results, it was concluded that the XBeach surfbeat showed better performance in generating the nearshore currents at B1 during Exp. 2. It is noted that the model errors in simulating the flows are likely because these 2-D models provided depth-averaged flow velocities whereas the observation data were measured near the bottom so that the vertical variation of flow structure could not be calculated by the models. The statistics of the model data such as the root mean square error ($\mathrm{RMSE} = \sqrt{\langle (x_c - x_m)^2 \rangle}$) and BIAS= ($\langle x_c - x_m \rangle$) for the sea surface elevation and the longshore and cross-shore velocities at B1 are listed in **Table 2**.

Once the hydrodynamic data were validated, the next step was to validate the XBeach surfbeat in simulating the morphological change (it is noted that Telemac-2D was used to provide forcing conditions for XBeach surfbeat, and not used to calculate morphology change). In **Figures 10A**, **B**, the morphological changes obtained from bathymetry measurements on September 17 and October 21, 2020 are compared with those calculated by XBeach surfbeat during Exp. 2 from September 15 to October 21, 2020. In general, the model reasonably generated the pattern of morphological change during the period, as shown in the green rectangles of the figure. For example, both of the severe erosions in L0, at the outer part of the breakwater, and L2, in the lee area of the island 'MunMu-daewang-neung', was nicely simulated by the model. In addition, the seabed erosion in in the southern part of the beach in L4 was also in an agreement between the observation and model data, which confirms the validation of XBeach surfbeat in simulating the morphology in general. However, there are areas where there were discrepancies if compared in detail. For example, the beachface in the northern part (L1) were deposited by the observation but eroded by the model. In addition, the erosion and deposition pattern in L3 and L5 occurred oppositely between the model and observation. In order for the additional validation of the model, the beach profiles calculated by XBeach surfbeat model are compared with the observation along the line marked in **Figure 10C** on two days in 16 September and 21 October, 2020 (**Figures 10D**, **E**). It was observed that there were dramatic changes in the bottom topography in the nearshore during the period, but the model nicely reproduced this rapid change. For example, a pit was observed just seaside of the shoreline with maximum depth of ~8 m in 16 September 2020, which was recovered in 21 October, 2020, which was successfully simulated by the model. The pit was formed in the edge of the salient located in the lee of the island before the attack of the storm (**Figure 10C**). After the storm, however, the salient moved to the south (yellow line in

TABLE 2 | Validation by statistics at B1.

Xbeach				**Telemac-2D**			
	Elevation(m)	**U-vel.(m/s)**	**V-vel. (m/s)**		**Elevation(m)**	**U-vel. (m/s)**	**V-vel. (m/s)**
RMSE	0.063	0.037	0.051	RMSE	0.057	0.048	0.072
BIAS	0.004	-0.001	-0.005	BIAS	-0.002	-0.010	-0.021

Figure 10C) and the pit was filled. The profiles in **Figures 10D, E** show that this process was reasonably simulated by Xbeach surfbeat. The model results also quantitatively agreed with the measured data. However, the model accuracy decreased at the nearshore area outside the pit (x = 543880 – 543950 m) where the modeled seabed topography in October, 2020 was lower than the observation with maximum discrepancy of ~2 m.

The model validation based on the data in Exp. 2 might not correctly reflect the damages in Exp. 1 in 2019 because the severe damages (e.g. dune erosion in the southern part) by Typhoon Tapah in 2019 were not recovered in Exp. 2. As shown in **Figure 10A**, however, the seabed morphology was also significantly changed during Exp. 2. In addition, the profiles in **Figure 5B** show that the seabed could be significantly changed after Typhoon Tapah until Exp. 2 started in 2020, which indicates that the seabed was adjusted for ~1 year since Tapah in 2019. Therefore, the seabed changes observed in Exp. 2 was mainly occurred during the period of EXP. 2 once the seabed morphology was considerably adjusted after Tapah, thus the data measured in Exp. 2 was still effective for the model validation.

4.2 Simulation of Shoreline Retreat in 2019

In this section, the results by XBeach surfbeat for Exp. 1 in 2019 are presented. The model was run for two cases during Exp. 1. In the first case, it was run from September 15 to September 24, 2019 so as to identify the impact of Typhoon Tapah only and to exclude the impact of Typhoon Mitag by stopping the model before the event of Mitag. In the second case, the model was run from September 15 to October 3, 2019 so that the impacts of both Tapah and Mitag was considered. **Figure 11** compares the results of morphological changes between the two cases. Although minute differences are observed, the two results are basically the same, which indicates that the significant morphological changes captured in **Figure 3** were caused by Tapah only, and the impact by Mitag was not significant in this site.

The similar model results of morphological changes between the two cases supported the witness from the dwellers in the study area, as mentioned in Section 2.2, that the severe damages in the southern part of the beach was observed just after Typhoon Tapah. If that is the case, the reason that Typhoon Mitag did not make significant impacts in the nearshore morphology needs to be explored. One of the direct indications was the discrepancy in the wave height between the two typhoons. As shown in **Figure 4**, the maximum H_s reached ~7 m during the attack of Tapah whereas it was less than 4 m during Mitag. Therefore, the wave energy that proportional to the square of the wave height would be higher in the study site during Tapah than Mitag. However, it should be also noted that the wave energy during Mitag was likely high enough to cause the erosions. As shown in the wave rose in **Figures 2C**, **D**, more than 90% of wave height were less than 2 m in this area. Therefore, the maximum wave height of ~4 m during Mitag could provide sufficient wave energy to cause erosions. For example, the data measured by a video monitoring system confirmed that the shorelines in another beach in the eastern coast of the Korean Peninsula (i.e. the beach with similar wave conditions with Bonggil Beach) significantly changed when the storm waves with maximum H_s lower than 4 m attacked the site (Oh et al., 2021). This unusual phenomenon was likely related with the recovery process. Once severe erosion occurred during Typhoon Tapah, the beach was gradually recovered under milder wave conditions followed by the storm (Hsu and Hanes, 2004), and the time that was required for the recovery could take months or even years (Forbes et al., 2004; Ranasinghe et al., 2012; Vousdoukas et al., 2012; Morales-Márquez et al., 2018). Therefore, it was likely that the severely eroded condition resulted from the attack of Tapah would not be recovered yet when Typhoon Mitag attacked the site again ~10 days later. Therefore, the impact by Typhoon Mitag whose wave energy at Bonngil Beach was relatively lower than that of Typhoon Tapah could not be sufficient to cause additional erosion. This result indicates that, in analyzing the storm impacts and planning the mitigation/adaptation measures, it is important to consider the resilience of the beach recovery in the study site, which will be revisited in the discussion section 5.1.

Although the model result of the morphological change by XBeach surfbeat could not be verified due to the lack of observation data during Exp. 1, the severe erosion in the southern part of the beach (**Figure 3**) was successfully simulated by the model as shown in the green rectangle, L6, in **Figure 11**. However, the model result also shows some errors because it was overestimated for the dune erosion. Although the erosion generally occurred along the beachface of the beach, it was less severe when compared with that simulated by the model, especially in the areas marked by rectangles L7 and L8. Therefore, the model results were likely exaggerated even though the general pattern of dune erosion was in agreement with the observations, which is discussed in the next section. The reason for the model's overestimation was still unclear. However, one of the factors that could affect the model results was the sediment size. As shown in **Figures 2A**, **B**, the beachface of Bonggil Beach was covered by a mixture of sand and gravel. Although gravels are more stable than sand in starting the incipient motion due to the gravity, they could be more active in motions once started and the fraction of sand and gravel in **Figures 8D**, **E** could be a controlling factor that determined the amount of eroded sediments. However, the model input in **Figure 8** was determined by the field survey during Exp. 2, which might be different from the sediment distribution during the time of Typhoon Tapah and Mitag (Exp. 1). Therefore, the insufficient information on the sediment distribution for the sand and gravel mixture possibly contributed to the overestimation of dune erosion along the beachface.

4.3 Simulation With Coastal Structures

The goal of this study was to develop a plan that can be used to protect the beach from future damages by similar or even more severe storm attacks. To achieve this goal, we tested three cases of model runs to examine the effectiveness of coastal structures as engineering measures. For the engineering structure, submerged breakwater (SB) and submerged groin (SG) were used as they have been commonly used for the hard structures on the east coast of South Korea. The first case (**Case 1**) was to place an SB in front of the northern part of Bonggil Beach (**Figure 12B**). This

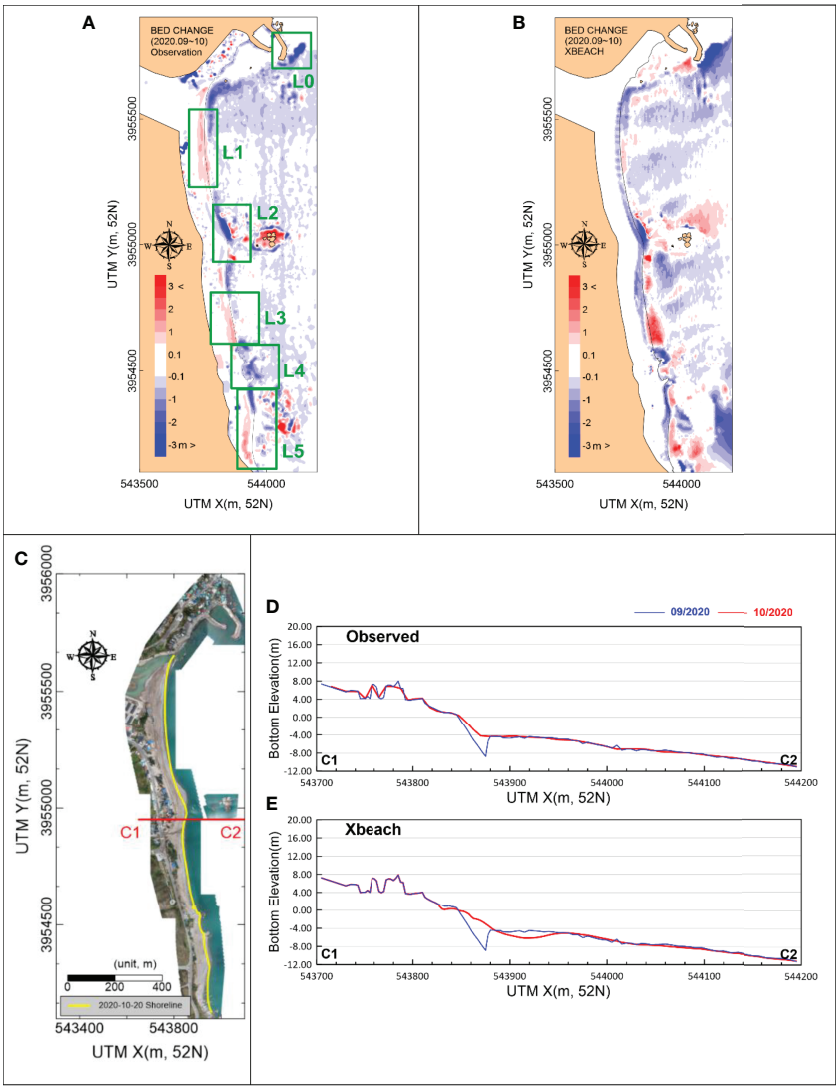

FIGURE 10 | Comparison of the **(A)** observed and **(B)** modeled morphological changes for Exp. 2. The observation data were obtained by the bathymetry measurements on September 17 and October 21, 2020. The model data were calculated by running XBeach surfbeat from September 15 to October 21, 2020. The green rectangles, L0 – L5, in the left panel mark the areas where the morphological change was in agreement or in disagreement between the observation and model data, **(C)** map of the site measured by the drone on September 10, 2020, before the attack of the storm. The yellow line on the map was the shoreline measured after the storm (October 20, 2020), showing that the salient formed behind the island moved to the south. The red line from C1 to C2 is a beach profile line selected for comparison between observational and modeled bottom topography, **(D)** beach profile measured in 16 September (blue) and 21 October (red), 2020 along the line from C1 to C2 in **(C**, **E)** beach profile calculated by XBeach surfbeat in September (blue) and October (red), 2020 along the line **(C)**. The pit formed in the edge of the salient before the storm attack was filled as shown in **(C)**, which was nicely simulated by the model as shown in **(E)**.

was a direct measure to protect the northern part of the beach. Although the erosion was more severe in the southern part, this plan was considered to protect the facilities that were mostly located in the northern part. The second plan (**Case 2**) was to place a SB in front of the southern part of the beach (**Figure 12C**), which was a direct measure to protect the southern part where severe erosion occurred. The third plan (**Case 3**) was to place a SG at the southern end of the beach (**Figure 12D**). This was an indirect measure for the beach protection because the SG would be used to capture the sediments that could leave the coastal cell of the beach by erosion instead of directly preventing the erosion. In fact, additional cases might be designed for the model simulation, and the performance of all cases could be compared by calculating the effectiveness in numeric. However, this type of effectiveness could not be verified without observation data to prove it. Therefore, we selected the three cases, instead of increasing test cases, because they represented hard stabilization measures that directly disturbed sediment motions and a soft

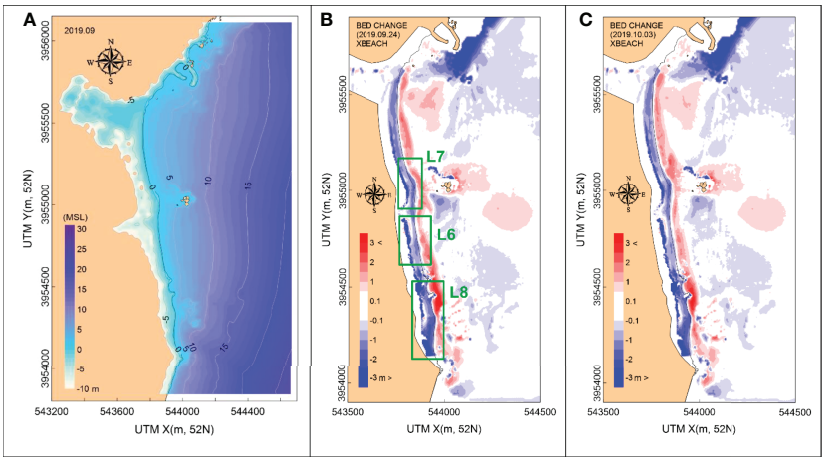

FIGURE 11 | (A) Geographical set up of XBeach surfbeat for Exp. 1, and **(B)** the model result of the morphological change that considered the impacts of Typhoon Tapah only by running the model from September 15 to September 24, 2019, and **(C)** the model result that considered the impacts of both Tapah and Mitag by running the model from September 15 to October 3, 2019.

stabilization measure that could conserve the sediments within the coastal cell.

In **Figure 12**, the model results of the morphological changes by XBeach surfbeat are compared between the three cases of coastal structure arrangement. For all cases, the model was set up with the storm wave conditions used for Typhoon Tapah, and was run for 15 days from September 15 to October 3, 2019 to observe the impacts by Tapah and Mitag with the structures, although Mitag could not make a significant impact. The model results are compared to the case without any structures (**Figure 12E**). For the first case of the run (SB in the northern part, **Figure 12F**), the beach was protected in the northern part as the sediments in the beachface were less eroded, and sediments were deposited in the lee of the SB, as shown in L9 of **Figure 12F**. However, side effects were also observed as the seabed was severely eroded in the north end of the SB (L9). In addition, the seabed in the south end of the SB was eroded (L10), which was not observed in the case of the run without the structure. It is also noted that the eroded sediments were cumulated in the southern end of Bonggil Beach as found in L11.

The side effects of SB were also observed in the second case of the simulation (SB in the southern part, **Figure 12G**). Although the beachface was less eroded, and sediments were cumulated in the lee of the SB as shown in L12, there could be a serious seabed erosion in the southern end of the SB (L13). In addition, the beachface in L13 was more severely eroded than the case without any structure (**Figure 12E**). These eroded sediments were cumulated in the southern end of the beach (L14). In the third case (SG in the southern end of the beach, **Figure 12H**), the side effect was minimal, although the protection of the beachface was also minimal. The erosion pattern in the beachface was similar to the case without structure, which indicates that the beach could not be protected in the future attacks of similar storm waves as Typhoon Tapah. However, the eroded sediments might not be lost from the coastal cell but cumulated in the area around the SG (L15). It is also noted that the sediments were eroded in L16, which was opposite to the findings of other cases because the sediments were cumulated in this area as observed in L14 of **Figure 12G**. This opposite pattern of sediment deposition/erosion is important because this area L16 is located in front of the WNPP and thus outside of the coastal cell. Therefore, the sediments cumulated in this area indicate that they would not return to Bonggil Beach but lost for good. This possibility of sediment loss from the coastal cell might be reduced by constructing the SG as in **Figure 12H**.

The simulation results indicated that the protection of the beach from the loss of sediments in the northern and southern parts could be more effective by constructing the SBs (**Case 1 and 2**). However, these cases might cause significant side effects of additional erosions at the unexpected seabed locations in the nearshore. Considering that these rapid seabed erosions were caused in a short-term period (days) during an attack of the harsh storm such as Typhoon Tapah, they could lead to longer-term (months) erosions in other parts of the nearshore areas when the post-storm process occurred to reach an equilibrium status. In contrast, the use of SG (**Case 3**) might have results with lower performance in directly preventing the severe erosion in the southern part of the beach. However, the side effect of unexpected seabed erosion would be much reduced. In addition, the loss of total sediments within the littoral cell could be reduced by preventing the outgoing sand movement through P4, by using the SG to save the transported sediments around it. Therefore, we suggest that **Case 3** as a favorable measure out of the three cases. Considering the goal of this study to protect the beach from future storm attacks, the possibility of additional erosions due to SBs would make it hesitant to choose the plans by **Case 1** and **2** because it would be no remedy because the SBs would only switch the locations of erosion if the additional erosions were to occur at other unexpected nearshore locations. Although recommended, it is noted that **Case 3** is still not be a perfect protection plan

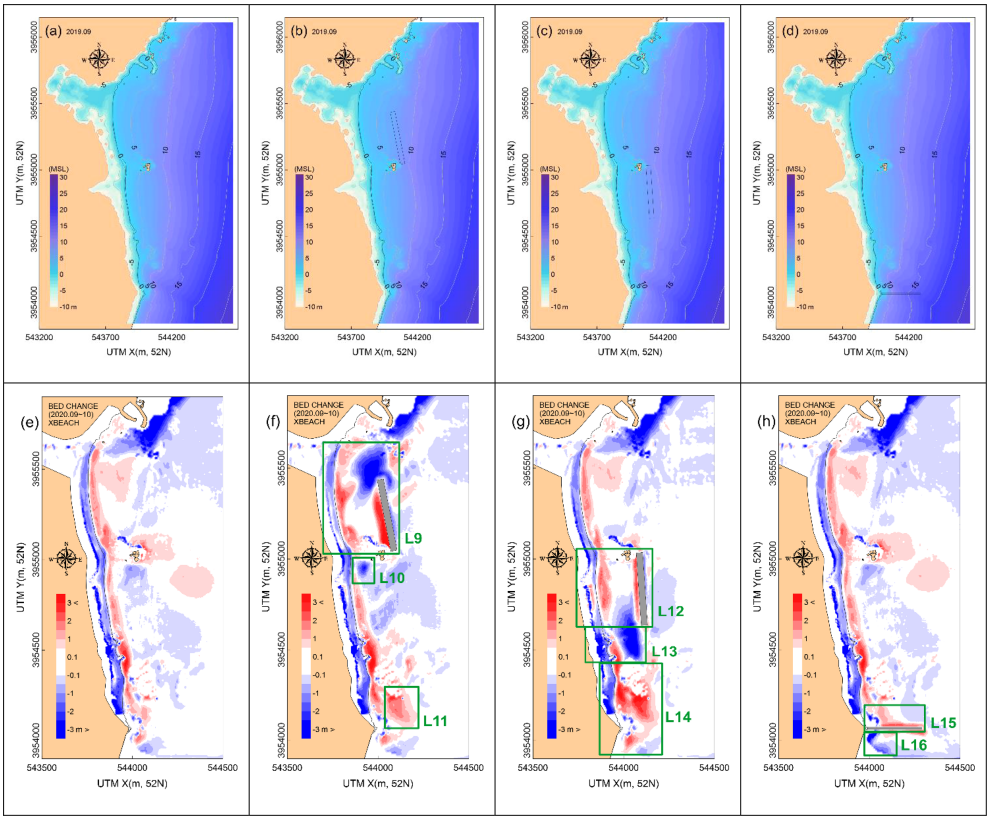

FIGURE 12 | Plan view of the test cases for simulation with coastal structures, **(A)** without structure, **(B)** with a submerged breakwater (SB) placed in front of the northern part of Bonggil Beach, **(C)** with a submerged breakwater (SB) placed in front of the southern part of the beach, **(D)** with a submerged groin (SG) placed in the southern end of the beach, and comparison of model results of morphological changes by XBeach surfbeat for the four different cases, **(E)** without structure, **(B)** with a SB placed in front of the northern part of Bonggil Beach, **(C)** with a SB placed in front of the southern part of the beach, **(D)** with a SG placed in the southern end of the beach. The model was run for 15 days from September 15 to October 3, 2019 that included the impacts of Typhoon Tapah and Mitag.

for the beach as it could still cause dune erosion in the southern part of the beach. Considering previous studies, hard structures might increase coastal variability and could worsen erosion (van Rijn, 2011; Do et al., 2021a). Therefore, measures that could conserve the equilibrium condition should be more desirable in preventing unexpected side effects.

5 DISCUSSION

The primary goal of the present study was to find out a measure to protect the beach by mitigating the erosional damage from future attacks of storm waves. For this, it was important to carefully analyze the causes of the erosional damages by the storm waves. One of the most significant observations in terms of the erosion during Typhoon Tapah and Mitag in 2019 was the discrepancy in the damage between the southern and northern parts of the beach as it was more severe in the southern part. As observed in the previous sections, the direct reason for this discrepancy was the difference in the water depths between both sides as the seabed was steeper in the nearshore area of the southern part. Due to the shoaling of the propagating waves, the wave energy dissipation was greater in the northern part, whereas more energy could be focused in the southern part, causing the severer damage. The reason for this difference in the bathymetry can be found in the characteristic pattern of geography in Bonggil Beach. The mouth of Daejong Stream was located in the northern part, and thus the sediment input through the stream was focused in this area (P2 in **Figure 1B**). In addition, the island, 'MunMu-daewang-neung', located in the middle of the beach (P3) and the salient in the lee area of P3 likely disturbed the movement of the input sediment to the southern part, which has resulted in the discrepancy in the bathymetry between the two parts. Besides the natural cause, there might be an anthropogenic factor as well that contributed to the bathymetry difference. As shown in **Figure 1B**, the artificial bank (P5) was built to protect the WNPP, which has deepened in the front area of P5 as shown in **Figure 7A**. Therefore, the sediments in the southern part would not return to this area if they were transported to the P5 area through P4, which was confirmed by the XBeach surfbeat simulations shown in L14, L15, and L16 of **Figure 13**. L14 shows that the sediments were transported to P5 through P4 during the

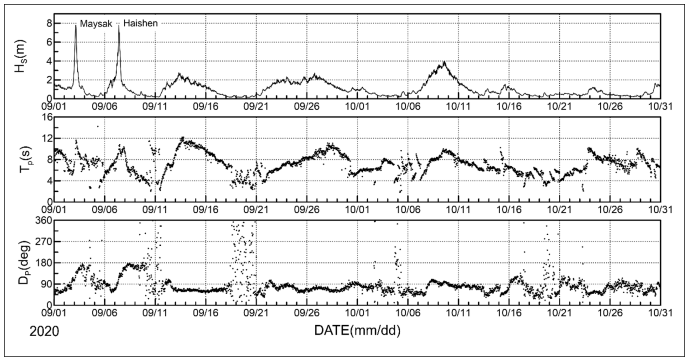

FIGURE 13 | Time series of significant wave height (H_s), peak wave period (T_p), and peak wave direction (D_p) for two months from September 1 to October 31, 2020, covering the times of Typhoons Maysak and Haishen, measured by the AWAC at A1. It is noted that Exp. 2 started on September 15, 2020, after these typhoon events.

storm attack which might not be recordable, and L15 and L16 indicates that the sediments were protected within the coastal cell with construction of the submerged groin.

As for the numerical model results, XBeach surfbeat simulated the pattern of erosion with reasonable agreement. In terms of the quantity, however, the model overestimated the degree of erosion in both experiments of Exp. 1 in 2019 and Exp. 2 in 2020. The reason for this has not been clearly understood yet. As described previously, the sediment input data might be correctly obtained as they were elaborately sampled at 72 locations inside/outside the water, which turned out that gravels were mixed with sand. XBeach model possibly had lower accuracy when the bottom was covered by the gravel of much larger size than sand (D50 = 0.44 mm sand and 2.34 mm for gravel). There have been numerous studies to run the XBeach model in the sandy beds so that the model could have been correctly tuned for sand. However, the studies for gravel beds was relatively rare as described in the introduction. Therefore, the model setup for gravel beds could show less accuracy. One of the ways to check this was to use 1-D XBeach-G model to apply in the gravel beach, similar to the previous researches by Jamal et al. (2014) & McCall et al. (2015), and to compare the results with observation data. In case the model performance becomes lower for the gravel beach, then the model setup could be tuned to increase the accuracy. Then, the new setup can be applied in Bongil Beach using the 2-D Xbeach surfbeat model, which is planned for a future study.

In addition to the understanding of the erosional process during the storm events, it is also necessary to compare the impacts of storm waves between different typhoon events so as to develop an effective measure considering the diversity of various storm conditions. For example, there was a discrepancy in the storm damages done by the typhoons in 2019 and 2020. As described in the previous sections, the damage in the study site was greater by the attacks of Tapah (and additionally by Mitag) in Exp. 1 of 2019 than that by the storm waves in Exp. 2 of 2020. Although the wave heights of the storm waves in Exp. 2 were lower than those in Exp.1, their durations were longer (**Figure 6**), which might be an important factor for nearshore morphological changes as well (Almar et al., 2010; Coco et al., 2014; Do et al., 2021b). For example, Almar et al. (2010) analyzed the data of a double-sandbar system in Truc Vert Beach, France. During their two-month observational period, four storms attacked the site. The pre-existing crescentic sandbar system was straightened and migrated offshore ~100 m by the severest second storm with maximum H_s of ~8 m. However, significant changes in the bar system also occurred during the longest fourth storm of ~10 day duration and H_s of 2 – 4 m as the bar developed crescentic pattern and migrated ~200 m southward. Similarly, Coco et al. (2014) suggested that the duration of consistently large waves and their effect on beach morphodynamics made the event comparable to an extreme storm. In addition, Do et al. (2021b) observed that a crescent sandbar system was fully developed from a straight sandbar system, during the longer second storm of ~6 day duration and maximum H_s of ~4 m, rather than during the stronger first storm of ~2 day duration and maximum H_s of ~5 m, which indicates that the duration of storm waves might play role in changing nearshore seabed morphology. Although direct comparison was not possible, the longer storm durations in Exp.2 than Exp. 1 could provide a favorable condition for additional erosion in Bonggil Beach but it did not occur, which will be further discussed later in this section.

It is also noted that two typhoons (Typhoon Mysak and Heishen) consecutively attacked the site just before the period of Exp. 2 (Mysak on September 3, 2020; Heishen on September 8, 2020). Considering that both Mysak and Heishen were Category 4 storms (Tapah and Mitag were Category 1 and 2 storms, respectively), the impacts by Mysak and Heishen would have been significant as their H_s measured in A1 was greater than that by Tapah (**Figure 13**). In addition, a favorable condition to morphological change was also observed under a series of storm events (Vousdoukas et al., 2012; Morales-Márquez et al, 2018; Rutten et al, 2018), which corresponds to the case of Mysak and Heishen. However, the erosional damage during Exp. 2 was much less than that during Exp. 1, and the significant discrepancy in the erosional damage between Exp. 1 and Exp. 2 was still unexpected, and additional investigation might be necessary.

One of the other factors to consider was the wave propagation direction. Although the amount of total sediment transport

depends on the wave power that is contributed by the wave height and period (Oh et al., 2021), the ratio between the cross-shore and longshore transport may be related to the wave direction, and it can result in the locality of erosional process, especially in the beaches with complex geography such as Bonggil Beach. The results in **Figure 4** show that the waves were approaching the shore in E direction (~82°) consistently for ~3 days during Tapah. In contrast, the wave propagation direction rapidly changed from ENE (60°) to SE (140°) during the course of both Mysak and Heishen. Therefore, the consistency of the wave direction during the storm event might be important in causing the coastal erosion, which requires further analysis in future studies.

Another factor that may contribute to the discrepancy between 2019 and 2020 events is the resilience of the beach for recovery. As described in the introduction, it is a natural process that beaches would be recovered after erosion due to onshore sediment motions under mild wave conditions (Hsu and Hanes, 2004). This recovery process usually took a longer time than the erosional process that occurred within a short-time scale in days during the attack of storm waves, as observed in this study. Previous studies suggested that the temporal scale of the recovery process was various from days to years or even to decades. The factors that affected the recovery process could be coastal morphology, wave energy, shoreline orientation, nearshore circulation, and local sediment supply. For example, individual large storms could cause local rapid erosion from which recovery might take years or even decades if the impacts were large but sand supply after that was not sufficient (Forbes et al., 2004). As for other cases, the recovery process could take months with slower paces of the recovery than the erosion. Vousdoukas et al. (2012) observed that sub-aerial beach volume reduction was up to 30 m^3/mon in steep-sloping beaches whereas the following recovery of the intertidal area was reaching ~10 m^3/mon. Morales-Márquez et al. (2018) found out that a group of storm waves generated significant erosion in three days but only half of the sediment was recovered during the next two months. In contrast, Ranasinghe et al. (2012) analyzed video monitoring data and wave measurements to quantify the nearshore morphological recovery time scale, T_{mr} and observed that T_{mr} could be as short as 5 days in Duck in North Carolina, United States. This result showed that the wave conditions and longshore current developed after the storms could be important indicators for T_{mr} In addition to the hydrodynamic conditions, the antecedent morphological condition could be a crucial factor for the recovery process as the beach might respond quite differently to the same hydrodynamic input conditions, depending on the morphodynamic status. For example, storm attack on susceptible beach could lead to catastrophic breakdown that might not be reversible or require long time for recovery (Forbes et al., 1995). Morales-Márquez et al. (2018) observed that, when a sequence of storms affiliated the beach, the storms developed later could hardly affect the morphology although their intensity was similar to the former ones that caused damages, confirming that the antecedent morphological condition might be crucial for the response of the beach. The antecedent condition could be also applied in the Bonggil Beach when Typhoon Mysak and Heishen attacked the site in 2020. The severe damage by Typhoon Tapah in 2019 might not be recovered and the morphological condition in the beach was not favored for additional erosion when the two severe typhoons affiliated the site again in ~1 year later. The temporal scale of the recovery process has not been estimated in Bonggil Beach yet. However, a similar observation was made in Yeongildae Beach that is located ~35 km north of Bonggil Beach (Oh et al., 2021), in which it took ~1.5 yrs for the shoreline of the beach to be recovered back to the level before the time of Typhoon Tapah's attack. Considering that Yeongildae Beach is located inside a bay, and thus the damage by Tapah was smaller than that in Bonggil Beach, it is likely that Bonggil Beach was still in the recovery process when Typhoon Mysak and Heishen affiliated the site in 2020, which was also clear from the profile measurement in **Figure 5B**. Therefore, the less erosional damage during the attack of Mysak and Heishen was likely because the beach was still in the recovery process, and the antecedent morphological condition was not favorable for additional erosions at the time of 2020 typhoons.

In designing the long-term mitigation/adaptation plans from extreme storm impacts in the study area, it is important to carefully consider the post-event recovery processes in order to reduce unexpected/unwanted side effects that might be caused by the implementation of the plan. The decision from the simulation results in Section 4.3 were based on such consideration. Out of the three cases, **Case 3** that planed the SG to conserve the sediments within the coastal cell was suggested for a preferred measure whereas **Case 1 and 2** that planned SBs were not suggested due to the predicted additional erosions in the unexpected nearshore locations. Because the hard stabilization structures of SBs would not only reduce the wave energy but they also directly block the cross-shore sediment motions, they could also disturb the post-event recovery process by blocking the onshore sediment movement under milder wave conditions. In addition, such plans can be designed more economically if both destructive (erosion by storms) and constructive (post-event recovery) processes are considered, than those that only consider the destructive process. For example, the plan by **Case 3** could also be economical when comparing the initial costs that were required in constructing the coastal structures. For example, the cost to construct the SG by **Case 3** would be cheaper than those to construct the SBs by **Case 1 and 2** because the SG would not need to be built high above the seabed, whereas the SBs should be high and wide to effectively reduce the wave energy. The plan by **Case 3** could be also economical because the sediments were conserved in the nearshore area without losing them from the littoral cell and they could be replenished back to the eroded area. However, the outcome of this study suggests that the considerations on the mitigation/adaptation from storm impacts should be confined in the study area. One of its reasons is that the resilience of post-storm recovery could be site-specific, as previously discussed, even under similar hydrodynamic and wave conditions, thus studies are required to be carefully conducted for specific site in developing mitigation/adaptation plans from storms.

One of the examples of such studies was done for Miami-Dade County, United States (Klima et al., 2012). In this research paper, hurricane adaptation plans to reduce damages from the attack of

tropical cyclones were developed by calculating surge height and wind speed as a function of return period and by estimating costs and economic losses using a damage model, for five areas along the county's coastline. In particular, the study noted that the five areas would have different susceptibilities even to same hurricane due to different bathymetry/topography and infrastructure. Therefore, the plans were developed site-specifically for each area by suggesting, for example, a surge barrier as the best method to reduce storm surge damage in one area but suggesting the best method to be varied with return period in another area. This result corresponded to the suggestion in the present study that such adaptation plan should be considered specifically for different site. In Bonggil Beach, a coastal management project was planned by the local government before the severe erosion damages by Typhoon Tapah occurred in 2019. According to this plan, a SB was designed to be placed in the northern part of the beach's nearshore, similar to the second plan (Case 2) shown in **Figure 12B**, to protect the commercial places located behind the northern part. Once Tapah affiliated the beach, however, the plan might require modification to consider beach conservation/adaptation from storm attacks. The results of the present study were then provided to suggest a design of engineering structure for future conservation specified in Bonggil Beach, considering the beach's characteristic pattern.

6 CONCLUSION

In the present study, field observations and numerical model experiments were carried out to analyse the severe erosion in the beachface of Bonggil Beach during the attack of Typhoon Tapah in September 2019. The models were validated with a reasonable agreement with observational data. Telemac-2D showed good performance in generating the wave conditions during both of the 2019 (Exp. 1) and 2020 (Exp. 2) experimental period. When comparing the Telemac-2D and XBeach surfbeat, XBeach showed better performance because the measured current data were more accurately generated by Xbeach surfbeat than Telemac-2D. The morphological changes simulated by the XBeach surfbeat for Exp. 2 were also agreed with the bathymetry measurements in general. However, the model overestimated the degree of erosion because the amount of modeled sediments that were eroded from the beachface was greater than that measured from field observation. The reason was likely due to the complicated sediment characteristics as the sediment in Bonggil Beach was a mixture of sand and gravel. To implement the impact of this sediment mixture in the model, the sand and model fraction of the erodible sediment part was elabolately determined based on the sediment samples obtained at 72 locations along the beachface and inside the water in the nearshore. However, the existence of gravel whose size (1.34 mm) was much larger than that of sand (0.44 mm), which might increase the simulation error. Considering that the gravels would be more stable in starting initial motion but more active once started the bedload motions, the errors in the sand/gravel fraction in the model setup might lead to the wrong estimation of the amount of eroded/deposited sediments, although the pattern their distribution was successfully simulated by the model.

The application of the XBeach surfbeat for the Typhoon Tapah event for Exp. 1 also resulted in general agreement of the sediment transport pattern even though the model also overestimated the degree of erosion along the beachface. In particular, the locality of the erosional pattern, the severe dune erosion in the southern part, was successfully simulated by the model. The locality was caused because the slope of the water depth was steeper in the southern part, which likely kept the propagating wave energy higher when reaching the shore during the attack of Typhoon Tapah. In Bonggil Beach, the sediments were input to the coastal cell from a stream connected to the northern end of the beach. However, the input sediments could have hardly reached the southern part due to the blocking of the island, 'MunMu-daewang-neung', located in the middle of the beach. In addition, the sediments in the southern part could not return to the coastal cell once they crossed the southern boundary of the beach. It was because the water depth outside the boundary was deepened due to the construction of the bank in front of a nuclear power plant. Due to the combined effect of natural and anthropogenic causes, the nearshore of the southern part of the beach has been kept deeper than that in the northern part, causing the locality in the erosional damage.

Additional simulations with three cases of engineering measures were performed in order to find out an effective measure in protecting/conserving the beach from future attacks of similar storm waves – construction of a submerged breakwater (SB) in front of the northern part of the beach; construction of a SB in the southern part; and construction of a submerged groin (SG) at the southern end of the beach to prevent the loss of sediments from the coastal cell. It turned out that, out of the three measures, the use of SG was most effective in conserving the beach because the two measures with SB might cause the side effect of additional erosions at unexpected seabed locations even though they were useful for directly protecting the shore in the lee side of the SBs. Although the direct impact of dune erosion could not be avoided, the SG would be an environmentally friendly measure with reduced side effects, and by keeping the sediments within the coastal cell around the SG that could be used for future replenishment, even though sediments could be conserved by the SG on specific situations, mainly depending on the wave directions that caused longshore sediment drift. In addition, the construction of SG might require less initial construction cost than SBs because the SG did not necessarily high above the seabed by only capturing the bedload sediments. Considering that the SBs could prevent the long-term recovery process of the onshore sediment motions under milder wave conditions, the measure with the SG was also recommended as it allowed the natural recovery although it was still not a perfect measure in protecting the beach from dune erosion.

One of the restrictions of this study was that its outcomes were site-specific and might not be applied in other areas. However, this study focused the importance of the locality in establishing storm adaptation plans, in even within the same area of the littoral cell. Due to the climate change and the subsequent sea-level rise or the possiblility of increasing storm intensity, it is essential to prepare for long-term adaptaion plans in many coatal regions globally. The result of this study noted that these plans should

consider the characteristic patterns of the site that might include the bathymetry, topography, wave climae, and the resilience of the site for post-storm recovery process. For this, preliminary researches are required to be carefully conducted for the sites of interest, considering their values.

DATA AVAILABILITY STATEMENT

The raw data supporting the conclusions of this article will be made available by the authors, without undue reservation.

AUTHOR CONTRIBUTIONS

JDD, J-YJ, WMJ and Y C contributed to conception and design of the study. JDD, BL, JYC, SKH and KK organized the database. JDD, BL, JYC, SKH and KK performed the statistical analysis. JDD and YC wrote the manuscript. All authors contributed to manuscript revision, read, and approved the submitted version.

FUNDING

This work was supported by the Korea Institute of Ocean Science and Technology [grant number PEA0031], and the Ministry of Oceans and Fisheries [grant number PM62850].

SUPPLEMENTARY MATERIAL

The Supplementary Material for this article can be found online at: https://www.frontiersin.org/articles/10.3389/fmars.2022.825359/full#supplementary-material

Supplementary Table 1 | Information on the sediment samples (sampling location, sediment size and type).

Supplementary Table 2 | Information on the wind and wave parameters during Exp.1. The data measured during the period of Typhoon Tapah are highlighted (21 - 24 September, 2019).

REFERENCES

Almar, R., Castelle, B., Ruessink, B., Sénéchal, N., Bonneton, P. and Marieu, V. (2010). Two-And Three-Dimensional Double-Sandbar System Behaviour Under Intense Wave Forcing and a Meso–Macro Tidal Range. *Continental. Shelf. Res.* 30, 781–792. doi: 10.1016/j.csr.2010.02.001

Anthony, E. J., Brunier, G., Besset, M., Goichot, M., Dussouillez, P. and Nguyen, V. L. (2015). Linking Rapid Erosion of the Mekong River Delta to Human Activities. *Sci. Rep.* 5, 1–12. doi: 10.1038/srep14745

Asaro, G. and Paris, E. (2000). The Effects Induced by a New Embankment at the Confluence Between Two Rivers: TELEMAC Results Compared With a Physical Model. *Hydrological. Processes.* 14, 2345–2353. doi: 10.1002/1099-1085(200009)14:13<2345::AID-HYP33>3.0.CO;2-X

Bender, M. A., Knutson, T. R., Tuleya, R. E., Sirutis, J. J., Vecchi, G. A., Garner, S. T., et al. (2010). Modeled Impact of Anthropogenic Warming on the Frequency of Intense Atlantic Hurricanes. *Science* 327, 454–458. doi: 10.1126/science.1180568

Bergillos, R. J., Masselink, G., Mccall, R. T. and Ortega-Sánchez, M. (2016). Modelling Overwash Vulnerability Along Mixed Sand-Gravel Coasts With XBeach-G: Case Study of Playa Granada, Southern Spain. *Coast. Eng. Proc.* 1, 13. doi: 10.9753/icce.v35.sediment.13

Berkhoff, J. (1973). "Computation of Combined Refraction—Diffraction," in *13th International Conference on Coastal Engineering 1972.)*, Vancouver, Canada, 471–490. doi: 10.1061/9780872620490.027

Coco, G., Senechal, N., Rejas, A., Bryan, K. R., Capo, S., Parisot, J., et al. (2014). Beach Response to a Sequence of Extreme Storms. *Geomorphology* 204, 493–501. doi: 10.1016/j.geomorph.2013.08.028

Davidson-Arnott, R., Bauer, B. and Houser, C. (2019). *Introduction to Coastal Processes and Geomorphology* (Cambridge University Press).

Do, J. D., Jin, J.-Y., Hyun, S. K., Jeong, W. M. and Chang, Y. S. (2020). Numerical Investigation of the Effect of Wave Diffraction on Beach Erosion/Accretion at the Gangneung Harbor, Korea. *J. Hydro-environment. Res.* 29, 31–44. doi: 10.1016/j.jher.2019.11.003

Do, J. D., Jin, J. Y., Jeong, W. M. and Chang, Y. S. (2019). Observation of Rapid Seabed Erosion Near Closure Depth During a Storm Period at Hujeong Beach, South Korea. *Geophysical. Res. Lett.* 46, 9804–9812. doi: 10.1029/2019GL083910

Do, J. D., Jin, J.-Y., Jeong, W. M., Lee, B., Choi, J. Y. and Chang, Y. S. (2021a). Collapse of a Coastal Revetment Due to the Combined Effect of Anthropogenic and Natural Disturbances. *Sustainability* 13, 3712. doi: 10.3390/su13073712

Do, J. D., Jin, J.-Y., Jeong, W. M., Lee, B., Kim, C. H. and Chang, Y. S. (2021b). Observation of Nearshore Crescentic Sandbar Formation During Storm Wave Conditions Using Satellite Images and Video Monitoring Data. *Mar. Geology.* 442, 106661. doi: 10.1016/j.margeo.2021.106661

Forbes, D., Orford, J., Carter, R., Shaw, J. and Jennings, S. (1995). Morphodynamic Evolution, Self-Organisation, and Instability of Coarse-Clastic Barriers on Paraglacial Coasts. *Mar. Geology.* 126, 63–85. doi: 10.1016/0025-3227(95)00066-8

Forbes, D. L., Parkes, G. S., Manson, G. K. and Ketch, L. A. (2004). Storms and Shoreline Retreat in the Southern Gulf of St. Lawrence. *Mar. Geology.* 210, 169–204. doi: 10.1016/j.margeo.2004.05.009

Galland, J.-C., Goutal, N. and Hervouet, J.-M. (1991). TELEMAC: A New Numerical Model for Solving Shallow Water Equations. *Adv. Water Resour.* 14, 138–148. doi: 10.1016/0309-1708(91)90006-A

Gurov, K. and Fomin, V. (2021). Mathematical Modeling the Dynamics of the Bottom Sediments Granulometric Composition in the Balaklava Bay Affected by the Wind Waves. *Phys. Oceanography.* 28, 78–89. doi: 10.22449/1573-160X-2021-1-78-89

Harter, C. and Figlus, J. (2017). Numerical Modeling of the Morphodynamic Response of a Low-Lying Barrier Island Beach and Foredune System Inundated During Hurricane Ike Using XBeach and CSHORE. *Coast. Eng.* 120, 64–74. doi: 10.1016/j.coastaleng.2016.11.005

Hervouet, J. M. (2000). A High Resolution 2-D Dam-Break Model Using Parallelization. *Hydrological. processes.* 14, 2211–2230. doi: 10.1002/1099-1085(200009)14:13<2211::AID-HYP24>3.0.CO;2-8

Holthuijsen, L., Herman, A. and Booij, N. (2003). Phase-Decoupled Refraction–Diffraction for Spectral Wave Models. *Coast. Eng.* 49, 291–305. doi: 10.1016/S0378-3839(03)00065-6

Hsu, T. J. and Hanes, D. M. (2004). Effects of Wave Shape on Sheet Flow Sediment Transport. *J. Geophysical. Research-Oceans.* 109. doi: 10.1029/2003JC002075

Jamal, M., Simmonds, D. and Magar, V. (2014). Modelling Gravel Beach Dynamics With XBeach. *Coast. Eng.* 89, 20–29. doi: 10.1016/j.coastaleng.2014.03.006

Klima, K., Lin, N., Emanuel, K., Morgan, M. G. and Grossmann, I. (2012). Hurricane Modification and Adaptation in Miami-Dade County, Florida. *Environ. Sci. Technol.* 46, 636–642. doi: 10.1021/es202640p

Knutson, T. R., Mcbride, J. L., Chan, J., Emanuel, K., Holland, G., Landsea, C., et al. (2010). Tropical Cyclones and Climate Change. *Nat. Geosci.* 3, 157–163. doi: 10.1038/ngeo779

Masselink, G. and Russell, P. (2013). Impacts of Climate Change on Coastal Erosion. *MCCIP. Sci. Rev.* 2013, 71–86. doi:10.14465/2013.arc09.071-086

McCall, R., Masselink, G., Poate, T., Roelvink, J. and Almeida, L. (2015). Modelling the Morphodynamics of Gravel Beaches During Storms With XBeach-G. *Coast. Eng.* 103, 52–66. doi: 10.1016/j.coastaleng.2015.06.002

Mentaschi, L., Vousdoukas, M. I., Pekel, J.-F., Voukouvalas, E. and Feyen, L. (2018). Global Long-Term Observations of Coastal Erosion and Accretion. *Sci. Rep.* 8, 1–11. doi: 10.1038/s41598-018-30904-w

Morales-Márquez, V., Orfila, A., Simarro, G., Gómez-Pujol, L., Ãlvarez-Ellacuría, A., Conti, D., et al. (2018). Numerical and Remote Techniques for Operational Beach Management Under Storm Group Forcing. *Natural Hazards. Earth System. Sci.* 18, 3211–3223. doi: 10.5194/nhess-18-3211-2018

Oh, J.-E., Jeong, W.-M., Ryu, K.-H., Park, J.-Y. and Chang, Y.-S. (2021). Monitoring of Recovery Process at Yeongildae Beach, South Korea, Using a Video System. *Appl. Sci.* 11, 10195. doi: 10.3390/app112110195

Phillips, B. T., Brown, J. M. and Plater, A. J. (2020). Modeling Impact of Intertidal Foreshore Evolution on Gravel Barrier Erosion and Wave Runup With Xbeach-X. *J. Mar. Sci. Eng.* 8, 914. doi: 10.3390/jmse8110914

Ranasinghe, R., Holman, R., De Schipper, M., Lippmann, T., Wehof, J., Duong, T. M., et al (2012). "Quantifying Nearshore Morphological Recovery Time Scales Using Argus Video Imaging: Palm Beach, Sydney and Duck, North Carolina," in ICCE 2012: Proceedings of the 33rd International Conference on Coastal Engineering, Santander, Spain, Coastal Engineering Research Council, 1–6 July 2012.

Robins, P. and Davies, A. (2011). "Application of TELEMAC-2D and SISYPHE to Complex Estuarine Regions to Inform Future Management Decisions," in Proceedings of the XVIIIth Telemac & Mascaret User Club 2011, EDF R&D, Chatou, 19-21 October 2011. 86–91.

Roelvink, D., Reniers, A., Van Dongeren, A., De Vries, J. V. T., Mccall, R. and Lescinski, J. (2009). Modelling Storm Impacts on Beaches, Dunes and Barrier Islands. *Coast. Eng.* 56, 1133–1152. doi: 10.1016/j.coastaleng.2009.08.006

Roelvink, J. and Van Banning, G. (1995). Design and Development of DELFT3D and Application to Coastal Morphodynamics. *Oceanographic. Literature. Rev.* 11, 925.

Russell, P. E. (1993). Mechanisms for Beach Erosion During Storms. *Continental. Shelf. Res.* 13, 1243–1265. doi: 10.1016/0278-4343(93)90051-X

Rutten, J., Ruessink, B. and Price, T. (2018). Observations on Sandbar Behavior Along a Man-Made Curved Coast. Earth Surf. *Process. Landf.* 43, 134–149. doi: 10.1002/esp.4158

Syvitski, J. P., Vörösmarty, C. J., Kettner, A. J. and Green, P. (2005). Impact of Humans on the Flux of Terrestrial Sediment to the Global Coastal Ocean. *science* 308, 376–380. doi: 10.1126/science.1109454

Van Geer, P., Den Bieman, J., Hoonhout, B. and Boers, M. (2015). XBeach 1d–Probabilistic Model: ADIS, Settings, Model Uncertainty and Graphical User Interface. *Tec. Rep.* 1209436.

van Rijn, L. C. (2011). Coastal Erosion and Control. *Ocean. Coast. Manage.* 54, 867–887. doi: 10.1016/j.ocecoaman.2011.05.004

Vousdoukas, M. I., Almeida, L. P. M. and Ferreira, Õ. (2012). Beach Erosion and Recovery During Consecutive Storms at a Steep-Sloping, Meso-Tidal Beach. *Earth Surface. Processes. Landforms.* 37, 583–593. doi: 10.1002/esp.2264

Wong, A. (2016). *Wave Hydrodynamics in Ports: Numerical Model Assessment of XBeach*. MSc Thesis, Delft University of Technology (repository.tudelft.nl).

Zhang, K., Douglas, B. C. and Leatherman, S. P. (2004). Global Warming and Coastal Erosion. *Climatic. Change* 64, 41–58. doi: 10.1023/B:CLIM.0000024690.32682.48

Conflict of Interest : Author SH is employed by Sekwang Engineering Consultants Company Limited, and author KK is employed by GeoSystem Research Corporation.The remaining authors declare that the research was conducted in the absence of any commercial or financial relationships that could be construed as a potential conflict of interest.

frontiers | Frontiers in Marine Science

TYPE Original Research
PUBLISHED 23 September 2022
DOI 10.3389/fmars.2022.889820

OPEN ACCESS

EDITED BY
Felice D'Alessandro,
University of Milan, Italy

REVIEWED BY
Robert V. Rohli,
Louisiana State University,
United States
Patrick Biber,
University of Southern Mississippi,
United States

*CORRESPONDENCE
Ernesto Tonatiuh Mendoza
ernesto.tonatiuh@univ-rouen.fr

SPECIALTY SECTION
This article was submitted to Coastal Ocean Processes, a section of the journal Frontiers in Marine Science

RECEIVED 04 March 2022
ACCEPTED 08 September 2022
PUBLISHED 23 September 2022

CITATION
Mendoza ET, Torres-Freyermuth A, Ojeda E, Medellín G, Rioja-Nieto R, Salles P and Turki I (2022) Seasonal changes in beach resilience along an urbanized barrier island. *Front. Mar. Sci.* 9:889820. doi: 10.3389/fmars.2022.889820

Seasonal changes in beach resilience along an urbanized barrier island

Ernesto Tonatiuh Mendoza[1*], Alec Torres-Freyermuth[2,3], Elena Ojeda[4], Gabriela Medellín[2,3], Rodolfo Rioja-Nieto[5,6], Paulo Salles[2,3] and Imen Turki[1]

[1]Univ Rouen Normandie, Univ Caen Normandie, CNRS, M2C, UMR 6143, Rouen, France, [2]Laboratorio de Ingeniería y Procesos Costeros, Instituto de Ingeniería, Universidad Nacional Autónoma de México, Sisal, Mexico, [3]Laboratorio Nacional de Resiliencia Costera (LANRESC), Laboratorios Nacionales CONACYT, Sisal, Mexico, [4]Univ Caen Normandie, Univ Rouen Normandie, CNRS, M2C, UMR 6143, Caen, France, [5]Escuela Nacional Estudio Superiores, Universidad Nacional Autónoma de México, Mérida, Mexico, [6]Laboratorio de Análisis Espacial de Zonas Costeras (COSTALAB), Unidad Multidisciplinaria de Docencia e Investigación-Sisal, Facultad de Ciencias, Universidad Nacional Autónoma de México, Sierra Papacal, Mexico

Beach width, dune height, and vegetation coverage are key parameters to assess beach resistance and resilience to storms. However, coastal development often causes beach ecosystem degradation due to poor coastal management. We propose a Coastal Resilience Index from Remote Sensors (CRIfRS) for urbanized coasts based on aerial photogrammetry. The study area, located along a 7.8 km stretch of coast on a barrier island, is characterized by persistent alongshore sediment transport and the presence of coastal structures and beach-front houses. Contrary to previous studies, we focus on anthropogenic perturbations (coastal urbanization and coastal structures), instead of hydrodynamic conditions (storms), since erosion in this region is mainly associated with alongshore sediment transport gradients induced by coastal structures. Thus, the CRIfRS is based on the relation of three indicators that affect the beach functionality for coastal protection: beach width, coastal structure influence area, and vegetation coverage. The CRIfRS was divided into five categories: Very Low resilience (VL), Low resilience (L), Medium resilience (M), High resilience (H), and Very High resilience (VH). The CRIfRS presented an important spatial and temporal variability due to changing environmental conditions and the deployment of new coastal structures. For the study period, the percentage of the coast within the VL and L resilience classification increased, whereas the percentage of the coast classified as M, H, and VH resilience decreased. During the winter storm season, the resilience increased mainly due to the cross-shore transport whilst during mean wave conditions (i.e., sea-breeze conditions) the long-shore transport becomes more persistent and thus the coastal structures play an important role interrupting the sediment flux. Additionally, the CRIfRS trajectory shows an overall increase of the L resilience and an overall decrease of the H resilience values. This study highlights the important role of anthropogenic perturbations on the assessment of coastal resilience for highly urbanized coasts. The CRIfRS

can help to improve the coastal management by assessing the coastal protection capability of beaches considering both natural and anthropogenic factors.

KEYWORDS

Beach resilience, UAVs flights, coastal structures, beach width, coastal vegetation

Introduction

Barrier islands are highly dynamic and are constantly modified due to different forcing agents (Kombiadou et al., 2019; Velasquez-Montoya et al., 2021). During low energy season, the beach width and dune volume increase and during high energy season or extreme events the vegetated sand dunes act as natural barriers (Aubrey, 1979; Feagin et al., 2019). Although the barriers can erode to some extent, they prevent further erosion of the coast. This cycle is affected by human action when infrastructure is built, without the proper knowledge of sediment transport dynamics, on top of the sand dunes or in the nearshore to try to mitigate chronic erosion, disregarding the natural beach cycle (Jiménez et al., 2011). Furthermore, this natural cycle will be affected in future scenarios with increasing storm activity (Emanuel, 2005; Ojeda et al., 2017) and sea level rise (Warrick et al., 1990; Devoy, 2021) associated with climate change. This is particularly important on barrier islands (Irish et al., 2010).

The northern Yucatan coast is fronted with a series of low-lying barrier islands which historically have supported small communities until the settlement of the town of Progreso, the main Yucatan port, and its subsequent train connection in 1881 (Meyer-Arendt, 2001). By the mid-1900s the construction of a road boomed the establishment of housing along the coastal fringe and by 1940 a major port had been finished, causing some erosion on its downdrift side. Beach house construction often removed the primary dune and vegetation. In the late 60s and early 70s a series of shelter harbors (small ports mainly used for minor vessels) were built along the Northern Yucatan coast, resulting in an accelerated erosion on the down-drift side of each port (Franklin et al., 2021). As a result, a series of uncontrolled strategies have been implemented to this day, which range from private homeowners illegally building rock and-timber groins -locally known as espolones or escolleras- (Tereszkiewicz et al., 2018) to government plans that include the construction and the removal of structures (Medellín et al., 2015) and the deployment of geotextile tubes filled with sand near the shoreline (Torres-Freyermuth et al., 2019). Assessments of coastal vulnerability of the Yucatan coast based on beach-dune characteristics and coastal hazards (erosion and flooding) have been addressed in previous studies (Mendoza et al., 2013; Cuevas-Jiménez et al., 2016; Mendoza et al., 2016). These studies represent the beach conditions for a given time and hence do not capture the seasonal variability. Moreover, neither of these studies considered the important role that coastal structures have on controlling shoreline stability.

In 2017 the Yucatan government deployed two detached breakwaters made of geotextiles filled with sand as a mitigation measure against beach erosion. High-resolution Real Time Kinematics Differential Global Positioning System (RTK-DGPS) beach surveys were conducted in the vicinity of these coastal structures, revealing a significant negative downdrift effect (Torres-Freyermuth et al., 2019). Moreover, this beach erosion triggered illegally built structures in downdrift areas. The latter implies that the coastal landscape is continuously changing due to human interventions and hence the beach monitoring using traditional RTK-GPS is insufficient. Recent studies have evaluated the use of Unmanned Aerial Vehicles (UAVs) in coastal monitoring (Gonçalves and Henriques, 2015; Turner et al., 2016; Clark, 2017; Franklin et al., 2021). Among other advantages are the low cost of operation and the extent of the surveyed area. Furthermore, UAVs permit the simultaneous collection of additional information regarding urban expansion, vegetation coverage, and the presence of coastal structures. Despite numerous interventions, few studies in this area allow quantitative evaluation of the beach resilience i.e., its capacity to cope with disturbances induced by factors such as extreme events or human impacts, by adapting whilst maintaining their essential functions (Masselink and Lazarus, 2019).

Resilience has an extensive variety of definitions and uses. However, most definitions concur that resilience is the capability of a system to absorb, recover, and adapt to an external perturbation (Zodrow et al., 2020). The term was originally coined in engineering and further developed in ecology (Masselink and Lazarus, 2019). Its use in coastal sciences is more recent and has been mostly based on the physical response of beaches to natural (e.g., storms) and anthropogenic (e.g. coastal structures) disturbances like extreme wave conditions (Angnuureng et al., 2017; Medellín et al., 2018). Dong et al. (2018) proposed the use of beach and dune morphometrics and storm hazards (flooding and erosion)

to obtain a Coastal Resilience Index (CRI). This methodology was employed in this region by Torres-Freyermuth et al. (2021) to investigate beach resilience of a 2-km stretch of coast using high-resolution beach profiles and numerical modelling results finding the important role of coastal structures on controlling beach resilience in this region. However, in this study we focus on the beach resilience due to anthropogenic perturbations (i.e., urbanization and coastal structures). The beach system plays a key function as a protection agent and a key element of the beach system is the beach width. In the case of urbanized coastal systems, it is unlikely to start with a non-perturbed case and hence coastal resilience can be assessed by analyzing the spatial and temporal evolution. Thus, to determine the resilience of a coastal system, it is required to have knowledge about the evolution of their key indicators over time. The trajectory describes the temporal changes in response to (natural and anthropogenic) perturbations of the resilience index. Piégay et al. (2020) propose a classification of the trajectories in terms of the equilibrium state (i.e., static equilibrium, dynamic equilibrium, meta-static dynamic equilibrium). The trajectory of a system is a key element that allow us to analyze and describe the capability to resist, adapt, and recover from a given perturbation. Hence, a more frequent assessment of the beach state allows us to capture the beach response to shocks occurring at different temporal scales and hence a better understanding of beach resilience.

In this work, we used UAV-derived data to survey the location and number of structures, the beach width, and the presence of vegetation along a 7.8 km stretch of coast during a fourteen-month period (six surveys from October 2016 to December 2017). The aim of this work is to develop indicators related to these three parameters and employ them to derive a Coastal Resilience Index from Remote Sensors (CRIfRS) applied to the study area and characterize its temporal evolution during the study period. The outline of this paper is the following. First, the study area is described in Section 2. The beach monitoring program conducted at the study site, the characteristics of the different coastal indicators, and the integration of the index are described in Section 3. The results of the spatio-temporal variability are presented in Section 4. A discussion on the CRIfRS is included in Section 5 followed by the concluding remarks in Section 6.

Study area

The study area is located on a barrier island in the northern Yucatan Peninsula, Mexico (Figure 1). The beach is composed of carbonaceus medium sand (0.3 mm) backed by a low sandy

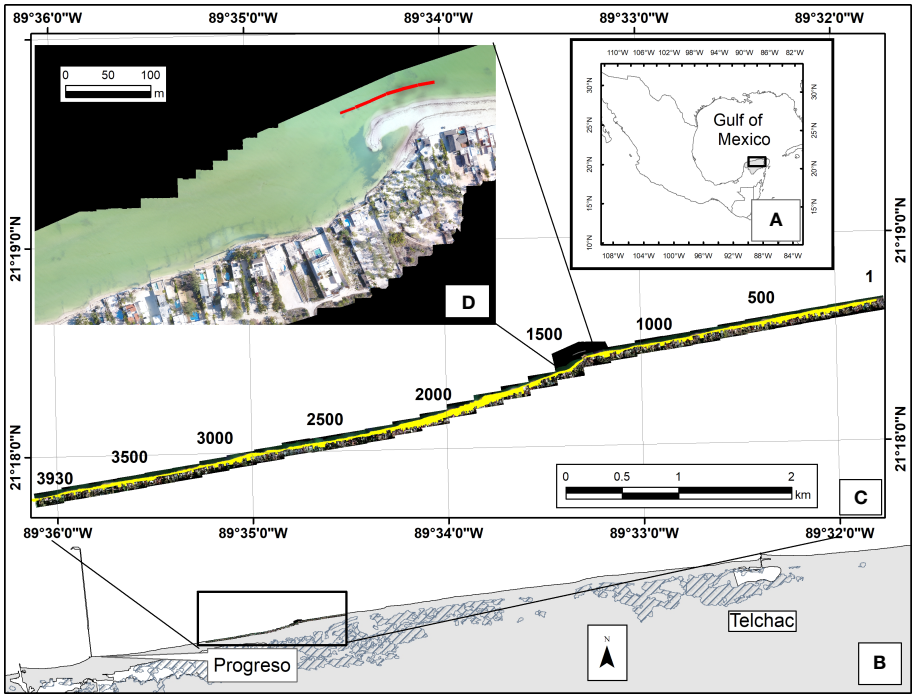

FIGURE 1
Study area location: **(A)** the beach stretch placed in the northern Yucatan Peninsula in the Gulf of Mexico; **(B)** between the ports of Progreso and Telchac. **(C)** the 7.8 km stretch was divided into 2-m transects numbered from east to west totaling 3930 transects. **(D)** detail of the Punta San Miguel with coastal structures (groins and geo textiles), infrastructure in the back part of the beach and vegetation coverage. The red line denotes the 120-m long low-crested detached breakwater made of geo textile tubes filled with sand.

dune in some sectors, often highly degraded due to human interventions and to the presence of beach houses along the coast. The study was conducted along a 7.8-kilometer stretch of highly urbanized coast located in the Progreso area (21° 09′ 56.20′′ N, 90° 02′′ 26.44′′ W; 807320 m E, 2343344 m N, UTM Zone 16 N coordinate system). The coast is characterized by a diurnal micro-tidal regime with a 0.75 m spring tidal range (Valle-Levinson et al., 2011) and a seasonal variation in the mean sea level which can reach up to 0.30 m (Zavala-Hidalgo et al., 2003). Sea breezes are highly energetic and although they occur all year long, they are more frequent and stronger during springtime (Figueroa-Espinoza et al., 2014). Central American Cold Surge (CACS) events take place throughout the fall and winter months (Kurczyn et al., 2021) and Tropical Cyclones (TC) take place from June to November although TCs less often make a landfall in this coast due to its orientation facing the North.

The prevailing wave conditions are driven by local sea breezes and CACS events. During sea breeze periods low energy waves approach from the NE causing a strong westward direction (Torres-Freyermuth et al., 2017) with a net sediment transport of 20,000–80,000 m^3/year along the northern Yucatan coast (Appendini et al., 2012). CACS events produce high energy NNW swell which is dissipated by the wide (200 km) and shallow (1 to 1000 slope) continental shelf (Enriquez et al., 2010). In CACS conditions the alongshore circulation is towards the East with significant sediment transport towards the coast (Briggs et al., 2020).

Materials and methods

Data acquisition

Six UAV flights were conducted over a 14-month period (October, and December 2016 July, September, October, and December 2017) in order to acquire images and construct ortho-mosaics of the area (Table 1). Flights were performed by trained operators using a fixed wing C-Astral Bramor UAV flying at an altitude of 120 m, following the Mexican Secretariat of Communications and Transport (SCT) legal requirements valid at the time of the study. The UAV was equipped with a Micasense RedEdge multispectral camera (red, green, blue, red-edge, and near-infrared) placed underneath to obtain images at a 90° angle from the ground. The camera was programmed to ensure that the images were obtained with an 80% overlap. Before the first flight, 67 Ground Control Points (GCPs) were placed on a zig-zag pattern along the study area. The GCPs were georeferenced with RTK-DGPS using the UTM Zone 16 N coordinate system.

Data analysis

The obtained images were processed with the Pix4DMapper (version 4.3.x) software to construct ortho-mosaics. The process was performed in three basic steps: initial processing, point cloud, and mesh generation, Digital Surface Model (DSM), and ortho-mosaics construction. The GCPs were used to georeference all the images to the UTM Zone 16 N coordinate system. A spatial resolution of 8 cm with an average error (X, Y, Z) between 7 and 15 cm was obtained. The ortho-mosaics were exported into a Geographic Information System (GIS).

In the GIS, a baseline parallel to the coastline was defined for the entire 7.8-km study region. Transects perpendicular to the baseline were automatically created with a 2-meter spacing and a 100 m length. This initial length was reduced using the intersection of each transect with a second, manually-digitized baseline: the line corresponding to the first structure landward (Figure 2). Transects were numbered from East to West, totaling 3930 transects (Figure 1C). The CRIfRS was then calculated for each transect based on three indicators: beach width, vegetation coverage, and presence/proximity of man-made structures. The evaluation of the three indicators was performed for each flight. The selection of the limits of goodness for each of the indicators was based on field observations from previous studies and will be further discussed herein.

Beach width indicator

The beach provides protection against storms by adjusting its shape to dissipate the wave energy more efficiently. However, such capability depends not only on the availability of sediment but also on the constraints of the hinterland of the beach (e.g., sea wall, houses). Thus, the beach width (BW) is a common

TABLE 1 Flight time and dates with the corresponding sea level and tidal correction distance.

Flight date	Initial time	Final time	Mean sea level (m)	Tide correction distance (m)
Oct-05-2016	10:55	11:30	0.1054	-1.05
Dec-16-2016	10:30	10:57	-0.0344	+0.34
Jul-26-2017	10:15	10:44	-0.0388	+0.38
Sept-07-2017	10:30	10:59	0.1054	-1.05
Oct-09-2017	9:05	9:32	0.3644	-3.6
Dec-11-2017	10:10	10:38	0.2130	-2.13

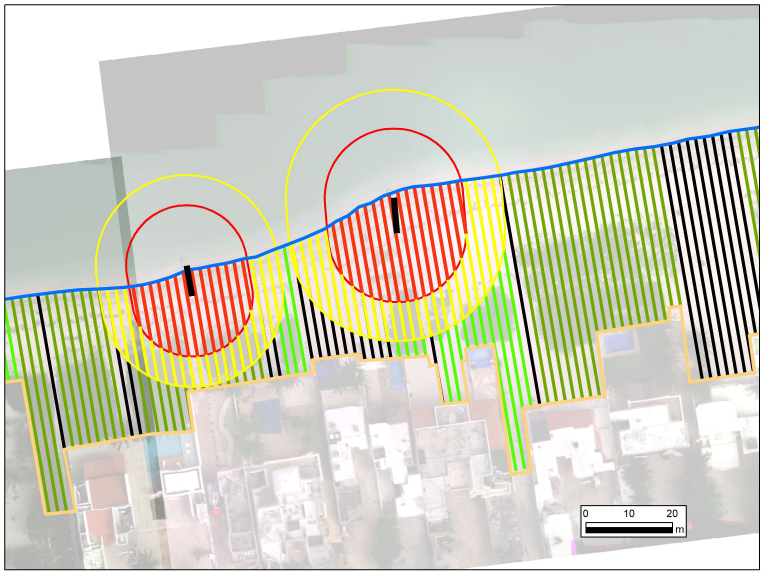

FIGURE 2
Example of the three selected indicators. The beach width indicator is the horizontal distance marked between the shoreline -blue line- and the first infrastructure landward -orange line. The vegetation coverage indicator is marked for each transect in colors: black transect denotes absence of vegetation, light green transects denote partially vegetated transects and dark green transects denotes transects with a high vegetation coverage. The coastal infrastructure indicator is marked with red transects which are within the direct zone of influence of the infrastructure, while the yellow transects are in the indirect zone of influence.

indicator used in previous studies (Mendoza et al., 2013; Cuevas-Jiménez et al., 2016) to establish a buffering zone. The BW was determined as the horizontal distance between the shoreline and the baseline corresponding to the first structure landward (Figure 2). As previously mentioned, this baseline was digitized manually along the landward part of the study area based on the first UAV flight, and its position did not change during the study period (i.e., no new houses or sea walls were built or removed).

The shoreline position was defined for each transect and each survey as the beach profile intersection with the mean water level. It was determined by the instantaneous wet-dry interface (e.g., Ruiz-Beltran et al., 2019) and, therefore, its position depended on the wave conditions and the tidal level during the image acquisition. The flights were conducted during calm wave conditions (Figure 3A; also, half hourly images in a nearby location can be obtained from http://tepeu.sisal.unam.mx), and therefore no wave corrections were required to the shoreline dataset. To adjust the differences in tidal level during each survey, the shoreline positions were corrected for the measured tidal level at the moment of the survey (Figure 3B), considering a mean beach slope of 0.1 for the study area. According to the five-year high-resolution survey accomplished by (Medellín and Torres-Freyermuth, 2021), the beach slope in the region varies between 0.05 and 0.15. To have an idea of the possible errors introduced by assuming a constant beach slope of 0.1, the tidal correction of the BW was repeated for each case considering the extreme slope values (i.e., 0.05, 0.15). Table 1 displays the tide correction applied for each survey considering a 0.1 slope.

A previous study in the region by Torres-Freyermuth et al. (2021), found that 10 m beach recession was associated to storms that are typically exceeded once a year, while the maximum shoreline recession found was close to 20 m associated with a storm sequence. Taking these results into account, a three-level BW classification was implemented considering a Highly Impacted beach will present a width of less than 10 m, an Impacted beach will have values between 10 and 20 m, and a Conserved beach will have values higher than 20 m (Table 2).

Vegetation coverage indicator

Vegetation coverage (VC) in the beach systems has been proven to increase their protective capacity, reducing erosion by attenuating wave energy (Kindermann and Gormally, 2013; Feagin et al., 2019). The seasonal change of the covered area is also important, given that high energy storms might deplete the vegetated dune which might not recover for several seasons, thus losing its protective capacity (Maximiliano-Cordova et al., 2021). On the other hand, if a mild winter season did not have major wave events, the VC might have grown, thus increasing the protection capacity. In this sense, the VC was assessed, for each of the sampled flights along the transects, by manually dividing

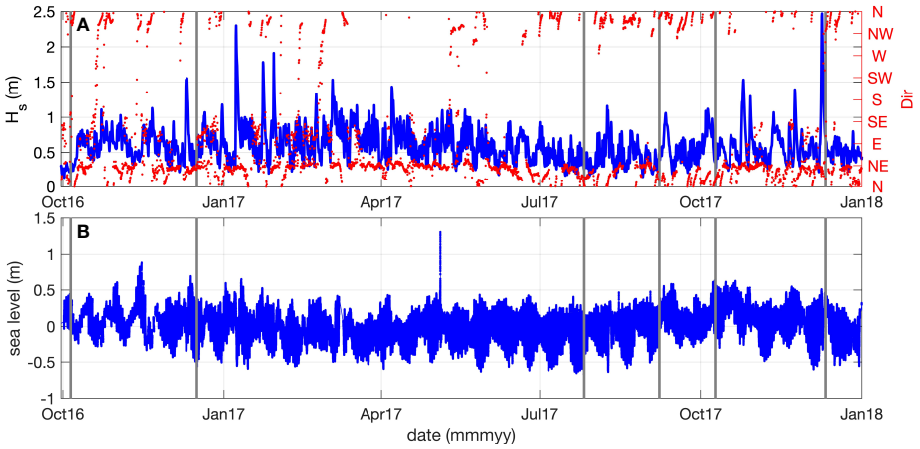

FIGURE 3
Wave and tide conditions in the study area: **(A)** significant wave height -blue line- and mean wave direction -red dots-; **(B)** sea level. Grey lines denote the dates of the UAV flights.

into three categories: absence of vegetation, partially vegetated, and fully vegetated. Initially, the limits for the categories were based on satellite resolution, to make the results compatible with Sentinel 2 images, with a pixel resolution of 10 m, the extension of the vegetation patch required to be larger than 10 m in the alongshore and cross-shore directions. However, following this criterion the VC was biased by the BW as the study site presents regions where the beach width does not reach a 10-m value (up to 21% of the transects in some cases). For this reason, the limits were finally set as: absence of vegetation (VC = Highly Impacted), was assigned when the area presented no vegetation along the selected transect. Partially vegetated (VC = Impacted), was assigned when the VC was found forming clusters smaller than 10 m alongshore and 5 m cross-shore. Fully vegetated (VC = Conserved), was assigned to clusters of vegetation with larger dimensions than the previous level (Table 2). An example of this classification can be seen in Figure 2.

Coastal structures indicator

Anthropogenic interventions play an important role in beach morphodynamics in this area. The deployment of unauthorized structures to try to mitigate erosion is a common practice and therefore there is no official record to be incorporated in formal analysis. The persistent littoral transport and significant downdrift effects associated with coastal structures (CS) in this area suggest the importance of CS for determining beach resilience. Thus, high-spatial and temporal resolution monitoring allows for tracking the number and type of CS along the study area.

The main materials used for these structures are rocks, sacks filled with sand or debris, geotextiles, a combination of wood and rocks, and concrete groins. The importance of these attributes resides in the longevity of the structures and their permeability. Sacks or geotextiles are usually deployed for a short period, they are easily torn and are usually left at the beach, ending as another source of microplastic contamination (Bai et al., 2022). Rock or concrete groins are more resistant and are deployed as a long-lasting solution.

For each survey, the location and length of coastal structures were digitized. The impact of the structure was evaluated in terms of its permeability (they were classified as permeable or impermeable) and in terms of their capability to cause a visible effect on the shoreline at the moment of the survey (actual or relict). Relict structures were considered when no visible effect on the coastline were found or when the entire structure was buried. Depending on these characteristics, a direct and indirect zone of influence were defined. In the case of impermeable structures, the direct zone was established as twice the length of the structure and the indirect zone as three times the length of

TABLE 2 Beach width, coastal structure and vegetation coverage threshold values used in the CRIfRS.

	Highly Impacted	Impacted	Conserved
Numerical value	0	1	2
Beach width	BW< 10 m	10 m< BW< 20 m	BW >20 m
Coastal structure	Within direct zone	Within indirect Zone	No influence
Vegetation coverage	Absence	Partially covered	Covered with sand dunes

the structure. In the case of permeable and relict structures, the direct zone was half the length of the structure and the indirect zone was equal to the length of the structure. The values for this indicator were assigned as Highly Impacted to transects within the direct influence zone, a value of Impacted to transects within the indirect influence zone and, a value of Conserved to transects that were located out of any influence zone (Table 2 and see example of this classification in Figure 2). The criteria to determine the influence area of CS was based on the work by Medellín et al. (2018) in the area, which employed field observations to calibrate a numerical model. The numerical model showed that, for typical sea breeze conditions, the area of influence of a 10-m impermeable groin was approximately 2.5 times its length. We decided to use the three- and two-times length criteria for the impermeable groins and decrease the values for the permeable cases as less impact would be expected.

Coastal resilience index from remote sensors

The CRIfRS helps to evaluate the loss of the beach functionality to provide coastal protection due to anthropogenic perturbations. The beach functionality for coastal protection is site specific and hence threshold values need to be determined at each coastal site. Here, we employed threshold values for the study area obtained from previous studies based on numerical models and field observations. This index is focused on the coastal protection functionality provided by the beach system. However, the index implicitly considers the conservation of habitats for key species such as the sea turtle (Eretmochelys imbricate and Chelonia mydas) that is highly correlated with the beach width.

The CRIfRS is constructed considering the relation of the three indicators that denote the relative resilience of the coast due to the seasonal variation: the BW, the presence of CS, and changes in VC. Every transect is assigned a three-level value (0, 1 or 2) for each of the three indicators (Table 2). Then, the CRIfRS is calculated using a ratio scale normalization (Equation 1),

$$CRIfRS = \sqrt[2]{\frac{BW + VC + CS}{3}} \quad (1)$$

where BW = beach width, VC = vegetation coverage, CS = coastal structures. The CRIfRS is divided into a five-classification structure according to the 20, 40, 60, and 80 quantile cumulative percentage, analogously to Thieler and Hammar-Klose (1999).

Mitigation measures often considers the deployment of coastal structures. However, it is well known that groins will cause negative downdrift effects if the net littoral transport is significant. The study site is characterized by the presence of hundreds of non-authorized coastal structures that exacerbated the beach erosion. Moreover, beach houses often remove the foredune vegetation. Beach width and vegetation coverage are key elements to provide coastal protection. Therefore, coastal management tools that provide spatio-temporal information on beach resilience are valuable for decision making regarding removal of structures and the implementation of engineering solutions.

Results

Beach width

Figure 4 shows the progression of the percentage of transects for the three categories of the beach indicator along the 14-month period of study. The highest percentage of transects were in the Conserved category (BW >20 m). The temporal evolution of the percentage of transects within this category shows an increase between October and December 2016 followed by a maintained decrease until October 2017 and a break in the decreasing trend between October 2017 and December 2017, instead of the pronounced increase found in the previous year. The temporal evolution of the percentage of transects within the Impacted (10 m< BW< 20 m) and Highly Impacted (BW< 10 m) categories were a mirror reflection of the evolution of the Conserved transects. The results suggest a differentiated seasonality of BW depending on the degree of conservation. The Conserved areas increase their beach width during winter storms and decrease during sea-breeze conditions. This is consistent with the natural shoreline dynamics in the study area where the main erosion occurs during sea-breeze conditions, associated with gradients in alongshore sediment transport (Medellín and Torres-Freyermuth, 2021).

In order to correct for the effect of the selection of a fixed beach slope of 0.1 on the calculation of beach width, the potential error associated with using the extreme slope values of 0.05 and 0.15, respectively, are also presented in Figure 4. The histogram and the lines within the bars indicate the percentage of transects falling within each category of the BW indicator in case of selecting the different beach slopes for the tide correction (i.e., initially the shoreline position change associated to each slope was calculated and then the BW indicator was classified using the thresholds given in Table 2). As expected, the largest differences are associated to i) the selection of the 0.05 slope, which represents a higher horizontal difference related to the 0.10 slope than that of the 0.15 slope; and ii) to the cases when the tide conditions were afar from the mean tide level.

Vegetation coverage

This indicator was the one that presented the least variability. Approximately half of the study site presented an absence of vegetation (Highly Impacted transects) with a

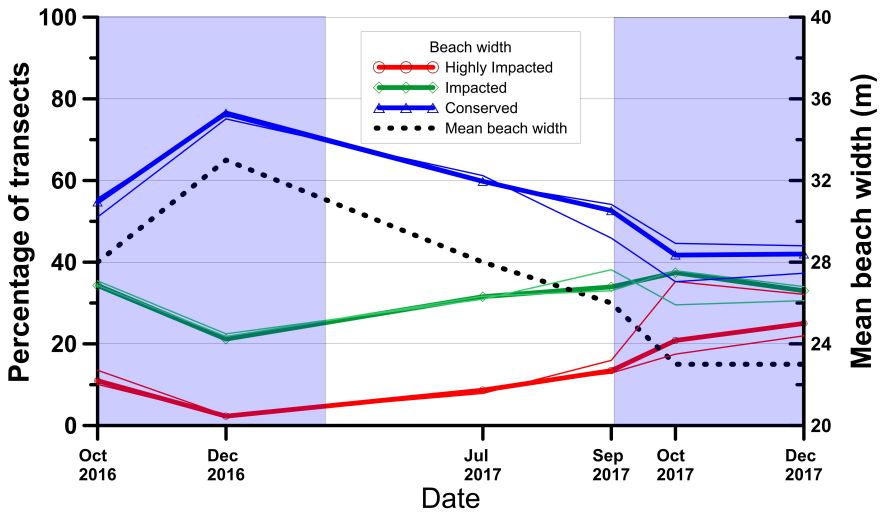

FIGURE 4
Progression of the beach width indicator presented as the percentage of transects belonging to each of the three different categories (red line - Highly Impacted class, green line - Impacted class and blue line - Conserved class) and the mean beach width for all the transects (black dotted line) along the 14 months of study. Blue shaded areas correspond to *Nortes* season and white areas correspond to sea breeze dominating conditions.

sustained increase during the study period. The Impacted category (which represents around 2.1 km) presented a decrease from 31% to 25% of the transects. Figure 5 suggests that such variability can be explained by the transformation from Impacted to Highly Impacted. On the other hand, the Conserved category remained around 20% of the transects with a small amount of seasonal variability (Figure 5).

Coastal structures

Figure 6 presents the temporal evolution of the CS impact, expressed as the percentage of transects influenced by CS for the three different categories along the 14 months of study. Overall, the highest percentage of the coast was within the Highly Impacted class, which started with 47% of the

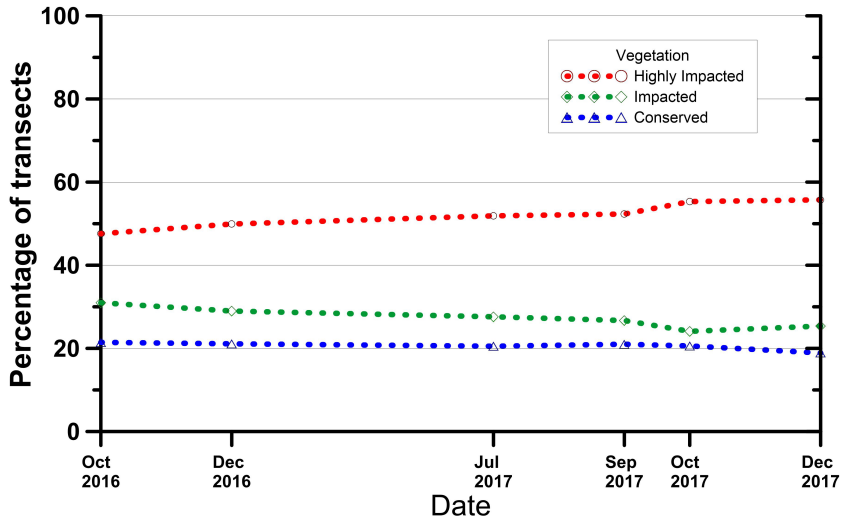

FIGURE 5
Progression of the vegetation coverage expressed in percentage of transects for the three different categories along the 14 months of study. In dotted red line the Highly Impacted class, in dotted green line the Impacted class and in dotted blue line the Conserved class.

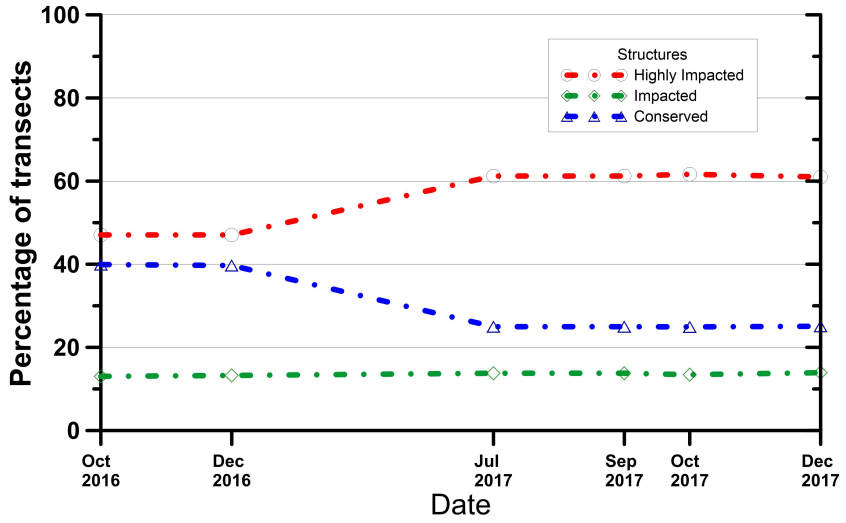

FIGURE 6
Temporal evolution of the Coastal Structure Indicator expressed as the percentage of transects within each of the three different categories along the 14 months of study.

transects and increased by July 2017 to 61% and remained near this level for the rest of the study. This abrupt change was a consequence of the deployment of new CS which changed in number from 170 to 281 (Figure 8). The Impacted class remained between 13 and 14%. The Conserved class was a clear result of the construction of new structures, presenting a value of 40% for the first two months, decreasing to 25% by July 2017, and remaining at this value for the rest of the study. This is consistent with the variation of the Highly Impacted class.

Coastal resilience index from remote sensors

Considering the previous three-level classification of the indicators and the results from the six evaluated surveys, we obtained the histograms of the frequency of occurrence and the cumulative percentage to obtain the final classification. Following the 20, 40, 60, and 80 quantile cumulative percentages, values lower than 0.6 were considered Very Low (VL) resilience; those between 0.6 - 0.9 were considered Low (L)

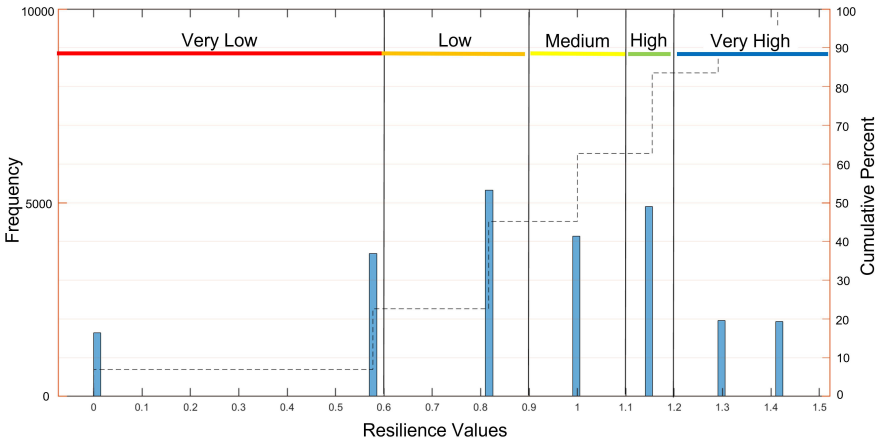

FIGURE 7
Frequency of occurrence expressed in histograms and cumulative percent of the CVIfRS values for the Yucatan coast. Color lines show the range between categories, Very Low (red), Low (orange), Medium (yellow). High (green) and Very High (blue).

resilience; values between 0.9 - 1.1 were considered Medium (M) resilience; those between 1.1 - 1.2 were considered High (H) resilience; and values > 1.2 were considered Very High (VH) resilience (Figure 7).

The evolution of the CRIfRS during the first three months of the study (October-December 2016) shows that the percentage of transects within the VL and L classification decreased (from 1.2 km to 0.7 km of beach corresponding to transects with VL values, and from 1.7 km to 1.2 km of beach corresponding to transects with L values) whilst the M, VH, and H classifications increased (from 1.2 km to 1.5 km, 1.6 km to 1.9 km, and 1.4 km to 1.6 km, respectively). These variations were due to the increase of the BW (Figure 4) while no significant changes occurred in the VC and the CS. Subsequently during the following ten months corresponding to the next three surveys (July, September, and October) the VL, and L values increased up to 2.2 km and 1.6 km, respectively, whereas the M, H, and VH values consistently decreased down to 1 km, 1.1 km, and 0.9 km correspondingly. This was caused by the increase of the total number of structures (a 165% increase) and the general decrease of BW (Figure 4). On December 2017, half of the surveyed beach had VL and L resilience, 1.1 km of the beach presented M resilience, 1.4 km of the transects were labeled as H, whilst the lowest number of transects (1 km) corresponded to the VH resilience value (Figure 8).

Application to Punta San Miguel case

The previously presented results show the evolution of the CRIfRS at a medium spatial scale (regional scale). The high-resolution of the results permits to analyze in detail any specific stretch of coast. As an example, the local case of Punta San Miguel (located 10.5 km east of Progreso port in Figure 1) is presented (local scale). The 0.9-km stretch of coast (Figure 9) was subjected during the study period to the deployment of a series of geotextile detached breakwaters designed to stabilize a coast section. We analyze, from an initial non-perturbed condition, the sequence of variations of the CRIfRS estimates following the perturbation due to the geotextile structure (Figure 9).

In October 2016, the VL, L, M, and H categories presented percentage values between 24 and 26 whilst VH had 9% of the transects. In December 2016, the VL and L values decreased, the M and H values increased while the VH percentage remained constant. This change was mainly due to the increase of the BW (Figure 9A). In July 2017 a geo-textile structure had been fully deployed consisting of six 20-m sections separated to form two detached breakwaters. The structure caused a BW increase concentrated only in the eastern section of the structure, while a downdrift erosion occurred in the western area (Torres-Freyermuth et al., 2019). Moreover, unauthorized CS were deployed by the home-owners to mitigate the downdrift erosion effect. These changes caused a significant increase in the VL percentage and a slight increase in the L values, while the rest of the classes decreased. The percentage values remained constant until October 2017 except for the M values which decreased, while the VL increased to more than half of the San Miguel area (57%). The downdrift beach loss initiated the removal of a western 20 m section of the geo-textile structure in November 2017, which was reflected on the December 2017 survey with an evident VL decrease and VH and M increase.

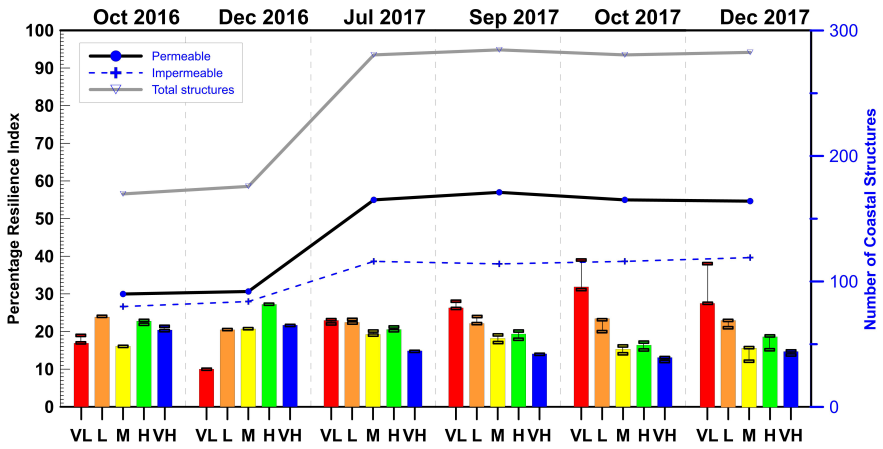

FIGURE 8
Histogram representing the percentage of transects within each category of the Coastal Resilience Index (VL: Very Low in red, L: Low in orange, M: Medium in yellow, H: High in green and VH: Very High in blue). Bar lines represent the variability range related to the selection of beach slope using the 0.05 and 0.15 values. Lines (right axis) represent the evolution of the number of coastal structures at each surveyed date within the study area. The gray line represents the total number of coastal structures, the black line represents the number of permeable structures, and the blue dotted line represents the number of impermeable structures.

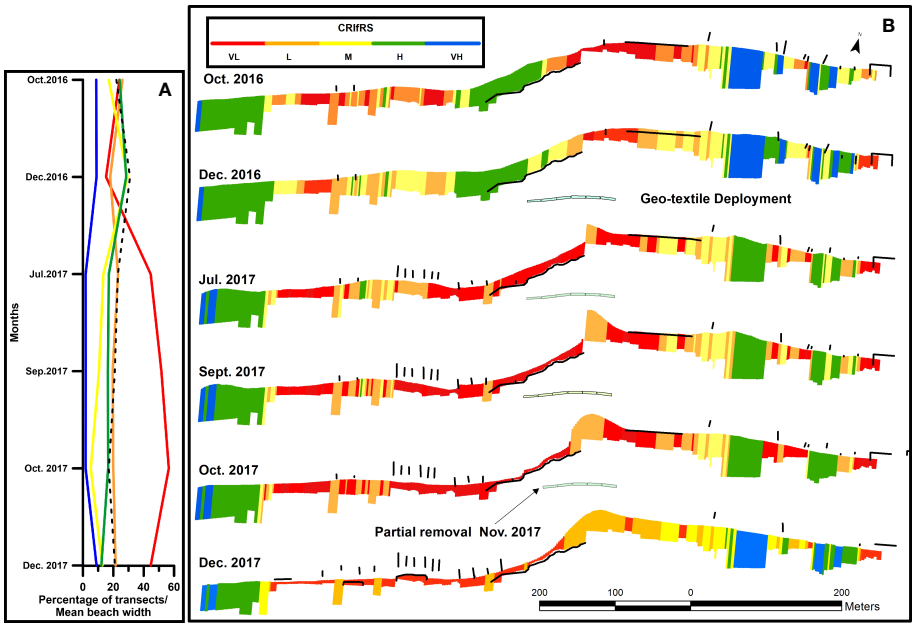

FIGURE 9
(A) CRIfRS assessment for Punta San Miguel, expressed as the percentage of transects for the five different categories (Very Low in red, Low in orange, Medium in yellow, High in green and Very High in blue) and mean beach width value (dashed black line) along the study period **(B)**. Spatial distribution of the CRIfRS along the study period with the deployment of structures (black lines) and the geo-textile structure -July 2017- and partial removal of the western section -November 2017- (right panel).

Comparison of December 2016 and December 2017 shows that Very Low and Low resilience values increased from 33% to almost 70% illustrating the complexity of implementing erosion mitigation measures in this region.

Discussion

The presented results show the evolution of the CRIfRS during a 14-month period instead of a fixed-image of the CRIfRS. This allows improved understanding of the importance of the different factors affecting beach resilience over time. The knowledge of the temporal evolution, or trajectory, of the key indicators is a fundamental component to assess beach resilience.

Limitations of the CRIfRS

From the three indicators used, the BW presented the highest variability. The increase of the percentage of transects classified as Conserved from October 2016 to December 2016, as well as the break of the previously decreasing trend from October 2017 to December 2017, may be due to the increased importance of cross-shore sediment transport and to seasonal changes of mean sea level that contribute to onshore sediment transport during those months (Medellín and Torres-Freyermuth, 2021). The difference found in the percentages of conserved BW transects from October 2017 to December 2017 with respect to the same months of 2016, might be related to a storm event that took place on December 9th, just before the December 2017 survey (Figure 3A). The short time lapse between the event and the beach survey probably did not allow for the expected natural recovery of the system in the days following the event. On the other hand, during prevailing sea-breeze conditions which occur all year long but are more persistent during springtime, the alongshore transport becomes more important and hence the downdrift effect of coastal structures becomes larger, accreting the beach updrift of the structure but eroding it downdrift.

Regarding the VC indicator, the slight changes observed during the study period are related to the urbanized character of the study area. Figure 10 shows three examples of the configuration of this stretch of coast to confirm its anthropic character: the largest beach sections that are not backed by man-made structures correspond to sections of< 50 m of alongshore extension. In the study area, the largest changes in vegetation were related to repopulation/removal of beach vegetation by human actions rather than natural cycles as the growth of vegetation patches during the study period did not reach the required 5x10 m extension. This is related to the specific studied case, a region with a large anthropogenic

FIGURE 10
Examples of the heavily urbanized character, and low vegetation coverage, of the study area.

influence. However, vegetation can play a key role in other settings where natural cycles in vegetation growth are more evident; in those regions this indicator might be responsible for an added seasonal signal that would have a higher weight in the CRIfRS. In the case of the Yucatan Peninsula, the vegetation follows a natural seasonal cycle related to the hydrodynamics that is not clearly represented in our data set. It has been documented that the effect of storms in the foredune vegetation might be evident even a year after the occurrence of the storm (Gallego-Fernández et al., 2020). Therefore, the VC indicator should be considered as a primary element for coastal management due to the slow recovery rate of the vegetation and its important role on sediment stabilization (Hesp et al., 2011).

In the case of the CS indicator, this work considers that coastal structures have a negative effect on beach resilience, which might not be the case in other study regions. Our decision was based on the fragility and the short-lived character of the structures. The sections of beach protected by these types of rock and timber dykes, sacks full of sand or debris, or geotextiles filled with sand are prone to their destruction (which is a common practice among downdrift neighbors) or their removal during governmental campaigns to manage illegal structures. In the coastal region of Yucatan, local stakeholders consider the infrastructure development as one of the main threats to the ecosystem services provided by the beach (Mendoza-González et al., 2021).

The combination of these three indicators lead to the CRIfRS. The possible errors associated with the CRIfRS are twofold: firstly, the CRIfRS value classification (from VH to VL values) will depend on the definition of individual thresholds for each of the three indicators. In this sense, a previous knowledge of the studied region is imperative for the definition of the thresholds, because the selection of these thresholds imply "a transcendental management decision" as stated by Cuevas-Jiménez et al. (2016). Secondly, within the evaluation of each indicator there will be associated errors that may add up in the final results. In the studied case, the main source of error to the authors knowledge was related to the different tide level during each survey. To account for these, the shoreline was corrected to a mean tide level using a 0.1 beach slope. According to a previous study (Medellín and Torres-Freyermuth, 2021), values of beach slope within the region range from 0.05 to 0.15. Therefore, an estimation of the inaccuracy due to beach slope was attained by recalculating the BW and the associated CRIfRS for these extreme slopes; results are presented in Figures 4, 8. In both cases, the BW and the CRIfRS, the differences associated to the selection of the beach slope have an effect proportional to the absolute value of the tide during the survey and, therefore, they reached the highest values during the last surveys (October 2017 and December 2017). The asymmetry found in these results is related to the different slope using a maximum change of eleven percentage points while the majority remained beneath three percentage points.

Impact of the removal of coastal structures

The case of Punta San Miguel presented in Section 4.5, allows for an initial evaluation of the performance of interventions on a local scale and highlights how inadequate is the use of CS in the study area. The evolution of the morphology of Punta San Miguel following the deployment of the geotextiles have been well document by Torres-Freyermuth et al. (2019) using high-resolution RTK-DGPS surveys and UAV images. However, a major drawback in the aforementioned study is the lack of information regarding the construction of additional coastal structures (besides the geotextile breakwater) during the studied period. The local study presented in this paper provides further information on the degradation of the beach system, showing the appearance of a series of new structures after the deployment of the geotextile. The new structures corresponded to both, relict structures that emerged after the deployment of the geotextiles due to the shoreline retreat and new structures that were deployed at the beach to overcome erosion. Furthermore, contrary to the previous study, the local study allows the delimitation of the down-drift region highly affected by the intervention which extended more than 400 m.

This breakwater caused a succession of cumulative negative effects in terms of erosion (1 km downdrift) that not only caused damages to homes but triggered the deployment of additional coastal structures (Figure 9B). Although this study finished in December 2017, relative beach change can be estimated for the following years through satellite images from Sentinel-2 (Figure 11). The spatial and temporal variability of the relative beach change confirm the high impact of the structure and how the geotextile destruction (removal) allows the sediment accumulation to propagate as a wave pulse travelling along the coast at a velocity of 230 m/year. The beach condition in the intervention area (>5500 m in Figure 11) becomes more critical after the project removal than before the structure's deployment.

This study presents evidence that sand beach ecosystems have significant and meaningful value. When they are degraded or depleted, the cost of nourishing the beach or deploying protection structures aimed to protect the properties behind the beach might be greater than the cost of regenerating the dune ecosystem which is far more beneficial.

Conclusions

A coastal resilience index derived from data obtained exclusively from a UAV was defined and applied to a 7.8 km stretch of the Northern Yucatan coast. The evolution of the index was measured through the analysis of six georeferenced data sets spanning a 14-month period. The high-resolution procedure, implemented in this study with the selected 2-m spacing between transects, allows us to investigate the evolution of the CRIfRS at a regional and local scales.

At the regional scale, the percentage of the coast within the Very Low and Low resilience classification increased during

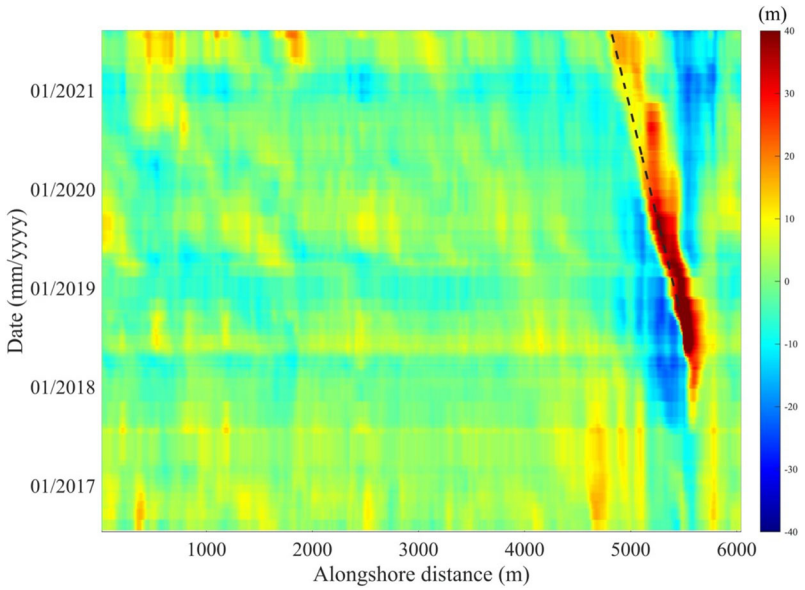

FIGURE 11
Spatial (alongshore) and temporal evolution of the relative beach width change, estimated from Sentinel-2, in the vicinity of the geotextile breakwater deployed in San Miguel. The dashed lined shows the sediment dispersion pattern after the breakwater destruction.

the period of study, while those classified as Medium, High, and Very High resilience decreased. The CRIfRS presented an important seasonal variability. During the CACS event season, the resilience at the conserved beach transects increased mainly due to the on-shore sediment transport. During the sea breeze season, the mean wave climate is important for the coastal resilience evolution given that the longshore transport becomes a determining factor. Thus, the CS play a crucial role given the interruption they cause in the sediment transport.

At a local scale, the example of the evolution of the CRIfRS for the stretch of coast surrounding Punta San Miguel was presented. This stretch of coast was subject to a man-made intervention during the study period. This example shows the complexity of implementing mitigation measures in this region where both natural and human disturbances play an important role on beach resilience. In this case, a mitigation measure that was intended to increase coastal resilience, caused major negative impacts on the beach conditions in the short-term. Thus, this approach demonstrates to be suitable to assess the performance of coastal protection projects.

Anthropogenic perturbations play an important role in coastal dynamics in this area and hence a tool is required for assessing their evolution through time. In the study area, beach houses are often built at the foredune location and hence dunes and the associated vegetation are removed. Beach erosion mitigation strategies traditionally employed groins and (more recently) breakwaters that are not suitable for this area due to the net littoral transport. Therefore, the CRIfRS can help to improve decision making in the coastal zone by pointing out the evolution of erosion hot spots, the degradation of the coastal dunes, and the construction of coastal structures that alter the sediment transport. This is contrary to traditional approaches that only focus on increasing the beach width without considering the degree of human degradation and how it evolves in time. A possible solution for this particular region must consider the removal of coastal structures that interrupt the alongshore sediment transport, must ensure that no further illegal structures are built, and must conserve the dune vegetation. However, taking into account the strong influence of alongshore sediment transport in the region, a more sustainable approach will be based on systematic beach nourishment and the regular bypass of sediments accumulated in shelter harbors and the re-design of the shelter harbors to decrease the sediment impoundment (Franklin et al., 2021). The repopulation of vegetated areas in front of beach houses will improve the protective effect of the beach. In this manner, the improvement of the three indicators evaluated by the CRIfRS are ensured. CRIfRS might help to evaluate the evolution of this solution.

The presented methodology to evaluate the CRIfRS is applicable to other locations taking into account that its correct evaluation requires a certain knowledge of the study area that will be addressed mainly to select the threshold values for each of the indicators. In this analysis, digital photogrammetry was used to evaluate the evolution of beach resilience. This methodology can be implemented in future works through the use of UAVs or also using satellite imagery (e.g., Sentinel 2, Pléiades, Planetscope) which will allow monitoring shoreline change and structure deployment with a high temporal resolution. However, satellite images are a useful tool, still in this particular study the smaller structures (<10 m) cannot be resolved although we can see its effect. Therefore, it is important to use the combination of different platforms such as UAVs and satellites. Additionally, multispectral sensors might be able to facilitate the automatization of the vegetation density and change assessment.

Data availability statement

The raw data supporting the conclusions of this article will be made available by the authors, without undue reservation.

Author contributions

EM, AT-F, EO, and GM conceived the study; RR-N, EM, AT-F, EO, and GM obtained/processed the field data collection and participated in writing the first draft. EM, AT-F, EO, GM, RR-N, PS, and IT assisted in the discussion, analysis of the results, writing, and reviewing. All authors contributed to the article and approved the submitted version.

Funding

This work was supported by SEDUMA- UNAM #6605. CONACYT through projects Catedras-1146, INFR-2014-01-225561, the Laboratorio Nacional de Resiliencia Costera [299063], CB-284819 and TAMU-CONACYT 19-20-013. PAPIIT DGAPA UNAM (Project IA101422).

Acknowledgments

The authors would like to thank Gonzalo Martín for IT support. José López González, Juan Alberto Gómez, Johnny Valdez Iuit, and Carlos Cruz Vázquez for additional support in field work. María Fernanda Medina Navarrete helped with the ortho-mosaic construction.

Conflict of interest

The authors declare that the research was conducted in the absence of any commercial or financial relationships that could be construed as a potential conflict of interest.

Publisher's note

References

Angnuureng, D. B., Almar, R., Senechal, N., Castelle, B., Addo, K. A., Marieu, V., et al. (2017). Shoreline resilience to individual storms and storm clusters on a meso-macrotidal barred beach. *Geomorphology* 290, 265–276. doi: 10.1016/j.geomorph.2017.04.007

Appendini, C., Salles, P., Mendoza, E., Lopez, J., and Torres-Freyermuth, A. (2012). Longshore sediment transport on the northern coast of the Yucatan peninsula. *J. Coast. Res.* 28 (6), 1404–1417. doi: 10.2112/JCOASTRES-D-11-00162.1

Aubrey, D. G. (1979). Seasonal patterns of onshore/offshore sediment movement. *J. Geophysical Research: Oceans* 84 (C10), 6347–6354. doi: 10.1029/JC084iC10p06347

Bai, X., Li, F., Ma, L., and Li, C. (2022). Weathering of geotextiles under ultraviolet exposure: A neglected source of microfibers from coastal reclamation. *Sci. Total Environ.* 804, 150168. doi: 10.1016/j.scitotenv.2021.150168

Briggs, T. R., Figlus, J., Torres-Freyermuth, A., Puleo, J. A., Warren, W., and Alrushaid, T. (2020). Variability in onshore sediment transport on a natural beach during a central American cold surge event. *J. Coast. Res.* 36 (3), 487–497. doi: 10.2112/JCOASTRES-D-19-00146.1

Clark, A. (2017). Small unmanned aerial systems comparative analysis for the application to coastal erosion monitoring. *GeoResJ* 13, 175–185. doi: 10.1016/j.grj.2017.05.001

Cuevas-Jiménez, A., Euán Ávila, J. I., Villatoro Lacouture, M. M., and Silva Casarín, R. (2016). Classification of beach erosion vulnerability on the Yucatan coast. *Coast. Manage.* 44 (4), 333–349. doi: 10.1080/08920753.2016.1155038

Devoy, R. J. N. (2021). "Sea-Level rise: causes, impacts and scenarios for change," in *Reference module in earth systems and environmental sciences* (Oxford: Academic Press, UK Elsevier).

Dong, Z., Elko, N., Robertson, Q., and Rosati, J. (2018). Quantifying beach and dune resilience using the coastal resilience index. *Coast. Eng. Proc.* 1 (36), 1-8. doi: 10.9753/icce.v36.papers.30

Emanuel, K. (2005). Increasing destructiveness of tropical cyclones over the past 30 years. *Nature* 436 (7051), 686–688. doi: 10.1038/nature03906

Enriquez, C., Mariño-Tapia, I. J., and Herrera-Silveira, J. A. (2010). Dispersion in the Yucatan coastal zone: Implications for red tide events. *Continental Shelf Res.* 30 (2), 127–137. doi: 10.1016/j.csr.2009.10.005

Feagin, R. A., Furman, M., Salgado, K., Martinez, M. L., Innocenti, R. A., Eubanks, K., et al. (2019). The role of beach and sand dune vegetation in mediating wave run up erosion. *Estuarine Coast. Shelf Sci.* 219, 97–106. doi: 10.1016/j.ecss.2019.01.018

Figueroa-Espinoza, B., Salles, P., and Zavala-Hidalgo, J. (2014). On the wind power potential in the northwest of the Yucatan peninsula in Mexico. *Atmósfera* 27 (1), 77–89. doi: 10.1016/S0187-6236(14)71102-6

Franklin, G. L., Medellin, G., Appendini, C. M., Gómez, J. A., Torres-Freyermuth, A., López González, J., et al. (2021). Impact of port development on the northern Yucatan peninsula coastline. *Regional Stud. Mar. Sci.* 45, 101835. doi: 10.1016/j.rsma.2021.101835

Gallego-Fernández, J. B., Morales-Sánchez, J. A., Martínez, M. L., García-Franco, J. G., and Zunzunegui, M. (2020). Recovery of beach-foredune vegetation after disturbance by storms. *J. Coast. Res.* 95 (sp1), 34–38. doi: 10.2112/SI95-007.1

Gonçalves, J. A., and Henriques, R. (2015). UAV photogrammetry for topographic monitoring of coastal areas. *ISPRS J. Photogrammetry Remote Sens.* 104, 101–111. doi: 10.1016/j.isprsjprs.2015.02.009

Hesp, P., Martínez, M., da Silva, G., Rodríguez, N., Gutiérrez, E., Humanes, A., et al. (2011). Transgressive dunefield landforms and vegetation associations, doña juana, veracruz, Mexico. *Earth Surf. Process. Landf.* 36, 285–295. doi: 10.1002/esp.2035

Irish, J. L., Frey, A. E., Rosati, J. D., Olivera, F., Dunkin, L. M., Kaihatu, J. M., et al. (2010). Potential implications of global warming and barrier island degradation on future hurricane inundation, property damages, and population impacted. *Ocean Coast. Manage.* 53 (10), 645–657. doi: 10.1016/j.ocecoaman.2010.08.001

Jiménez, J. A., Gracia, V., Valdemoro, H. I., Mendoza, E. T., and Sánchez-Arcilla, A. (2011). Managing erosion-induced problems in NW Mediterranean urban beaches. *Ocean Coast. Manage.* 54 (12), 907–918. doi: 10.1016/j.ocecoaman.2011.05.003

Kindermann, G., and Gormally, M. J. (2013). Stakeholder perceptions of recreational and management impacts on protected coastal dune systems: A comparison of three European countries. *Land Use Policy* 31, 472–485. doi: 10.1016/j.landusepol.2012.08.011

Kombiadou, K., Matias, A., Ferreira, Ó., Carrasco, A. R., Costas, S., and Plomaritis, T. (2019). Impacts of human interventions on the evolution of the ria Formosa barrier island system (S. Portugal). *Geomorphology* 343, 129–144. doi: 10.1016/j.geomorph.2019.07.006

Kurczyn, J. A., Appendini, C. M., Beier, E., Sosa-López, A., López-González, J., and Posada-Vanegas, G. (2021). Oceanic and atmospheric impact of central American cold surges (Nortes) in the gulf of Mexico. *Int. J. Climatology* 41 (S1), E1450–E1468. doi: 10.1002/joc.6779

Masselink, G., and Lazarus, E. D. (2019). Defining coastal resilience. *Water* 11 (12), 2587. doi: 10.3390/w11122587

Maximiliano-Cordova, C., Martínez, M. L., Silva, R., Hesp, P. A., Guevara, R., and Landgrave, R. (2021). Assessing the impact of a winter storm on the beach and dune systems and erosion mitigation by plants. *Front. Mar. Sci.* 8. doi: 10.3389/fmars.2021.734036

Medellín, G., Mariño-Tapia, I., and Euán-Ávila, J. (2015). The influence of a seawall on postnourishment evolution in a sea-breeze-dominated microtidal beach. *J. Coast. Res.* 31 (6), 1449–1458. doi: 10.2112/JCOASTRES-D-13-00194.1

Medellín, G., and Torres-Freyermuth, A. (2021). Foredune formation and evolution on a prograding sea-breeze dominated beach. *Continental Shelf Res.* 226, 104495. doi: 10.1016/j.csr.2021.104495

Medellín, G., Torres-Freyermuth, A., Tomasicchio, G. R., Francone, A., Tereszkiewicz, P. A., Lusito, L., et al. (2018). Field and numerical study of resistance and resilience on a sea breeze dominated beach in Yucatan (Mexico). *Water* 10 (12), 1806. doi: 10.3390/w10121806

Mendoza-González, G., Paredes-Chi, A., Méndez-Funes, D., Giraldo, M., Torres-Irineo, E., Arancibia, E., et al. (2021). Perceptions and social values regarding the ecosystem services of beaches and coastal dunes in Yucatan, Mexico. *Sustainability* 13 (7), 359. doi: 10.3390/su13073592

Mendoza, E. T., Ojeda, E., Meyer-Arendt, K. J., Salles, P., and Appendini, C. M. (2016). "Assessing coastal vulnerability in Yucatan Mexico," in *Coastal management*, (London: ICE publishing) 607–616.

Mendoza, E. T., Trejo-Rangel, M. A., Salles, P., Appendini, C. M., Gonzalez, J. L., and Torres-Freyermuth, A. (2013). Storm characterization and coastal hazards in the Yucatan peninsula. *J. Coast. Res. (SPEC. ISSUE* 65), 790–795. doi: 10.2112/SI65-134.1

Meyer-Arendt, K. J. (2001). Recreational development and shoreline modification along the north coast of Yucatan, Mexico. *Tourism Geographies* 3 (1), 87–104. doi: 10.1080/14616680010008720

Ojeda, E., Appendini, C. M., and Mendoza, E. T. (2017). Storm-wave trends in Mexican waters of the gulf of Mexico and Caribbean Sea. *Nat. Hazards Earth Syst. Sci.* 17 (8), 1305–1317. doi: 10.5194/nhess-17-1305-2017

Pieígay, H., Chabot, A., and Le Lay, Y.-F. (2020). Some comments about resilience: from ciclicity to trajectory, a shift in living and nonliving system theory. *Geomorphology* 367, 106527. doi: 10.1016/j.geomorph.2018.09.018

Ruiz-Beltran, A. P., Astorga-Moar, A., Salles, P., and Appendini, C. M. (2019). Short-term shoreline trend detection patterns using SPOT-5 image fusion in the northwest of Yucatan, Mexico. *Estuaries Coasts* 42 (7), 1761–1773. doi: 10.1007/s12237-019-00573-7

Tereszkiewicz, P., McKinney, N., and Meyer-Arendt, K. J. (2018). Groins along the northern Yucatan coast. *J. Coast. Res.* 34 (4), 911–919. doi: 10.2112/JCOASTRES-D-17-00062.1

Thieler, E. R., and Hammar-Klose, E. S. (1999). "National assessment of coastal vulnerability to sea-level rise: Preliminary results for the U.S. Atlantic coast," in *Open-file report*. (United Sates of America: USGS) doi: 10.3133/ofr99593

Torres-Freyermuth, A., Medellín, G., Mendoza, E. T., Ojeda, E., and Salles, P. (2019). Morphodynamic response to low-crested detached breakwaters on a sea breeze-dominated coast. *Water* 11 (4), 635. doi: 10.3390/w11040635

Torres-Freyermuth, A., Medellín, G., and Salles, P. (2021). Human impact on the spatiotemporal evolution of beach resilience on the northwestern Yucatan coast. *Front. Mar. Sci.* 8 (111). doi: 10.3389/fmars.2021.637205

Torres-Freyermuth, A., Puleo, J. A., DiCosmo, N., Allende-Arandía, M. E., Chardón-Maldonado, P., López, J., et al. (2017). Nearshore circulation on a sea breeze dominated beach during intense wind events. *Continental Shelf Res.* 151, 40–52. doi: 10.1016/j.csr.2017.10.008

Turner, I. L., Harley, M. D., and Drummond, C. D. (2016). UAVs for coastal surveying. *Coast. Eng.* 114, 19–24. doi: 10.1016/j.coastaleng.2016.03.011

Valle-Levinson, A., Mariño-Tapia, I., Enriquez, C., and Waterhouse, A. F. (2011). Tidal variability of salinity and velocity fields related to intense point-source submarine groundwater discharges into the coastal ocean. *Limnology Oceanography* 56 (4), 1213–1224. doi: 10.4319/lo.2011.56.4.1213

Velasquez-Montoya, L., Sciaudone, E. J., Harrison, R. B., and Overton, M. (2021). Land cover changes on a barrier island: Yearly changes, storm effects, and recovery periods. *Appl. Geogr.* 135, 102557. doi: 10.1016/j.apgeog.2021.102557

Warrick, R. A., Oerlemans, J., Beaumont, P., Braithwaite, R. J., Drewry, D. J., Gornitz, V., et al. (1990). "Sea Level rise," in *Climate change* (Cambridge, UK: Cambridge University Press), 257–282.

Zavala-Hidalgo, J., Morey, S. L., and O'Brien, J. J. (2003). Seasonal circulation on the western shelf of the gulf of Mexico using a high-resolution numerical model. *J. Geophysical Research: Oceans* 108 (C12), 1–19. doi: 10.1029/2003JC001879

Zodrow, I., Hendel-Blackford, S., Mall, P., and Swanson, D. (2020). *Reducing risk & building resilience of SMES to disasters*. Ed. J. Bridger (United Nations: SENDAI Framework for Disaster Risk Reduction UNDRR).

Advantages of publishing in Frontiers

OPEN ACCESS
Articles are free to read for greatest visibility and readership

FAST PUBLICATION
Around 90 days from submission to decision

HIGH QUALITY PEER-REVIEW
Rigorous, collaborative, and constructive peer-review

TRANSPARENT PEER-REVIEW
Editors and reviewers acknowledged by name on published articles

Frontiers
Avenue du Tribunal-Fédéral 34
1005 Lausanne | Switzerland

Visit us: www.frontiersin.org
Contact us: frontiersin.org/about/contact

REPRODUCIBILITY OF RESEARCH
Support open data and methods to enhance research reproducibility

DIGITAL PUBLISHING
Articles designed for optimal readership across devices

FOLLOW US
@frontiersin

IMPACT METRICS
Advanced article metrics track visibility across digital media

EXTENSIVE PROMOTION
Marketing and promotion of impactful research

LOOP RESEARCH NETWORK
Our network increases your article's readership